
Electronic Thesis and Dissertation Repository

12-5-2018 2:30 PM

Understanding New Trends on Gold Mineralization at the Yellowknife City Gold Project, Northwest Territories, using Synchrotron X-ray Spectroscopy

Ramjay Jude L. Botor
The University of Western Ontario

Supervisor
Banerjee, Neil R.
The University of Western Ontario Co-Supervisor
Van Loon, Lisa L.
The University of Western Ontario

Graduate Program in Geology
A thesis submitted in partial fulfillment of the requirements for the degree in Master of Science
© Ramjay Jude L. Botor 2018

Follow this and additional works at: <https://ir.lib.uwo.ca/etd>

 Part of the [Geochemistry Commons](#), [Geology Commons](#), and the [Other Earth Sciences Commons](#)

Recommended Citation

Botor, Ramjay Jude L., "Understanding New Trends on Gold Mineralization at the Yellowknife City Gold Project, Northwest Territories, using Synchrotron X-ray Spectroscopy" (2018). *Electronic Thesis and Dissertation Repository*. 5915.
<https://ir.lib.uwo.ca/etd/5915>

This Dissertation/Thesis is brought to you for free and open access by Scholarship@Western. It has been accepted for inclusion in Electronic Thesis and Dissertation Repository by an authorized administrator of Scholarship@Western. For more information, please contact wlsadmin@uwo.ca.

Abstract

The Yellowknife City Gold Project (YCGP) currently encompasses 780 sq. km of contiguous land north, south and east of the city of Yellowknife. The project lies in the prolific Archean north-south trending Yellowknife Greenstone Belt, a suite of mafic and felsic volcanics and greywacke turbidites overlying a gneissic basement. Exploration and drilling efforts have been focused along 70 km of strike length on the southern and northern extensions of the mineralized shear zones and quartz veins associated with the past-producing high-grade Con (6.1 Moz @ 16.1 g/t Au) and Giant (8.1 Moz @ 16.0 g/t Au) gold mines.

Synchrotron analysis applied to mineral exploration can address industry-relevant questions and provide rapid solutions that add significant value using innovative, high-resolution analytical techniques without specialized sample preparation. Synchrotron radiation X-ray diffraction (SR-XRD) is a rapid technique for mineralogical analysis, providing critical mineralogical information on altered and mineralized samples. Synchrotron X-ray fluorescence (SR-XRF) spectroscopy is a nondestructive technique that provides *in-situ* trace element analysis for ore mineral mapping and zonation, as well as textural and spatial associations. X-ray absorption near edge structure (XANES) spectroscopy can determine the speciation of gold and other associated trace elements, useful for understanding geometallurgy and characterization of deleterious elements. We have created SR-XRD methods on rock pulps and powders contained in capillary tubes holding >100 mg of sample, capable of producing mineralogical data in a short time period. We have also developed new SR-XRF techniques that can be performed directly on half-core samples and produce trace element maps >10 cm long by up to 5 cm wide. The technique is non-destructive and provides critical trace-element associations in gold bearing sulphide minerals that provide integral information regarding the nature of mineralizing fluids. XANES spectroscopy on elements of interest, such as Au, can be done *in-situ* after SR-XRF analysis and interpretation, in turn providing critical information on the oxidation state of gold while determining its spatial association with other elements via SR-XRF.

Synchrotron X-ray diffraction of 71 powdered samples, and X-ray fluorescence maps of 73 slabs and half cores reveal similarities in mineralization styles between the Northbelt

Property and the Con-Giant Mines, hinting that both locations are derived from a single mineralizing system. Our results suggest the timing of mineralization is similar throughout the Yellowknife City Gold Project, with pyrite-arsenopyrite and sphalerite-galena forming first, followed by sericite-chlorite, and quartz-carbonate veining. Three main gold associations are present across the YCGP – gold+sulphide, gold+quartz-carbonate, and gold+sericite-chlorite with the two latter probably due to later remobilization during syn-mineralization metamorphic processes. XANES analyses of select samples with viable Au signals revealed the presence of only metallic Au within sulphides and quartz veins. No refractory gold associated with elevated arsenic levels has been observed, suggesting gold may be easier to recover than previously thought.

Keywords

Yellowknife City Gold Project, Yellowknife Greenstone Belt, synchrotron spectroscopy, X-ray fluorescence, X-ray diffraction, X-ray absorption near edge structure, gold residence, high-As sulphides, base metal sulphides, quartz-carbonate

Acknowledgments

Many people have been the keys to the completion of this project, which without their unending support, I could not have completed in due time.

The Banerjee Research Group (Neil, Lisa, Trevor, Jess, Hannah, Kelsey, and all work study students) have been very supportive and helpful in the analyses of the samples. Their enthusiasm and determination cannot be matched by any group I have worked with so far.

Without the patience and generous assistance of the beamline scientists at the Canadian Light Source, this project would have been impossible to accomplish. I give my thanks to David Muir of the IDEAS Beamline, and Michel Fodje, Kathryn Janzen, and Shaun Labiuk of the CMCF beamline for the technical guidance in data collection and sample setup. I also like to thank Peter Blanchard of the VESPERS Beamline for tips in data interpretation using PyMCA. Research described in this work was performed at the Canadian Light Source, which is supported by the Canada Foundation for Innovation, Natural Sciences and Engineering Research Council of Canada, the University of Saskatchewan, the Government of Saskatchewan, Western Economic Diversification Canada, the National Research Council Canada, and the Canadian Institutes of Health Research.

Without the people of TerraX Minerals, Inc., especially Alan Sexton, we would not have had samples to study. We are adamant in giving them a more improved approach to the mineralization trends of the several prospects within their property, which will in turn allow them to get a better understanding of the connections of the sites with the old mines. This, in turn, will increase confidence in future studies in the property, given that the north is connected to the Con and Giant.

My friends in North America have been very helpful in allowing me to settle here in London, To Jeremy and Emman, grad students who I have worked with back home, without our chats I could not have been more determined to finish my degree. I also like to thank the Department of Earth Sciences, especially the grad students, for bearing with me and including me in this huge social circle.

Table of Contents

Abstract	i
Acknowledgments.....	iii
Table of Contents	iv
List of Tables	vii
List of Figures	ix
List of Appendices	xv
Chapter 1	1
1 Introduction and Background Review	1
1.1 Orogenic Gold.....	1
1.2 The Slave Province	7
1.3 The Yellowknife Greenstone Belt	11
1.4 Yellowknife City Gold Project	15
1.5 Mineralogy of the Yellowknife Greenstone Belt.....	16
1.6 Invisible Gold.....	17
1.7 Local Geology.....	21
1.7.1 Summary of the Yellowknife City Gold Project.....	21
1.8 Synchrotron Radiation	26
1.8.1 Application of Synchrotron Spectroscopy in the Natural Sciences	26
1.9 Synchrotron Techniques in the Project.....	27
1.10 Other complementary techniques for synchrotron spectroscopy	30
1.11 Purpose.....	31
1.12 Objectives	32
1.13 Impact	32
1.14 Scope and Limitations.....	33
Chapter 2	34

2	Methods.....	34
2.1	Sample Selection.....	34
2.2	Synchrotron Radiation X-ray Diffraction	36
2.2.1	Experiment Setup at the CMCF.....	37
2.2.2	Remote Data Collection.....	40
2.2.3	Data Calibration and Integration of 2-Dimensional SR-XRD Results	40
2.2.4	Synchrotron X-ray Diffraction Data Analysis	42
2.3	Synchrotron Radiation X-ray Fluorescence.....	42
2.3.1	Experiment Parameters and Set-up.....	43
2.3.2	Data Interpretation	45
2.4	X-ray Absorption Near Edge Structure.....	46
2.4.1	Re-tracing of Au spot and XANES Spectroscopy of Au.....	47
2.4.2	Data Processing and Interpretation	47
	Chapter 3.....	49
3	Synchrotron X-ray Diffraction and Prospect Cogenuity.....	49
3.1	GSC Kerswill Suite.....	50
3.1.1	Yellowknife City Gold Project Northbelt Property	52
3.1.2	Summary.....	58
	Chapter 4.....	61
4	Synchrotron X-ray Fluorescence and Interpretation of Au Association.....	61
4.1	XRF MCA spectra	62
4.2	2-Dimensional X-ray Fluorescence Maps of the Yellowknife City Gold Project	62
4.2.1	GSC Kerswill Suite.....	64
4.2.2	Yellowknife City Gold Project Northbelt Property	65
4.3	Summary.....	76
	Chapter 5.....	80

5	X-ray Absorption Near Edge Structure (XANES) Spectroscopy on Au speciation	80
5.1	Summary	83
Chapter 6	87
6	Discussion	87
6.1	X-ray Diffraction and Mineralogy	87
6.2	X-ray Fluorescence, Geochemical Similarities, and Textural Implications	88
6.3	X-ray Absorption Near Edge Structure and Gold Speciation	94
6.4	Implications.....	97
6.5	Conclusions.....	101
6.6	Future Studies	102
References	103
Appendices	124

List of Tables

Table 1. Summary of the mineralization styles within the Northbelt section of the Yellowknife City Gold Project, with the boldfaced prospects studied in this thesis (data summarized from Geovector Management, 2017).	25
Table 2. Hole IDs and locations of the TerraX Northbelt samples. SCH – schist, MVL – mafic volcanic, SDS – sedimentary sand, IVL – intermediate volcanic, POR – porphyry, MAI – mafic intrusive, INI – intermediate intrusive, FVL – felsic volcanic, VEI – vein.....	35
Table 3. Locations of the Kerswill Suite samples, including their gold mineralization styles.	36
Table 4. Sample parameters of the X-ray diffraction experiments for the July 2017, March 2018, and May 2018 beam times.	38
Table 5. Parameters for SR-XRF data collection. Beam energy was set to allow excitation of elements of interest, especially Au (L3 binding energy: 11919 eV).	43
Table 6. List of element and line energies used to identify elements in the 2-dimensional fluorescence maps. For PyMCA, tolerance on the region of interest for each element is at ± 100 eV. Ar maps were indications of the ambient argon in front of the sample.	46
Table 7. Sample analysis parameters for XANES, using a 2x2 mm beam spot size and 13400 eV beam energy. The -60 to -20 eV from the absorption edge defined pre-edge line (needed not to be very precise, thus the 5 eV step), the -20 to 60 eV is the most crucial section of the XANES analysis, since it covers the absorption edge of Au (any shift from 11919 eV, including changes in the shape of the spectrum itself, indicate a different Au species), and the area 60 to 100 eV from absorption edge is for post-edge line refinement, may be helpful for EXAFS (not covered in this study).....	48
Table 8. Summary of the mineralogy in the nine representative mineralized suites in the YGB, or the Kerswill Sample Suite.	60

Table 9. Summary of the mineralogy in the seven prospects from the YCGP Northbelt Property 60

Table 10. Summary of the mineralogy in the Kerswill Suite and the TerraX Northbelt Property. Note the similarities in mineral presence, most notably the sulphides (pyrite, arsenopyrite, sphalerite, galena, and monor pyrrhotite), carbonates (dolomite, ankerite, and calcite). 89

List of Figures

- Figure 1. Gold deposition levels for epithermal, porphyry, and orogenic gold (greenstone-hosted quartz carbonate) systems, modified from Dube and Gosselin, 2007)..... 6
- Figure 2. Geologic map (A) and Stratigraphic column of the Slave Province, modified from Haugaard et al (2017). The stratigraphic column (B) also includes the intrusion ages of the various plutons in the Slave. Note the plutons from the Defeat Suite to the granite 'bloom' coincide with the mineralization ages in the Slave Craton. 8
- Figure 3. Map of the Yellowknife City Gold Project, with the seven prospects in purple stars. Modified from Geovector Management, 2018. 23
- Figure 4. Generalized geology of the Yellowknife City Gold Project, modified from Geovector Management (2017). Mapped faults are marked in black, and approximation of the Yellowknife River Fault Zone in red. 24
- Figure 5. Sample X-ray Fluorescence map of the the Fe content of a mafic volcanic with patchy chlorite and disseminated arsenopyrite needles. 28
- Figure 6. Sample X-ray fluorescence map of the same sample in Figure 4. Green to red spots indicate abundance of arsenopyrite..... 28
- Figure 7. Interpretation of Bragg's Law, from Pecharsky and Zavalij, 2005..... 29
- Figure 8. (Left) Raw data of XANES of InP, shown with fitted pre-and post-edge lines. (Right) Normalized data of the left spectrum. From Schnohr and Ridgway, 2015..... 29
- Figure 9. Inside the experiment hutch of the CMCF-BM. The robotic arm (1) moves the sample close to the beam (2) for SR-XRD analysis. The capillaries are stored in a flask containing the cassettes (3) with appropriate labels corresponding to each sample..... 39
- Figure 10. Typical setup for the slabs and half cores for synchrotron XRF and XANES spectroscopy. A wooden core box was cut in half and screwed on the x-z operating motor, and can hold 2 cores at a time for 2-dimensional SR-XRF mapping. The beam comes from

the lower right of the image, and the detector is set at 45 degrees with respect to the sample, effectively making a 90-degree arc for the beam to travel. The detector is pulled back approximately 15 cm from the core, moved closer or farther depending on the dead time counts. 44

Figure 11. X-ray diffractogram of sample C611 from the Con Mine, a gold-bearing quartz vein with minor sulphides. Base metal sulphides, such as galena, are only minor. Pyrrhotite and pyrite are the high-As sulphides present, while quartz is relatively the most abundant mineral. Pyrrhotite could be due to arsenopyrite alteration. Note that the sulphide peaks are very short compared to quartz..... 51

Figure 12. X-ray diffractogram of sample G13, from the Giant Mine a mineralized sample from the main orebody. Noticeable carbonates (calcite, dolomite), mica, and both base metal (sphalerite-galena) and As-rich sulphides (pyrite-arsenopyrite) are observed. Quartz is relatively the most abundant mineral, and is both host rock and vein components. Some traces of tourmaline (as elbaite) is also detected, and can be from the host rock. 51

Figure 13. X-ray diffractogram of sample R433857 from Crestaurum, a quartz-sericite-chlorite schist. Base metal (sphalerite-galena) and high-As (pyrite-arsenopyrite) sulphides are also apparent. Pyrrhotite is possibly due to the alteration of arsenopyrite. Ankerite and dolomite are the main types of carbonate, while chlorite and muscovite are also present. Quartz is relatively the most abundant mineral, and is both host rock and vein component.. 53

Figure 14. X-ray diffractogram of sample R115609 from the Barney Shear, a sericite-bearing chlorite schist. Ankerite and dolomite are the dominant carbonates, and chlorite and muscovite are also seen. Base metal (sphalerite-galena) and high-As (pyrite-arsenopyrite) As sulphides are also apparent. Quartz is relatively the most abundant mineral, and can be both host rock and vein components. 53

Figure 15. X-ray diffractogram of sample S521365 from Hébert-Brent, a portion of the mineralized feldspar quartz porphyry dyke. Both base metal and high-As sulphides (sphalerite and pyrite-arsenopyrite, respectively) are seen. Remnant plaioclase is still visible. Sericitization is reflected by muscovite, while quartz can be both part of the dyke and later veins. 55

Figure 16. X-ray diffractogram of sample V890298 from Sam Otto, a sheared mineralized gabbro. Base metal (sphalerite-galena) and high-As (pyrite-arsenopyrite) sulphides are also apparent. Biotite is observed, which could be due to higher grade metamorphism. Pyrrhotite may be the result of the alteration of arsenopyrite. Quartz is relatively the most abundant mineral, and is both host rock and vein component..... 55

Figure 17. X-ray diffractogram of sample V160414 from Dave’s Pond, a sericitic ash tuff. Traces of remnant plagioclase are detected, as well as traces of quartz. Base metal (sphalerite-galena) and high-As (pyrite-arsenopyrite) sulphides represent two periods of sulphidation, while pyrrhotite may be an indicator of arsenopyrite alteration. Quartz is part of the host rock and veins..... 56

Figure 18. X-ray diffractogram of sample S892089 from Mispickel, a mineralized greywacke. Remnants of metamorphic minerals (chlorite) and host rock components (plagioclase, quartz) are sericitized (muscovite), and sulphidised (pyrite). Pyrrhotite may be due to the alteration of arsenopyrite. Quartz exists as host rock and vein material..... 56

Figure 19. X-ray diffractogram of sample S345537 from Homer, a mineralized gabbro. Chloritization is seen due to the presence of clinocllore. Remnant plagioclase is still observed, representing the host rock. Base metal (sphalerite-galena) and high-As (pyrite-arsenopyrite) sulphides could represent two periods of sulphidation. Quartz is seen as both a host rock and vein mineral..... 57

Figure 20. An example of the mean MCA spectrum for sample S343811, which provides a representation of the relative abundance of elements in the section mapped. 63

Figure 21. Comparison of the average MCA (top) and a single pixel MCA (bottom) of sample S343811. Note that the counts are lower and peaks are noisier in the bottom spectrum, but elements can still be identified. 63

Figure 22. Element distribution map of sample C611 from the Con Mine, a gold-bearing quartz vein with minor sulphides (pixel size at 0.5 mm). Au mineralization is associated with Fe. Minor Zn and Cu exists as small clusters, as well as very minor K and quartz and Ca veining. Fe veinlets and clusters surround quartz margins. 66

Figure 23. Element distribution map of sample G13 from the Giant Mine, a mineralized sample from the main orebody (pixel size at 0.5 mm). Disseminated Au is hosted within As-Fe, and quartz and Ca, and minor K alteration is apparent. As-Fe clusters are overprinted by minor Zn, and overprinted by minor K. Minor quartz and Ca cut through the rest of the rock. Elements also display shearing along the NE-SW portion of the sample, indicating that the minerals associated with them were precipitated during tectonic events. 67

Figure 24. Element distribution map of sample R432250 from Crestaurum, a quartz-sericite-chlorite schist (pixel size at 0.5 mm). Au is spatially associated with Fe-As and Zn. Earlier quartz is cut by sericite (K), and eventually proliferated by later quartz and Ca veins. 70

Figure 25. Element distribution map of sample R115604 from the Barney Shear, a sericite-altered host rock with grey quartz veins and ankerite (pixel size at 2 mm). Au is spatially associated within As-Fe masses, with later Zn overprinting As and Fe. Early K (outside the main vein) is cut by As-Fe, while later K and minor quartz and Ca vein overprints the sulphides. Ti enrichment is seen within the sulphide mass, which can be correlated to later K. 71

Figure 26. Element distribution map of sample S521365 from Hébert-Brent, a portion of the mineralized feldspar quartz porphyry dyke (pixel size at 0.5 mm). Au is associated with As-Fe bands cut by later quartz-Ca. Early K is cut by later As-Fe bands and quartz-Ca veins. Minor Zn is contained within the As-Fe veins..... 72

Figure 27. Element distribution map of sample V156527 from Sam Otto, a mafic volcanic host with patchy chlorite (pixel size at 0.5 mm). Au is associated with quartz-Ca overprinting As-Fe and Zn. Early K-Ti and Ca-Fe (at the left portion of the core) is cut by As-Fe veining. Later K at the right portion of the sample is overprinted by quartz-Ca veining. Sb signatures are related to Au..... 74

Figure 28. Element distribution map of sample V160414 from Dave's Pond, a sericitic ash tuff (pixel size at 2 mm). Au is associated with K. Early K, which shows foliation, is cut by As-Fe and Zn veining, and eventually overprinted by secondary K alteration. Minor quartz-Ca veining cuts across the foliation bands. Remnant veinlets of As-Fe and disseminated Zn

are scattered along fringes of the host rock. Sb signatures are related to Au (orange to red pixels at the top right of the Sb map)..... 77

Figure 29. Element distribution map of sample S892089 from Mispickel, a greywacke host rock with foliation displayed by As-Fe and minor K (pixel size at 0.5 mm). Au is associated with As-Fe which cut through earlier K-Ti mineralization. Remnant Zn is overprinted by later K-Ti, which doesn't show foliation (centre mass at the K map), and are all cut by quartz-Ca veining. Sb signatures are related to Au..... 78

Figure 30. Element distribution map of sample S345537 from Homer, a gabbro host with prominent leopard-like As-Fe mineralization (pixel size at 0.5 mm). Au is associated with As-Fe clusters cutting through early K and chlorite Ca-Fe. Sparse Zn is an indication of low-As mineralization. Minor Sb is seen to be related to Au. 79

Figure 31. MCA spectrum of sample C611 from the Con Mine. Note that the Au L₃ peak proves that there is indeed Au in the sample. 81

Figure 32. Zoomed in MCA spectrum of the high intensity pixel of sample C611 from the Con Mine. Zn K β overlaps with Au L₃, but the Au peak is still prominent. 81

Figure 33. MCA spectrum of the high intensity pixel of sample V413296 from Dave's Pond. Note that there is strong Zn presence, and it overlaps with the Au signal. Still, if Au was indeed present, it will show as a distinct peak above Zn. 82

Figure 34. Zoomed in MCA spectrum of the high intensity pixel of sample V413296 from Dave's Pond. There is no distinct peak that represents Au, and it is overlapped by Zn..... 82

Figure 35. Sample C611 from the Kerswill Suite, a quartz vein with minor sulphide veins from the Con Mine. Encircled in the top image is the approximate spot where X-ray Fluorescence maps of As, Fe, and Au were made, and is used to locate the spot for Au XANES. 84

Figure 36. Sample S892089 from the Mispickel Suite, a mineralized greywacke. Encircled in the top image is the spot where X-ray Fluorescence maps of As, Fe, and Au were made, and used to pinpoint the spot for Au XANES. 84

Figure 37. XANES results of the spots with high Au, with the bottom graph showing XANES spectra of a gold in-house standard for reference. Both the Kerswill (top left) and Mispickel (top right) samples show the presence of Au⁰, or metallic gold, within the spot. . 85

Figure 38. Samples of Au XANES spectra of a gold foil (top, for Au⁰), gold sulphide (middle, corresponding to Au³⁺), and gold hydroxide (bottom, corresponding to Au¹⁺), from Ravel, 2016. Note the behaviour of the spectrum at the Au L₃ absorption edge (11919 eV) changes with respect to the oxidation state..... 86

Figure 39. X-ray fluorescence maps showing (top) Au distribution differences via Peakaboo (middle maps) and PyMCA (bottom maps), suspected to be due to variations in peak fitting, but the Fe map of the top left sample (bottom) shows similar trends..... 93

Figure 40. Representatives of sulphide-associated Au from the Kerswill Suite (top) and the Northbelt Property (bottom). Note that sulphide-hosted Au exists either as veinlets or pods.95

Figure 41. Representative of quartz-carbonate hosted (left) and sericite-chlorite (right) from the Northbelt Property. Quartz-carbonate veins cut through earlier textures, and is last in the order of mineralization, while heavy sericitization reflects foliation in both samples. 96

List of Appendices

Appendix A: Summary of X-ray Fluorescence Interpretations	124
Appendix B: X-ray Fluorescence Maps.....	144
Appendix C: Summary of XRD Data	196
Appendix D: XRD Diffractograms	200
Appendix E: PyMCA Tutorial	276
Appendix F: MCA spectra of samples analysed for Au XANES	299
Appendix G: Other peak types to consider in identifying elements via X-ray fluorescence, and how to prevent detector oversaturation	312

Chapter 1

1 Introduction and Background Review

1.1 Orogenic Gold

Orogenic gold provinces are the result of the accretion and collision of several terranes, forming metamorphic belts extending several kilometres. Its formation involved both thermal and lithospheric processes that, as mentioned by Groves (2003) and Goldfarb and Groves (2015), triggered several events, including 1) magmatic and forearc generation with accretionary prisms and back-arc formation with extensional basins; 2) deformation and metamorphism along with prevalent granitoid plutonism; 3) eventual uplift and erosion with penecontemporaneously-formed younger sedimentary basins, 4) introduction of K, S, CO₂, H₂O, Si, and Au, along with variable As, B, Bi, Na, Sb, Te, and W via hydrothermal fluids, and 5) production of supralithostatic, low salinity ore-forming fluids bearing H₂O, CO₂, CH₄, N₂, and H₂S. Common chemical characteristics of such deposits generally include low sulphide volume, low salinity and CO₂-rich fluids, and $\Delta^{18}\text{O}$ values of 5-10 ‰ (Goldfarb et al, 2001). Orogenic gold deposits were synthesized in areas previously deformed and metamorphosed, in temperatures ranging from 200 to 650°C, and pressures from 1 to 5 kbar (Groves, 1998). Hydrothermal veins, developing due to perforation of fluids along the developed cracks in a metamorphic terrane, originated from trapped fluids released after deformation and tectonism, carrying metals and other elements of economic value, such as rare-earth elements (Kerrick and Fyfe 1988a, b; Groves, 2003). Contact metamorphism and plutonic bodies also contributed to fluids responsible for mineralization, such as the Yellowknife Greenstone Belt (van Hees et al, 1999; 2006). Notable mineral assemblages in orogenic gold deposits are carbonates and sulphides, as well as pervasive chlorite alteration in host rocks of the greenschist to low amphibolite, with or without sericite (Isachsen and Bowring, 1994; Goldfarb, 2001), and abundance of quartz-carbonate veins (Goldfarb, 2001), which occasionally host gold, i.e., the Yellowknife Greenstone Belt (Geovector Management, 2017).

There were at least four major periods during the earth's history where orogenic gold deposition occurred. The earth experienced several pulses of orogenic gold deposition from 3.4-3.0 Ga, 2.8-2.55 Ga, 2.1 to 1.8 Ga, 570-250 Ma, and 250-65 Ma, and rare showings of orogenic gold deposition from 2.5 to 2.1 Ga, and 1.8 to 0.6 Ga, with some exceptions, (Meyer; 1981; Hutchinson, 1987; Goldfarb et al, 2001), supported by the lack of gold-enriched areas in greenstone belts and other related terranes, or the lack of abundant hydrothermal activities required for these deposit styles throughout the Proterozoic (Meyer, 1981; Goldfarb, 2001). The most important and largest Au deposits in the world were formed in the Archaean (Hutchinson, 1987). The Early Proterozoic bore only rare, insignificant Au showings, while the Late Proterozoic to Early Paleozoic and the Mesozoic demonstrated some showings of significant orogenic gold systems, such as the Mahd adh Dahab in the Arabian Peninsula and the Juneau in Alaska (Hutchinson, 1987). These periods experienced large-scale migration of fluids responsible for mineralization along moderate to high temperatures (>400 to 500 °C) in deep structures (Goldfarb et al, 2001).

Orogenic gold, previously named lode-gold or greenstone-hosted quartz-carbonate vein deposits (Groves et al, 1998; Dube and Gosselin, 2007), contain relatively large amounts of gold and silver hosted in quartz and quartz-carbonate veins. These deposits are situated in shear zones and faults related to greenstone belts, usually metamorphosed to greenschist to lower amphibolite facies, at depths ranging from 5 to 10 km. Iron-carbonate deposits are also associated with orogenic gold, where structurally-controlled quartz-carbonate veins are found in metamorphosed terranes. Such deposits appear as fault-fill veins in steep, brittle-ductile compressional shear zones and faults associated with local hydrothermal breccias and extensional veins (Dube and Gosselin, 2007). Hydrothermal fluids driving mineralization in these deposit types were commonly H₂O-CO₂-rich, low salinity fluids with anomalous CH₄, N₂, K, and S (Dube and Gosselin, 2007). Common gangue minerals in such deposit types are quartz, calcite, dolomite, ankerite, and siderite, with minor chlorite, white mica, tourmaline, and scheelite, while common sulphides include pyrite, pyrrhotite, chalcopyrite, and arsenopyrite, especially in the Slave Province (Dube and Gosselin, 2007). Vein thicknesses range from a few centimetres to 5 m, with lengths varying from 10 to 1000 m (Dube and Gosselin, 2007).

Gold exists both in quartz-carbonate veins and iron-enriched sulphidized wall rocks of orogenic gold deposits (Dube and Gosselin, 2007). A variety of terranes host gold, such as ultramafic and mafic volcanics, gabbros, metasedimentary rocks, and granitoids. Usual Au/Ag ratio in such deposits vary from 5 to 10, and display no vertical metal zoning, unlike epithermal systems which readily illustrate vertical zoning (Dube and Gosselin, 2007). Along with gold, metals such as Ag, As, W, B, Bi, Sb, Te, Mo, and seldom with anomalous Cu, Pb, and Zn, also exist in orogenic gold systems (Groves et al, 1998; Dube and Gosselin, 2007). Major fault lines and associated structures acted as conduits for hydrothermal fluids in greenstone-hosted quartz-carbonate vein deposits. These deposits were related to “2nd to 3rd-order compressional reverse-oblique to oblique brittle-ductile high-angle shear and high-strain zones” (Dube and Gosselin, 2007), located 5 km away from the 1st order fault, and were usually apparent within hanging walls (Robert, 1990). Such deposits synthesized during syn- or post-peak deformation and metamorphism in greenstone to amphibolite facies hosts, whereas world-class deposits were more common within greenstone belts. Locally, rock composition, competence and metamorphic grade greatly affected alteration, whereas halo dimensions were influenced by the type of host rock. Orogenic gold deposits in greenschist-facies belts are observed with iron-carbonate-sericite alteration, as well as sulphidation (pyrite and minor arsenopyrite) (Dube and Gosselin, 2007). Common alteration minerals within greenschist-facies hosts are Cr or V-rich micas, and ankerite-bearing quartz-carbonate stockwork zones, while in amphibolite-facies host rocks, common alteration minerals are biotite, amphibole, pyrrhotite, pyrite, and arsenopyrite, and biotite/phlogopite, diopside, garnet, pyrrhotite and arsenopyrite appeared at higher metamorphic grades (Mueller and Groves 1991; Witt, 1991; Hagemann and Cassidy 2000; Ridley et al 2000; Dube and Gosselin, 2007).

A multitude of studies attempted to understand the timing and mineralogical association of gold in Archaean orogenic gold provinces (i.e., Meyer and Saager, 1985; Witt, 1991; van Hees et al, 1999; Dube and Gosselin, 2007). Sulphide precipitation in the Main Hill prospect in the Pilbara Block in Western Australia was coeval with peak metamorphism, and gold was associated with the release from the löllingite structure, and precipitation along löllingite-arsenopyrite grain boundaries (Neumayr et al, 1993). Mumin et al (1994) believed that gold in the Ashanti Gold Belt in Ghana was derived from fluids from

dehydration and decarbonation at depth, eventually depositing sulphides such as arsenian pyrite and arsenopyrite. Invisible gold mineralization in the Cretaceous Coffee orogenic gold deposit in the Yukon was associated with fine-grained, disseminated arsenian pyrite within extensional fractures perforating along metamorphic foliation and post-metamorphic shears (MacKenzie et al, 2015). The association of gold with both pyrite and arsenopyrite in the Giant Mine, Northwest Territories, and fluids that precipitated the sulphides were believed to be heavily influenced by the metasedimentary rocks which gave their chemical imprint to the fluids percolating through the rocks within the Yellowknife Supergroup (van Hees et al, 1999). Gold, both visible and invisible, was contained with sulphides such as pyrite, arsenian pyrite, and arsenopyrite among various deposits around the world. Along with shear-zone hosted Au and quartz-carbonate-hosted Au, other notable deposits in Archaean greenstone belts were banded iron formations and volcanogenic massive sulphides. Banded iron formations were cut by quartz-sulphide veins, and gold was associated with either sulphides (Saager et al, 1987; Oberthur et al, 1990; Philips and Groves, 1998; Adrianjakavah et al, 2007; Haugaard et al, 2016, 2017) or existed as disseminations within the iron formations (Philips and Groves, 1998). There was a potential on BIFs in Madagascar to be extracted with both Fe and Au, as well as the presence of Au in both gneissic basement and mafic-ultramafic rocks adjacent to the BIFs (Andrianjakavah et al, 2007). Philips and Groves (1998) studied the distribution of gold in both the Pilbara and Yilgarn Cratons in Western Australia, where gold was associated with veins related to anticlines and structural highs, and some occurrences of BIF-hosted Au disseminations also existed in the Yilgarn block, both at Mt. Magnet and Bullfinch. Studies of quartz-carbonate veins in some of the BIFs in the Slave Craton, i.e., gold mineralization in the Goose Lake BIFs, exhibited elevated S values and high REE and Y numbers caused by the proliferation of post-metamorphic mineralizing fluids (Padgham, 1992; Haugaard et al, 2017). Volcanogenic massive sulphide deposits were also prominent in Archaean cratons, where base metals and/or Au may be extracted. Massive sulphide deposits in orogenic gold terranes were due to the overprinting and remobilization of fluids and pre-existing material during deformation and metamorphism (Goldfarb et al, 2001; Groves et al, 2003). Some examples of overprinted VMS in orogenic gold systems were the Bulyanhulu in Tanzania, Macalder in Kenya, and Mount

Gibson in Australia, where there was evidence of overprinting of a syngenetic, pyritic to base-metal VMS deposit by later orogenic gold-related mineralization (Goldfarb et al, 2001; Groves et al, 2003). Massive sulphide deposits were deformed and metamorphosed in the main stages of orogeny, and eventually uplifted and eroded (Groves et al, 2003).

There have been efforts to differentiate orogenic gold (Kerrich and Fyfe, 1981; Barnicoat et al, 1991) from both epithermal and porphyry copper systems. Porphyry Cu-Mo-Au and epithermal Au-Ag deposits are both part of a telescoped system produced by the ascent of hydrothermal fluids associated with calc-alkaline magmatism in subduction zones, with mineralization forming in both continental and accreted arcs (Figure 1) (Groves et al, 1998; Robb, 2005; Dube and Gosselin, 2007; Whitty, 2007; Morey et al, 2008; Corbett, 2009; Sillitoe, 2010). Zonation patterns are apparent in porphyry-epithermal systems, a result of prograde alteration of the host rock intruded by a mineralizing body. Porphyry copper systems are positioned 2 to 3 kilometres below and around the intrusive body, with minerals such as secondary biotite, potassium feldspar, magnetite, bornite, chalcopyrite, covellite, and pyrite hosted in the halo called the potassic zone (Corbett, 2009; Sillitoe, 2010). Other associated magmatic-hydrothermal systems within the porphyry-epithermal deposits also exist, such as proximal and distal skarns, and carbonate-replacement Zn-Pb-Ag-Au, and are usually affected by lithology of other surrounding rocks (Sillitoe, 2010). Other alteration zones emanate from the main dyke, serving as pathfinders for the main mineralized body. In epithermal systems, late fluids from the magmatic intrusion interacted with the walls of the host rock, altering local wallrock in shallow crustal levels (Robb, 2008). Depending on the chemistry, pH, and redox state of S, different epithermal mineralization styles and mineral presence are to be expected. High sulphidation epithermal systems are proximal to the volcanic vent (Robb, 2008), indicating mineralization coming directly from the magmatic source. Low sulphidation systems are mineralized by a mix of meteoric and magmatic fluids, and are located away from a volcanic source or a magmatic body. Common minerals associated with epithermal systems are quartz, kaolinite, illite, chlorite, montmorillonite, calcite, chalcedony, adularia (low sulphidation) and alunite (high sulphidation). Orogenic gold deposits, on the other hand, are associated with faults and shear zones contained in

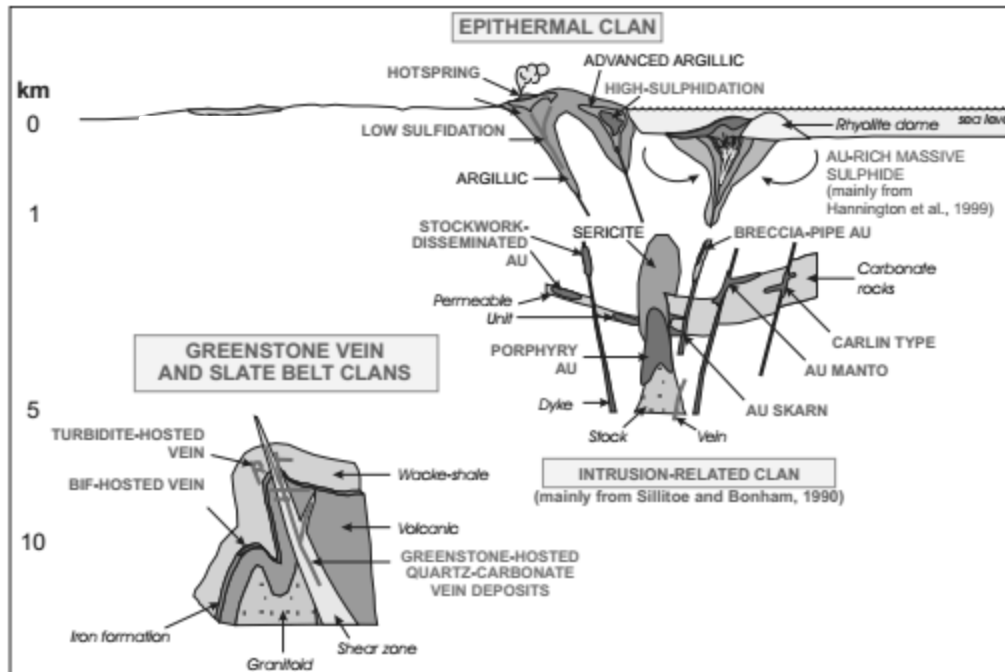


Figure 1. Gold deposition levels for epithermal, porphyry, and orogenic gold (greenstone-hosted quartz carbonate) systems, modified from Dube and Gosselin, 2007)

deformed terranes and are associated with rocks metamorphosed to greenschist facies (Figure 1), and are formed from low salinity, CO₂-rich fluids perforating through metamorphic terranes (Groves et al, 1998; Goldfarb et al, 2001; Groves et al, 2003; Dube and Gosselin, 2007).

1.2 The Slave Province

The Slave Province is an Archaean granite-greenstone terrane located at the northwest of the Canadian Shield, containing metals such as base-metal silver and gold, as well as rare earth element pegmatites, all related to 2.7 to 2.55 Ga supracrustal material (Kusky, 1989; Bleeker, 2002; Padgham, 1991; Webb, 1992; Ootes et al, 2011). The Slave is bordered by two Proterozoic provinces - the Bear Province along its north and west flanks, and the Churchill Province to its south and east. The Slave Craton is a remnant of a larger continental mass, with a Neoproterozoic supracrustal component (the Yellowknife Supergroup; Bleeker, 2002) covering a Mesoarchaean gneissic basement (Bleeker, 2003). The Yellowknife Supergroup (Figure 2, red box) was deposited during several tectonic phases (Isachsen et al., 1991; Isachsen and Bowring, 1997; Cousens, 2000; Bleeker, 2002; Davis et al., 2003; Cousens et al., 2006a; Bleeker and Hall, 2007; Ootes et al., 2009; in Ootes, 2011), including rifting and mafic volcanism during 2.73-2.70 Ga, which led to greenstone belt formation. The main event at 2.69 to 2.67 Ga was a bimodal, intraplate arc volcanism (Bleeker, 2002). Turbidite deposition, a result of back-arc basin rifting, was derived from older volcanic material and minor Middle Archaean basement rock (Yamashita and Creaser, 1999; Ootes et al, 2009; Ootes et al, 2011). The Slave Province exhibited variation in rock deformation throughout its units, displaying irregular orientations, while being controlled by basement rocks at the margins of upper units (Padgham and Fyson, 1992). Metamorphism to greenschist to amphibolite facies, as well as intrusion of granitic bodies, re-oriented structures pre-existing in the Slave (Padgham and Fyson, 1992). A progression from pre-metamorphic folding, as well as homoclines, to isoclinal folds and succeeding foliations, were prominent in the Slave, and syn-deformation intrusives introduced open folding (Padgham and Fyson, 1992). Several events of foliation and cleavage as minor folds are seen in the metasediments, and F₁ to F₂ folds were overprinted by schistosity and mineral cleavages due to metamorphism

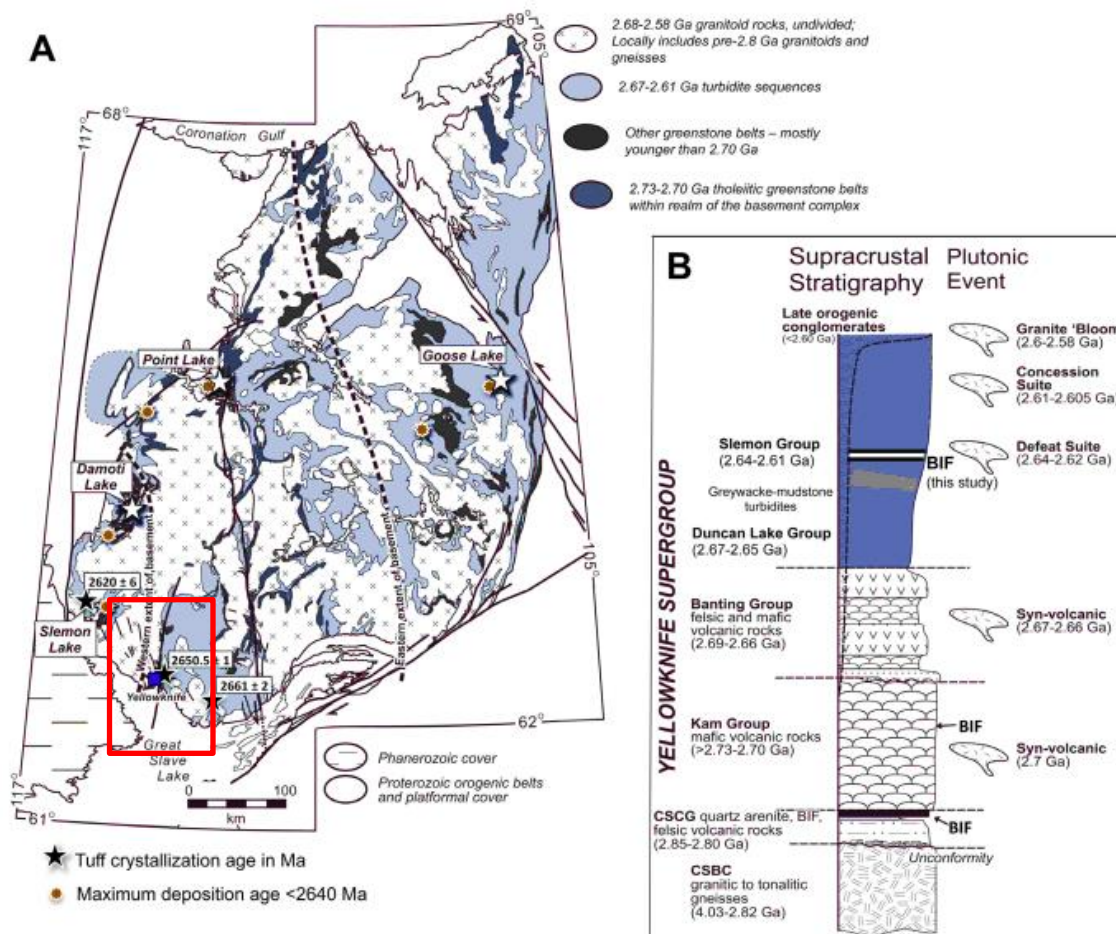


Figure 2. Geologic map (A) and Stratigraphic column of the Slave Province, modified from Haugaard et al (2017). The stratigraphic column (B) also includes the intrusion ages of the various plutons in the Slave. Note the plutons from the Defeat Suite to the granite' bloom' coincide with the mineralization ages in the Slave Craton.

(Padgham and Fyson, 1992). Syn-deformational intrusives modified the folds and foliations by flattening, yet such folds and foliations were shortened within unmodified folds and foliations, indicating little to no effect to country rock strain (Padgham and Fyson, 1992). Lineation of volcanic belts and plutons extend 50 kilometres, oriented northwesterly in the eastern flank of the craton. Late Archaean belts at the northwest edge are oriented north-northeast, forming due to the collision with the Wopmay Orogen during the Proterozoic (Padgham and Fyson, 1992). The southwestern Slave, however, demonstrates northwest to northeast-trending belts and intrusives in an angular fashion, and was controlled by crustal-scale fractures beneath the units (Padgham and Fyson, 1992). Shear zones were overprinted and covered by intrusions, and are seen to trail the boundaries of syn-volcanic plutons. Steep folds and cleavages were “inclined, overturned, and convexed westward” (Padgham and Fyson, 1992), with décollement zones seen in lower crustal points due to lack of surficial traces of major displacement within high-strain areas. Folds within metasediments were secondary and superimposed within larger folds, as well as local overturned limbs (Padgham and Fyson, 1992).

Bleeker (2002) and Padgham and Fyson (1992) considered the Slave Province to be analogous to the Superior Province. The abundance of tonalite, gneiss, migmatite, and late granitoid intrusions were common between the two provinces (Padgham and Fyson, 1992). The presence of gold and volcanogenic massive sulphide deposits in both cratons were the most noticeable similarities, with the systems in both cratons dating Late Archaean. Differences between the cratons were enumerated by Padgham and Fyson (1992), i.e., in the Slave Province, supracrustal rocks are volcanics and greywacke (metavolcanics and metasediments) formed between 2.71 to 2.65 Ga, and were penecontemporaneous with uplift, unlike the older units in the Superior (Card, 1990). The Slave was covered with more sedimentary rocks compared to the Superior – less than 20% of the latter is covered in sediment. Felsic to intermediate volcanic rocks were more common in the Slave, while komatiitic and alkalic volcanics proliferated the Superior. Volcanic rocks in the Superior were adjacent or within tholeiitic basalts (Card, 1990), while those in the Slave were not related with tholeiitic rocks (Padgham and Fyson, 1992). Felsic basement rocks were more prevalent in the Slave, i.e. the Acasta Gneiss in the west of the province (Bowring et al, 1989). Volcanogenic massive sulphide deposits

in the Slave exhibited zinc-lead-silver signatures compared to the copper-zinc-gold Superior VMS. Gold provinces in the Slave were synthesized before the peak of thermal metamorphism, granitic pluton intrusion, and deformation, unlike the gold deposits in the Superior being emplaced after major deformation, intrusion, and metamorphism (Padgham, 1992; Bleeker, 2002).

Two theories on how the Slave Craton evolved were presented by Kusky (1989) and Bleeker (2002). Kusky (1989) believed that the Slave present characteristics indicating an obducted oceanic lithosphere, revealing that the area was an accretionary prism formed due to the development of an island-arc system. Bleeker (2002), on the other hand, believed that the craton was allochthonous, due to the lack of a metamorphic sole and the eruption of pillow basalts through sialic crust. The Contwoyto terrane was a metamorphosed greywacke-mudstone turbidite body, with bases either truncated by faults or were poorly defined, which may suggest an allochthonous source (Kusky, 1987b, 1989). The greywackes were derived from an island-arc source, contemporaneous with volcanism, producing the Hackett River Arc (Lambert, 1978). The presence of sheeted dykes and pillow lavas were perceived to indicate an ophiolite sequence obducted over the gneissic basement. Bleeker (2002), on the other hand, debunked Kusky's (1989) assumption of an island arc-ophiolite origin for the Slave Province. There was a lack of mafic-ultramafic successions in the Slave, and the feeder dykes connecting the basement and volcanic rocks did not show signatures related to an ophiolite sequence (Bleeker, 2002). Rather, the dyke swarms were derived from a source other than an ultramafic body, and were indicative of basin extension. Pillow lavas were extruded through the felsic basement. No evidence of thrusting, obduction, or a metamorphic sole was seen in the Slave. Flat LREE patterns were present in the Slave, unlike the positive ϵ_{Na} isotopic signatures indicating oceanic origins. Bleeker (2002) proposed that the Slave Craton was allochthonous, overlain by a certain stratigraphic succession and with a single continuous basement (Bleeker et al 1999a, b, 2000).

The largest amount of gold in the Slave is hosted by shear zone deposits, especially those from the Con and Giant Mines in Yellowknife, with a combined historical production of about 14 Moz gold (Geovector Management, 2017). These large shear zones show

alteration and foliation due to perforation of silica and CO₂-rich fluids during mineralization (Boyle, 1961; Kerrich and Fyfe, 1988; Padgham, 1991; Goldfarb et al, 2001). Shear zones within the Con, Campbell, and Negus Mines in the Yellowknife Greenstone Belt were oriented northwest to northeast, dipping 40 to 70 degrees to the west, while portions deemed productive or ore-bearing were oriented northwards, dipping 50 degrees to the west (Webb, 1992). Such shear zones pre-dated or were contemporaneous with mineralization, with Webb (1992) showing that post-mineralization shears were barren of significant gold. Ootes et al (2011), on the other hand, presented the role of shear zones in acting as both conduits and reservoirs for Au mineralization within the Yellowknife Greenstone Belt.

1.3 The Yellowknife Greenstone Belt

The Yellowknife Greenstone Belt (YGB) is one of the more exposed and well-studied greenstone belts in the Slave Craton (Cousens, 2000), and is the southernmost belt of a north-south trending volcanic system in the Slave (Isachsen and Bowring, 1994). The belt is segregated into two distinct stratigraphic groups – the mafic tholeiitic, 2.72-2.70 Ga Kam Group, and the felsic, and the 2.66 Ga Banting Group (Helmstaedt and Padgham, 1986; Cousens 2000; Cousens et al, 2001). Both groups overlie the >2.8 Ga gneissic basement complex composed of tonalitic and granodioritic intrusions (Helmstaedt and Padgham 1986; Bleeker et al. 1999a; Bleeker et al. 1999b; Cousens et al, 2001; Bleeker, 2002). The Yellowknife Greenstone Belt was intruded by two, 2.64-2.61 Ga bodies at its western flank – the Defeat Plutonic Suite and Anton Complex (Henderson, 1985; Isachsen and Bowring, 1994; Cousens, 2000), while the northern segment was infringed by the 2.68 Ga Ryan Lake pluton and 2.61 Ga Duckfish aplite (Ootes et al, 2007). To the east, the greenstone belt was covered by the sedimentary Burwash and Walsh Formations, both derived from detrital material from the Yellowknife metavolcanic suites (Cousens et al, 2000). The basement for the Yellowknife Greenstone Belt is the Dwyer Group (Helmstaedt and Padgham, 1986; Isachsen and Bowring, 1994; Cousens, 2000; Cousens et al, 2001) is a >3.7 to 2.923 Ga quartzite, volcanoclastic, and iron formation group unconformable under the lower Kam Group, due to shearing and obscuring of gabbroic sills, and unconformable over the tonalitic basement. This Mesoarchean (>2.8

Ga) gneiss (Cousens, 2000; Cousens et al, 2001) is composed of banded iron formations, quartzites, and minor metavolcanics. The eastern Slave, however, lacks such basement (Bowring et al. 1989; Dudas 1989; Davis and Hegner 1992; Thorpe et al. 1992; Cousens, 2000).

The Kam Group (Helmstaedt and Padgham, 1986; Isachsen and Bowring, 1994; Cousens, 2000; Cousens et al, 2001) is a >2.72 to 2.70 Ga, northeast striking and steeply dipping, mafic to intermediate volcanic sequence, and embodies most of the Yellowknife Greenstone belt. The Kam group is divided into four formations – the lowermost Chan Formation, Crestaurum Formation, Townsite Formation, and the Yellowknife Bay Formation. The 2.8-2.71 Ga Chan Formation (Isachsen and Bowring, 1994; Cousens, 2000), the lowermost within the group, is composed of pillow basalts intruded by a gabbro dyke-sill system, originally classified as indicators of potential seafloor spreading and ophiolite obduction (Helmstaedt and Padgham, 1986), and was debunked by Bleeker (2002). The Ranney Tuff and Chert (2.8-2.64 Ga) serves as the boundary between the Chan and Crestaurum Formations, and represents either a back-arc basin associated with arc magmatism (Crestaurum to Yellowknife Bay Formations) or another event unrelated to volcanic activity (Isachsen and Bowring, 1994). The Crestaurum Formation (Isachsen and Bowring, 1994; Cousens, 2000) is a 2.71 Ga pillow basalt and mafic flow-dominated unit containing minor dacitic to rhyodacitic tuffs (Isachsen and Bowring, 1994; Cousens 2000). The 2.71 to 2.70 Ga Townsite Formation (Isachsen and Bowring, 1994; Cousens, 2000) is a dacitic to rhyodacitic flow, tuff, and breccia unit intruded by gabbroic sills. The 2.70 Ga Yellowknife Bay Formation (Isachsen and Bowring, 1994; Cousens, 2000) is a cherty tuff with a reversely graded conglomeratic unit named the Bay Formation (Padgham 1987b, Cousens, 2000). Cousens (2000) states that the shear zone-hosted Au deposits in Yellowknife are hosted within the Yellowknife Bay Formation.

The Banting Group (Isachsen and Bowring 1994; Cousens et al, 2001) is a 2.66 Ga felsic to intermediate volcanic unit, striking north and faulted against the Kam Group and Jackson Lake Formation (Isachsen and Bowring, 1994). Feeder dykes intruding the Kam Group and leading to Banting volcanism are consistent with the deposition of the latter over the Kam Group after a 35 to 40 million-year pause (Helmstaedt and Padgham,

1986). The Banting Group is divided into the Ingraham Formation, a quartz porphyry, ash flow tuff unit with intercalations of mafic flows, and the Prosperous Formation, bearing felsic tuff, mafic flows, and volcanoclastic sedimentary rocks (Cousens et al, 2002).

Two metasedimentary rock groups overlie the mafic volcanics, especially in the eastern section of the Yellowknife Greenstone Belt. The Duncan Lake Group (Helmstaedt and Padgham, 1986, Ootes et al, 2009; Haugaard et al, 2016) is a 2.67-2.65 Ga suite of turbidite rocks overlying the Banting Group, and includes the Burwash, Clover Lake, Itchen Lake, and Mosher Lake Formations. The Siemon Group (Haugaard et al, 2016) is a 2.64-2.61 Ga suite of tuff, greywacke-mudstone turbidites, and BIF-bearing turbidites overlying the Duncan Lake Group, and consists of the Siemon Lake, Goose Lake, Salmita, Contwoyto Lake, Damoti Lake, Kwejinne Lake, Emille River, Wheeler Lake, and James River (High Lake) Formations (additional information on the lithology of the units of both the Duncan Lake and Siemon Groups are in Haugaard et al, 2016).

A plethora of intrusive bodies cut through the metavolcanic and metasedimentary groups. A northeast-trending magmatic suite, the 2.63-2.62 Ga Defeat Suite, intrudes both the Duncan Lake and Siemon Groups at the southern edge of the exposed Slave Craton (van Breemen et al, 1992a; Davis and Bleeker 1999; MacLachlan and Davis 2002). Several other plutons intrude the supracrustal units of the Slave Craton, such as the 2.61-2.6 Ga Concession Suite (Davis et al, 1994) and a 2.66-2.6 Ga granite bloom (Ootes et al, 2009). Ootes and others (2011) believed that gold mineralization occurred in the active orogenic belt due to crustal thickening and deformation, and the intrusion of plutonic bodies at 2.6 to 2.58 Ga carried mineralizing fluids.

The <2.61 Ga Jackson Lake Formation (Isachsen and Bowring, 1994) is an extremely metamorphosed conglomerate-sandstone unit sitting unconformable over the Kam Group, and is coeval with the Superior's Timiskaming Conglomerate. This unit bears stretching lineations and steep to almost vertical dips, which are identical to older units in the Yellowknife Greenstone Belt, indicating that the units are deformed after 2.61 Ga. Tectonic events provided conduits for mineralizing fluids to proliferate and altered the host rocks and shear zones to deposit gold and associated sulphides.

Martel and Lin (2006) proposed four ductile structure periods within the Yellowknife River Fault Zone. The 1st generation, so-called G_1 structures, was seen in all formations older than the metaconglomerates of the Jackson Lake Formation. S_1 foliation was parallel to the bedding planes of the Banting Group, was transposed along later foliation events, and micas preserved such foliation within metasediments (Martel and Lin, 2006). F_1 folds were overprinted by S_2 foliation, especially within metasediments. G_2 structures were common along the rocks of the Yellowknife Greenstone Belt, where S_2 foliations were shown as a continuous fabric along the Banting Group volcanics, and developing millimetre-scale dark and light alternating bands within metasediments. S_2 foliations were axially planar to F_2 folds of S_1 and bedding planes (Martel and Lin, 2006). F_2 folds were outlined by Kam Group tuff within the Crestaurum Mine. Shearing during the G_2 event was marked with varied mineral assemblages based on host rock mineralogy (Martel and Lin, 2006). The Yellowknife River Fault Zone exhibited a 10-30 m mylonite zone with intense chloritization and carbonatization, as well as sulphide-rich banding along the contacts of the Kam and Banting Groups (Martel and Lin, 2006). G_3 structures, on the other hand, were prominent along the Yellowknife River Fault Zone and the Homer Lake Fault. S_3 foliation was a well-spaced, developed crenulation cleavage within the metavolcanic rocks of the Kam Group, and was oriented clockwise with respect to the metasediments of the Burwash Formation (Martel and Lin, 2006). G_3 shearing was dextral, shown by the counterclockwise orientation of S_3 with respect to S_2 and F_3 fold asymmetry. G_4 structures and shearing were prominent within the Yellowknife River Fault Zone, such as S_4 foliation parallel to shear zones, as well as crenulating S_3 foliation (Martel and Lin, 2006). The Yellowknife River Fault Zone, with its sulphide bands close to the metavolcanics, was one of the main conduits for Au mineralization in the Yellowknife Greenstone Belt (Martel and Lin, 2006).

Gold-bearing quartz veins are apparent within the Yellowknife Greenstone Belt. Boyle (1961) performed a geochemical study of the veins within the metasediments and metavolcanics in Yellowknife, and Fyson's (1986) study of the timing and geometry of such veins with respect to folding and foliation revealed gold association with quartz veins within the metavolcanics and metasediments. Bedding veins (Fyson, 1986) were localized in meta-sandstones and in close relationship with metagreywackes, and formed

before or synchronous with F_1 folding. Deformation of bedding veins were common within the hinges of F_3 folds. Echelon veins (Fyson, 1986) occurred as oblique lineations within subhorizontal rocks, and thinning near metagraywacke contacts. These echelon veins exhibited anticlockwise orientations with respect to the beddings in northwest to north-striking limbs (Fyson, 1986), forming after S_2 fabrics. Foliation veins (Fyson, 1986) were parallel to S_3 fabric, and discontinuous along the intruded rocks. Some foliation veins were offshoots from the bedding veins in the metasedimentary rocks. A plethora of discordant veins crossed folds, foliations, and even cross-bedding, and perforated widest on meta-sandstone (Fyson, 1986). These discordant veins intruded after the development of F_3 folding and S_3 foliation (Fyson, 1986). The quartz veins were emplaced in the metasedimentary rocks within the Yellowknife Greenstone belt, synchronous to the greenschist to amphibolite metamorphism in the area, as well as with syn-deformation plutonism. Veining developed from bedding-style to echelon, and then to foliation-style veining and discordant veins within the metagreywackes (Fyson, 1986).

1.4 Yellowknife City Gold Project

TerraX Minerals, Inc. owns 780 sq. km of explorable land near Yellowknife, and is exploring and drilling extensions of both the Con and Giant mines in the Southbelt, Eastbelt, and Northbelt properties. Company reports reveal that the Kam and Banting Groups are hosts of the gold-bearing shears in the areas, respectively (Geovector Management, 2017, 2018). The acquisition, named the Yellowknife City Gold Project (YCGP), was originally explored in 2013 to investigate the annexes to the shear zones and associated mineralization in both the Con and Giant mines. Further tests within the Northbelt segment reveal the presence of extensions of mineralized shears and prospects along the strike of the main host body (Geovector Management, 2017), all found east and south of the Con Mine, and all close to the Yellowknife River Fault Zone, which display potential for future extraction. The Southbelt property was acquired last 2014 to discover potential prospects south of the two original mines, and this section of the property included the Con Mine's largest gold producer, the Campbell Shear. Late 2016 foresaw the purchase of the Northbelt Property, and it bears showings of possible gold-bearing porphyries and plugs (Geovector Management, 2017) in a felsic intrusive area next to

mafic volcanics. Updates on the mineralogical and geological associations among the several prospects in the Yellowknife City Gold Project are to be investigated to gain a better understanding on the relationships of the property with the Con and Giant mines.

1.5 Mineralogy of the Yellowknife Greenstone Belt

Manifold (1947) and Coleman (1957) presented the first studies on the mineral assemblages of the Akaitcho Property and Giant Mine in the Yellowknife Greenstone Belt. Coleman (1957) proposed three mineralizing, magmatically sourced fluids in the Yellowknife area, with the first period precipitating the Au-bearing sulphides (pyrite and arsenopyrite). The second and third periods were post-deformation mineralizing events, with the third was a result of the reaction of fluids with minerals from the second period. Sphalerite, chalcopyrite, and pyrrhotite from the second mineralizing stage exhibited rims bearing Pb and Sb-bearing minerals of the third period. Gold was introduced during each mineralizing pulse, and filled fractures in the sulphides (Coleman, 1957). Gold was primarily associated with both arsenopyrite and pyrite as fracture fills and refractory blebs. Experiments by Coleman (1957) to separate solid-solution Au within sulphides revealed that Au within sulphides only comprised a minor portion of the total Au budget of the Giant Mine. Aurostibite formed due to the reaction of Au with the fluids from the third mineralizing phase, and was contained at rims of Au, or rims between native Au and younger sulphosalts and sulphides (Coleman, 1957). Manifold (1947) executed a study of the Akaitcho Property, contained within the current Northbelt Property of the YCGP. Mineralization was sparse, and ore minerals were finely textured. Pyrite and arsenopyrite were intimately associated with each other and appeared as either euhedral crystals within quartz-carbonate gangue or fractured and veined by quartz-carbonate. Stibnite was associated with sulphosalts, and contained minute Au inclusions. Chalcopyrite and sphalerite were associated with both pyrite and pyrrhotite, and were contained in quartz-carbonate gangue. Later precipitation of Sb-bearing species was initiated by a decrease in the As content of the fluids. Wallrock alteration was not touched by ore solutions, but sericitized areas held more sulphides. Chlorite content increased away from the ore, a good proxy for finding mineralized portions.

Van Hees et al (1999) studied the geochemical variations within the Giant Mine, and presented the role of metasedimentary rocks in Au mineralization. Na acted as the reflection of hydrothermal alteration, where $\text{Na}_2\text{O}/\text{Zr}$ ratios of 300-600 were consistent within all altered rock units. In alteration zones with low $\text{Na}_2\text{O}/\text{Zr}$, enrichment of K_2O was observed, and crosscut both metavolcanic and metasedimentary host rocks. In zones with anomalous As, Ag, S, and Sb, sericite was indicative of the reaction of ore-depositing fluids within such zones. Anomalous Sb and As were due to the influence of metasedimentary rocks, as fluids removed both Sb and As from the metasedimentary rocks (van Hees et al, 1999).

A study of the mineralogy of the Kam and Banting Group rocks at the northern end of the greenstone belt was done by Smith (2011). Sphalerite existed within the Kam Group as fracture infills and grain boundary replacements of early arsenopyrite and pyrite, or as larger masses within galena. The Banting Group, on the other hand, showed sphalerite infills within early arsenopyrite and late pyrrhotite fractures, and it was intergrown with galena. Smith (2011) believed that sphalerite was a component of a late-stage base-metal mineralizing event. Arsenopyrite grains hosted within the Kam Group exhibited no compositional zoning, while those from the Banting Group displayed, from core to rim, a decrease in S content, and increase in both Fe and As. Distinct fluid rock reservoirs for both the Kam and Banting Groups were proposed due to the lack of overlap in $\delta^{18}\text{O}$ values from fluid inclusions from both groups. Smith's (2011) work disproved the interaction of fluids between the metavolcanics and metasedimentary rocks, as earlier proposed by van Hees (1999), and stated that the metavolcanic and metasedimentary-hosted Au deposits and Yellowknife had distinct fluid sources.

1.6 Invisible Gold

Certain theories on the presence of invisible gold in the Yellowknife Greenstone Belt have been present over the years, yet there are no studies directly probing on its presence within the area. Refractory gold was known to be present in the YCGP, starting with Coleman (1957) explaining Au existing as refractory blebs within pyrite-arsenopyrite. After this, there were no works looking on the association of Au with sulphides on other mineralized sections of the Yellowknife Greenstone Belt.

Invisible gold was discovered by Burg (1930) while working on pyrites in Romania via optical microscopy. Boyle (1979) later classified invisible gold into either present in chemical combination in the pyrite and arsenopyrite, and in a submicroscopic state. Cook and Chryssoulis (1990) provided a more concise definition of invisible gold as either 1) lattice-bound gold or 2) gold nanoparticles. Their work involved analyzing multiple sulphides (pyrrhotite, arsenopyrite, pyrite, galena, marcasite, chalcopyrite, tetrahedrite-tennantite, bornite) for any invisible gold signatures using dynamic secondary ion mass spectrometry (D-SIMS) and electron microprobe microanalysis (EPMA). Cook and Chryssoulis (1990) suggested that arsenopyrite and arsenian pyrite are ample hosts for high invisible gold, and other sulphides exhibit insignificant values. Arsenopyrite was the main host for invisible gold, incorporating oxidized Au into its structure, while pyrite demonstrated abundance of structural gold with the enrichment of As, and finer grains were discovered to host higher invisible gold concentrations. Other sulphides such as pyrrhotite, marcasite, and others common in environments where pyrite and/or arsenopyrite existed only incorporated minor gold concentrations (Cook and Chryssoulis, 1990), but the study showcased the ability of sulphides, especially pyrite and arsenopyrite, in containing gold in their structure. Au^{3+} substituted for Fe^{3+} in the arsenian pyrite structure to balance the addition of As (Cook and Chryssoulis, 1990). Introduction of As in the pyrite structure produced $[\text{AsS}]^{3-}$ pairs, balanced by As^{3+} , Au^{3+} , and other trivalent cations. Arsenopyrite, on the other hand, already possessed the $[\text{AsS}]^{3-}$ modified structure, and was readily available for Au^{3+} substitution for Fe^{3+} .

Invisible gold is found in numerous types of deposits, such as orogenic gold (Meyer and Saager, 1985; Goldfarb et al, 1988, Cabri et al, 1989; McKeag and Craw, 1989, Cook and Chryssoulis, 1990; Witt, 1991; Neumayr et al, 1993; Mumin et al, 1994; Oberthur et al, 1997; Tarnocai et al, 1997; Genkin et al, 1998; Ashley et al, 2000; Saha and Venkatesh, 2002; Vaughan and Kyin, 2004; Zacharias et al, 2004; Morey et al, 2008; Sung et al, 2009; Large et al, 2011; Cook et al, 2013; MacKenzie et al, 2015), Carlin-type gold (Wells and Mullens, 1973; Simon et al, 2009; Palenik et al, 2004; Large et al, 2011;), large igneous provinces (Foya et al, 1999), and epithermal deposits (Cepedal et al, 2008; Deditius et al, 2008; Morishita et al, 2008; Deditius et al, 2014). Several techniques can discern the type of refractory gold inside sulphides, such as optical microscopy, chemical

dissolution, electron microprobe, secondary ion mass spectrometry, and Mössbauer spectroscopy (Cabri et al, 1989; Cook and Chryssoulis, 1990). Initially, these techniques demonstrated the presence of structural gold in bulk sulphides, and Cabri and others (1989) attempted to analyse individual grains for invisible gold. Experiments using D-SIMS, EPMA, and high-resolution transmission electron microscopy (TEM) uncovered the presence of invisible gold reaching 912 to 4400 ppm in arsenopyrite. Benzaazoua et al (2007) examined arsenopyrite grains via scanning electron microscopy, electron microprobe, secondary ion mass spectrometry, Mössbauer spectroscopy, and transmission electron microscopy, revealing presence of invisible gold correlated with high As, and within the rims of arsenopyrite. Pyrite grains, on the other hand, displayed variable Au contents dependent on As content. Zoning in pyrite and arsenopyrite showed positive correlation of Au and As, but not the reverse (Benzaazoua et al, 2017). Based on these studies, invisible gold is associated with elevated As content in pyrite, and with arsenopyrite.

Orogenic gold provinces are known to document invisible gold, i.e. within the As-bearing growth bands in both pyrite and arsenopyrite. The study of Au speciation and distribution in arsenopyrite and pyrite grains of the Ashanti Gold Belt in Ghana revealed the presence of both structural and nanoparticle-sized gold in arsenian pyrite and arsenopyrite (Mumin et al, 1994). Gold was concentrated along grain fractures and boundaries due to redistribution of Au during metamorphism. Au was initially incorporated in the structure of both arsenian pyrite and arsenopyrite, and were forced out from the lattice to migrate to voids and fractures within sulphides, to the grain margins, and out of the crystals (Mumin et al, 1994; Oberthur et al, 1997). Metamorphic processes decreased the refractory properties of the host mineral, squeezing structural Au out of the sulphide structure (Mumin et al, 1994). Au migrated as colloidal (nanoparticle) and micron-sized particles in fractures and voids, and then to grain boundaries, before being expelled and concentrated outside the precursor sulphides (Mumin et al, 1994). This method of Au mineralization contradicted the multi-stage Au mineralization concept of Bonnemaïson and Marcoux (1990), where invisible Au initially precipitated, and eventual dissolution by late sulphide-bearing hydrothermal fluids locked invisible gold in the sulphides precipitated by such late fluids. Mumin et al (1994) and Oberthur et al's (1997)

assumption was supported by Cook and others (2013) with evidence from pyrite and arsenopyrite grains from the Tanami Gold Province in Australia. Sulphides exhibited anomalous Au concentrations along grain margins, microfractures, and porous portions within sulphides. Along with Au, Bi and Pb were concentrated within microfractures and grain boundaries. Sulphide cores were Au-poor, while zones were practically enriched in Au, Co, Ni, Se, Sb, and Te. Cook and others (2013) believed that the elements were enriched along microfractures and zones due to their release during brittle deformation, which supported Mumin et al's (1994) claim that Au and other elements were released from the sulphide structure due to the decrease in its refractory properties.

Other techniques attempted to understand the speciation of invisible gold hosted in sulphides. Cabri and others (2000) examined arsenopyrite from four orogenic gold deposits via X-ray absorption near edge structure (XANES), supporting data collected from electron microprobe and secondary ion mass spectrometry. The Au L₃ (11919 eV) absorption line was collected for the arsenopyrite samples, and edge shifts were analysed to compare with standards of known Au valence. High concentration of As in the grains interfered with the Au edge shifts due to the background interference of As (As Ka – 11867 eV) (Cabri et al, 2000). Data gathered from Mössbauer spectroscopy (Genkin et al, 1998) were compared with linear combination fitting results from XANES measurements, and Cabri and others (2000) found that metallic Au (Au⁰) existed as gold nanoparticles in arsenopyrite samples from the Olympiada mesothermal gold deposit in Siberia. On the other hand, structural Au in arsenopyrite were recognized in three other mesothermal deposits (Sheba, São Bento, Sentachan), with Au enrichment along growth zones for Sheba and São Bento, and heterogenous Au distribution in the arsenopyrite from Sentachan samples. (Cabri et al, 2000). Results from Cabri and others' (2000) XANES analyses were compared with electron microprobe, SIMS, and Mössbauer spectroscopy data, and the two latter techniques complement the XANES results, revealing an alternative methodology for nondestructive, *in-situ* analysis of Au speciation in ore samples.

1.7 Local Geology

1.7.1 Summary of the Yellowknife City Gold Project

Seven prospects within the Yellowknife City Gold Project are drilled in drilling periods from 2014 to 2017, as well as core archived from the Giant Core yard. Details regarding the geology and structural information regarding the prospects are gathered from the August 2017 and January 2018 reports (Figures 3 and 4) (Geovector Management, 2017, 2018).

1.7.1.1 Ryan Lake Target

1.7.1.1.1 Crestaurum

The Crestaurum deposit is a multi-stage quartz-carbonate vein within mafic volcanics, oriented northerly to north northeastern, and dips vertically to 50° east. Alteration minerals within the rocks in the deposit include quartz, sericite, and chlorite, outward from centre of mineralization. Pervasive carbonatization is also present, as well as high Au percentages within quartz veining.

1.7.1.1.2 Barney Shear and Porphyry

The Barney Shear is a wide, multi-kilometre deformation zone with wide shears bearing plentiful quartz-carbonate veins which also enclose sulphides. A north-south mineralized zone dips sub-vertical to 50°. The best mineralization styles are hosted within shear flexures that plunge flatly, as veins and pods. The gold to silver ratio of the deposit is at 1:10. The porphyry intrusion, on the other hand, is laden with stockwork quartz and carbonate alteration, and bore significant enrichment of chalcopyrite, Mo, and Ag.

1.7.1.1.3 Hébert-Brent

The Hébert-Brent deposit is a deposit exhibiting sericitic alteration with replacement-style Au located within arsenopyrite- needles, and rare to absent quartz veining. Mineralization is restricted within a flat plunging zone, hosted within mafic volcanic and intrusive rocks cut by felsic porphyry dykes. The deposit strikes at 120 degrees, and dips

90 degrees with respect to the shear fabric. The felsic intrusive outside the deformation zone does not exhibit traces of mineralization

1.7.1.2 Sam Otto Target

1.7.1.2.1 Dave's Pond

Dave's Pond is a shear hosted, multi-stage quartz-carbonate vein deposit within felsic and mafic volcanics, and demonstrates multiple sulphide occurrences. Sericitization is prevalent in the deposit's core zone, which progressed into chlorite outward. The deposit is hosted within felsic to intermediate volcanic rocks located within a major crustal tear, and the footwall of Dave's Pond is seen to be akin to that of the Con Shear Zone.

1.7.1.2.2 Sam Otto

The Sam Otto deposit is an unusual low grade, bulk tonnage deposit with a sericitized intermediate to felsic volcanic host, and is the largest deposit in the Yellowknife City Gold Project. Finely disseminated sulphides are discovered within a N-S striking, subvertical dipping host.

1.7.1.3 Walsh Lake Target

1.7.1.3.1 Mispickel

The Mispickel deposit is situated within wide (>200 m) deformation zones with plentiful quartz veins. Such veins are found to host visible Au and sulphides such as pyrite, arsenopyrite, and pyrrhotite. There are hints of biotite presence, as well as subtle sericitization and chlorite alteration. The deposit strikes northwards, and dipped almost vertically, exhibiting a steep to moderate southerly plunge. The prospect hosts high-grade Au lodes, which can reach almost 200 g/t. The mineralized zone is within isoclinally folded turbidites, revealing steep to almost vertical southerly axes.

1.7.1.4 Homer

The Homer target is a base metal (Zn-Pb) deposit which exhibits relatively high Au and values (1-100 g/t Au) over a 2 km zone. As of January 2018, TerraX is eager to drill over the zone to better understand pervasive mineralization.

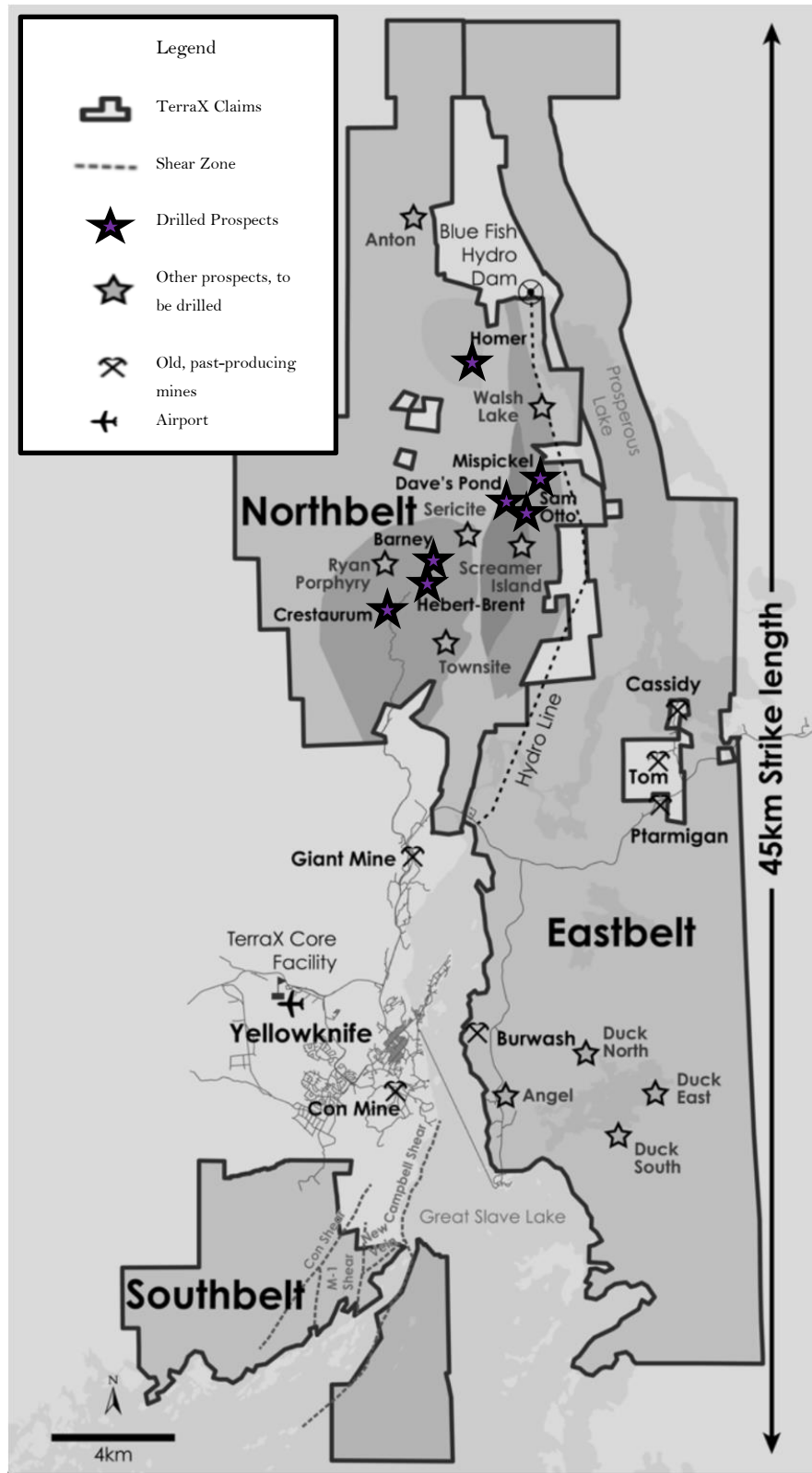


Figure 3. Map of the Yellowknife City Gold Project, with the seven prospects in purple stars. Modified from Geovector Management, 2018.

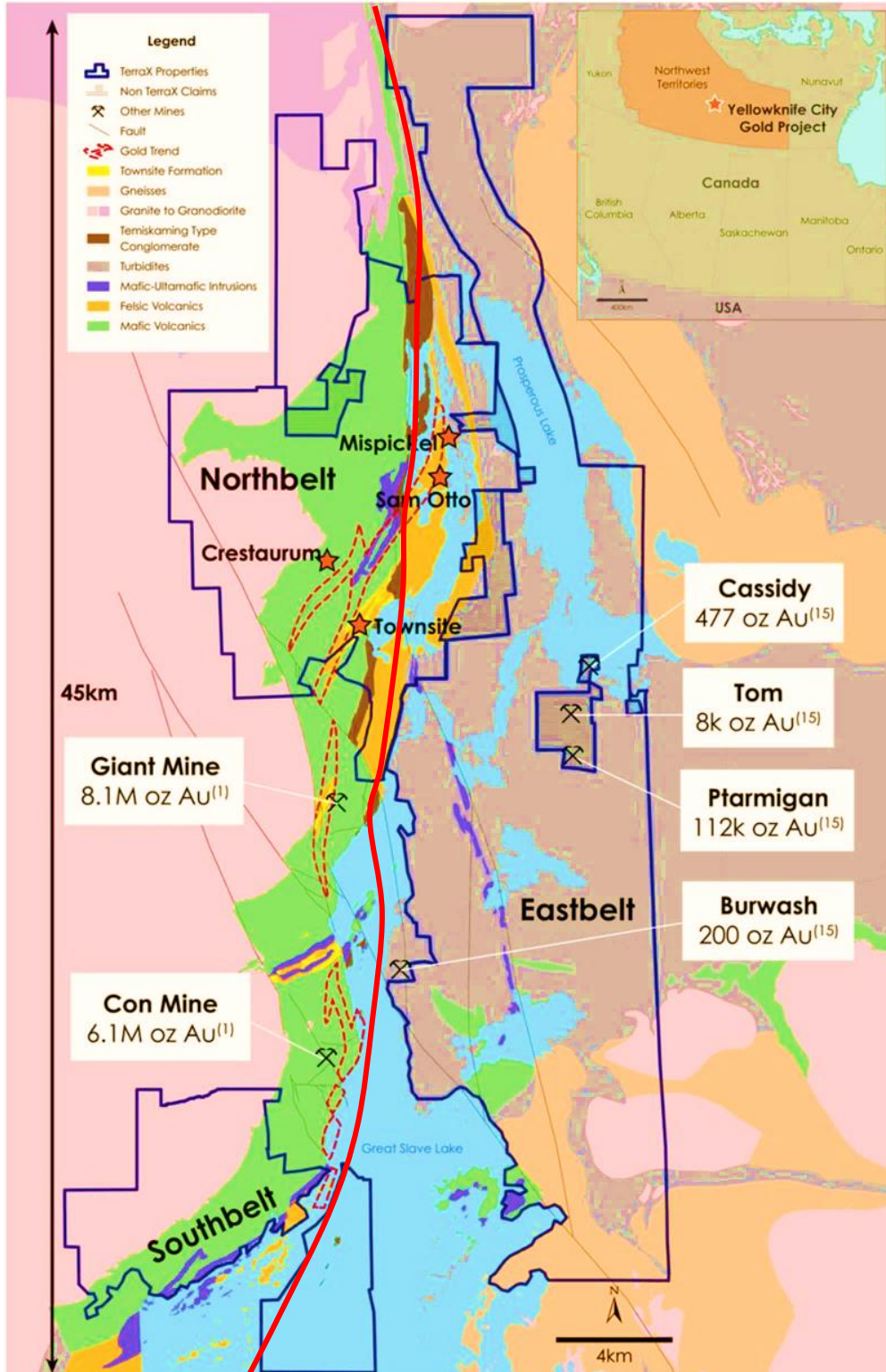


Figure 4. Generalized geology of the Yellowknife City Gold Project, modified from Geovector Management (2017). Mapped faults are marked in black, and approximation of the Yellowknife River Fault Zone in red.

Table 1. Summary of the mineralization styles within the Northbelt section of the Yellowknife City Gold Project, with the boldfaced prospects studied in this thesis (data summarized from Geovector Management, 2017).

Prospect	Mineralization Style
Crestaureum	Narrow shear hosted multi-stage quartz (ankerite veining); Low to moderate sulphides; arsenopyrite, pyrite, stibnite; core zone sericitization outward to chlorite within mafic volcanics and intrusive; mineralization as py, arsenopyrite, Au, stibnite, chalcopyrite, sph, galena, and other quartz-veining associated minerals; Au associated with sericite, minor chlorite; high Au within steeply-plunging structures controlled by a poorly-studied feature; can bear 200 g/t Au in veins
Barney Shear	Wide (>200 m) long lived strike trend deformation zones; with coarse grained moderate to high massive sulphides (arsenopyrite, py, gal, chalcopyrite, po, sph); within sericitic alt surrounded by carbonate alt; in mafic volcanics and intrusives with proximal ultramafic volcanics and intrusives; surface exposures as 1-5 m wide brown carbonate veins, common within deformation zone; lode-like gold distribution, with lower Au closer to where porphyry and shear intersects quartz veins and massive sulphides with >30 g/t Au, >200 g/t Ag ~7% Pb
Hébert-Brent	Flat plunging zones with sericite alt; replacement-style Au-bearing fine to medium-grained sulph such as py, needle arsenopyrite along contacts of and within felsic intrusive porphyry dykes intruding mafic volc and intrusive; quartz veining rare to absent; 1-5 g/t Au related to felsic intrusive; ~30 g/t Au related to contact mafic rock (hanging and footwall contacts)
Sam Otto	Wide (~120 m) shear hosted finely disseminated sulphides such as pyrite and arsenopyrite; 0.1-5 g/t Au over 30-120 m widths; sheared and sericitized within intermediate to felsic fragmental volcanic rocks; rare >3 g/t Au, but considered to be the largest system within the YCGP
Dave's Pond	Narrow discrete shear-hosted multi-stage quartz-ankerite veining within the main crustal break in the Yellowknife district, with moderate sulphides (arsenopyrite, pyrite, stibnite), with core zone sericitization outward to chlorite; hosted within felsic to intermediate volcanic rocks; 30 g/t Au
Mispickel	Wide (>200 m) deformation zones with shears bearing abundant narrow (1-50 cm) quartz veins with coarse grained visible gold and low to moderate sulphides (arsenopyrite, pyrite, pyrrhotite) within subiotite chloritic to sericitic alteration; hosted within turbiditic sediments; weathered 2-7 m oxidised highly fissile shear zones on surface; quartz veins with biotite and ~300 g/t Au
Barney Porphyry Zone	Porphyry intrusion hosted quartz vein stockworks w/ carbonate alt and sericitic edges on veins ~1 m wide with 30 g/t Au, sulphides and base metals such as chalcopyrite, Mo, and Ag
Homer Lake Base Metal	Shear controlled disseminated to massive base metal; sphalerite, galena, arsenopyrite, pyrite, chalcopyrite; 200 g/t Ag and 10 g/t Au; hosted w/in mafic volcanics and felsics (high level intrusive to extrusive); sulphide zones 1-7 m wide with max 20% Pb+Zn (average 5-7 %)
Homer Lake Gold	Fracture and/or shear ctrlled quartz-carb veins with ±ser-chl-carb alt and ± base metal (Zn, Pb) and Ag (~100 g/t); mineralization controlled by N-trending deformation zones

1.8 Synchrotron Radiation

Synchrotrons were primarily utilized for studying nuclei, but were later discovered to produce light with variable wavelengths for a variety of purposes (Aquilanti et al, 2015). Third-generation synchrotron facilities are constructed for such experiments, tackling on topics such as structural biology, condensed matter physics, earth sciences, and others (Aquilanti et al, 2015). Synchrotron radiation is generated by accelerating electrons by magnetic fields at relativistic speeds along curved trajectories (Balerna and Mobilio, 2015). Typical synchrotron facilities are composed of an electron gun, linear accelerator, booster ring, storage ring, bending magnets, and insertion devices (Wilmott, 2018). Linear accelerators receive accelerated electrons in vacuum from the electron gun, booster rings raised electron energies, and storage rings held electrons in relativistic velocities and GeV-level energies. Beamlines are attached into either bending magnets or insertion devices, where bending magnets keep electrons in a closed path and force electrons to emit light due to their curved trajectory; or into insertion devices where brilliance increases compared to bending magnets due to a special arrangement of N-S, S-N dipole magnets (Wilmott, 2018). Beamlines provide intense, monochromatic, parallel X-rays with a small source point. Beamlines are composed of radiation-cleaning front end optics, primary optics with slits and monochromators, beamline optics which clean up the radiation, and detectors which convert signals from chemical reactions, visible light, and electrons emitted by samples upon interaction with X-rays.

1.8.1 Application of Synchrotron Spectroscopy in the Natural Sciences

Several studies attempted to utilize the high brightness of synchrotron facilities to understand a variety of questions which cannot be fully answered by conventional laboratory equipment. Yang et al (2013) investigated Cu speciation in soils via bulk XANES and EXAFS for remediation. Mumm et al (2010) used 3- and 4-dimensional X-ray Tomography to study fluid motion in geological processes, such as upper crust convection of fluids. Henderson et al (1995), on the other hand, studied the geological applications of synchrotron radiation using mostly X-ray Absorption, Fluorescence, and Diffraction, with XRF for discovering XANES spots, XRD analysis of synthetic leucites

for determining structure and studying compressibility, and XANES for revealing Fe oxidation states in synthetic leucites. Fuisseis et al (2013, 2014) utilized X-ray microtomography to investigate significance of fluid-rock interaction within reservoirs, as well as structural geology and rock mechanics. Brugger et al (2010) investigated trace element variations in minerals using synchrotron radiation for fluid inclusion studies, soil carbonates for geochemical Au exploration, redox state of fluids, and invisible Au within arsenian pyrite and arsenopyrite. Bassett and Brown (1990) summarized several applications of synchrotron radiation in geology, such as XAS experiments of crystalline and noncrystalline materials, XRD studies of high pressure/temperature materials, and spatial XRF analysis of several materials for compositional variations. Liu et al (1989) compared results of synchrotron radiation with other geochemical techniques such as electron microprobe (EPMA), particle-induced X-ray emission (PIXE), particle-induced gamma-ray spectroscopy (PIGE), nuclear reaction analysis (NRA), and secondary-ion mass spectroscopy (SIMS). These works proved the advantages of synchrotron radiation over conventional sources, such as the use of smaller sample sizes due to efficient focusing of the beam through mirrors, and the ability to selectively excite certain elements with the use of monochromators.

1.9 Synchrotron Techniques in the Project

Three synchrotron spectroscopy techniques were utilized in this project to investigate mineralogical and geochemical associations of the rocks within the Yellowknife Greenstone Belt. Such techniques proved efficient in collecting data for later interpretation of the relationships between the Northbelt Property and the Geological Survey of Canada's Extech III: Kerswill Sample Suite.

X-ray fluorescence is a technique where an electron from the inner shell of an atom is ejected due to the introduction of photons from an X-ray source. One outer shell electron will fill up the missing electron from the innermost shell, releasing a photon with a characteristic energy and wavelength, which will be used to identify the element of interest. X-ray fluorescence can also be utilized to create two-dimensional element distribution maps (i.e., Figures 5 and 6). X-ray diffraction, on the other hand, reflects the

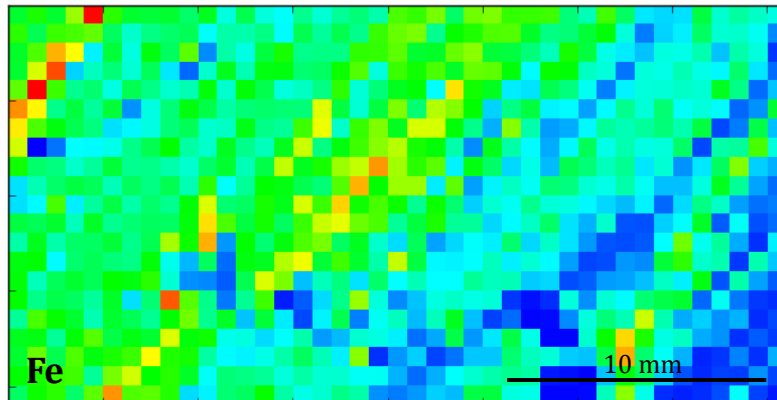


Figure 5. Sample X-ray Fluorescence map of the the Fe content of a mafic volcanic with patchy chlorite and disseminated arsenopyrite needles.

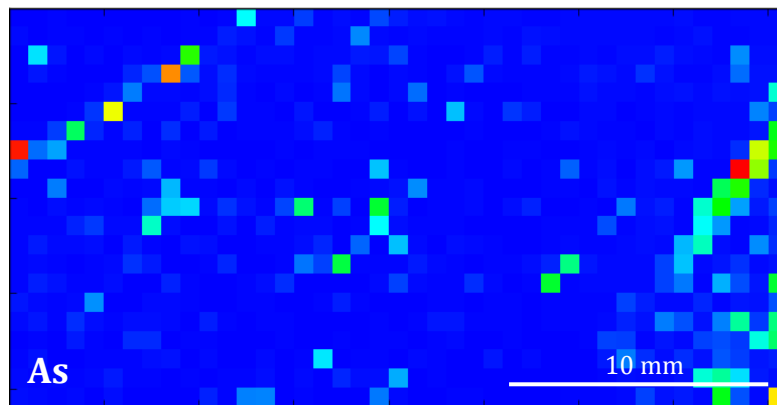


Figure 6. Sample X-ray fluorescence map of the same sample in Figure 4. Green to red spots indicate abundance of arsenopyrite.

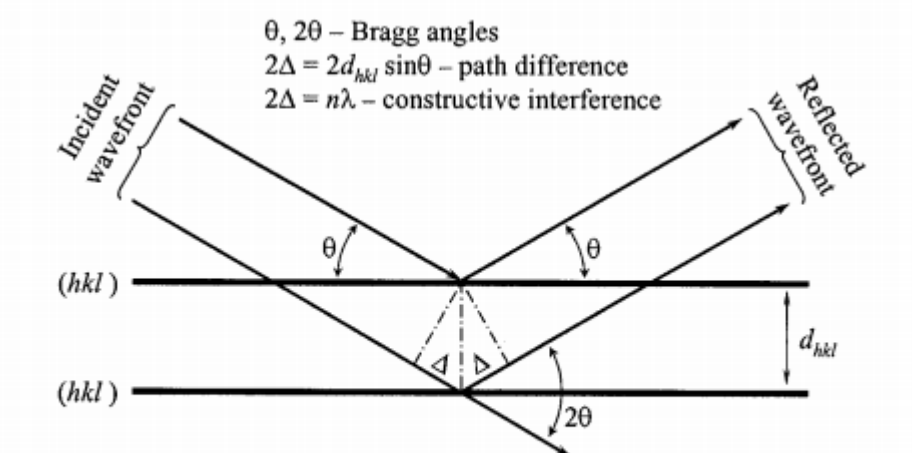


Figure 7. Interpretation of Bragg's Law, from Pecharsky and Zavalij, 2005

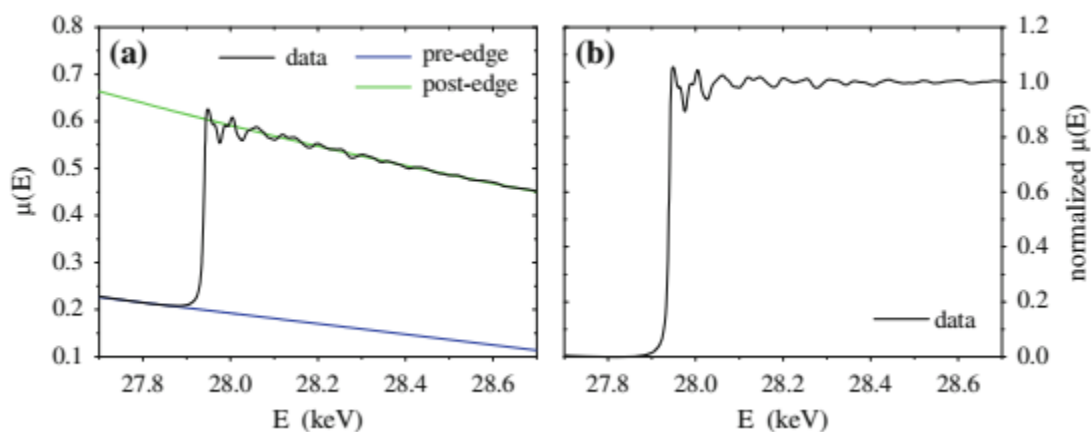


Figure 8. (Left) Raw data of XANES of InP, shown with fitted pre-and post-edge lines. (Right) Normalized data of the left spectrum. From Schnohr and Ridgway, 2015.

internal arrangement of the atoms in a mineral specimen. Using Bragg's Law (Figure 7), the calculation of d-spacings for each 2θ value given by the diffractometer is used to identify the mineral phases present in a sample. Powder diffraction of sample pulps are performed to look for mineral associations among the numerous prospects of the company. X-ray Absorption Near Edge Structure (XANES) spectroscopy is a technique which deals with identifying photoelectron transitions to empty bound states. Since this technique is critical with chemical bonds, it can be used to decipher oxidation states of an element of interest, such as Figure 8. Identification of oxidation states via XANES is performed by examining the behaviour of the near-edge spectrum of the element of interest, and comparing with the spectra of known standards through visual inspection, or linear combination fitting (explained further in Chapter 5).

1.10 Other complementary techniques for synchrotron spectroscopy

Several techniques complement the results gathered by synchrotron spectroscopy techniques such as SR-XRF and SR-XRD. Quantitative Evaluation of Materials by Scanning Electron Microscopy (QEMSCAN) and Mineral Liberation Analysis (MLA) are techniques integrating backscatter electron imaging and energy-dispersive X-ray spectroscopy to identify minerals, and define distribution and liberation characteristics in crushed samples, grain mounts, and even polished sections. Several authors have utilized QEMSCAN and MLA to look for indicator minerals in petroleum prospects (Sliwinski et al, 2009; de Block et al, 2015), process mineralogy (Lotter et al 2003, 2011a, 2011b, 2013; Baum, 2004), and exploration (Santoro et al 2014, 2015; Pirrie et al 2011; Grammatikopoulos et al 2011; Gabler et al, 2011; Field and Atkins, 2012). Results gathered from QEMSCAN and MLA are also compared with complementary technologies such as X-ray diffraction and X-ray tomography (Li et al, 2007). X-ray tomography is a nondestructive technique to decipher 3-dimensional mineral distribution in a variety of samples, such as drill cores (Godel, 2013), and is complemented by diffraction and fluorescence studies as well. Hyperspectral logging is another nondestructive technique in exploring for metallic deposits, such as the gangue minerals correlated to metallic minerals are readily seen (Yang et al, 2011). Hydrothermally

altered deposits, such as REEs (Möller and Williams-Jones, 2018), porphyry copper (Holliday and Cooke, 2007), and even orogenic Au (Huntington, 2016) were explored and their cores mapped via hyperspectral mapping to create a library of minerals and alteration patterns directly on half cores. Laser ablation Inductively Coupled Plasma-Mass Spectrometry (LA ICP-MS) is another complementary technique to synchrotron studies on mineralized samples, such as the one done by Lintern et al (2009) to investigate invisible gold in calcrete in Western Australia. LA-ICPMS, synchrotron XRF, and XANES were used to investigate the method of Au remobilization in soils in the Bounty Gold Deposit (Lintern et al, 2009). Other *in-situ* analyses using LA-ICPMS were done on garnets (Zhai et al, 2014), metavolcanics for dating (Storey et al, 2007), and galena (2014). LA-ICPMS is destructive, with ablation spots eliminating the opportunity for further studies on that same area to confirm and compare results. Micro X-ray fluorescence using a benchtop machine (Tonzetic, 2017) is also complemented by synchrotron micro-XRF, with the former working similar to the principles of MLA and QEMSCAN.

1.11 Purpose

Since the acquisition of the 780 sq. km Yellowknife City Gold Project, TerraX Minerals, Inc. has been determined to gather additional drill cores in select prospects for future mine development. Gold residence is not fully understood, due to the lack of prior studies on the potential presence of structural gold in sulphides, and information regarding gold residence will allow better planning for actual mining operations. The relationships of the Con and Giant mines with other prospects in the YCGP are still unclear due to lack of information. Offering the company novel techniques, such as synchrotron X-ray fluorescence mapping and X-ray absorption near edge structure spectroscopy, will increase confidence on data gathered and modeled by the company's geoscientists. In the scientific standpoint, additional knowledge on the associations of the mineralized zones, as well as deciphering overprinting relationships, will be beneficial in understanding how world-class deposits such as the Con and Giant mines developed.

1.12 Objectives

The Northbelt Property exhibits nine possible styles within the property, all initially identified to be likely related to Con-style mineralization (Table 1). Investigation of the similarities of the prospects of the Northbelt Property and the mineralized sections of the Yellowknife Greenstone Belt will provide more information if these are part of a single, giant mineralizing source. Mineralogical similarities and relative timing of mineral formation, examined via geochemical signatures, textures, crosscutting, and overprinting relationships, will also increase the understanding of the processes that were occurring during the formation of the mineralized sections of the Yellowknife Greenstone Belt. The association of gold with alteration minerals will be studied to simplify the current knowledge of different relationships of Au within each prospect (Table 1). The oxidation state of gold will be revealed, determining if gold is either metallic or structural, which will affect decision-making on processing and extraction of Au. This project also aims to apply synchrotron spectroscopy techniques in the earth sciences, allowing the use of a large sample suite to understand mineralization, alteration patterns, and crosscutting relationships in a sizeable project such as the Yellowknife City Gold Project.

1.13 Impact

The knowledge on the relationships of the numerous prospects of the property will be helpful in deciphering the timing of mineralization, as well as delineating possible extensions of the Northbelt Property exhibiting similar patterns with the Con and Giant Mines. Association of gold with mineralization periods, as well as its oxidation state, will allow the company to identify the most reasonable extraction methods upon production. Showing the utility of novel techniques such as synchrotron techniques for more rapid, accurate, *in-situ* analyses of a plethora of half cores and slabs will prove useful not just for the company, but for students aiming to utilize similar methods in mineral exploration, providing better alternatives on conventional, lab-based equipment. The techniques used in this project are not limited to mineral exploration, but can also be used in process mineralogy studies of mill feeds, and even remediation of tailings and waste material.

1.14 Scope and Limitations

Seventy-one representative half cores and slabs, with their corresponding rock pulps and powders from both the YCGP Northbelt Property and Kerswill Suite were provided for the study to identify geochemical, textural, and mineralogical associations within the Yellowknife City Gold Project. Thin sections were not prepared for the study, since the project was intended to prove that macro-scale X-ray fluorescence maps are adequate for identifying geochemical and textural associations, showing that the technique can be complementary to petrography, providing more information even before selection of sections of the half core to be cut and polished. Only the surfaces of the slabs and half cores were mapped using SR-XRF, thus it is possible that gold may not be directly analysed. Limited beam time is also a factor in choosing the best possible samples for analyses, especially for XANES spectroscopy, thereby also affecting the design of the experiments.

Chapter 2

2 Methods

2.1 Sample Selection

This project was done in cooperation with TerraX Minerals, Inc. on seven prospects of the Northbelt Property. Fifty-eight drill core sections from twenty-two drill holes of the seven prospects were gathered based on the complexity of alteration patterns, best representing areas of mineralization contained within various types of lithology. Core sections were collected from the company's 2013 to 2017 drill periods, with focus on areas of geophysical anomalies close to the main fault zone, sections of pervasive wallrock alteration or greenschist to amphibolite metamorphic facies, and locations where high-grade grab samples were initially collected. Sections from the Giant Core yard were also included, as these were originally drilled from two prospects (Crestaurum and Barney). These sections were selected to complement fourteen slabs from the Geological Survey of Canada's Extech III: 3D Drillhole Database for the Yellowknife Mining Camp (Kirkham et al, 2003), aptly named the Kerswill Suite. These slabs represent mineralized sections of the Yellowknife City Gold Project, focusing on the Con and Giant Mines. Thirty-nine rock powders from the Kerswill Suite were also provided, including powders from the fourteen slabs, to represent other mineralized sections of the Yellowknife Greenstone Belt. Rock pulps of the half cores from prior geochemical and assay studies were retrieved, while rock powders from the slabs were also provided by the GSC. Thirty-two rock pulps from the original fifty-nine samples from TerraX and thirty-nine rock powders from the Kerswill Suite were chosen for mineralogical studies and prepared in-house at Western University. Pulps and powders were mounted in 2 cm polyimide tubings, also called capillaries (outer diameter - 0.05461 cm, inner diameter - 0.04953 cm), sealed with super glue on both ends, and mounted on B3S ALS-style reusable goniometer bases. Samples were selected based on Au and As contents of low to high grade sections to represent mineralization trends within the YCGP.

Table 2. Hole IDs and locations of the TerraX Northbelt samples. SCH – schist, MVL – mafic volcanic, SDS – sedimentary sand, IVL – intermediate volcanic, POR – porphyry, MAI – mafic intrusive, INI – intermediate intrusive, FVL – felsic volcanic, VEI – vein

Belt	Prospect	Zone	Hole ID	Sample ID	Dip	Azimuth	Easting	Northing	From	To	Lith1
Northbelt	Barney		NB-95-16-W1	R115609					335.66	335.79	SCH
Northbelt	Barney		NB-95-16-W1	R115621					343.67	343.82	MVL
Northbelt	Barney		NB-95-16-W1	R115622					344.64	344.77	MVL
Northbelt	Barney		NB-95-16-W1	R115604					331.94	332.89	VEI
Northbelt	Barney Porphy	Porphyry	TBY16-013	S519135					518.97	519.09	INI
Northbelt	Hebert-Brent		TCG16-034	S520992	-80	30	636796	6942503	2.04	2.19	POR
Northbelt	Hebert-Brent		TCG16-034	S520998	-80	30	636796	6942503	7.45	7.58	MAI
Northbelt	Hebert-Brent		TCG16-040	S521155	-60	30	636834	6942469	2.00	2.10	MVL
Northbelt	Hebert-Brent		TCG16-052	S521365	-45	135	636817	6942499	17.89	17.99	POR
Northbelt	Hebert-Brent		TCG16-052	S521371	-45	135	636817	6942499	22.43	22.58	POR
Northbelt	Crestaaurum		TCR15-003	R432247			635712	6941567	99.54	99.69	SCH
Northbelt	Crestaaurum		TCR15-003	R432250			635712	6941567	100.47	100.59	SCH
Northbelt	Crestaaurum		TCR15-052	R433857	-45	304	635739	6941688	51.19	51.34	SCH
Northbelt	Crestaaurum		TCR15-052	R433866	-45	304	635739	6941688	56.72	56.84	SCH
Northbelt	Homer		THL16-008	S345459	-47	90	638195	6950030	33.94	34.05	MVL
Northbelt	Homer		THL16-008	S345464	-47	90	638195	6950030	37.89	38.02	MVL
Northbelt	Homer		THL16-009	S345537	-47	90	638195	6950005	18.69	18.83	MAI
Northbelt	Homer		THL16-009	S345563	-47	90	638195	6950005	43.88	43.99	MAI
Northbelt	Homer Lake		THL16-010	S520925	-62	120	638259	6950234	196.59	196.70	MAI
Northbelt	Barney		TNB14-010	R115110					134.08	134.25	MVL
Northbelt	Barney		TNB14-010	R115123					143.10	144.00	MVL
Northbelt	Sam Otto	Hanging Wall Zone	TSO16-006	V156522	-45	270	639810	6944845	21.00	22.00	MVL
Northbelt	Sam Otto	Hanging Wall Zone	TSO16-006	V156527	-45	270	639810	6944845	26.00	26.50	MVL
Northbelt	Sam Otto	Hanging Wall Zone	TSO16-006	V156517	-45	270	639810	6944845	17.00	18.00	MVL
Northbelt	Sam Otto	Hanging Wall Zone	TSO16-006	V156518	-45	270	639810	6944845	18.00	19.00	MVL
Northbelt	Sam Otto	Hanging Wall Zone	TSO16-006	V156519	-45	270	639810	6944845	19.00	20.00	MVL
Northbelt	Sam Otto	Hanging Wall Zone	TSO16-006	V156526	-45	270	639810	6944845	25.00	26.00	MVL
Northbelt	Daves Pond	Hanging Wall Zone	TSO17-019	V160414	-45	270	639658	6945159	62.50	63.54	FVL
Northbelt	Daves Pond	Foot Wall Sb Zone	TSO17-019	V413119	-45	270	639658	6945159	341.70	342.70	MVL
Northbelt	Daves Pond	Hanging Wall Zone	TSO17-019	V413124	-45	270	639658	6945159	346.30	346.42	IVL
Northbelt	Daves Pond	Hanging Wall Zone	TSO17-019	V413125	-45	270	639658	6945159	347.79	347.90	IVL
Northbelt	Daves Pond	Foot Wall Sb Zone	TSO17-020	V413294	-45	270	639577	6945151	265.85	266.90	IVL
Northbelt	Daves Pond	Foot Wall Sb Zone	TSO17-020	V413296	-45	270	639577	6945151	267.75	268.50	IVL
Northbelt	Daves Pond	Foot Wall Sb Zone	TSO17-020	V413285	-45	270	639577	6945151	258.98	259.11	IVL
Northbelt	Sam Otto	Main Zone	TSO17-025	V890298	-45	270	639860	6944902	161.96	163.00	MAI
Northbelt	Sam Otto	Hanging Wall Zone	TSO17-027A	V892232	-65	270	639899	6944551	193.05	193.85	IVL
Northbelt	Sam Otto	Hanging Wall Zone	TSO17-027A	V892234	-65	270	639899	6944551	194.85	196.00	IVL
Northbelt	Sam Otto	Main Zone	TSO17-027A	V892336	-65	270	639899	6944551	306.75	307.80	IVL
Northbelt	Sam Otto	Main Zone	TSO17-027A	V892341	-65	270	639899	6944551	311.00	312.00	IVL
Northbelt	Sam Otto	Main Zone	TSO17-027A	V892345	-65	270	639899	6944551	314.60	315.60	IVL
Northbelt	Sam Otto	Hanging Wall Zone	TSO17-028	V892625	-58	270	639861	6944800	51.20	52.70	IVL
Northbelt	Daves Pond	Main Zone	TSO17-029	V892939	-58	270	639861	6944800	77.00	78.50	MVL
Northbelt	Daves Pond	Main Zone	TSO17-029	V892959	-58	270	639861	6944800	102.30	103.30	MVL
Northbelt	Daves Pond	Main Zone	TSO17-029	V892979	-58	270	639861	6944800	119.30	120.30	MVL
Northbelt	Daves Pond	Hanging Wall Zone	TSO17-030	V738327	-50	270	639664	6945119	46.92	47.70	MVL
Northbelt	Sam Otto	Main Zone	TWL16-011	S343808	-45	270	639739	6944566	42.00	43.00	IVL
Northbelt	Sam Otto	Main Zone	TWL16-011	S343813	-45	270	639739	6944566	45.50	46.20	IVL
Northbelt	Sam Otto	Main Zone	TWL16-011	S343815	-45	270	639739	6944566	47.20	48.10	IVL
Northbelt	Sam Otto	Main Zone	TWL16-011	S343816	-45	270	639739	6944566	48.10	48.70	IVL
Northbelt	Sam Otto	Main Zone	TWL16-011	S343811	-45	270	639739	6944566	43.90	44.75	IVL
Northbelt	Sam Otto	Main Zone	TWL16-011	S343819	-45	270	639739	6944566	50.45	51.25	IVL
Northbelt	Mispickel	North Zone	TWL16-032	S892044	-51	270	640700	6946106	252.00	253.50	SDS
Northbelt	Mispickel	North Zone	TWL16-032	S892089	-51	270	640700	6946106	307.50	308.00	SDS
Northbelt	Mispickel	North Zone	TWL16-032	S892043	-51	270	640700	6946106	250.50	252.00	SDS
Northbelt	Mispickel	North Zone	TWL16-032	S892045	-51	270	640700	6946106	253.50	255.00	SDS
Northbelt	Mispickel	North Zone	TWL16-032	S892082	-51	270	640700	6946106	299.42	300.60	SDS
Northbelt	Mispickel	North Zone	TWL16-032	S892084	-51	270	640700	6946106	301.60	302.60	SDS
Northbelt	Mispickel	North Zone	TWL16-032	S892087	-51	270	640700	6946106	305.00	306.00	SDS
Northbelt	Mispickel	North Zone	TWL16-032	S892102	-51	270	640700	6946106	321.50	323.00	SDS

Table 3. Locations of the Kerswill Suite samples, including their gold mineralization styles.

Belt	Property	Sample ID	Locale	Easting	Northing	Style
Kerswill	TerraX Yellowknife City Property ???	AN14	Anne-ZnPb-F	640832	6941968	Free-milling
Kerswill	Other	BP1X5	Clan Lake-Beaver Pond-Nose-F	640270	6979163	Free-milling
Kerswill	Con Mine Property	C511	Con-Campbell Zone-F	635863	6925219	Free-milling
Kerswill	Con Mine Property	C611	Con-Campbell Zone-F	635863	6925219	Free-milling
Kerswill	Con Mine Property	C131	Con-Campbell Zone-X	636532	6924327	Unclassified
Kerswill	Con Mine Property	C421	Con-Campbell Zone-X	636532	6924327	Unclassified
Kerswill	TerraX Yellowknife City Property	CR16	Crestaurum-Main Zone-R	635481	6941536	Refractory
Kerswill	TerraX Yellowknife City Property	CRW1	Crestaurum-Other Zone-R	635768	6941765	Refractory
Kerswill	TerraX Yellowknife City Property	CRW2	Crestaurum-Other Zone-R	635768	6941765	Refractory
Kerswill	Other	D21	Discovery	655985	7010040	Background
Kerswill	Other	DX2	Discovery-F	656250	7010420	Free-milling
Kerswill	TerraX Yellowknife City Property	DF11	Duckfish-F	637098	6950117	Free-milling
Kerswill	TerraX Yellowknife City Property	DF21	Duckfish-F	637101	6950123	Free-milling
Kerswill	Giant Mine Property	BRX2	Giant-Brock-F	635585	6932841	Free-milling
Kerswill	Giant Mine Property	DWC41	Giant-DWC-R	635727	6930821	Refractory
Kerswill	Giant Mine Property	G13	Giant-LAW-R	636090	6934172	Refractory
Kerswill	Giant Mine Property	G15	Giant-LAW-R	636090	6934172	Refractory
Kerswill	Giant Mine Property	G32	Giant-Supercrest-R	636120	6935212	Refractory
Kerswill	Giant Mine Property	G42	Giant-Supercrest-R	636120	6935212	Refractory
Kerswill	Giant Mine Property	G51	Giant-Supercrest-R	636120	6935212	Refractory
Kerswill	Gold Lake Property	GL11	Gold Lake-Lynx-R	635855	6937245	Refractory
Kerswill	Gold Lake Property	GL41	Gold Lake-Lynx-R	635862	6937262	Refractory
Kerswill	Gold Lake Property	GL82	Gold Lake-Lynx-R	635960	6937470	Refractory
Kerswill	TerraX Yellowknife City Property	HL44	Homer-As-F	638183	6949936	Free-milling
Kerswill	Other	JL21	Jackson Lake-X	636170	6918480	Unclassified
Kerswill	TerraX Southbelt Property ???	MQ12	MacQueen-F	635859	6921080	Free-milling
Kerswill	Other	MN12	Mon-F	635775	6976957	Free-milling
Kerswill	TerraX Yellowknife City Property ???	MOS14	Mos-VMS	639447	6938695	VMS/BIF
Kerswill	TerraX Yellowknife City Property ???	MOS16	Mos-VMS	639447	6938695	VMS/BIF
Kerswill	Other	NLR1	Nicholas Lake-Trench-F	662720	7017375	Free-milling
Kerswill	Other	OMX011	Ormsby Zone-F	654880	7008430	Free-milling
Kerswill	Other	RS12	Rod-F	632649	6932060	Free-milling
Kerswill	Other	SL23	Sito Lake-F	638513	6975150	Free-milling
Kerswill	Other	TO11	Tom-F	644120	6936733	Free-milling

Visual description on the samples were done after the cores and slabs were sent to Western University. Half-cores up to 6x20 cm and slabs up to 5x12 cm were photographed and described using a 20x hand lens. Systematic descriptions based on texture, alteration patterns, and major minerals are at Appendix A, and findings were utilized to set where maps were to be collected.

2.2 Synchrotron Radiation X-ray Diffraction

Synchrotron radiation X-ray diffraction studies of the rock pulps and powders was inspected at the Canadian Macromolecular Crystallography Facility (CMCF) at the Canadian Light Source in Saskatoon, SK. The beamline focuses on macromolecular crystallography for studying structures of proteins and other macromolecules. The

Bending Magnet (08B1-1) port of the CMCF is situated at a 7.14287 m bend radius, capable of energies from 4 to 18 KeV (3.1 to 0.69 Å wavelength). The beamline uses a collimating mirror with Si and Rh/Pt stripes, a Rh/Pt toroidal focusing mirror, and a Si (111) crystal. The flux is set at $1e^{11}$ photons/second at 250 mA using a 1 mrad horizontal fan, and energy is tuned by a KOHZU double crystal monochromator (DCM) with a water-cooled first crystal and a flat, long second crystal. The beamline uses a Stanford Automated Mounting system (SAM), where either Unipuck or SSRL-style cassettes can be set up for automated sample changing. A Rayonix MX300HE CCD X-ray detector, with 16 CCDs and 16 tiled fiber-optic tapers, collects 2-dimensional X-ray diffraction data, with detector distance variable from 115 to 700 mm, and a resolution of 4096 x 4096 pixels (73 µm pixel size), while Vortex ME4 and Röntec XFlash 1001 detectors permit the collection of XANES, EXAFS, MAD/SAD, and XRF data. An Epson robotic arm mounts capillary samples from the SSRL-style cassette. The beamline is currently capable of collecting XRD, MX (macromolecular crystallography), SAD (single wavelength anomalous diffraction), MAD (multi-wavelength anomalous diffraction), XRF, and XANES in cryogenic or room temperatures using capillary tubes or single crystal mounts. CMCF uses the MxDC in-house software in conjunction with the MxLive online data platform and NoMachine for remote analysis.

2.2.1 Experiment Setup at the CMCF

Three beamtimes at the Canadian Macromolecular Crystallography Facility (CMCF) Beamline at the Canadian Light Source in Saskatoon, Saskatchewan were granted to investigate rock pulps and powders collected for the project. Samples were prepared in-house at the Department of Earth Sciences, Western University by storing them in 2 cm-long polyimide (capillary) tubes (outer diameter at 0.05461 cm, inner diameter 0.04953 cm), sealed with superglue, which were then mounted in B3S ALS-style reusable goniometer bases. The robot used an SSRL-style sample cassette with 96 sample slots sample storage, with each slot provided with a unique code (i.e. A1) for labeling. Sample codes were written in a spreadsheet and transferred to MxLIVE, the CMCF's online data management software.

The experiments were carried out on both automated and manual sampling conditions in ambient air, with automated sampling employed after tests on the number of frames and beam exposure time were figured out after five samples were analysed via manual data collection. Analysis parameters for automated and manual collection for both July 2017 and May 2018 beamtimes were set at 0.6888 Å (18 KeV), while automated and manual data sampling for the March 2018 beam time were set at 0.9795 Å (12.658 KeV) and 0.6888 Å, respectively. The capillary was rotated 180 degrees per frame to collect representative peaks for each side of the homogeneous sample. Exposure time was fixed at 5 seconds per frame, for 6 frames in the July 2017 time, and 24 frames in the March and May 2018 periods. A Rayonix MX300HE CCD X-ray detector collected 2-dimensional X-ray diffraction data, with detector distance at 250 mm for both automated and manual data collection, while information collected via automated sampling at the March 2018 beamtime had the detector set at 150 mm. An Epson robotic arm collected and mounted capillary samples from the SSRL-style cassette storing the samples. Other essential parameters, especially those to be utilized during sample integration, are listed in Table 4.

Table 4. Sample parameters of the X-ray diffraction experiments for the July 2017, March 2018, and May 2018 beam times.

	July 2017, 18 KeV	March 2018, 18 KeV	March 2018, 12.658 KeV	May 2018, 18 KeV
Detector distance	250 mm (unless otherwise stated)	250 mm	150 mm	250 mm
Pixel size	73.24x 73.24 µm	73.24x 73.24 µm	73.24x 73.24 µm	73.24x 73.24 µm
Angle of detector tilt	0.217447131215°	0.2801°	0.1359°	0.2233°
Angle of detector rotation	220.817823667°	44.84°	61.48°	43.09°
Maximum 2θ	40°	40°	56°	40°
Polarisation factor	0.990	0.990	0.990	0.990

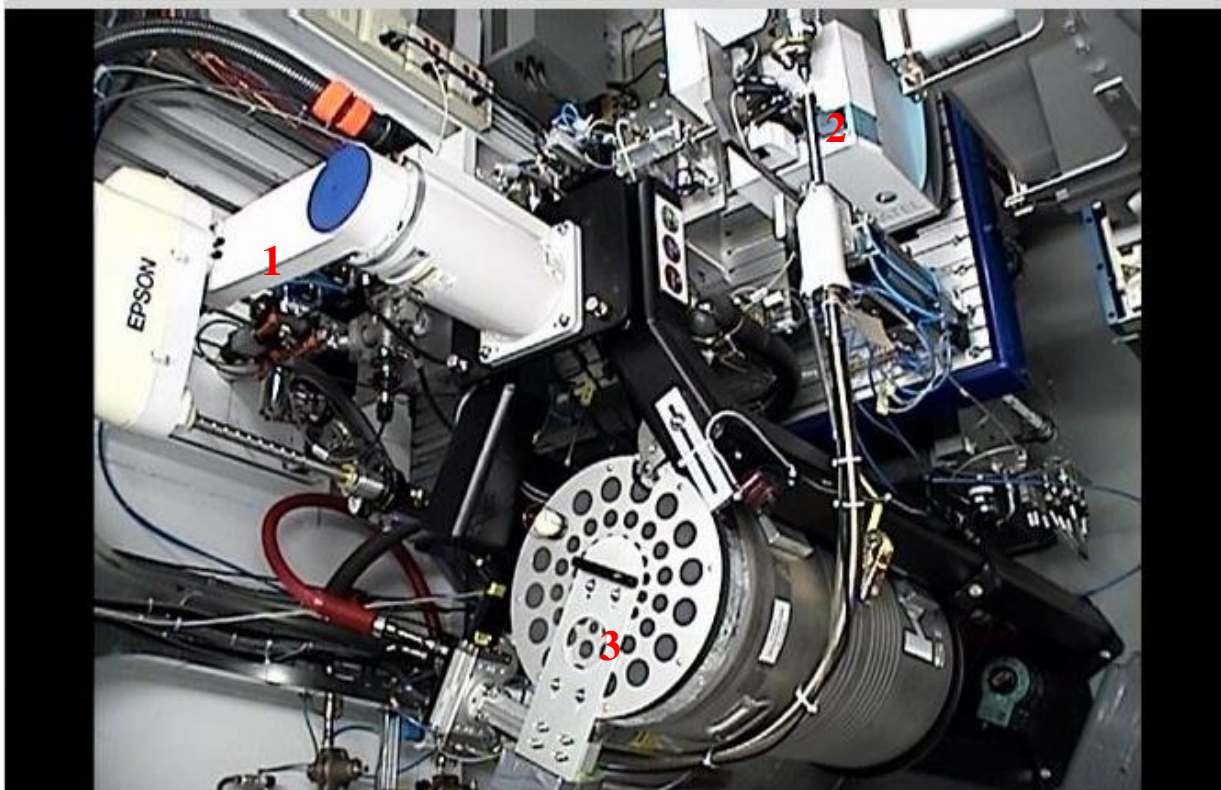


Figure 9. Inside the experiment hutch of the CMCF-BM. The robotic arm (1) moves the sample close to the beam (2) for SR-XRD analysis. The capillaries are stored in a flask containing the cassettes (3) with appropriate labels corresponding to each sample.

2.2.2 Remote Data Collection

Two in-house programs and one remote operation software were utilized for sample collection and management. MxLIVE is the online sample management system by the CMCF (accessible via <https://mxlive.lightsource.ca/login/?next=/>), which permitted the user to name sample groups, and label them based on their position in the SSRL-style cassette (e.g., A1). Data collected during the experiment(s) were saved in the same platform and downloaded after the experiment. MxDC is the in-house software of the CMCF, remotely operated using the NoMachine platform (<https://www.nomachine.com/>). MxDC allowed the use of either manual or automated data collection, based on set parameters, i.e. energy, detector distance, etc. Automated capillary centring was refined during the March and May 2018 beam times, since the July 2017 run only allowed manual centring due to software and remote operation issues.

2.2.3 Data Calibration and Integration of 2-Dimensional SR-XRD Results

Data calibration for the correction of relative intensities and slight peak deviations were made for the three beam times. For the July 2017 and May 2018 data, an in-house lanthanum hexaboride (LaB_6) sample was analysed first and last to establish experiment parameters (Table 4) to be applied to subsequent data processing. Lanthanum hexaboride (LaB_6) is one of the most common standards for powder diffraction, especially for correcting peak width errors (Mezouar et al, 2005). Internal standards were utilized for the March 2018 data due to lack of LaB_6 – a zinc fume oxide sample for 18 KeV data, and the Kerswill Suite sample CRW1 (diffractogram is at Appendix D) for samples analysed at 12.658 KeV and were inspected thoroughly to display clear rings and lack of specks or dots.

Calibration parameters were collected and data integration was done via two software packages, GSAS-II and auto.powder. GSAS-II is a software developed for the APS at the Argonne National Laboratory, Chicago, IL (Toby and Von Dreele, 2013), which allows collection of calibration data and integration of 2-D diffractograms to 1-D based on analysis parameters listed in Table 4. Calibration using GSAS-II employed the selection

of a frame of a known calibrant (i.e., LaB₆), and employing the Calibration function, which calculated analysis parameters based on other fixed values such as detector distance and wavelength, as well as the fit of the result of the calibrant with the internal fitting values of the software. Stacking of six to twenty-four diffractograms produced by GSAS by addition of relative intensities was done manually using Microsoft Excel, which increased total counts. Integration of two-dimensional XRD data for auto.powder was performed using the Auto Integrate function, converting 2-D to 1-D data with parameter values. Instrument parameters were configured via auto.powder's Calibration function, which allows selection of any sample with clear rings of diffraction, and calculating to establish instrument parameters based on known parameters (Table 4). Conversion and integration of the several 2-dimensional files were simpler compared to GSAS-II, with calibration and integration made easier by using a single command line via the Linux terminal. Auto.powder uses Fit2D algorithms (Hammersley et al, 1996; Hammersley, 1997) to integrate multiple diffractograms by using the line:

```
auto.powder /<folder1>/<folder2>/.../<filename>*.img
```

where all files with the same file name before the asterisk within the folders are calibrated against the calibrant parameters used, and integrated into separate .xdi file containing 2theta, d-spacing, counts for each file, and the integrated counts. Auto.powder is a faster, more efficient method of data integration compared to GSAS-II, since it automatically adds all integrated data of the same file or sample name.

Integrated results, which included total counts for each 2theta value, were then saved as separate .dat files for each sample, and converted using ConvX (Bowden, 1998). The software is a multi-tool conversion software for XRD-readable file types of various programs, such as ASCII, to the Bruker-readable .raw file. The only parameter required for conversion is the wavelength used (0.6888 Å for 18 KeV, 0.9795 Å for 12.658 KeV) for a batch of files.

2.2.4 Synchrotron X-ray Diffraction Data Analysis

Bruker's proprietary software, DIFFRAC.EVA (Bruker, 2018) grants peak matching and semi-quantitative analysis of mineralogical presence and abundance. In this study, the ICDD's PDF 2001 database was used for peak identification. Background subtraction was applied in all samples to remove interferences and noise. In peak matching, the subfile "Mineral" was selected, and major mineral phases were selected based on the best matches which corresponded to the peaks. Minor phases were identified using the same methods for major minerals, through information from visual descriptions of the corresponding half core or slab.

2.3 Synchrotron Radiation X-ray Fluorescence

Synchrotron Radiation X-ray fluorescence (SR-XRF) data collection was conducted at the Industry Development Education Applications Students (IDEAS) beamline at the Canadian Light Source (CLS) in Saskatoon, SK. The IDEAS beamline is a flexible, general purpose beamline focusing on in-house science, educational outreach and supporting instrumentation and experimental design and development within the CLS, situated within port 08B2-1. The beamline is of a simple design with a constant beam height double crystal monochromator providing an energy range of 1.8 keV – 15 keV using InSb(111), Ge(220), and Si(311) crystal pairs. The energy was tuned using a Ge(220) double crystal monochromator, with the flux set at $5e^{10} - 7e^{11}$ photons/second at 100 mA. Resolution was at 1.5 eV using the collimated beam maintained at a constant exit height. Data collection was performed using a KETEK AXAS-M (M5T1T0-H80-ML5BEV) Silicon Drift Detector using a XIA DXP Mercury pulse processor. The beamline is capable of XRF, XANES and EXAFS in air or in vacuum, with the available ion chambers and silicon drift detector. 2-dimensional XRF mapping with sub-millimetre resolution can be performed in air on large samples up to 9x20 cm. IDEAS uses an implementation of the in-house developed Acquaman software suite for powerful, user-friendly data acquisition and management.

2.3.1 Experiment Parameters and Set-up

Two-dimensional X-ray fluorescence mapping of the slabs and half cores was done at the IDEAS Beamline at the Canadian Light Source on ambient air conditions. Incident X-ray energies for analyses were set from 13140 to 13800 eV for the December 2016 to November 2017 beamtimes, respectively, and were calibrated against an Au foil standard (Au L₃ binding energy – 11919 eV). Beam energy was deemed enough to excite elements of interest, especially Au. Map dimensions were set to varying sizes to cover a large portion of the sample, averaging 10 x 4 cm, and the assembly was placed on a wooden core holder mounted on an x-z operating motor (Figure 10). The 1-element KETEK AXAS-M (M5T1T0-H80-ML5BEV) Silicon Drift Detector was positioned 15 cm away from sample, moved further in or out if counts are either too low or if the detector will hit the sample. Dead time counts were kept below 35% to prevent oversaturation of the detector. Beam spot sizes were set at 0.5x0.5 mm, 1x1 mm, and 2x2 mm, with interaction volumes negatively correlated to the atomic number (larger interaction volumes with smaller atomic numbers). Sample parameters were set using the Acquaman software (Table 5). Results were saved as ASCII files representing fluorescence spectra for each pixel. Fluorescence spectra collected were either analysed directly in Peakaboo (for December 2016, January and June 2017 data), or further processed via data conversion to .edf file formats to be analysed in PyMCA (June and November 2017 data). Each pixel corresponded to a full fluorescence (as MCA) spectrum, representing relative element abundances, and used to identify the presence of key elements such as Au.

Table 5. Parameters for SR-XRF data collection. Beam energy was set to allow excitation of elements of interest, especially Au (L3 binding energy: 11919 eV).

	December 2016	January 2017	June 2017	November 2017
Beam energy	13150 eV	13700 eV	13840 eV	13400 eV
Beam spot size(s)	0.5x0.5mm, 1x1 mm, 2x2 mm	0.5x0.5mm, 1x1 mm, 2x2 mm	2x2 mm	2x2 mm
Mean Detector Distance	15 cm	15 cm	15 cm	15 cm

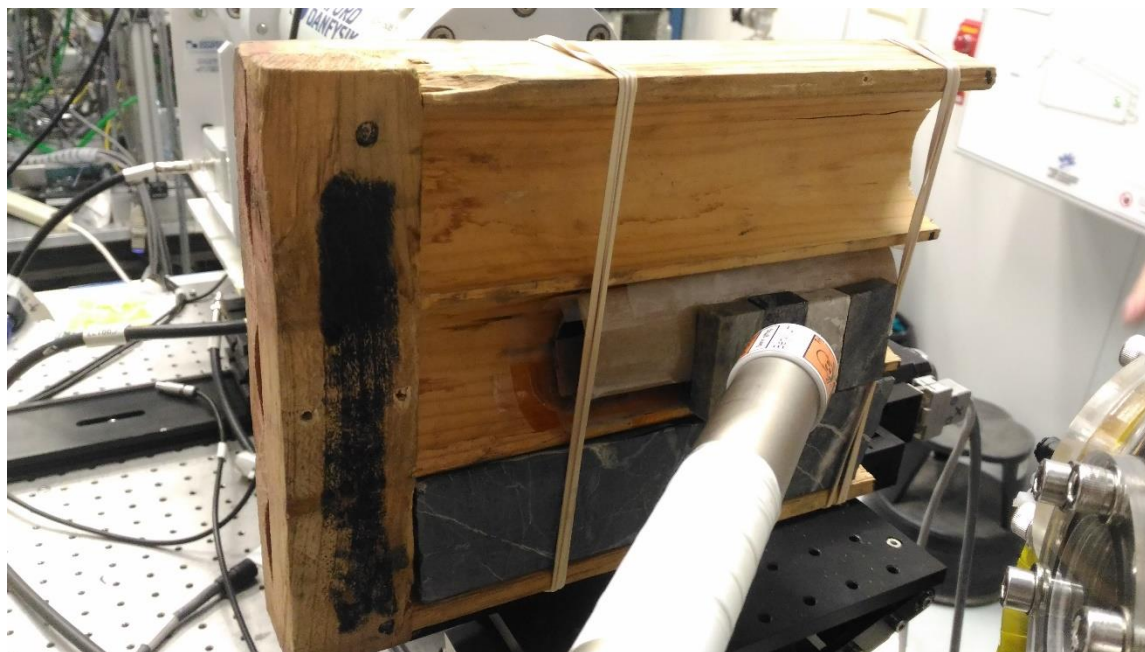


Figure 10. Typical setup for the slabs and half cores for synchrotron XRF and XANES spectroscopy. A wooden core box was cut in half and screwed on the x-z operating motor, and can hold 2 cores at a time for 2-dimensional SR-XRF mapping. The beam comes from the lower right of the image, and the detector is set at 45 degrees with respect to the sample, effectively making a 90-degree arc for the beam to travel. The detector is pulled back approximately 15 cm from the core, moved closer or farther depending on the dead time counts.

2.3.2 Data Interpretation

Geochemical association and element maps of key components were interpreted using Sherry et al's (2009) Peakaboo and Solé et al's (2007) PyMCA software. Data from the December 2017 to June 2017 beam times were first analysed in Peakaboo, with the energy set at the corresponding beam energy for each time. Background subtraction was done using Brukner background subtraction, which "smooths data over several data iterations and calculating the minimum of the unsmoothed and smoothed data for each channel on each pass" (Sherry et al, 2018). The software utilizes Pseudo-Voigt fitting function by default to fit spectra, and single curve fitting is done by using the Max under Curve fitting algorithm, which fits directly under the full width at half maximum (FWHM) area, and is deemed to be conservative (Sherry et al, 2018). The spectrum was an average of each individual MCA spectrum corresponding to each pixel of the two-dimensional map, and elements in the spectrum were identified using Guided Fitting and Element Lookup, which matches fluorescence energies for each emission line of an element (Table 6). Peak intensities were also measured, and is positively correlated to relative abundance. Maps of elements of interest were then produced and compiled. An option to select the escape peak type (silicon for this project) is available in Peakaboo to adjust for the reduction in energy for major elements (Sherry et al, 2018)

Data collected from the June 2017 beam time were re-analysed, and results from November 2017 were entirely interpreted using PyMCA (Solé, et al, 2007). Data was calibrated against both the energy used and the Fe K_{α} fluorescence peak (6405.2 eV), due to the Fe peak being common and prominent across all samples. Background removal was done using the SNIP tool, which dealt with statistical fluctuations to correct for background removal (Solé et al, 2007). Peaks were measured using Hypermet fitting functions by default, utilizing linear least-squares fitting of entire elements, not single peaks (Solé et al, 2007). The energy used was re-inputted, and elements were identified using their corresponding energies on the calibrated spectrum. Like Peakaboo, the average MCA spectrum was representative of the average of each individual pixel with its own MCA spectrum, and peak intensities were also positively correlated with element abundance. After fitting the elements, regions of interest were fitted on the average

spectrum (tolerance of 100 eV) based on their emission energies (Table 6), and element maps were produced based on the area within the region of interest established for each element. Further information on using PyMCA is in Appendix E.

2.4 X-ray Absorption Near Edge Structure

The two-dimensional XRF maps were examined to identify samples with gold spots, indicated by intense signals in the Au maps. Fourteen samples with twenty-seven intense Au spots were selected for further XANES analysis to identify the oxidation state of gold in the samples (Harris. 1990; Simon et al, 1999; Hinchey et al, 2003). The intense spots were then further examined by looking at the MCA spectrum of the pixel corresponding to test for interferences of other fluorescence emission lines, such as Zn K_{β} (9567.4 eV), via PyMCA. Two samples were then selected for Au XANES analysis to investigate the oxidation state of Au.

Table 6. List of element and line energies used to identify elements in the 2-dimensional fluorescence maps. For PyMCA, tolerance on the region of interest for each element is at ± 100 eV. Ar maps were indications of the ambient argon in front of the sample.

Element	Line	Energy (eV)
Ar	$K\alpha_1$	2957.5
K	$K\alpha_1$	3313.8
Ca	$K\alpha_1$	3692.3
Ti	$K\alpha_1$	4512.2
V	$K\alpha_1$	4952.9
Cr	$K\alpha_1$	5414.9
Mn	$K\alpha_1$	5900.3
Fe	$K\alpha_1$	6405.2
Co	$K\alpha_1$	6930.9
Ni	$K\alpha_1$	7480.3
Cu	$K\alpha_1$	8046.3
Zn	$K\alpha_1$	8637.2
As	$K\alpha_1$	10543.4
Sb	Lg_2	4602.4
Au	$L\alpha_1$	9713
Pb	$L\alpha_2$	10449

2.4.1 Re-tracing of Au spot and XANES Spectroscopy of Au

After 2-dimensional XRF maps of the samples were studied after data processing via Peakaboo and PyMCA, and Au hotspots, as well as mineralogical and textural associations, were delineated, fourteen samples were re-mapped to approximate the location of the Au signal via detailed maps by performing X-ray fluorescence mapping of a 2x2 cm area surrounding the Au spot, with a 2x2 mm beam spot size at a beam energy of 13400 eV, enough to produce Au emission lines. Maps were also collected below the Au L₃ binding energy (11919 eV) to investigate possible interferences. The beam was repositioned to the Au spot, and analysis was switched to X-ray Absorption Near Edge Structure (XANES) in the IDEAS beamline at the Canadian Light Source. The analysis was set at XAS (X-ray absorption spectroscopy) mode in Acquaman, and necessary parameters were established (Table 7).

The XANES spot in the analysis was set at 2 mm beam size for increased flux to the spot, as well as allowing the best representation of the Au spot detected via prior SR-XRF analysis. The L₃ absorption edge of Au (11919 eV) was measured. An in-house gold foil standard was first examined to represent metallic gold, and subsequent analyses used the same parameters as the Au foil, shown in Table 7. Detector parameters were the same as SR-XRF, with the 1-element KETEK detector positioned 15 cm from the sample.

2.4.2 Data Processing and Interpretation

Data processing was done in Athena (Ravel, 2005), an X-ray Absorption Spectroscopy data processing software, to normalize spectra for further examination. Pre- and post-edges of the XANES spectrum were normalized to relatively horizontal to correct for noise and allow statistical calculations (not covered in this study). X-Y values of the normalized spectra were then transferred to OriginPro 2017 (OriginLab Corporation, 2017), a data analysis and graphing software, to make intensity versus energy spectra, and to identify the behaviour of the Au L₃ edge of the samples. Comparison of XANES spectra with the Au foil standard allowed the identification the oxidation state of gold in the samples.

Table 7. Sample analysis parameters for XANES, using a 2x2 mm beam spot size and 13400 eV beam energy. The -60 to -20 eV from the absorption edge defined pre-edge line (needed not to be very precise, thus the 5 eV step), the -20 to 60 eV is the most crucial section of the XANES analysis, since it covers the absorption edge of Au (any shift from 11919 eV, including changes in the shape of the spectrum itself, indicate a different Au species), and the area 60 to 100 eV from absorption edge is for post-edge line refinement, may be helpful for EXAFS (not covered in this study).

Electron energy distance from absorption edge, start	Step size	Electron energy distance from absorption edge, start	Duration
-60 eV	5 eV	-20 eV	2 sec
-20 eV	1 eV	60 eV	2 sec
60 eV	2 eV	100 eV	2 sec

Chapter 3

3 Synchrotron X-ray Diffraction and Prospect Cogeneity

X-ray diffractograms of thirty-nine Kerswill Suite representative samples and thirty-two TerraX core pulps were collected to identify mineral phases and compare similarities in mineralogy. The Kerswill Sample Suite is the best representative of the mineralized sections of the Yellowknife Greenstone Belt, and will best embody the mineralization of the Con and Giant mines, as well as other suites within the Yellowknife Greenstone Belt, with drill core pulps from the seven prospects of the Northbelt property. Mineralogical assemblages would provide necessary information to prove that the deposits in the Northbelt are indeed associated with the Con and Giant Mines, signifying that the YCGP and YGB is part of a single, giant mineralizing system. Mineral phases will also support geochemical data collected via 2-dimensional synchrotron radiation X-ray fluorescence spectroscopy (Chapter 4) to confirm *in-situ* mineralogical, textural, and spatial associations in lieu of petrography, as well as providing information on the macro scale. Information on the presence of certain minerals, i.e., quartz as host rock and vein component, was identified using data gathered from hand sample descriptions.

Experiments on the optimum number of frames and exposure times were carried out on all three beam times. Exposure time was set at 5 seconds per frame since it provided decent (>5000) counts while being rapid enough for gathering more data. Multiple frames of each sample were stacked, or added to each other, to provide Rietveld-quality data (average counts reaching approximately 40000), as well as improving the signal-to-noise ratio. The collection of more frames with short exposure times also served as a precautionary measure in case of beam disruption or machine failure, preventing data loss.

Minor phases were identified in the diffractograms, supporting geochemical data provided by SR-XRF maps, and/or drill core data based on visual inspection. X-ray diffraction data were then compared with each other to identify similarities in remnant

host rock lithology, alteration mineralogy and sulphide presence, which will confirm the similarities in the prospects and the other mineralized portions of the YCGP.

3.1 GSC Kerswill Suite

Thirty-nine samples from the Kerswill Suite were analysed from July 2017 to May 2018, and were picked to represent the mineralized sections of ore bodies and pits within the Yellowknife Greenstone Belt. Thirteen of the thirty-three samples (refer to Appendix D for other diffractograms), embodying nine mineralized portions of the YGB, were deemed representative of the various mineralization styles in the project area. X-ray diffraction results of these samples will reveal mineralogical similarities, as well as their relationship with the deposits within the YCGP. A summary of the mineralogy of the representative Kerswill Suite samples is in Table 8.

Con Mine samples show plentiful quartz, and minor and muscovite, and pyrite and arsenopyrite are the most common sulphides (Figure 11), while galena and sphalerite are apparent in arsenopyrite-poor samples. Little pyrrhotite is seen, while dolomite and ankerite are the main carbonates, and plagioclase is still seen. Giant Mine samples, on the other hand, show abundant carbonate veining as dolomite, ankerite, and calcite (Figure 12). Common sulphides are both high (pyrite and arsenopyrite) and base metal-bearing (sphalerite and galena). Chlorite is also prevalent in the Giant Mine.

Mineralized samples outside the Con-Giant Mine complex show similar trends with pulps from both mines, with their diffractograms in Appendix D. The Anne Trench sample is a base-metal prospect which demonstrates base metal sulphides, sphalerite and galena. Sito Lake rocks display quartz, plagioclase, muscovite, pyrite, and arsenopyrite, as well as prominent chlorite. The Duckfish Granite, a mineralizing intrusive, bears quartz, muscovite, biotite, and plagioclase, while the most common sulphides are pyrite and arsenopyrite. The Crestaurum Main Zone demonstrates quartz, ankerite, and dolomite with minor arsenopyrite. Mineralized conglomerates from the Jackson Lake Formation are enriched with quartz, dolomite and calcite, as well as chlorite, indicating carbonate veining and chloritization. Pyrite-arsenopyrite and sphalerite are apparent within the conglomerate, and sericitization as muscovite and biotite is also common. A sample from

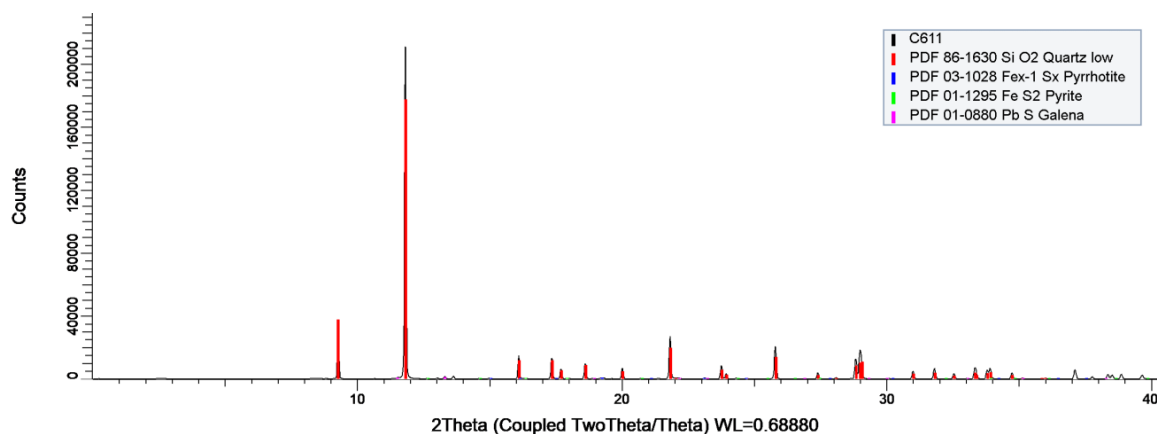


Figure 11. X-ray diffractogram of sample C611 from the Con Mine, a gold-bearing quartz vein with minor sulphides. Base metal sulphides, such as galena, are only minor. Pyrrhotite and pyrite are the high-As sulphides present, while quartz is relatively the most abundant mineral. Pyrrhotite could be due to arsenopyrite alteration. Note that the sulphide peaks are very short compared to quartz.

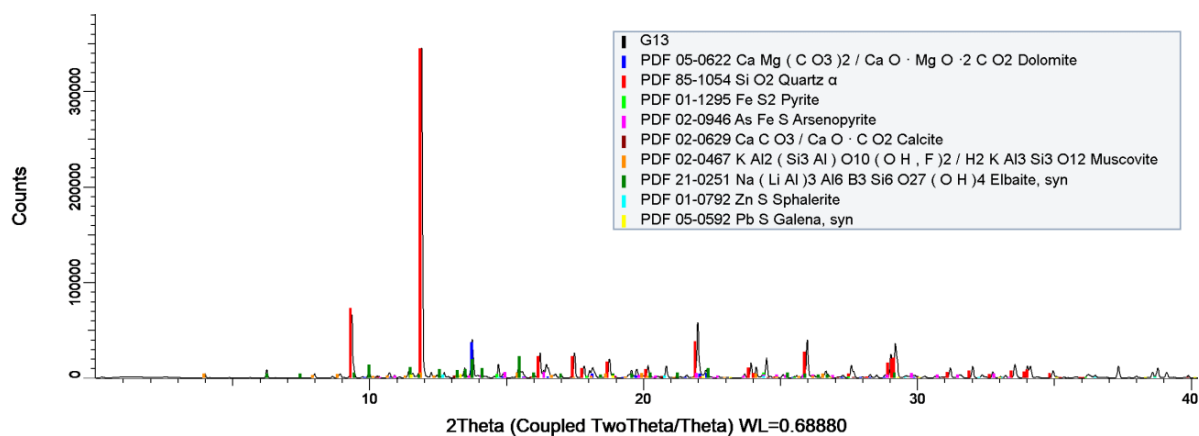


Figure 12. X-ray diffractogram of sample G13, from the Giant Mine a mineralized sample from the main orebody. Noticeable carbonates (calcite, dolomite), mica, and both base metal (sphalerite-galena) and As-rich sulphides (pyrite-arsenopyrite) are observed. Quartz is relatively the most abundant mineral, and is both host rock and vein components. Some traces of tourmaline (as elbaite) is also detected, and can be from the host rock.

the Discovery Mine possesses both base metal (sphalerite-galena) and high-As (pyrite-arsenopyrite) sulphides. Quartz-carbonate (calcite and dolomite), muscovite, and biotite are also present within the Discovery Suite. The MacQueen Prospect is similar to the Discovery Suite in bearing both base metal and high-As sulphides, sericite, and quartz-carbonate (carbonate as dolomite).

3.1.1 Yellowknife City Gold Project Northbelt Property

Thirty-two pulps from the seven prospects of the Yellowknife City Gold Project are analysed to compare mineralogy, as well as to identify any relationships with the Con and Giant Mines. Quartz, sulphides, muscovite, and chlorite are the most common minerals within the Northbelt Property. Differences among the prospects are discussed in more detail below, and a summary of the results are found in Table 9. Diffractograms of the other samples not listed in this section can be found in Appendix D.

3.1.1.1 Crestaurum

Three samples from Crestaurum were examined. The diffractogram for sample R433857 is shown in Figure 13. The Crestaurum prospect with quartz-sericite-chlorite schist hosts exhibits both base metal (sphalerite-galena) and As-rich (pyrite-arsenopyrite) sulphides, as well as pyrrhotite. Gangue minerals include muscovite, quartz, dolomite and ankerite. Pyrrhotite is suspected to be the result of alteration of arsenopyrite, explained further in Chapter 6.

3.1.1.2 Barney

Two samples from Barney were analysed, and the diffractogram for sample R115609 is shown in Figure 14. Hosts for Au mineralization within the Barney Shear include both quartz-sericite-chlorite schist and chloritized mafic volcanics. Samples exhibit both As-rich (pyrite-arsenopyrite) and base metal sulphides (sphalerite-galena) (Figure 14), while dolomite and ankerite are the main carbonates. Sericitization is reflected by muscovite, while chloritization is also apparent. Dolomite and ankerite act as the main carbonates. Quartz is possibly a minor part of the host rock, and is a major vein component.

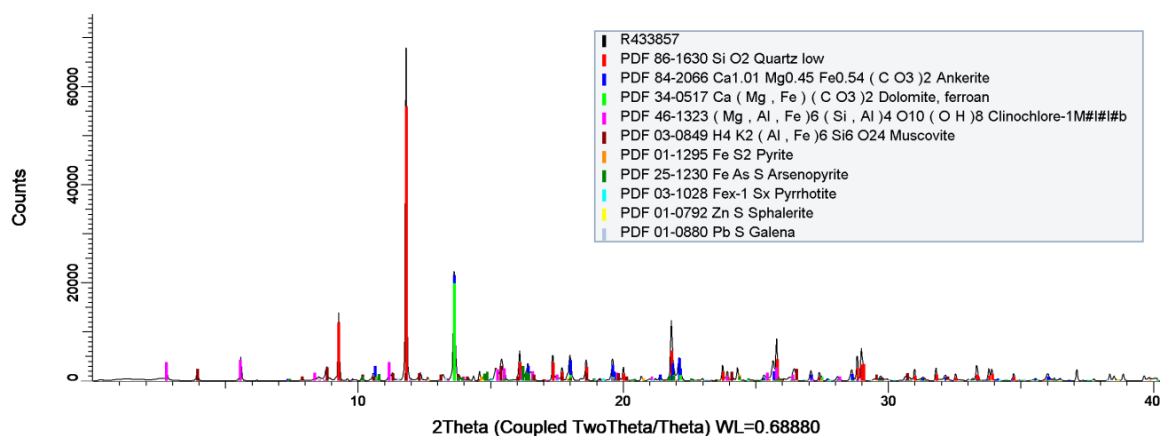


Figure 13. X-ray diffractogram of sample R433857 from Crestaurum, a quartz-sericite-chlorite schist. Base metal (sphalerite-galena) and high-As (pyrite-arsenopyrite) sulphides are also apparent. Pyrrhotite is possibly due to the alteration of arsenopyrite. Ankerite and dolomite are the main types of carbonate, while chlorite and muscovite are also present. Quartz is relatively the most abundant mineral, and is both host rock and vein component.

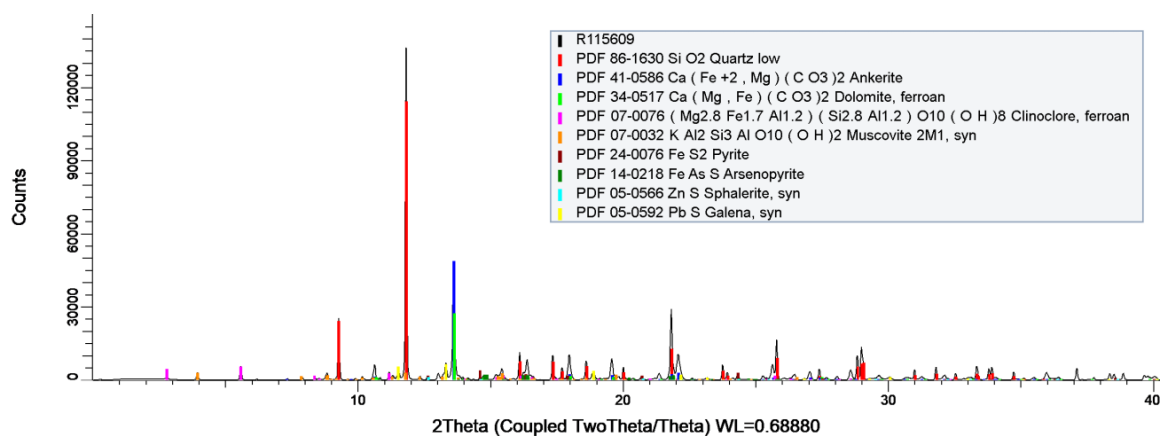


Figure 14. X-ray diffractogram of sample R115609 from the Barney Shear, a sericite-bearing chlorite schist. Ankerite and dolomite are the dominant carbonates, and chlorite and muscovite are also seen. Base metal (sphalerite-galena) and high-As (pyrite-arsenopyrite) As sulphides are also apparent. Quartz is relatively the most abundant mineral, and can be both host rock and vein components.

3.1.1.3 Hébert-Brent

Three samples from Hébert-Brent were examined, with the representative sample S521365 shown in Figure 15. Samples from the Hébert-Brent prospect host Au within both bleached gabbro and feldspar quartz porphyry dykes. The feldspar quartz porphyry dyke exhibits both base metal (sphalerite-galena) and high-As (pyrite-arsenopyrite) sulphides. Bleached gabbro samples show similar mineralogical features as of those of the dykes, as well as sphalerite, in gabbro. For both host rocks, quartz, sericite, and chlorite are mostly apparent. Remnant plagioclase is a component of the protolith.

3.1.1.4 Sam Otto

Ten samples from Sam Otto were inspected, and the diffractogram for the representative sample V890298 is shown in Figure 16. Hosts for gold mineralization in Sam Otto include mafic volcanics and lapilli tuff. Samples from the deposit exhibit both As-rich (pyrite-arsenopyrite) and base metal (sphalerite-galena) sulphides. Pyrrhotite is suspected to be due to the alteration of arsenopyrite due to later mineralization reacting with arsenopyrite. No sample is exhibiting solely pyrrhotite, probably due to incomplete alteration of arsenopyrite to pyrrhotite (more explanation in Chapter 6). Chlorite (as clinocllore) is evidence of metamorphism, as well as a component of the percolating fluids during orogenic gold deposition. Sericitization as muscovite and biotite is also apparent. Minor carbonates are represented by calcite and very rare dolomite. Quartz is a minor part of the host rock, and is present in veins. Some plagioclase reflects host rock mineralogy.

3.1.1.5 Dave's Pond

Six samples from Dave's Pond were investigated, and the diffractogram for sample V160414 is shown in Figure 17. Host rocks in Dave's Pond include ash tuff, intermediate volcanics and mafic volcanoclastics. Some remnant plagioclase from the host is seen in the samples, and the rocks are laden with chlorite, probably due to metamorphism. Muscovite is the main mica, with biotite only comprising minor amounts. Calcite is the main component of the carbonate veins. Both base metal (sphalerite-galena) and high-As

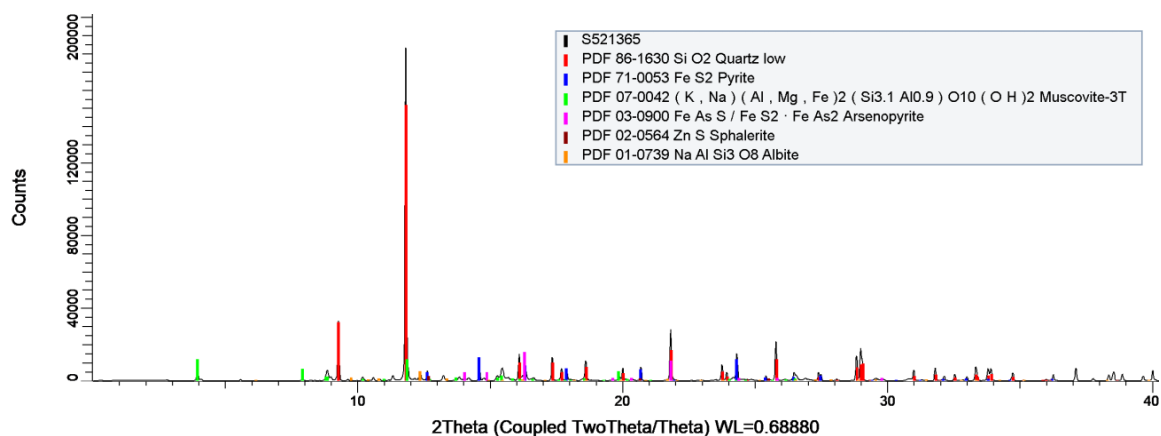


Figure 15. X-ray diffractogram of sample S521365 from Hébert-Brent, a portion of the mineralized feldspar quartz porphyry dyke. Both base metal and high-As sulphides (sphalerite and pyrite-arsenopyrite, respectively) are seen. Remnant plaioclase is still visible. Sericitization is reflected by muscovite, while quartz can be both part of the dyke and later veins.

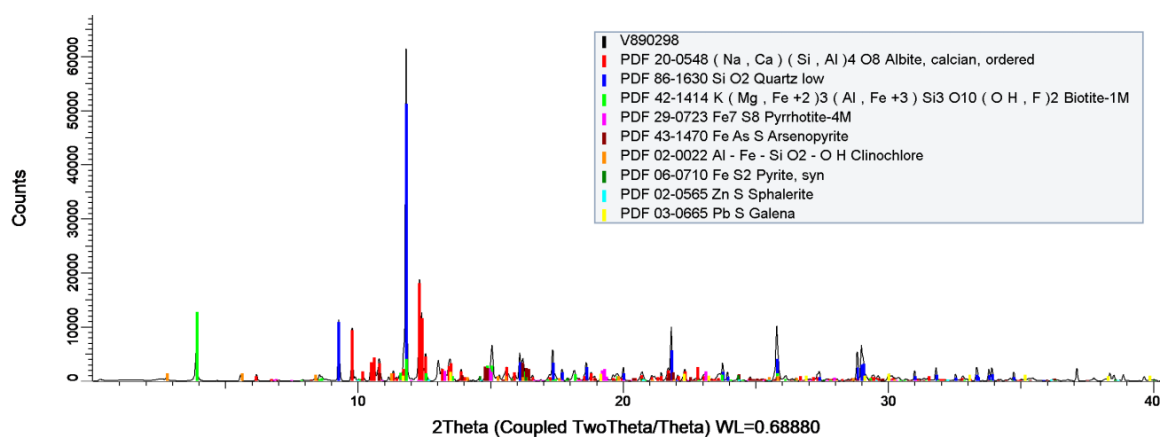


Figure 16. X-ray diffractogram of sample V890298 from Sam Otto, a sheared mineralized gabbro. Base metal (sphalerite-galena) and high-As (pyrite-arsenopyrite) sulphides are also apparent. Biotite is observed, which could be due to higher grade metamorphism. Pyrrhotite may be the result of the alteration of arsenopyrite. Quartz is relatively the most abundant mineral, and is both host rock and vein component.

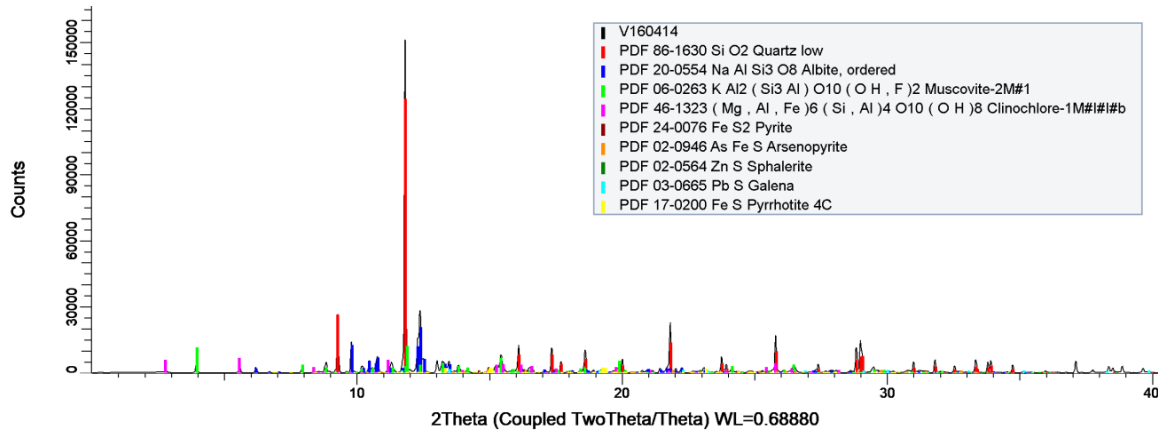


Figure 17. X-ray diffractogram of sample V160414 from Dave's Pond, a sericitic ash tuff. Traces of remnant plagioclase are detected, as well as traces of quartz. Base metal (sphalerite-galena) and high-As (pyrite-arsenopyrite) sulphides represent two periods of sulphidation, while pyrrhotite may be an indicator of arsenopyrite alteration. Quartz is part of the host rock and veins.

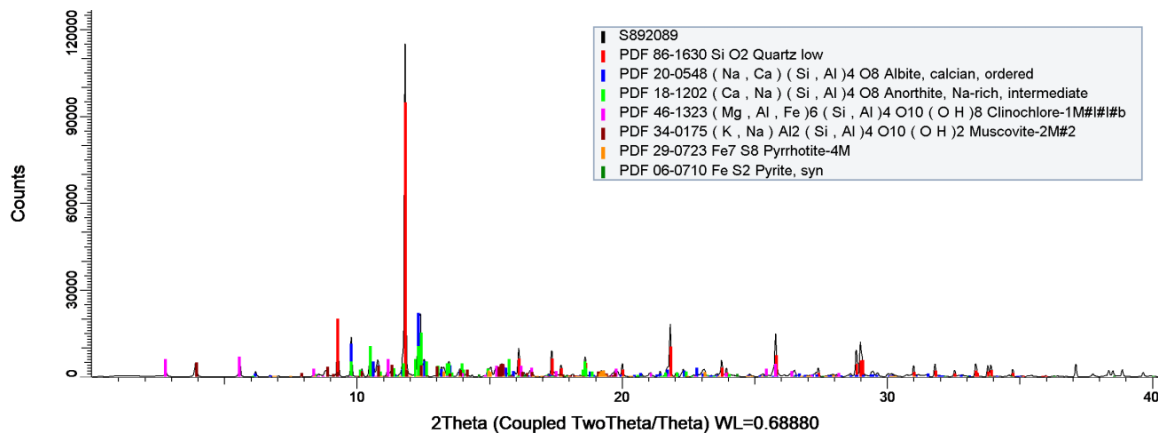


Figure 18. X-ray diffractogram of sample S892089 from Mispickel, a mineralized greywacke. Remnants of metamorphic minerals (chlorite) and host rock components (plagioclase, quartz) are sericitized (muscovite), and sulphidised (pyrite). Pyrrhotite may be due to the alteration of arsenopyrite. Quartz exists as host rock and vein material.

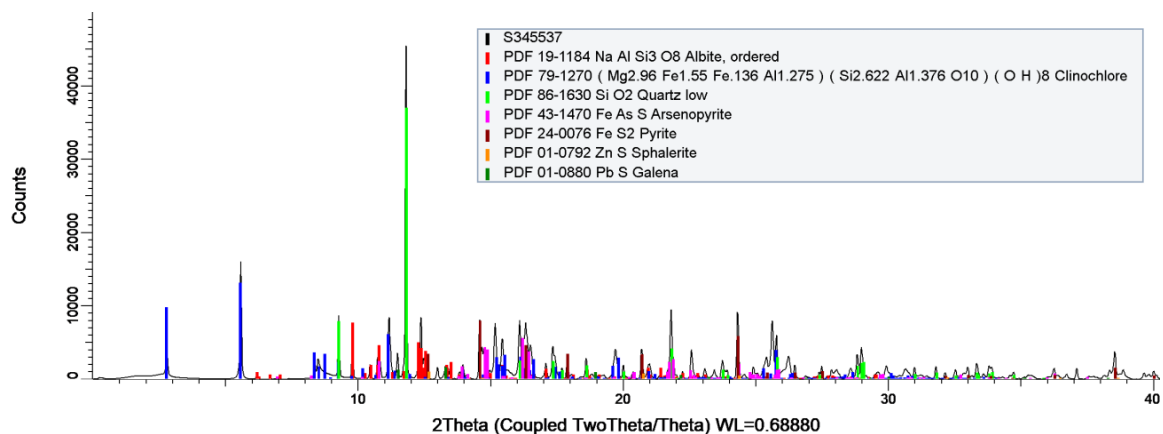


Figure 19. X-ray diffractogram of sample S345537 from Homer, a mineralized gabbro. Chloritization is seen due to the presence of clinocllore. Remnant plagioclase is still observed, representing the host rock. Base metal (sphalerite-galena) and high-As (pyrite-arsenopyrite) sulphides could represent two periods of sulphidation. Quartz is seen as both a host rock and vein mineral.

(pyrite-arsenopyrite) sulphides are seen, as well as pyrrhotite, probably derived from altered arsenopyrite.

3.1.1.6 Mispickel

Five samples from Mispickel were tested, with the representative diffractogram (S892089) shown in Figure 18. The samples from the Mispickel prospect show traces of host rock (greywacke) material, such as plagioclase. Sericite as muscovite and biotite, as well as quartz, are still prevalent, which can be both part of the host rock and mineralized sections. Pyrite, sphalerite, and galena are the principal sulphides in Mispickel, with arsenopyrite comprising only a minor fraction of the sulphide budget, likely due to almost complete alteration to pyrrhotite (further explained in Chapter 6). Pervasive chloritization is also observed, as well as the lack of carbonates.

3.1.1.7 Homer

Three samples from Homer were researched, and the representative sample S345537 is shown in Figure 19. Base metal (sphalerite-galena) and As-rich (pyrite-arsenopyrite) sulphides are both common within the massive flow and gabbroic host rocks within the Homer prospect. Chloritization is prominent and quartz is abundant, but the deposit lacks carbonates. Muscovite and biotite are very minor, and pyrrhotite is also observed. Remnant plagioclase from the host rocks is still prevalent.

3.1.2 Summary

Mineralogical data derived from synchrotron radiation X-ray diffraction dictates that similar minerals are found in both the Kerswill Suite and the Northbelt Property of the Yellowknife City Gold Project. Dominant minerals include quartz, calcite, ankerite, dolomite, plagioclase, muscovite, and biotite, while minor minerals are pyrite, arsenopyrite, sphalerite, galena, and pyrrhotite. Muscovite and biotite are probably related to sericitization events. Pyrite, arsenopyrite, sphalerite, galena, pyrrhotite are indicators of sulphide mineralization, with pyrrhotite suspected to be a result of the incomplete alteration of arsenopyrite. Calcite, ankerite, and dolomite are the most common carbonates in quartz-carbonate veins, and a combination of these three minerals

can exist in the deposits. Chlorite is related to chloritization during metamorphism, as well as fluid percolation during orogenic gold deposition (Isachsen and Bowring, 1994; Goldfarb, 2001). Plagioclase signifies host rock mineralogy, while quartz is present as a protolith mineral in felsic volcanics and metasedimentary rocks, and as veins in most samples.

Table 8. Summary of the mineralogy in the nine representative mineralized suites in the YGB, or the Kerswill Sample Suite.

	quartz	plagioclase	muscovite	biotite	pyrite	arsenopyrite	galena	sphalerite	pyrrhotite	dolomite	ankerite	calcite	chlorite
Con Mine	1	1	1		1	1	1	1	1	1	1		
Giant Mine	1		1		1	1	1	1		1	1	1	1
Anne Trench	1						1	1					
Crestaurum Main Zone	1					1				1	1		
Duckfish Granite	1	1	1		1	1	1	1					
Discovery Mine	1		1	1	1	1	1	1		1		1	
Jackson Lake	1		1	1	1	1		1			1	1	1
MacQueen Prospect	1		1		1	1	1	1		1			
Sito Lake	1	1	1		1	1	1	1					1

Table 9. Summary of the mineralogy in the seven prospects from the YCGP Northbelt Property.

	quartz	plagioclase	muscovite	biotite	pyrite	arsenopyrite	galena	sphalerite	pyrrhotite	dolomite	ankerite	calcite	chlorite
Crestaurum	1		1		1	1	1	1	1	1	1		1
Barney	1		1		1	1	1	1		1	1		1
Hebert-Brent	1	1	1	1	1	1		1					1
Sam Otto	1	1	1	1	1	1	1	1	1	1		1	1
Dave's Pond	1	1	1	1	1	1	1	1	1			1	1
Mispickel	1	1	1	1	1	1	1	1	1				1
Homer	1	1	1	1	1	1	1	1	1				1

Chapter 4

4 Synchrotron X-ray Fluorescence and Interpretation of Au Association

Fifty-eight samples from the seven prospects of the Yellowknife City Gold Project were scanned for Au and any elements related to it for vectoring geochemical, mineralogical, and textural relationships to aid in revealing the distribution of gold and any associated elements. The half cores from twenty-two drill holes were compared with thirteen selected slabs from the Geological Survey of Canada's Extech III – Kerswill Sample Suite to test for any common characteristics, which complement mineralogy, as well as the determination of any relationships between gold mineralization on the YCGP with the Con and Giant mines. Geochemical distribution of the elements is directly related to mineralogical, textural, structural, and even temporal features. Element maps were produced based on the fitting of fluorescence spectra with the respective emission energies of elements, compiled, and prepared in a grid-like fashion to exhibit spatial associations (see Appendix B). Maps were then compared with high-resolution photographs of the samples, as well as mineralogical data provided by X-ray diffraction, providing clues on the spatial distribution of mineralization periods and gold associations, as well as structures, cross-cutting, and alteration relationships.

Semi-quantitative XRF analysis of the half cores were done with beam spot sizes of 0.5x0.5, 1x1, and 2x2 mm, and the latter was deemed ample for rapid, accurate analysis of geochemical relationships without compromising resolution. Increasing the beam size also increased the flux on the sample, improving data quality by presenting more counts per pixel.

Start and end points of maps were matched with the experiment setup for comparison with the high-resolution photographs of the cores and slabs. Element distribution patterns and associations were studied and compared with high-resolution photographs, focusing on the relationship of Au with the other elements. Spatial intensity distribution of elements was plotted as relative abundances using a temperature spectrum (red – higher relative abundance). The technique is one of the first attempts in nondestructive, *in-situ*

mapping to investigate elemental associations. X-ray fluorescence maps were then used to discern geochemical associations and textural information via comparison with high-resolution photographs of the scanned areas of the core or slab.

4.1 XRF MCA spectra

The mean MCA spectrum of each sample was fit for a series of elements: Ar (as ambient argon in front of the sample), K, Ca, Ti, Sb, V, Cr, Mn, Fe, Co, Ni, Cu, Zn, Au, As, and Pb, with an example shown in Figure 20. The average MCA spectrum represents the mean distribution of elements within the sample. The MCA spectrum of each individually mapped pixel, or a group of pixels, can also be analysed (i.e., Figure 21). Although the spectrum of an individual pixel exhibits more noise, peaks for individual elements are still visible and identifiable. 2D XRF maps were constructed from the fitted, mean MCA spectra. A sample with a mapped area of 4 cm x 10 cm with a 2 mm beam spot size contains over 700 pixels that can each be individually examined, i.e. to confirm the presence of an element. Chapter 2 provides information on the method of interpretation of the presence of elements based on the mean MCA spectra for each sample.

The mean XRF spectra were compared for overall similarities and differences in element distribution in samples from across the YGB and YCGP. Major elements identified include As, Fe, and Zn which are likely found in sulphides, Ca from carbonates, and K for sericite. Other identified elements include Cu, Ti, Cr, V, Ni, Pb, and Sb, and are possibly minor components of major minerals, such as Ti in sericite, Sb in sulphides, etc. The presence of Au pixels was identified in fifty-five samples.

4.2 2-Dimensional X-ray Fluorescence Maps of the Yellowknife City Gold Project

Two-dimensional SR-XRF maps for a series of elements of interest were prepared for each sample. Elements identified include Ar, K, Ca, Ti, Sb, V, Cr, Mn, Fe, Co, Ni, Cu, Zn, Au, As, and Pb. Spatial relationships between elements can be determined using the element maps, especially those related to Au. Arsenic distribution was also a focus, as it is deemed to be a pathfinder element for Au in the YGB (Groves et al, 1998; Dube and

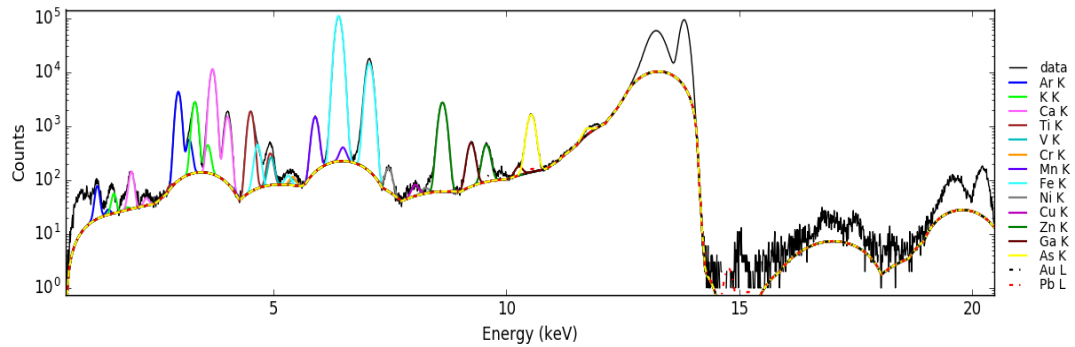


Figure 20. An example of the mean MCA spectrum for sample S343811, which provides a representation of the relative abundance of elements in the section mapped.

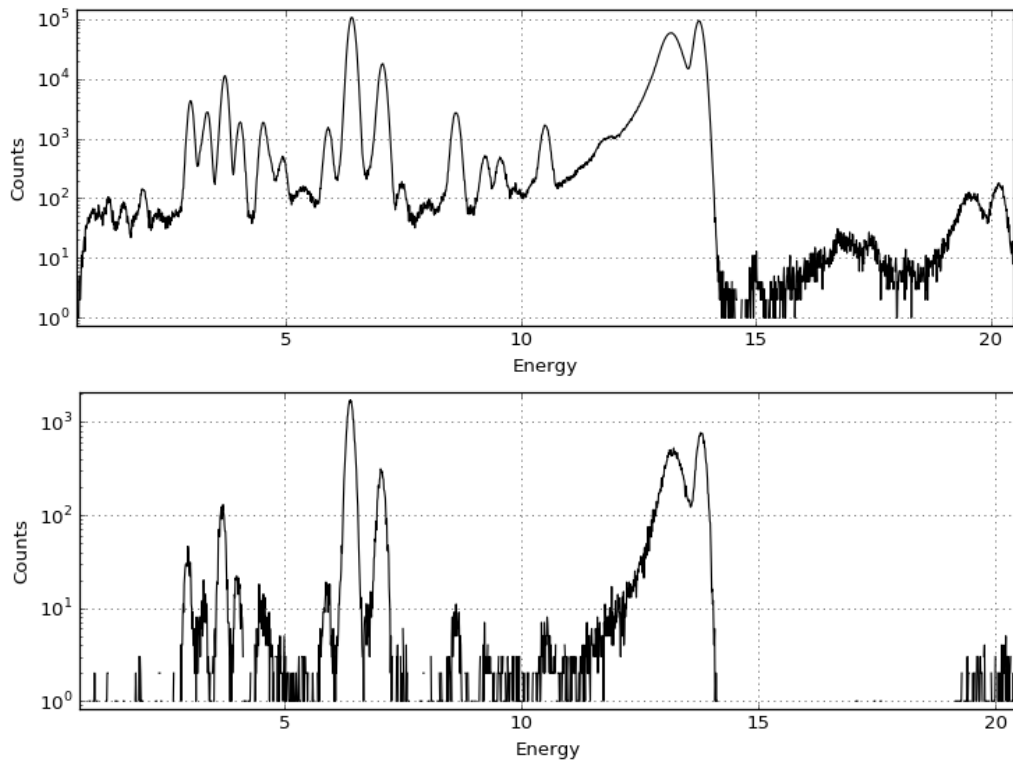


Figure 21. Comparison of the average MCA (top) and a single pixel MCA (bottom) of sample S343811. Note that the counts are lower and peaks are noisier in the bottom spectrum, but elements can still be identified.

Gosselin, 2007). The elements mapped were chosen as they indicate spatial associations with elements that make up their composition (i.e., Fe-As – arsenopyrite, Ca – carbonate, K – sericite, Fe – pyrite and pyrrhotite, Zn – sphalerite, Pb – galena, Ca-Fe – chlorite, etc.), and were supported by mineralogical data provided by X-ray diffraction (refer to Chapter 3), as well as investigations via visual description. Quartz was not detected using element maps due to the inability of the experiment setup to identify Si, since the emission line for Si (Si K α – 1739.8 eV) was too low and was readily absorbed by ambient air (refer to Chapter 2 for experiment setup and conditions). The presence of quartz was inferred by comparing high-resolution photographs with XRF maps, based on prior visual inspection of the samples, and observing areas of white veins showing no element presence (i.e., no counts).

4.2.1 GSC Kerswill Suite

Thirteen samples from the Geological Survey of Canada's Extech III – Kerswill Suite were chosen to represent the mineralized sections of several test pits and orebody samples scattered within the Yellowknife Greenstone Belt. Gold assay values for these representative samples ranged from 0.2 to almost 1000 grams per tonne (Appendix A) (i.e., Con-Campbell Shear Zone F sample C611, with 1054.8 g/t Au, Figure 22). Such samples were analysed to compare geochemical, mineralogical, and textural similarities with the Northbelt property. These samples are the best representatives of the mineralized sections within the YGB, permitting the study of the association of the Con and Giant Mines with the prospects of the Northbelt property.

Six representative samples from both the Con and Giant Mines (XRF maps in Appendix B) consist of Au hosted by quartz-carbonate veining and sulphide mineralization. XRF maps of the Con Mine samples show Au within As, Fe, (Figure 22, C611) and Ca. Zn overprints regions rich in As-Fe, and in turn by later K, and then by quartz and Ca. Giant Mine samples demonstrate Au correlated with both As-Fe, and quartz and Ca (Figure 23, G13), which also show some shear fabrics. Zn and Pb are indicative of later overprinting of early As-Fe clusters.

Seven other Kerswill Suite samples collected from various mineralized sites within the Yellowknife Greenstone Belt were classified as free-milling gold, with grades ranging from 0.5 to 145 g/t Au (Appendix A), and corresponding maps can be located in Appendix B. Varied hosts for gold mineralization are present, such as Zn and Pb within base-metal sulphide mineralization in the Anne Trench, while other slabs indicate either As-Fe or quartz and Ca correlated with Au. The Sito Lake prospect demonstrates As-Fe rich regions overprinted by later Zn-Pb, and later proliferation by K, and quartz and Ca. A slab from one of the mineralizing intrusives (Duckfish Granite) shows Au within As-Fe overprinted by K and cut by later quartz and Ca. As-Fe pods within the Crestaurum Main Zone are associated with Au, and are overprinted by Zn-Pb and cut by later quartz and Ca. Conglomerates in the Jackson Lake Formation were derived from older, mineralized metavolcanics and metasedimentary rocks, and display Au disseminations within As-Fe overprinted by K and cut by later, vein-like quartz and Ca. A sample from the Discovery Suite illustrates Au related to quartz and Ca veining with minor Zn disseminations. A mineralized sample from the MacQueen Prospect bears As-Fe associated Au cut by stockwork-like quartz and Ca signatures.

4.2.2 Yellowknife City Gold Project Northbelt Property

Fifty-eight half-cores were gathered from the seven prospects within the Yellowknife City Gold Project to identify associations of Au for later XANES analysis. Au is hosted within sericite, quartz-carbonate veins, and sulphide masses. Differences in element distribution and associations are explained in detail below, and XRF maps for other samples are in Appendix B.

4.2.2.1 Crestaurum

Four samples from Crestaurum were examined, and 2D SR-XRF single element maps for the representative sample R432250 are shown in Figure 24. The elements present in Crestaurum samples are As, Fe, Ca, Zn, K, Sb, Ti, V, Pb, and Mn. Gold signals were identified in all samples. Comparing the single element maps with the high-resolution photographs, it can be observed that As and Fe are found on the edges of the quartz veins. Gold is located on As-Fe veinlets on the margins of the quartz veins. The spatial

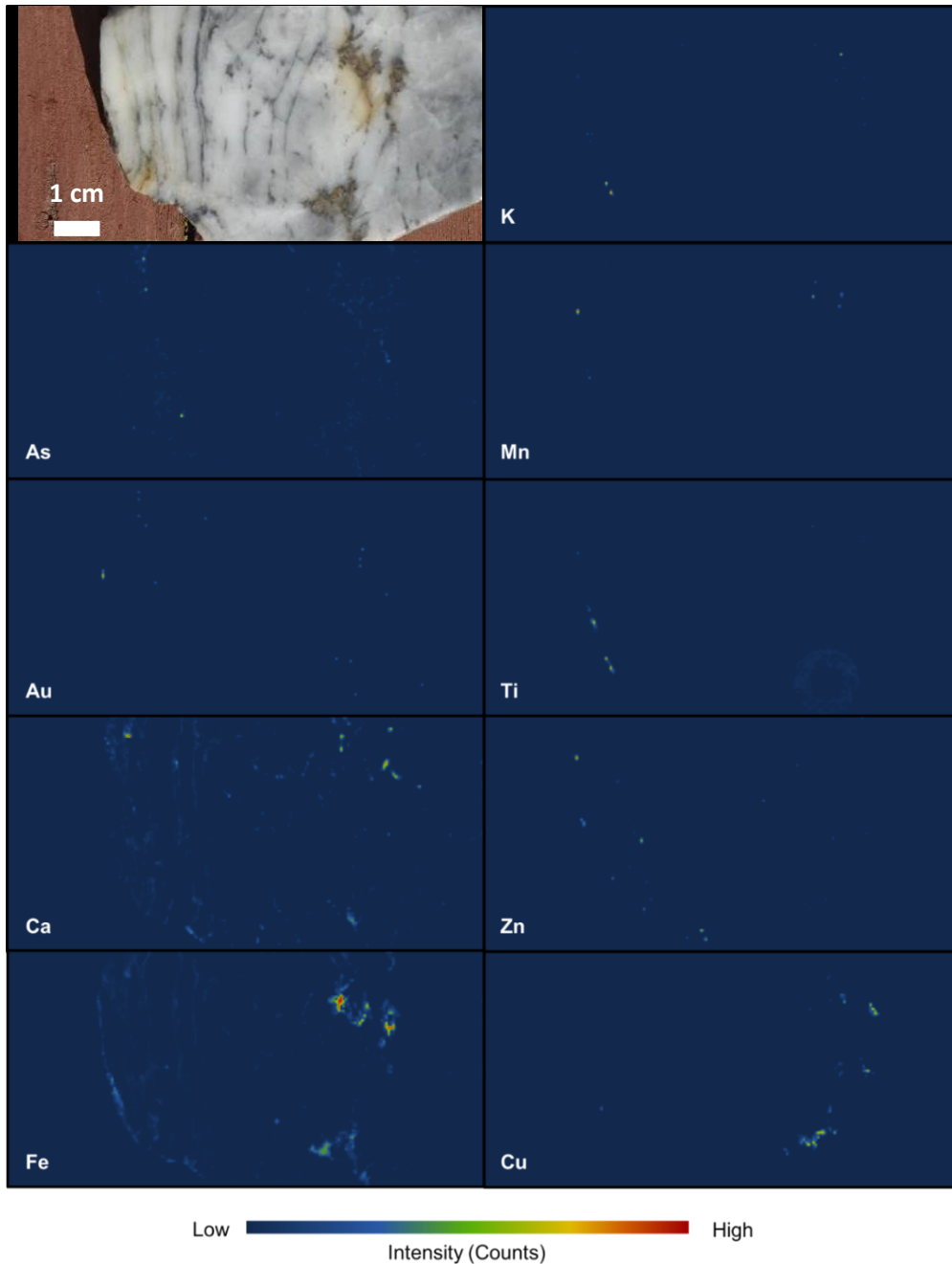


Figure 22. Element distribution map of sample C611 from the Con Mine, a gold-bearing quartz vein with minor sulphides (pixel size at 0.5 mm). Au mineralization is associated with Fe. Minor Zn and Cu exists as small clusters, as well as very minor K and quartz and Ca veining. Fe veinlets and clusters surround quartz margins.

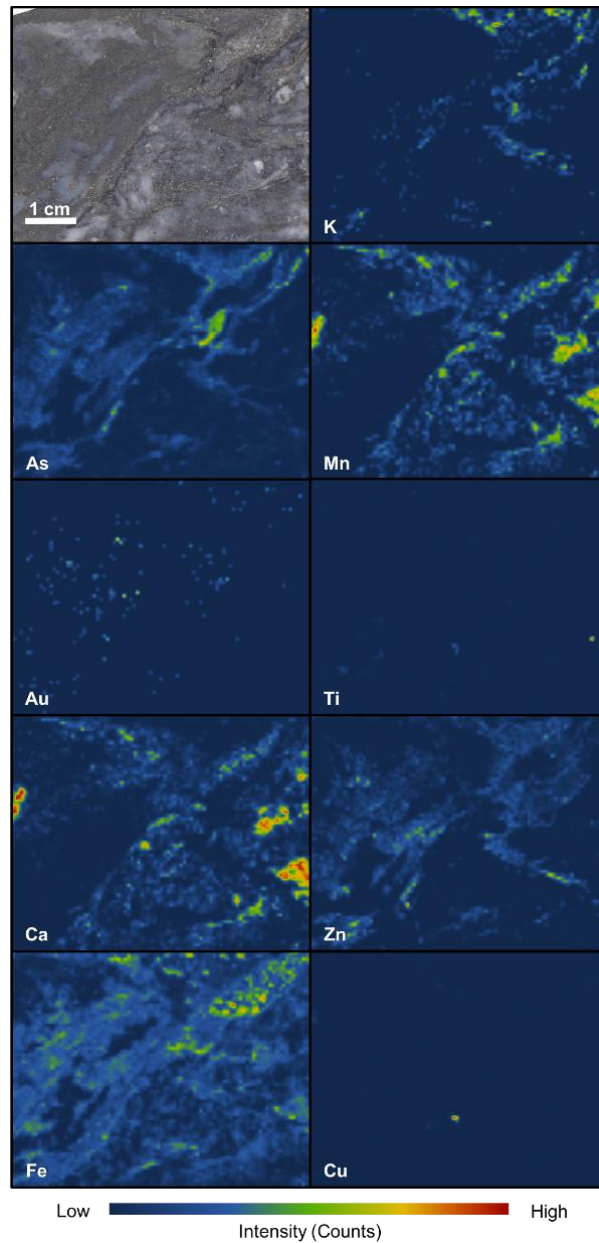


Figure 23. Element distribution map of sample G13 from the Giant Mine, a mineralized sample from the main orebody (pixel size at 0.5 mm). Disseminated Au is hosted within As-Fe, and quartz and Ca, and minor K alteration is apparent. As-Fe clusters are overprinted by minor Zn, and overprinted by minor K. Minor quartz and Ca cut through the rest of the rock. Elements also display shearing along the NE-SW portion of the sample, indicating that the minerals associated with them were precipitated during tectonic events.

distribution of As follows that of Fe, and Au sits on margins close to As-Fe. Early K is cut by Fe-As and later quartz and Ca.

Half cores from the Crestaurum prospect demonstrate Au associated with sulphides within quartz-sericite-chlorite schist. Evidence of Au within quartz-Ca veins are also apparent. Highest Au values are hosted within shear-hosted veins bearing disseminated As-Fe and Zn (Figure 24). Later As-poor mineralization is indicated by the presence of Zn, seen to overprint As-Fe veinlets and masses. Quartz and Ca veins are boudinaged, proving that mineralization occurred syn-deformation.

4.2.2.2 Barney

Seven samples from Barney were examined, and 2D SR-XRF single element maps for the representative sample R115604 are shown in Figure 25. Elements present in Barney samples are As, Fe, Ca, Zn, K, Cu, Sb, Ti, V, Pb, and Mn. Gold signals were identified in five samples. Comparing the single element maps with the high-resolution photograph, it can be observed that As and Fe are found as disseminations, clusters, or veinlets surrounding quartz-carbonate mineralization, and. Gold is located within both the As-Fe masses, or within the quartz-carbonate veins. The spatial distribution of As follows that of Fe, and Au sits on margins close to As-Fe. Early K is cut by Fe-As and later quartz and Ca.

Two variants of gold mineralization are present in the Barney Shear– Au correlated with As-Fe and quartz. Hosts for gold mineralization within the Barney Shear include both quartz-sericite-chlorite schist and chloritized mafic volcanics. Low Au samples from the Barney Shear show abundance of disseminated Pb within quartz veins. Au correlated with As-Fe, on the other hand, are more focused on the sericite-chlorite schist cut by quartz veins. Au is preferentially deposited within the As-Fe mass (Figure 25). Abundance of Ti are apparent in samples with high gold grades (Appendix A).

4.2.2.3 Hébert-Brent

Five samples from Hébert-Brent were examined, and 2D SR-XRF single element maps for the representative sample S521365 are shown in Figure 26. The major elements

present in Hébert-Brent samples are As, Fe, Ca, Zn, K, Sb, Ti, V, Pb, and Mn. Gold signals were identified in three samples. As and Fe are found either as veinlets cut by the quartz veins, or as masses proliferated by minor quartz-carbonate. Gold is located within As-Fe veinlets on the margins of the quartz veins. The spatial distribution of As follows that of Fe, and Au sits on masses close to As-Fe. Early K is cut by As-Fe and later quartz and Ca.

Hébert-Brent samples exhibit Au associated with As-Fe. Two Au-bearing host rocks are present – bleached mafic rocks and feldspar quartz porphyry dykes. Bleached mafic rock hosts are proximal to the contact with the dyke, and are cut by Fe bands and As-Fe needles. Low Au is associated with As-Fe (i.e., Figure 26), while high Au grades are contained in flow breccias consisting of bleached mafic rock clasts. Mineralization within the dykes, on the other hand, exhibit Au associations with As-Fe bands cutting through early K and proliferated by later by quartz-Ca veins. Some traces of Zn within high Au samples signify mineralization of low-As sulphides after Fe-As.

4.2.2.4 Sam Otto

Nineteen samples from Sam Otto were mapped, and 2D SR-XRF single element maps for the representative sample V156527 are shown in Figure 27. The elements present in Sam Otto samples are As, Fe, Ca, Zn, K, Sb, Ti, V, and Mn. Gold signals were identified in eleven samples. As and Fe are found either as veinlets cut by the quartz veins, or as masses proliferated by minor quartz-carbonate. Gold is located within As-Fe veinlets on the margins of the quartz veins, as well as within quartz-Ca gangue. The spatial distribution of As follows that of Fe, and Au sits on As-Fe stringers on the margins of quartz veins, close to K-Fe-Ca masses, and within quartz-Ca veins. Early K is cut by Fe-As and later quartz and Ca. Ca-Fe patches are intimately associated with K overprints.

Three main Au associations are present in the Sam Otto prospect. Au associated with quartz-Ca veins are hosted within mafic volcanics and lapilli tuff. Highest Au grades are hosted within intermediate lapilli tuff. Quartz bands are spatially associated with Au (i.e., Figure 27), and needly As-Fe bands are cut by such quartz veins. Very low to high (0.023 to 2.44 g/t) (Appendix A) Au grades are recorded in mafic volcanic-hosted Au-bearing

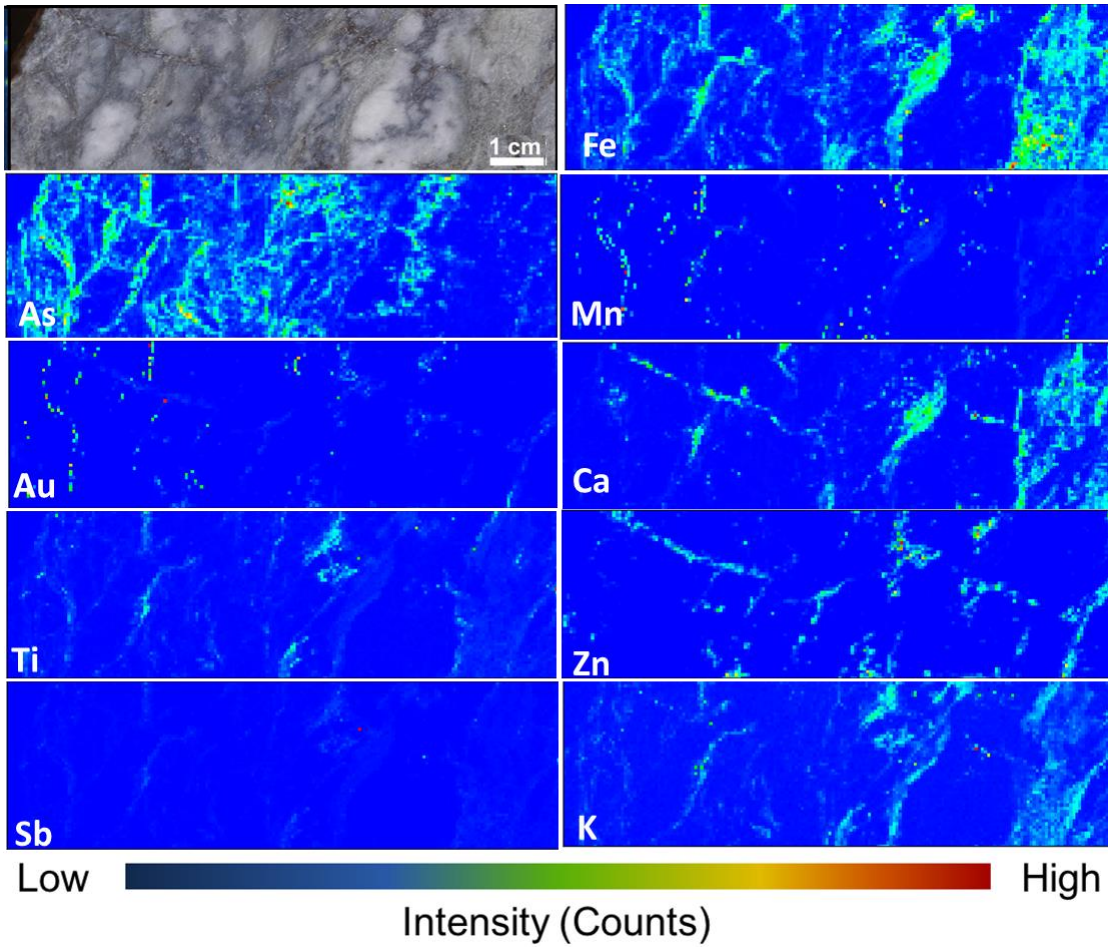


Figure 24. Element distribution map of sample R432250 from Crestaurum, a quartz-sericite-chlorite schist (pixel size at 0.5 mm). Au is spatially associated with Fe-As and Zn. Earlier quartz is cut by sericite (K), and eventually proliferated by later quartz and Ca veins.

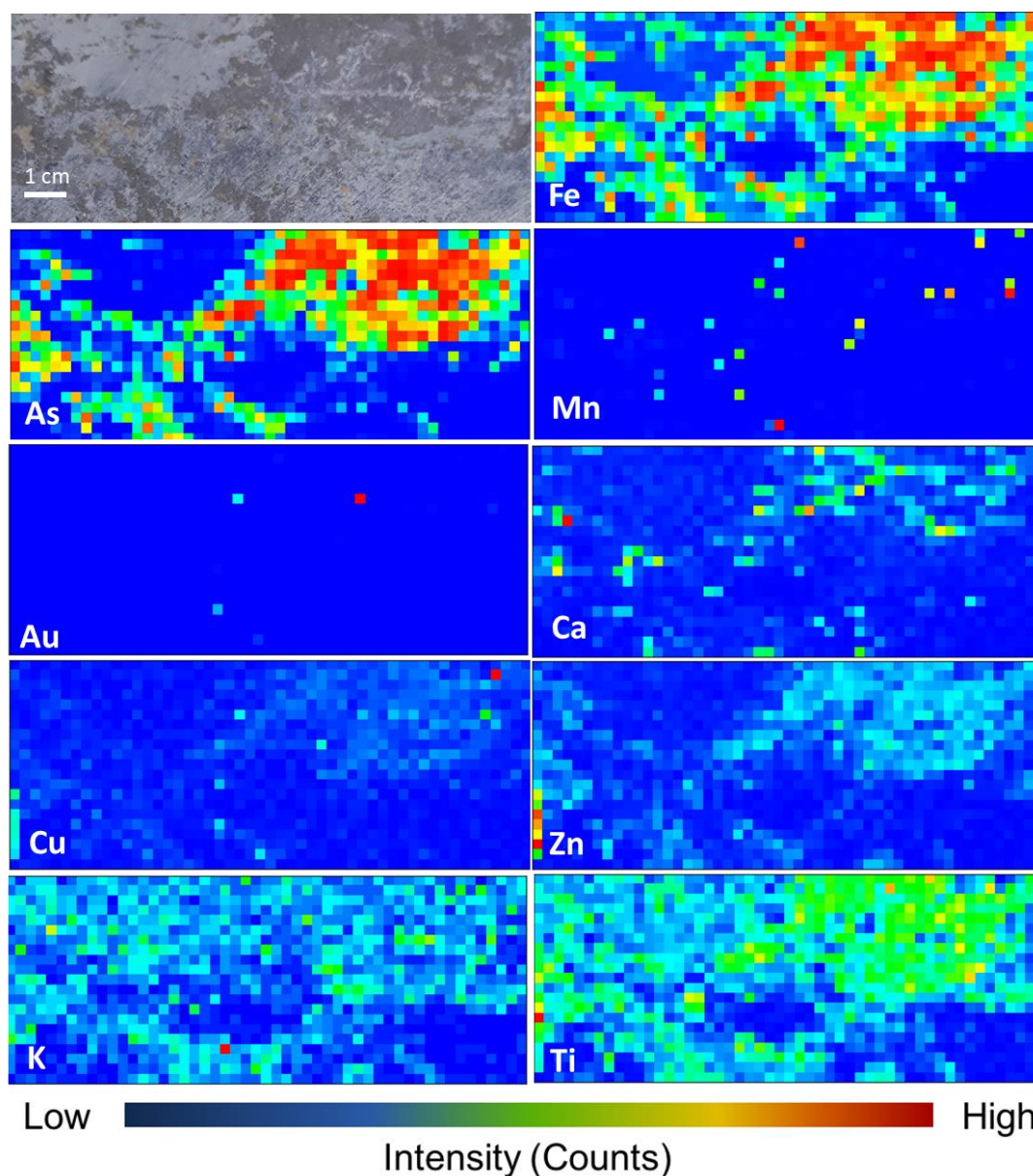


Figure 25. Element distribution map of sample R115604 from the Barney Shear, a sericite-altered host rock with grey quartz veins and ankerite (pixel size at 2 mm). Au is spatially associated within As-Fe masses, with later Zn overprinting As and Fe. Early K (outside the main vein) is cut by As-Fe, while later K and minor quartz and Ca vein overprints the sulphides. Ti enrichment is seen within the sulphide mass, which can be correlated to later K.

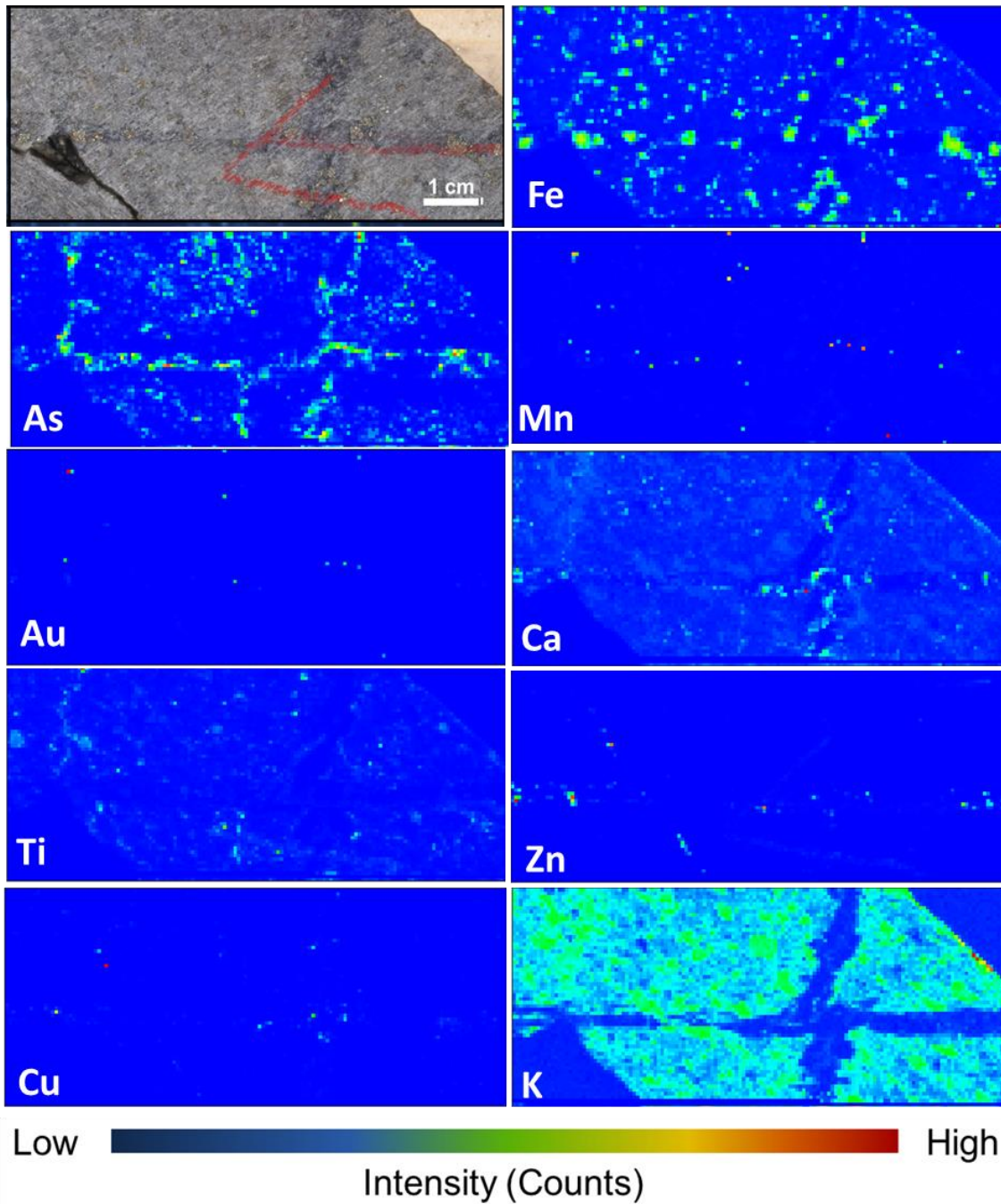


Figure 26. Element distribution map of sample S521365 from Hébert-Brent, a portion of the mineralized feldspar quartz porphyry dyke (pixel size at 0.5 mm). Au is associated with As-Fe bands cut by later quartz-Ca. Early K is cut by later As-Fe bands and quartz-Ca veins. Minor Zn is contained within the As-Fe veins.

quartz veins. Early K and Ca-Fe is proliferated by sulphide mineralization. Needly to disseminated As-Fe are overprinted by K-Ti and cut by bluish quartz veining. Sericite-hosted Au is also apparent, suggesting that later sericite-mineralizing fluids remobilized Au from pyrite-arsenopyrite. Sulphide-hosted Au within the Sam Otto prospect bared varied percentages within a multitude of host rocks. Insignificant to relatively high (0.054 to ~5 g/t, Appendix A) Au grades are seen in mafic volcanic hosts, where disseminated to needly As-Fe are overprinted by patchy K and cut by bluish quartz veins. Low Au samples are enriched with Zn instead of As-Fe. Varied Au grades (0.6 to 6 g/t, Appendix A) are hosted within volcanoclastic rocks and both lapilli and ash tuff. Disseminated to needly As-Fe are cut by K and quartz-Ca. Some signatures of later Zn overprint earlier As-Fe. Evidence of strong As-Fe mineralization are present along the foliation bands of the volcanoclastics. Wallrock samples display prominent K. Sheared gabbro hosts (averaging 3.75 g/t Au, Appendix A) show As-Fe bands overprinted by Zn and cut by later K-Ti and quartz-Ca veining. Minor Sb is seen to be associated with Au.

4.2.2.5 Dave's Pond

Thirteen samples from Dave's Pond were mapped, and 2D SR-XRF single element maps for the representative sample V160414 are shown in Figure 28. The elements present in Dave's Pond samples are As, Fe, Ca, Zn, K, Sb, Ti, V, Pb, and Mn. Gold signals were identified in eleven samples. As and Fe are found either as veinlets cut by the quartz veins, or as masses proliferated by quartz-carbonate. Gold is located within As-Fe veinlets on the margins of the quartz veins, as well as minor Sb within quartz-Ca. The spatial distribution of As follows that of Fe, and Au sits on As-Fe stringers on the margins of quartz veins, close to K-Fe-Ca masses, and within quartz-Ca veins. Early K shows foliation, and is cut by Fe-As and later quartz and Ca.

Dave's Pond half cores exhibit Au hosted in quartz-Ca veins, K, and As-Fe hosted in sheared ash tuff, intermediate volcanics, and mafic volcanoclastics. Higher Au grades are situated within moderately sheared zones within the tuff, and are related to plentiful K and Zn. Zinc mineralization is fracture-controlled. Au correlated with K possesses relatively lower (~0.5 g/t, Appendix A) grades (Figure 28), and is also hosted within ash

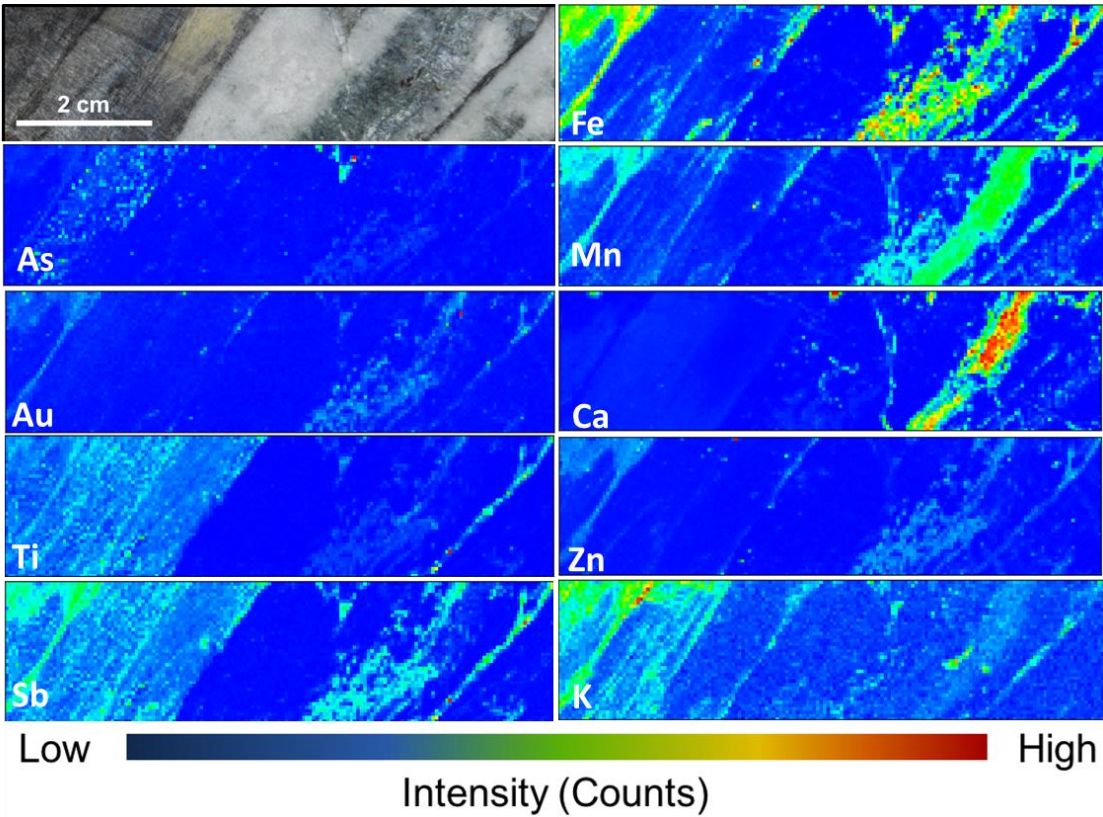


Figure 27. Element distribution map of sample V156527 from Sam Otto, a mafic volcanic host with patchy chlorite (pixel size at 0.5 mm). Au is associated with quartz-Ca overprinting As-Fe and Zn. Early K-Ti and Ca-Fe (at the left portion of the core) is cut by As-Fe veining. Later K at the right portion of the sample is overprinted by quartz-Ca veining. Sb signatures are related to Au.

tuff. As-Fe veinlets are still apparent within the K-hosted Au, and exists as veinlets at the margins of quartz-Ca. Au associated with As-Fe are common within the shear zone, and are overprinted by K and cut by quartz-Ca veins. Minor Au can be also seen to be related to Sb.

4.2.2.6 Mispickel

Nine samples from Mispickel were mapped, and 2D SR-XRF single element maps for the representative sample S892089 are shown in Figure 29. The elements present in Mispickel samples are As, Fe, Ca, Zn, K, Sb, Ti, V, and Mn. Gold signals were identified in eight samples. As and Fe are found either as veinlets cut by the quartz veins, within masses or veinlets of K, or proliferated by quartz-carbonate. The spatial distribution of As follows that of Fe, and Au sits on As-Fe stringers on the margins of quartz veins, and within quartz-Ca veins. Early K shows foliation, and is cut by Fe-As, and proliferated by later quartz and Ca.

The Mispickel Suite is a greywacke-hosted mineralized prospect with evidence of two Au associations. Insignificant Au is seen within K, while variable, low Au grades are seen hosted within quartz-Ca veins. Foliation is displayed by early K and As-Fe mineralization. Small to significant Au assay values (0.2 to 5.6 g/t, Appendix A) (Figure 29) are located within As-Fe. Bluish quartz veins proliferate within the greywacke host. Later K is cut by quartz-Ca veining.

4.2.2.7 Homer

Four samples from Homer were mapped, and 2D SR-XRF single element maps for the representative sample S345537 are shown in Figure 30. The elements present in Homer samples are As, Fe, Ca, Zn, K, Sb, Ti, V, and Mn. Gold signals were identified in all samples. As and Fe are found either as veinlets cut by the quartz veins, or as pod-like masses proliferated by quartz-carbonate. Gold is located within As-Fe veinlets on the margins of the quartz veins. The spatial distribution of As follows that of Fe, and Au sits on As-Fe stringers on the margins of quartz-Ca veins, or within the As-Fe pods. Early K is cut by Fe-As and later quartz and Ca.

Samples from the Homer prospect exhibit Au associated with As-Fe hosted in both massive flow and gabbroic hosts. Host rocks are chloritized and sericitized due to metamorphism and percolation of mineralizing fluids. Early Ca-Fe and K are overprinted by As-Fe, and are eventually cut by quartz-Ca veining. Lower Au counts are associated with minor Ca infills and Zn, while higher Au grades are present within strong As-Fe pods, such as Figure 30.

4.3 Summary

Based on the geochemical and textural associations examined via 2-dimensional X-ray fluorescence maps, timing of mineralization as well as mineralogical relationships are established. Metamorphic processes acting on a variety of host rocks on both the Kerswill Suite and the Northbelt Property, from mafic and felsic volcanics to greywackes, and these were altered by early Ca-Fe and K. Mineralization of As-Fe followed suit, and were overprinted by Zn and minor Pb. Another wave of K mineralization overprinted the sulphides, and quartz-Ca veining proliferated through the mineralized masses. Enigmatic Sb signatures are associated with elevated gold counts, but is to be investigated further. Au is seen to be associated with three main types of mineralization, such as K and Ca-Fe, quartz-Ca, and As-Fe.

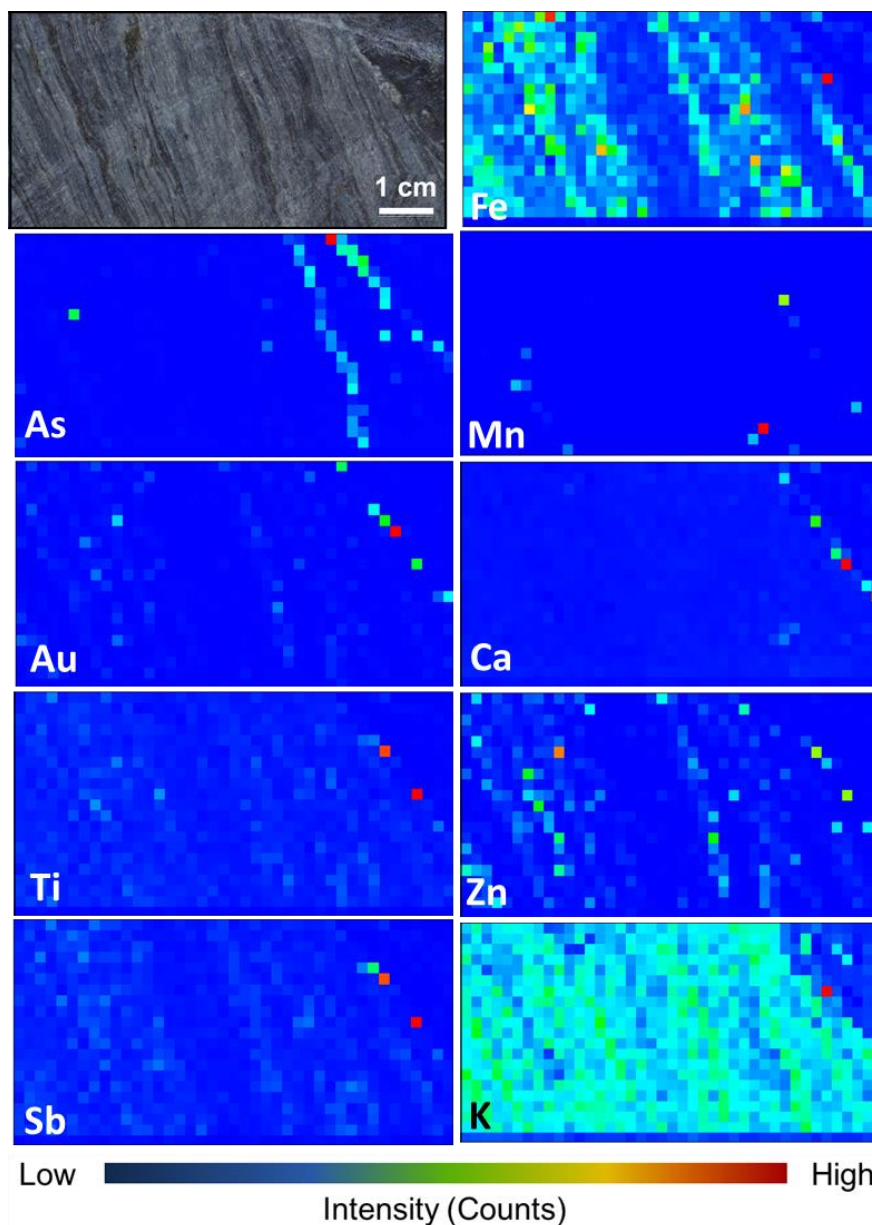


Figure 28. Element distribution map of sample V160414 from Dave's Pond, a sericitic ash tuff (pixel size at 2 mm). Au is associated with K. Early K, which shows foliation, is cut by As-Fe and Zn veining, and eventually overprinted by secondary K alteration. Minor quartz-Ca veining cuts across the foliation bands. Remnant veinlets of As-Fe and disseminated Zn are scattered along fringes of the host rock. Sb signatures are related to Au (orange to red pixels at the top right of the Sb map).

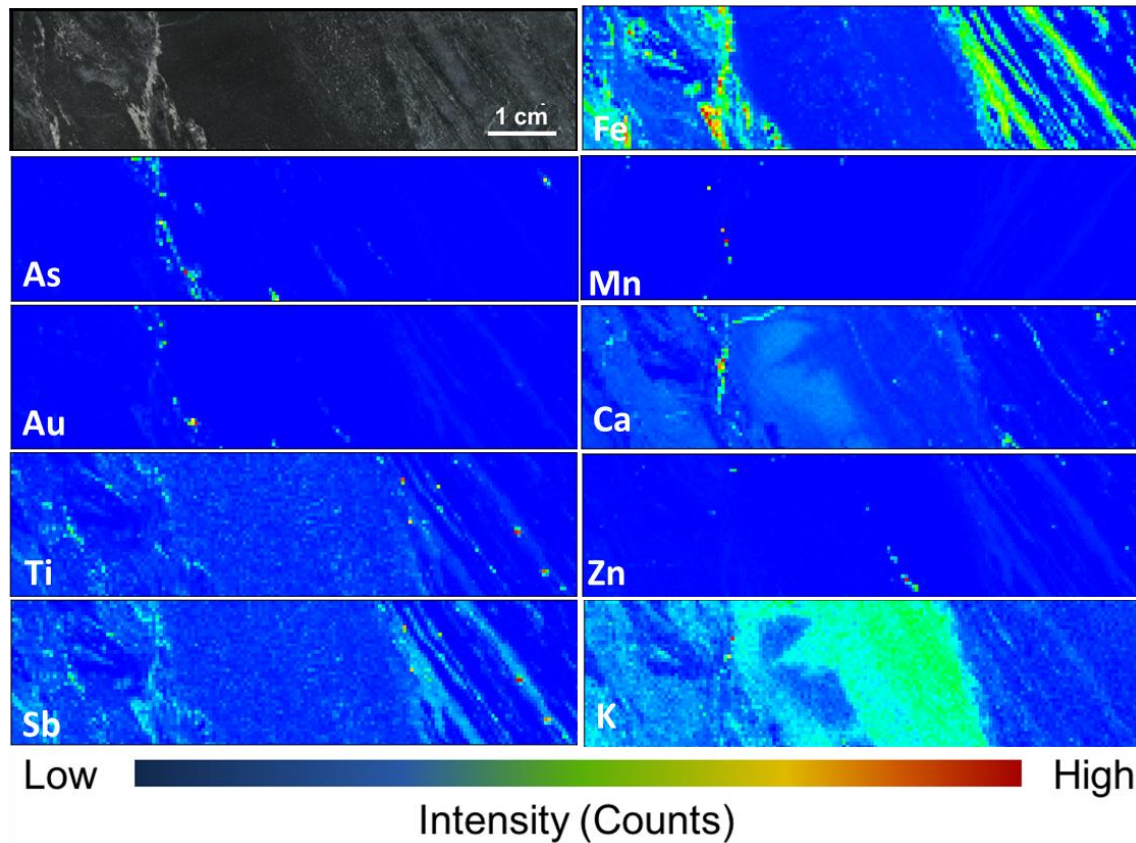


Figure 29. Element distribution map of sample S892089 from Mispickel, a greywacke host rock with foliation displayed by As-Fe and minor K (pixel size at 0.5 mm). Au is associated with As-Fe which cut through earlier K-Ti mineralization. Remnant Zn is overprinted by later K-Ti, which doesn't show foliation (centre mass at the K map), and are all cut by quartz-Ca veining. Sb signatures are related to Au.

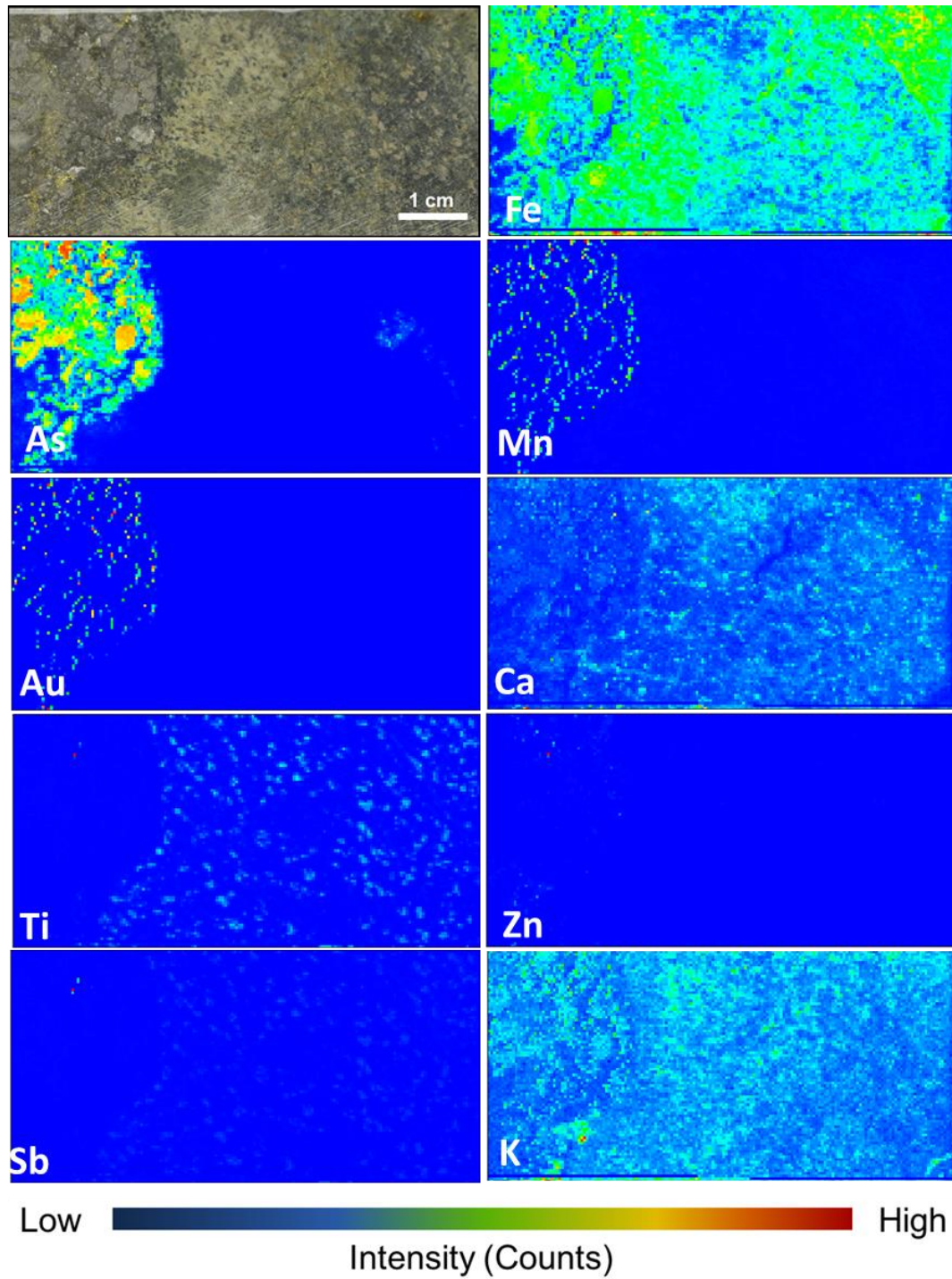


Figure 30. Element distribution map of sample S345537 from Homer, a gabbro host with prominent leopard-like As-Fe mineralization (pixel size at 0.5 mm). Au is associated with As-Fe clusters cutting through early K and chlorite Ca-Fe. Sparse Zn is an indication of low-As mineralization. Minor Sb is seen to be related to Au.

Chapter 5

5 X-ray Absorption Near Edge Structure (XANES) Spectroscopy on Au speciation

XANES studies of fourteen slabs and half cores with the most promising Au signals were selected for further analysis. In these samples, the XRF gold maps showed hot spots for Au. Examination of the MCA spectra showed a fluorescence peak at 9713 eV for gold. X-ray fluorescence maps of a 2x2 cm area surrounding the identified high Au pixel were collected, and the MCA spectra were analysed for Au presence and interferences. There are known spectral interferences that may give a false positive gold signal, such as Zn K_{β} (9570.4 eV) or W L_2 (9672 eV) (Ravel et al, 2005). Of the initial 14, twelve samples were identified to exhibit zinc interference, identified by observing the characteristic Zn K_{β} emission pattern and comparing with the relative fit of the Au L_3 emission line (Figure X). Two samples were determined to have gold signals for XANES analysis.

After X-ray fluorescence mapping, spots representing Au were further studied by looking at its corresponding MCA spectrum to see if it indeed coincides with the fluorescence emission line of Au L_3 . Twenty-seven spots corresponding to the fourteen slabs and half cores were mapped to locate the intense Au spot. To check for issues regarding interference, additional XRF maps were collected using beam energies below the Au L_3 binding energy (11919 eV; refer to Chapter 2 for SR-XRF map collection methods). Twelve of the samples exhibited interference with Zn K_{β} (9567.4 eV), as well as a mismatch of the Au L_3 emission line (i.e., Fig. 33 and 34) (MCA spectra of the Au hotspots are in Appendix F). Two samples were identified to exhibit MCA spectra matching the Au L_3 line, the Con Mine sample C611 (Figures 31 and 32), and the Mispickel sample S892089 (see Appendix F for the MCA fit of Au). Sample selection for Au XANES is easily affected by such peak interferences, giving a false impression of the presence of Au in the pixel. Also, other samples which undergone Au XANES did not show any spectra corresponding to Au presence, proving that there is no gold contained in the pixel examined, such as the Dave's Pond sample V413296 (Figures 33 and 34).

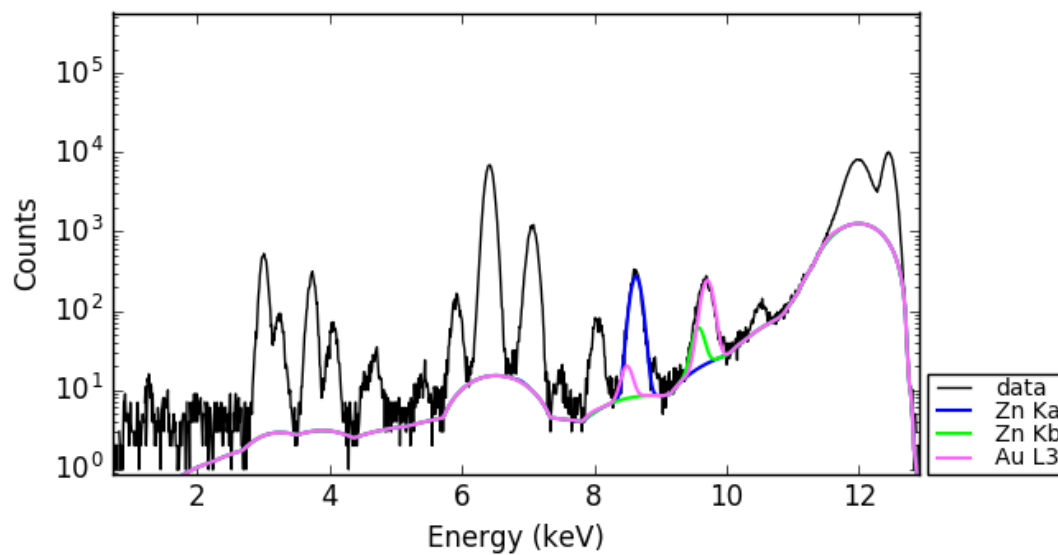


Figure 31. MCA spectrum of sample C611 from the Con Mine. Note that the Au L₃ peak proves that there is indeed Au in the sample.

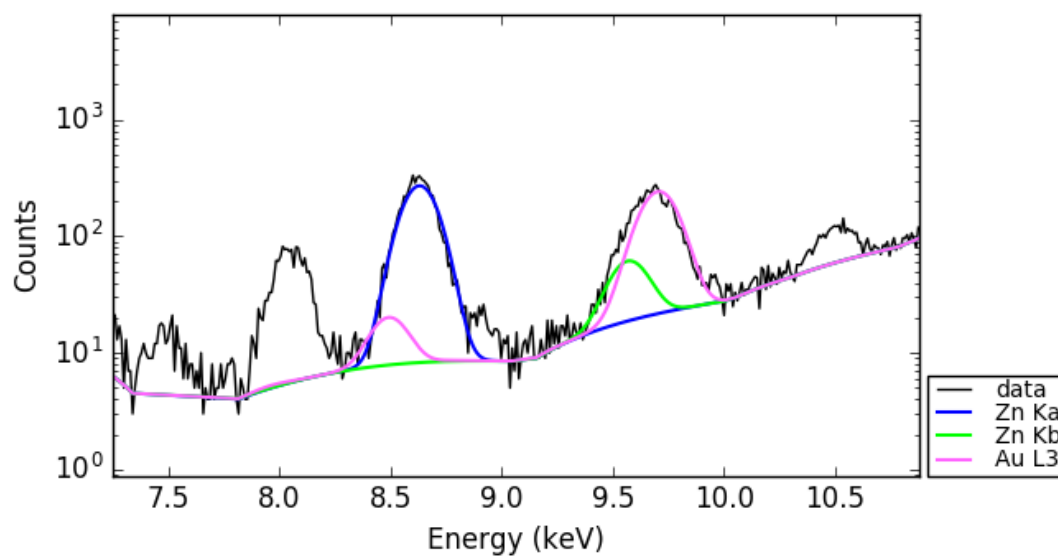


Figure 32. Zoomed in MCA spectrum of the high intensity pixel of sample C611 from the Con Mine. Zn K β overlaps with Au L₃, but the Au peak is still prominent.

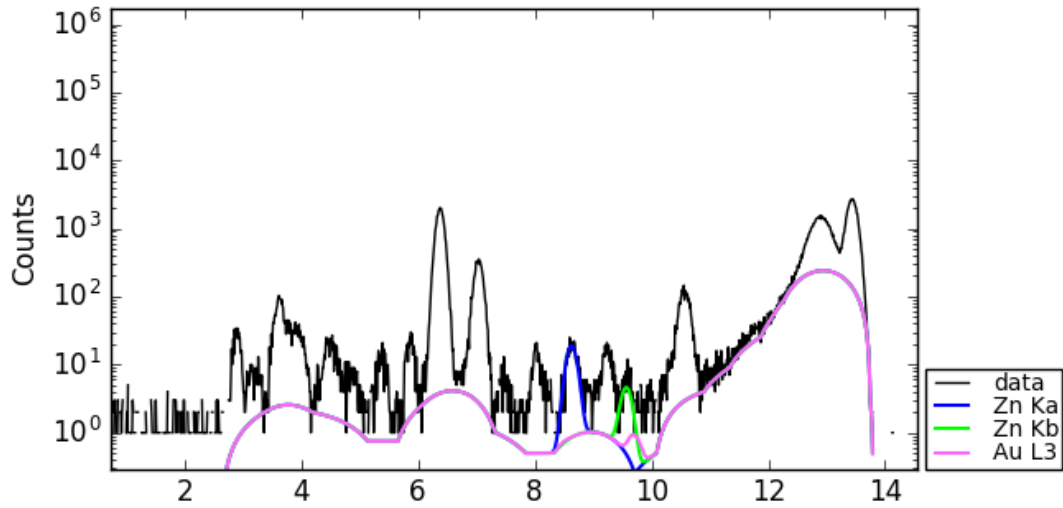


Figure 33. MCA spectrum of the high intensity pixel of sample V413296 from Dave's Pond. Note that there is strong Zn presence, and it overlaps with the Au signal. Still, if Au was indeed present, it will show as a distinct peak above Zn.

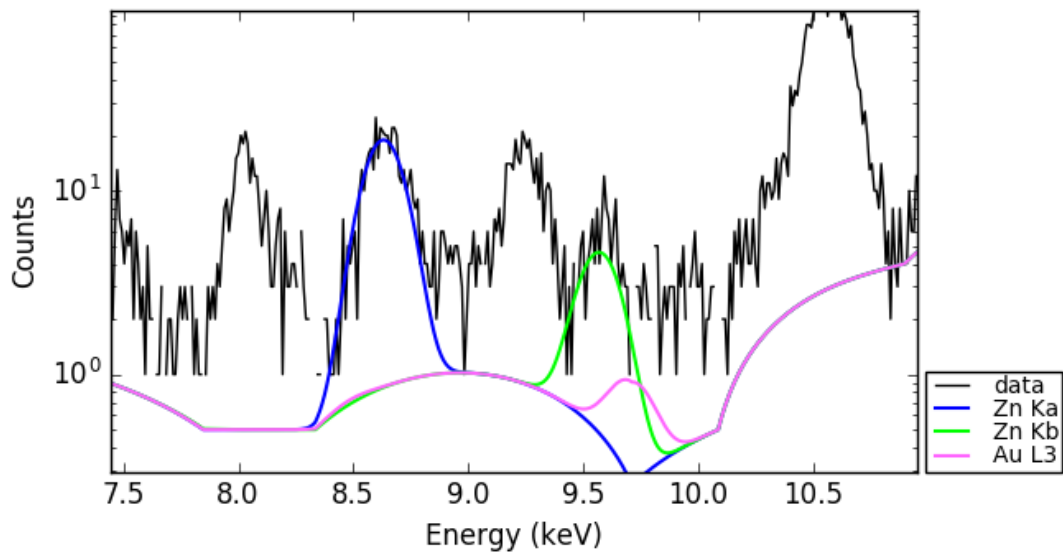


Figure 34. Zoomed in MCA spectrum of the high intensity pixel of sample V413296 from Dave's Pond. There is no distinct peak that represents Au, and it is overlapped by Zn.

Identification of the speciation of Au is usually described using least squares linear combination fitting (i.e., Van Loon et al, 2015), which involves fitting the sample spectrum with several weighted standards of Au. However, the lack of Au standards in hand prevented the use of such a method, as only a gold foil standard was present during the experiment. Hence, Au speciation was determined using visual matching of the Au XANES spectrum of the gold foil. It is not recommended to utilize the Au XANES spectrum of known standards gathered from data libraries, since these were not analysed under the same conditions as the unknowns.

The sample from the Kerswill Suite (C611, Figure 35) is a slab from the Con Mine, with Au hosted within a minor sulphide (arsenopyrite-pyrite-pyrrhotite) vein along a quartz vein. The gold grade for the slab averages ~1058 g/t Au (Appendix A). The gold spot was then analysed using XANES, and its signal (Figure 37, top left) matches the spectrum of an Au foil in-house standard (Figure 37, bottom centre) examined prior, stating that Au in the Con Mine slab is metallic gold. A sample from the Mispickel Suite (S892089, Figure 36) also bears metallic Au (Figure 37, top right). Figure compares the XANES spectra of metallic versus oxidised gold in different anion pairs.

5.1 Summary

Based on the collected XANES spectra, it can be concluded that metallic gold is indeed present in the Northbelt Property. No other oxidation states of Au were identified (i.e. Figure 38), hinting that gold is not incorporated into the lattice structures of the sulphides. Interference of Zn in the Au spots does not automatically state that there is no gold in the whole sample, but instead states that spectral interference misrepresented the presence of gold in the pixel or spot analysed.

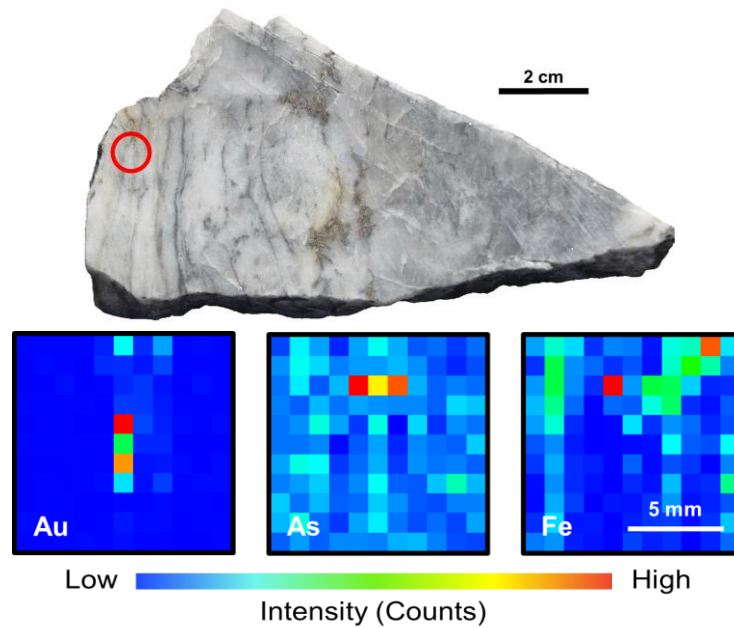


Figure 35. Sample C611 from the Kerswill Suite, a quartz vein with minor sulphide veins from the Con Mine. Encircled in the top image is the approximate spot where X-ray Fluorescence maps of As, Fe, and Au were made, and is used to locate the spot for Au XANES.

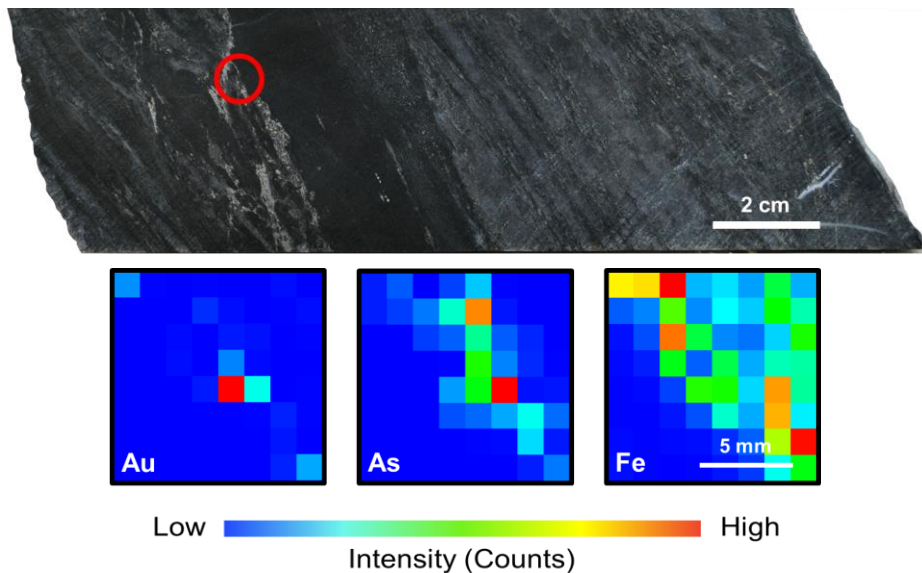


Figure 36. Sample S892089 from the Mispickel Suite, a mineralized greywacke. Encircled in the top image is the spot where X-ray Fluorescence maps of As, Fe, and Au were made, and used to pinpoint the spot for Au XANES.

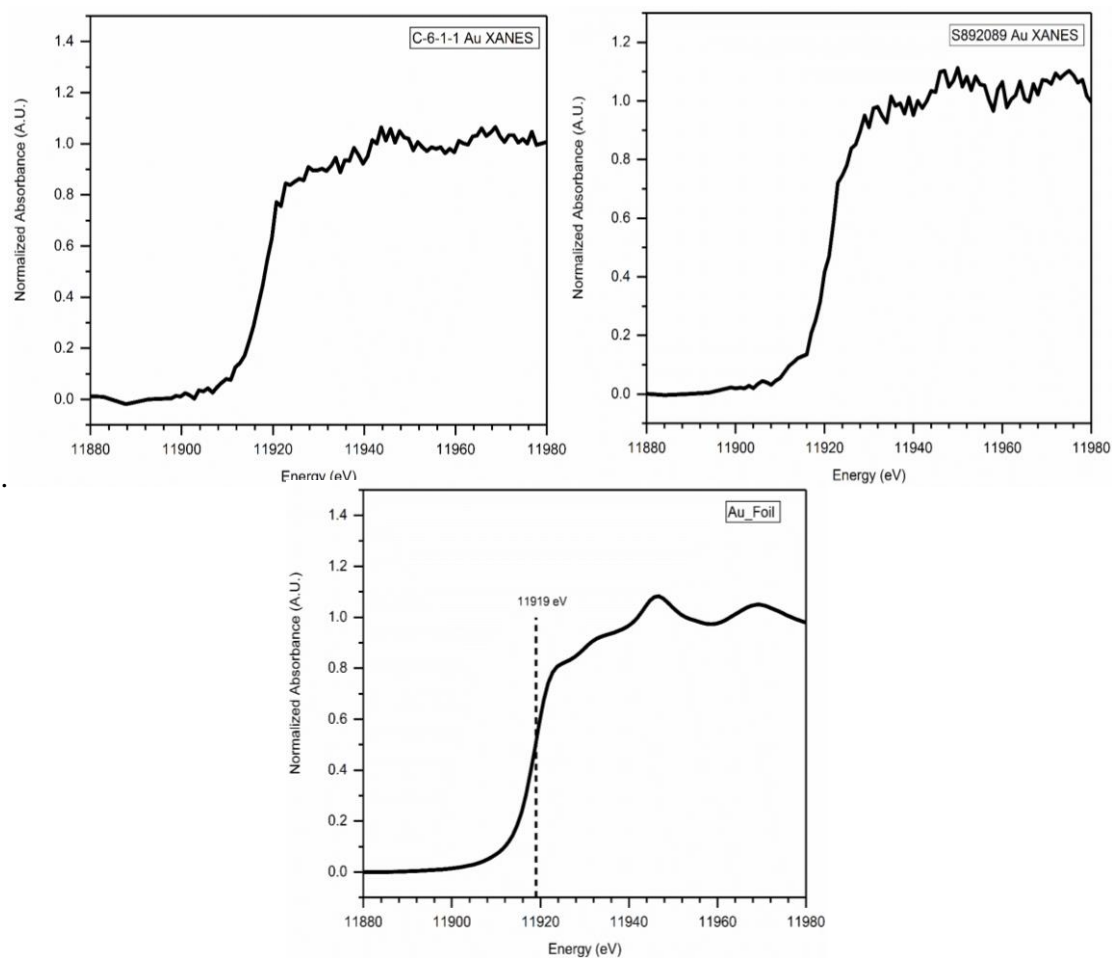


Figure 37. XANES results of the spots with high Au, with the bottom graph showing XANES spectra of a gold in-house standard for reference. Both the Kerswill (top left) and Mispickel (top right) samples show the presence of Au⁰, or metallic gold, within the spot.

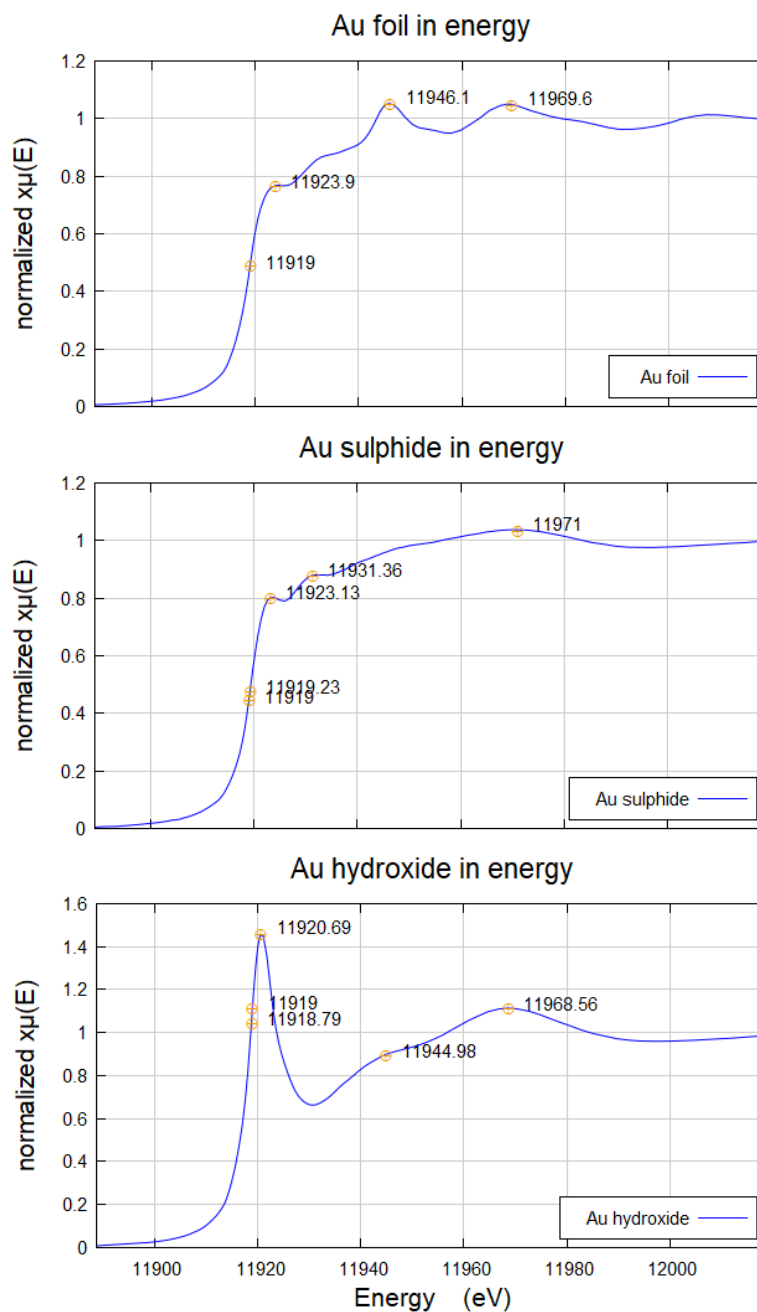


Figure 38. Samples of Au XANES spectra of a gold foil (top, for Au^0), gold sulphide (middle, corresponding to Au^{3+}), and gold hydroxide (bottom, corresponding to Au^{1+}), from Ravel, 2016. Note the behaviour of the spectrum at the Au L₃ absorption edge (11919 eV) changes with respect to the oxidation state.

Chapter 6

6 Discussion

The goals of the project were to determine if the YCGP is part of the same gold mineralizing system as the prolific Con and Giant mines in the YGB, and if these are a part of a single, giant mineralizing system, investigate vectors for Au mineralization, and identify the oxidation state of gold. Synchrotron XRD, XRF and XANES spectroscopy techniques were applied to determine similarities and differences between samples collected across the YCGP property and various locations in the YGB. Mineralogy, elemental spatial relationships, mineral textures, overprinting associations, cross-cutting, and gold speciation were all examined to develop a picture of how a single system was responsible for gold mineralization in the YGB. Mineralogical and geochemical vectors for Au mineralization were identified to allow future exploration efforts to readily identify spatial associations for gold in the field and during drilling periods. The oxidation state of gold will be important in planning for future production, and will also contribute to the decision if gold is indeed viable to be produced.

6.1 X-ray Diffraction and Mineralogy

Common minerals in both the YCGP and the mineralized sections of the YGB involve abundant quartz, calcite, dolomite, ankerite, muscovite, biotite, chlorite, and plagioclase, while the more apparent sulphides include pyrite, arsenopyrite, pyrrhotite, sphalerite, and galena, summarized in Table 10. Evidence of arsenopyrite being altered to pyrrhotite was based on visual descriptions on the half cores, with remnant arsenopyrite grains showing alteration and further work is required to understand the mechanism and timing of arsenopyrite alteration to pyrrhotite. Both locations show prevalent quartz, muscovite, biotite, and chlorite, while a combination of carbonates are present, e.g., dolomite and ankerite are present in the Con Mine, while all dolomite and calcite are in Sam Otto. A lack of carbonates is seen in the Sito Lake, Anne Trench, and the Duckfish Granite for the YGB, and Hébert-Brent, Mispickel, and Homer for the YCGP. For sulphides, all locations show prevalence of pyrite, arsenopyrite, pyrrhotite, sphalerite, and galena.

Remnant plagioclase is more common in the Northbelt, except for Crestaurum and Barney, and an appearance in the Con Mine, Duckfish granite, and Sito Lake. Only low-As sulphides are present in the Anne Trench due to its location in a base-metal sulphide prospect.

Two types of sulphide mineralization are discovered within both the Kerswill Suite and Northbelt samples. Both low (sphalerite-galena), and high-As (pyrite-arsenopyrite) sulphides are observed across deposits. Pyrrhotite is likely due to the alteration of arsenopyrite, especially in the Mispickel Suite, where there are relatively low amounts of arsenopyrite relative to pyrrhotite (further explained in Chapter 6). Quartz is also seen as the most abundant mineral, either as part of a later veining event, silicification, or of the host rock, especially for felsic volcanics, tuff, schist, and greywacke. Carbonates such as calcite, dolomite, and ankerite are plentiful in some prospects, e.g. Crestaurum and Sam Otto, and are very minor, up to almost undetectable, in others, e.g. Homer and Hébert-Brent. A combination of carbonate minerals is present in the deposits, with the type probably due to the influence of host rock mineralogy. Chloritization as clinocllore is apparent in all samples, and developed either due to metamorphic processes or fluids percolating during orogenic gold deposition. Sericitization is also apparent as muscovite, and biotite is prevalent, especially in Sam Otto, which may indicate wallrock alteration by another set of percolating fluids. Remnant host rock minerals such as plagioclase are still present. Diffraction data proves that the Northbelt Property of the YCGP and the high-grade gold samples from the Kerswill Suite from the YGB are indeed similar mineralogically.

6.2 X-ray Fluorescence, Geochemical Similarities, and Textural Implications

Mineralogical data identified by X-ray diffraction data is linked to the geochemical signatures collected via X-ray fluorescence, along with the help of visual observations on the half cores. Minerals were identified based on spatial associations of elements, such as As-Fe for arsenopyrite, Fe for pyrite and pyrrhotite, Zn for sphalerite, Pb for galena, Ca for carbonates, Ca-Fe for chlorite (for Fe areas with lack of As and abundance of Ca, as well as spatial association with K) and K for sericite (inclusive for muscovite and biotite),

Table 10. Summary of the mineralogy in the Kerswill Suite and the TerraX Northbelt Property. Note the similarities in mineral presence, most notably the sulphides (pyrite, arsenopyrite, sphalerite, galena, and monor pyrrhotite), carbonates (dolomite, ankerite, and calcite).

	quartz	plagioclase	muscovite	biotite	pyrite	arsenopyrite	galena	sphalerite	pyrrhotite	dolomite	ankerite	calcite	chlorite
GSC Kerswill													
Con Mine	1	1	1		1	1	1	1	1	1	1		
Giant Mine	1		1		1		1	1		1	1	1	1
Anne Trench	1						1	1					
Crestaurum Main Zone	1						1			1	1		
Duckfish Granite	1	1	1		1		1	1					
Discovery Mine	1		1	1	1		1	1		1		1	
Jackson Lake	1		1	1	1		1	1			1	1	1
MacQueen Prospect	1		1		1		1	1		1			
Sito Lake	1	1	1		1		1	1					1
TerraX Northbelt	quartz	plagioclase	muscovite	biotite	pyrite	arsenopyrite	galena	sphalerite	pyrrhotite	dolomite	ankerite	calcite	chlorite
Crestaurum	1		1		1	1	1	1	1	1	1		1
Barney	1		1		1		1	1		1	1		1
Hebert-Brent	1	1	1	1	1		1	1					1
Sam Otto	1	1	1	1	1		1	1	1	1		1	1
Dave's Pond	1	1	1	1	1		1	1	1			1	1
Mispickel	1	1	1	1	1		1	1	1				1
Homer	1	1	1	1	1		1	1	1				1

since XRD data and visual descriptions were the only sources for any mineralogical information. Statistical evaluations, such as principal component analysis (PCA), was not considered for the project since the intention of producing the maps was to provide further information on geochemical and textural distributions of elements to be used in decision-making, but PCA may be done in future work to understand element occurrence and distribution. Quartz is associated with map areas lacking any counts, which matches areas of bluish and whitish veins in high-resolution photographs (see Chapter 4 for explanations). Quartz is, coincidentally, also related to carbonate veining, based on visual descriptions of hand samples. Elements include Ti, Sb, V, Mn, Co, Ni, and Cu are spatially associated with sulphides, where they may be present as trace components, i.e. Ti in sericite, or Sb in sulphides.

Two-dimensional maps of both the YGB and YCGP display the relative timing of mineralization of minerals, common in both units. The maps reveal the mineralization of early chlorite and sericite, which was overprinted by high-As sulphides (pyrite-arsenopyrite), and eventually proliferated by base metal sulphides (sphalerite-galena). A second phase of sericitization and chloritization altered the older minerals, and quartz-carbonate veining cut through the other units. Textural associations were also observed (refer to Chapter 4 for the images). with the fluorescence maps, such as veinlets surrounding quartz-carbonate veins (C611, Fig. 22), boudinaged veins (R432250, Fig. 24), sulphide pods (S345537, Fig. 30), and foliation as indicated by sericite (V160414, Fig. 28) Detailed XRF maps of other samples can be found in Appendix B.

Three main Au associations are observed among the seven prospects within both the YGB mineralized suites and the YCGP Northbelt Property. Au is related to mineralization of pyrite-arsenopyrite (Figure 39), sericite-chlorite (Figure 40, right), and quartz-carbonate veining (Figure 40, left). These associations are also prevalent in the Kerswill Suite, representatives of the mineralized samples of the Yellowknife City Gold Project. The presence of Au within such spots were examined by looking at their corresponding MCA spectra to prove that gold is indeed present in the site.

Only sulphide-associated Au is seen in the Crestaurum deposit. Highest Au grades are located within shear-hosted sulphide veins, while low Au samples are distal from the shear zones. Both high and low Au samples exhibit similar features, such as boudinaged quartz-carbonate (dolomite-ankerite) veins and early sericitization.

Au within both sulphides and quartz-carbonate veining in schist and mafic volcanics are apparent in the Barney prospect. Low Au is seen in samples with disseminated galena in quartz-hosted gold, while highest gold grades within sulphides are associated with Ti enrichment. Later sericitization and quartz-carbonate veining eventually overprint sulphides.

Only sulphide-hosted Au is seen within Hébert-Brent. Relatively moderate to high Au grades are hosted in both flow breccia and feldspar quartz porphyry dyke hosts. Bands of pyrite-arsenopyrite are seen to cut through the sericitized host rock. Sphalerite is indicative of base metal sulphide mineralization after pyrite-arsenopyrite deposition. Arsenopyrite needles replaced ferromagnesian clasts, contributing to the chemical budget within the deposit.

The Sam Otto prospect show all three gold association types. Highest gold grades are seen within sulphide-hosted Au in sheared gabbro, while arsenopyrite and banded pyrite stringers are hosted within tuff, volcanoclastics, and mafic volcanics. Pyrrhotite mineralization can be attributed to altered arsenopyrite. Overprinting of As-rich sulphides (pyrite and arsenopyrite) by later base metal sulphides (sphalerite-galena) are also present, overprinted by later sericite and cut by quartz-carbonate veins. Relatively high Au grades within quartz-carbonate veins cut through intermediate lapilli tuff, while there are minor Au showings in sericite-hosted Au compared to quartz-carbonate and sulphide-hosted gold. Sericite appears to reflect foliation due to metamorphism.

The Dave's Pond prospect display all three Au associations, hosted within both ash tuff and mafic volcanoclastics. Gold is hosted within both quartz-carbonate and sulphides. Low Au is seen within sericitic ash tuff, while highest Au is observed within sulphides in shear zones in both host rock types. Sulphide-hosted Au also shows sphalerite, as well as sericite and quartz-carbonate proliferation. Sericite patterns indicate foliation due to

metamorphic processes. All samples within Dave's Pond display prior As-poor sulphide mineralization overprinted by As-rich sulphides. Sb-Au association, especially in samples with high gold assay values, may be probable in the deposit.

Three Au associations are present in the Mispickel property. The highest Au grades are associated with sulphides, while variable, low Au is seen within quartz-carbonate veining. Very weak to insignificant Au signals are seen within sericite-chlorite. There is clear evidence of arsenopyrite being replaced by pyrrhotite, due to minor arsenopyrite in sulphide veins. Quartz cuts through the greywacke host, and intrudes Au-hosting secondary sericitization. Sericite also occurs as markers of foliation as an effect of metamorphism.

Homer shows only Au associated with sulphides such as pyrite and arsenopyrite. Lower Au grades are within calcite infills and strong sphalerite-galena signatures, while higher Au counts are observed within zones of weak silicification, leopard-like sulphide masses, and low chlorite content. Antimony-gold associations may be present in the deposit, especially for high-grade samples such as Fig. 30 in Chapter 4.

Both the Con and Giant Mine samples exhibit similar Au associations as the Northbelt properties – Au is seen within quartz-carbonate veins and sulphide mineralization. Evidence of later sulphide-galena mineralization is overprinting prior As-rich sulphides, sericite, and quartz-carbonate veining. Similar trends of sulphide-hosted (pyrite-arsenopyrite) mineralization are also evident with other Kerswill Suite samples, such as the mineralizing intrusive (Duckfish Granite). Also, gold-hosting, base metal mineralization is also apparent in some samples from within the Northbelt property, such as the Anne Trench. Conglomerates of the Jackson Lake Formation display the trend of As-rich sulphides hosting Au. X-ray Fluorescence results suggest the similarities of the Con and Giant Mine samples, as well as other mineralized samples within the Yellowknife Greenstone Belt, with the prospects of the Yellowknife City Gold Project.

Differences in maps produced via Peakaboo and PyMCA, especially for Au distribution, can be attributed to the curvefitting of the peaks corresponding to identified elements. Peakaboo uses Pseudo-Voigt fitting with Max under Curve algorithm to fit the peaks

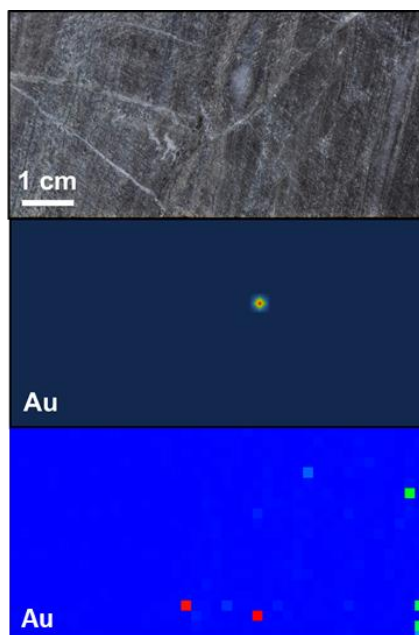
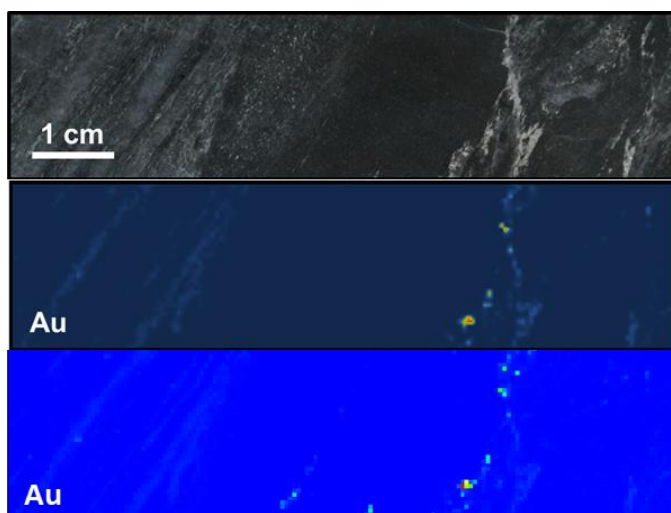
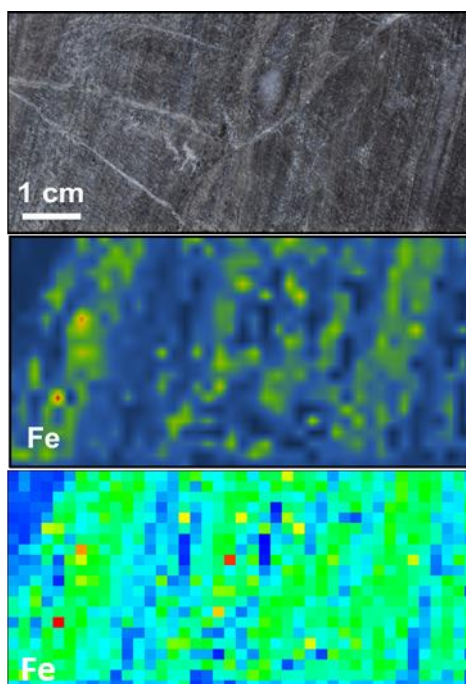
Dave's Pond, V738327, Au**Mispickel, S892089, Au****Dave's Pond, V738327, Fe**

Figure 39. X-ray fluorescence maps showing (top) Au distribution differences via Peakaboo (middle maps) and PyMCA (bottom maps), suspected to be due to variations in peak fitting, but the Fe map of the top left sample (bottom) shows similar trends.

of identified elements via Peak Search or Guided Fitting, whereas PyMCA allows the selection of regions of interest within the emission spectra of elements using Hypermet and linear least-squares fitting, and the size of the regions of interest will depend on the choice of the user. Background removal is also different between the two software packages (more on Chapter 2). Distribution of elements of low relative abundance, such as Au, may be different when comparing the element maps created via both software packages simply because of the differences in the method of fitting peaks, but were not major issues when comparing the maps of elements of high relative abundances, or elements identified using K lines, like Fe, in Fig 39.

6.3 X-ray Absorption Near Edge Structure and Gold Speciation

Representative samples from both the Kerswill Suite (Con Mine, C611) and the Northbelt Property (Mispickel, S892089) prove that metallic Au is present, and no structural gold is apparent, observed via the lack of any oxidised Au species suggesting that gold may be easily recoverable than previously thought.

One of the major issues on the setup was the pre-selection of samples which display very intense (red pixels) Au hotspots (see Chapters 4 and 5 for the XRF maps showing intense Au spots). Due to limited beam time, the system only allowed the pre-selection of a small subset of the samples, chosen based on the best possibility of getting good XANES data of intense Au spots. Gold might have been also located in areas of low to moderate intensities (i.e., orange or yellow, based on a temperature scale). The lack of gold in such intense spots does not indicate the absence of gold in the sample, rather, gold may just not have been present in the spot. Future experiment setups will be considering gold spots of medium intensity for XANES spectroscopy. Also, sample selection will be carefully examined to select samples with gold associated with either quartz-carbonate or sericite-chlorite to avoid the issue of the interference of zinc.

A limitation that the experiments for XRF and XANES is the use of energy-dispersive spectrometry (EDS) in data collection. EDS spectrum is broad, such that Zn K_{β}

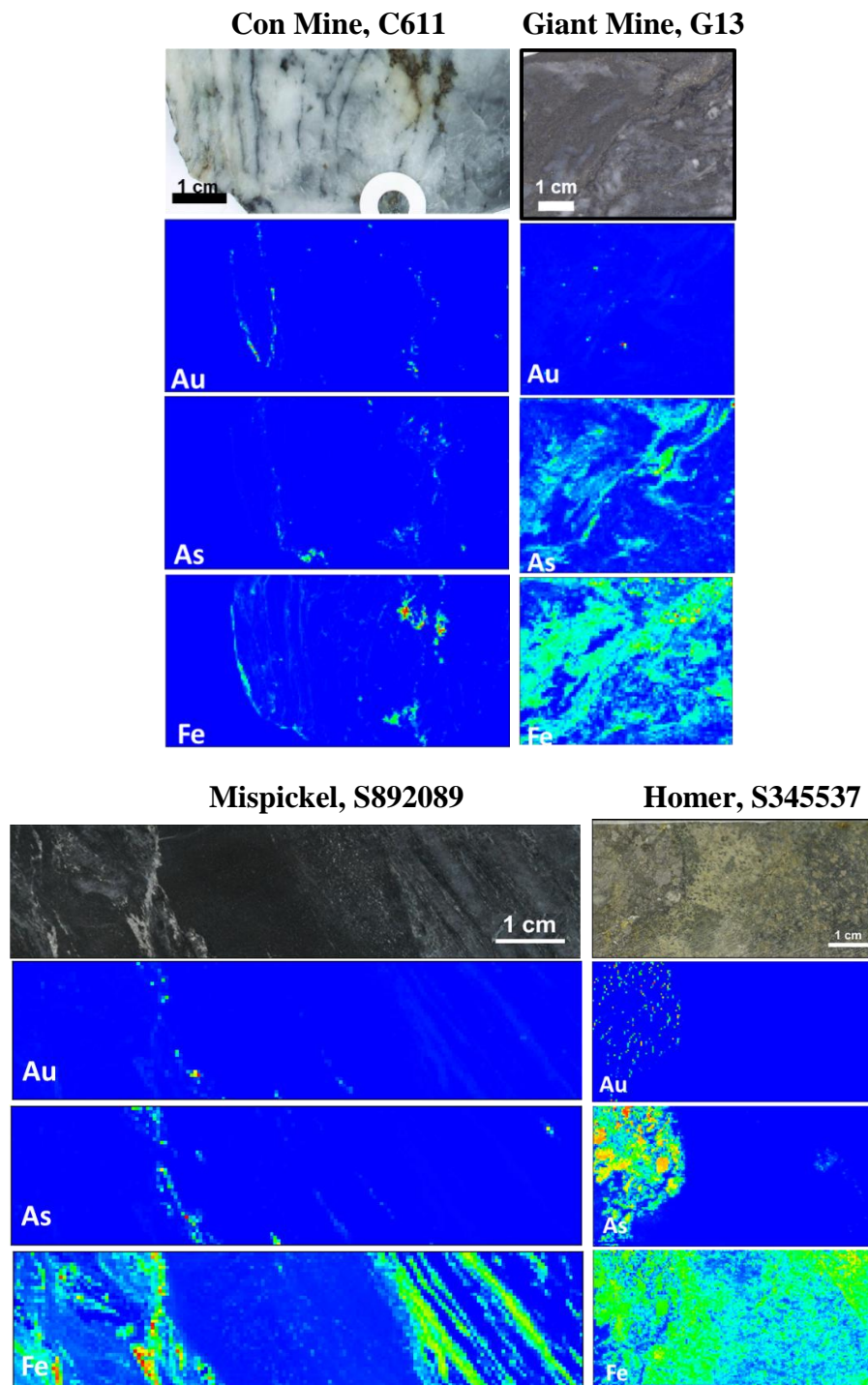


Figure 40. Representatives of sulphide-associated Au from the Kerswill Suite (top) and the Northbelt Property (bottom). Note that sulphide-hosted Au exists either as veinlets or pods.

Sam Otto, V156527

Dave's Pond, V160414

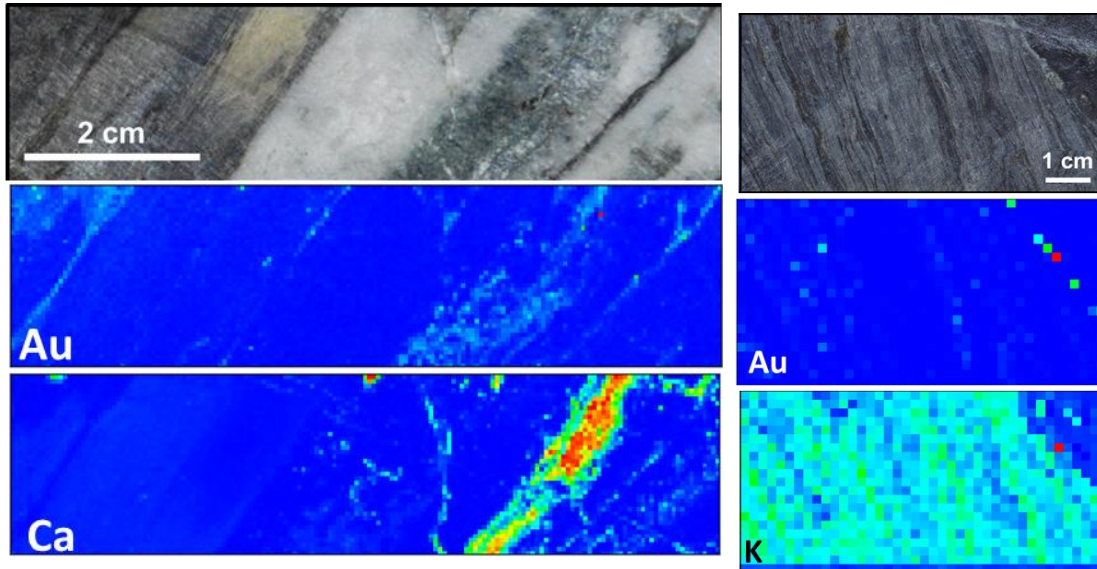


Figure 41. Representative of quartz-carbonate hosted (left) and sericite-chlorite (right) from the Northbelt Property. Quartz-carbonate veins cut through earlier textures, and is last in the order of mineralization, while heavy sericitization reflects foliation in both samples.

interference with Au L₃ peaks is not easily resolvable. For the samples in this study, peak interference is due to Zn K_β (9570.4 eV) obstructing Au L₃ (9713 eV), which can lead to misrepresentation of gold. Zinc interference is due to either a matrix issue, where Zn-rich minerals, such as sphalerite, surrounds Au, or gold is indeed absent in the spot, indicating misrepresentation, such as Figures 33 and 34 in Chapter 5. Sum peaks may also present issues, such as Fe K_α + Ar K_α (more information on Appendix G), especially since gold is associated with Fe-bearing sulphides. Other emission lines of gold, such as Au M_α (2118.4 eV), are too weak to produce signals and are interfered easily by other light elements, or beyond the capacity of the beam energy to be reachable, i.e. Au K edge at 80725 eV. Interference of other elements were eventually solved by using PyMCA to study the fit of Au in the spectrum of the data collected, and determining if the Au spots in the maps were indeed indicating Au or Zn.

Wavelength-dispersive X-ray fluorescence detectors could have resolved issue of peak overlaps, such as the study of Verita et al (1994) and McSwiggen and Associates (2005), where possible peak overlaps collected via EDS detectors can be resolved using WDS methods to easily discriminate fluorescence peaks. Once peak overlaps are resolved, XANES spectroscopy can then be resumed. Although, issues of using WDS detectors for X-ray fluorescence are present, such as the need for pre-selection of elements, inability to gather a full MCA spectrum with all possible elements in a spot, longer acquisition periods, and the use of several diffraction crystals, which all defeats the purpose of rapid analysis. WDS detectors cannot be used for XANES spectroscopy. Investigations of probable issues in peak interferences, such as petrography, knowledge on possible interferences with elements of interest (sum peak identification or element interferences), or even the selection of other emission spectra for identification, will help in resolving such issues.

6.4 Implications

Synchrotron radiation X-ray diffraction and fluorescence studies of the samples in the project complement each other to support the mineralogical distributions in the deposit, as well as the associations of Au within such samples. Mineralogy was investigated and associated with geochemical data based on results from X-ray diffraction and visual

inspection of the slabs and half-cores. Evidence of several mineralization periods are confirmed by mineralogical data, and fluorescence maps reveal the distributions of such minerals, as well as associations with Au, using relatively large beam spot sizes with high flux. Gold speciation studies prove that metallic Au is indeed present within the YCGP. This project also highlights the use of synchrotron techniques in the study, which prove to be great alternatives to conventional, lab-based equipment.

Samples within the Northbelt property of the YCGP show varied host rock types, from greywackes and mafic rocks to schists, exhibiting similar mineralization styles with the Kerswill Suite of the YGB. Sulphide mineralization is both low (sphalerite-galena) and high (pyrite-arsenopyrite) As, with Au preferentially related to the latter, and sphalerite-galena overprint pyrite-arsenopyrite. Pyrrhotite may be the result of arsenopyrite alteration. Sericite and chlorite are prominent, with biotite being evidence of wallrock alteration, and muscovite and chlorite are indicative of both metamorphism and orogenic gold-related mineralization. Quartz and carbonates are seen within veins, hosting Au through remobilization from high-As sulphides. Minor aurostibite may be present in the YCGP, and further studies are required to confirm its presence.

Three types of gold associations are present within the YCGP, and these are similar to the associations observed in the mineralized slabs from the Kerswill Suite of the YGB. Gold is associated with sulphides, quartz-carbonate veining, and sericite-chlorite. Spatial relationships of the minerals are also similar throughout the YGB and YCGP. Both sample groups exhibit abundant sericitization and carbonate veining. Low and high-As (sphalerite-galena and pyrite-arsenopyrite, respectively) sulphides are present, where the former overprints the latter. Sericitization and chloritization is prominent, and quartz-carbonate veining cuts through earlier alteration. Prospects seen west of the Yellowknife River Fault Zone (Homer, Crestaurum, Barney, and Hébert-Brent) do not show Au associated with sericite-chlorite, and gold is hosted within mafic volcanics and their metamorphic counterparts. Meanwhile, prospects at the east of the fault zone (Mispickel, Dave's Pond, Sam Otto) show Au within sericite-chlorite. Mispickel is the only greywacke-hosted deposit, with the other two bearing gold within intermediate to felsic volcanic rocks.

XANES analysis of representative samples from both the Kerswill Suite and the Northbelt property of TerraX reveal the presence of metallic Au. Lack of evidence on the existence of structural Au (gold within the sulphide structure) may be partly due to the limitation in the resolution of the beamline used in the experiments (majority of the samples were collected using 2x2 mm beam spot size), or interference of other elements in the maps, from Zn to Fe+Ar sum peaks, such that the Au signal is false. The lack of Au in the sites or spots analysed does not automatically conclude that gold, be it structural or metallic, is absent in the sample. Pixels exhibiting low to moderate intensities were not considered in the XANES setup, given the limited time provided for beam time use. Despite such issues, proof of the presence of metallic gold is indeed confirmed within the YCGP.

Synchrotron spectroscopy techniques such as XRD, XRF, and XANES prove that there are better alternatives to conventional methods such as petrography, conventional XRD, and lab-based microprobe. The ability to collect a huge amount of high quality and high resolution data with low detection limits, and using rapid, nondestructive techniques without prior sample preparation allows interpretation of results and making decisions faster than ever before. Half cores analysed using SR-XRF and XANES were directly mounted on the sample holders, without polishing or thin sections prepared, and SR-XRD powders were prepared in small capillaries which hold ~100 mg of sample, and were readily available for XRF and XANES studies at the same beamline. Petrography involves selection of a small portion of the half core or slab, is time-consuming, and only provides micro-scale textures, whereas SR-XRF provides the ability to analyse geochemical and textural relationships from centimeter to even micrometer scale on large sample areas, such as half cores and slabs, as well as identifying representative sections for further analysis. Conventional XRD machines involve the use of ~5 to 10 grams of powder, and takes five to ten minutes for a single sample, whereas SR-XRD permits data collection for 5 seconds per sample, which can already be processed using conventional diffraction software. Speciation of elements can be performed using lab-based equipment, e.g. SIMS, but further sample preparation by mounting on pucks, whereas XANES can be done in the same setup as SR-XRF, and can be done *in-situ* after XRF analysis. The experiments prove that synchrotron techniques provide better alternatives to conventional

techniques due to the ability to provide huge amounts of data without special sample preparation.

Other common analytical techniques are currently considered efficient enough for mineral exploration, but synchrotron techniques are advantageous over tabletop machinery. Conventional QEMSCAN and MLA analyses are not readily available for drill core mapping, as they focus on pebble to granule-sized particles, which need to be collected from ground representatives, and analytical scales are usually in the order of millimeters. Microprobe analysis needs polished slabs and thin sections, and involves pre-selection of elements to be analysed. LA-ICPMS is useful for *in-situ* studies, but is destructive, leaving ablation spots. Samples for LA-ICPMS need to be cut into approximately 5x2 cm polished blocks or thin sections, which are time-consuming to prepare. Hyperspectral mapping, while indeed fast, doesn't cover metallic minerals (Yang et al, 2011), i.e., sulphides, which are of main importance to orogenic gold studies.

The major advantage of synchrotron techniques is the ability to perform rapid, nondestructive analysis in a single setup. Spots with interesting elements such as Au can be readily analysed by XANES without transferring the sample to another beamline or instrument, with spot sizes from 10 microns to up to 2 mm, depending on the beamline capabilities. Interpretation of synchrotron XRF can be done as fast as 10 to 30 minutes upon acquiring data thanks to readily available software packages such as Peakaboo and PyMCA, and does not need preselection of elements. Sample preparation is low to nil, with unpolished half cores and slabs readily available to be examined, unlike microprobe and LA-ICPMS which require polishing and thin section preparation, or QEMSCAN and MLA which needs millimeter scale granules which will represent the whole half core or slab. All elements excited by the beam will be represented in the MCA spectrum, while hyperspectral mapping cannot identify metals. All elements excited by the beam will be represented in the fluorescence spectrum, and doesn't need pre-selection of elements of interest, unlike EPMA which needs a pre-determined suite of elements. Conventional X-ray diffraction is slow, whereas synchrotron XRD permits rapid analyses producing Rietveld-quality data, with the option for subsequent XRF and XANES experiments without sample changing. Synchrotron techniques prove that there are readily available

alternatives to conventional geochemical and mineralogical techniques that allow collection of a huge amount and variety of data in a short time span without changing instruments.

6.5 Conclusions

Based on evidence collected from both X-ray diffraction and X-ray fluorescence studies, the Northbelt Property prospects are indeed related to the Con-Giant mines. All areas are derived from a single mineralizing system separated by host rock lithology. The Yellowknife River Fault Zone and its various splays are the conduits for fluid percolation and eventual mineralization during metamorphism (Martel and Lin, 2006; Ootes et al, 2011). A variety of host rocks, from metavolcanics to metasedimentary rocks, reveal similar alteration patterns, such as sulphides overprinted by sericite-chlorite and cut by later quartz-carbonate veining. Host rock mineralogy and percolating fluids play some factors in alteration mineralogy, which can be traced to the variety of carbonates and presence or absence of certain sulphides such as sphalerite and galena, similar to the study by van Hees et al (1999). The timing of mineralization is similar throughout the Yellowknife Greenstone Belt, with early sericite-chlorite as indicators of metamorphism, followed by As-rich pyrite-arsenopyrite, As-poor sphalerite-galena, pyrrhotite, secondary sericite-chlorite, and quartz-carbonate, which supports Coleman (1957) Manifold (1947), and Smith's (2011) hypothesis on the order of mineralization within the Yellowknife Greenstone Belt. Three mineral assemblages are seen to host Au – sulphides (mainly pyrite-arsenopyrite), quartz-carbonate, and sericite-chlorite. The two latter assemblages host Au remobilized due to fluid motion liberating Au from the sulphides (van Hees et al, 1999). XANES spectroscopy results reveal that Au is metallic, indicating that gold may be easier to recover via cyanidation or ball milling, compared to structural gold which needs to be released from the sulphide structure through roasting.

Synchrotron techniques such as SR-XRD, SR-XRF, and XANES prove very useful and efficient in deciphering gold residence and mineralogical associations within the Northbelt Property in the Yellowknife City Gold Project. This novel, rapid approach to geochemical and mineralogical investigations of mineral deposits prove that synchrotron spectroscopy is as reliable as conventional techniques, even surpassing them with the

number of samples and amount of data in a time period, as well as minimal sample preparation. Results gathered from this study will be helpful in future complementary studies, such as better constraints in sample selection for petrography, micro-scale analyses of sulphides, and XANES spectroscopy of low to medium-intensity pixels of Au.

6.6 Future Studies

Further work for the study will include oxygen isotope studies to study fluids within quartz veins and carbonates, as well as fluid inclusion studies to support chemistry and salinity of fluids percolating during mineralization, will also help to properly discern the order of mineralizing stages. Differences between the deposits lying left and right of the fault zone are to be further tackled, since host rock lithology can be of great importance to the subtle differences in mineral composition and texture. Additional micro-XRF studies and petrography of sulphides, especially arsenopyrite, will confirm Smith's (2011) original conclusion that variations of arsenopyrite zoning reveals slight variations on metavolcanic versus metasedimentary-derived fluids, highlighting reservoir differences. Understanding which carbonate mineral is associated with higher Au values in quartz-carbonate hosted areas will also serve as vectors for hunting gold. Micro-XRF and XANES studies of sulphides will confirm the presence of invisible Au, be it metallic or structural, with focus on areas believed to exhibit refractory gold, such as the Giant Mine, focusing on arsenopyrite grains in thin sections. Sb presence is to be confirmed within high Au samples, and prove antimony peaks are not interference by Ti. Selection of a more diverse sample set for Au XANES will be considered, especially low to moderate pixel intensities, since these may also show the presence of gold.

References

- Adam, M.A. "Gold Mineralisation at the FAT Deposit, Courageous Lake Greenstone Belt, Northwest Territories, Canada." Western University, 2016. Print.
- Andrianjakavah, P., et al. "Textural and Fluid Inclusion Constraints on the Origin of the Banded-Iron-Formation-Hosted Gold Deposits at Maevatanana, Central Madagascar." *Mineralium Deposita*, 2007. 385-98. Vol. 42. Print.
- Aquilanti, G. "Instrumentation at Synchrotron Radiation Beamlines." *Synchrotron Radiation: Basics, Methods, and Applications*. Eds. Mobilio, S., F. Boscherini and C. Meneghini. Vol. Berlin: Springer-Verlag, 2015. 65-104. Web.
- Arai, T. "Introduction." *Practical X-ray Fluorescence Analysis*. Eds. Beckhoff, B., et al. Berlin: Springer-Verlag Berlin Heidelberg, 2006. 1-26. Print.
- Armitage, A.E., R.S. James, and S.P. Goff. "Gold Mineralization in Archaean Banded Iron Formation, Third Portage Lake Area, Northwest Territories, Canada." *Exploration and Mining Geology*, 1996. 1-15. Vol. 1996. Print.
- Ashley, P.M., C.J. Creagh, and C.G. Ryan. "Invisible Gold in Ore and Mineral Concentrates from the Hillgrove Gold-Antimony Deposits, Nsw, Australia." *Mineralium Deposita*, 1999. 285-301. Vol. 35. Print.
- Balerna, A., and S. Mobilio. "Introduction to Synchrotron Radiation." *Synchrotron Radiation: Basics, Methods, and Applications*. Eds. Mobilio, S., F. Boscherini and C. Meneghini. Vol.: Springer-Verlag, 2015. 3-28. Web.
- Barnicoat, A.C., et al. "Synmetamorphic Lode-Gold Deposits in High-Grade Archean Settings." *Geology*, 1991. 921-24. Vol. 19. Print.
- Baruchel, J., P. Bleuet, and A. Bravin. "Advances in Synchrotron Hard X-ray Based Imaging." *Comptes Rendus Physique*, 2008. 621-41. Vol. 9. Print.

- Bassett, W.A., and G.E. Brown Jr. "Synchrotron Radiation: Applications in the Earth Sciences." *Annual Review of Earth and Planetary Sciences*, 1990. 387-447. Vol. 18. Print.
- Bateman, R., Ayer J.A., and B. Dube. "The Timmins-Porcupine Gold Camp, Ontario: Anatomy of an Archean Greenstone Belt and Ontogeny of Gold Mineralization." *Economic Geology*, 2008. 1285-308. Vol. 103. Print.
- Baum, W., N.O. Lotter, and P.J. Whittaker. "Process Mineralogy - a New Generation for Ore Characterization and Plant Optimization." *SME Annual Meeting*. 2004. Print.
- Benzaazoua, M., et al. "Gold-Bearing Arsenopyrite and Pyrite in Refractory Ores: Analytical Refinements and New Understanding of Gold Mineralogy." *Mineralogical Magazine*, 2007. 123-42. Vol. 71. Print.
- Bleeker, W. "Archean Tectonics: A Review, with Illustrations from the Slave Craton." London: Geological Society of London, 2002. 151-81. Vol. 199. Print.
- Bleeker, W. "The Late Archean Record: A Puzzle in Ca. 35 Pieces." *Lithos*, 2003. 99-134. Vol. 71. Print.
- Bleeker, W., and B. Hall. "The Slave Craton: Geology and Metallogenic Evolution": Geological Association of Canada, Mineral Services Division, Special Publication, 2007. 749-849. Print.
- Bleeker, W., J.W.F. Ketchum, and W.J. Davis. "The Central Slave Basement Complex, Part II: Age and Tectonic Significance of High-Strain Zones Along the Basement-Cover Contact." *Canadian Journal of Earth Sciences*, 1999a. 1111-30. Vol. 36. Print.
- Bleeker, W., et al. "The Central Slave Basement Complex, Part I: Its Structural Topology and Autochthonous Cover." *Canadian Journal of Earth Sciences*, 1999b. 1083-109. Vol. 36. Print.

- Bleeker, W., R. Stern, and K. Sircombe. "Why the Slave Province, Northwest Territories, Got a Little Bigger." Geological Survey of Canada Current Research, 2000. Print.
- Bonnemaison, M., and E. Marcoux. "Auriferous Mineralization in Some Shear-Zones: A Three-Stage Model of Metallogenesis." Mineralium Deposita, 1990. 96-104. Vol. 25. Print.
- Bowden, M. "Convex." 1998. Web, 2018.
- Deposition Environment of Gold-Bearing Arsenopyrite in Mesothermal Deposits. Current Research in Geology Applied to Ore Deposits. 1993. University of Granada. Print.
- Bowring, S. A., et al. "Neodymium and Lead Isotope Evidence for Enriched Early Archaean Crust in North America." Nature, 1989. 222-25. Vol. 340. Print.
- Boyle, R.W. "The Geochemistry of Gold and Its Deposits (Together with a Chapter on Geochemical Prospecting for the Element)." Geological Survey of Canada Bulletin, 1979. Vol. 280. Print.
- Boyle, R.W.. "The Geology, Geochemistry, and Origin of the Gold Deposits of the Yellowknife District, N.W.T." Geological Survey of Canada, 1961. Print.
- Brugger, J., et al. "Probing Ore Deposits Formation: New Insights and Challenges from Synchrotron and Neutron Studies." Radiation Physics and Chemistry, 2010. 151-61. Vol. 79. Print.
- Bruker. "XRD Software: Diffrac.Suite EVA." 2018. Web, 2018.
- Burg, G.H. "Die Sichtbarmachung Des Feinverteilten Goldes in Goldhaltigen Erzen Und Ihre Wirtschaftliche Bedeutung." Metall und Erz, 1930. 333-38. Vol. 27. Print.
- Cabri, L.J., et al. "The Nature Of "Invisible" Gold in Arsenopyrite." The Canadian Mineralogist, 1989. 353-62. Vol. 27. Print.

- Cabri, L.J. "Chemical Speciation of Gold in Arsenopyrite." *The Canadian Mineralogist*, 2000. 1265-81. Vol. 38. Print.
- Card, K.D. "A Review of the Superior Province of the Canadian Shield, a Product of Archean Accretion." *Precambrian Research*, 1990. 99-156. Vol. 48. Print.
- Cepedal, A., et al. "Gold-Bearing as-Rich Pyrite and Arsenopyrite from the El Valle Gold deposit, Asturias, Northwestern Spain": *The Canadian Mineralogist*, 2008. 233-47. Vol. 46. Print.
- Chen, T.T., L.J. Cabri, and J.E. Dutrizac. "Characterizing Gold in Refractory Sulfide Gold Ores and Residues." *Journal of Mineralogy*, 2002. 20-22. Vol. 54. Print.
- Coleman, L.C. "Mineralogy of the Giant Yellowknife Gold Mine, Yellowknife, Nwt." *Economic Geology*, 1957. 400-25. Vol. 52. Print.
- Cook, N.J., and S.L. Chryssoulis. "Concentrations Of "Invisible Gold" In the Common Sulfides." *The Canadian Mineralogist*, 1990. 1-16. Vol. 28. Print.
- Cook, N.J., et al. "Arsenopyrite-Pyrite Association in an Orogenic Gold Ore: Tracing Mineralization History from Textures and Trace Elements." *Economic Geology*, 2013. 1273-83. Vol. 108. Print.
- Corbett, G. "Anatomy of Porphyry-Related Au-Cu-Ag-Mo Mineralised Systems: Some Exploration Implications." *Australian Institute of Geoscientists North Queensland Exploration Conference*, 2009. 1-13. Print.
- Corbett, G. "Epithermal Au-Ag Deposit Types - Implications for Exploration." *Poexplo Conference Peru*, 2005. 1-15. Print.
- Cousens, B., K. Facey, and H. Falck. "Geochemistry of the Late Archean Banting Group, Yellowknife Greenstone Belt, Slave Province, Canada: Simultaneous Melting of the Upper Mantle and Juvenile Mafic Crust." *Canadian Journal of Earth Sciences*, 2001. 1635-56. Vol. 39. Print.

- Cousens, B.L. "Geochemistry of the Archean Kam Group, Yellowknife Greenstone Belt, Slave Province, Canada." *Journal of Geology*, 2000. 181-198. Vol. 108. Print.
- Cousens, B.L., et al. "Bedrock Geochemistry of the Yellowknife Greenstone Belt and Adjacent Areas: Regional Correlations, Tectonic Settings, and Stratigraphic Solutions.": Geological Association of Canada Mineral Deposits Division, Special Publication, 2006a. 70-94. Print.
- Cutler, J., et al. "The Brightest Light in Canada: The Canadian Light Source." *Quantum Beam Science*, 2017. 1-10. Print.
- Davis, J., and W. Bleeker. "Timing of Plutonism, Deformation, and Metamorphism in the Yellowknife Domain, Slave Province, Canada." *Canadian Journal of Earth Sciences*, 1999. 1169-87. Vol. 36. Print.
- Davis, W. J., and E. Hegner. "Neodymium Isotopic Evidence for the Tectonic Assembly of Late Archean Crust in the Slave Province, Northwest Canada." *Contributions to Mineralogy and Petrology*, 1992. 493-504. Vol. 111. Print.
- Davis, W.J., B.J. Fryer, and J.E. King. "Geochemistry and Evolution of Late Archean Plutonism and Its Significance to the Tectonic Development of the Slave Craton." *Precambrian Research*, 1994. 207-41. Vol. 67. Print.
- Davis, W.J., et al. "Lithosphere Development in the Slave Craton: A Linked Crustal and Mantle Perspective." *Lithos*, 2003. 575-89. 71 vols. Print.
- De Block, M. Hoffmann, A., et al. "A New Solution for the Characterization of Unconventional Shale Resources Based on Analysis of Drill Cuttings." Abu Dhabi International Petroleum Exhibition and Conference. Society of Petroleum Engineers, 2015. Print.
- Deditius, A.P., et al. "The Coupled Geochemistry of Au and As in Pyrite from Hydrothermal Ore Deposits." *Geochimica et Cosmochimica Acta*, 2014. 644-70. Vol. 140. Print.

- Deditius, A.P., et al. "A Proposed New Type of Arsenian Pyrite: Composition, Nanostructure and Geological Significance." *Geochimica et Cosmochimica Acta*, 2008. 2919-33. Vol. 72. Print.
- Dencker, I., A. Moeller, and H. Schleicher. "Synchrotron Radiation X-ray Fluorescence (Srxrf) Microprobe Analyses of Metasomatized Xenoliths." 2000. Print.
- Dube, B., and P. Gosselin. "Greenstone-Hosted Quartz-Carbonate Vein Deposits." Geological Association of Canada, Mineral Deposits Division, Special Publication, 2007. 49-73. Print.
- Dudas, F. O., J. B. Henderson, and J. K. Mortensen. "U-Pb Ages of Zircons from the Anton Complex, Southern Slave Province." *Geological Survey of Canada Radiogenic Age Isotopic Studies*, 1990. 39-44. Vol. 3. Print.
- Field, B., and C. Atkins. "Characterization of Fine Grained Sediment in The and-2a Drillhole Core (Southern Mcmurdo Sound, Antarctica) Using Qemscan®." *GNS Science Report*, 2012. 18. Print.
- Foya, S.N., et al. "Pixe Microanalysis of Gold-Pyrite Associations from the Kimberley Reefs, Witwatersrand Basin, South Africa." *Nuclear Instruments and Methods in Physics Research*, 1999. 588-92. Vol. 158. Print.
- Fraser, S.J., et al. "Mineralogical Face-Mapping Using Hyperspectral Scanning for Mine Mapping and Control." Darwin, Northern Territory, Australia: 6th International Mining Geology Conference, 2006. 227-32. Print.
- Fusseis, F., et al. "A Low-Cost X-ray-Transparent Experimental Cell for Synchrotron-Based X-ray Microtomography Studies under Geological Reservoir Conditions." *Journal of Synchrotron Radiation*, 2013. 251-53. Vol. 21. Print.
- Fusseis, F., et al. "A Brief Guide to Synchrotron Radiation-Based Microtomography in (Structural) Geology and Rock Mechanics": *Journal of Structural Geology*, 2014. 1-16. Vol. 65. Print.

- George, L., et al. "Trace and Minor Elements in Galena: A Reconnaissance La-Icp-MS Study ": *American Mineralogist*, 2015. 548-69. Vol. 100. Print.
- Genkin, A.D., et al. "A Multidisciplinary Study of Invisible Gold in Arsenopyrite from Four Mesothermal Gold Deposits in Siberia, Russian Federation." *Economic Geology*, 1998. Vol. 93. Print.
- Geovector Management, Inc. "Terrax Minerals Inc.; Summary Report on the Yellowknife City Gold Project." Geovector Management Inc., 2017. 1-43. Print.
- Geovector Management, Inc. "Terrax Minerals: First Mover in a Major Canadian Gold District." 2018. 23. Ed. Inc., Geovector Management. Print.
- Godel, B. "High-Resolution X-Ray Computed Tomography and Its Application to Ore Deposits: From Data Acquisition to Quantitative Three-Dimensional Measurements with Case Studies from Ni-Cu-Pge Deposits." *Economic Geology*, 2013. 2005-19. Vol. 108. Print.
- Goldfarb, R.J., and D.I. Groves. "Orogenic Gold: Common or Evolving Fluid and Metal Sources through Time." *Lithos*, 2015. 2-26. Vol. 233. Print.
- Goldfarb, R.J., D.I. Groves, and S Gardoll. "Orogenic Gold and Geologic Time: A Global Synthesis." *Ore Geology Reviews*, 2001. 1-75. Vol. 18. Print.
- Goldfarb, R.J., et al. "Origin of Lode-Gold Deposits of the Juneau Gold Belt, Southeastern Alaska." *Geology*, 1988. 440-43. Vol. 16. Print.
- Goldstein, J.I., et al. *Scanning Electron Microscopy and X-ray Microanalysis*. 4th Edition ed. New York: Springer Science+Business Media LLC, 2014. Print.
- Gordon, R.A., et al. "Chemical Speciation of Gold in Arsenopyrites by Micro-X-ray Analysis." In Press. Print.

- Grammatikopoulos, T., et al. "Quantitative Characterization of the Ree Minerals by Qemscan from the Nechalacho Heavy Rare Earth Deposit, Thor Lake Project, Nwt, Canada." *SGS Minerals Services*, 2011. 1-12. Vol. 07. Print.
- Groves, D.I., et al. "Orogenic Gold Deposits: A Proposed Classification in the Context of Their Crustal Distribution and Relationship to Other Gold Deposit Types." *Ore Geology Reviews*, 1998. 7-27. Vol. 13. Print.
- Groves, D.I., et al. "Gold Deposits in Metamorphic Belts: Overview of Current Understanding, Outstanding Problems, Future Research, and Exploration Significance." *Economic Geology*, 2003. 1-29. Vol. 98. Print.
- Gäbler, H-E., et al. "Speeding up the Analytical Workflow for Coltan Fingerprinting by an Integrated Mineral Liberation Analysis/LA-ICP-MS Approach": *Geostandards and Geoanalytical Research*, 2011. 431-48. Vol. 35. Print.
- Hagemann, S.G., and K.F Cassidy. "Archean Orogenic Lode Gold Deposits." *Gold in 2000*. Vol. 13. Hagemann, S.G. Brown, P.E. Society of Economic Geologists, *Reviews in Economic Geology*, 2000. 9-68. Print.
- Hammersley, A.P. "Fit2d: An Introduction and Overview." *ESRF Internal Report*, ESRF97HA02T, 1997. Print.
- Hammersley, A.P., et al. "Two-Dimensional Detector Software: From Real Detector to Idealised Image or Two-Theta Scan." *High Pressure Research*, 1996. 235-46. Vol. 14. Print.
- Harris, C.M., and B.K. Selinger. "Single-Photon Decay Spectroscopy, II - the Pile-up Problem." *Australian Journal of Chemistry*, 1979. 2111-29 Vol. 32. Print.
- Harris, D.C. "The Mineralogy of Gold and Its Relevance to Gold Recoveries." *Mineralium Deposita*, 1990. S3-S7. Vol. 25. Print.

- Haugaard, R., et al. "Depositional Timing of Neoproterozoic Turbidites of the Slave Craton - Recommended Nomenclature and Type Localities." *Canadian Journal of Earth Sciences*, 2016. 15-32. Vol. 54. Print.
- Haugaard, R., L. Ootes, and K. Konhauser. *Precambrian Research*, 2017. 130-51. Vol. 292. Print.
- Helmstaedt, H., and W.A. Padgham. "A New Look at the Stratigraphy of the Yellowknife Supergroup at Yellowknife, N.W.T. - Implications for the Age of Gold-Bearing Shear Zones and Archean Basin Evolution." *Canadian Journal of Earth Science* 23 (1985): 454-75. Print.
- Henderson, C.M.B., G. Cressey, and S.A.T. Redfern. "Geological Applications of Synchrotron Radiation." *Radiation Physics and Chemistry*, 1995. 459-81. Vol. 45. Print.
- Henderson, J.B. "Geology of the Yellowknife-Hearne Lake Area, District of Mackenzie: A Segment across an Archean Basin." *Geological Survey of Canada Memoirs*, 1985. 135. Vol. 414. Print.
- Hinchey, J.G., Derek H.C. Wilton, and M.N. Tubrett. "A Lam-Ilcp-MS Study of the Distribution of Gold in Arsenopyrite from the Lodestar Prospect, Newfoundland, Canada." *The Canadian Mineralogist*, 2003. 353-64. Vol. 41. Print.
- Holliday, J. R., and D. R. Cooke. "Advances in Geological Models and Exploration Methods for Copper ± Gold Porphyry Deposits." *Proceedings of Exploration 07: Fifth Decennial International Conference on Mineral Exploration*. Ed. Milkereit, B.2007. 791-809. Print.
- Huntington, J. "Uncovering the Mineralogy of the Australian Continent: The Auscope National Virtual Core Library. A National Hyperspectrally Derived Drillcore Archive." *Australian Journal of Earth Sciences*, 2016. 923-28. Vol. 63. Print.
- Hutchinson, R.W. "Metallogeny of Precambrian Gold Deposits: Space and Time Relationships." *Economic Geology*, 1987. 1993-2007. Vol. 82. Print.

- Isachsen, C.E., and S.A. Bowring. "Evolution of the Slave Craton." *Geology*, 1994. 917-20. Vol. 22. Print.
- Isachsen, C.E., S.A. Bowring, and W.A. Padgham. "U-Pb Zircon Geochronology of the Yellowknife Volcanic Belt, Nwt, Canada: New Constraints on the Timing and Duration of Greenstone Belt Magmatism." *Journal of Geology*, 1991. 55-68. Vol. 99. Print.
- Kemp, B., et al. "A Simple Format for Exchange of Digitized Polygraphic Recordings." *Electroencephalography and Clinical Neurophysiology*, 1992. 391-93. Vol. 82. Print.
- Kerrich, R., and W.S. Fyfe. "The Formation of Gold Deposits with Particular Reference to Archean Greenstone Belts and Yellowknife: I. Geological Boundary Conditions and Metal Inventory." *Contrib. Geol. Northwest Territories*, 1988a. 37-62. Vol. 3. Print.
- Kerrich, R., and W.S. Fyfe. "The Formation of Gold Deposits with Particular Reference to Archean Greenstone Belts and Yellowknife: II. Source of Hydrothermal Fluids, Alteration Patterns and Genetic Models." *Contrib. Geol. Northwest Territories*, 1988b. 63-96. Vol. 3. Print.
- Kerrich, R., and W.S. Fyfe. "The Gold-Carbonate Association: Source of Co₂ and Co₂ Fixation Reactions in Archean Lode Deposits." *Chemical Geology*, 1981. 265-94. Vol. 33. Print.
- Kirkham, G. et al. "EXTECH III: 3D Drillhole Database for the Yellowknife Mining Camp." Open File 1583, 2003. 1CD. Digital.
- Kretschmar, U., and S.D. Scott. "Phase Relations Involving Arsenopyrite in the System Fe-as-S and Their Application." *The Canadian Mineralogist*, 1976. 364-86. Vol. 14. Print.
- Kusky, T.M. "Accretion of the Archean Slave Province." *Geology* 17 (1989): 63-67. Print.

- Kusky, T.M. "Are Greenstone Belts in the Slave Province, Nwt, Allochthonous?": Workshop on the tectonic evolution of greenstone belts: Lunar and Planetary Institute Technical Report, 1986. 135-39. Vol. 86-10. Print.
- Lambert, M.B. "The Back River Volcanic Complex—a Cauldron Subsidence Structure of Archaean Age." Geological Survey of Canada, 1978. 153-57. Print.
- Large, R.R., S.W. Bull, and V.V. Maslennikov. "A Carbonaceous Sedimentary Source-Rock Model for Carlin-Type and Orogenic Gold Deposits." Economic Geology, 2011. 331-58. Vol. 106. Print.
- Li, J., et al. "Characterization of a Low-Grade Copper-Sulphide Ore to Assess Its Suitability for *in-situ* Recovery." Powder Diffraction, 2017. S78-S84. Vol. 32. Print.
- Lintern, M.J., et al. "Ionic Gold in Calcrete Revealed by LA-ICP-MS, Sxrf and Xanes." Geochimica et Cosmochimica Acta, 2009. 1666-83. Vol. 73. Print.
- Lötter, N.O. "Modern Process Mineralogy: An Integrated Multi-Disciplined Approach to Flowsheeting." Minerals Engineering, 2011a. 1229-37. Vol. 24. Print.
- Lötter, N.O., et al. "Modern Process Mineralogy: Two Case Studies." Minerals Engineering, 2011b. 638-50 Vol. 24. Print.
- Lötter, N.O., et al. "Sampling and Flotation Testing of Sudbury Basin Drill Core for Process Mineralogy Modelling." Minerals Engineering, 2003. 853-64. Vol. 16. Print.
- Lötter, N.O., et al. "Flowsheet Development for the Kamoia Project – a Case Study." Minerals Engineering, 2013. 8-20. Vol. 52. Print.
- Lu, F.Q., et al. "Synchrotron X-ray Fluorescence Analysis of Rock-Forming Minerals: 1. Comparison with Other Techniques, 2. White-Beam Energy-Dispersive Procedure for Feldspars." Chemical Geology, 1989. 123-43. Vol. 75. Print.

- Mackenzie, D., D. Craw, and C. Finnigan. "Lithologically Controlled Invisible Gold, Yukon, Canada." *Mineralium Deposita*, 2015. 141-57. Print.
- MacLachlan, K., and W.J. Davis. "Uranium-Lead Ages of Deformed Granitoid Rocks near the Con Mine, Yellowknife, Northwest Territories." *Geological Survey of Canada Current Research*, 2002. 9 p. Vol. 2002-F1. Print.
- Maddox, L.M., et al. "Invisible Gold: Comparison of Au Deposition on Pyrite and Arsenopyrite." *American Mineralogist*, 1998. 1240-45. Vol. 83. Print.
- Manifold, A.H. "The Mineralogy and Geology of the Akaitcho Area, Yellowknife, Northwest Territories." University of British Columbia, 1947. Print.
- McIntyre, N.S., et al. "X-ray Fluorescence Spectroscopy and Mapping Using Excitation from White and Broad Bandpass Synchrotron Radiation." *Journal of Analytical Atomic Spectrometry*, 2010. 1381-89. Vol. 25. Print.
- McKeag, S.A., and D. Craw. "Contrasting Fluids in Gold-Bearing Quartz Vein Systems Formed Progressively in a Rising Metamorphic Belt: Otago Schist, New Zealand." 1989. 22-33. Vol. 84. Print.
- McSwiggen and Associates. "Tech Notes: Wds Vs. Eds." McSwiggen and Associates. Web. May 2018.
- Mezouar, M., et al. "Development of a New State-of-the-Art Beamline Optimized for Monochromatic Single-Crystal and Powder X-ray Diffraction under Extreme Conditions at the ESRF." 5 ed: *Journal of Synchrotron Radiation*, 2005. Vol. 12. Print.
- Mobilio, S., F. Boscherini, and Meneghini. "Synchrotron Radiation: Basics, Methods, and Applications." Berlin: Springer-Verlag, 2015. Print.
- Mountjoy, G. "X-ray absorption Spectroscopy." Canterbury: University of Kent, undated. Presentation.

- Meyer, C. "Ore-Forming Processes in Geologic History." *Economic Geology*, 1981. Vol. 75th Anniversary. Print.
- Meyer, M., and R. Saager. "The Gold Content of Some Archaean Rocks and Their Possible Relationship to Epigenetic Gold-Quartz Vein Deposits." *Mineralium Deposita*, 1985. 284-89. Print.
- Mikhlin, Y.L., A.S. Romanchenko, and I.P. Asanov. "Oxidation of Arsenopyrite and Deposition of Gold on the Oxidized Surfaces: A Scanning Probe Microscopy, Tunneling Spectroscopy and XPS Study." *Geochimica et Cosmochimica Acta*, 2006. Vol. 70. Print.
- Mobilio, S., F. Boscherini, and Meneghini. "Synchrotron Radiation: Basics, Methods, and Applications." Berlin: Springer-Verlag, 2015. Print.
- Morey, A.A., et al. "Bimodal Distribution of Gold in Pyrite and Arsenopyrite: Examples from the Archean Boorara and Bardoc Shear Systems, Yilgarn Craton, Western Australia." *Economic Geology*, 2008. 599-614. Vol. 103. Print.
- Morishita, Y., N. Shimada, and K. Shimada. "Invisible Gold and Arsenic in Pyrite from the High-Grade Hishikari Gold Deposit, Japan." *Applied Surface Science*, 2008. 1451-54. Vol. 255. Print.
- Mueller, A.G., and D.I Groves. "The Classification of Western Australia Greenstone-Hosted Gold Deposits According to Wallrock-Alteration Mineral Assemblages." *Ore Geology Reviews*, 1991. 291-331. Vol. 6. Print.
- Mumin, A.H., M.E. Fleet, and S.L. Chryssoulis. "Gold Mineralization in as-Rich Mesothermal Gold Ores of the Bogosu-Prestea Mining District of the Ashanti Gold Belt, Ghana: Remobilization Of "Invisible" Gold": *Mineralium Deposita*, 1994. 445-60. Print.
- Mumm, A.S., et al. "Fluids in Geological Processes — the Present State and Future Outlook." *Journal of Geochemical Exploration*, 2010. 1-7. Vol. 106. Print.

- Möller, V., and A.E. Williams-Jones. "A Hyperspectral Study (V-NIR-SWIR) of the Nechalacho REE-Nb-Zr Deposit, Canada." *Journal of Geochemical Exploration*, 2018. 194-214. Vol. 188. Print.
- Neumayr, P., et al. "Syn-Amphibolite Facies Archaean Lode Gold Mineralisation in the Mt. York District, Pilbara Block, Western Australia." *Mineralium Deposita*, 1993. 457-68. Print.
- Oberthur, T., R. Saager, and H.P. Tomschi. "Geological, Mineralogical and Geochemical Aspects of Archean Banded Iron-Formation-Hosted Gold Deposits: Some Examples from Southern Africa." *Mineralium Deposita*, 1990. S125-S35. Vol. 25. Print.
- Oberthur, T., et al. "Mineralogical Siting and Distribution of Gold in Quartz Veins and Sulfide Ores of the Ashanti Mine and Other Deposits in the Ashanti Belt of Ghana: Genetic Implications." *Mineralium Deposita*, 1997. 2-15. Vol. 32. Print.
- Ootes, L., et al. "Re-Os Molybdenite Ages from the Archean Yellowknife Greenstone Belt: Comparison to U-Pb Ages and Evidence for Metal Introduction at ~2675 Ma ": *Economic Geology*, 2007. 511-18. Vol. 102. Print.
- Ootes, L., et al. "Two Distinct Ages of Neoproterozoic Turbidites in the Western Slave Craton: Further Evidence and Implications for a Possible Back-Arc Model." *The Journal of Geology*, 2009. 15-36. Vol. 117. Print.
- Ootes, L., et al. "The Timing of Yellowknife Gold Mineralization: A Temporal Relationship with Crustal Anatexis?": *Economic Geology*, 2011. 713-20. Vol. 106. Print.
- OriginLab Corporation. "Origin Pro 2017": OriginLab Corporation, 2007.
- Padgham, W.A. "Field Guide: Yellowknife Mining District": Northwest Territories Geological Association Canada, 1987b. 11-20. Print.

- Padgham, W.A. "Mineral Deposits in the Archean Slave Structural Province; Lithological and Tectonic Setting." *Precambrian Research*, 1991. 1-24. Vol. 58. Print.
- Padgham, W.A. "Mineral Deposits in the Archean Slave Structural Province; Lithological and Tectonic Setting." *Precambrian Research*, 1992. 1-24. Vol. 58. Print.
- Padgham, W.A., and W.K. Fyson. "The Slave Province: A Distinct Archean Craton." *Canadian Journal of Earth Sciences*, 1992. 2072-86. Vol. 29. Print.
- Palenik, C.S., et al. "'Invisible' Gold Revealed: Direct Imaging of Gold Nanoparticles in a Carlin-Type Deposit." *American Mineralogist*, 2004. 1359-66. Vol. 89. Print.
- Pecharsky, V.K., and P.Y. Zavalij. "Fundamentals of Diffraction." *Fundamentals of Powder Diffraction and Structural Characterization of Materials*. Springer Science+Business Media, Inc., 2005. 148-63. Print.
- Philips, G.N., and D.I. Groves. "The Nature of Archaean Gold-Bearing Fluids as Deduced from Gold Deposits of Western Australia." *Journal of the Geological Society of Australia*, 1983. 25-39. Vol. 30. Print.
- Pirrie, D., and G.K. Rollinson. "Unlocking the Applications of Automated Mineral Analysis." *Geology Today*. Vol. 27: Blackwell Publishing Ltd., 2011. 226-35. Print.
- Ravel, B., and M. Newville. "Athena, Artemis, Hephaestus: Data Analysis for X-ray Absorption Spectroscopy Using Ifeffit." *Journal of Synchrotron Radiation*, 2005. 537-41. Vol. 12. Print.
- Ravel, B. "Hephaestus v. 0.9.25, A souped-up periodic table for the X-ray absorption spectroscopist." 2016. Program.
- Reich, M., et al. "Solubility of Gold in Arsenian Pyrite." *Ceochimica et Cosmochimica Acta*, 2005. 2781-96. Vol. 69. Print.

- Ridley, J.R., D.I. Groves, and J.T Knight. "Gold Deposits in Amphibolite and Granulite Facies Terranes of the Archean Yilgarn Craton, Western Australia: Evidence and Implications for Synmetamorphic Mineralization." *Metamorphosed and Metamorphogenic Ore Deposits*. Eds. Spry, P.G., B. Marshall and F.M. Vokes. Vol. 11: Society of Economic Geologists, Reviews in Economic Geology, 2000. 265-90. Print.
- Robb, L. "Introduction to Ore-Forming Processes". Oxford, UK: Blackwell Publishing, 2005. Print.
- Robert, F. "An Overview of Gold Deposits in the Eastern Abitibi Belt." *The Northwestern Quebec Polymetallic Belt; a Summary of 60 Years of Mining Exploration*. Ed. Rive, M., Verpaelst, P., Gagnon, Y., Lulin, J.-M., Riverin, G., and Simard, A. Vol. 43: Canadian Institute of Mining and Metallurgy Special Volume, 1990. 93-105. Print.
- Robert, F. "Structural Setting and Control of Gold-Quartz Veins of the Val D'or Area, Southeastern Abitibi Subprovince, ." *Gold and Base-Metal Mineralization in the Abitibi Subprovince, Canada, with Emphasis on the Quebec Segment*. Eds. Ho, S.E., F. Robert and D.I. Groves. Vol. 24: University of Western Australia, Short Course Notes, 1990. 167-210. Print.
- Saager, R., T. Oberthur, and H.P. Tomschi. "Geochemistry and Mineralogy of Banded Iron-Formation-Hosted Gold Mineralization in the Gwanda Greenstone Belt, Zimbabwe." *Economic Geology*, 1987. 2017-32. Vol. 82. Print.
- Saha, I., and A.S. Venkatesh. "Invisible Gold within Sulfides from the Archean Huttimaski Schist Belt, Southern India." *Journal of Asian Earth Sciences*, 2002. 449-57. Print.
- Santoro, L., et al. "Mineralogical Characterization of the Hakkari Nonsulfide Zn(Pb) Deposit (Turkey): The Benefits of Qemscan." *Minerals Engineering*, 2014. 29-39. Vol. 69. Print.

- Santoro, L., et al. "Automated Scanning Electron Microscopy (QEMSCAN)-Based Mineral Identification and Quantification of the Jabali Zn-Pb-Ag Nonsulfide Deposit (Yemen)." *Economic Geology*, 2015. 1083-99. Vol. 110. Print.
- Schnohr, C.S., and M.C. Ridgway. "Introduction to X-ray Absorption Spectroscopy." *X-ray Absorption Spectroscopy of Semiconductors*. Berlin: Springer-Verlag Berlin Heidelberg, 2015. 1-26. Print.
- Seward, T.M. "The Transport and Deposition of Gold in Hydrothermal Systems." *Gold '82*. A.A. Balkema Publishers, 1984. 165-81. Print.
- Sherry, N., et al. "Science Studio: A Computer Network and Software for the Collection and Management of Scientific Data from Remote Sites." Print.
- Sherry, N., et al. "Using Peakaboo Xrf Spectral Analysis and Imaging Software with Vespers Microbeams: Mineralogical and Metallurgical Applications." *Canadian Light Source*, 2009. Print.
- Sherry, N. et al. "Peakaboo 5 User Manual." 2018. Print.
- Sillitoe, R.H. "Porphyry Copper Systems." *Economic Geology*, 2010. 3-41. Vol. 105. Print.
- Simon, G., et al. "Oxidation State of Gold and Arsenic in Gold-Bearing Arsenian Pyrite." *American Mineralogist*, 1999. 1071-79. Vol. 84. Print.
- Sliwinski, J., M. Le Strat, and M. Dublonko. "A New Quantitative Method for Analysis of Drill Cuttings and Core for Geologic, Diagenetic and Reservoir Evaluation." *CSPG CSEG CWLS Convention*. 2009. Print.
- Smith, A.D. "Characterizing the Relative Timing and Conditions of Gold and Base-Metal Deposition in the Northern Part of the Yellowknife Greenstone Belt, Northwest Territories, Canada." *University of Missouri-Columbia*, 2011. Print.

- Solé, V.A., et al. "A Multiplatform Code for the Analysis of Energy-Dispersive X-ray Fluorescence Spectra." *Spectrochimica Acta Part B*, 2007. 63-68. Vol. 62. Print.
- Storey, C.D., M.P. Smith, and T.E. Jeffries. "*In-situ* LA-ICP-MS U-Pb Dating of Metavolcanics of Norrbotten, Sweden: Records of Extended Geological Histories in Complex Titanite Grains." *Chemical Geology*, 2007. 163-81. Vol. 240. Print.
- Sung, Y.H., et al. "Invisible Gold in Arsenian Pyrite and Arsenopyrite from a Multistage Archaean Gold Deposit: Sunrise Dam, Eastern Goldfields Province, Western Australia." *Mineralium Deposita*, 2009. 765-91. Vol. 44. Print.
- Tarnocai, C.A., K. Hattori, and L.J. Cabri. "'Invisible' Gold in Sulfides from the Campbell Mine, Red Lake Greenstone Belt, Ontario: Evidence for Mineralization During the Peak of Metamorphism." *The Canadian Mineralogist*, 1997. 805-15. Vol. 35. Print.
- Tauson, V. "Gold Solubility in the Common Gold-Bearing Minerals: Experimental Evaluation and Application to Pyrite." *European Journal of Mineralogy*, 1999. 937-47. Vol. 11. Print.
- Thorpe, R. I., G. L. Cumming, and J. K. Mortensen. "A Significant Pb Isotope Boundary in the Slave Province and Its Probable Relation to Ancient Basement in the Western Slave Province." *Geological Survey of Canada Open File Reports*, 1992. 179-84. Vol. 2484. Print.
- Toby, B.H., and R.B. von Dreele. "GSAS-II: The Genesis of a Modern Open-Source All-Purpose Crystallography Software Package." *Journal of Applied Crystallography*, 2013. 544-49. Vol. 46. Print.
- Tonzetic, I. "Micro-Xrf: A New Automated Mineralogical Analysis Paradigm." *Cape Town: Process Mineralogy*, 2017. 19. Vol. 4. Print.
- Ubaladini, S., et al. "Biooxidation of Arsenopyrite to Improve Gold Cyanidation: Study of Some Parameters and Comparison with Grinding." *International Journal of Mineral Processing*, 1997. 65-80. Vol. 52. Print.

- Van Breemen, O., W. J. Davis, and J. E. King. "Temporal Distribution of Granitoid Plutonic Rocks in the Archean Slave Province, Northwestern Canadian Shield." *Canadian Journal of Earth Sciences*, 1992a. 2186-99. Vol. 29. Print.
- Van Hees, E.H., et al. "Metasedimentary Influence on Metavolcanic-Rock-Hosted Greenstone Deposits: Geochemistry of the Giant Mine, Yellowknife, Northwest Territories, Canada." *Geology*, 1999. 71-74. Vol. 27. Print.
- Van Hees, E.H., et al. "Genesis of the Ptarmigan Gold Deposit: Is It of Magmatic Affinity?" Geological Association of Canada Mineral Deposits Division, 2006. 270-85. Print.
- Van Loon, L.L., et al. "Comparison of nickel speciation in workplace aerosol samples using sequential extraction analysis and X-ray absorption near-edge structure spectroscopy." *Environmental Science: Processes and Impacts*. 922. Vol. 17. Print.
- Vaughan, J.P., and A. Kyin. "Refractory Gold Ores in Archaean Greenstones, Western Australia: Mineralogy, Gold Paragenesis, Metallurgical Characterization and Classification." *Mineralogical Magazine*, 2004. 255-77. Vol. 68. Print.
- Vearncombe, J. "Shear Zones, Fault Networks, and Archaean Gold." *Geology*, 1998. 855-58. Vol. 26. Print.
- Walker, S.R., et al. "The Speciation of Arsenic in Iron Oxides in Mine Wastes from the Giant Gold Mine, N.W.T.: Application of Synchrotron Micro-Xrd and Micro-Xanes at the Grain Scale." *The Canadian Mineralogist*, 2005. 1205-24. Vol. 43. Print.
- Webb, D. "The Geochemistry and Structural Controls of Auriferous Shear Zones at Yellowknife, Mackenzie District, Northwest Territories, Canada." The University of Western Ontario, 1992. Print.

- Wells, J.D., and T.E. Mullens. "Gold-Bearing Arsenian Pyrite Determined By Microprobe Analysis, Cortez and Carlin Gold Mines, Nevada." *Economic Geology*, 1973. 187-201. Vol. 68. Print.
- Whitty, W.H.R. "Structural and Metamorphic Evolution of the Ormsby Zone and Relative Timing of Gold Mineralization: A Newly-Defined Archean Orogenic Gold Prospect Hosted on the Discovery Property, Yellowknife Greenstone Belt, Slave Province, Canada." The University of British Columbia, 2007. Print.
- Wilmott, P. "Synchrotrons and X-ray Free Electron Lasers". edX, 2018.
- Witt, W.K. "Regional Metamorphic Controls on Alteration Associated with Gold Mineralization in the Eastern Goldfields Province, Western Australia: Implications for the Timing and Origin of Archean Lode-Gold Deposits." *Geology*, 1991. 982-85. Vol. 19. Print.
- Witt, W.K. "Regional Metamorphic Controls on Alteration Associated with Gold Mineralization in the Eastern Goldfields Province, Western Australia: Implications for the Timing and Origin of Archean Lode-Gold Deposits." *Geology*, 1991. 982-85. Vol. 19. Print.
- Wood, B.J., and R.G.J. Strens. "Diffuse Reflectance Spectra and Optical Properties of Some Sulphides and Related Minerals." *Mineralogical Magazine*, 1979. 509-18. Vol. 43. Print.
- Yamashita, K., and R.A. Creaser. "Geochemical and Nd Isotopic Constraints for the Origin of Late Archean Turbidites from the Yellowknife Area, Northwest Territories, Canada." *Geochimica et Cosmochimica Acta*, 1999. 2579-98. Vol. 63. Print.
- Yang, J., et al. "Speciation and Distribution of Copper in a Mining Soil Using Multiple Synchrotron-Based Bulk and Microscopic Techniques." *Environmental Science and Pollution Research*, 2014. 2943-54. Vol. 21. Print.

Yang, K., et al. "Hylogging for Quantifying Gangue Minerals for Geometallurgy."
Antofagasta, Chile: GEOMIN 2011, 2011. 7. Print.

Zacharias, J., et al. "Arsenopyrite and as-Bearing Pyrite from the Roudny Deposit,
Bohemian Massif ": Mineralogical Magazine, 2004. 31-46. Vol. 68. Print.

Zhai, D.G., et al. "Origin of Oscillatory Zoned Garnets from the Xieertala Fe – Zn Skarn
Deposit, Northern China: *in-situ* LA – ICP-MS Evidence." Lithos, 2014. 279-
91. Vol. 190-191. Print.

Appendices

Appendix A: Summary of X-ray Fluorescence Interpretations

Kerswill Suite Samples

Prospect	Zone	Hole ID	Sample ID	Description	Other Comments:	Au_ppm	pixel size	Interpretation	Notes
YCGP	Anne-ZnPb-F	N/A	AN-1-4	mineralized sample from main trench	Free-milling	40.20	0.5 mm	A mineralized slab from the main trench, with sphalerite(?), galena within Au-free mineralization (Au might be nugget(s) somewhere in the sample, not mapped); sparse arsenopyrite within sphalerite and galena - indicative of minor As-rich sulphides perforated by As-poor mineralization	Au might not have been in sample, or not within surface
YCGP	Crestaurem-Main Zone-R	N/A	CR-1-6	mineralized sample from northern pit on Crestaurem shear	Refractory	12.90	0.5 mm	Au associated with arsenopyrite mineralization; quartz veining overprinting sulphide and carbonate veining; galena (?) and minor sphalerite present within sulphide veins; rare sericitization	
YCGP	Duckfish-F	N/A	DF-1-1	mineralized sample from trench near shore of "Arseno" lake	Free-milling	0.51	0,5 mm	Au associated with pyrite-arsenopyrite-pyrrhotite mineralization; very minor sericite and carbonate alteration; rare sphalerite and chalcopyrite, sericitization very weak; quartz veining not associated with mineralization.	

YCGP	MacQueen-F	N/A	MQ-1-2	mineralized sample from main trench; approximate location	Free-milling	5.07	0.5 mm	Quartz vein was cut by both carbonate and sulphide veining (asp-py); Au was associated with asp-py mineralization; minor sericitization was overprinted by sulphides; sphalerite and cpy(?) in minor amounts within sulphides; carbonates appeared as stockwork-like veining cutting through qz and sulphides
Other	Discovery-F	N/A	D-X-2	mineralized sample from "old" rock pile north of headframe	Free-milling	5.83	0.5 mm	Au was found within carbonate (Pb-Ca-Fe) veining; little to no arsenopyrite was seen; sparse sphalerite seen as disseminations within carbonates
Other	Jackson Lake-X	N/A	JL-2-1	mineralized sample of Jackson Lake Fm from small pit on enigmatic zone on sub-island	Unclassified	0.23	0.5 mm	Au disseminated within pyrite-arsenopyrite-pyrrhotite; sphalerite-galena-Ti mineralization (ilmenite?) overprinting py-asp (?); very weak sericitization; quartz vein cutting through all mineralized parts - very late qz fluid(?), quartz not deformed, might be post-mineralization
Other	Mon-F	N/A	MN-1-2	mineralized sample from main vein at workings	Free-milling	145.00	0.5 mm	no Au observed; qz vein cut by py-sphalerite and carbonate (Mn-rich) veining, very minor arsenopyrite-pyrite-pyrrhotite mineralization, seemed to be cut by As-poor mineralization

Other	Sito Lake-F	N/A	SL-2-3	mineralized sample from trench	Free-milling	39.40	0.5 mm	Au was associated with asp-py mineralization; As-poor sulphides overprinting py-asp mineralization; high-As sulphides eventually overprinted by sericitization (including Au spots), and then by qz-carbonate veining; weak Zn as sphalerite, Pb as galena, within asp-py-po; asp as small, 0.2-0.4 cm veins cutting through host rock, and overprinted by sericite and qz-carbonate veining	
Giant Mine Property	Giant-Brock-F	N/A	BR-X-2	mineralized sample from Brock Pit	Free-milling	98.3	1 mm	Au was associated with both sphalerite and arsenopyrite - in between As-poor and As-rich mineralization(?); presence of Fe-Ti(?).	
Giant Mine Property	Giant-LAW-R	N/A	G-1-3	mineralized sample from LAW orebody: Stope 452, "refractory" variety	Refractory	24.80	1 mm	disseminated Au within sulphide-carbonate veins (Au within carbonate veins due to remobilization?); minor sericitization; sphalerite and pyrite-arsenopyrite-pyrrhotite present (overprinted by later As-poor fluids?); minor cpy; quartz veining proliferate both sulphide and carbonate veins	
Giant Mine Property	Giant-Supercrest-R	N/A	G-4-2	mineralized sample from Supercrest orebody: Stope 370-P South, "refractory" variety	Refractory	40.90	0.5 mm	No Au was present at surface; pyrite-arsenopyrite-pyrrhotite(?) mineralization within qz-carbonate and sericitization (late sulphide cut by quartz-carbonate and sericite?); minor sphalerite and cpy within sulphides; mineralization observed to deformed,	Au might not have been in sample, or not within surface

								with boudinage-like forms displayed by both sulphides and qz-carbonate.	
Con Mine Property	Con-Campbell Zone-X	stope vs oc	C-4-2-1	mineralized sample from Campbell shear: Stope 3187-AW, "refractory"/enigmatic variety	Unclassified	5.06	0.5 mm	Quartz vein with small carbonate and sericite veining, very rare sulphides (sphalerite, arsenopyrite, cpy?), Ti assoc with carbonates(?) and minor sphalerite(?)	
Con Mine Property	Con-Campbell Zone-F	N/A	C-5-1-1	mineralized sample from deep in Campbell Zone; location is for Robertson shaft	Free-milling	79.7	0.5 mm	Free Au within quartz vein (remobilized from sulphides?); also associated with arsenopyrite-pyrite-po mineralization; carbonate veining present; Cu-Zn (sphaerite-chalcopyrite(?), or carbonate(?)) of another mineralization phase; minor sericite overprinted by quartz-carbonate mineralization	
Con Mine Property	Con-Campbell Zone-F	N/A	C-6-1-1	mineralized sample from deep in Campbell Zone; location is for Robertson shaft	Free-milling	1054.8	0.5 mm	Au mineralization within minor sulphide (asp-py-po) vein overprinted by quartz veining; minor sphalerite and cpy; minor sericitization; carbonate veining present, albeit quartz is more dominant.	

Crestaurum

Prospect	Zone	Hole ID	Sample ID	Lith1	Lith2	Description	Au_ppm	pixel size	Interpretation	Notes
Crestaurum		TCR15-052	R433866	SCH	SCS	light coloured unit distinguished by density of deformed qtz-ank veins (similar to 51.06m), veins range from 0.5-27cm, grey-white-cream/locally smokey with chlorite filling fractures; veins are both deformed/sub-parallel to foliation as well include angular fragments of mineralized wall rock (e.g. 60.07-60.74m); 2-5% fg py-asp disseminated in finely laminated host (S2 @60-75 TCA), bands of semi-massive vfg asp +/- py up to 2cm along qtz-carb vein margins common; sections of the interval are moderately to strongly broken; distinct lower contact @75 TCA	3.97	0.5 mm	Au was associated with sulphide (py-asp) veining and quartz-carbonate (remobilized from sulphides?); quartz-carbonate veining prominent and overprinting sulphide, chlorite, and sericite, mild sericitization overprinting sulphides; very weak ilmenite sig nature within sericite (may also be biotite); sphalerite was overprinting As-rich sulphidation	
Crestaurum		TCR15-052	R433857	SCH	CSS	well foliated sericite-chlorite schist w/ sericite alt decreasing down the hole; unit hosts ~10% boudinaged to deformed qtz-ank veins sub-parallel to foliation @60-70 TCA; 51.06-51.35m represents a zone of mineralization w/ asp-py spatially associated with ser altered wallrock, VG sites at: 51.19m, 51.25m and 51.28m; distinct lower contact @74 TCA	18.85	0.5 mm	Au assoc with sulphide (py-asp-po) veining; qz carbonate veining overprinting sulphide (py-asp-po), sericite (bt), chlorite, and , as well as ilmenite; 1 cm sulphide vein as main sulphide (asp-py-po) vein cutting through earlier sericite and qz-carbonate mineralization (2 nd pulse?), as well as sulphide veins overprinting sericite and qz-carbonate some cm away from 1 cm vein	qz-carbonate vein may be early mineralization (unlike other qz-carb veins which are post sulphide veining), evidenced by encapsulated carbonates (Ca, Mn) within 1 cm sulphide vein,

										and some sericite as well
Crestaurem		TCR15-003	R432247	SCH	QSS	Quartz sericite shear. Shear fabric includes 5% fg pyrite, 1% arseno, 0.5% stibnite. Veins are mineralized along fractures/crystal planes with pyrite/arseno/stibnite/sphal/galena and VG. VG at 99.80, 100.55, 100.75m.	27.8	0.5 mm	Au present within sulphide (py-asp-po) veining; quartz overprinting both carbonate and sulphide veining; minor sphalerite overprinting As-rich mineralization; very rare ilmenite within asp-py-pop veining	
Crestaurem		TCR15-003	R432250	SCH	QSS	Quartz sericite shear. Shear fabric includes 5% fg pyrite, 1% arseno, 0.5% stibnite. Veins are mineralized along fractures/crystal planes with pyrite/arseno/stibnite/sphal/galena and VG. VG at 99.80, 100.55, 100.75m.	50.9	0.5 mm	Au associated with both sulphides and sericite (remobilized?); carbonate and sericite vein overprinted by quartz-carbonate; sphalerite veins overprinted by sericite and carbonate; very weak ilmenite traces within asp-py-po; traces of galena within the quartz-carbonate vein	

Barney

Prospect	Zone	Hole ID	Sample ID	Lith1	Lith2	Description	Other Comments:	Au_ ppm	pixel size	Interpretation
Barney		TNB14-010	R115110	MVL	MVL	Massive, fine grained, light to dark green mafic volcanic, locally very strongly sheared.		0.85	0.5 mm	No Au observed; ilmenite (?), galena as sulphides and oxides (minor disseminated sphalerite); quartz-carbonate veining cutting through sulphides; disseminated galena

										encapsulating quartz pods, cutting through the other sulphides
Barney		TNB14-010	R115123	MVL	MVF	Massive, fine grained, light to dark green mafic volcanic, locally very strongly sheared.	From Dec '16 Intake - Mineralization Test - uXRF for Au assoc.	12.9 5	2 mm	Au noticeable within quartz, overprinted, asp-py-po vein; vein deformed as pod-like, boudinaged structures; sericitization at host rock was intruded by quartz-carbonate veining.
Barney		NB-95-16-W1	R115621	MVL	MVL	Buff to light green sericite-chlorite schist	Test Aspy speciation: Needles vs Coarse gr	16.8	2 mm	Au hosted within sericite and qz-carbonate-altered blob of asp-py-po; carbonate veinlets not cutting through mass - later veining?; sericite overprinted by qz-carbonate alteration
Barney		NB-95-16-W1	R115609	SCH	CSS	chlorite schist, local sericite		1.84	0.5 mm	Au associated with py-asp-po, sericite, chlorite alt, carbonate veining (suspected to have remobilized Au); carbonate veining prominent, overprinting sulphide veining; disseminated ilmenite(?) within sulphides
Barney		NB-95-16-W1	R115604	VEI	QAV	grey quartz with increasing ankerite. Sericite altered host rock	From Dec '16 Intake - Mineralization Test - uXRF for Au assoc.	11.1 5	2 mm	Au associated within pods of asp-py-po(?) S-C fabric-style(?); As-poor mineralization overprinting As-rich sulphides, sericite, and qz-carbonates; noticeable Ti enrichment within asp-py-po (ilmenite, sericite?)
Barney		NB-95-16-W1	R115622	MVL	MVL	Buff to light green sericite-chlorite schist	Test Aspy speciation: Needles vs Coarse gr	37.7	2 mm	Au related to sulphide (asp-py-po) mass overprinted by As-poor mineralization; all are altered by sericitization; noticeable Sb mineralization accompanied by Zn and Ti

Barney Porphyry	Porph yry	TBY16-013	S519135	INI	IPT	Felsic intrusive - granodiorite? Plag-qtz-bio-musc, zones of chlorite alteration of bio, local patches of epidote alteration, qz mostly has bluish tint. Veins, especially above 540 m, common and often mineralized with py, po, cpy, aspy, mo, sb, possibly electrum.	Mineralization Test - uXRF for Au assoc.	16	2 mm	No Au; qz vein overprinting early sulphide, sericite alteration; minor calcite veining present, might have occurred before quartz overprinting; strong Sb signals within overprinted mass indicate stibnite(?) presence in earlier mineralization
-----------------	-----------	-----------	---------	-----	-----	---	--	----	------	---

Hébert-Brent

Prospect	Zone	Hole ID	Sample ID	Lith1	Lith2	Description	Other Comments:	Au_ppm	pixel size	Interpretation
Hébert-Brent		TCG16-034	S520998	MAI	MBG	Bleached gabbro, mineralized near the FQP contact (footwall). Presence of leucoxene, pyrite bands and arsenopyrite needles.		3.47	0.5 mm	Au associated with py-asp bands; very minor sericitization could be seen; sphalerite present in small sulphide cluster; Ti assoc with leucoxene(?), or might be rt; Fe rich band patchy, pyrite(?)
Hébert-Brent		TCG16-040	S521155	MVL	MVF	Bleached mafic volcanic rock, flow breccia. Pervasive carbonate alteration and in breccia matrix. Cross-cut carbonate veins.	Flow Breccia with clasts containing fgr Aspy needles	24.4	2 mm	No Au at surface of rock; prominent As- and Sb-rich veining indicative of asp and stibnite(?); minor calcite veining; As and Sb overprinted by sericitization.
Hébert-Brent		TCG16-052	S521365	POR	FQP	FQP dyke, mineralized (arsenopyrite-pyrite; traces of sphalerite and		0.903	0.5 mm	sericitized sample with py-asp bands; Au assoc with such sulphide bands; carbonate veining cutting through early sericite alteration,

							stibnite).				carrying some asp-py with associated Au; Zn indicates sphalerite
Hébert-Brent			TCG16-052	S521371	POR	FQP	FQP dyke, mineralized (arsenopyrite-pyrite; traces of sphalerite and stibnite).		18.85	0.5 mm	Disseminated py-asp overprinted by sericitization; carbonate veining (Ti) present, as well as late qz-carbonate veining cutting through host rock (post-mineralization?); chloritization as patches within host rock; sericite minor; traces of sphalerite within host rock
Hébert-Brent			TCG16-034	S520992	POR	FQP	Feldspar quartz porphyry dyke; mineralized. With ferro-magnesian angular "clasts", locally replaced by arsenopyrite.		18.9	0.5 mm	Noticeable sulphide mineralization (py-asp-po) overprinted by sericitization; Au associated with sulphides (py-asp), rare cpy and sph; Ti might be of ilmenite or chlorite, patches within foliation, and overprinted by asp-py-po; sericite also with bt(?)

Sam Otto

Prospect	Zone	Hole ID	Sample ID	Lith1	Lith2	Description	Au_ppm	pixel size	Interpretation
Sam Otto	Main Zone	TSO17-027A	V892336	IVL	IVC	Ash tuff. Not Mineralized.	0.006	2 mm	no Au counts; no mineralization - element signatures reflect ash tuff geochem (host rock mineralogy still present, i.e. Ti, Ca, Fe in px)
Sam Otto	Hanging Wall Zone	TSO17-027A	V892234	IVL	IVC	Altered Ash tuff. Pluri-mm wide S&P stringer-barren	0.023	2 mm	No Au spots; sulphides cut by series of quartz-carbonate veins; sericite overprinted by qz-carb vein; traces of possible host rock minerals (ilm?, px?) still apparent.

Sam Otto	Hanging Wall Zone	TSO16-006	V156518	MVL		Mafic volcanic with patchy sericite, 1%, disseminated arsenopyrite needles. <1% disseminated pyrrhotite. Local silicification and bluish quartz veins.	0.495	2 mm	no Au present; sparse py-asp veining; sericitization overprinting sulphides and host rock; carbonate veins apparent, cutting through sulphides and host rock; Ti within sericite and ilmenite/px
Sam Otto	Hanging Wall Zone	TSO16-006	V156526	MVL		Mafic volcanic with patchy chlorite, 1%, disseminated arsenopyrite needles. <1% disseminated pyrrhotite. Local silicification and bluish quartz veins.	0.846	2 mm	no Au observed; sulphides overprinted by sericitization, and cut by qz-carbonate veining, single qz vein as wormlike intrusion cutting through host rock (late post-deformation vein?)
Sam Otto	Hanging Wall Zone	TSO16-006	V156527	MVL		Mafic volcanic with patchy chlorite, 1%, disseminated arsenopyrite needles. <1% disseminated pyrrhotite. Local silicification and bluish quartz veins.	1.775	0.5 mm	Au associated with qz-carbonate veining, remobilized in qz-carbonate vein; sulphide overprinted by sericite, chlorite and qz-carbonate veining - remobilizing Au?
Sam Otto	Hanging Wall Zone	TSO16-006	V156519	MVL		Mafic volcanic with patchy sericite, 1%, disseminated arsenopyrite needles. <1% disseminated pyrrhotite. Local silicification and bluish quartz veins.	2.44	2 mm	No Au was observed; py-asp overprinted by sericitization and quartz-carbonate veining; remnant As-poor sulphides (sph) still seen; galena signatures overprinted asp-py-po and sericitization; Ti associated with sericite.
Sam Otto	Main Zone	TWL16-011	S343819	IVL	ITL	Intermediate lapilli tuff. Moderate sericite, 2-3% quartz-chlorite veins, 1% arsenopyrite needles, 1-2% pyrite bands.	5.07	2 mm	Au was associated with quartz-carbonate overprinting sulphides - Au might be remobilized from sulphides; Zn within sphalerite; very minor sericite overprinted by qz-carbonate veining (Ti might be in bt)
Sam Otto	Main Zone	TWL16-011	S343811	IVL	ITL	Intermediate lapilli tuff - not mineralized	0.053	2 mm	No Au at surface; evidence of minor quartz-carbonate and heavy sericitization, quartz-carbonate veining may just have only little

									influence on rock
Sam Otto	Hanging Wall Zone	TSO16-006	V156517	MVL		Mafic volcanic - not mineralized	0.054	2 mm	No Au observed; with prominent sphalerite mineralization overprinted by carbonate veining and sericitization; presence of Ti (along with assoc Fe) might indicate ilmenite mineralization (or may be px!), as well as Ti-bearing sericite (musc, bt); very minor asp
Sam Otto	Main Zone	TWL16-011	S343813	IVL	ITL	Intermediate lapilli tuff. Moderate sericite, 2-3% quartz-chlorite veins, 1% arsenopyrite needles, 1-2% pyrite bands.	0.622	0.5 mm	Au assoc with sulphide veining (py-asp); chlorite, sericite alt, and quartz-carbonate veining overprinting sulphides; Zn in carbonates; Ti within sericite; minor cpy; shearing episode provided pathway for carbonate veining cutting almost perpendicular to foliation
Sam Otto	Main Zone	TSO17-027A	V892345	IVL	IVC	Ash tuff. dark smoky grey coloured qtz vein, banded / slight crustiform texture. Contains up to 15% very fine disseminated aspy and 5% fine diss Po. Selvages strongly sericite altered along with wisps of ser internally.	0.63	2 mm	Au along stringers of asp-py overprinted by sericite and chlorite; qtz-carbonate veining overprinting sulphides, sericite, and chlorite; boudinaged qz-carb veins sign of pre-deformation mineralization
Sam Otto	Main Zone	TWL16-011	S343808	IVL	ITL	Intermediate lapilli tuff. Moderate sericite, 2-3% quartz-chlorite veins, 1% arsenopyrite needles, 1-2% pyrite bands.	2.12	0.5 mm	Au assoc with sulphide veining (py-asp-po) overprinted by chlorite alteration (metamorphic?) and quartz-carbonate (Fe, Zn, Ca) veining; disseminated galena within sulphide veining (formed before py-asp?, overprinted?); very rare sphalerite within qz-carbonate veins (earlier As-poor sulphides?)

Sam Otto	Main Zone	TSO17-027A	V892341	IVL	IVC	Ash tuff. tightly spaced hairline chlorite rich salt and pepper stringers. Veins contain trace fine diss Po. Wall rock strongly biotite altered (medium brown colour) and contains up to 1% needle like aspy and 1% fine diss Po. Stringer selvages also contain biotite rich halos.	2.44	2 mm	no Au observed; qz-carbonate vein overprinting chloritization at right of sample; sulphides (asp, py, po?) overprinted by chlorite; bt assoc with Fe, Ti(?)?, or may be indicative of ilmenite(?) or chlorite(?), seen to be slightly overprinted by qz-carbonate
Sam Otto	Hanging Wall Zone	TSO17-028	V892625	IVL	IVC	Intermediate Volcaniclastic. strong po mineralization in foliation parallel bands to lower contact	2.45	2 mm	Au intimately related with asp-py-po stringers, overprinted by sericite and qz-carbonate alteration
Sam Otto	Main Zone	TWL16-011	S343815	IVL	ITL	Intermediate lapilli tuff. Moderate sericite, 2-3% quartz-chlorite veins, 1% arsenopyrite needles, 1-2% pyrite bands.	3.5	0.5 mm	Au within sulphide veins (py-asp); sericitization and qz carbonate veining prominent; galena as disseminations within both qz-carb-ser and sulphide veining (remobilized?); late qz-pyrite?/Fe oxide?/chlorite? vein cutting through older veins (no Au); remnant splaherite within qz-Fe vein; Ti within sericite as bt(?)
Sam Otto	Main Zone	TSO17-025	V890298	MAI	GAB	sheared and mineralized fg gabbro.	3.75	2 mm	Au associated with pyrite-arsenopyrite; host rock cut by qz-carbonate veins; sulphides overprinted by qz-carbonate; minor As-poor sulphides (Zn) overprinted by later quartz-carbonate; strings of ilmenite(?) or px of host rock(?) indicating deformation
Sam Otto	Hanging Wall Zone	TSO16-006	V156522	MVL		Mafic volcanic with patchy sericite, 1%, disseminated arsenopyrite needles. <1% disseminated pyrrhotite. Local silicification and bluish quartz veins.	4.98	0.5 mm	Au associated with pyrite-arsenopyrite; sulphides overprinted by sericitization and quartz-carbonate veining; sparse sphalerite-galena as indication of later As-poor mineralization.

Sam Otto	Hanging Wall Zone	TSO17-027A	V892232	IVL	IVC	Altered ash tuff. mix of very tightly spaced hairline qtz stringers, and coarse grained, smoky qtz veins up to 5cm wide with very fine grained aspy. Wall rock contains 2-3% very fine disseminated Po and 1% very fine needle like aspy. Wall rock over interval is moderately biotite altered, medium brown in colour.	5.76	2 mm	Possible Au associated with py-asp-po mineralization; sulphides overprinted by quartz-carbonate veining; weak sericite overprinted by quartz-carbonate
Sam Otto	Main Zone	TWL16-011	S343816	IVL	ITL	Intermediate lapilli tuff. Moderate sericite, 2-3% quartz-chlorite veins, 1% arsenopyrite needles, 1-2% pyrite bands.	6.01	0.5 mm	Au associated with sulphides (py-asp-po); chlorite alt and quartz-carbonate veining prominent and overprinting sulphide; sericite alt minor; minor sphalerite within sulphides; stibnite(?) as disseminations within sulphide veining, as well as within qz-carbonate veins and within chlorite masses; late carbonate (ankerite?) vein cutting through foliations, post-deformation fluids?

Dave's Pond

Prospect	Zone	Hole ID	Sample ID	Lith1	Lith2	Description	Other Comments:	Au_ppm	pixel size	Interpretation
Daves Pond	Main Zone	TSO17-029	V892939	MVL	MVC	Ash tuff. Not Mineralized.		0.0025	2 mm	no Au; sericite, biotite(?) altered rock overprinting Fe sulphides, and cut by qz-carbonate veining; Zn may be indicative of prior As-poor sulphide mineralization; late qz-carb veining may indicate post-metamorphism mineralization

Daves Pond	Hanging Wall Zone	TSO17-019	V413124	IVL	IVC	Feldspar crystals in a biotite-rich matrix. Crystals locally preserved in sericitic mineralized zones.	Mineralization Test - disseminated sulfides in less altered, vs sericite alt'd and veined - Wondering about background levels of Sb too	0.031	2 mm	no Au; sericite altered rock with some veinlets of asp-py-po; minor quartz-carbonate veining, cutting through sericite mass; biotite overprinting sulphides.
Daves Pond	Hanging Wall Zone	TSO17-019	V413125	IVL	IVC	Feldspar crystals in a biotite-rich matrix. Crystals locally preserved in sericitic mineralized zones.	Mineralization Test - disseminated sulfides in less altered, vs sericite alt'd and veined - Wondering about background levels of Sb too	0.39	2 mm	No Au; disseminated asp-py-po within sericite altered host rock, minor quartz-carbonate (Mn-bearing) cutting through sericite (biotite, muscovite) and sulphide mass.
Daves Pond	Foot Wall Sb Zone	TSO17-020	V413285	IVL	IVC	Biotite-rich matrix; sericite where mineralization occurs. Chlorite-carbonate near downhole contact. Mudstone bed at 283.25m - 283.33m.	As & Sb + veins sample uXRF for Au	0.472	2 mm	no Au; prominent As and Sb sulphide-rich veining, with minor calcite veins; Ti, Cr enrichment within sulphide zone, may be bt overprint;

Daves Pond	Foot Wall Sb Zone	TSO17-020	V413296	IVL	IVC	moderately sheared intermediate volcanic. Sb rich.		0.039	2 mm	Au associated with qz-carbonate veining; sericite overprinted by qz-carbonate alteration/veining; remnant pyrite-arsenopyrite-po vein still observed; Sb veining overprinted by sericite and qz-carb veining
Daves Pond	Foot Wall Sb Zone	TSO17-020	V413294	IVL	IVC	Moderately sheared intermediate Volcanic. aspy, sb rich vein sets		0.259	2 mm	Au associated with qz-carbonate veining (remobilized from sulphides); prominent qz-carbonate alt overprinting sulphides and minor sericite; minor stibnite veining overprinted by qz-carb
Daves Pond	Hanging Wall Zone	TSO17-030	V738327	MVL	MVC	weakly sheared ash tuff. milky qtz veins with local blebby aspy		1.065	2 mm	Au associated with qz-carbonate veining (Au remobilized from sulphides?); sericitization overprinted by qz-carbonate veining; post-deformation carbonate veins cutting through everything; Ti assoc with sericitization
Daves Pond	Main Zone	TSO17-029	V892979	MVL	MVC	Moderate shear zone developed in mafic ash tuff. blue-grey folded and locally dismembered qtz veins with patchy to strong sericite selvages and spotty fracture controlled rubyjack spalerite		11.9	2 mm	Au intimately associated with quartz veining - might have been remobilized from As-rich sulphide mineralization (asp, py, po); sheared asp-py-po(?) overprinted by quartz veining; evidence of later As-poor mineralization (sphalerite) evident, and overprinted As-rich sulphides
Daves Pond	Hanging Wall Zone	TSO17-019	V160414	FVL	FVC	Sericitic Ash tuff. 3% stringer Po, 0.5% medium grained aspy. Local dark smoky qtz veins.		0.518	2 mm	Au associated with sericite (remobilized from As-rich sulphidation); remnant veinlets of As along fringes of sericite altered host rock.
Daves Pond	Foot Wall Sb Zone	TSO17-019	V413119	MVL	MVC	Mafic Volcaniclastic. Mod shear. series of veins at a 2-3cm interval, sb / aspy rich.		0.93	2 mm	Au associated with disseminated sulphides within qz veins; 4-5 cm qz vein cutting through host and sulphide altered mass; sericite overprinted by qz-

										carboante veining
Daves Pond	Main Zone	TSO17-029	V892959	MVL	MVC	Shear zone with stringer smoky and grey to s and p stringers,		4.97	2 mm	Au associated with py-asp-po veins; foliation bands of sulphides overprinted by sericite, and intruded/alterd by qz-carbonates; prior As-poor mineralization overprinted by As-rich sulphides

Mispickel

Prospect	Zone	Hole ID	Sample ID	Lith1	Lith2	Description	Au_ppm	pixel size	Interpretation
Mispickel	North Zone	TWL16-032	S892087	SDS	GWK	Greywacke - not mineralized	0.065	2 mm	Au associated with chloritization (remobilized from sulphides); sericite, quartz-carbonate veining and sulphides heavily overprinted by chloritization.
Mispickel	North Zone	TWL16-032	S892045	SDS	GWK	Greywacke - not mineralized	0.095	2 mm	Au hosted within qz-carbonate veining, remobilized from sulphides(?); sericite overprinted by qz-carbonate veining; poor As in sulphides (mostly py?, sph?); sericite with Ti association; carb with Zn component; sericite overprinted by qz-carb
Mispickel	North Zone	TWL16-032	S892082	SDS	GWK	Greywacke with 1% disseminated arsenopyrite and 2% pyrrhotite laminations. Locally pyrrhotite replacinf arsenopyrite. Local bluish quartz veins and matrix silica alteration.	0.674	2 mm	Au associated with quartz-carbonate veining (mainly qz); Au might have been remobilized from sulphides; sulphides strongly overprtned by quartz-carbonate veining; Ti and K in sericite, overprinted by carbonate; Zn as sphalerite, indicating later As- poor sulphidation overprinted qz-carb; late py-ilm(?) vein crosscutting qz-carb (post-deformation fluids?)
Mispickel	North Zone	TWL16-032	S892084	SDS	GWK	Greywacke with 1% disseminated arsenopyrite and 2% pyrrhotite laminations. Locally pyrrhotite	1.58	2 mm	Au associated with qz-carbonate veining (qz), might be remobilized from overprinted asp-py; prominent py vein crosscutting qz-carb (late barren mineralization?);

						replacinf arsenopyrite. Local bluish quartz veins and matrix silica alteration.			very minor sericitization (might be heavily overprinted, or part of host rock heavily altered)
Mispickel	North Zone	TWL16-032	S892102	SDS	GWK	Greywacke with 1% disseminated arsenopyrite and 2% pyrrhotite laminations. Locally pyrrhotite replacinf arsenopyrite. Local bluish quartz veins and matrix silica alteration.	0.201	2 mm	no Au; sulphides and sericite overprinted by qz-carbonate and chloritization (qz-carbonate as last alt episode?); Ti within sericite; Ca, Fe, Zn within qz-carbonate; asp replaced by py-po
Mispickel	North Zone	TWL16-032	S892043	SDS	GWK	Greywacke with 2-3% , 1-2mm, disseminated arsenopyrite with pyrrhotite replacement in pressure shadows.	0.654	2 mm	Au assoc with py-asp-po mineralization; overprinted by qz-carbonate veining; late sheared carbonate vein cuts through host rock, might be post-foliation mineralization (but note that it is still sheared)
Mispickel	North Zone	TWL16-032	S892044	SDS	GWK	Greywacke with 2-3% , 1-2mm, disseminated arsenopyrite with pyrrhotite replacement in pressure shadows.	2.53	0.5 mm	Au associated with py-asp mineralization, overprinted by sericitization and qz-carbonate veining; some Au remobilized into qz-carbonate; disseminated Pb observed (galena overprinted by qz-carb?); sericite heavily overprinted by qz-carb alt and veining; Ti might be either ilm or rutile, and Zn might be sph (As-poor sulphidation still present, within qz-carb veining)
Mispickel	North Zone	TWL16-032	S892089	SDS	GWK	Greywacke with 1% disseminated arsenopyrite and 2% pyrrhotite laminations. Locally pyrrhotite replacinf arsenopyrite. Local bluish quartz veins and matrix silica alteration.	5.59	0.5 mm	Au associated with sulphides (py-asp-po); sericitization overprinted by qz-carbonate veining (Ca, Fe, Zn); remnant low As sulphides overprinted by sericite; pyrite veins cutting through qz-carbonate (late barren sulphides?); sericite with Ti; some signatures of Pb indicating remnant galena (As-poor mineralization overprinting earlier As-rich mineralization)

Homer

Prospect	Hole ID	Sample ID	Lith1	Lith2	Description	Other Comments:	Au_ppm	pixel size	Interpretation
Homer Lake	THL16-010	S520925	MAI	GAB	Dark, fg-mg, massive, possible massive flow (?), 5-15% variably oriented fractures filled with epi-cal, 10-20% white calcite veins filling fractures or parallel to localized foliation fabrics (S1 - 24-64 TCA), pluri-cm convoluted to routeless cal veins not uncommon; several intercepts of semi-massive sph-po +/- py-gal-cpy spatially associated w/ calcite veins/fill displaying a strong chl halo overprinting wallrock, weak to moderate leucoxene throughout; sharp lower contact (@43)	Base Metals sample	1.34	2 mm	Au associated with asp-py-po veining, slightly altered by qz-carbonate veining; base metals such as Zn, Sb within sulphides, while Ti and Mn enriched within asp-poor zones; slight qz-carbonate veining apparent
Homer	THL16-009	S345537	MAI	GAB	Variable section of gabbro, overall fg with occasional mg sections which are more massive. Intermittent weak-mod foliation, rarely strong. Just above 2.9m, 9.4m and 30.38m the gabbro gradually becomes more fine grain before a distinct contact and coarse grain gabbro. Intermittently strongly magnetic. Massive below 21m. Sharp, undulating lower contact.		5.49	0.5 mm	Au associated with py-asp-po clusters; chloritization prominent; minor sericitization, Ca might be indicative of chlirite alt; minor traces of cpy (?) within asp-py-po mass; sparse Zn as indication of possible sphalerite

Homer	THL16-008	S345459	MVL	MVF	<p>Very fine grain mafic flow, no leucoxene altn. Possibly a finer grain and altered version of the gabbro above. Few veins in this section, but there is an overall weak-mod siliceous altn; most veins are overprinted by sulfides or associated with semi-massive sulfides from 34-34.68m. Broken core from 31.67-31.77m and 0.5cm fault gouge along the lower margin of broken core at 31.77m (30 TCA). Second fault zone (broken/fractured core) from 38-39.26m, with possible fault gouge at 39.26m. Lower contact is obscured by increased sulfides, marked by the appearance of leucoxene.</p>	10.6	0.5 mm	<p>prominent sericite-chlorite alteration; Au associated with sulphides (py-asp); chlorite with Ca-Ti-Fe components; minor cpy within sulphide veins; weak to no qz-carbonate alt; shearing might have introduced pathways for sericite alt, as well as chlorite (?)</p>
Homer	THL16-009	S345563	MAI	GAB	<p>Gabbro is fg-mg, massive and mottled texture. Gabbro has the 'leopard' rock texture. There is weak epidote altn throughout the matrix. Section of bleached/silicified mafics with bands of semi-massive sulfides from 43.81-44.65m, similar to the section of mineralization between two faults in hole THL16-008. Weak leucoxene altn that locally increases in short sections. Sharp lower contact at 50 TCA (no beta).</p>	13.85	0.5 mm	<p>Au associated with disseminated to leopard-like sulphide mineralization (asp, py); minor sericitization and carbonate alteration; chloritization prominent, as well as epidote mineralization (metamorphic?); minor indications of cpy within Fe altered mass</p>

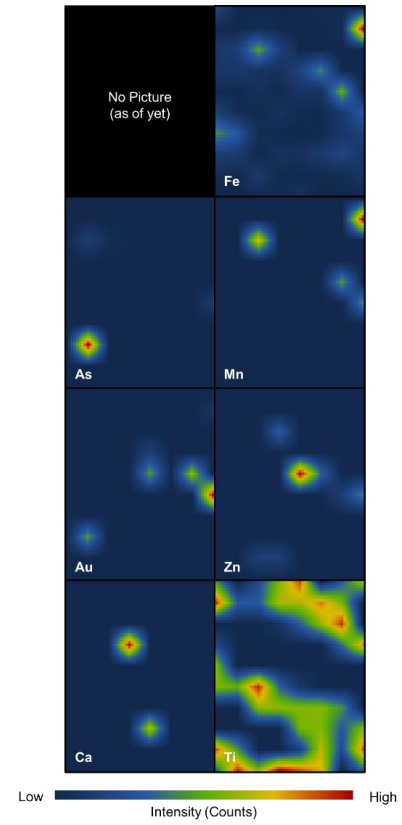
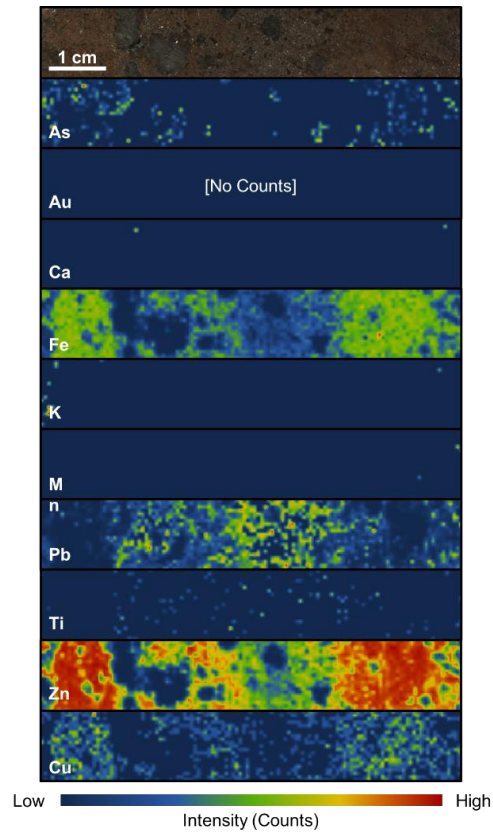
Homer	THL16-008	S345464	MVL	MVF	<p>Very fine grain mafic flow, no leucoxene altn. Possibly a finer grain and altered version of the gabbro above. Few veins in this section, but there is an overall weak-mod siliceous altn; most veins are overprinted by sulfides or associated with semi-massive sulfides from 34-34.68m. Broken core from 31.67-31.77m and 0.5cm fault gouge along the lower margin of broken core at 31.77m (30 TCA). Second fault zone (broken/fractured core) from 38-39.26m, with possible fault gouge at 39.26m. Lower contact is obscured by increased sulfides, marked by the appearance of leucoxene.</p>	0.695	0.5 mm	beamline error
-------	-----------	---------	-----	-----	--	-------	--------	----------------

Appendix B: X-ray Fluorescence Maps

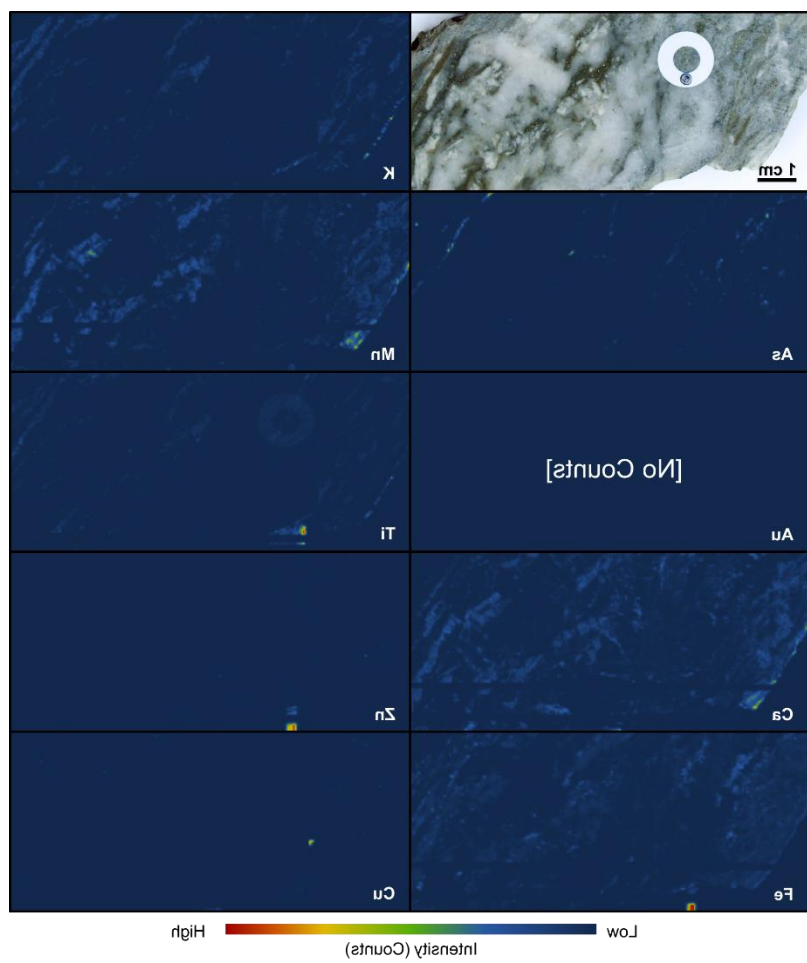
Kerswill Suite

BRX2

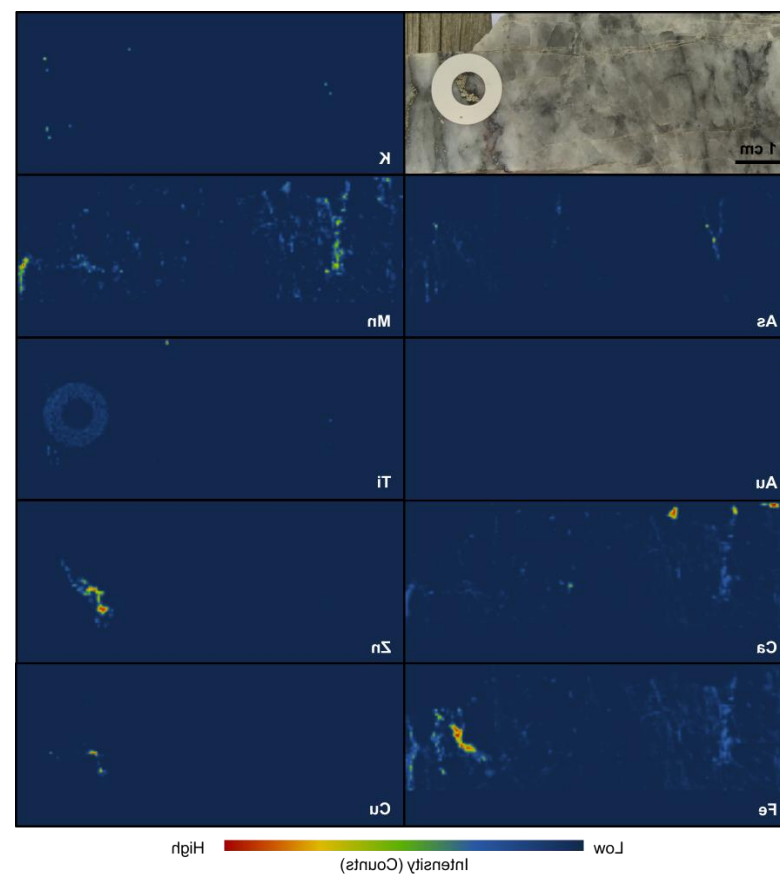
AN14



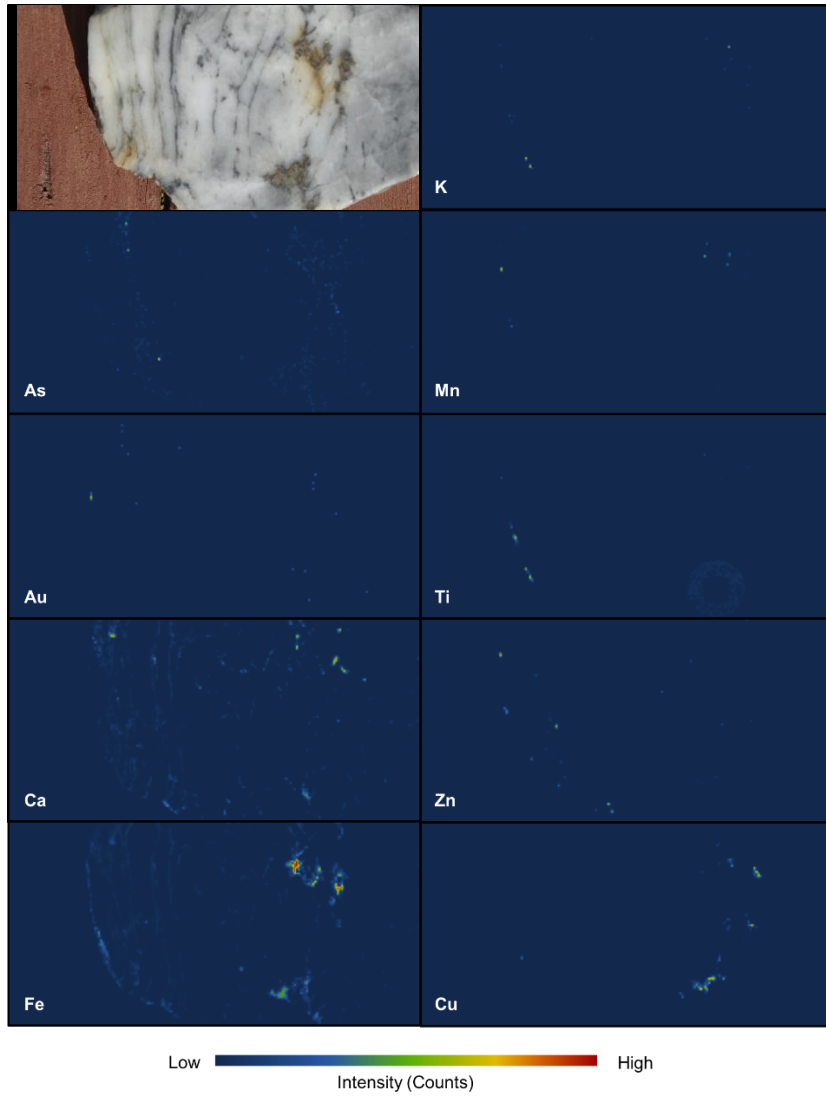
C421



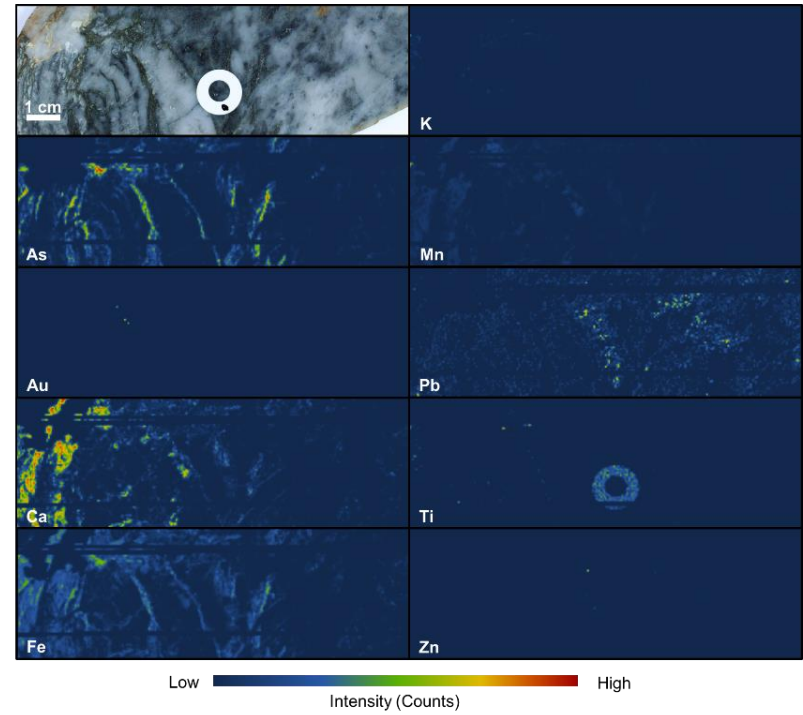
C511



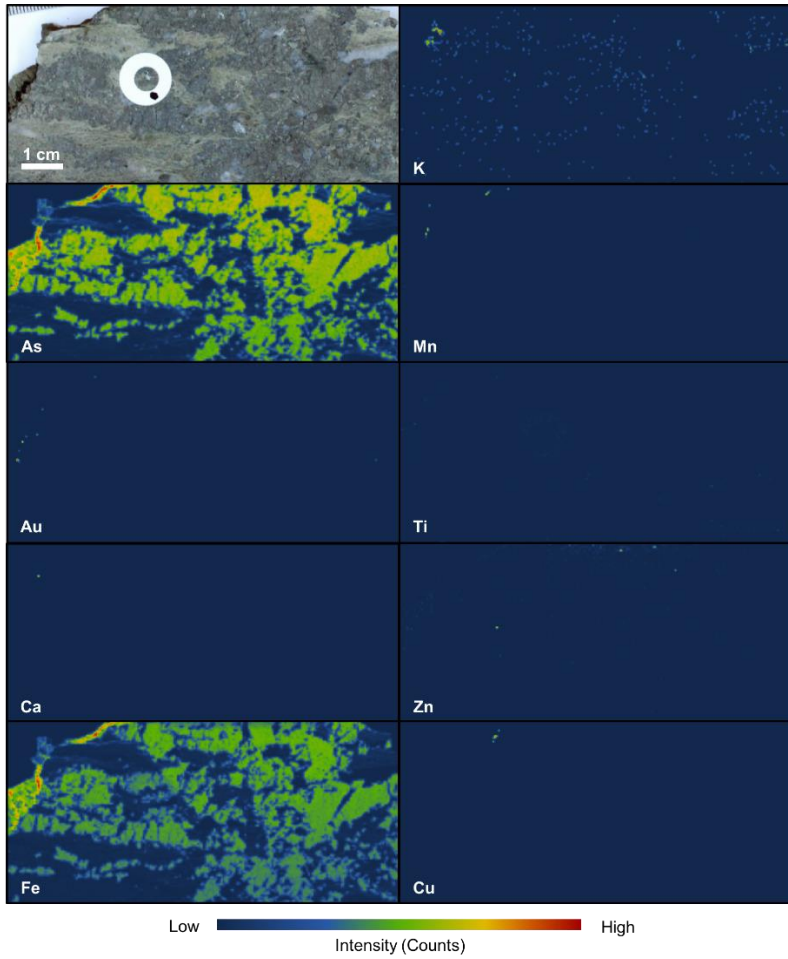
C611



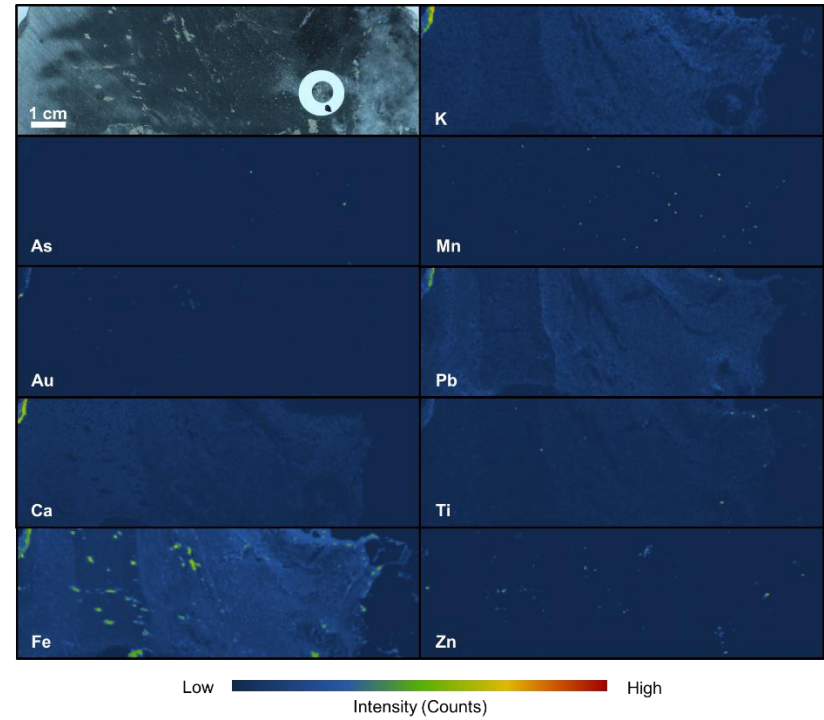
CR16



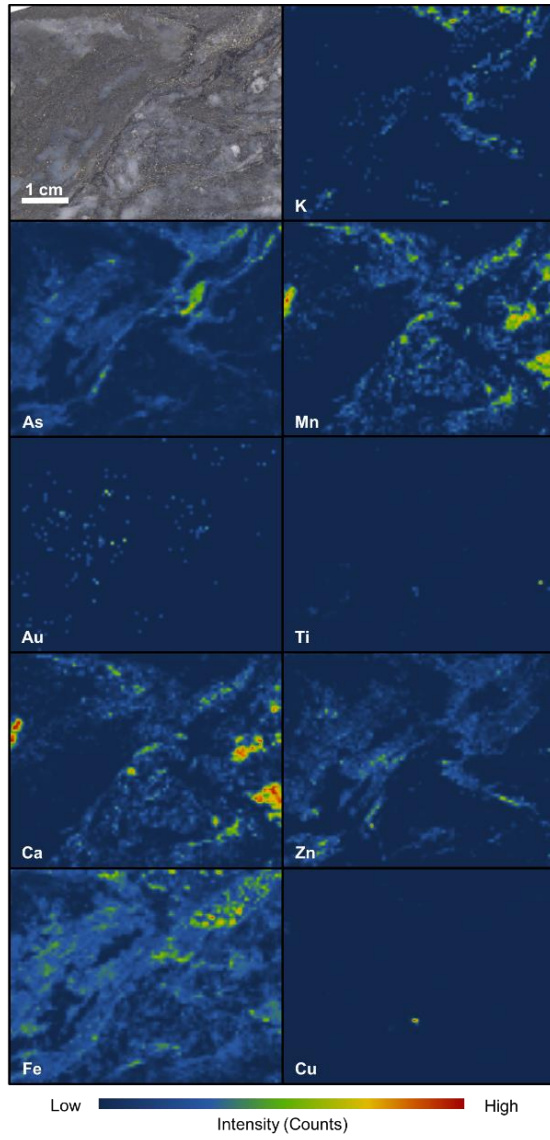
DF11



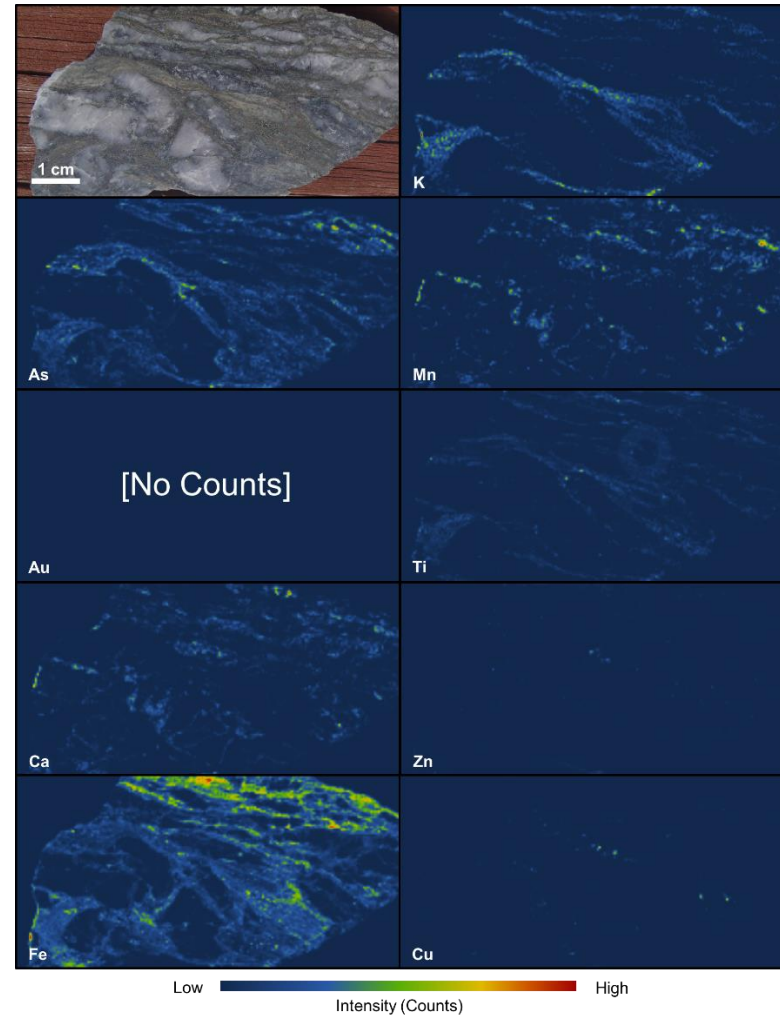
DX2



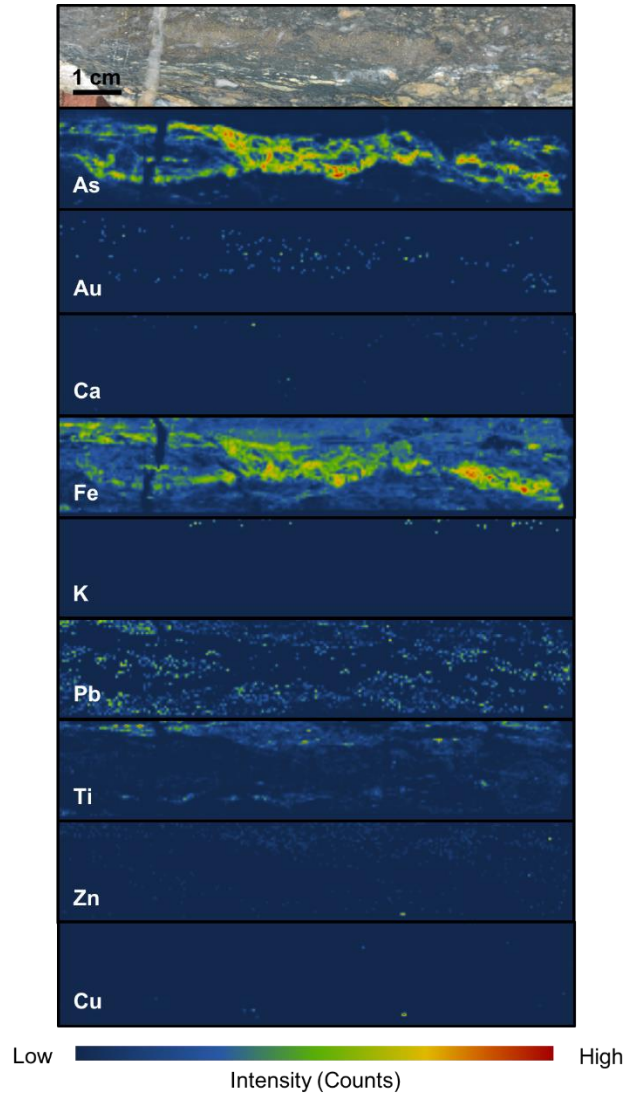
G13



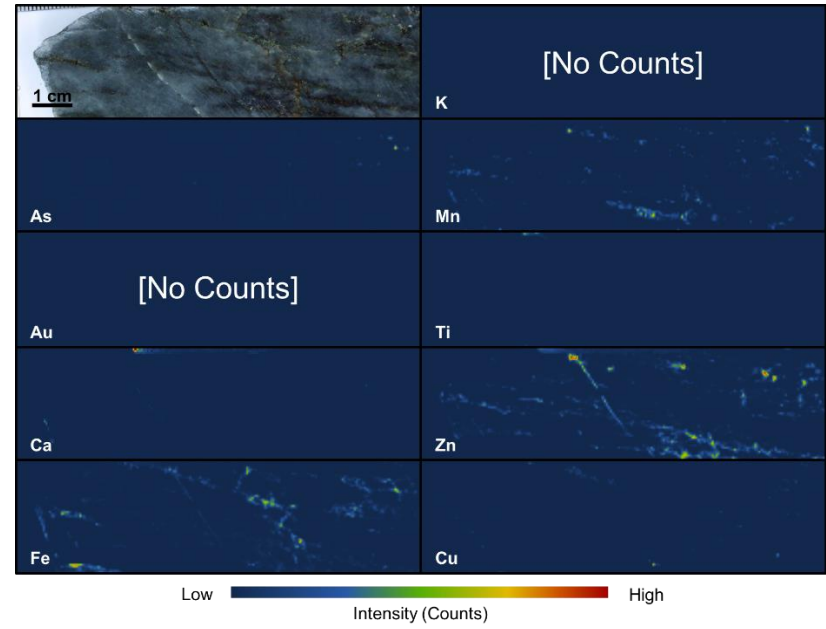
G42



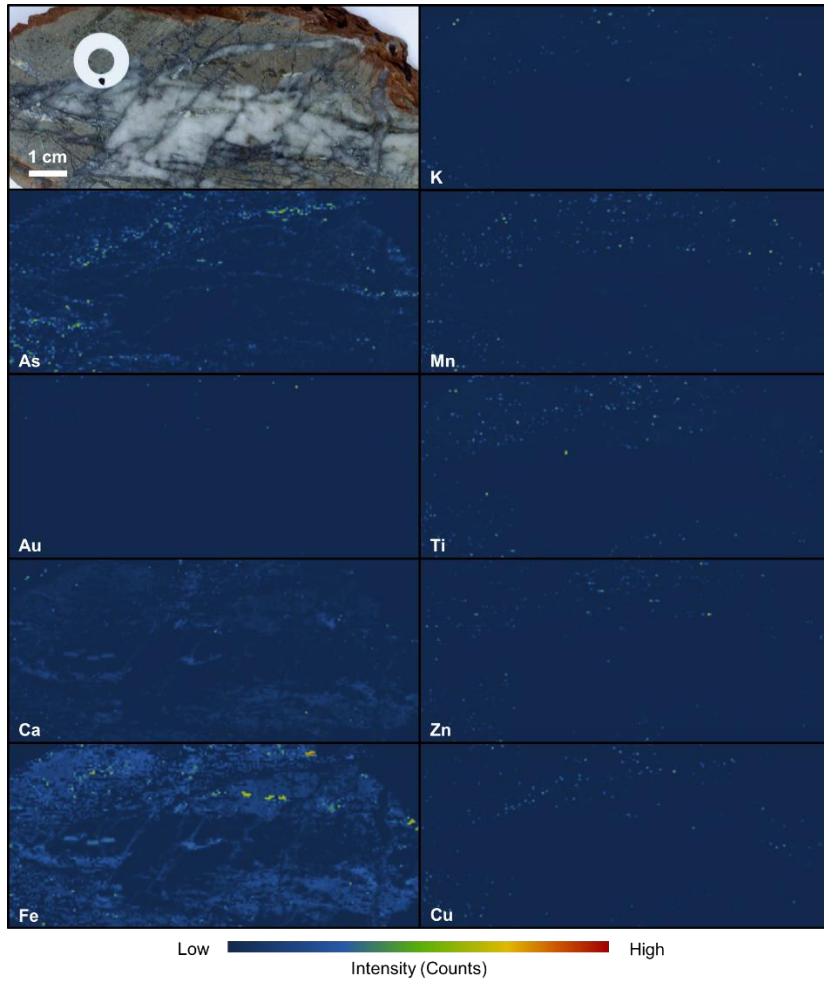
JL21



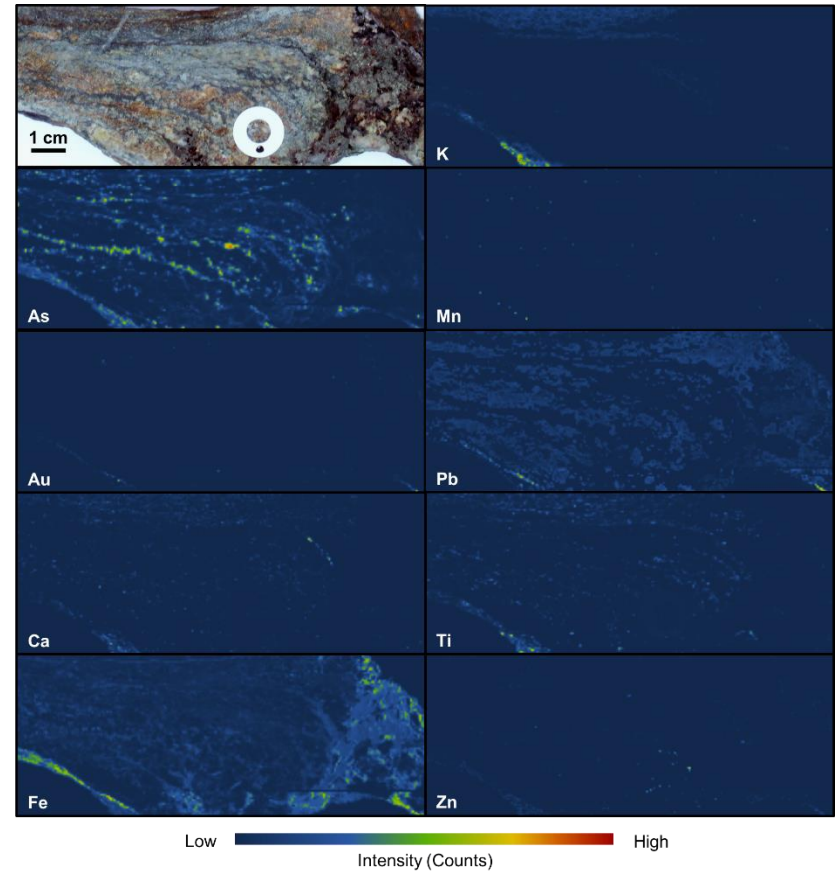
MN12



MQ12

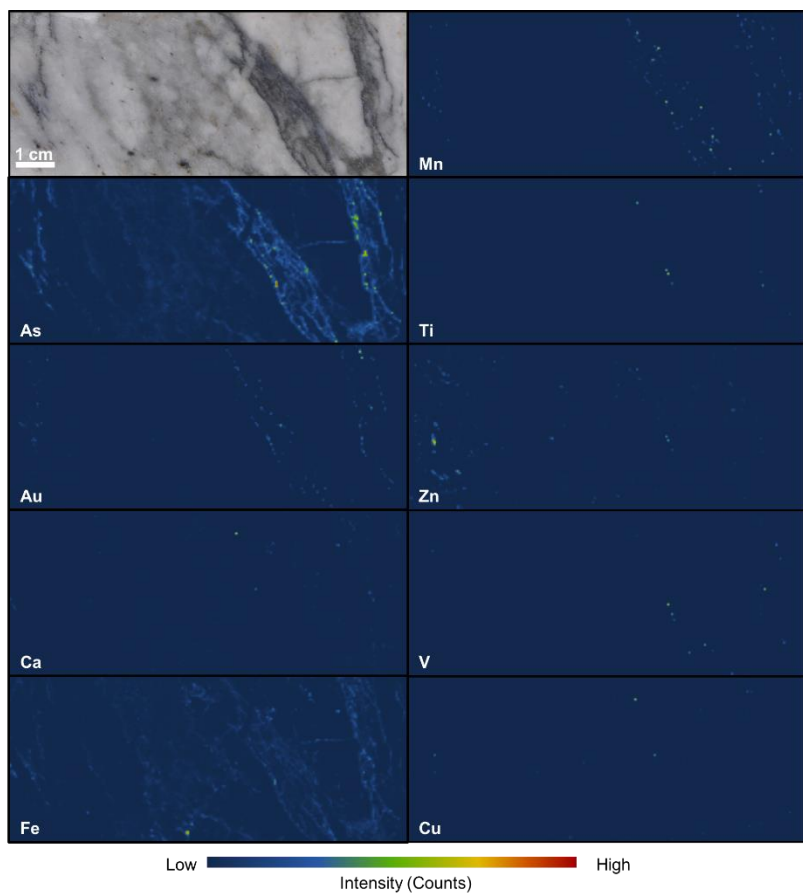


SL23

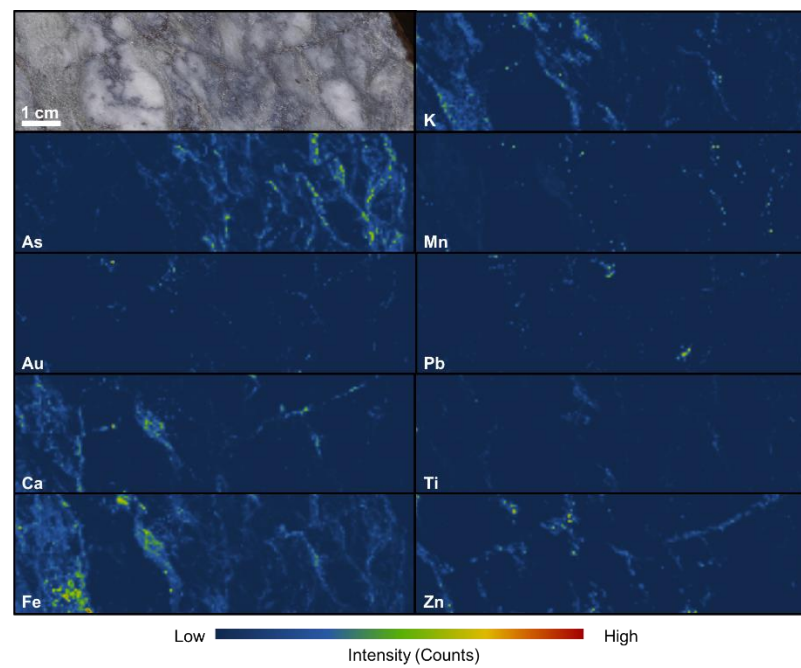


Crestaaurum

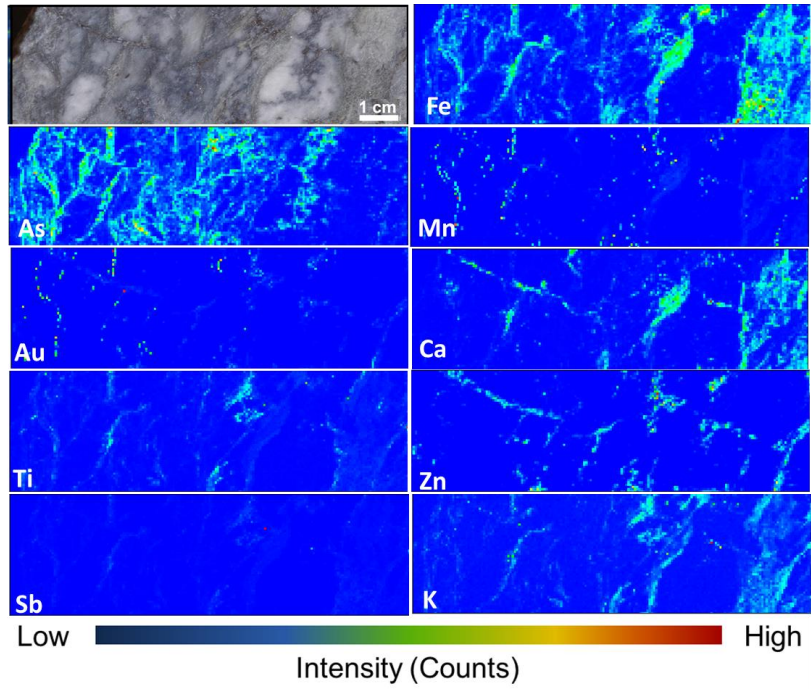
R432247



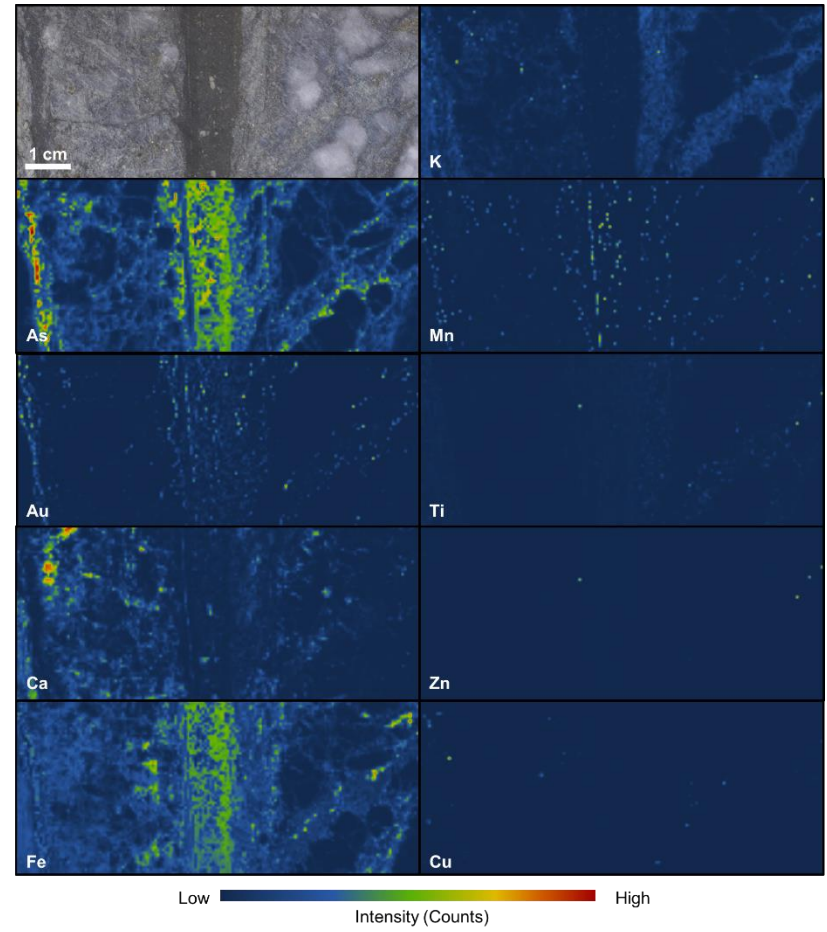
R432250, Peakaboo (flipped)



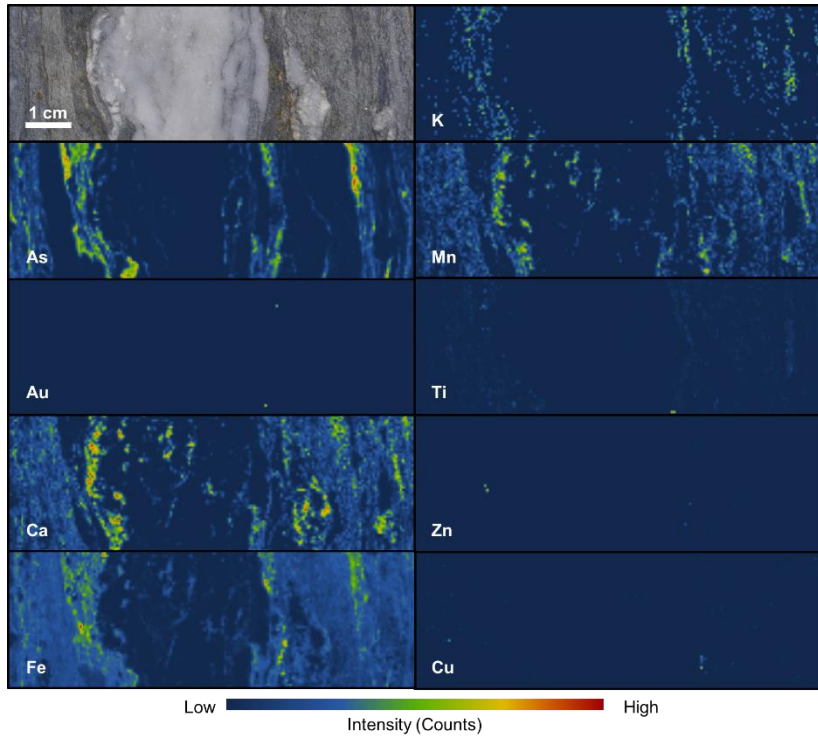
R432250, pyMCA



R433857

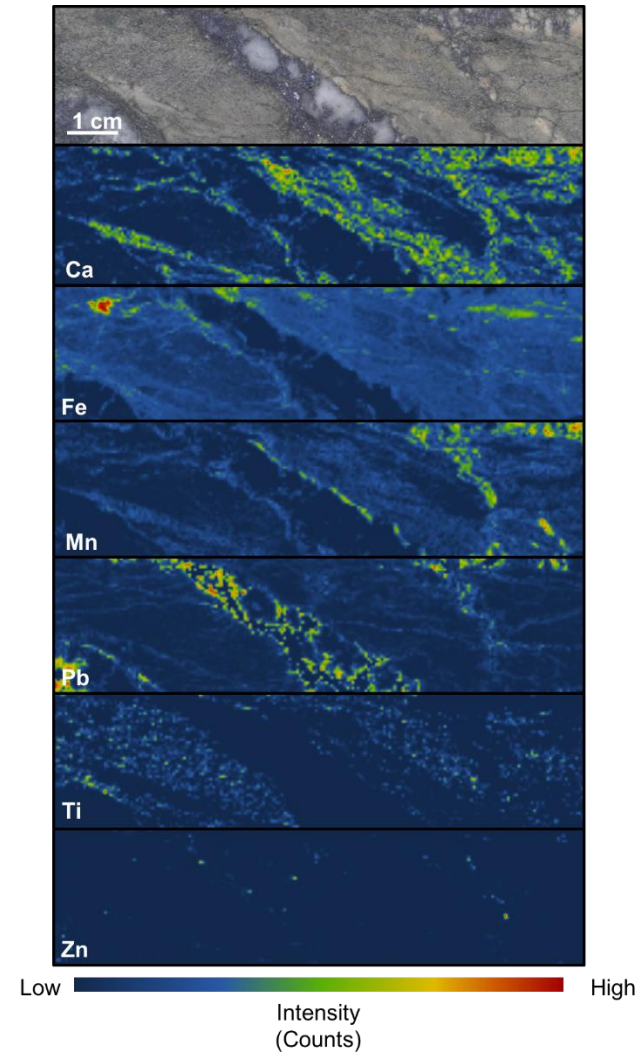


R433866

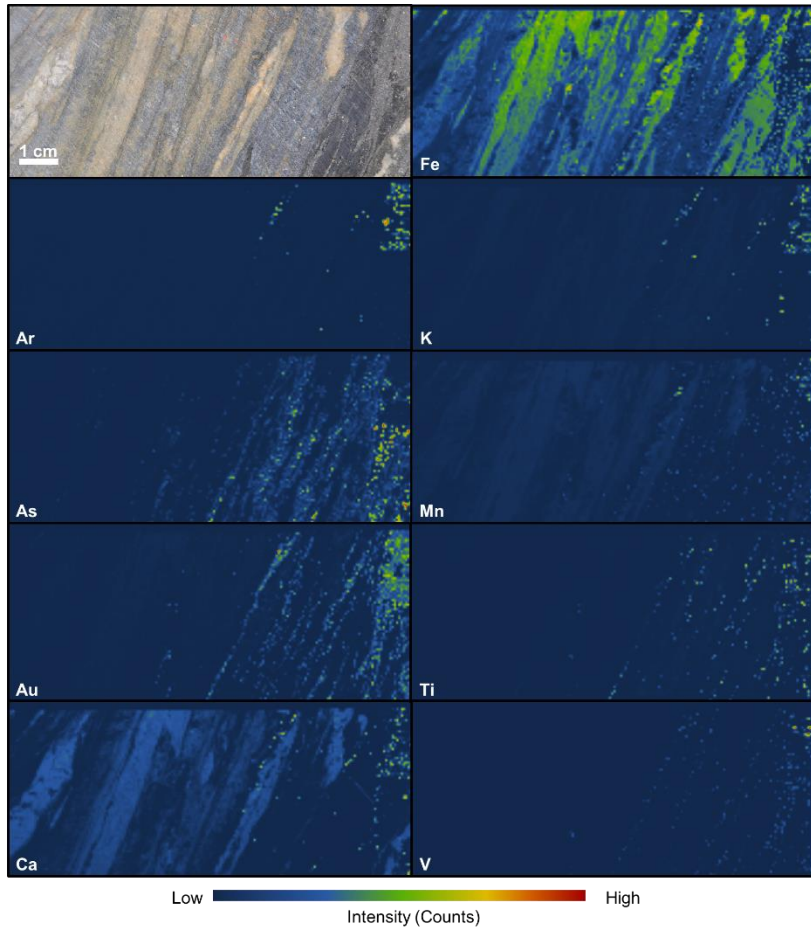


Barney

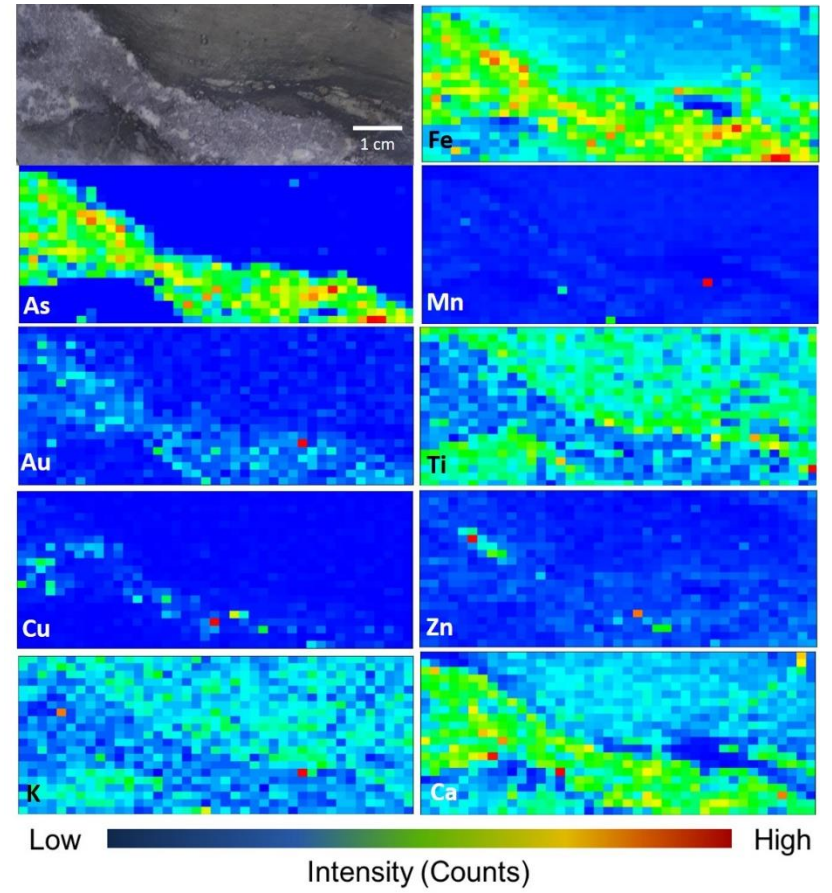
R115110



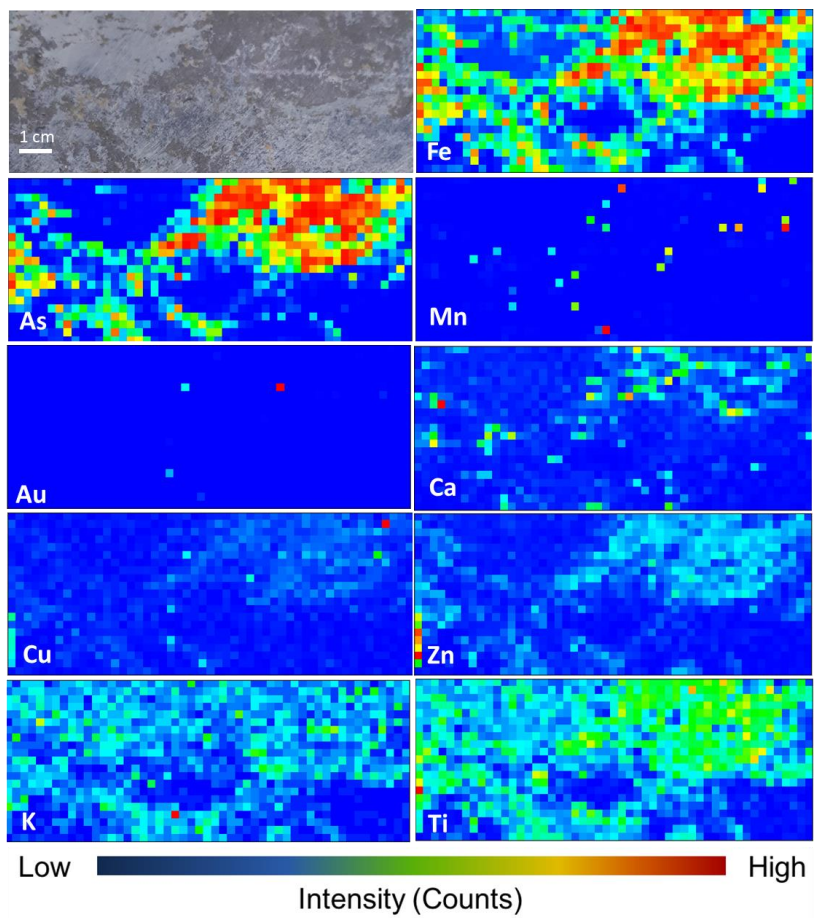
R115609



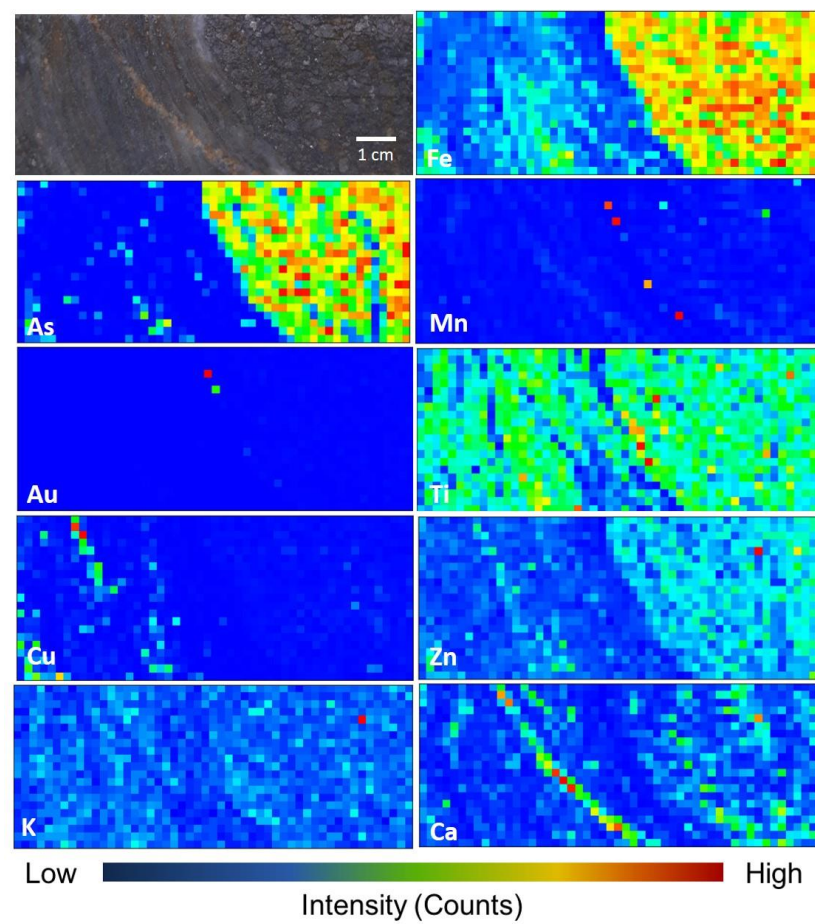
R115123



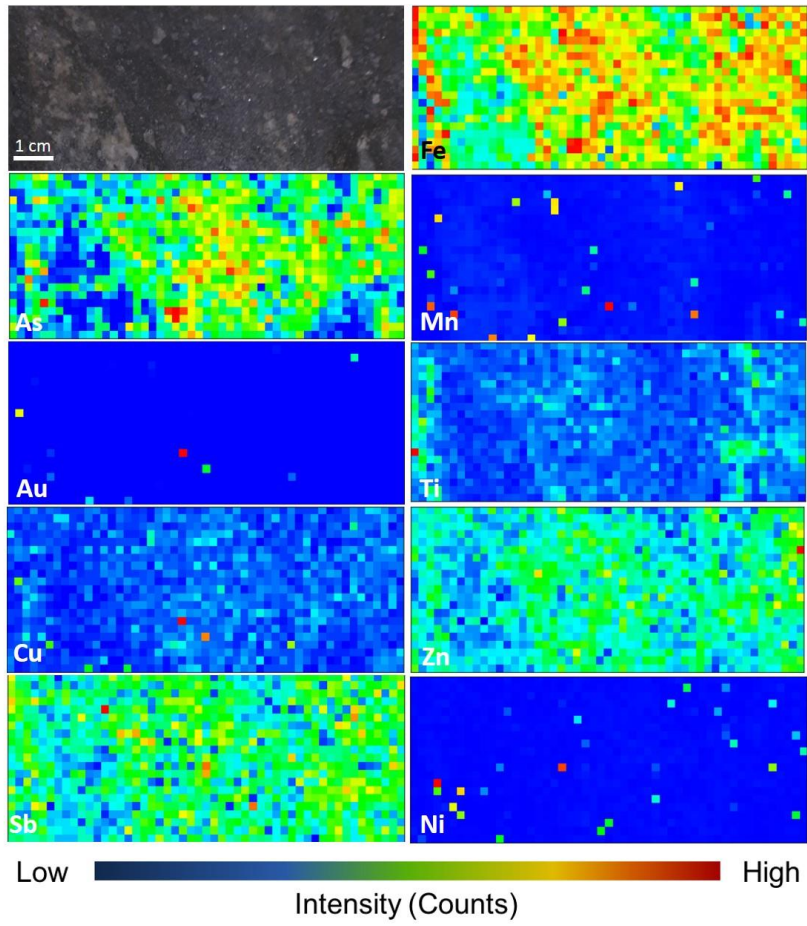
R115604



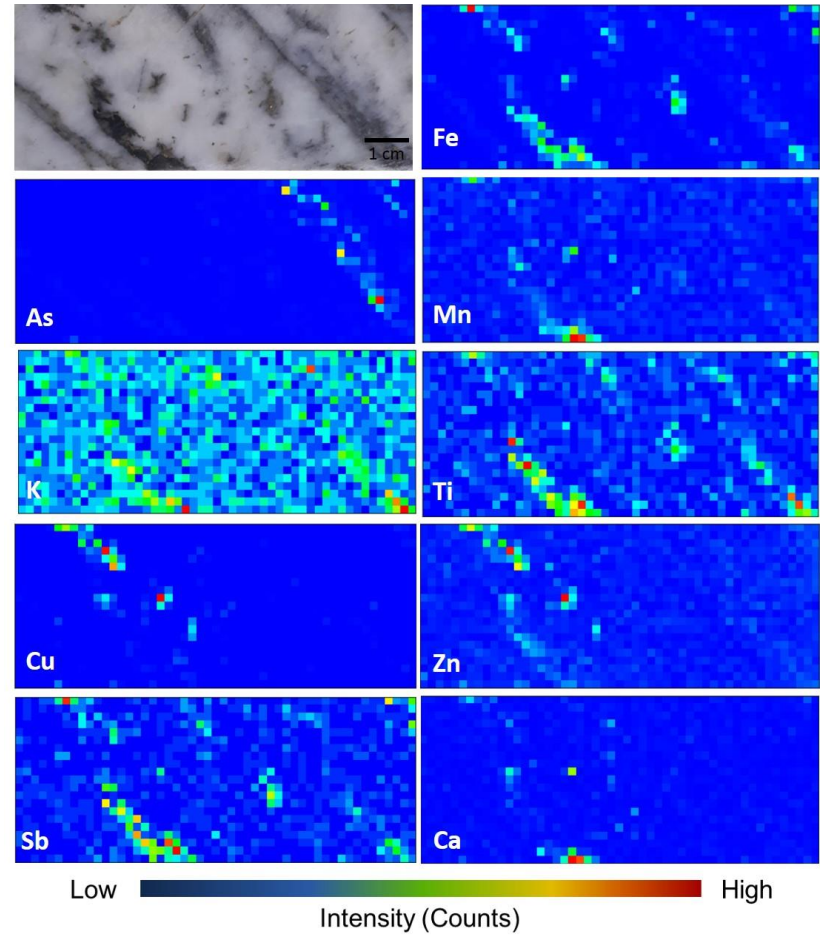
R115621



R115622

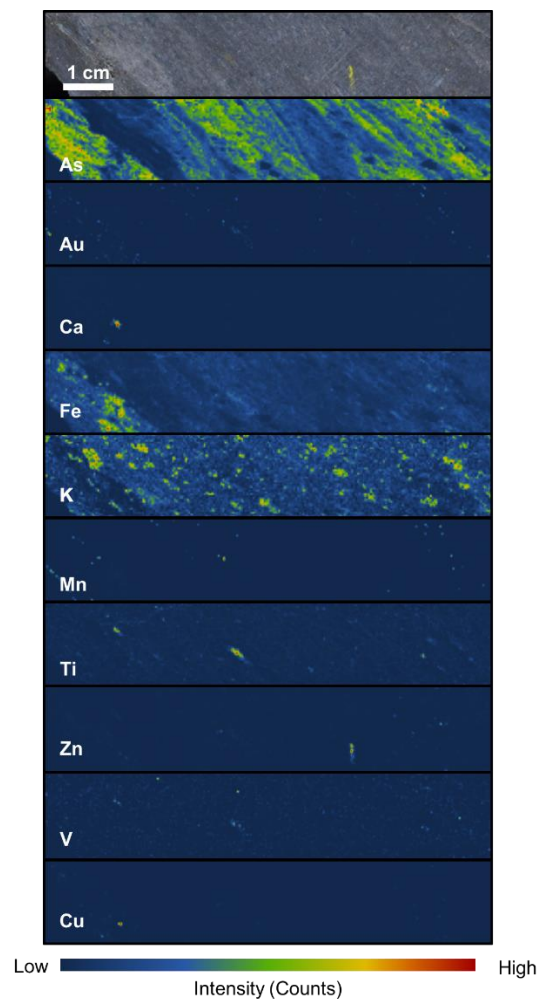


S519135

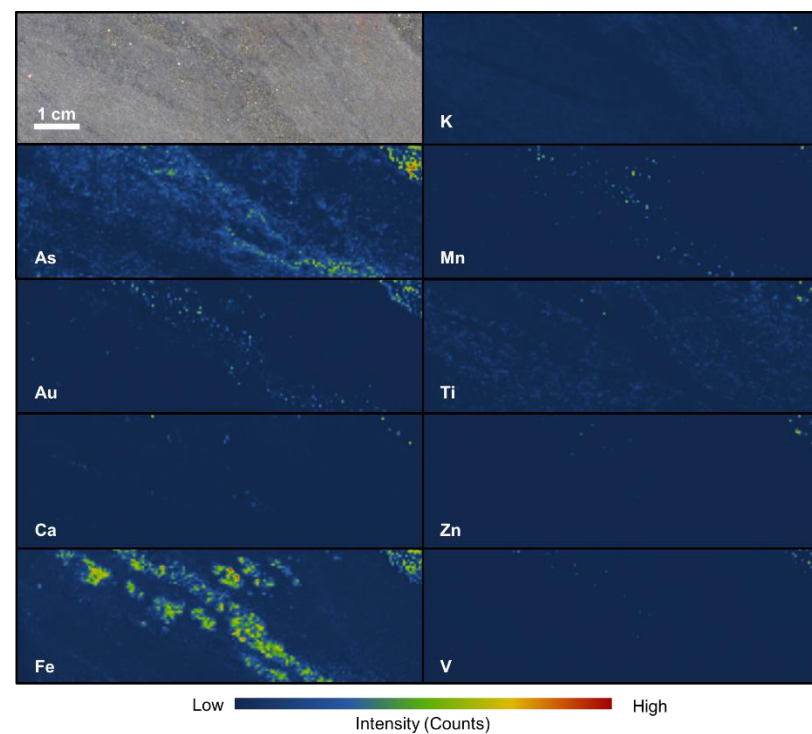


Hébert-Brent

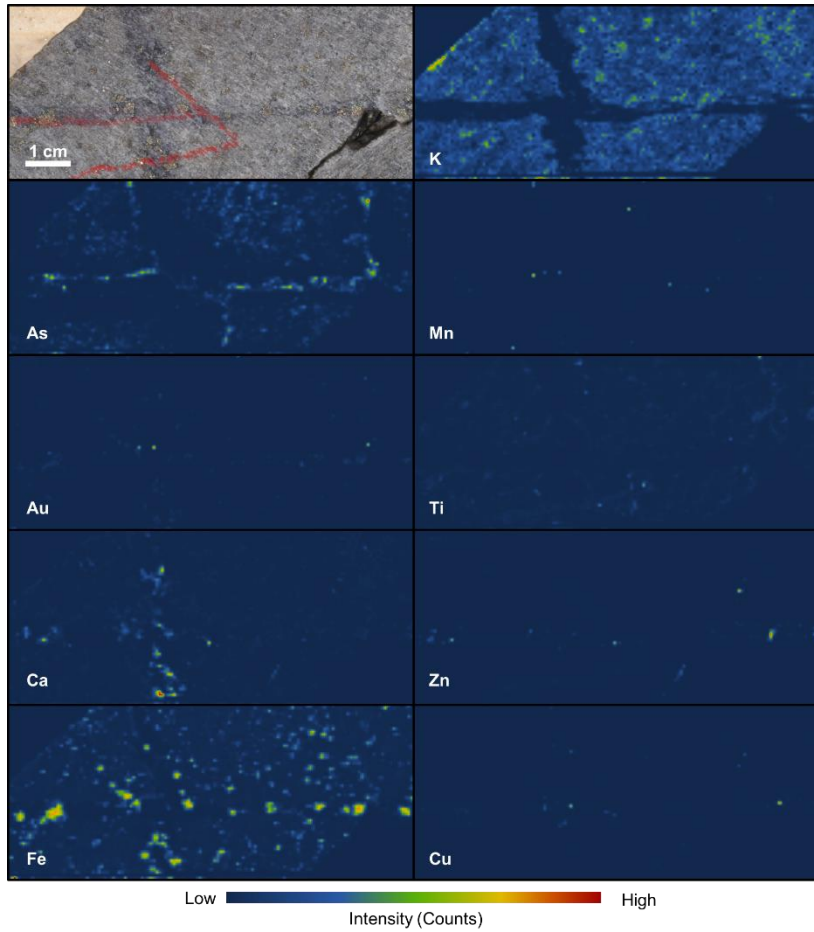
S520992



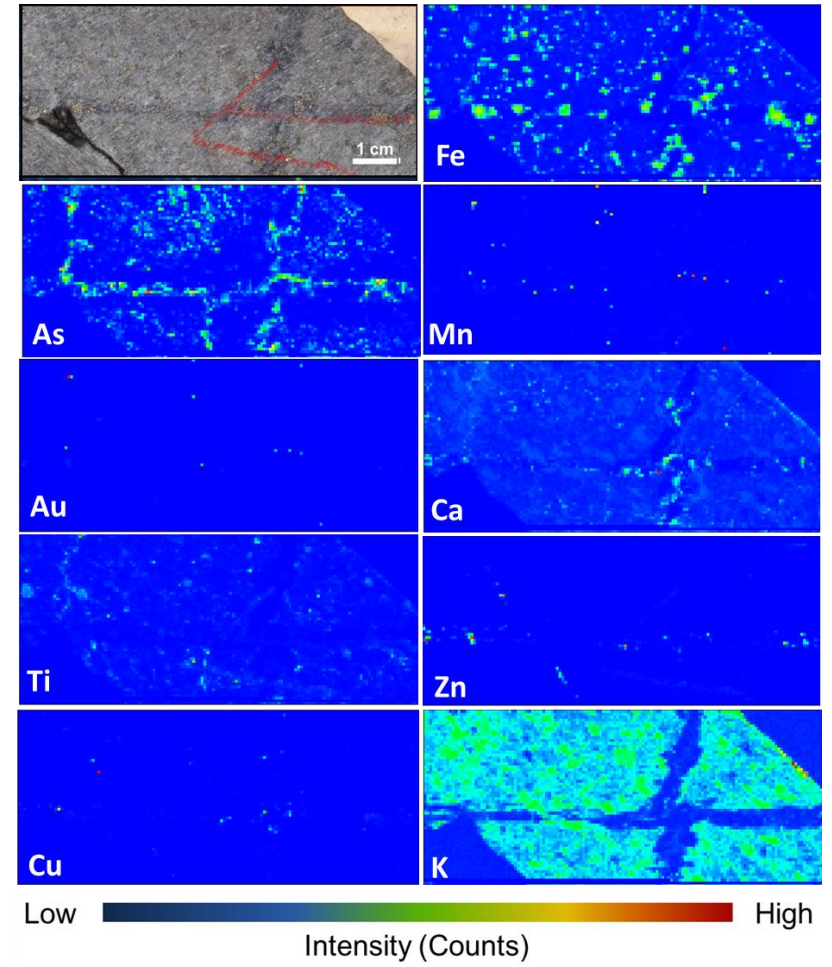
S520998



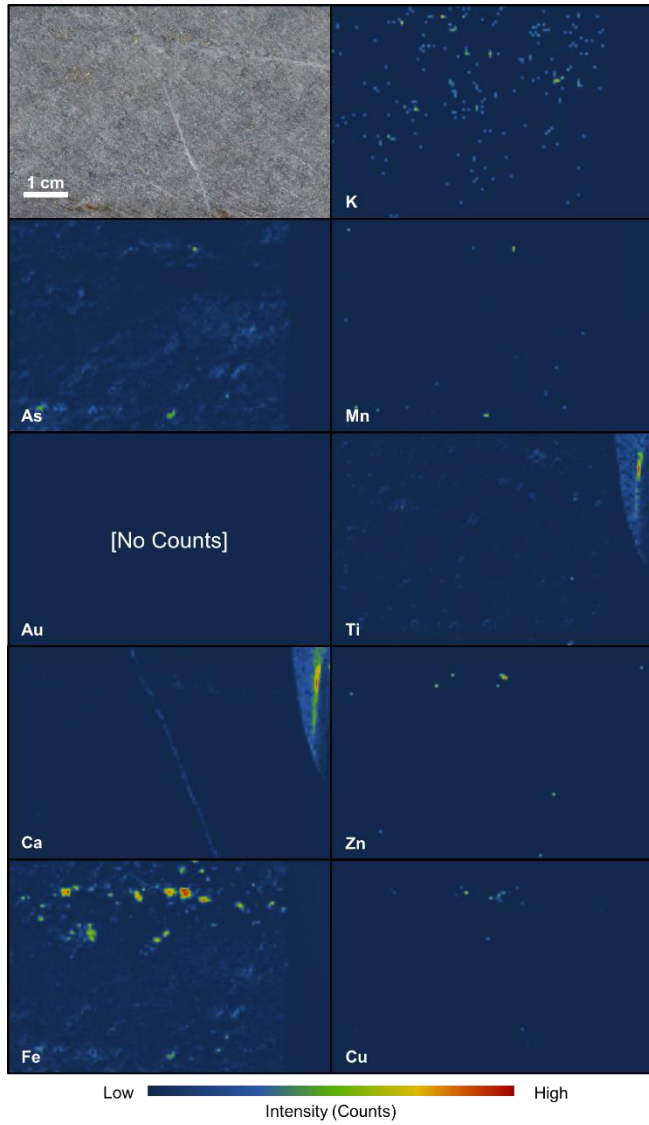
S521365, Peakaboo (flipped)



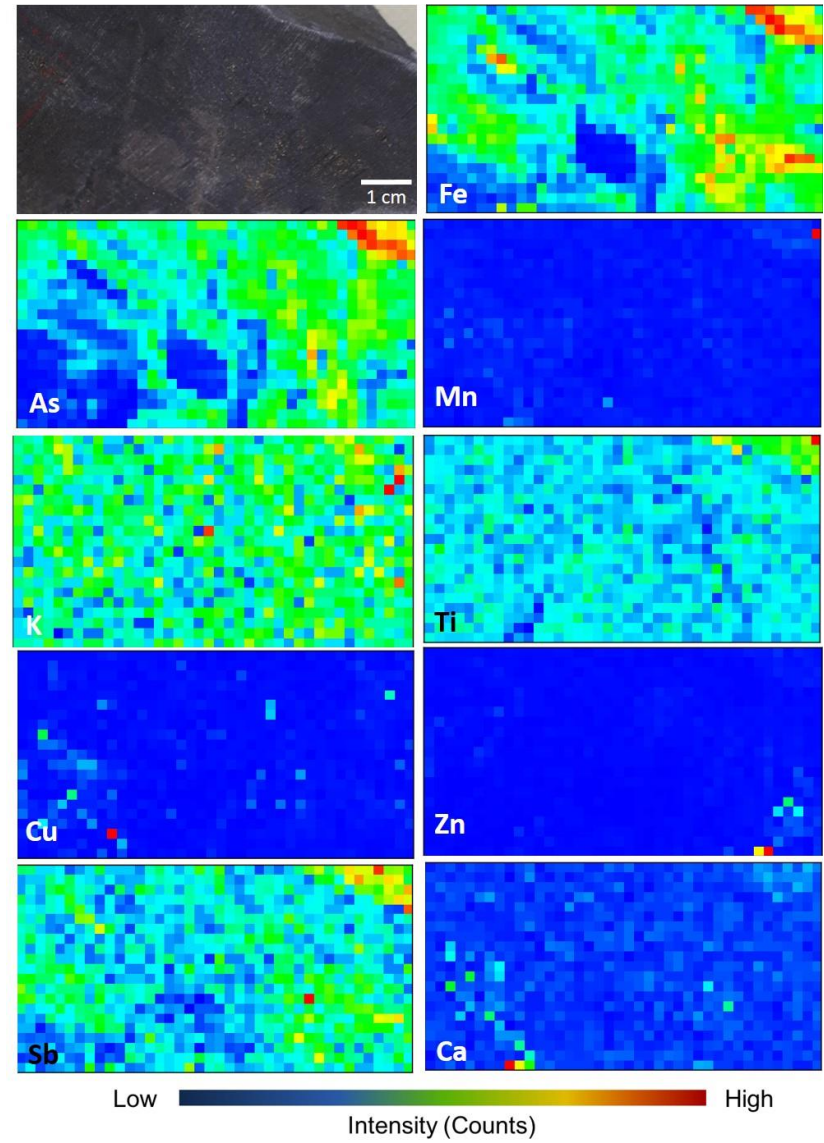
S521365, pyMCA



S521371



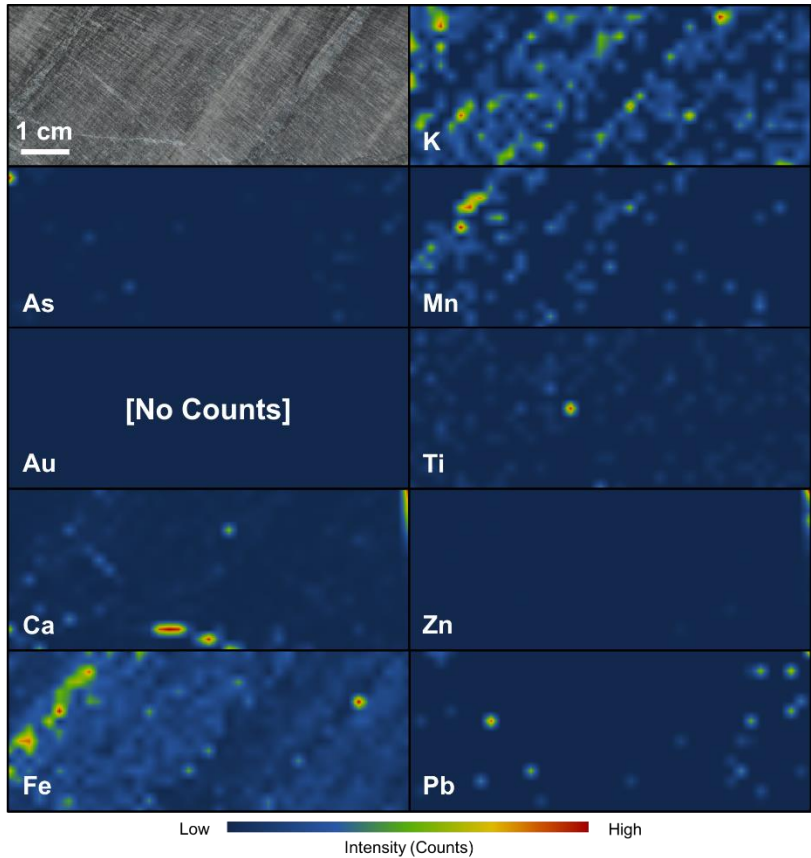
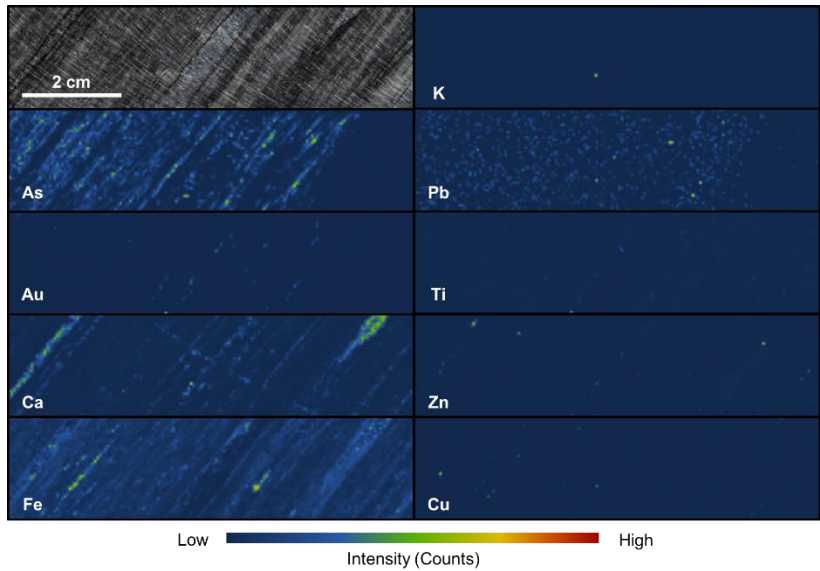
S521155



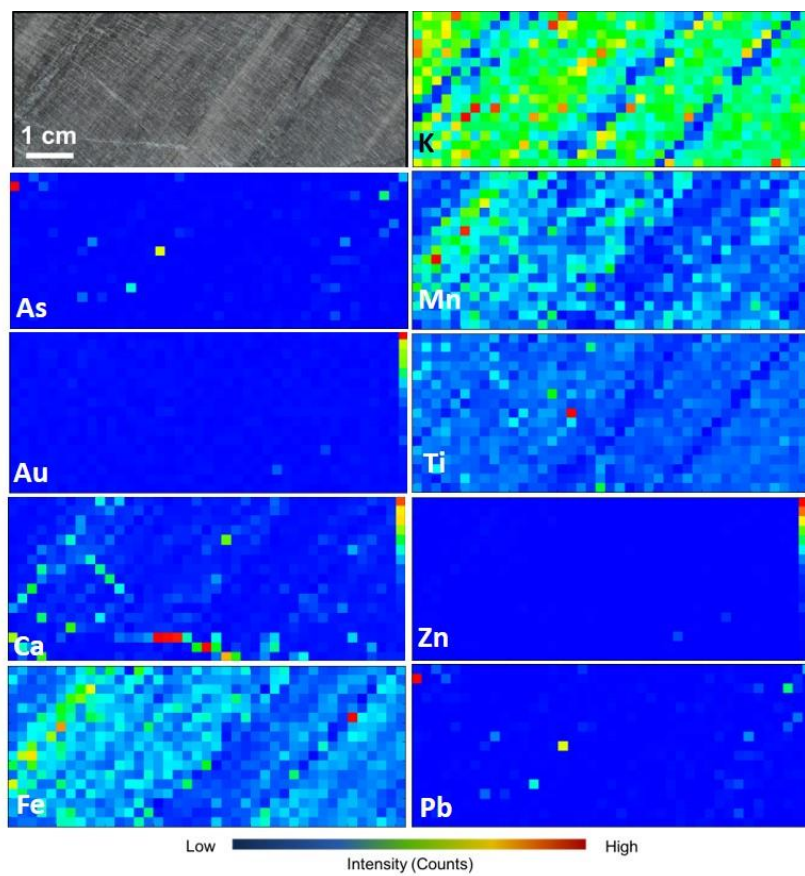
Sam Otto

S343811, Peakaboo

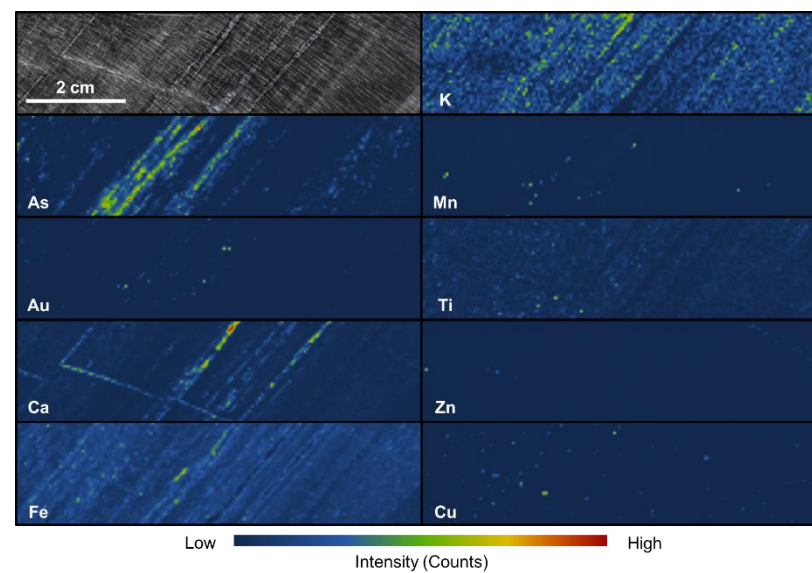
S343808



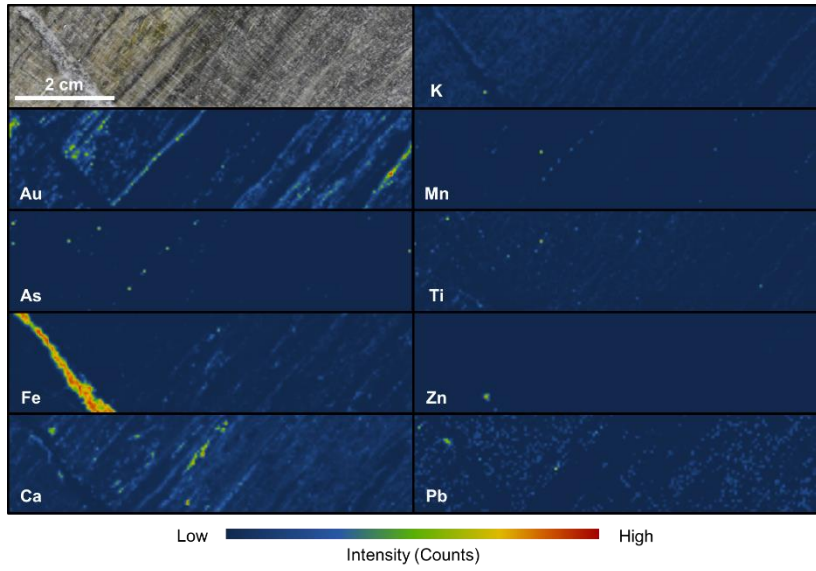
S343811, pyMCA



S343813



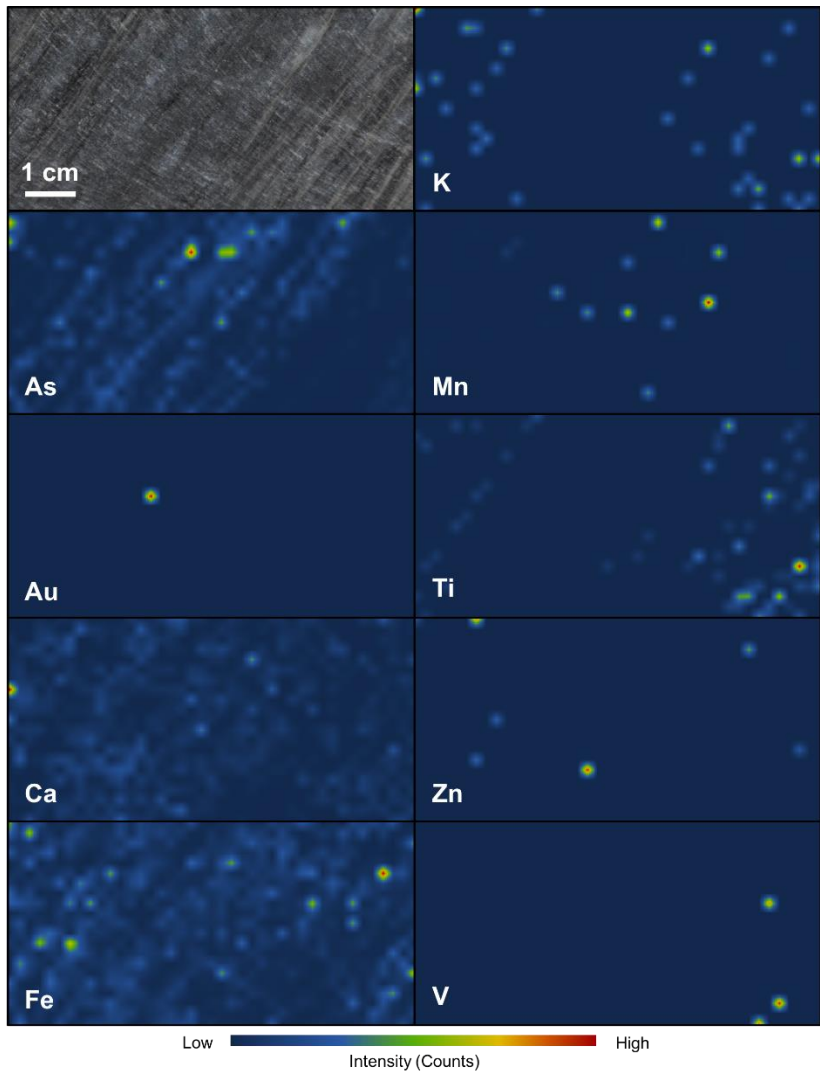
S343815



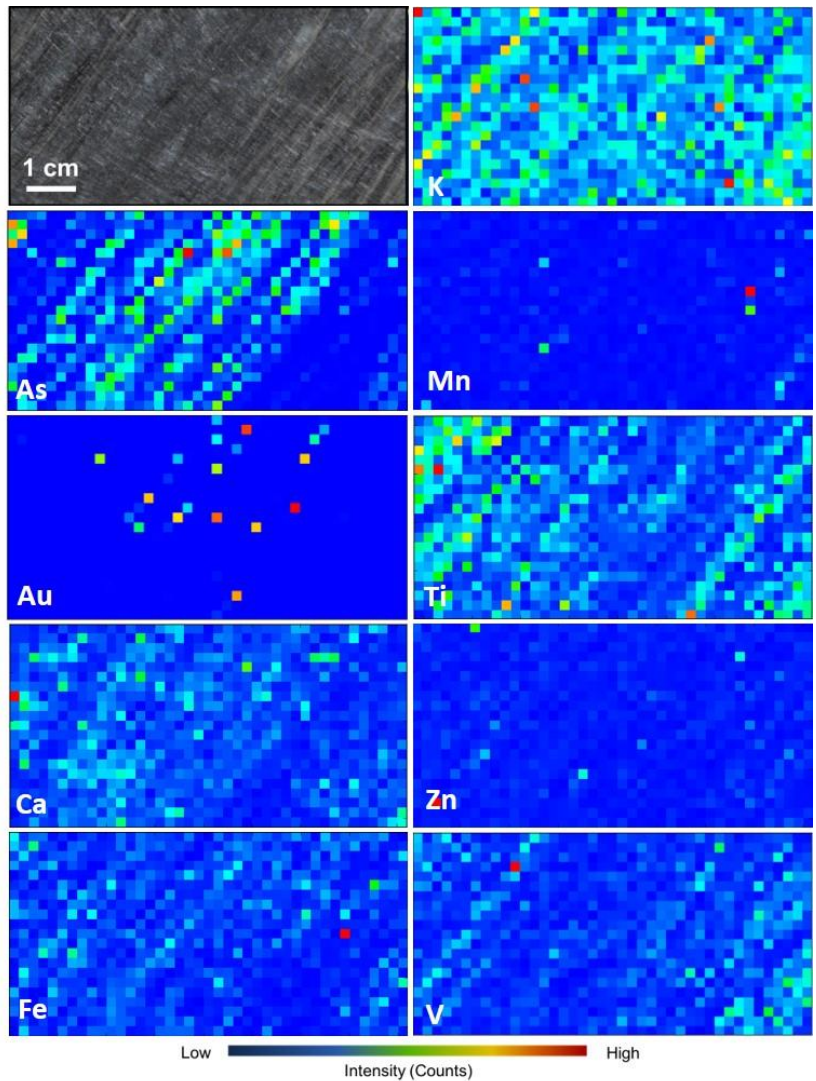
S343816



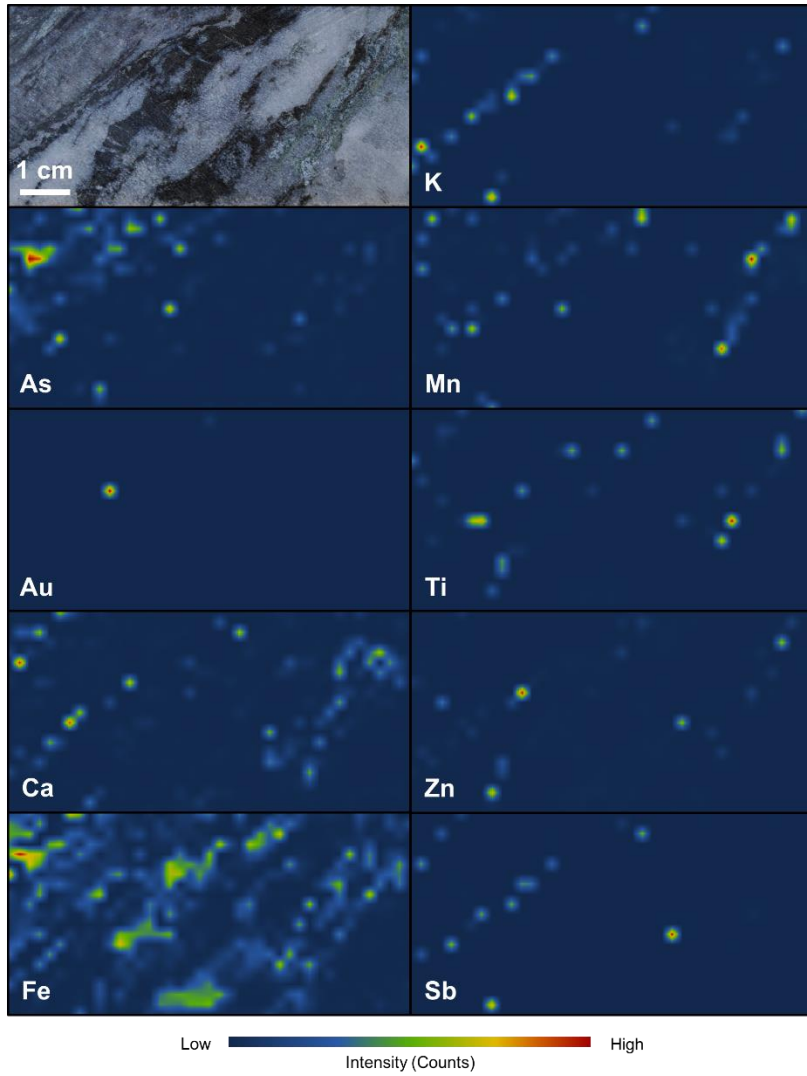
S343819, Peakaboo



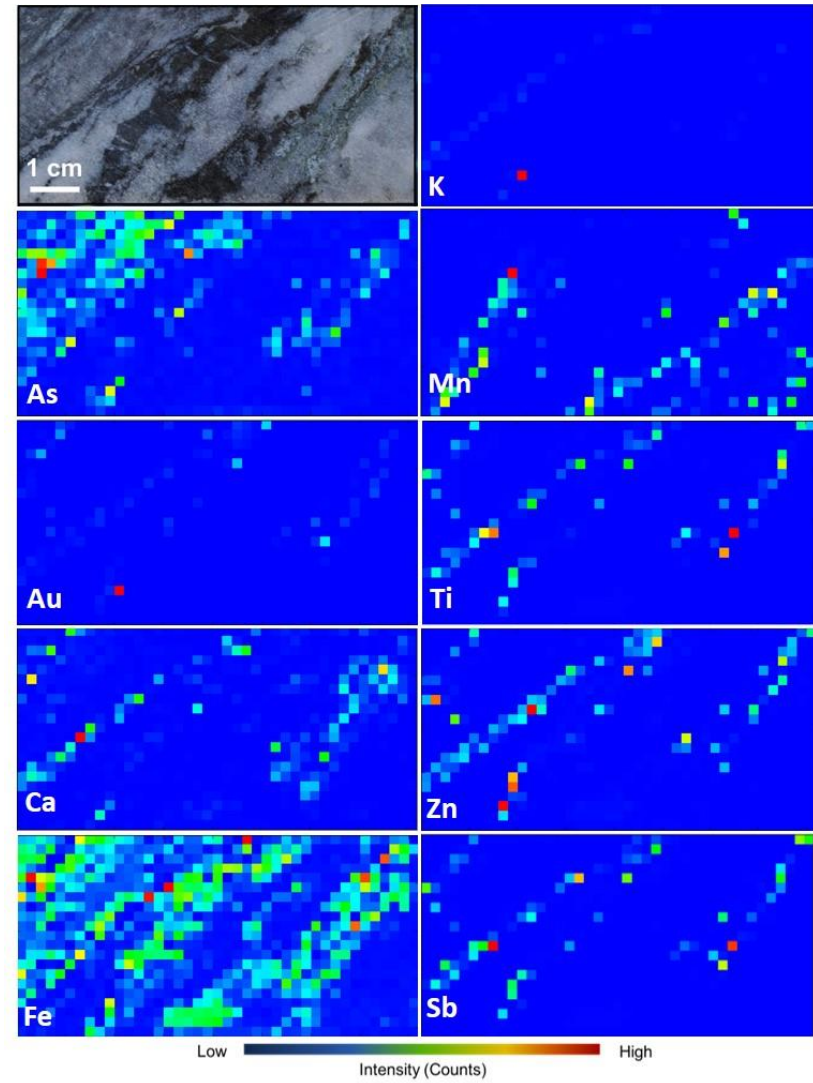
S343819, pyMCA



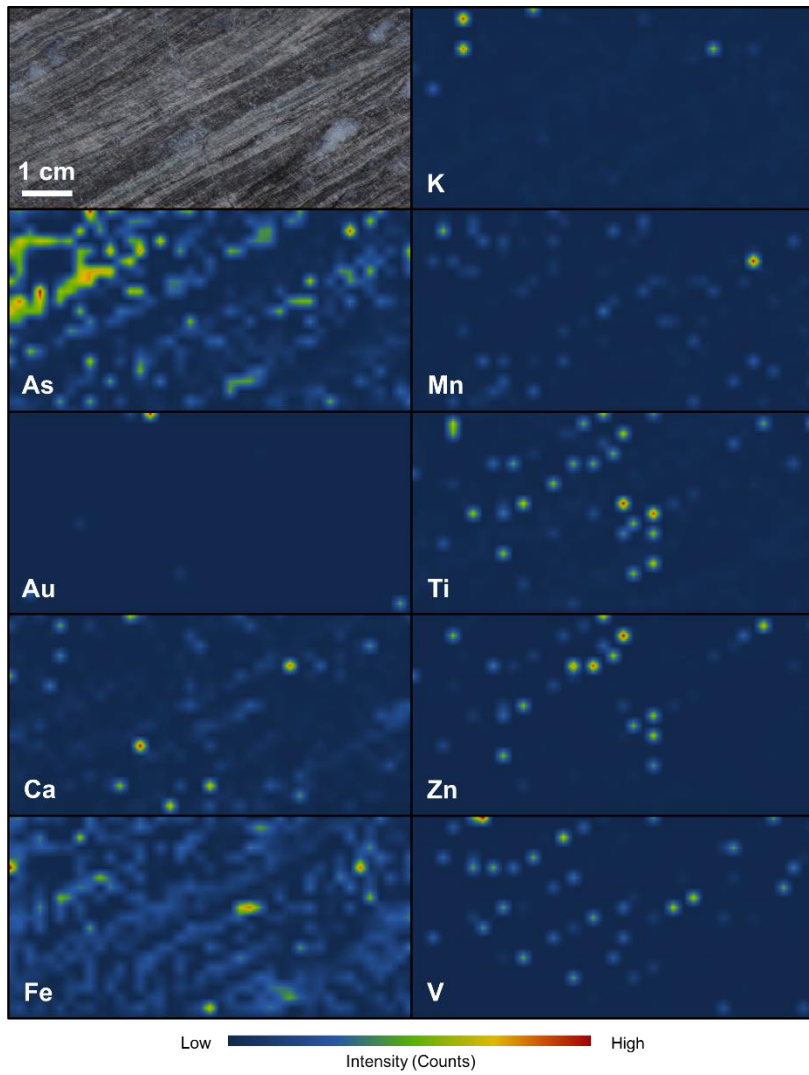
V890298, Peakaboo



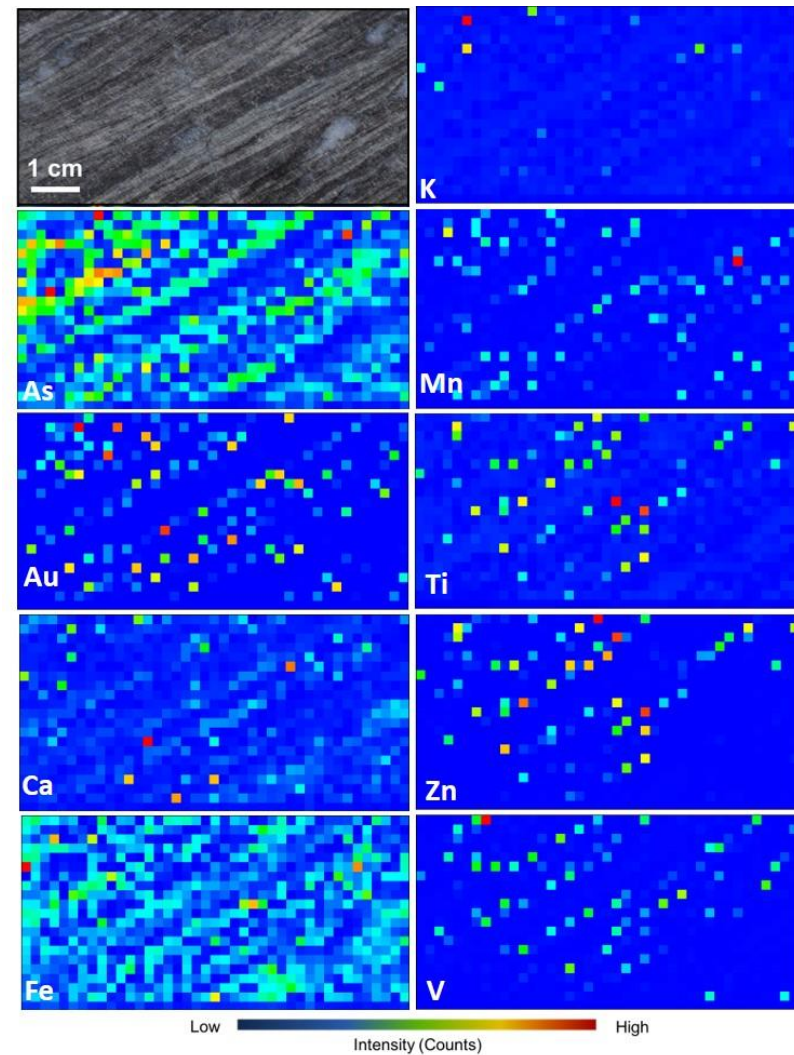
V890298, pyMCA



V892232, Peakaboo

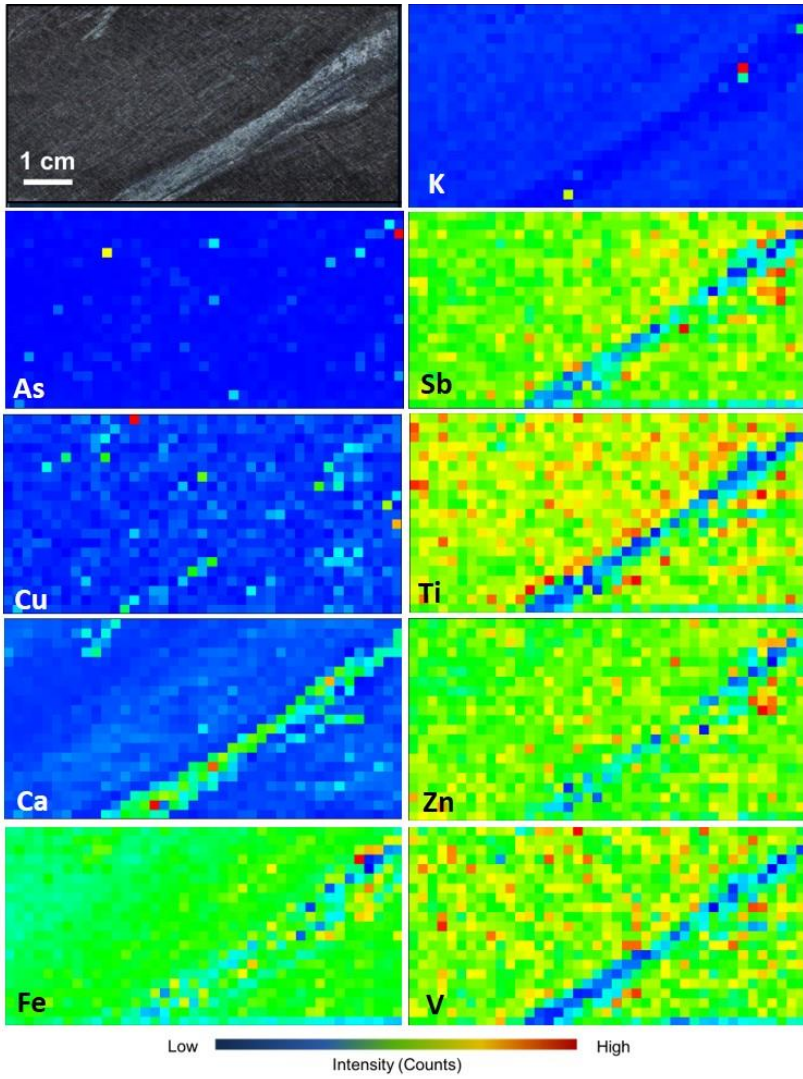
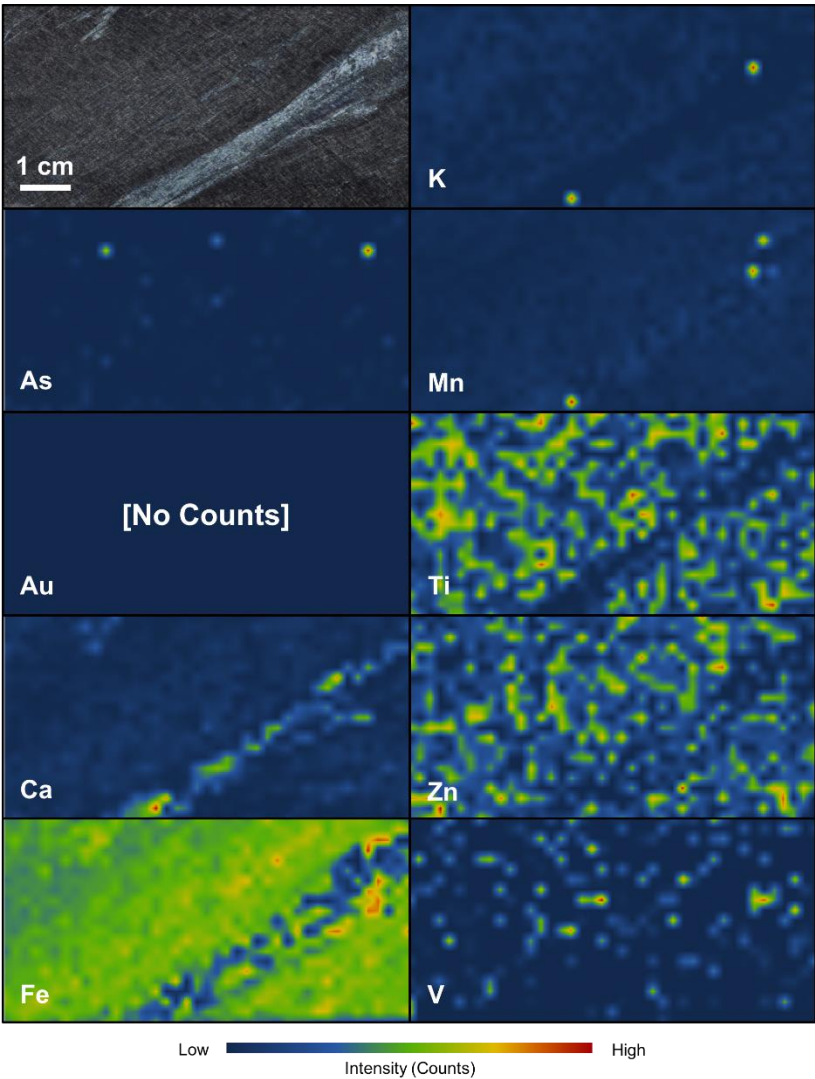


V892232, pyMCA

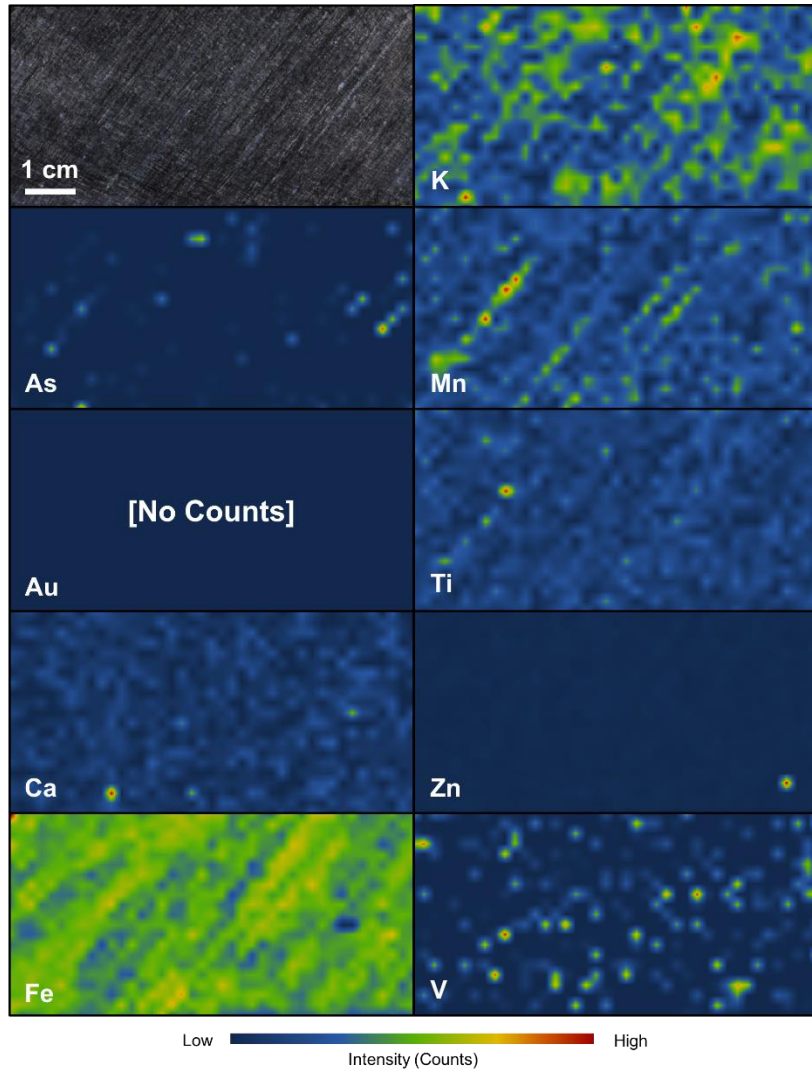


V892234, Peakaboo

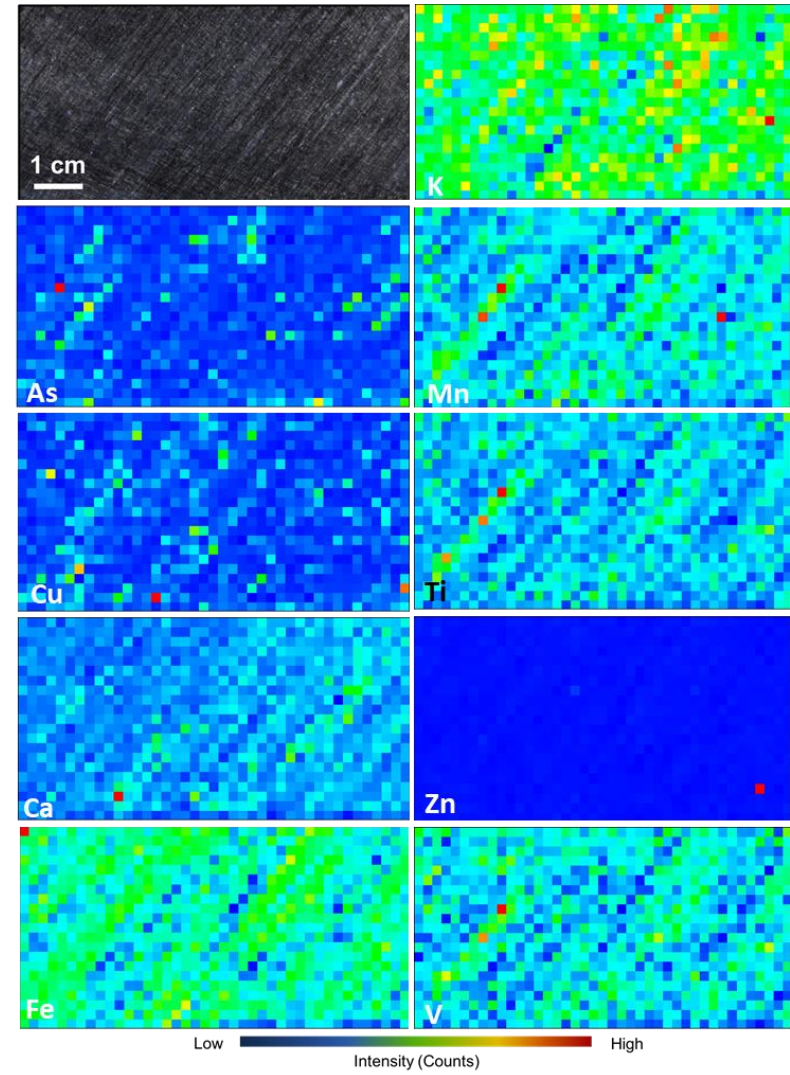
V892234, pyMCA



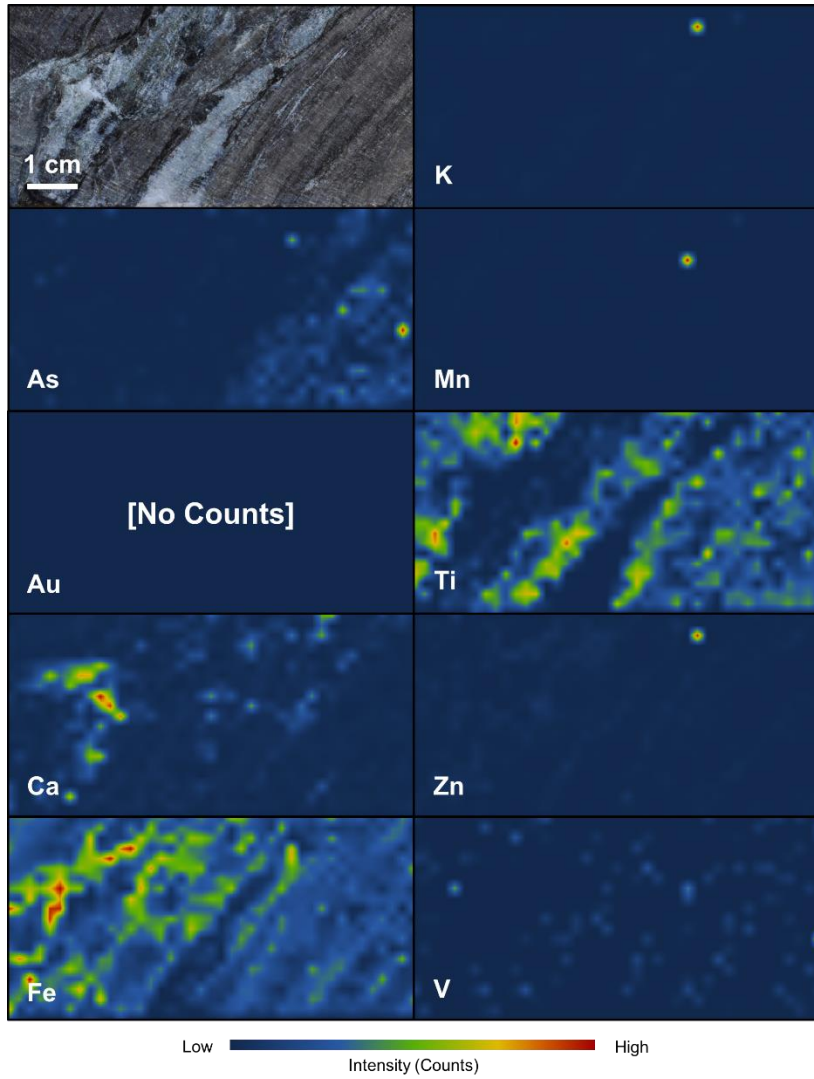
V892236, Peakaboo



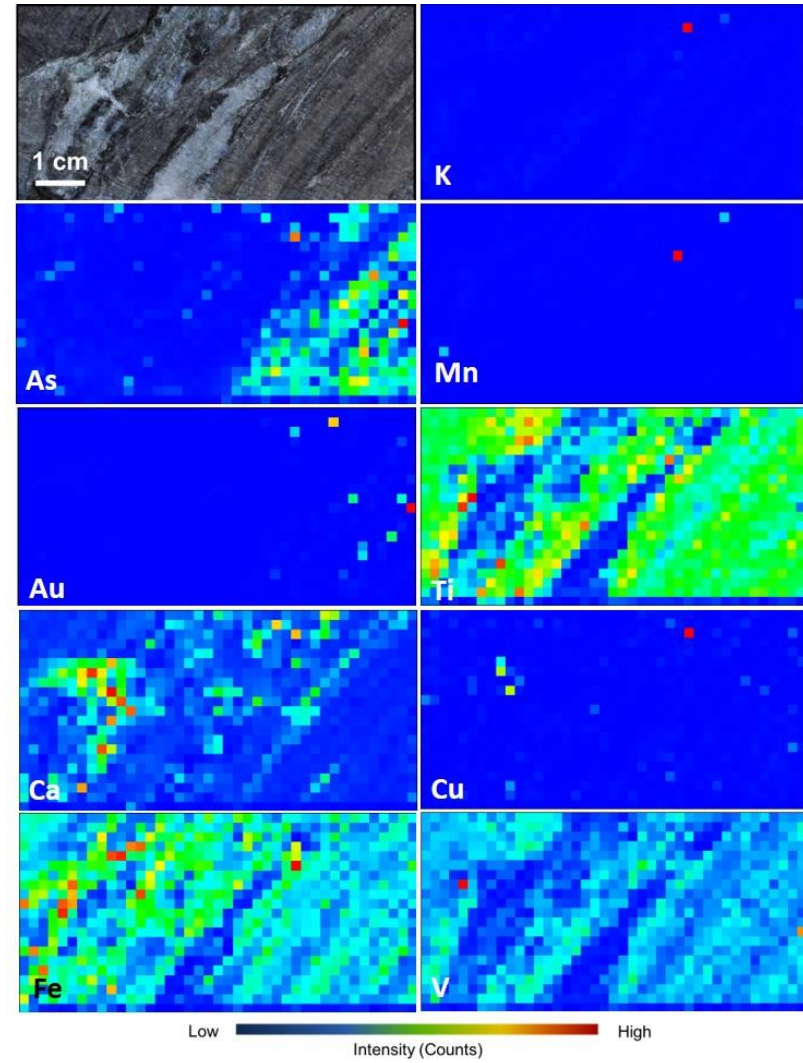
V892236, pyMCA



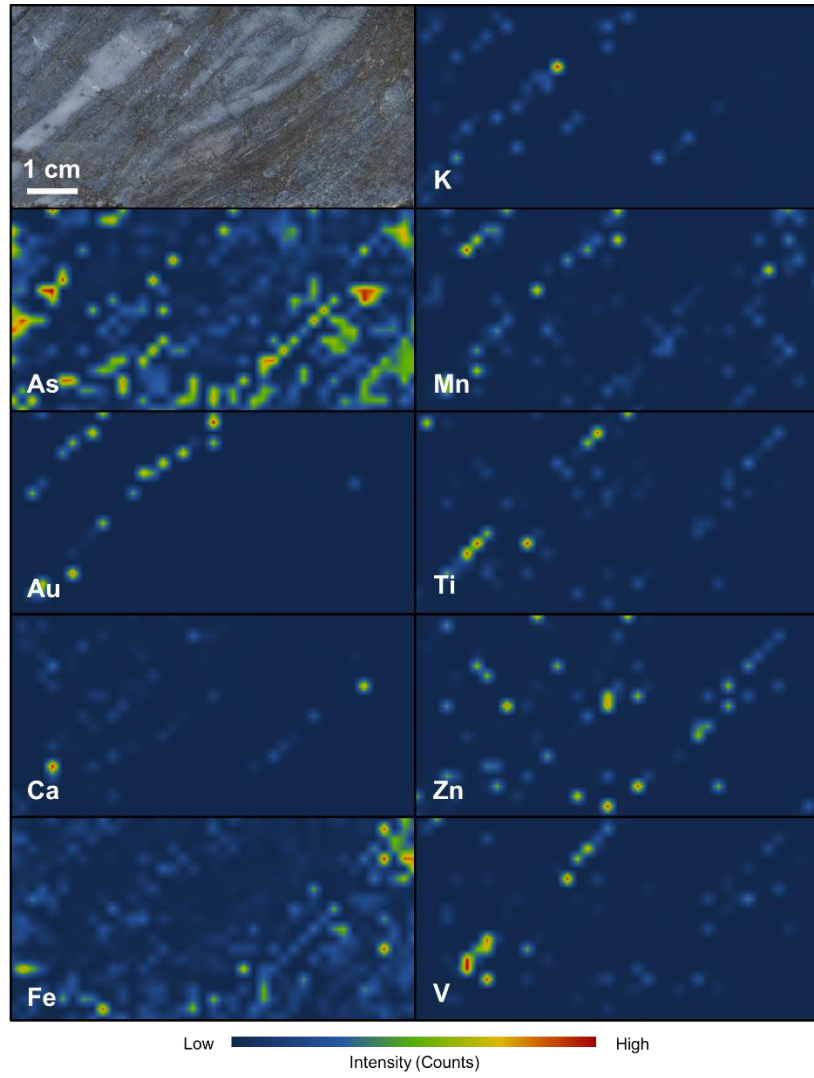
V892341, Peakaboo



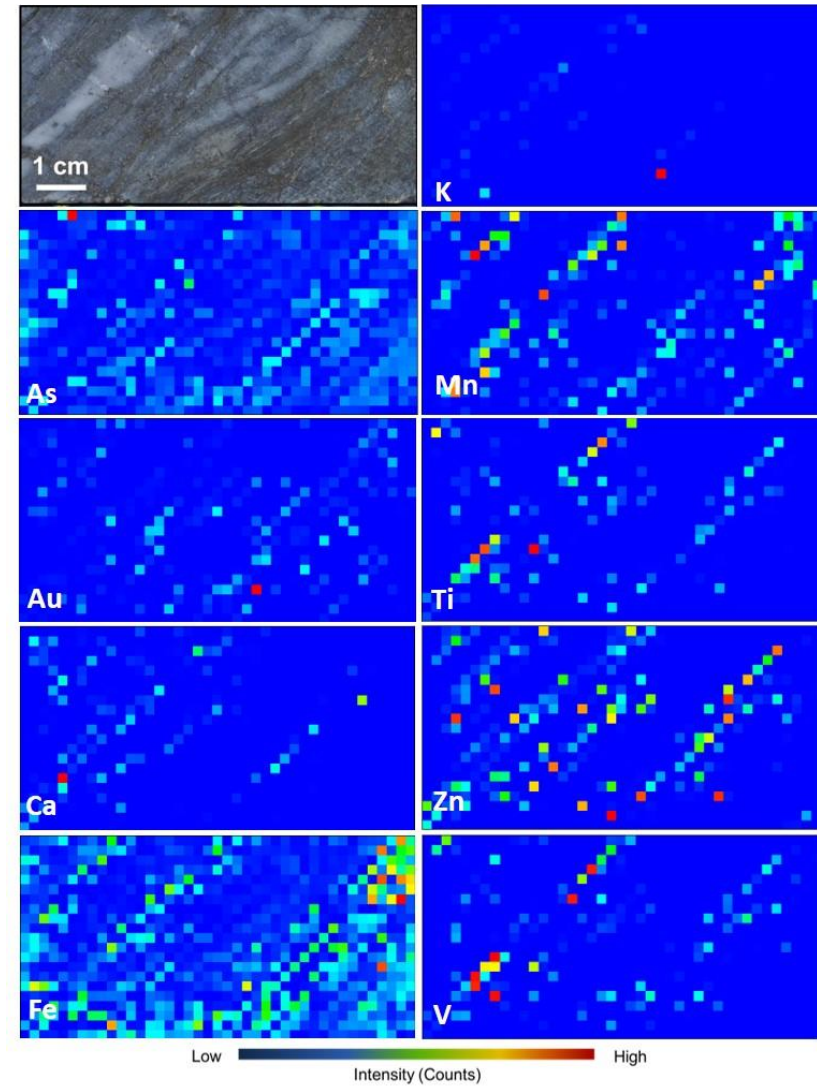
V892341, pyMCA



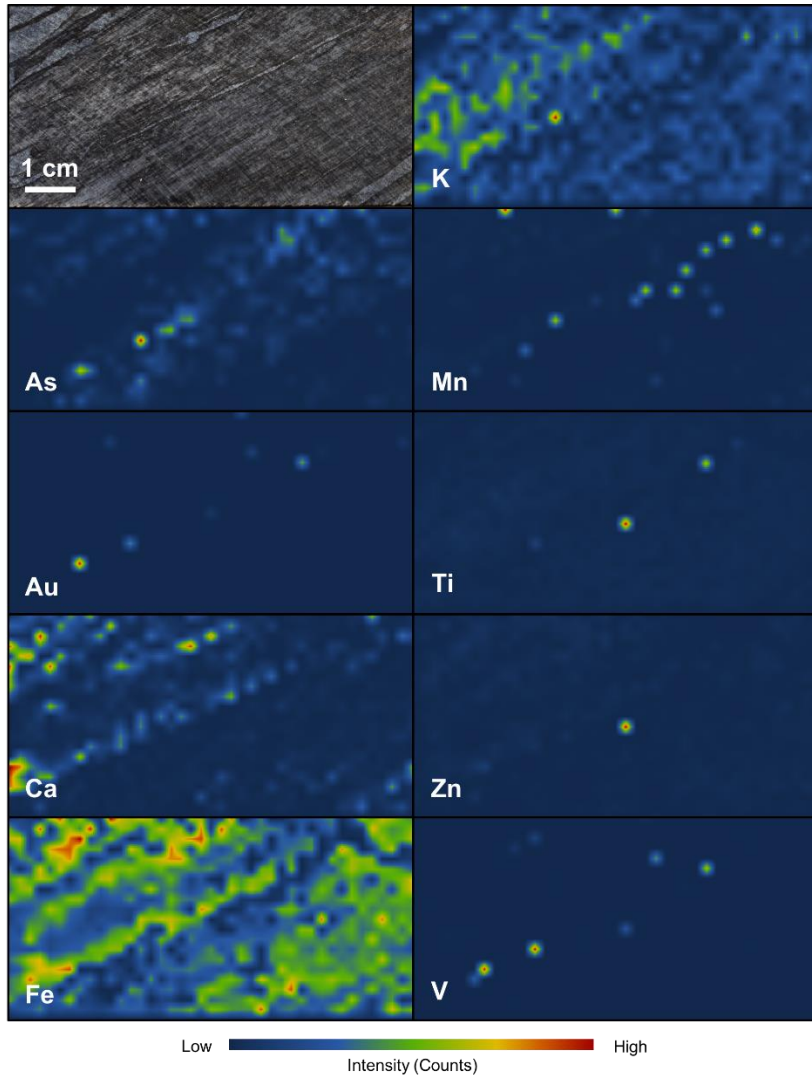
V892345, Peakaboo



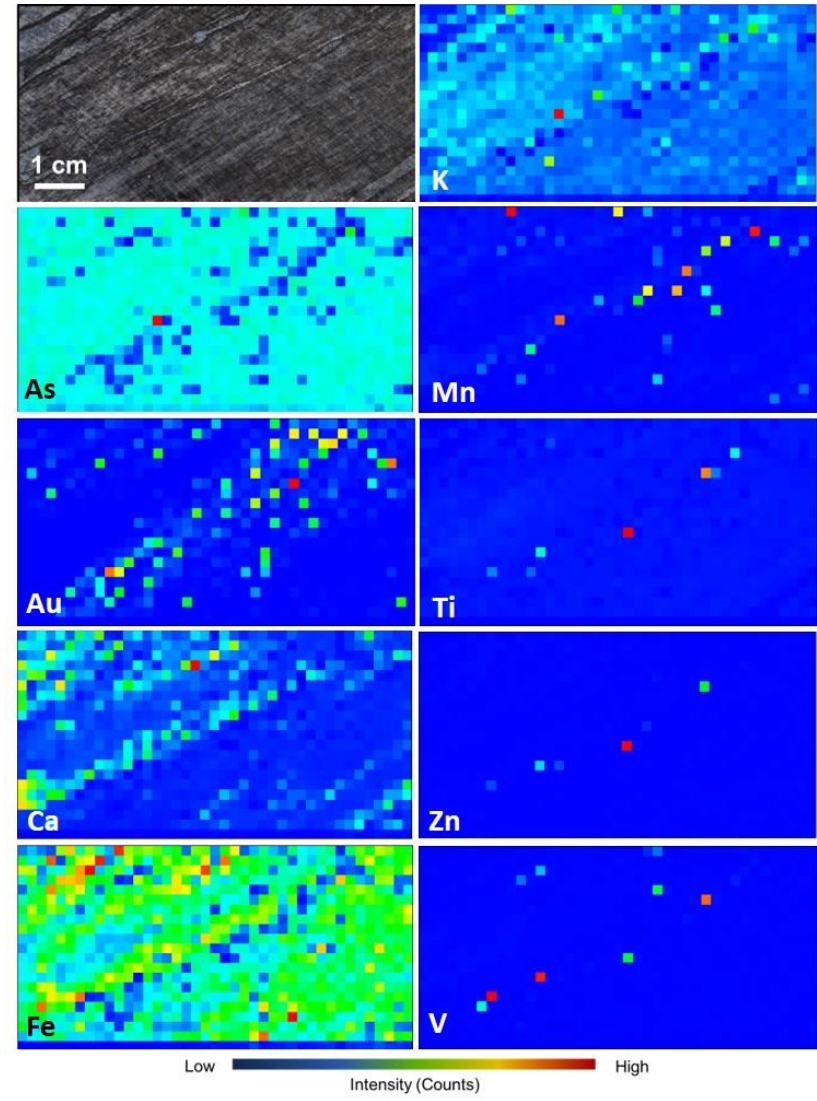
V892345, pyMCA



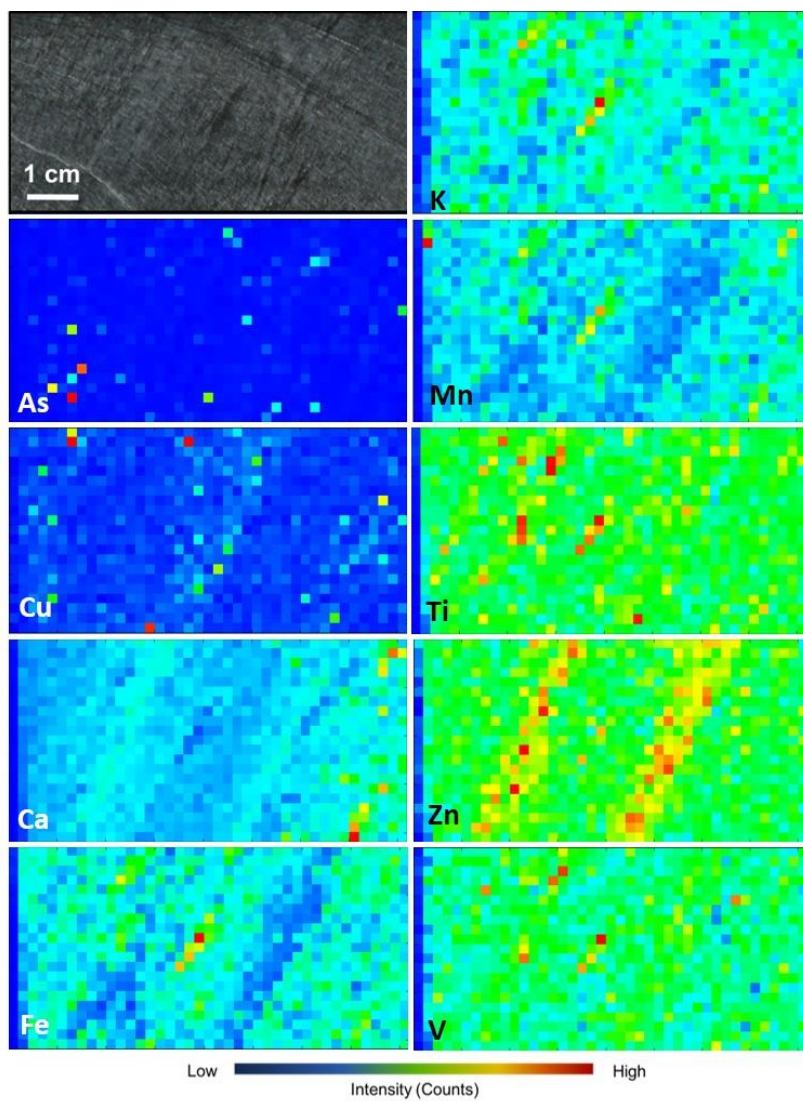
V892625, Peakaboo



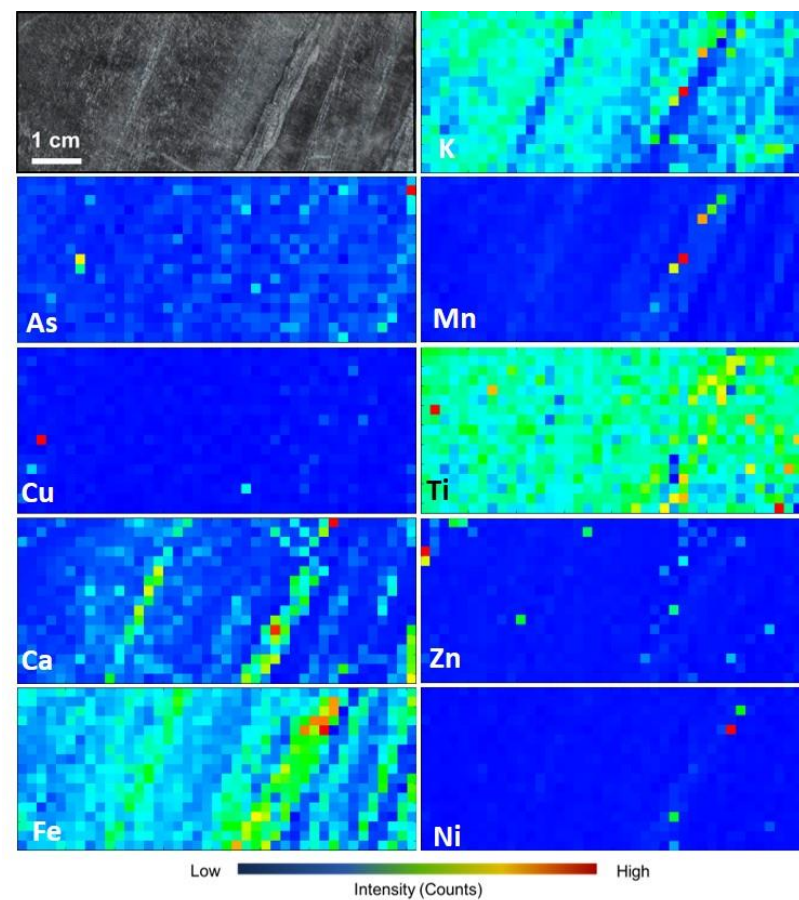
V892625, pyMCA



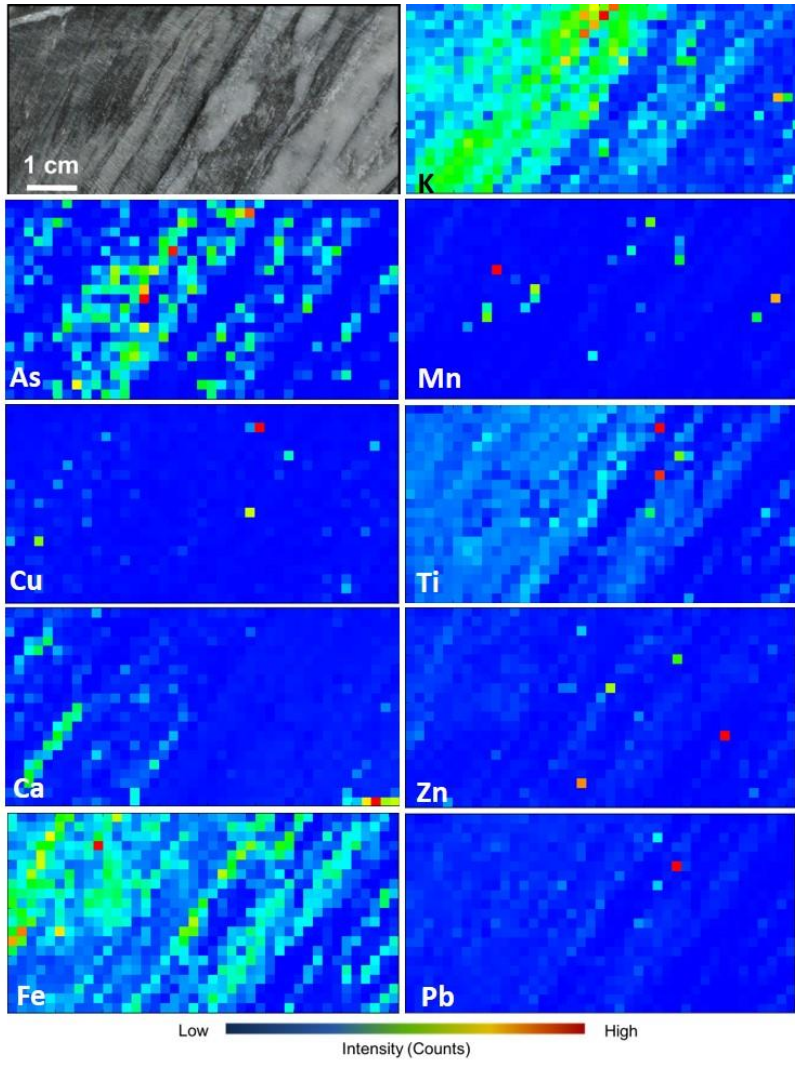
V156517



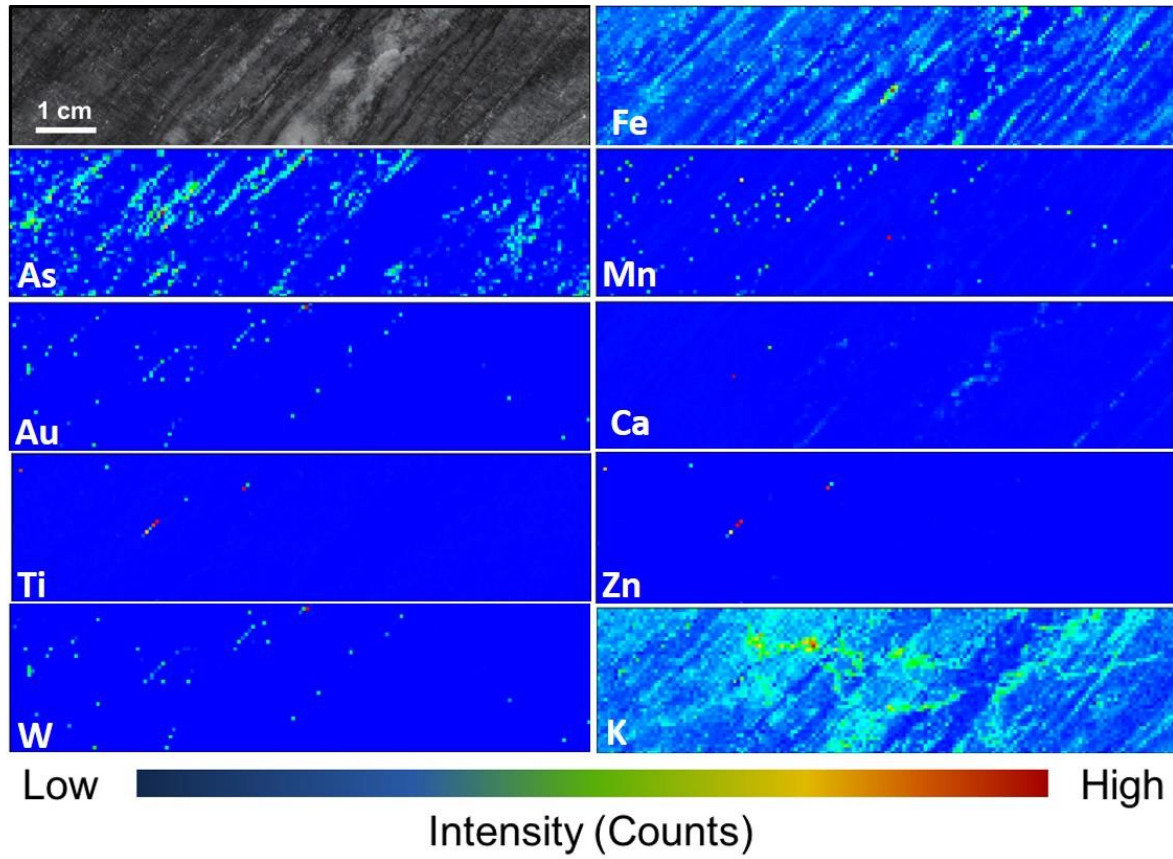
V156518



V156519

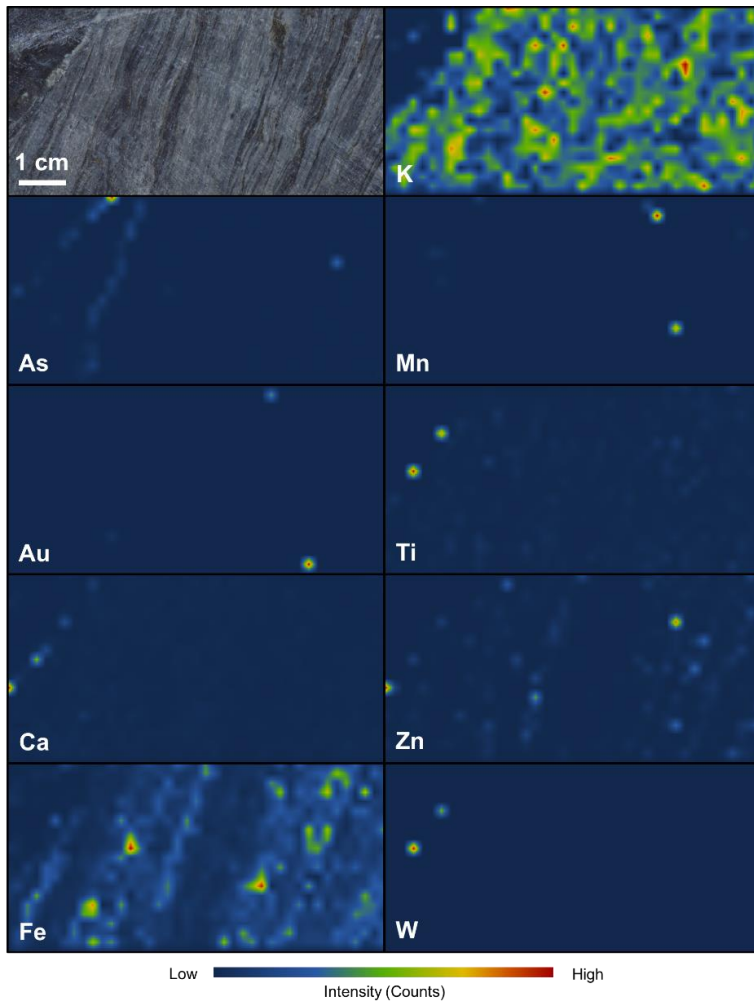


V156522

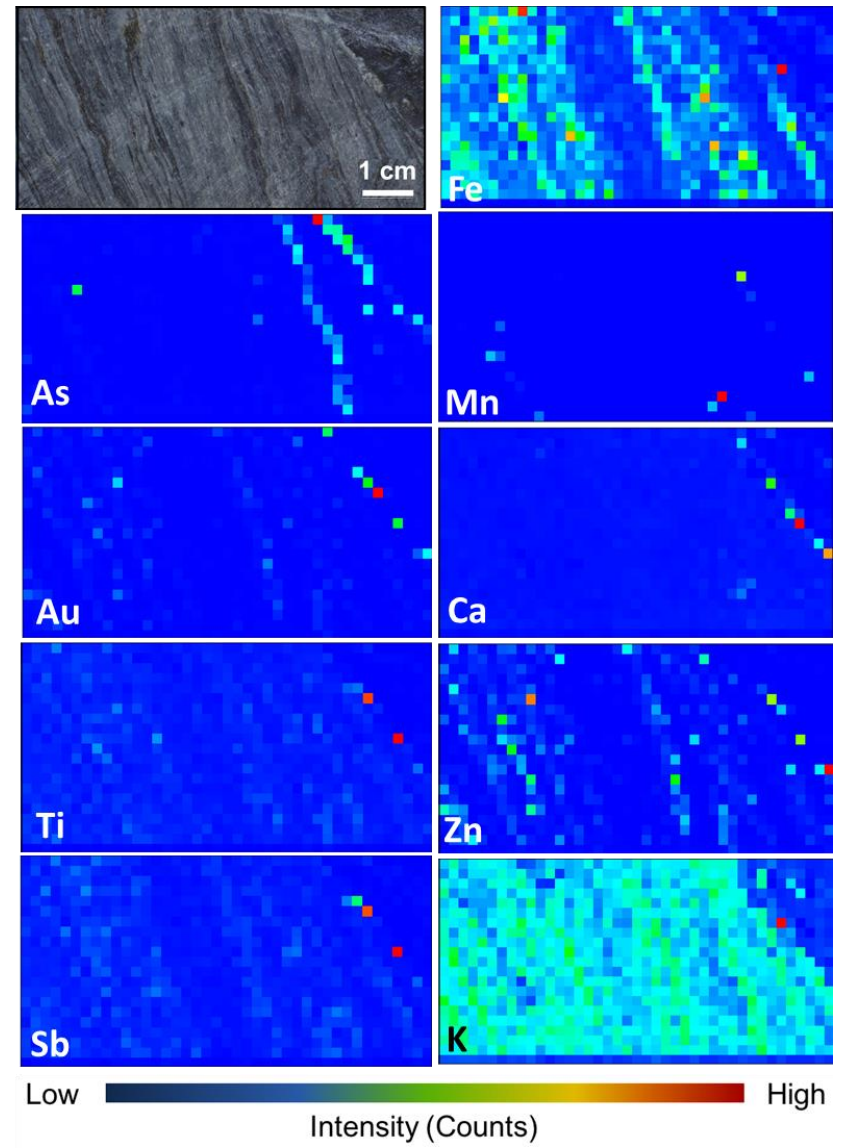


Dave's Pond

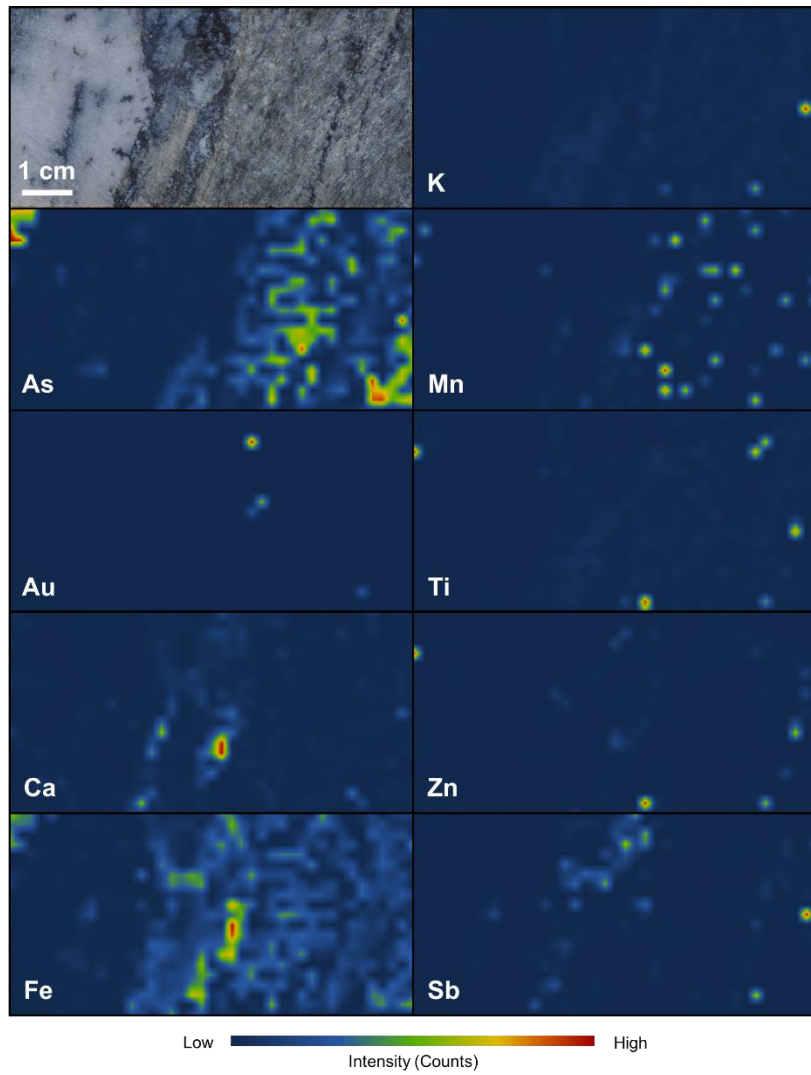
V160414, Peakaboo, flipped



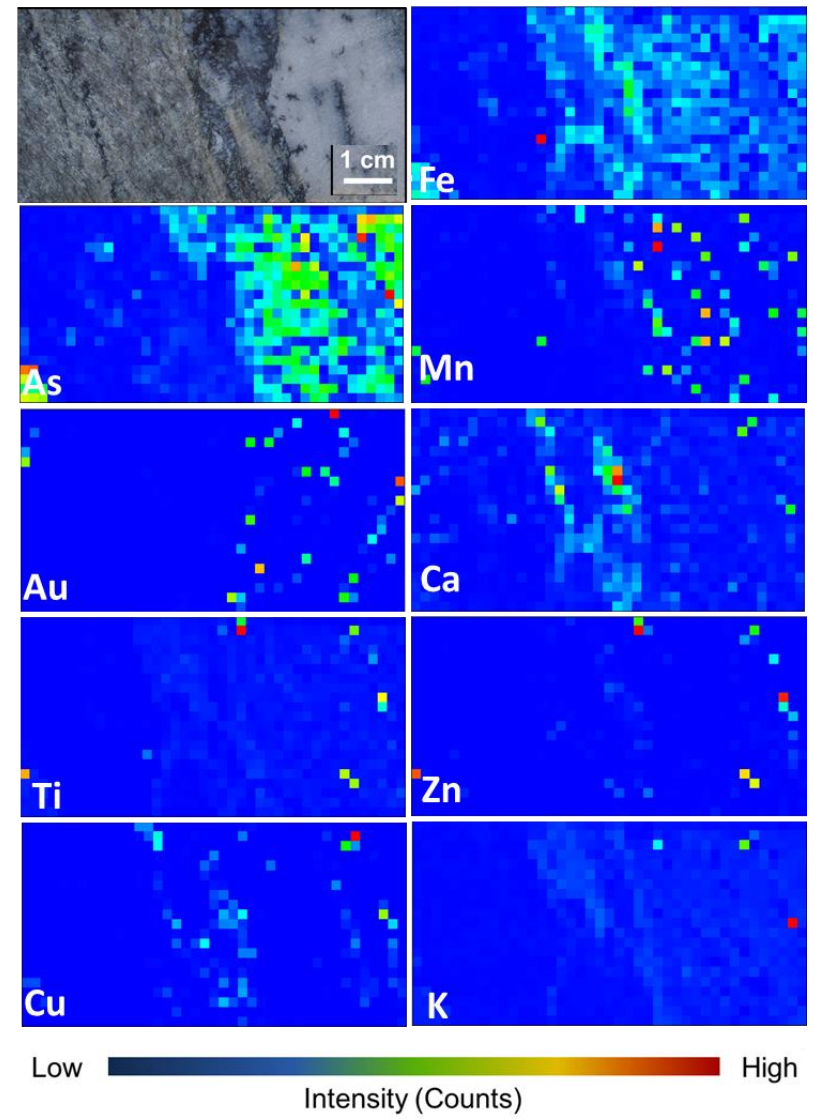
V160414, pyMCA



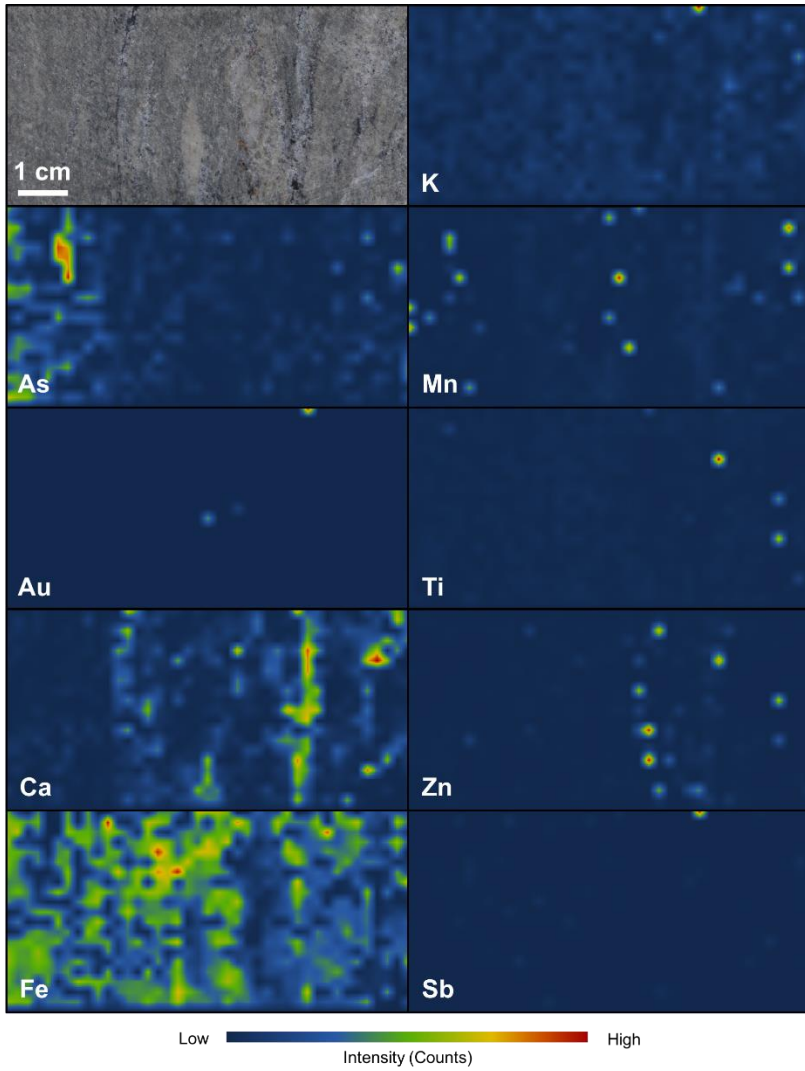
V413119, Peakaboo, flipped



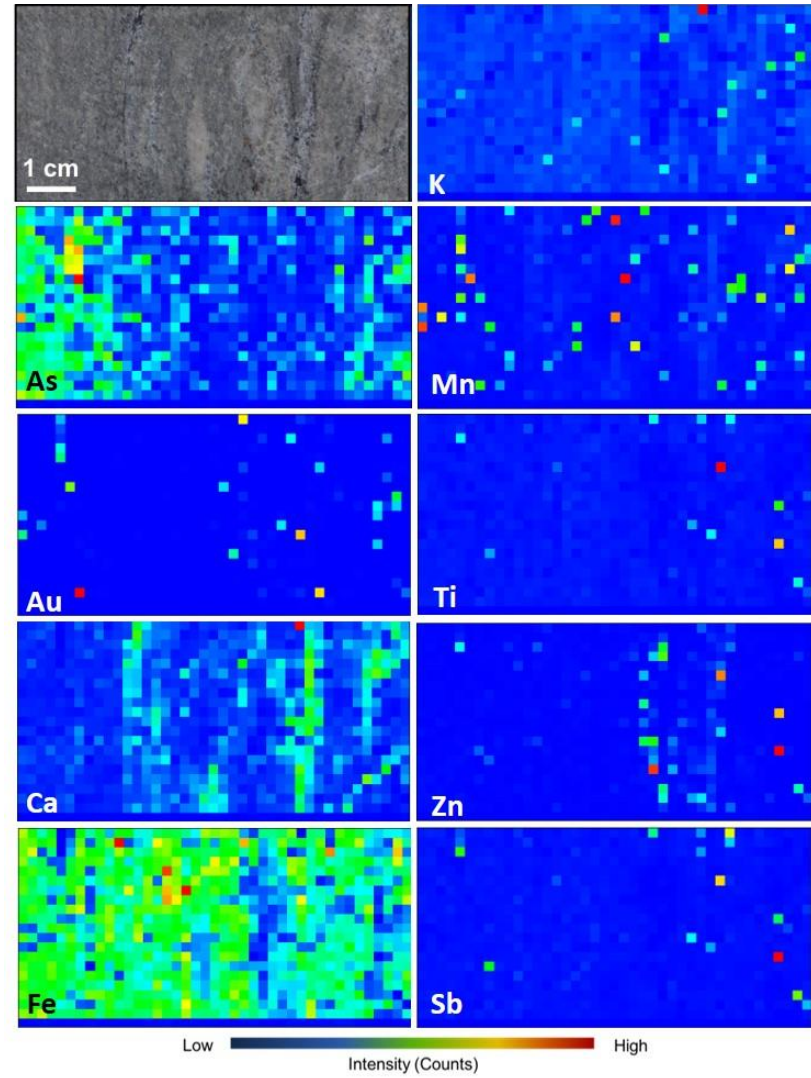
V413119, pyMCA



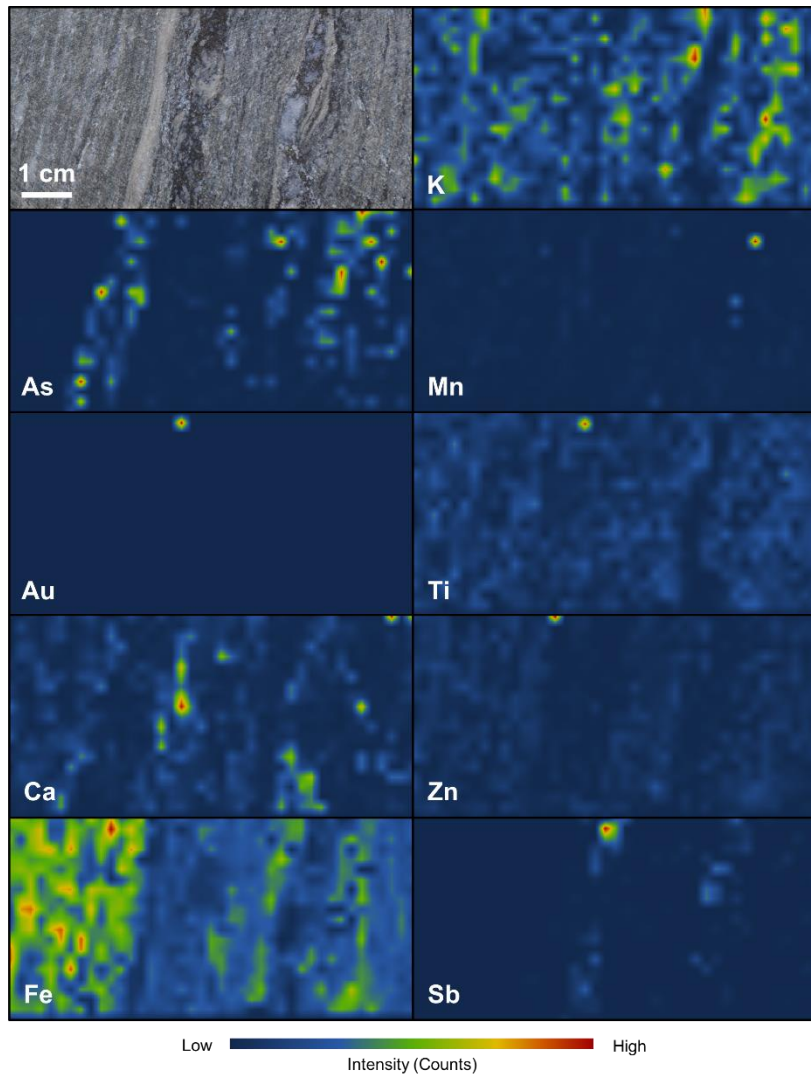
V413294, Peakaboo



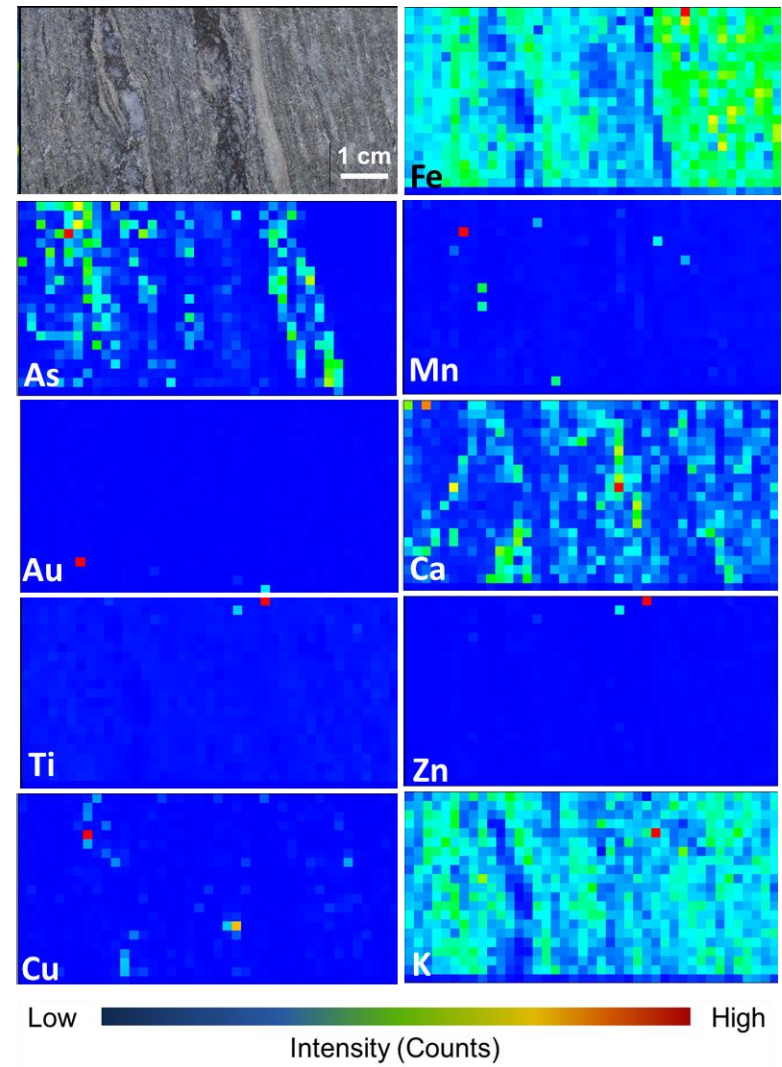
V413294, pyMCA



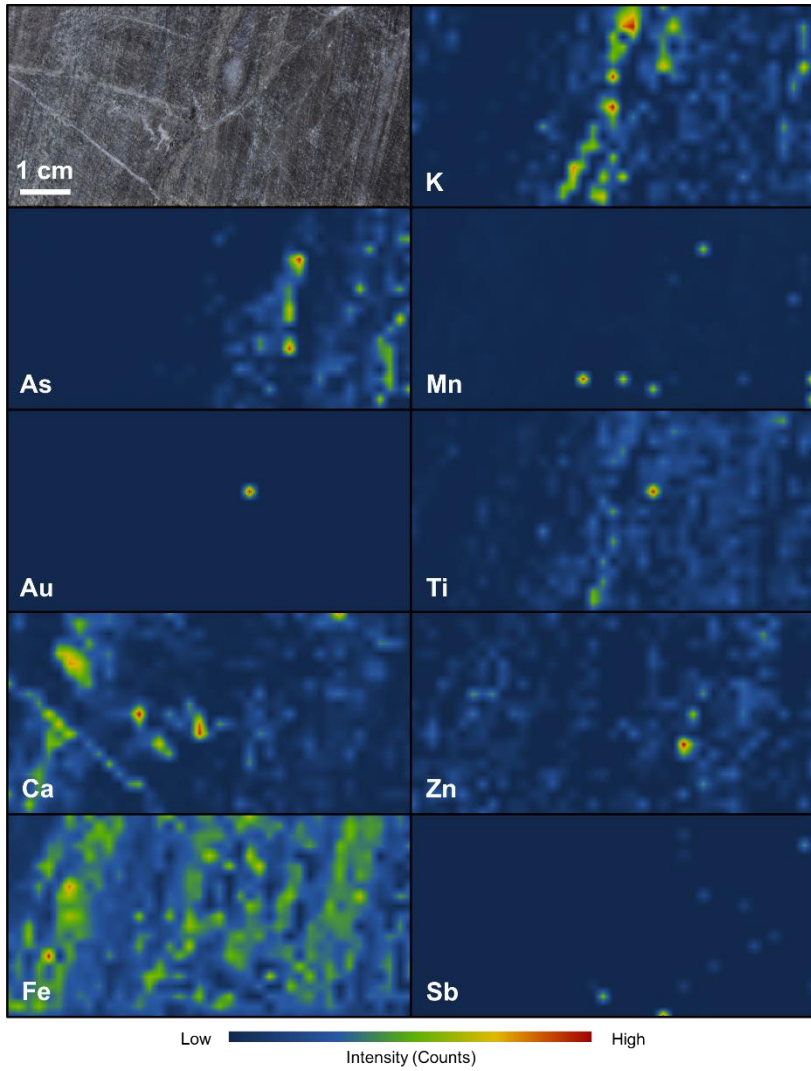
V413296, Peakaboo, flipped



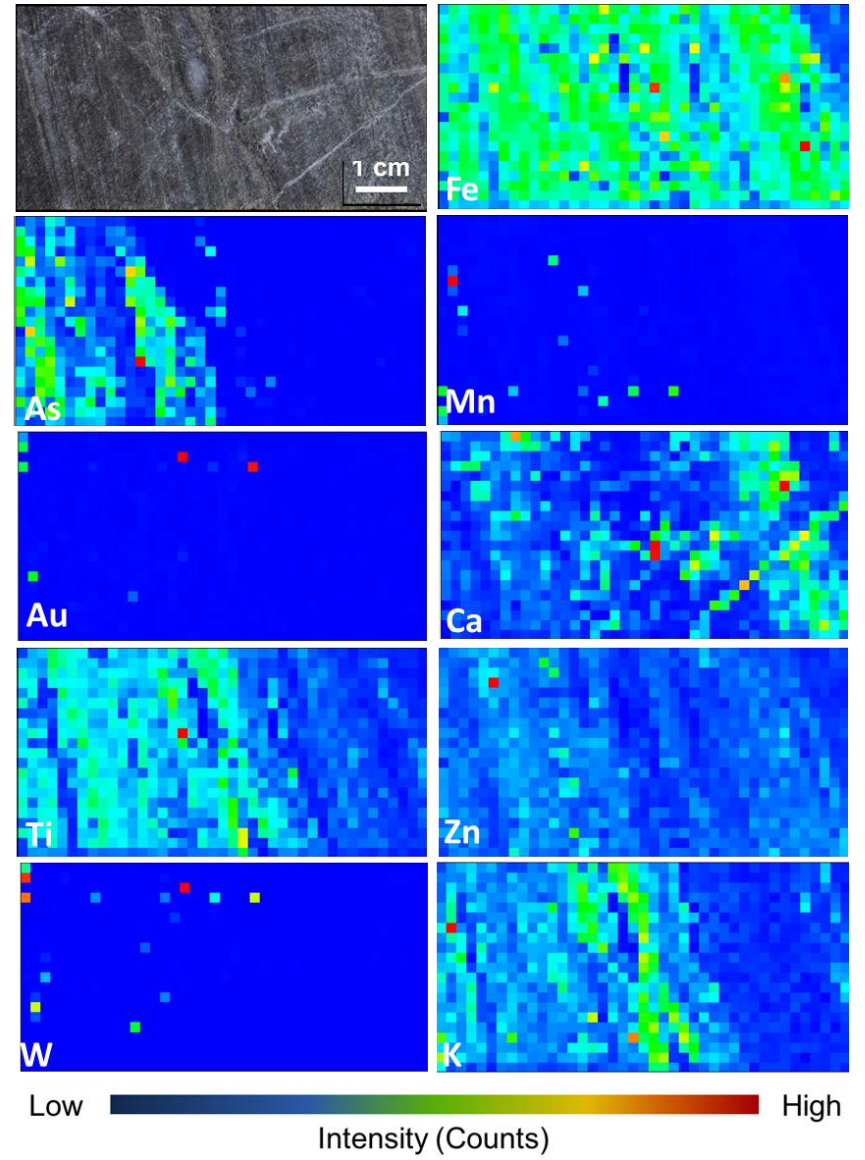
V413296, pyMCA



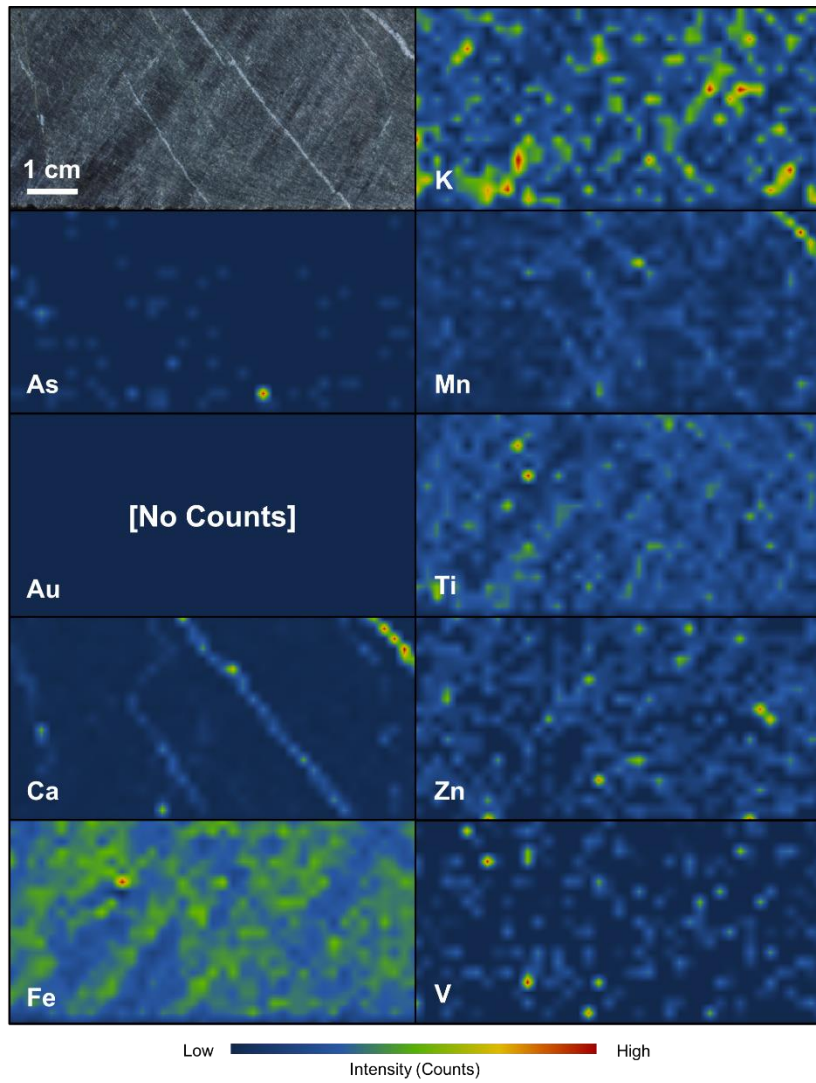
V738327, Peakaboo, flipped



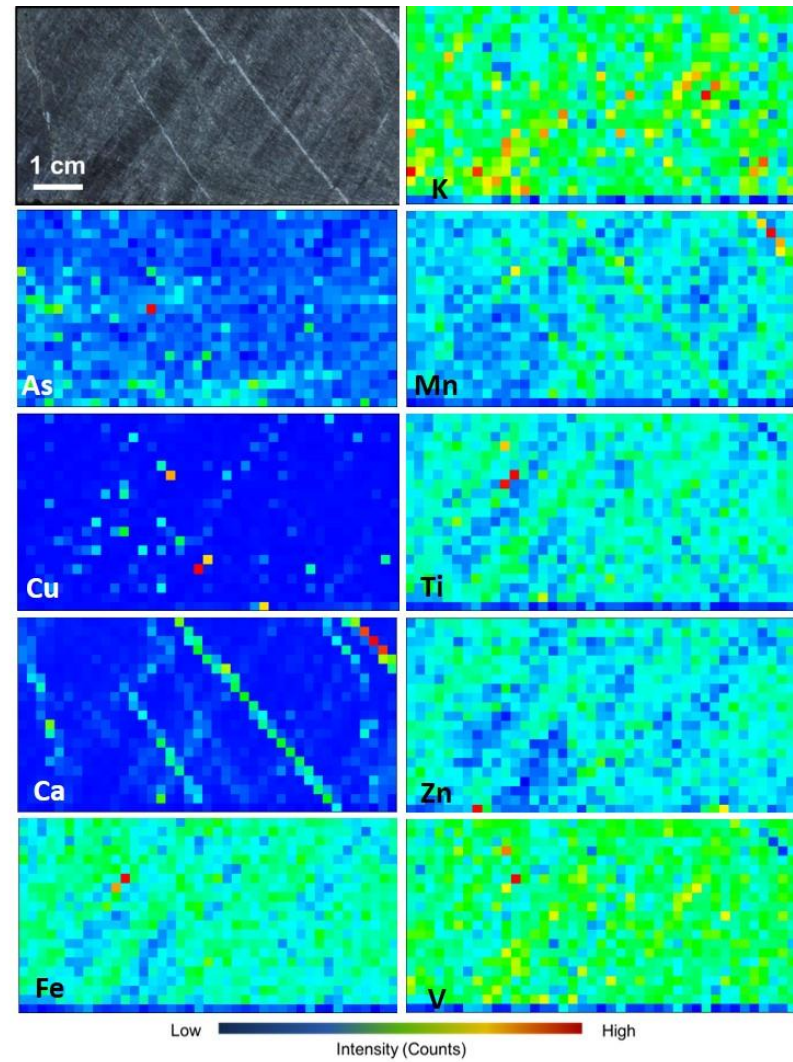
V738327, pyMCA



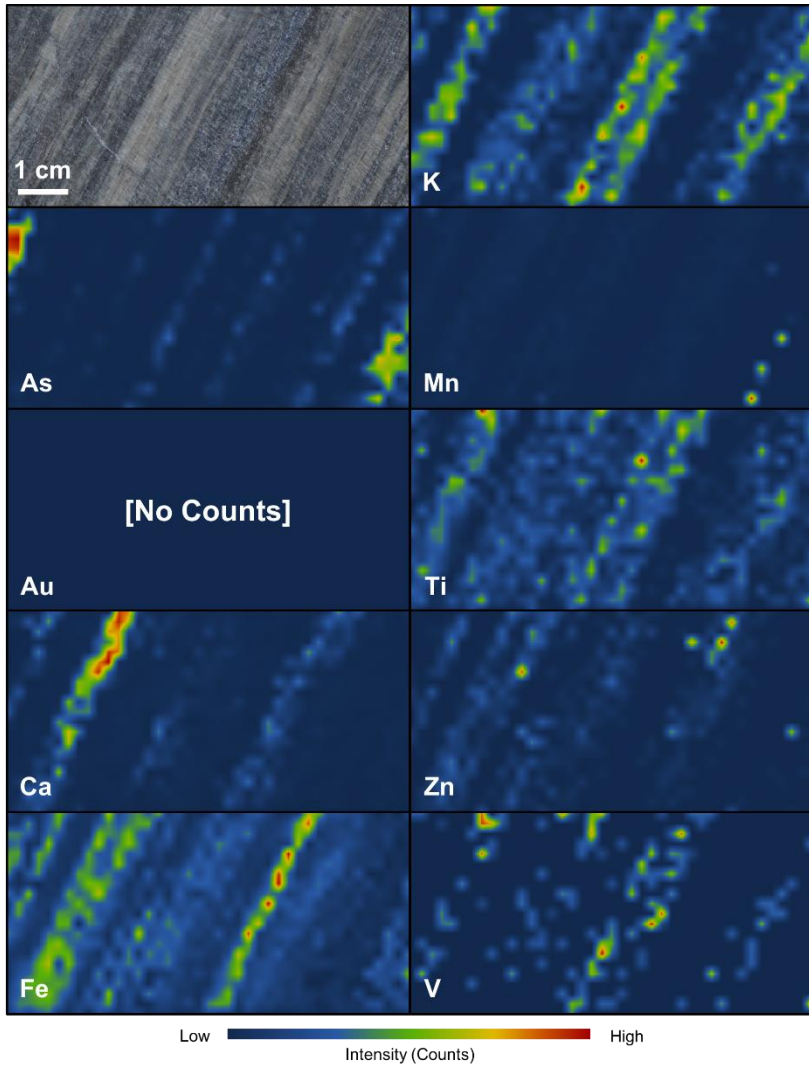
V892939, Peakaboo



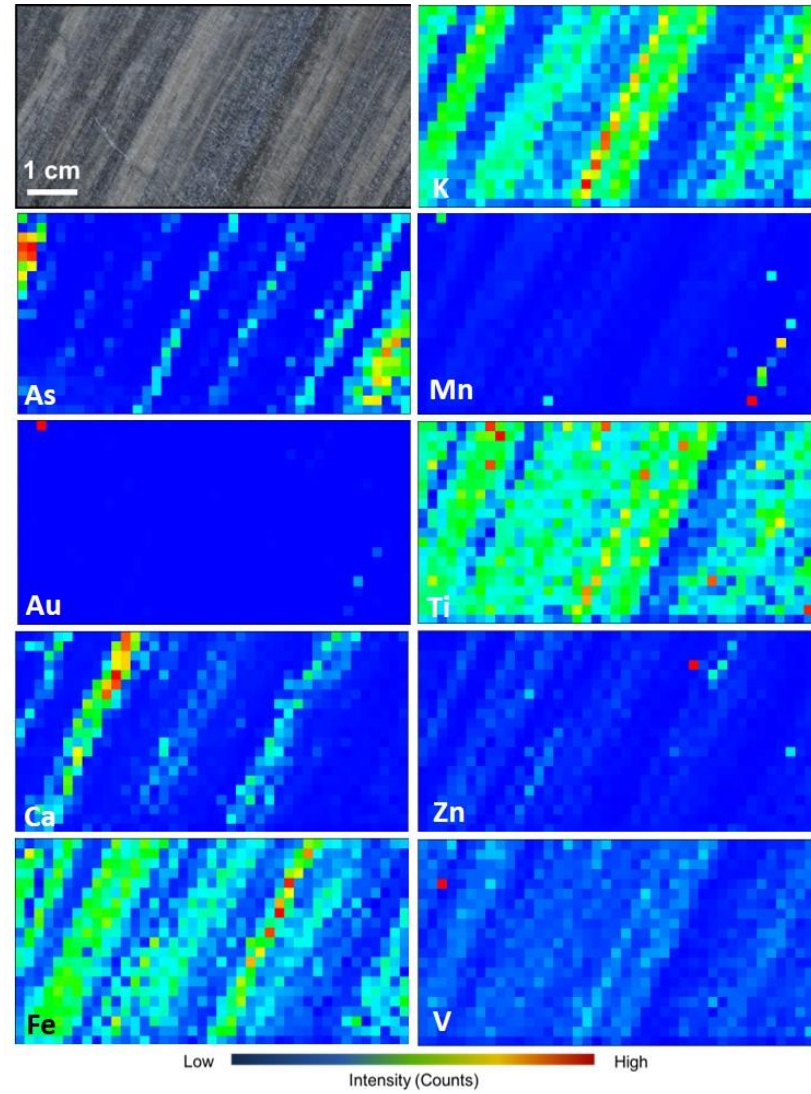
V892939, pyMCA



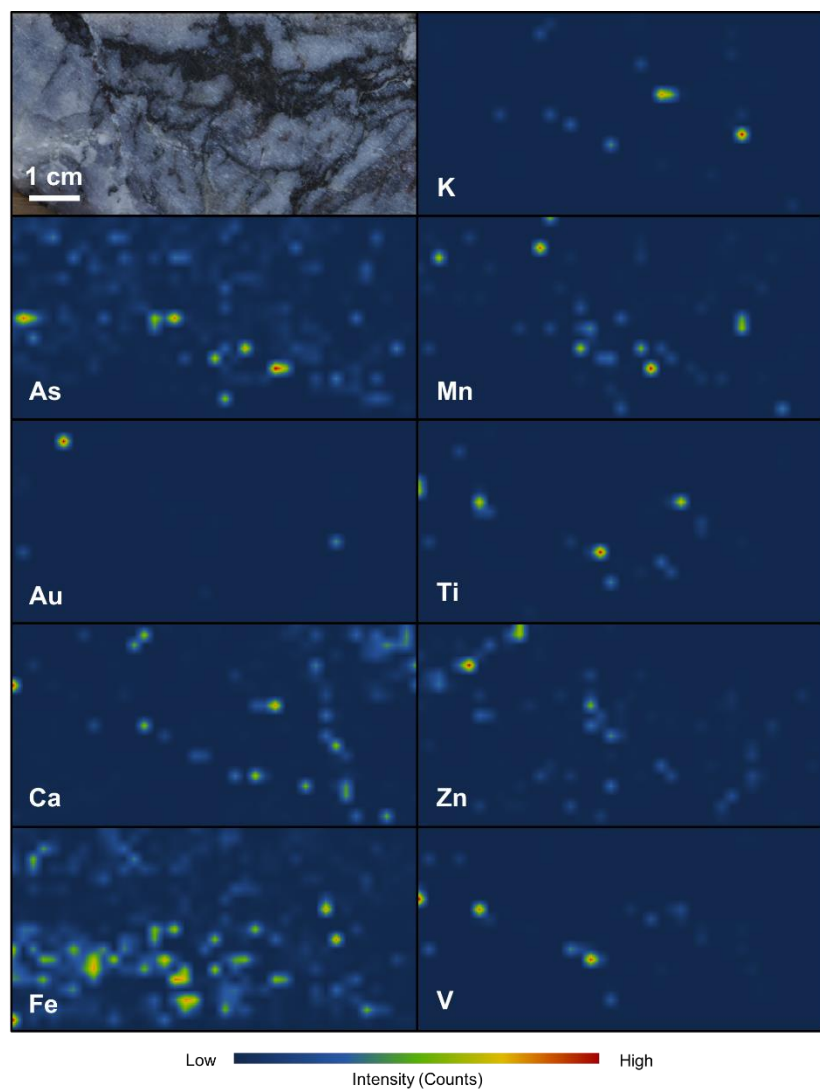
V892959, Peakaboo



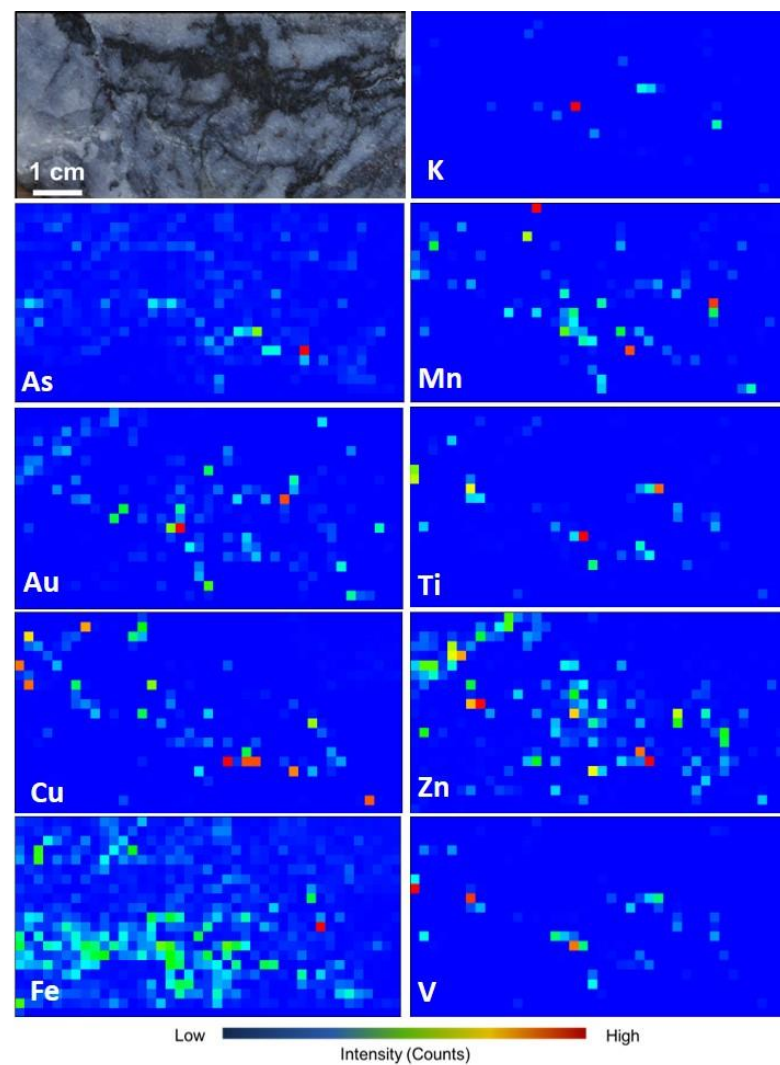
V892959, pyMCA



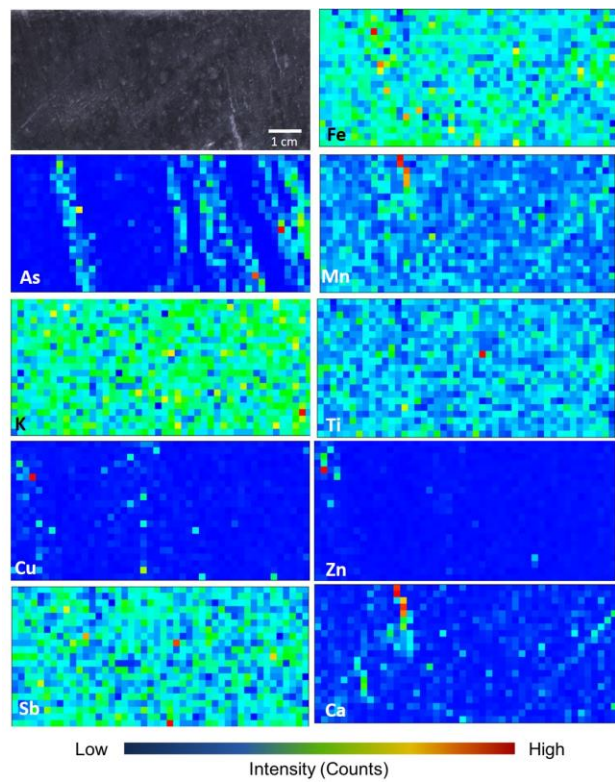
V892979, Peakaboo



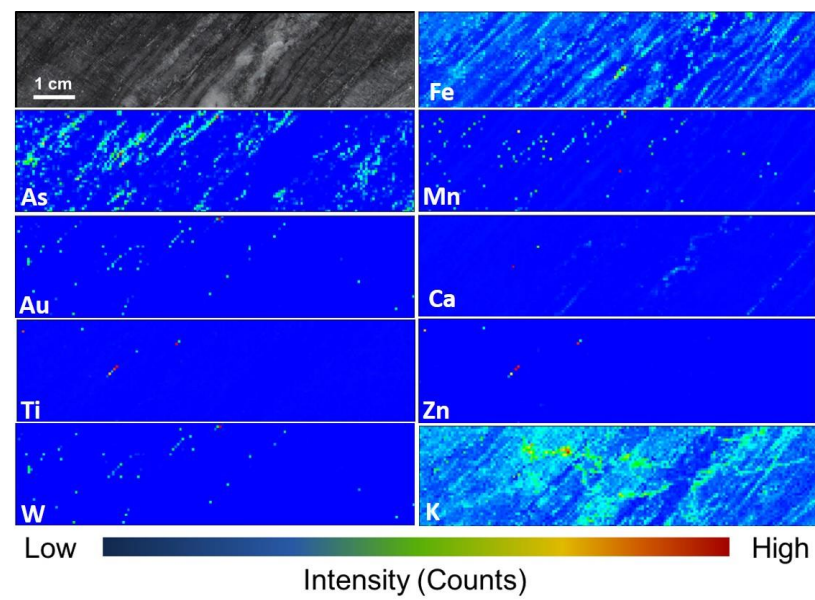
V892979, pyMCA



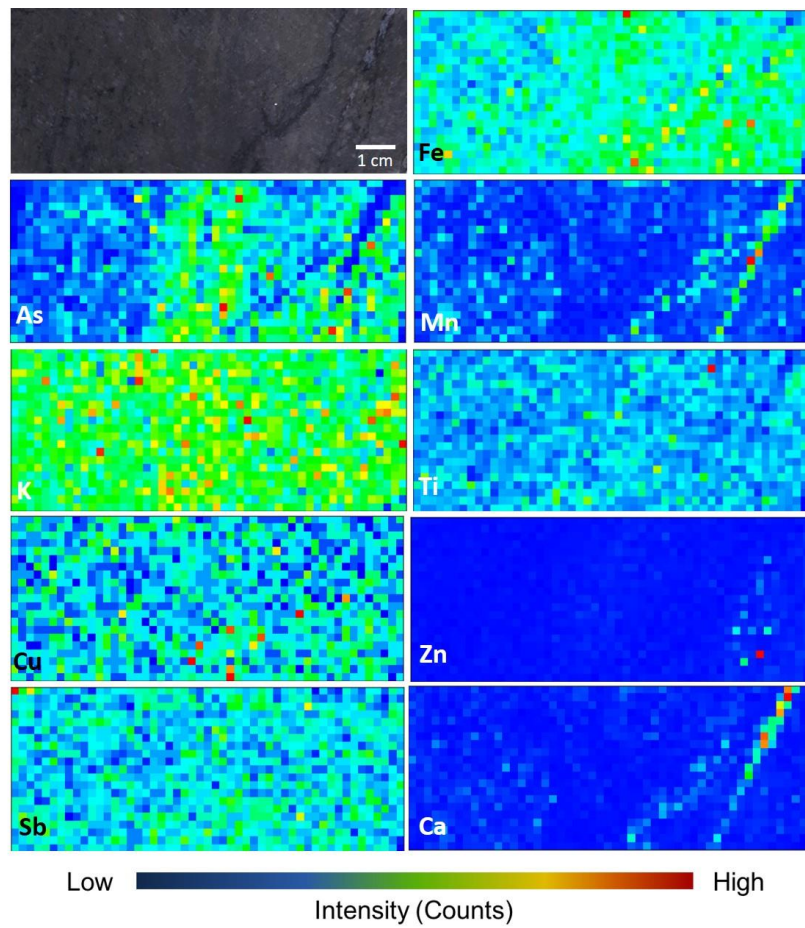
V413124



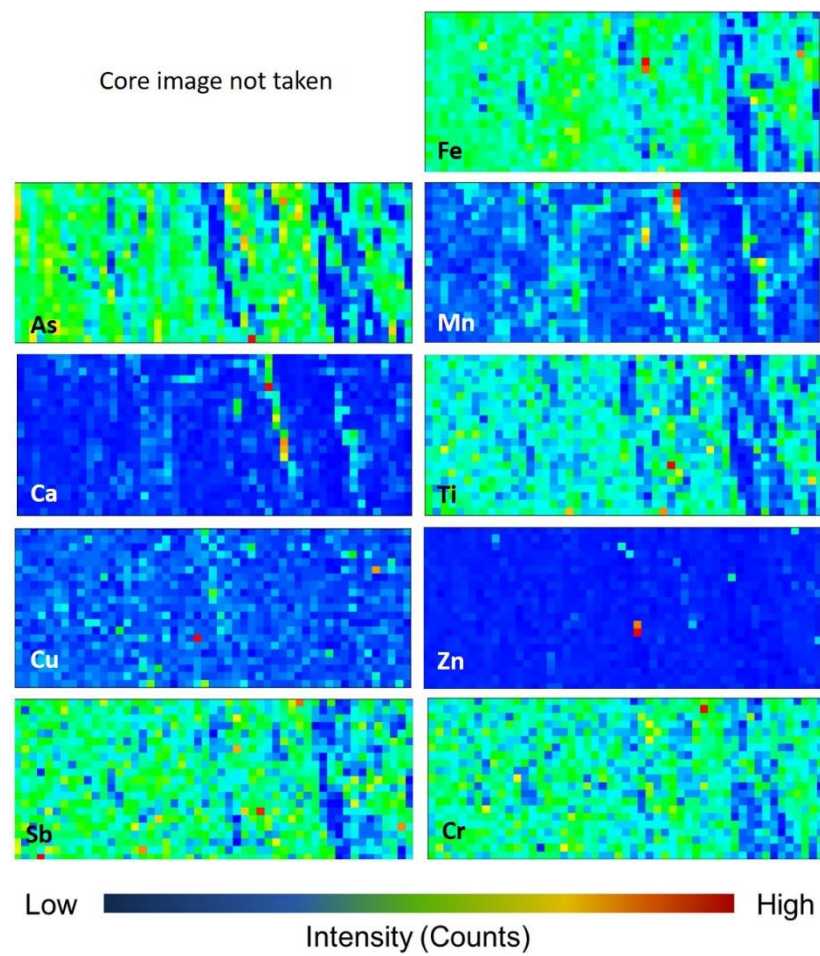
V156522



V413125

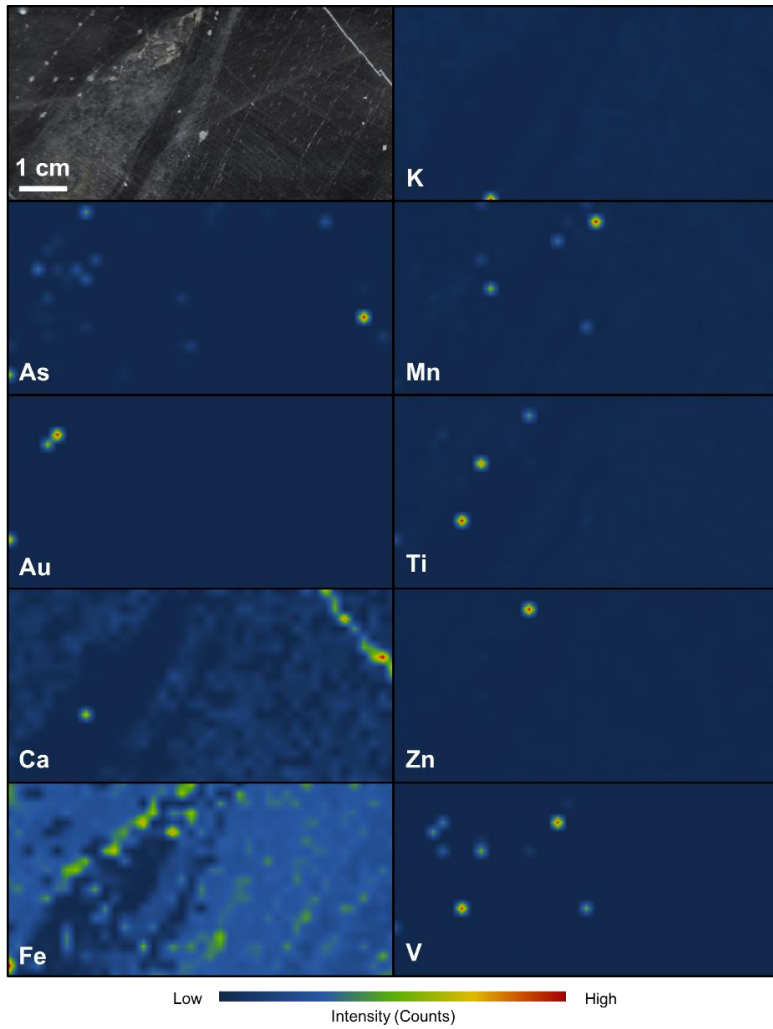


V413285

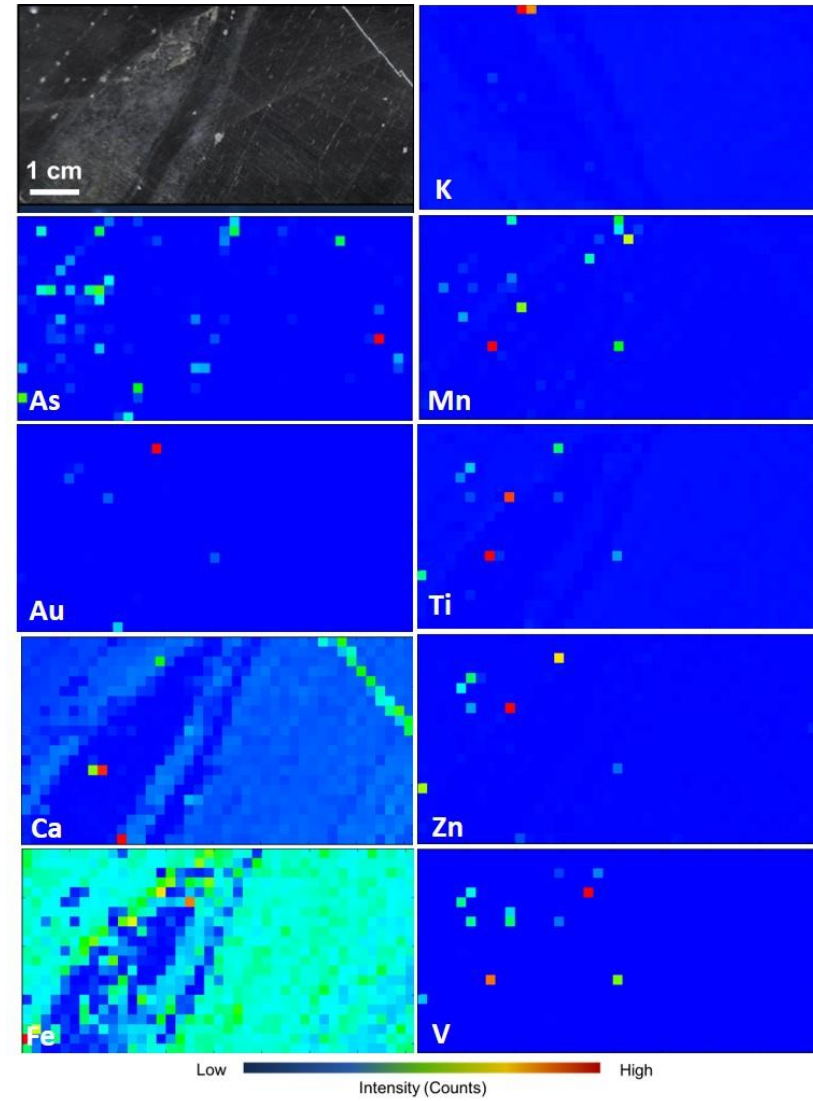


Mispickel

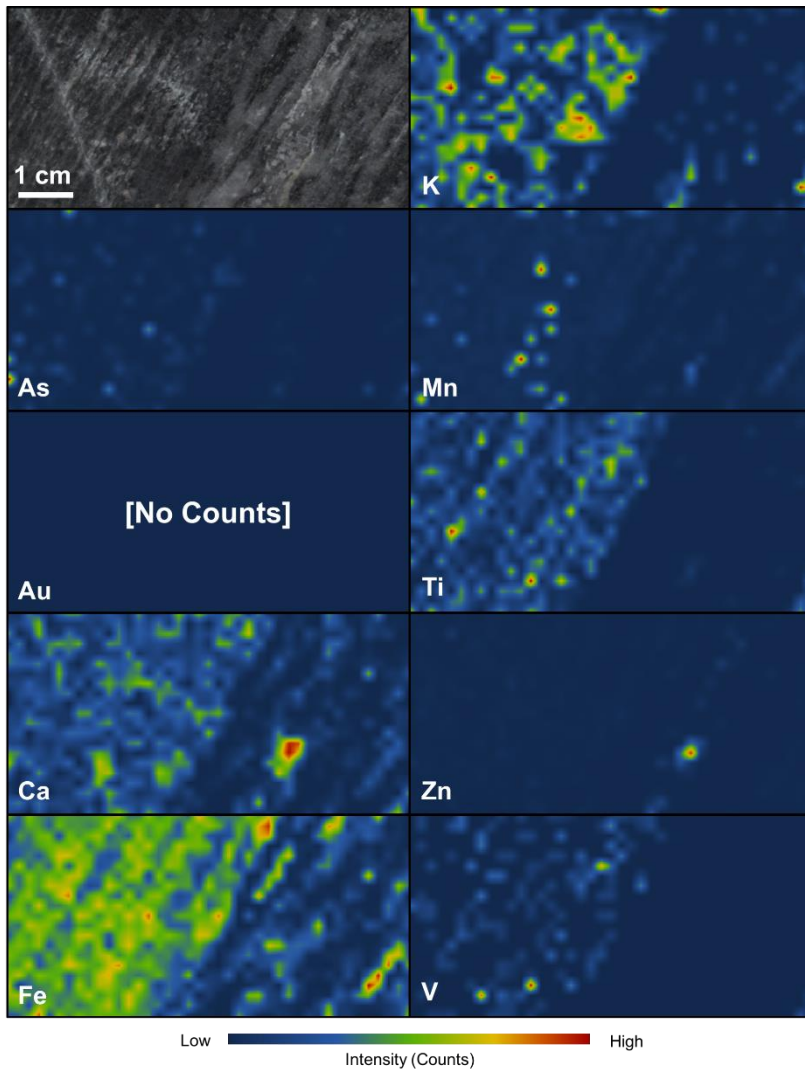
S892043, Peakaboo



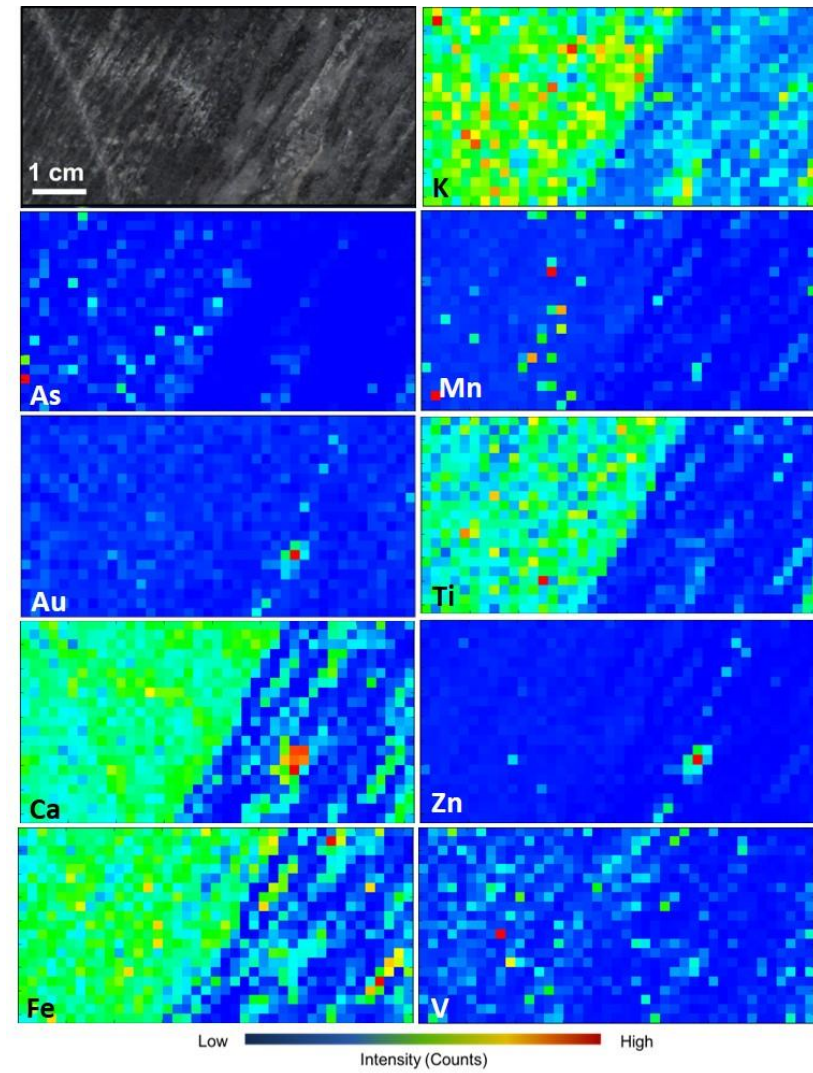
S892043, pyMCA



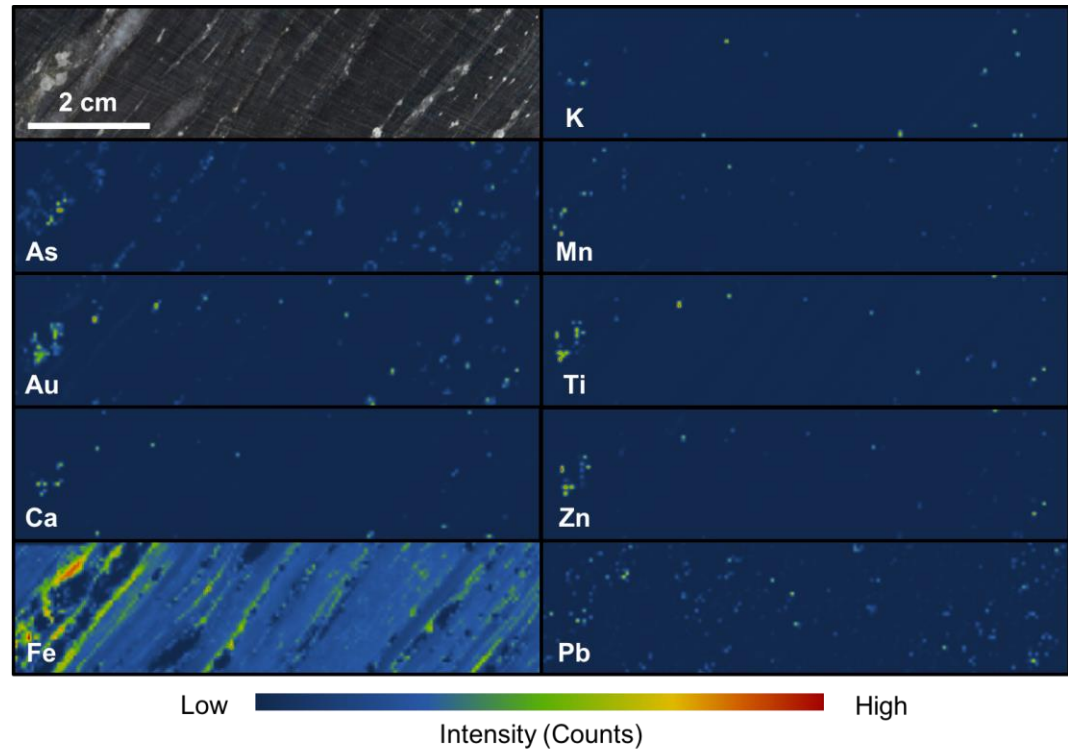
S892045, Peakaboo



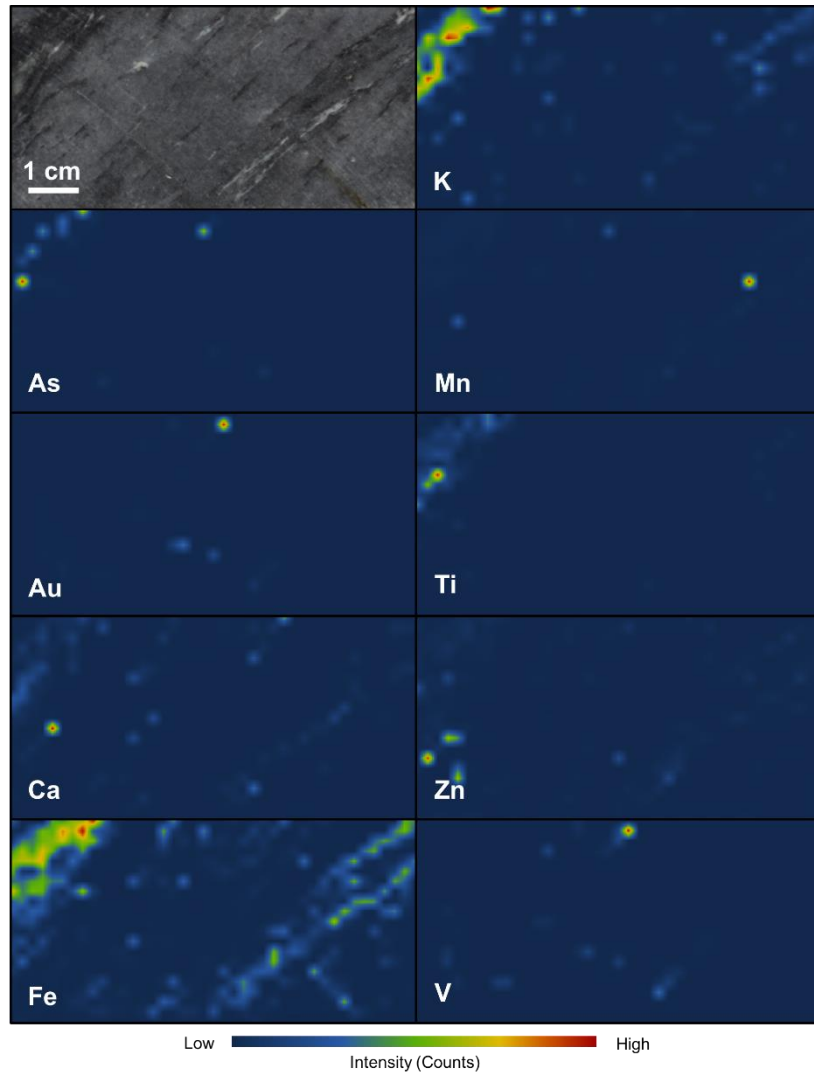
S892045, pyMCA



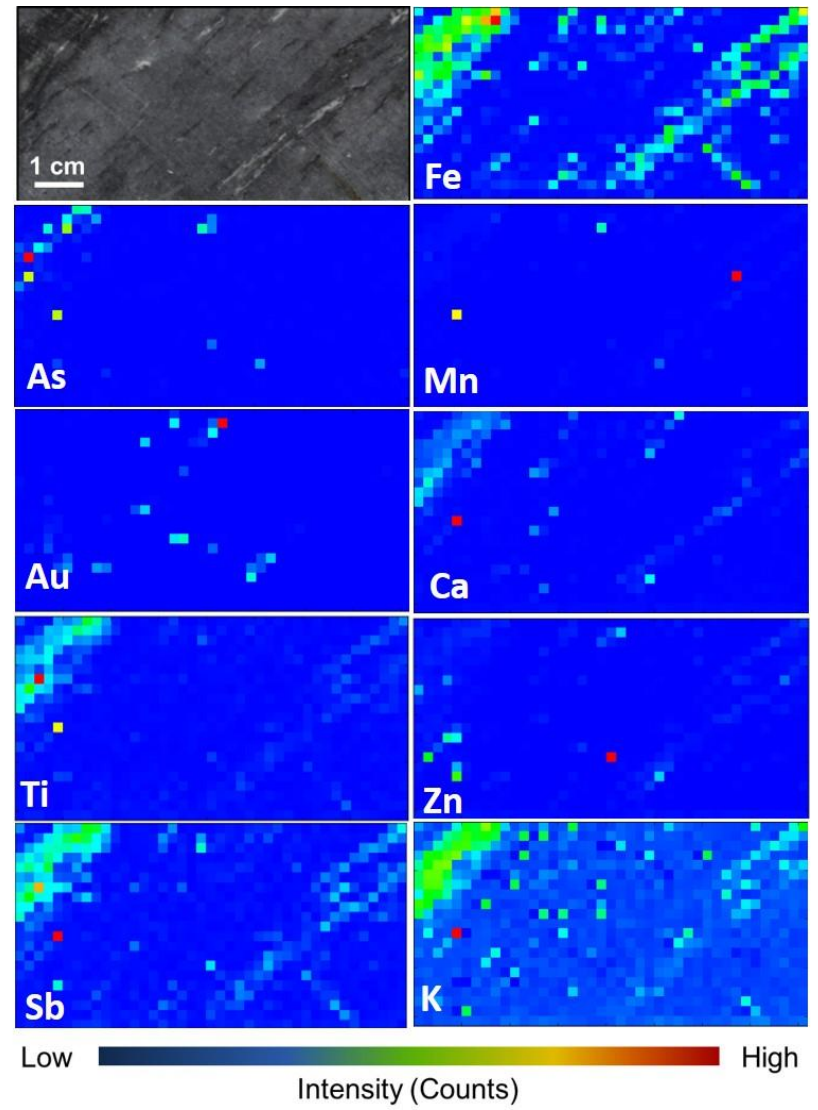
S892044



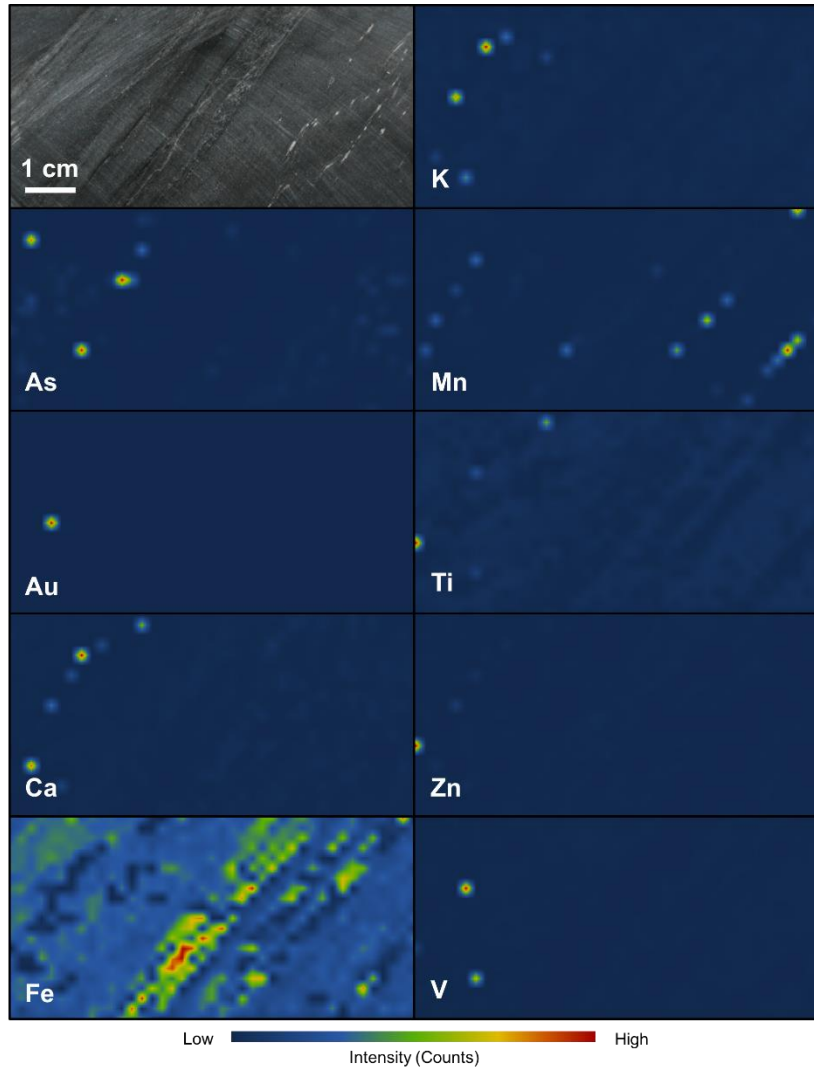
S892082, Peakaboo



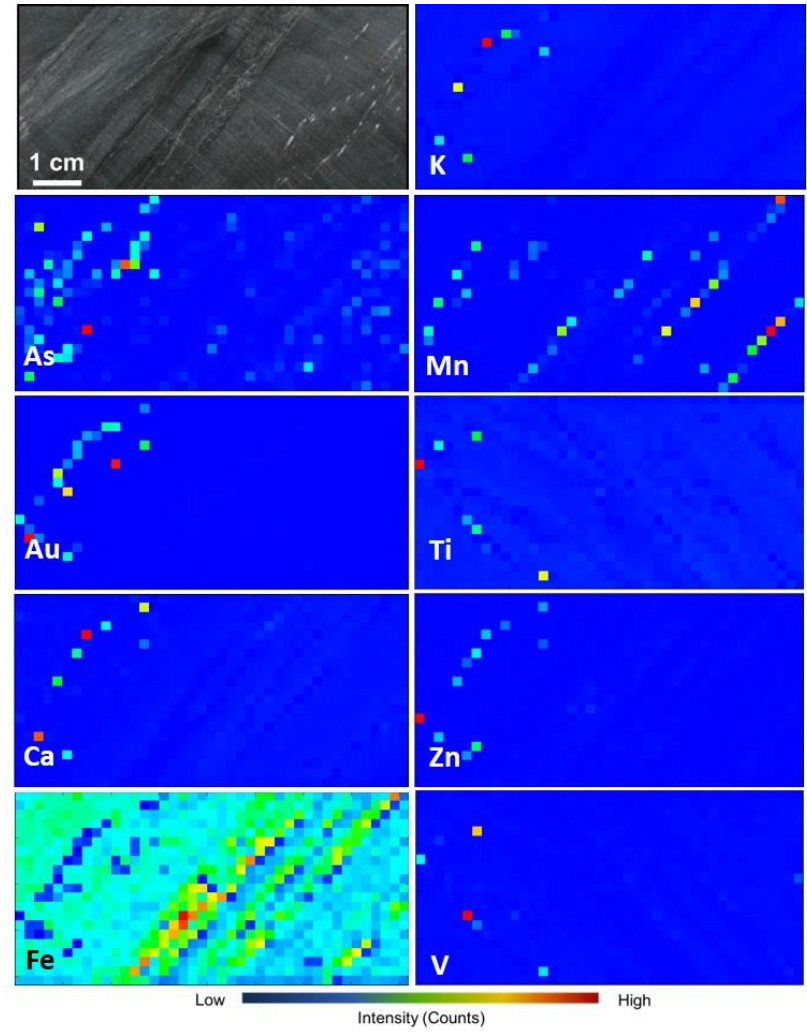
S892082, pyMCA



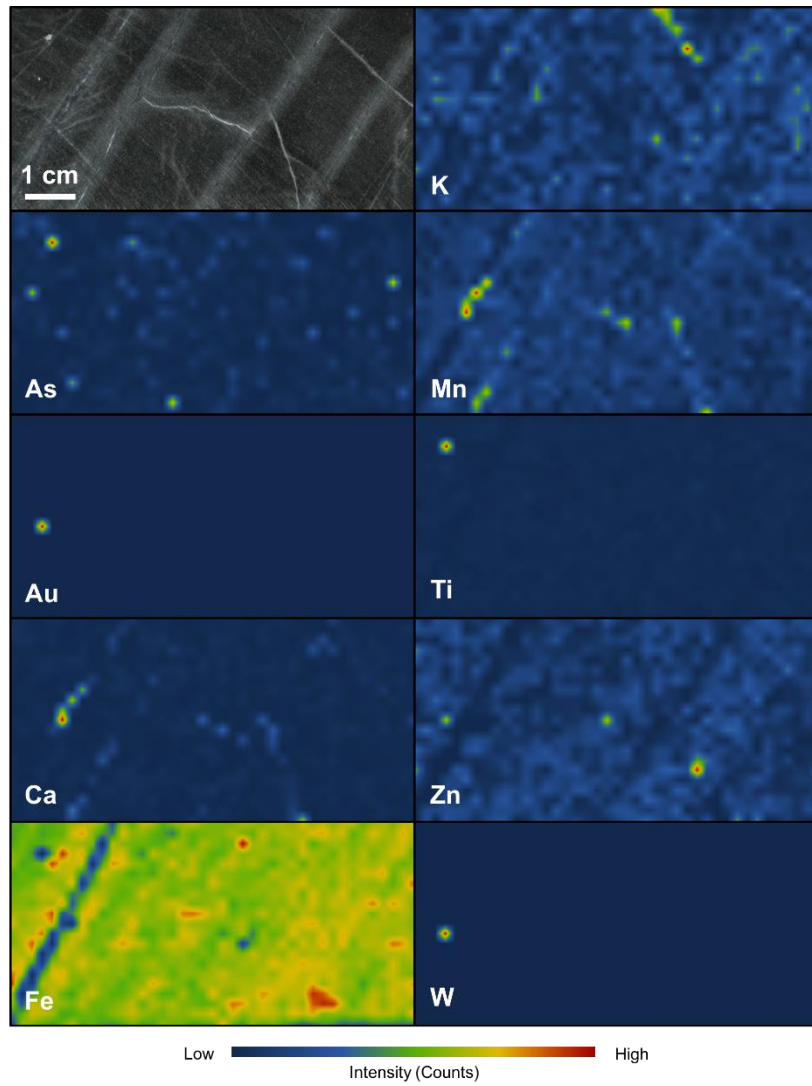
S892084, Peakaboo



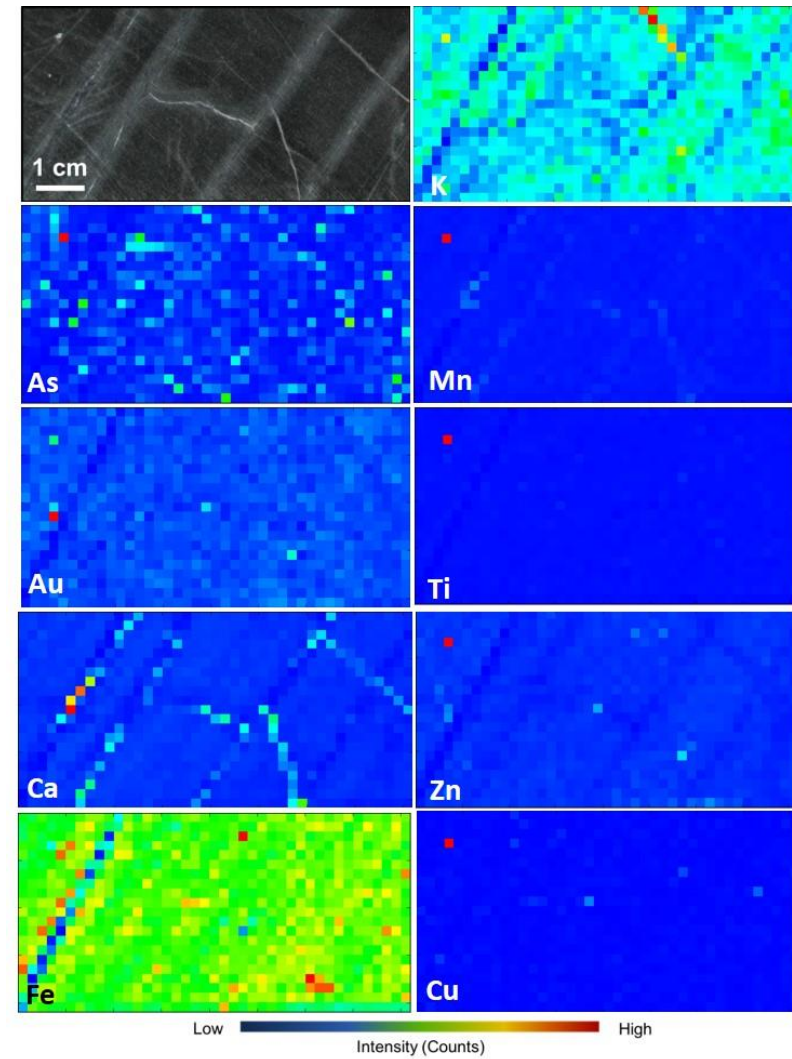
S892084, pyMCA



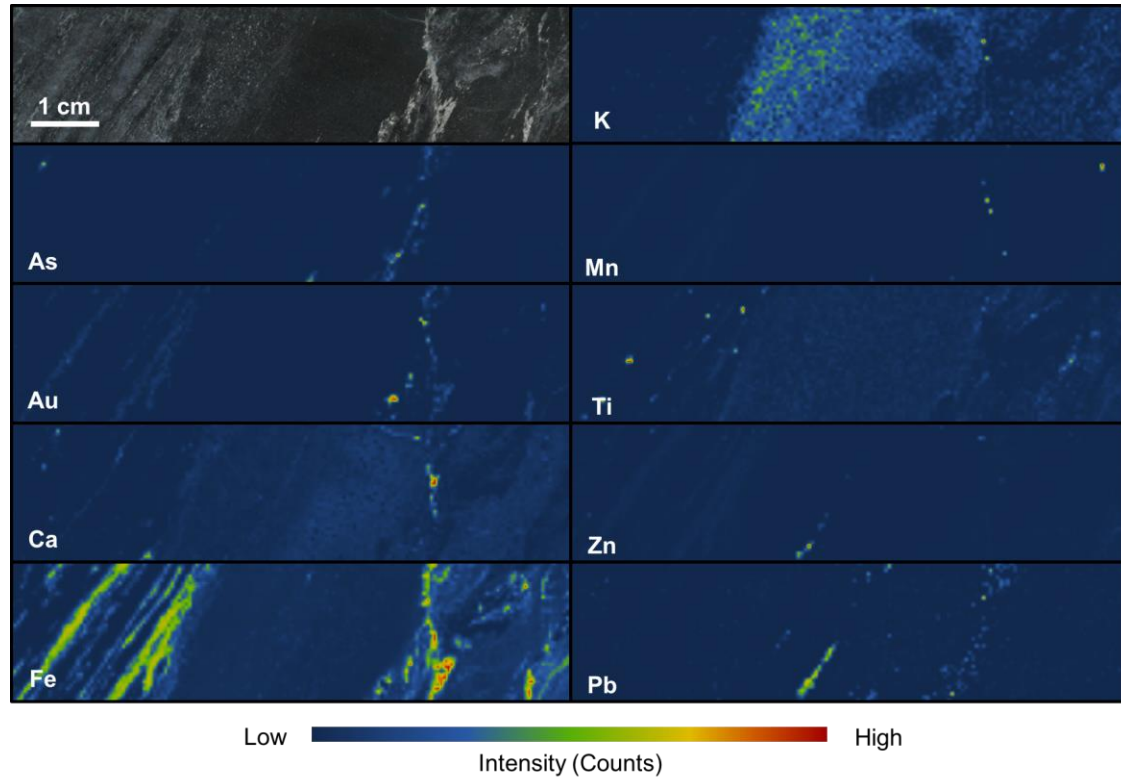
S892087, Peakaboo



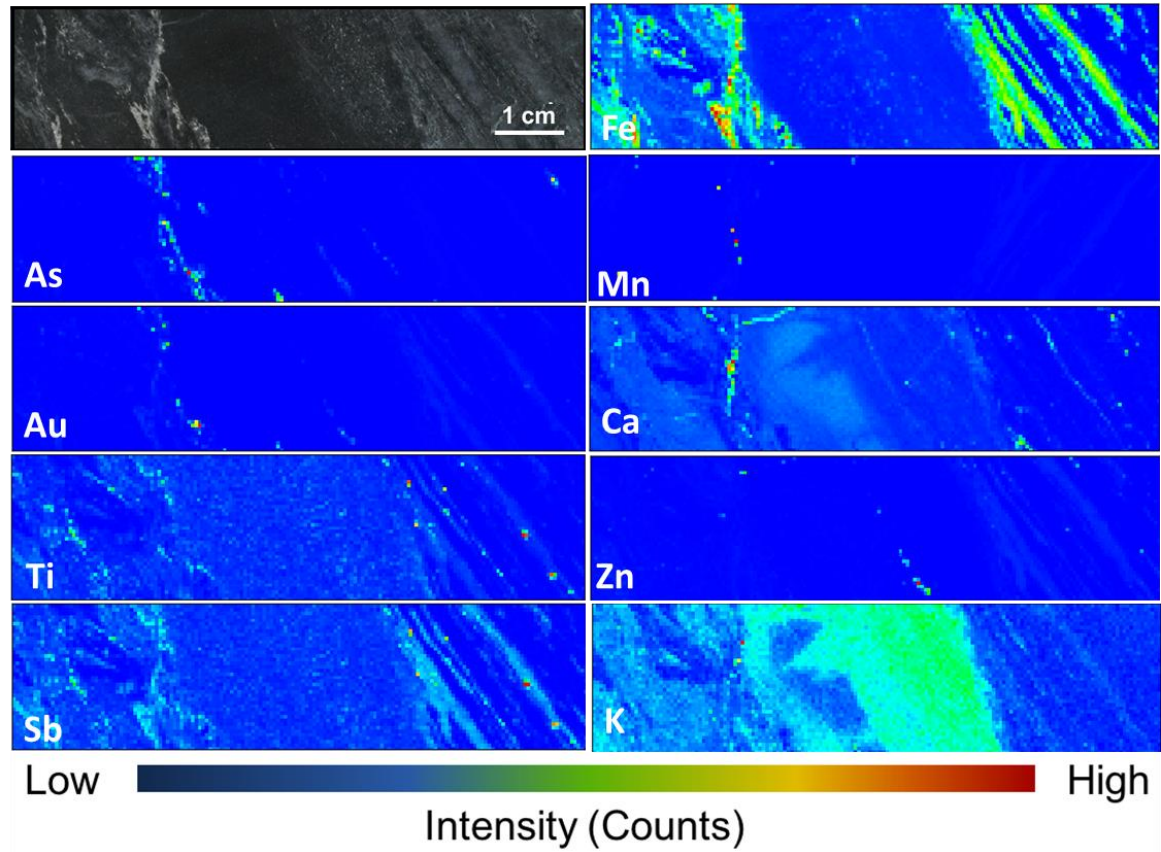
S892087, pyMCA



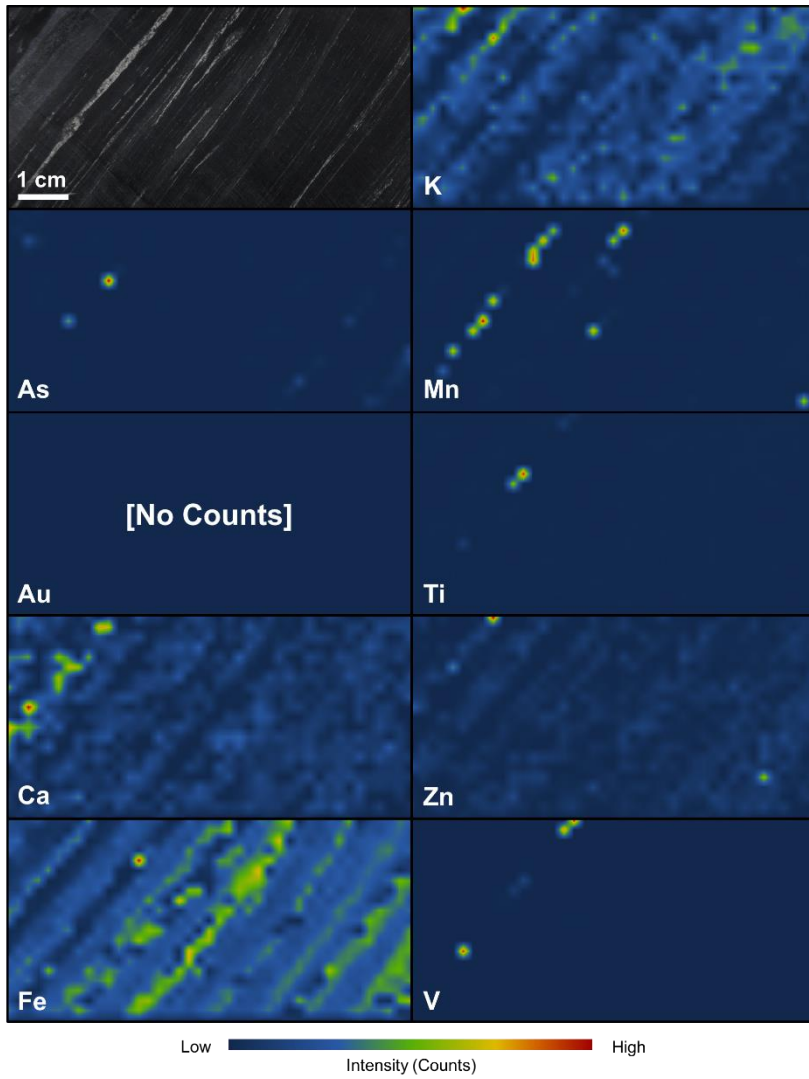
S892089, Peakaboo, flipped



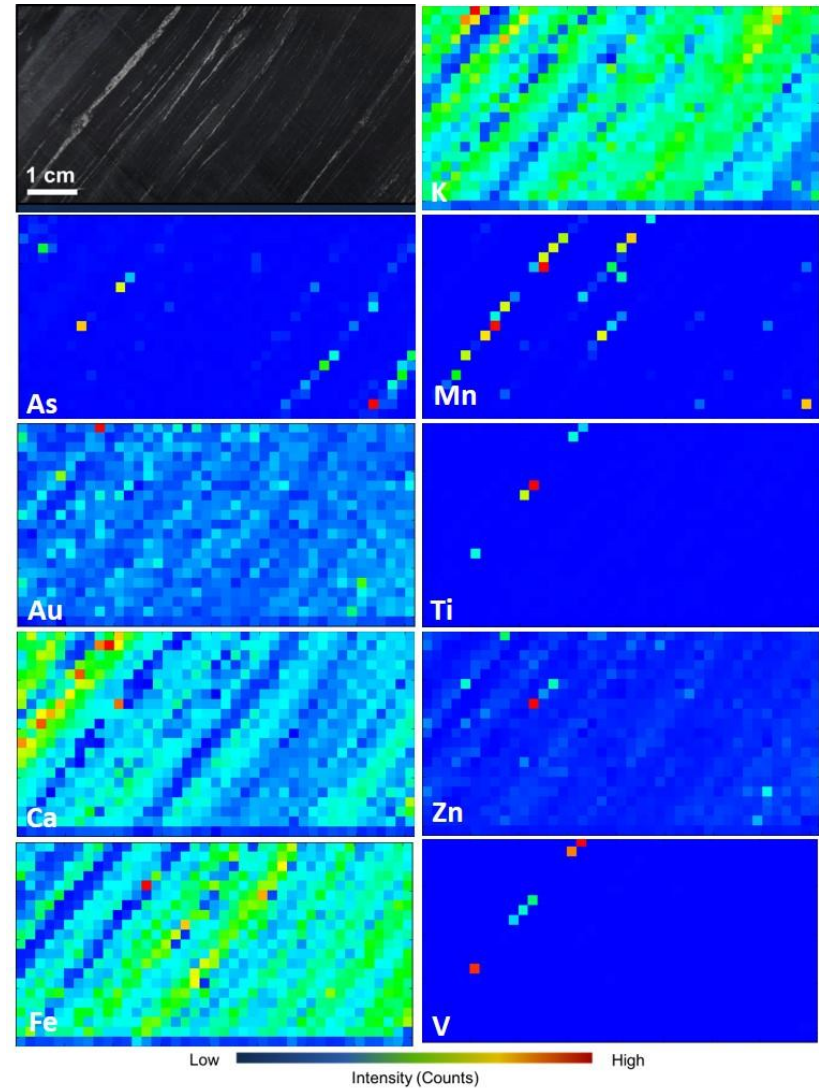
S892089, pyMCA



S892102, Peakaboo

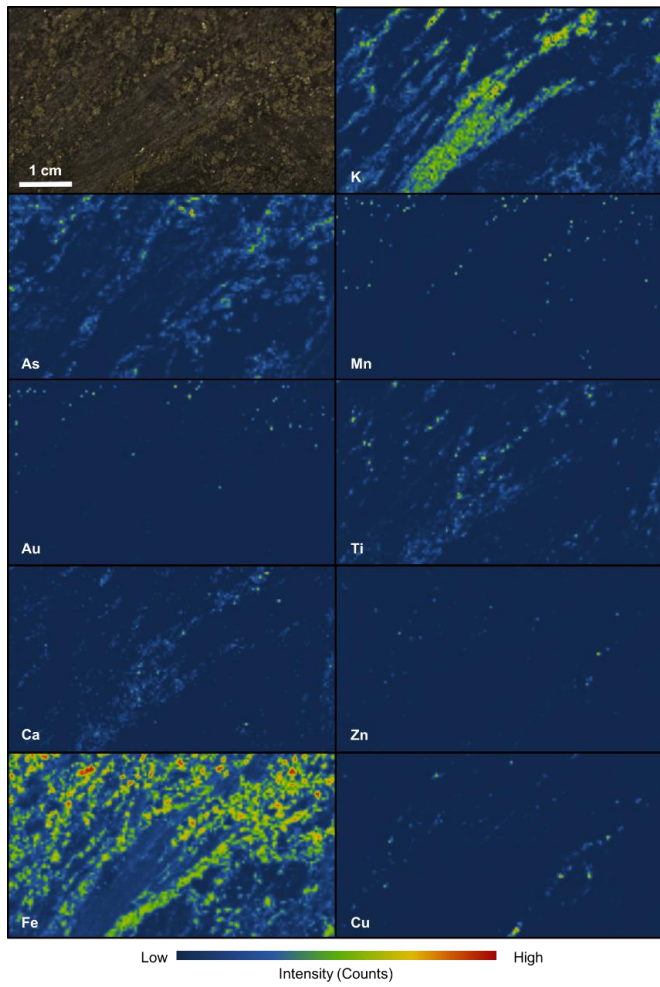


S892102, pyMCA

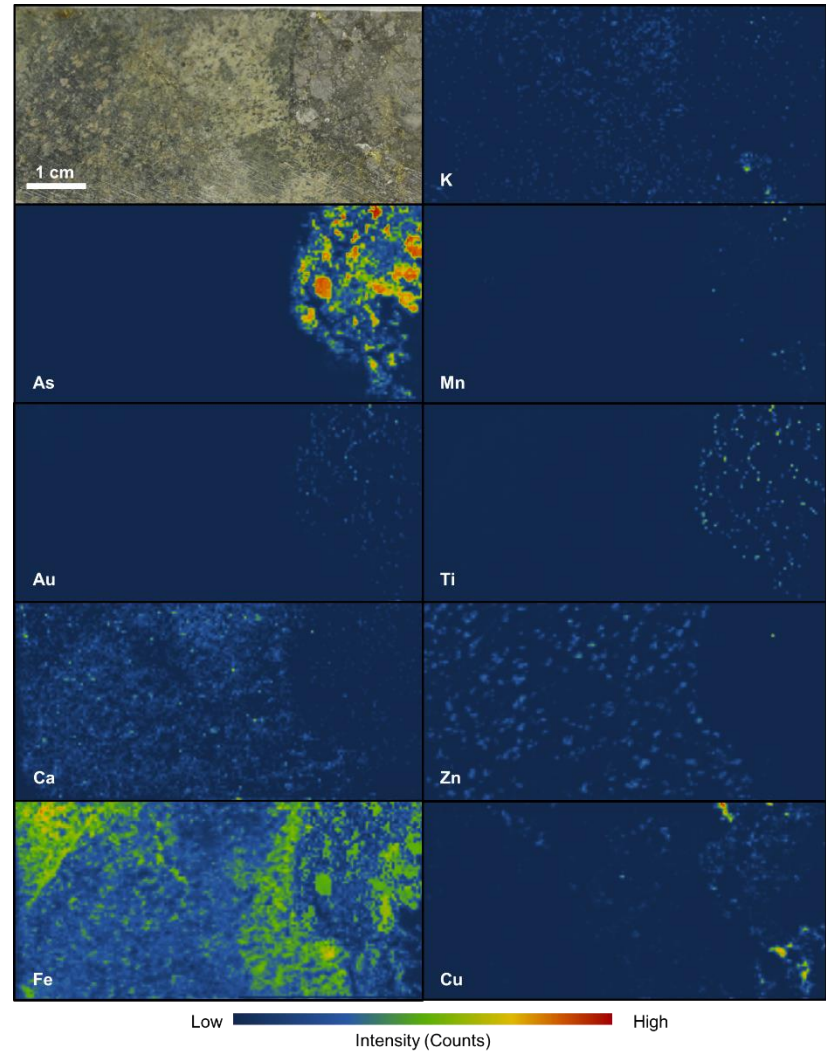


Homer

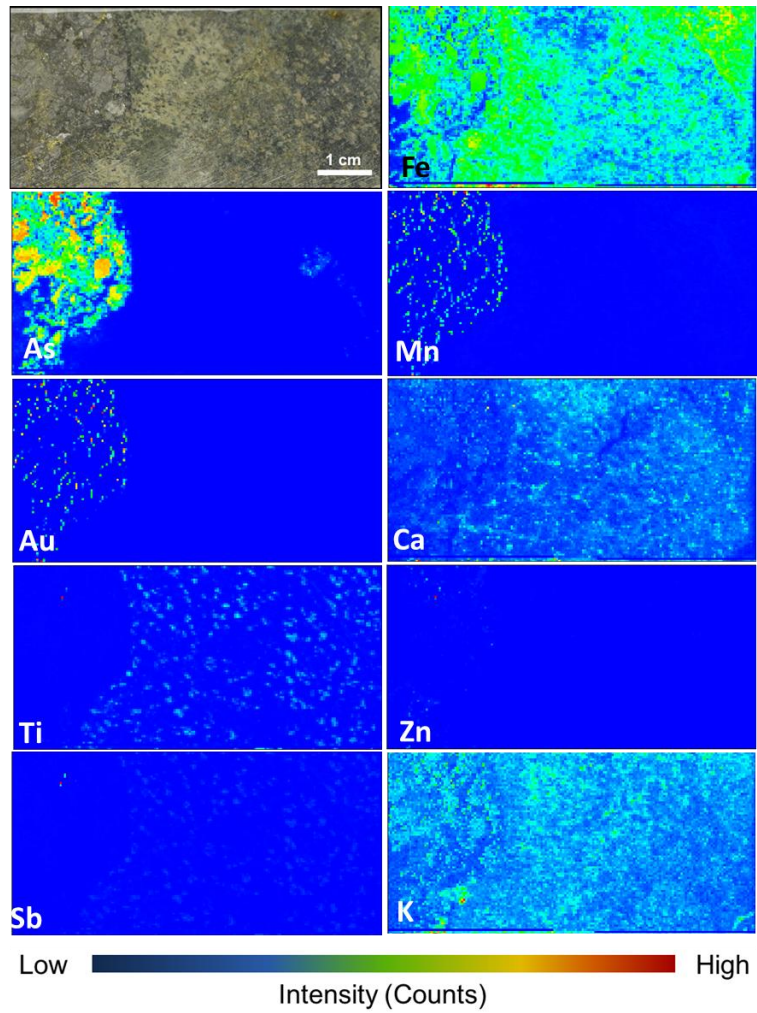
S345459



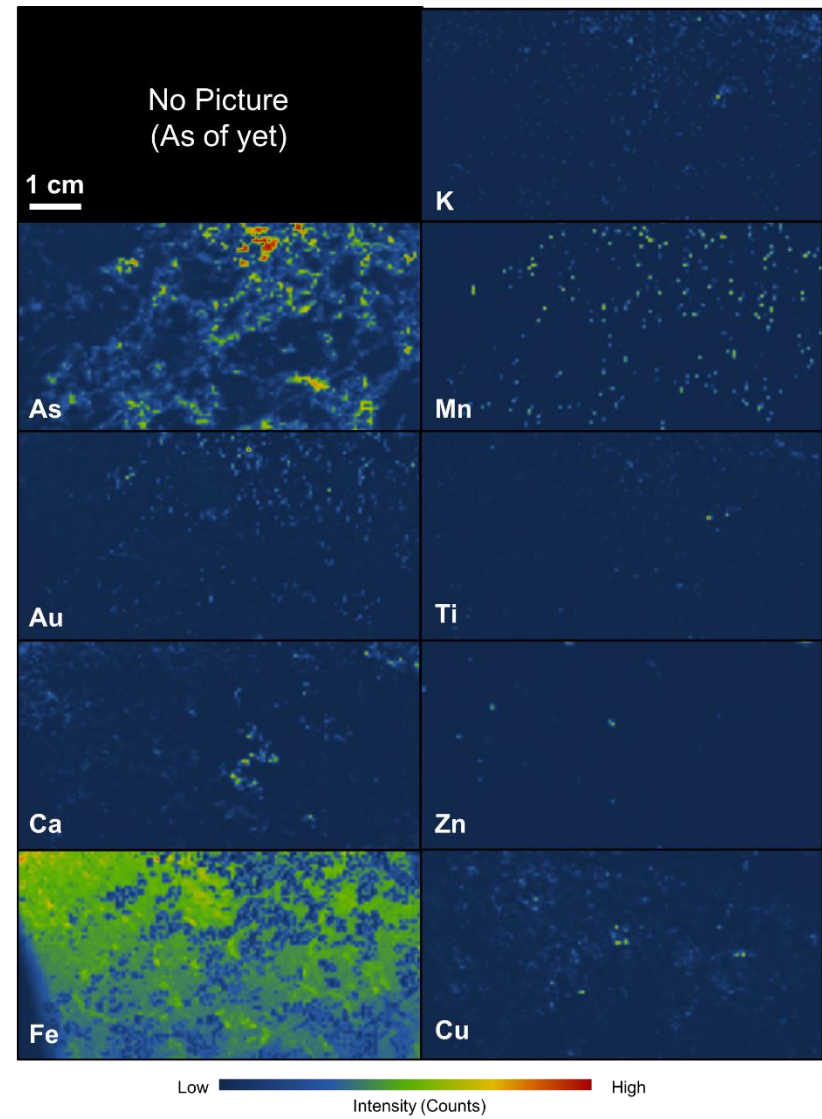
S345537, Peakaboo, flipped



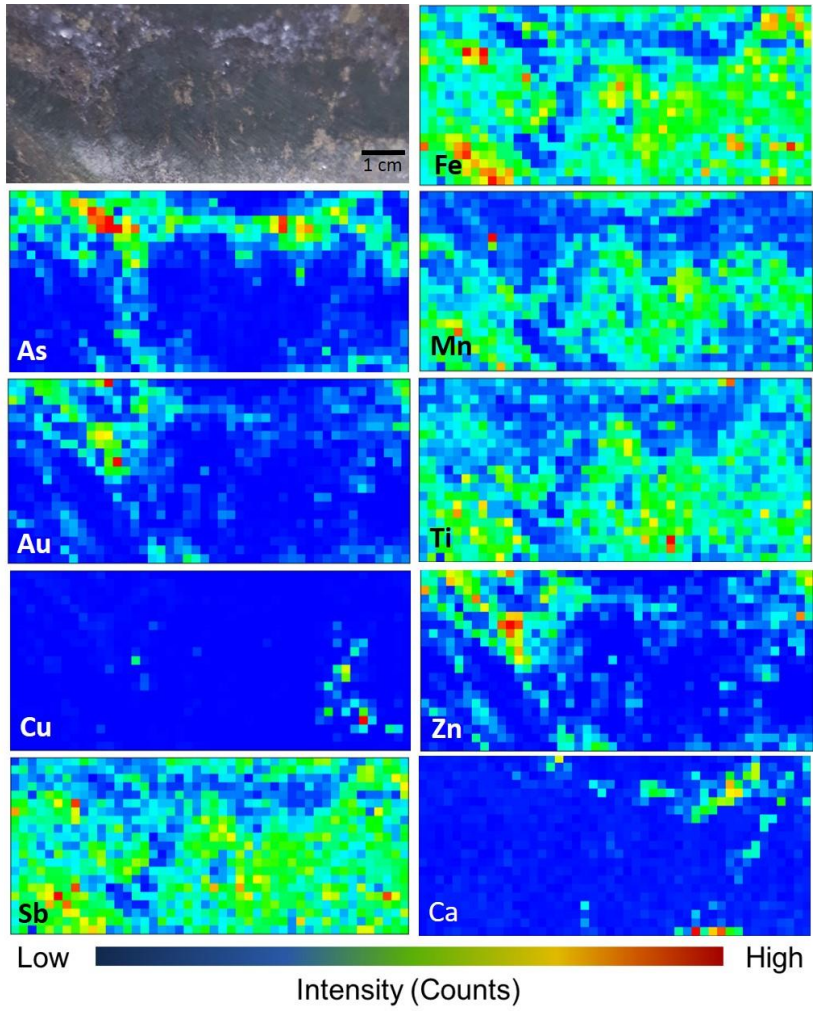
S345537, pyMCA



S345563



S520925



May 2018, TerraX

	quartz	plagioclase	muscovite	biotite	pyrite	arsenopyrite	galena	sphalerite	dolomite	ankerite	calcite	pyrrhotite	chlorite	diopside
Barney														
R115110	1		1		1		1	1		1			1	
R115609	1		1		1	1	1	1	1	1			1	
Crestaurem														
R432250	1		1		1	1	1	1	1	1		1		
R433857	1		1		1	1	1	1	1	1		1	1	
R433866	1		1		1	1	1	1	1	1		1		
Sam Otto														
S343808	1	1	1	1	1	1		1			1		1	
S343813	1	1	1	1				1					1	
S343816	1	1	1	1	1	1		1			1		1	
S343819	1	1		1		1					1	1	1	
V156519	1	1	1	1		1			1				1	
V156526	1	1	1	1	1	1	1				1		1	
V890298	1	1		1		1	1	1				1	1	
V892232	1	1	1	1	1	1		1			1	1		
V892234	1	1		1			1						1	
V892336	1	1		1	1		1	1					1	
Homer														
S345459	1		1	1	1	1	1	1				1	1	
S345537	1	1			1	1	1	1					1	
S345563	1	1			1	1	1	1				1	1	
Hébert-Brent														
S520992	1		1		1	1							1	
S520998	1		1	1	1	1							1	
S521365	1	1	1		1	1		1						
Mispickel														
S892045	1	1	1	1	1		1	1					1	
S892082	1	1	1	1										
S892084	1	1	1		1		1	1					1	1
S892089	1	1	1		1							1	1	
S892102	1	1	1		1	1		1					1	
Dave's Pond														
V160414	1	1	1		1	1	1	1				1	1	
V413294	1	1	1		1	1		1			1	1	1	
V413296	1	1	1	1	1			1			1		1	
V892939	1	1	1	1	1	1	1					1	1	
V892959	1	1	1		1	1	1	1			1		1	

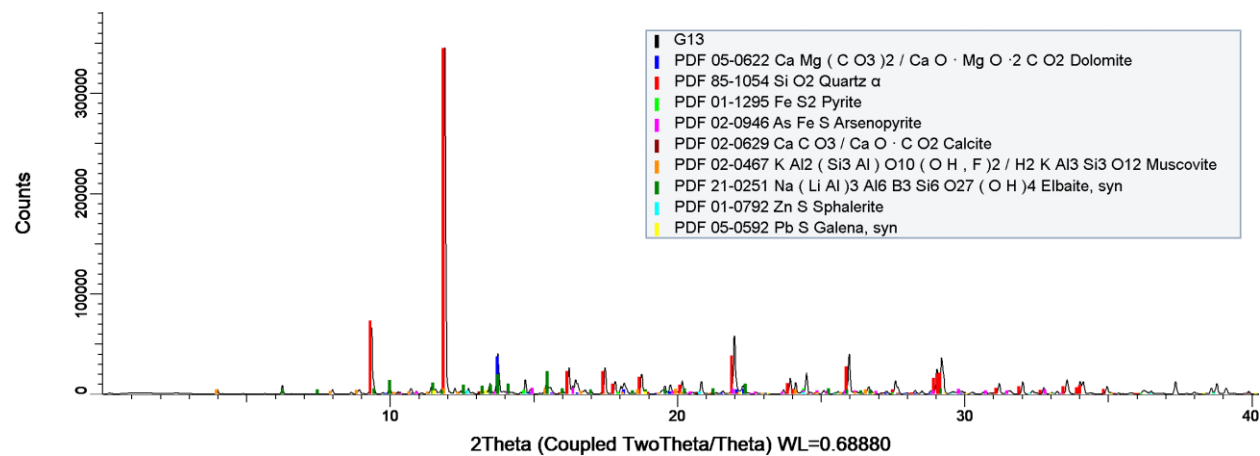
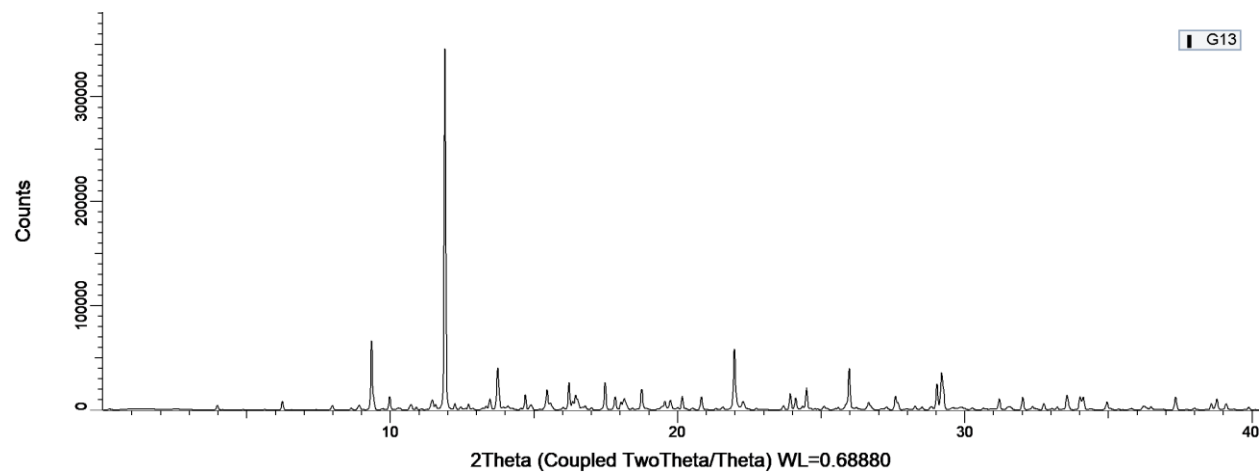
Appendix D: XRD Diffractograms

Appendix D – X-ray Diffractograms

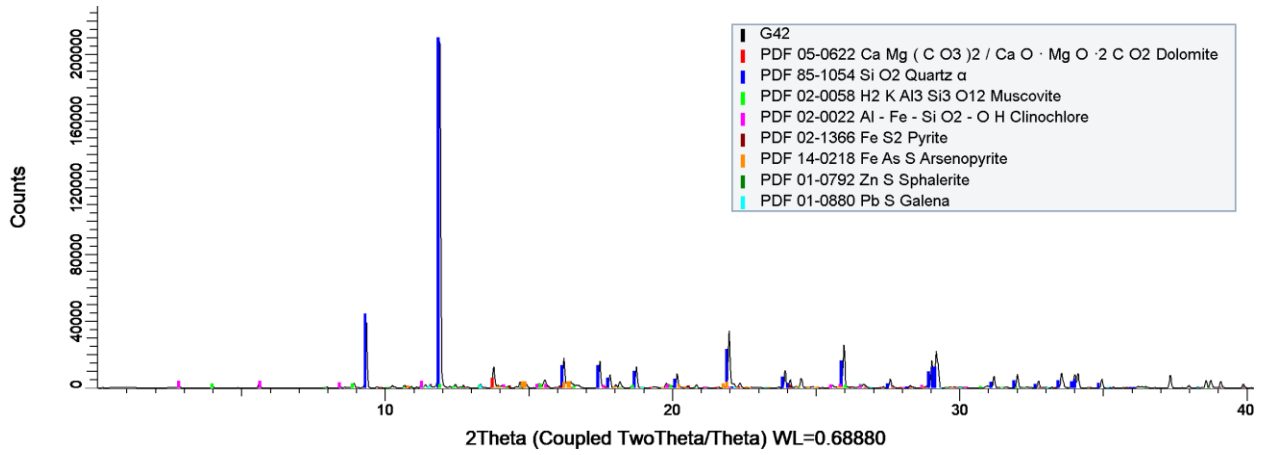
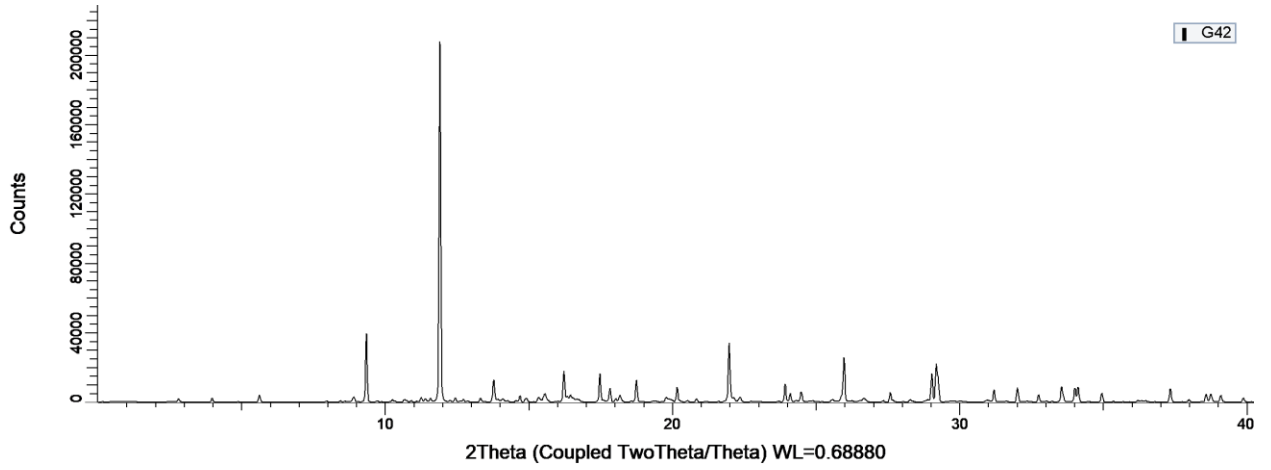
Kerswill Suite

March 2018 Data

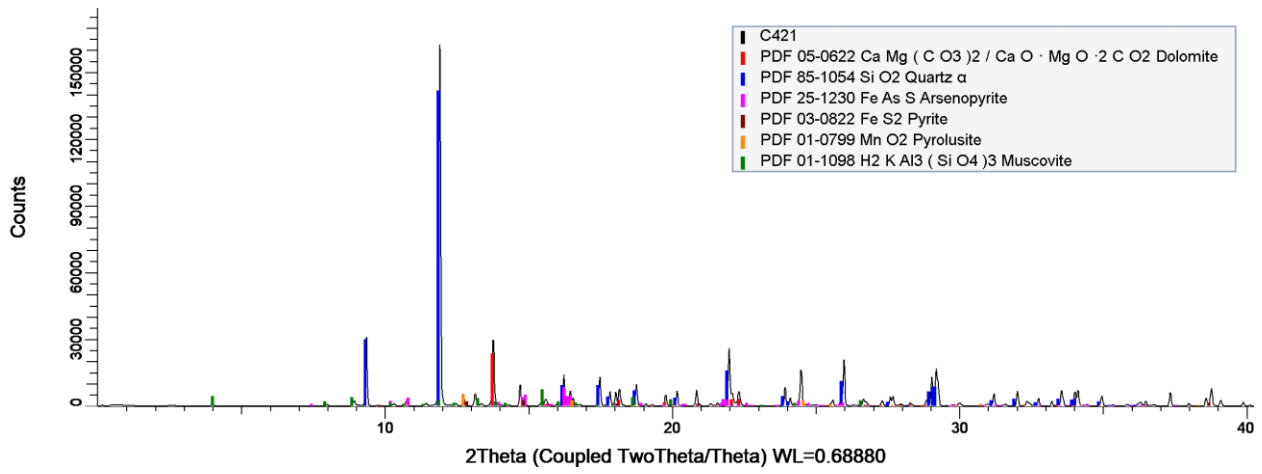
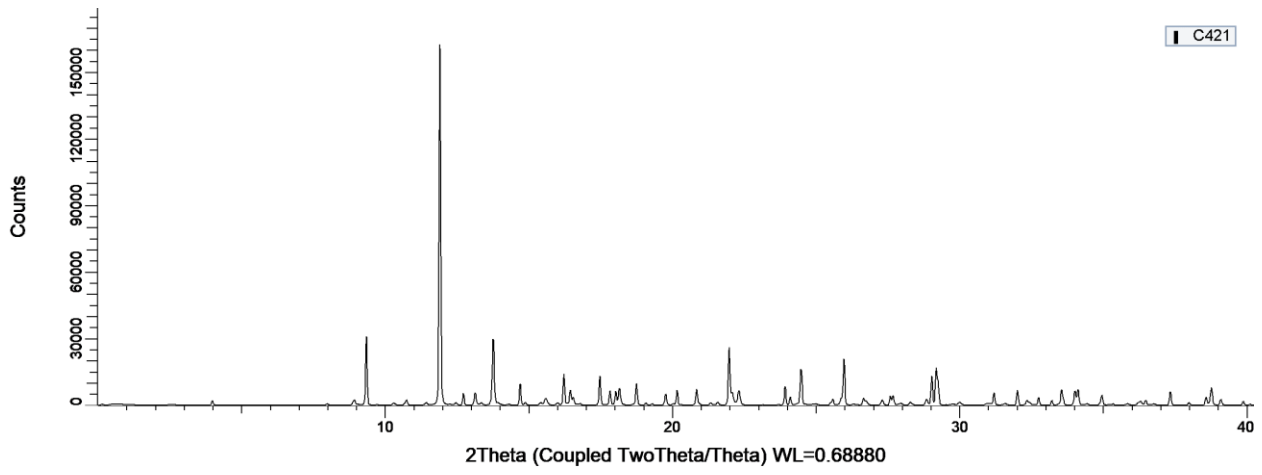
G13



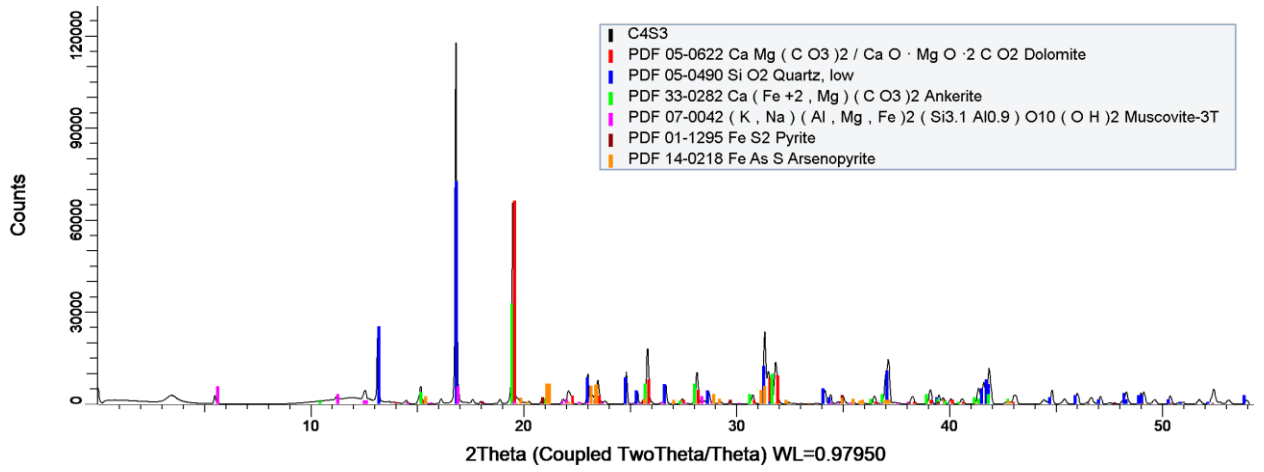
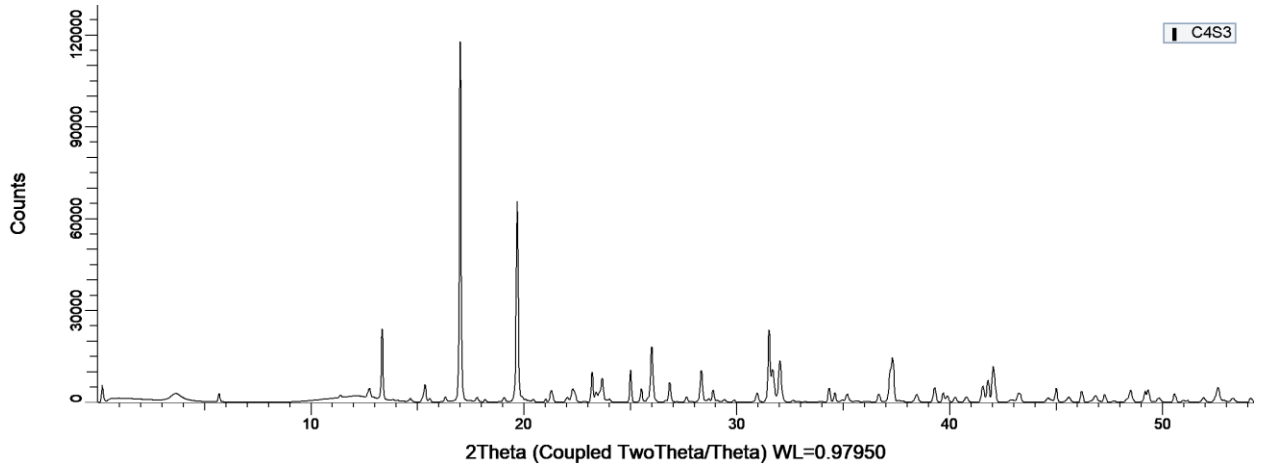
G42



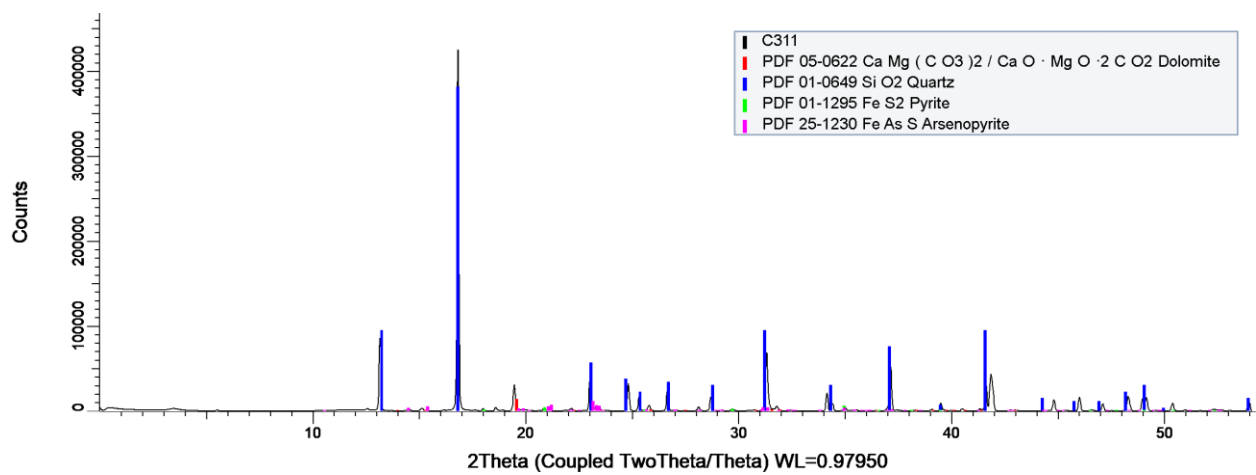
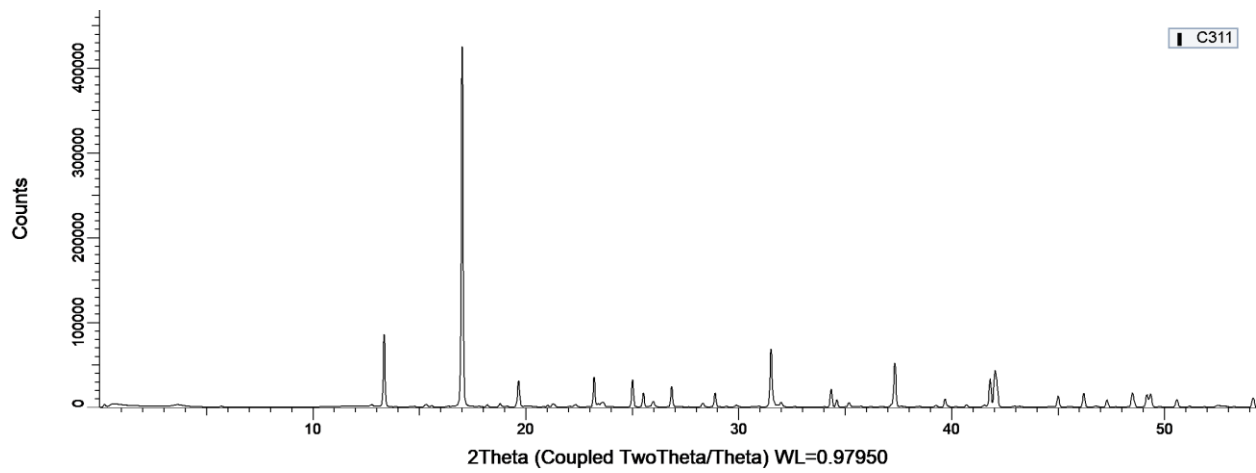
C421



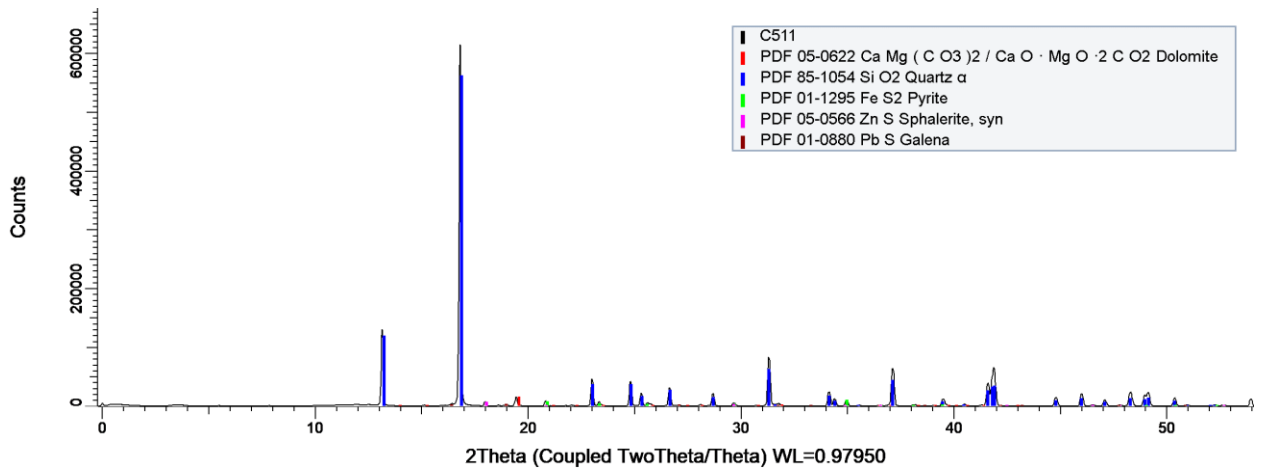
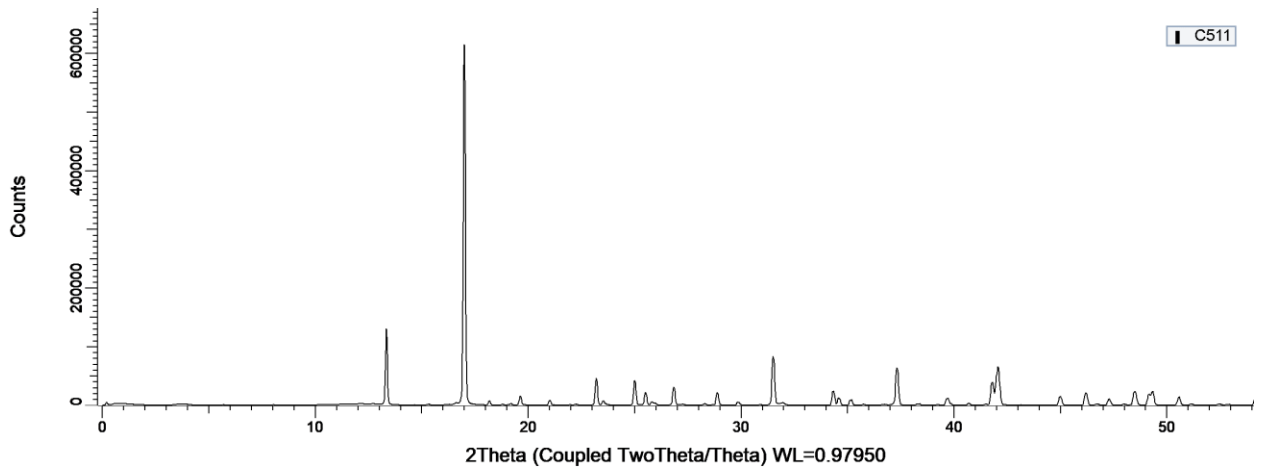
C4S3



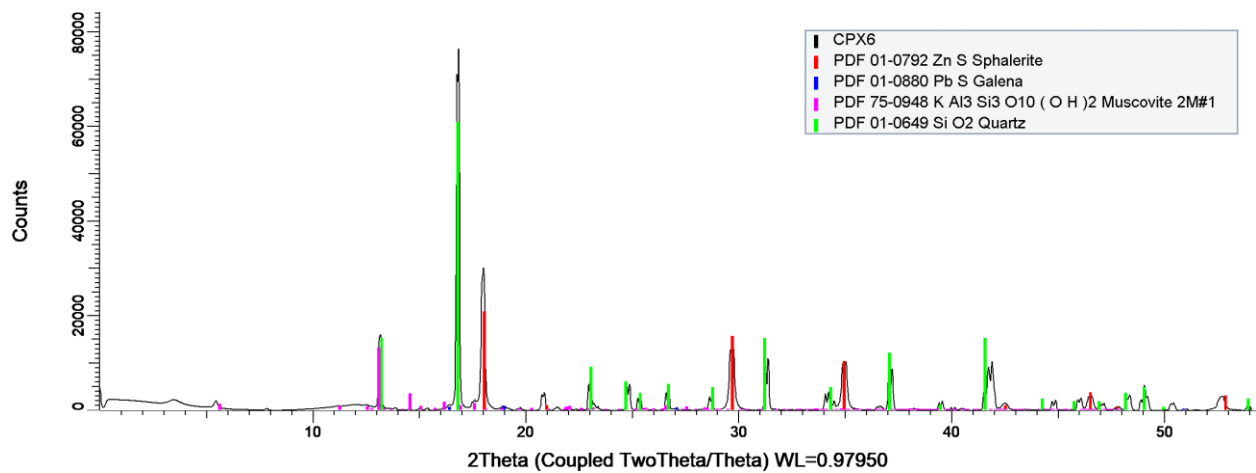
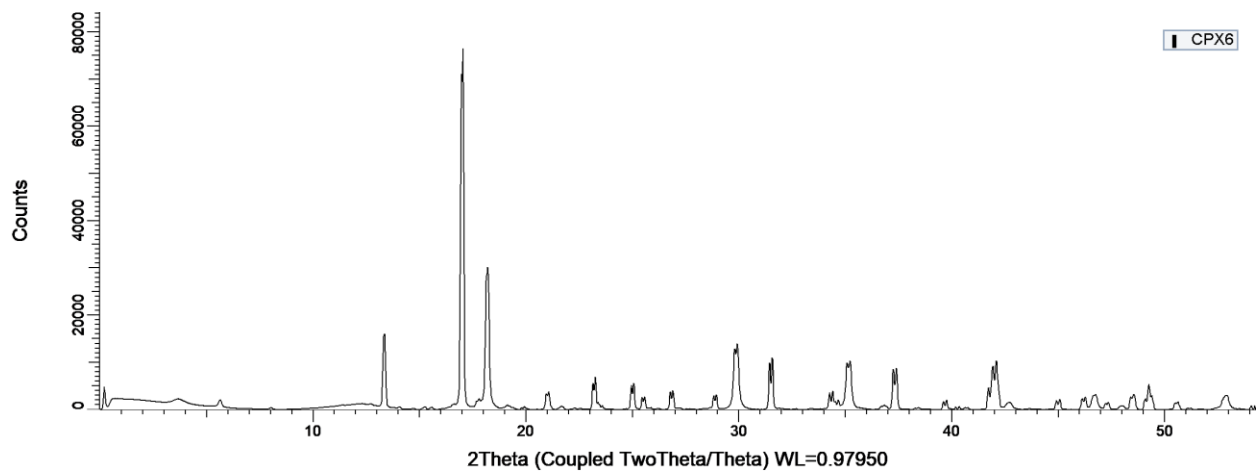
C311



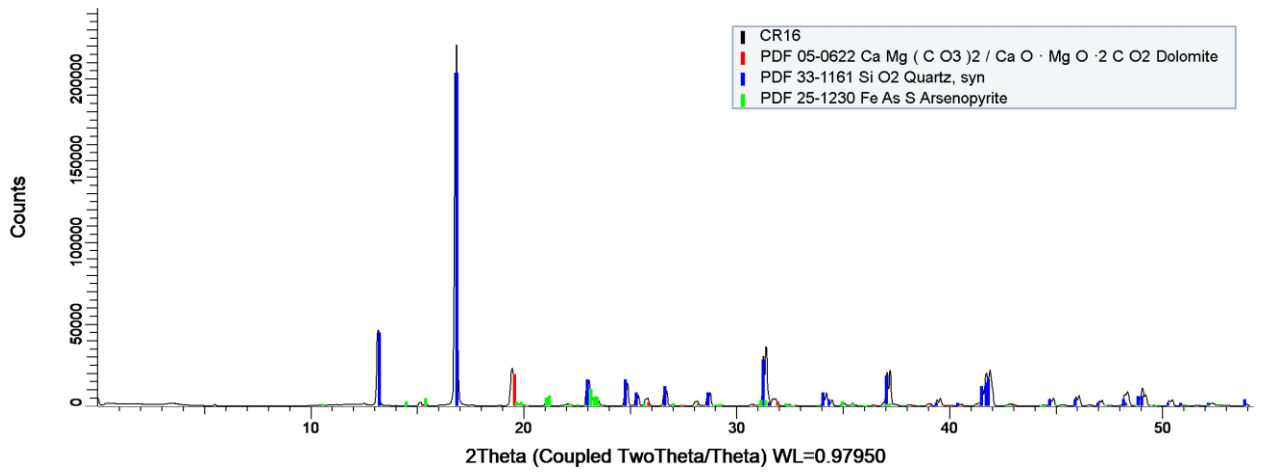
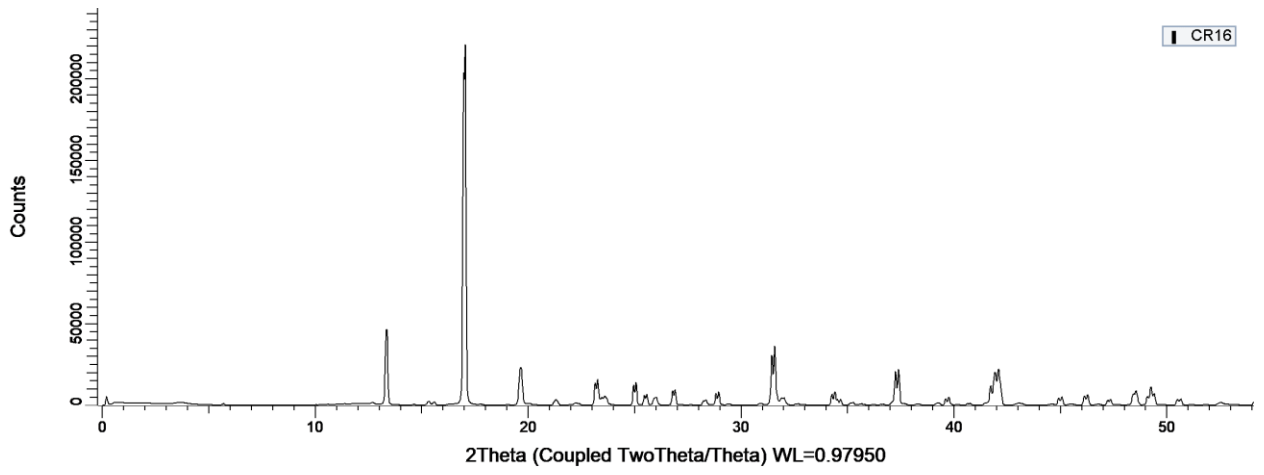
C511



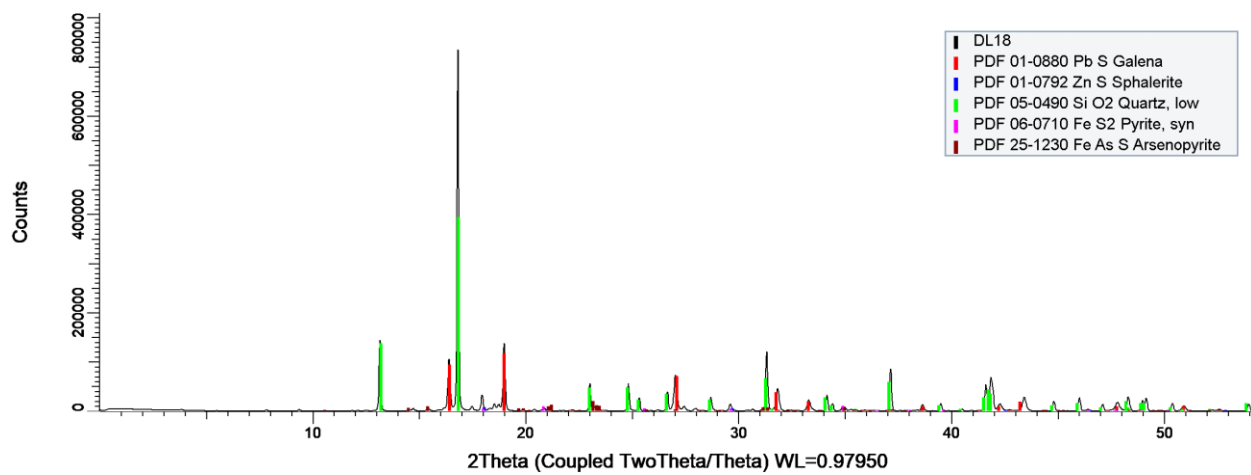
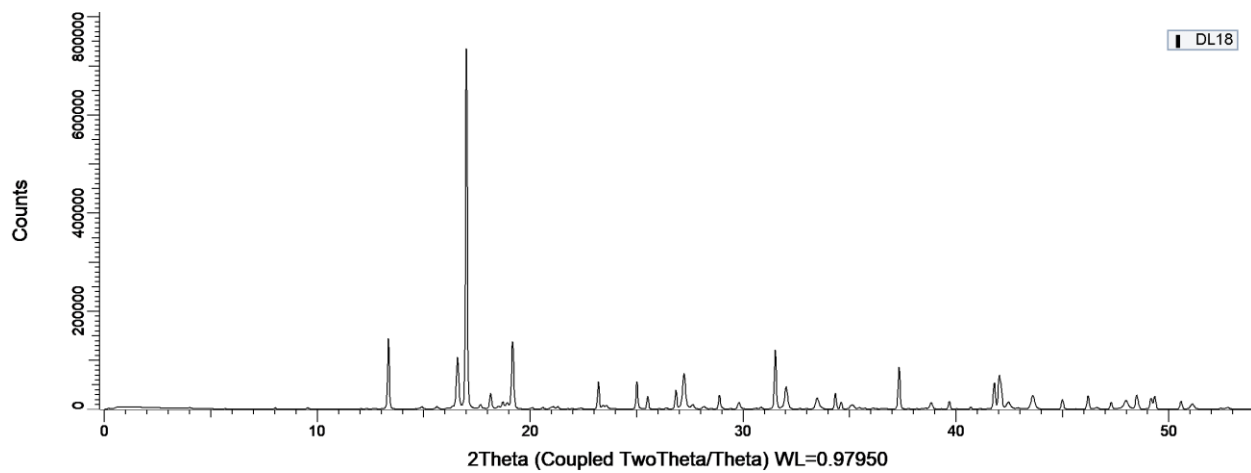
CPX6



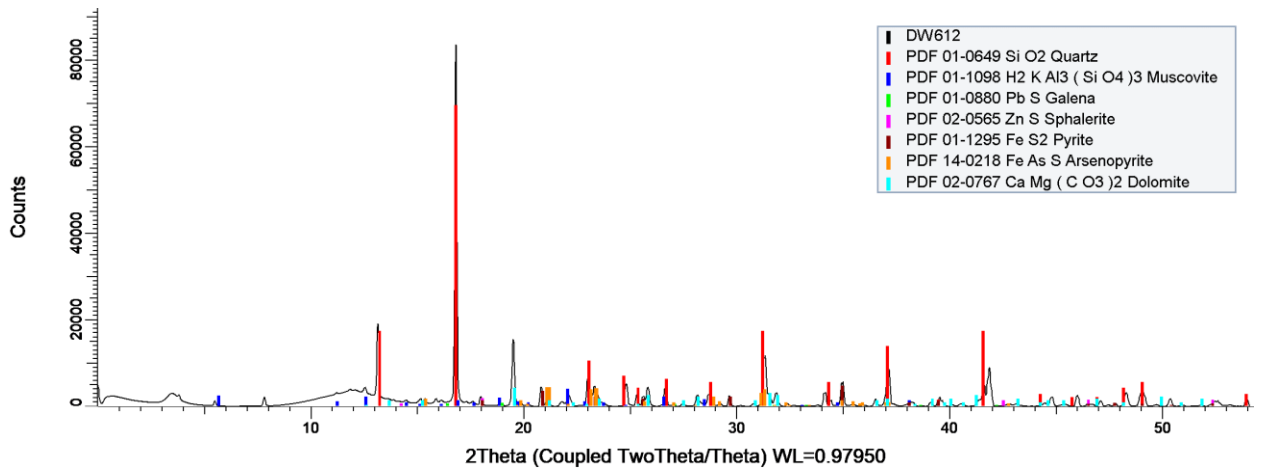
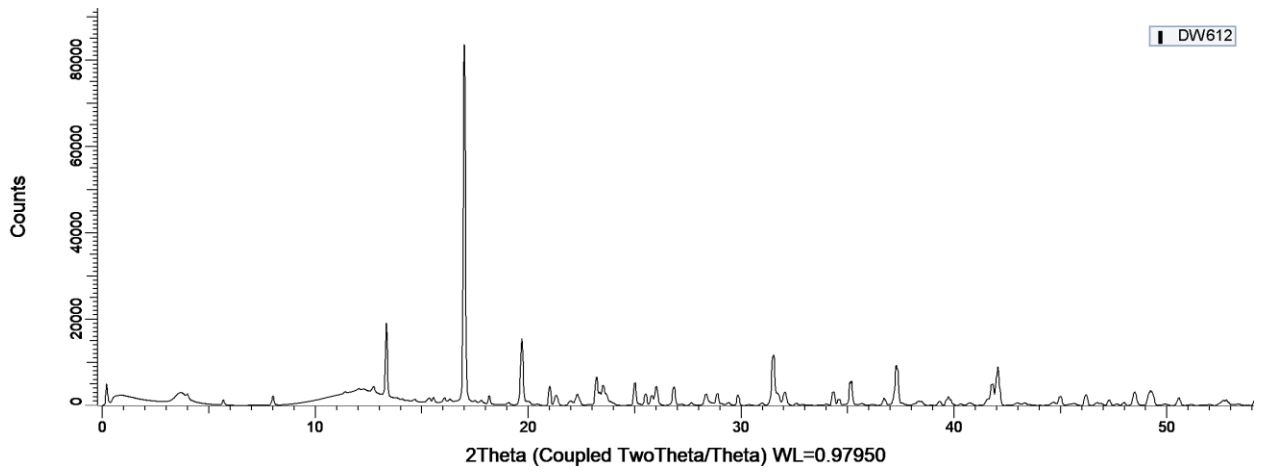
CR16



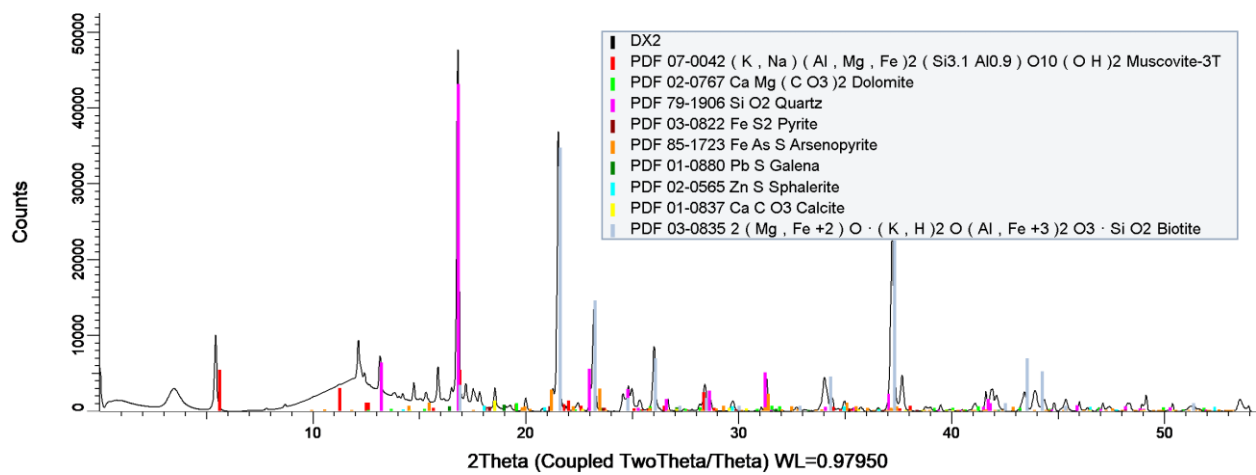
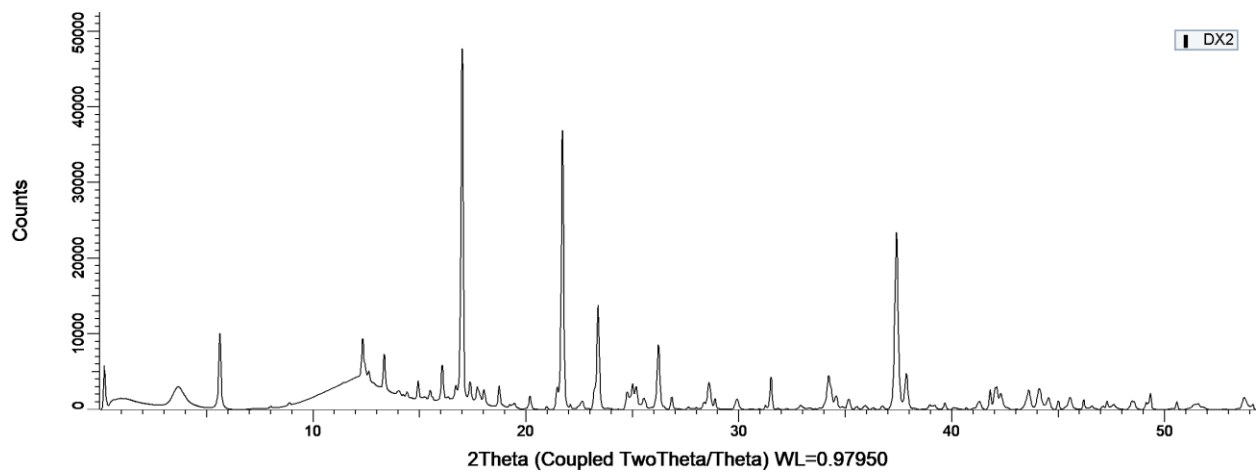
DL18



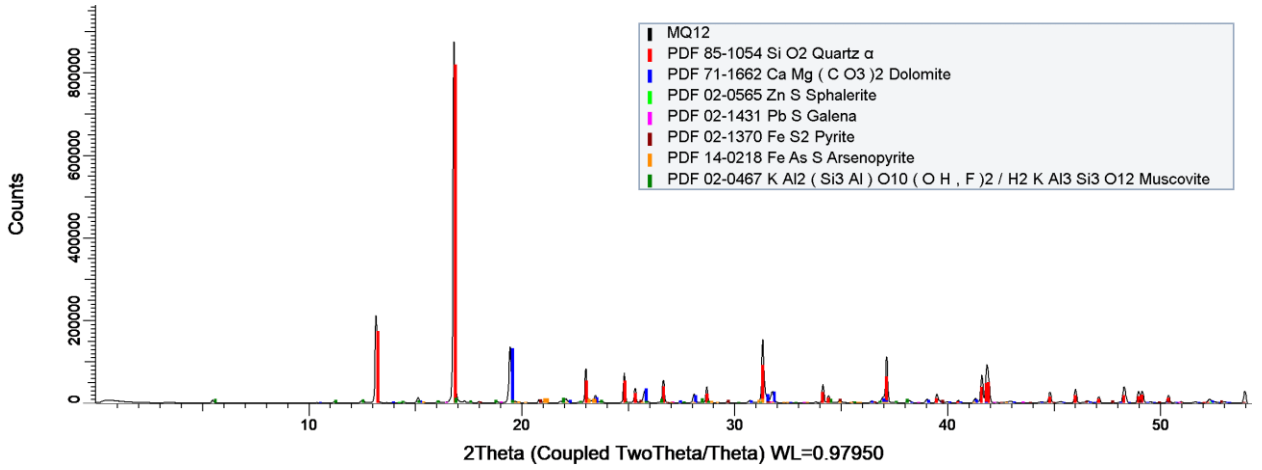
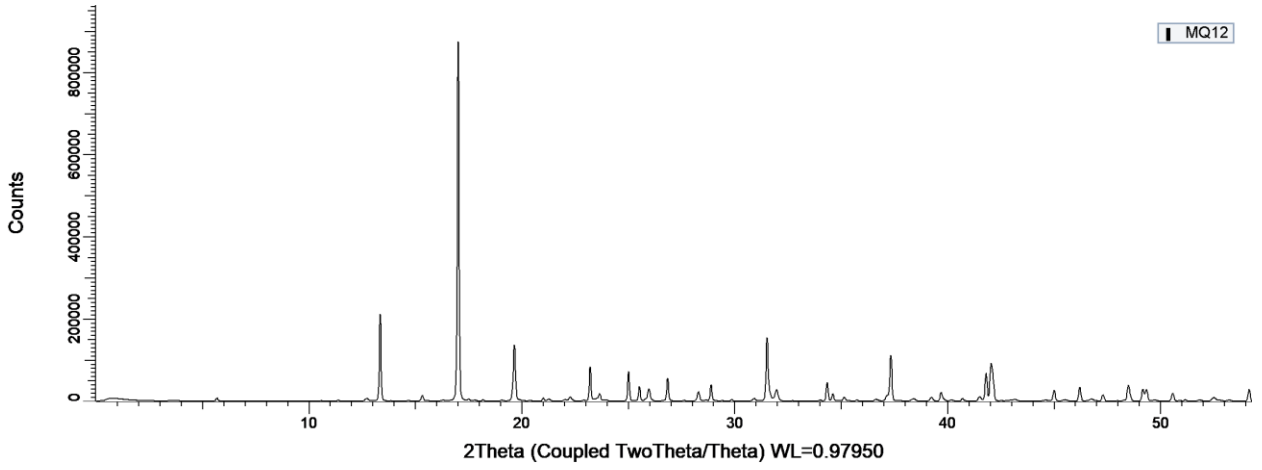
DW612



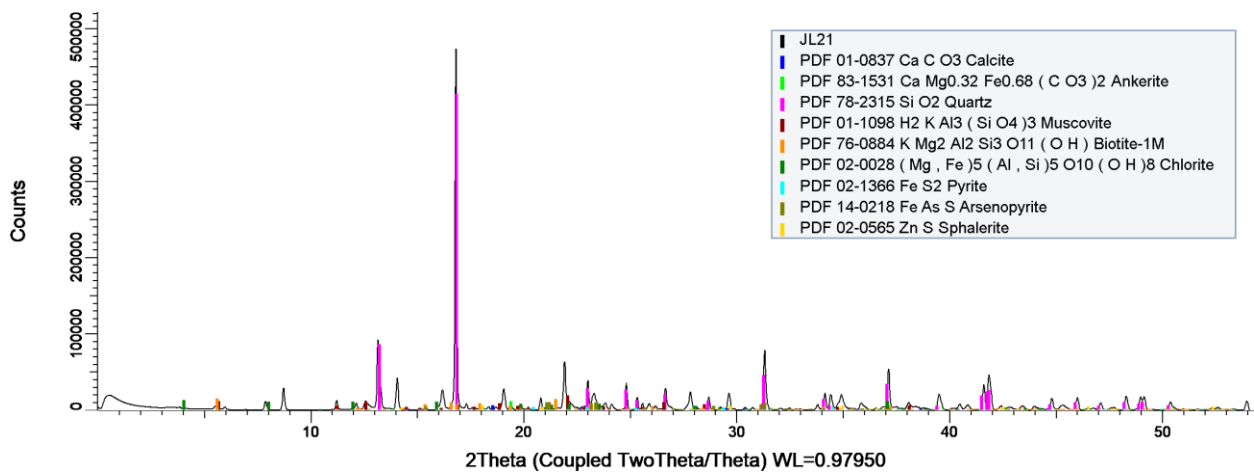
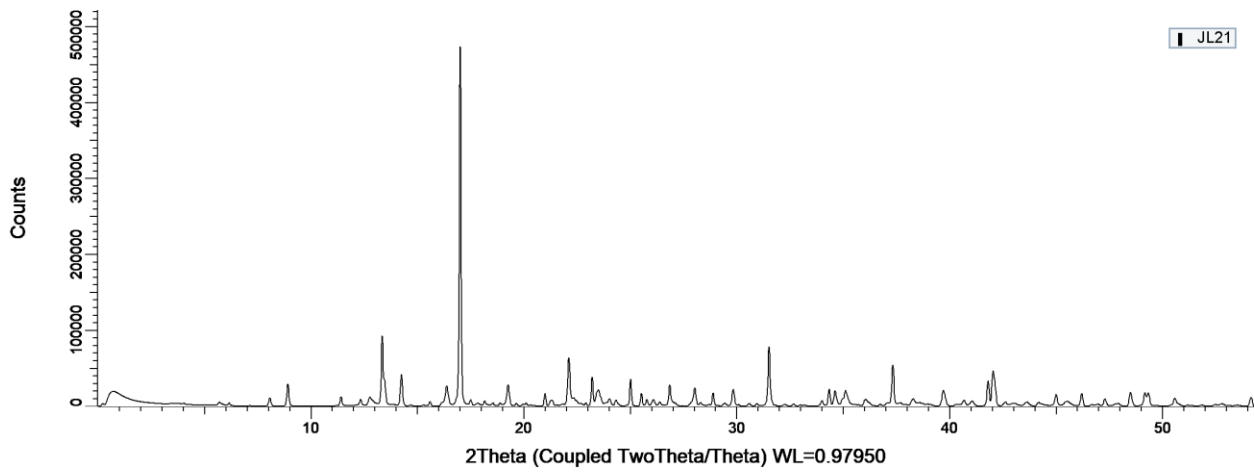
DX2



MQ12

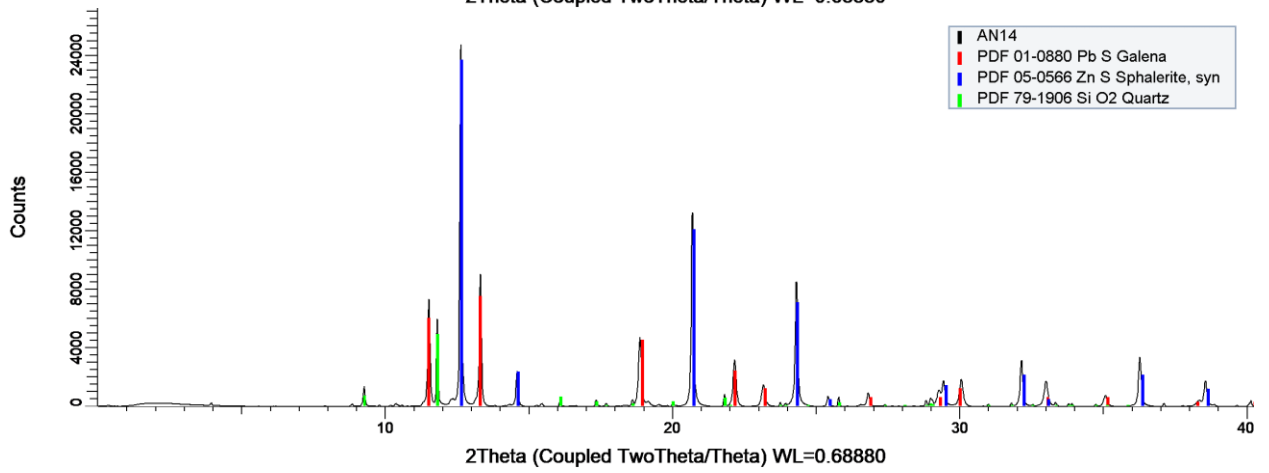
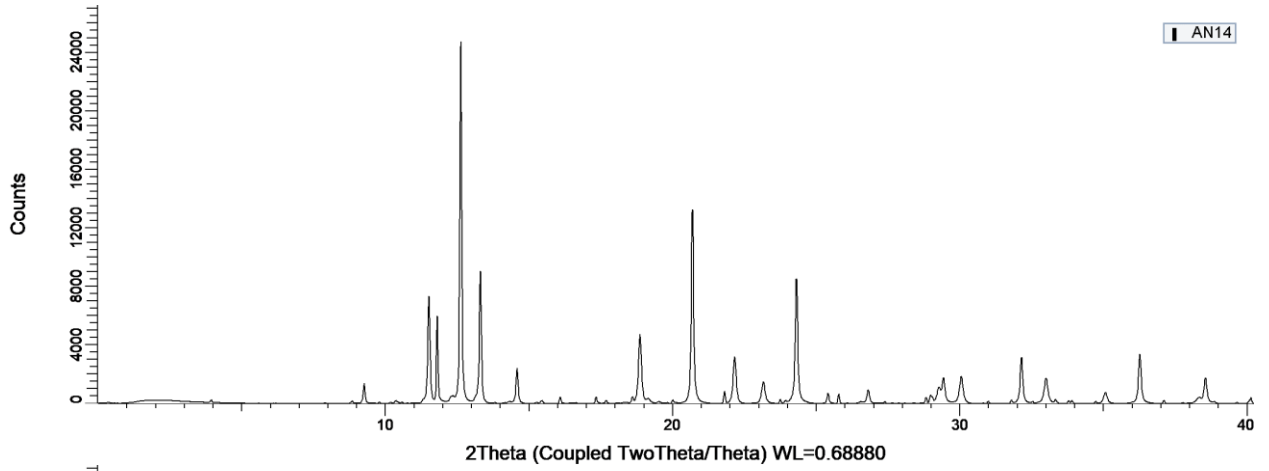


JL21 (analysed at 12.658 KeV) –

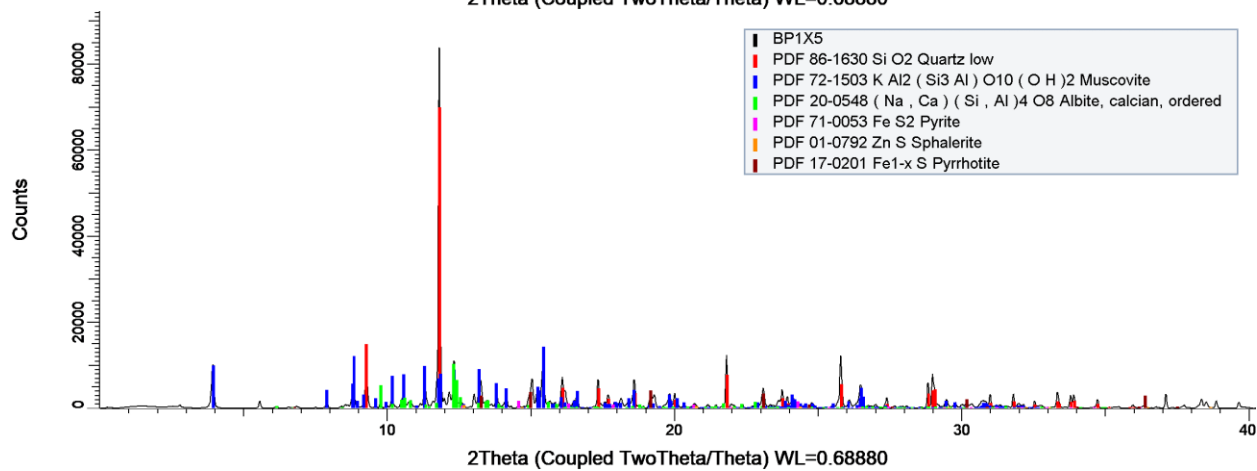
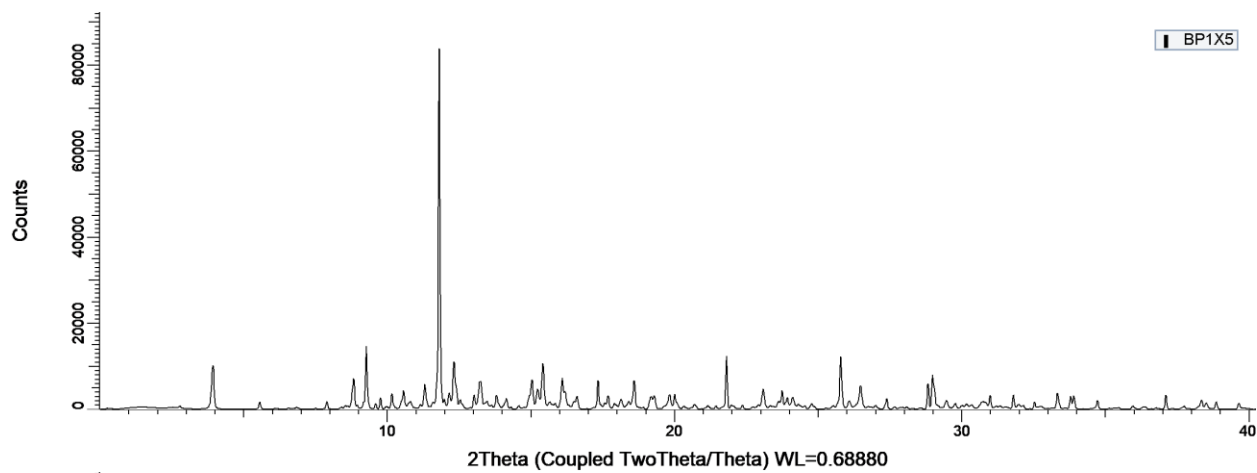


May 2018

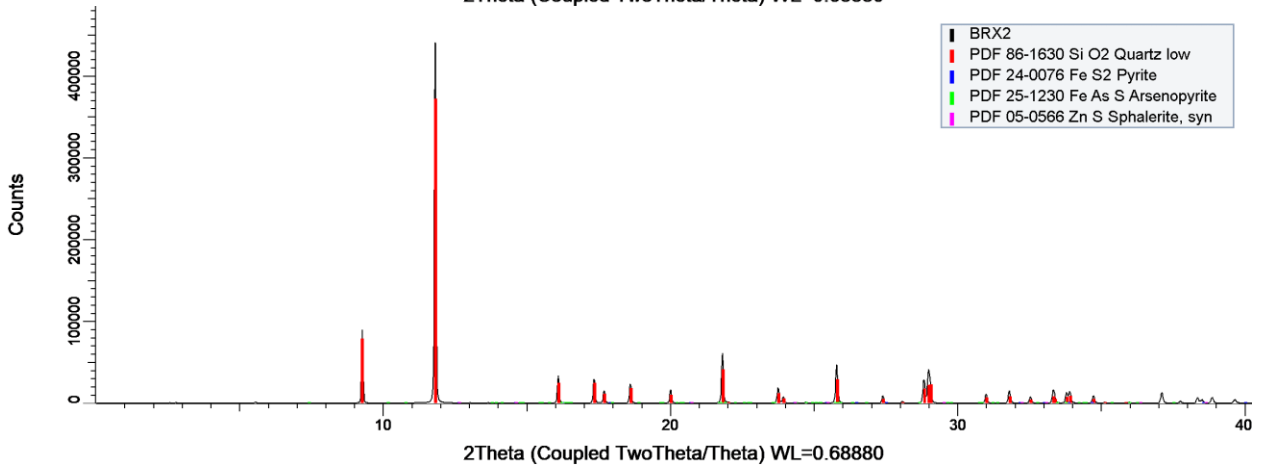
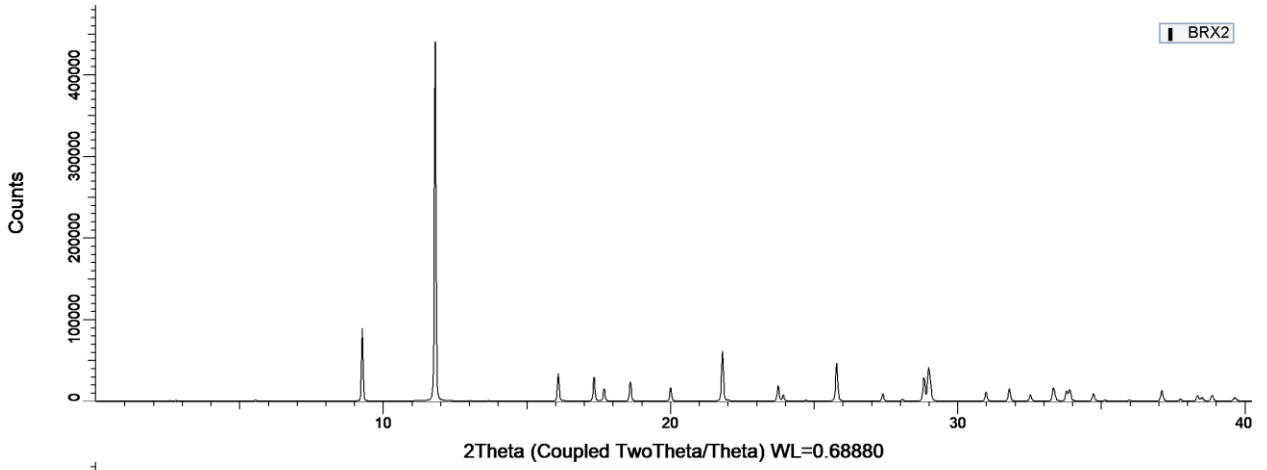
AN14



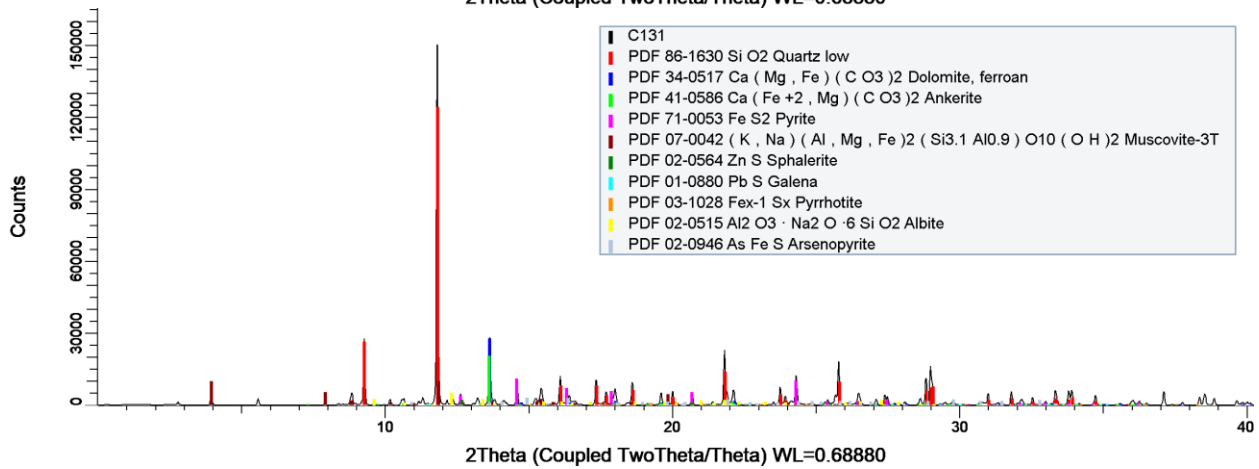
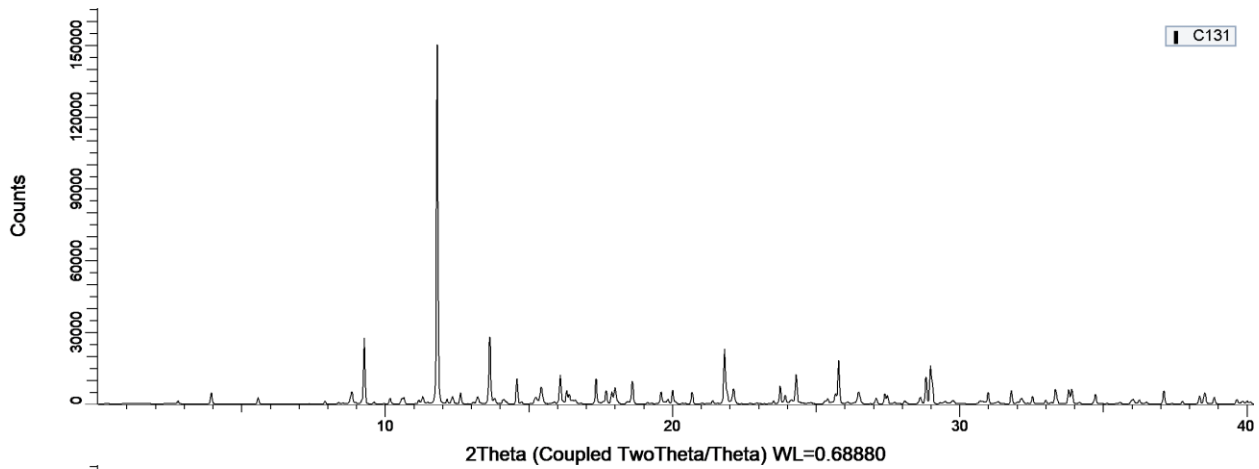
BP1X5



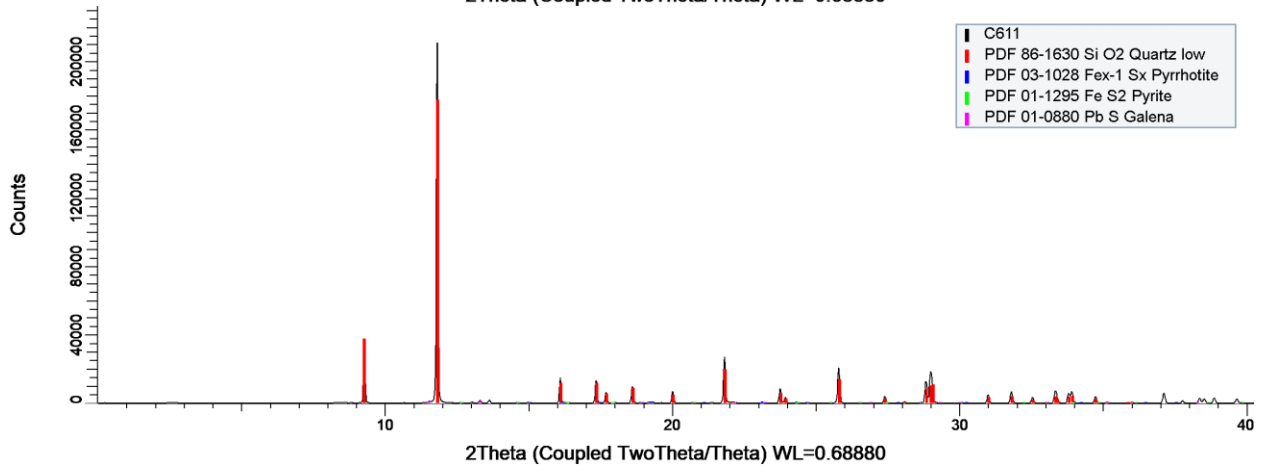
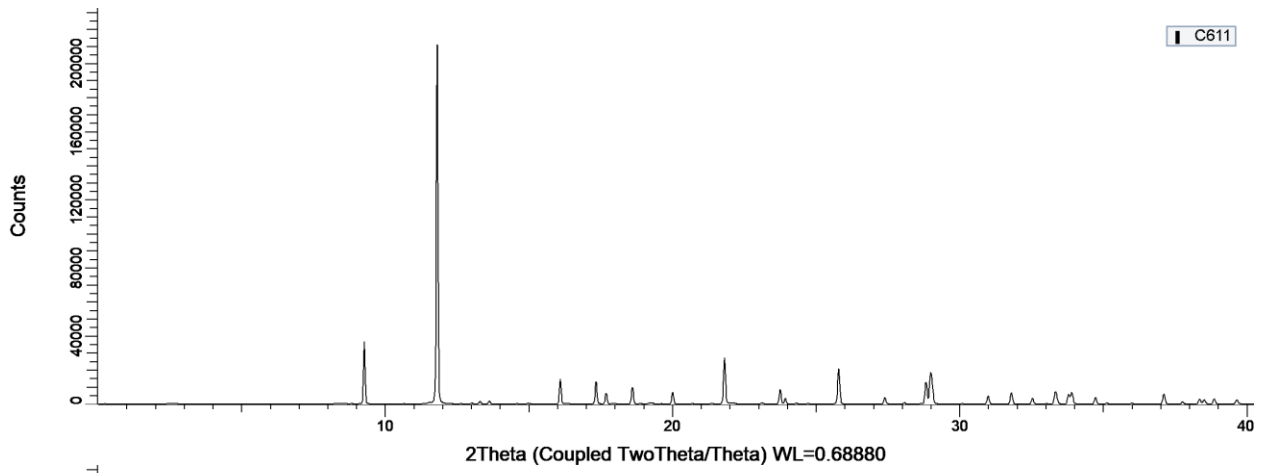
BRX2



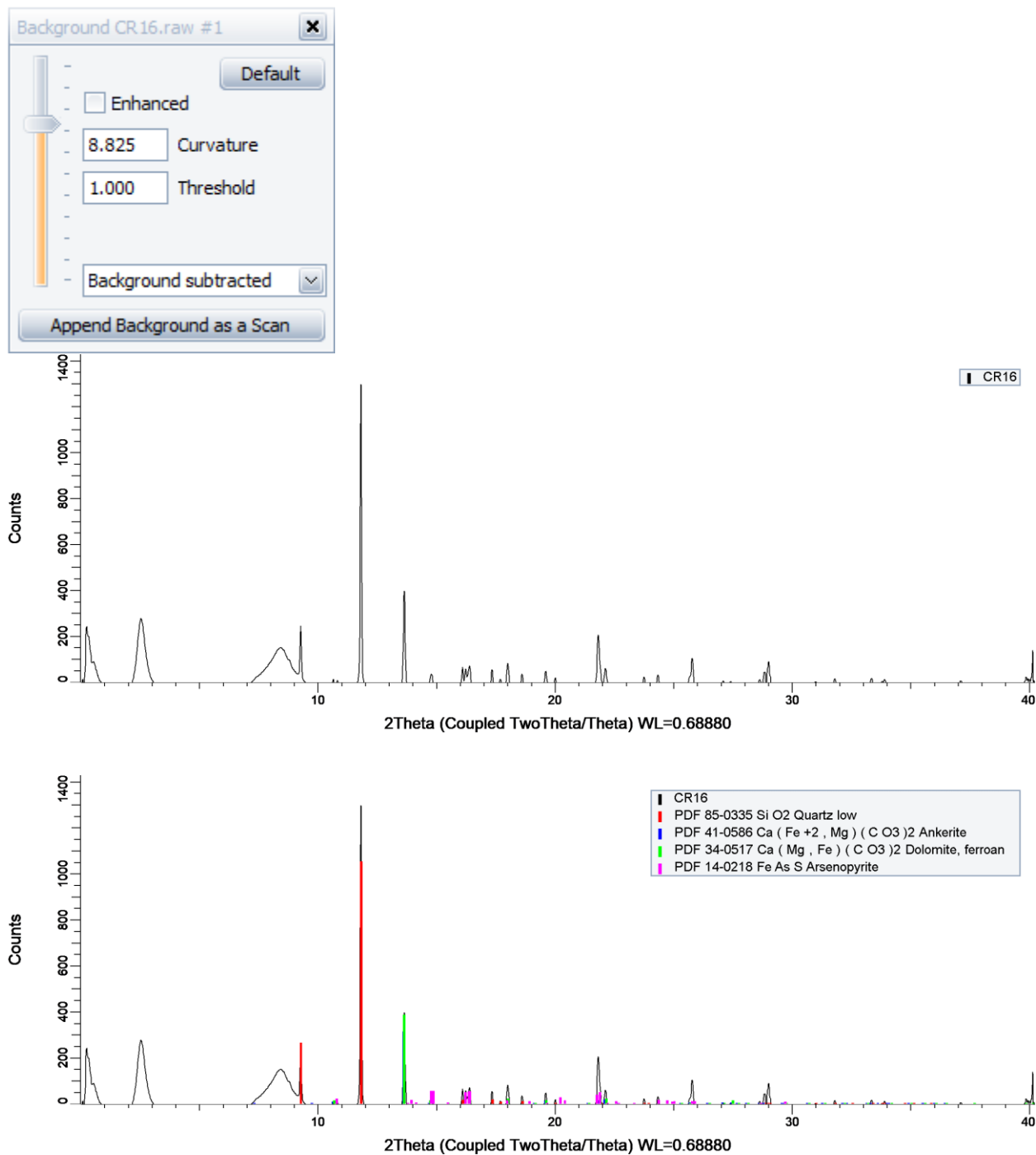
C131



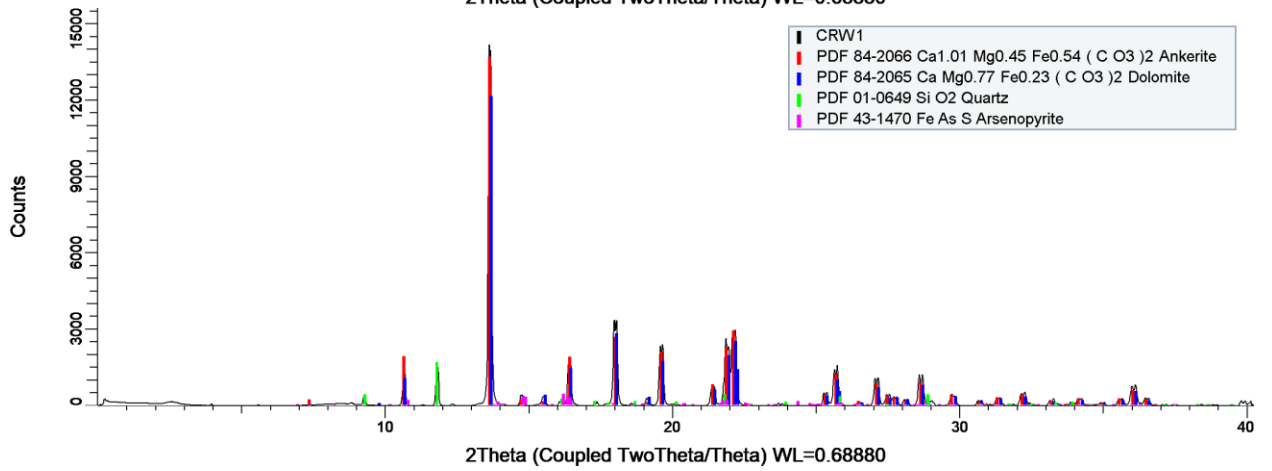
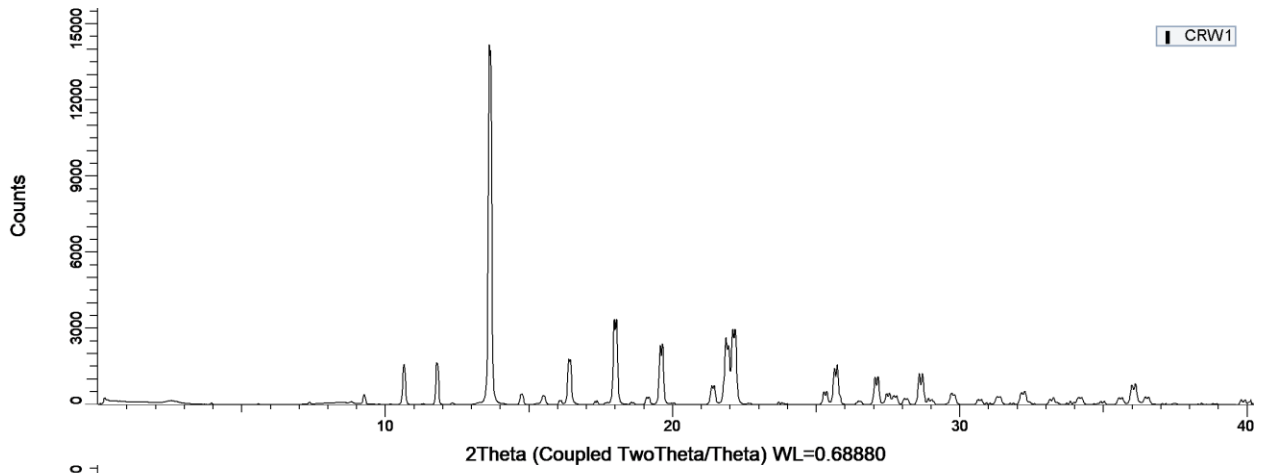
C611



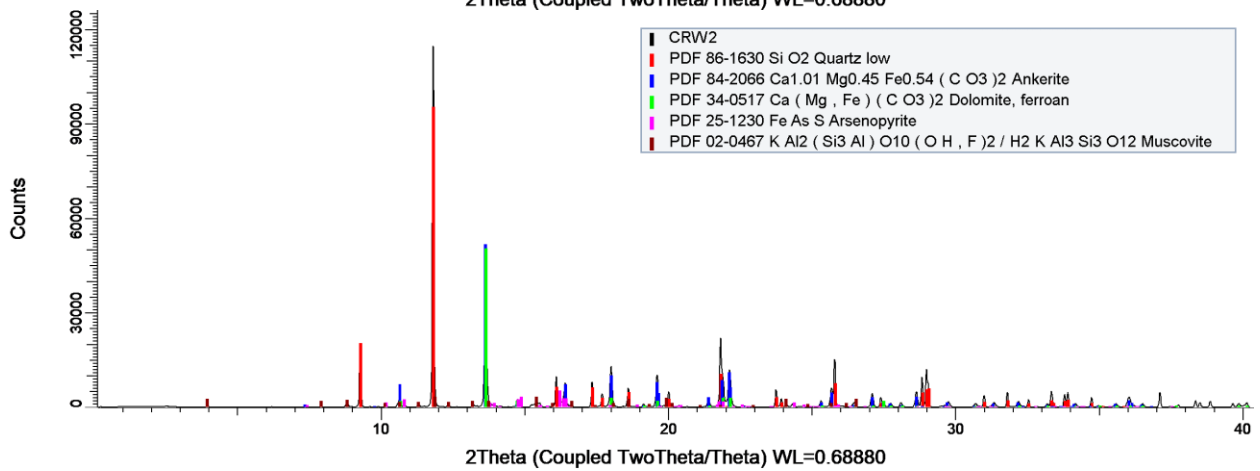
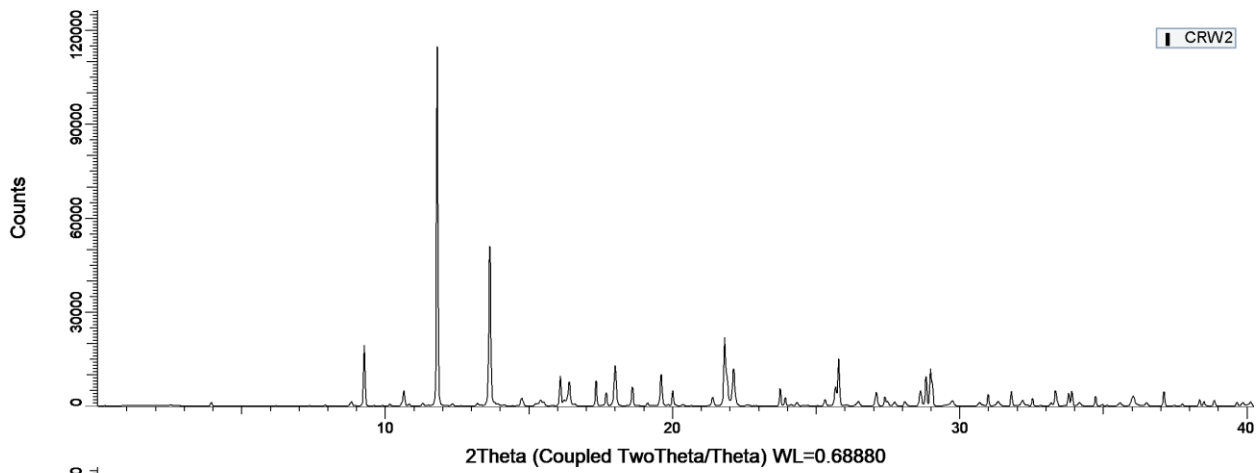
CR16 – bad data



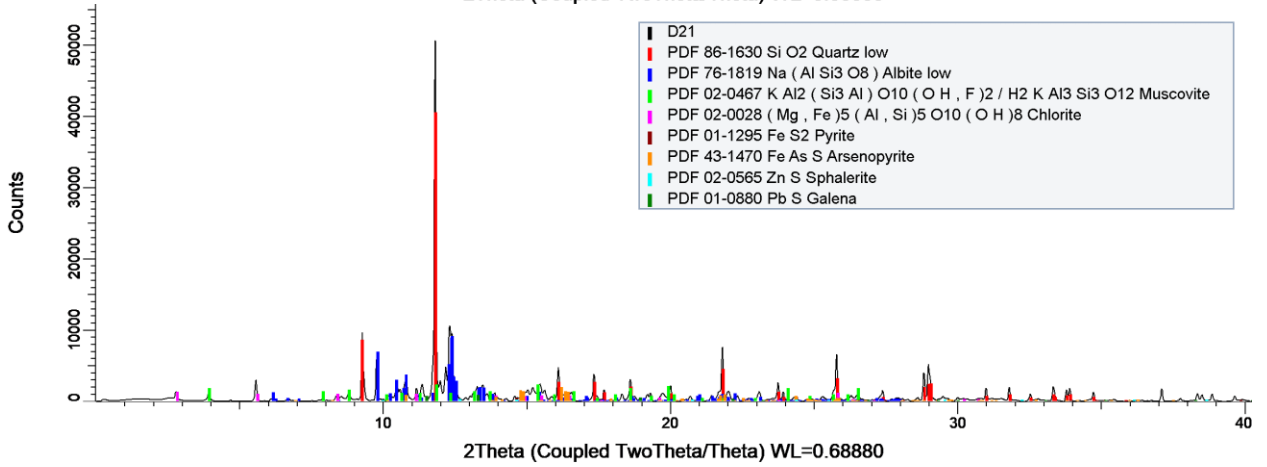
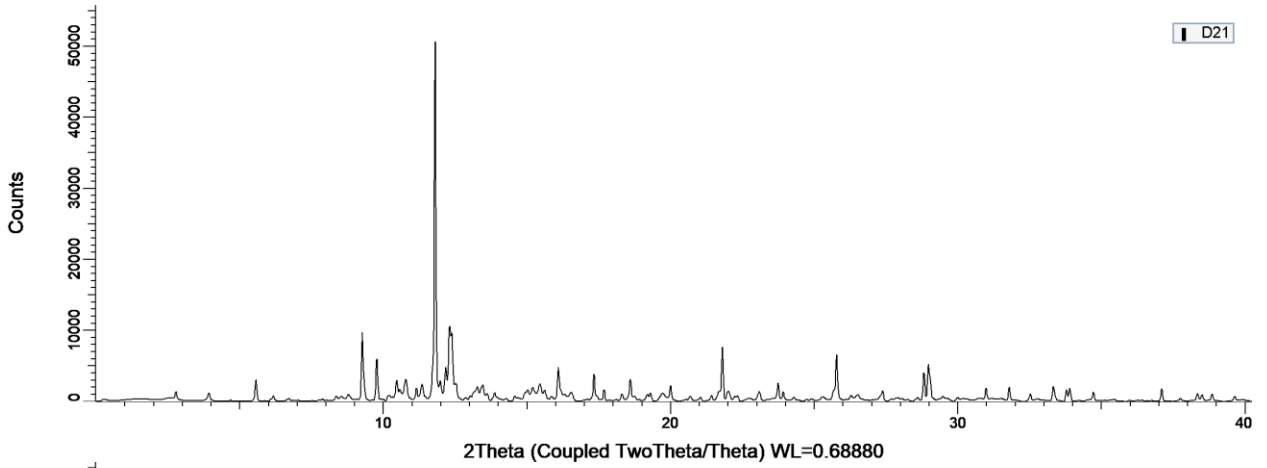
CRW1



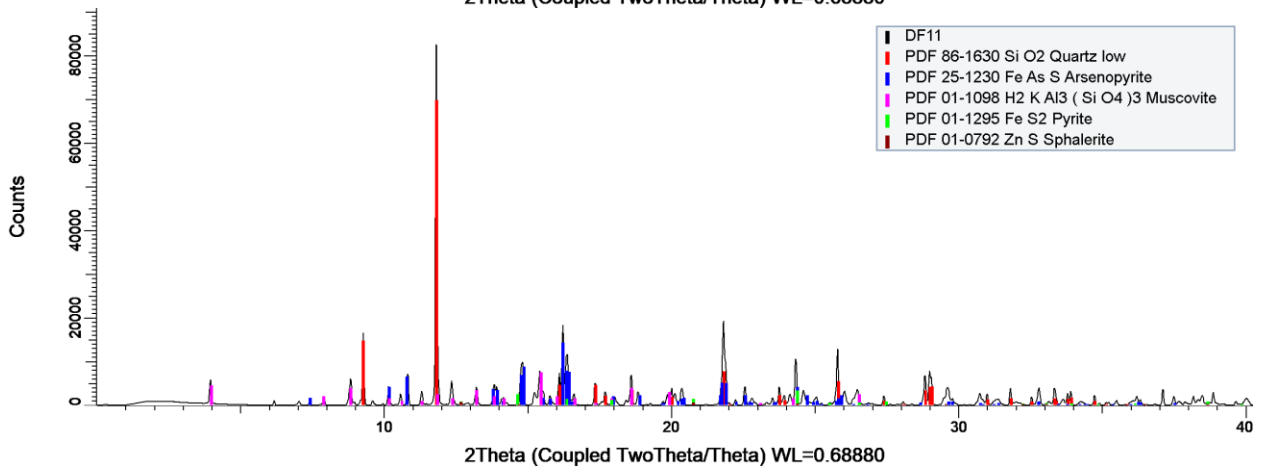
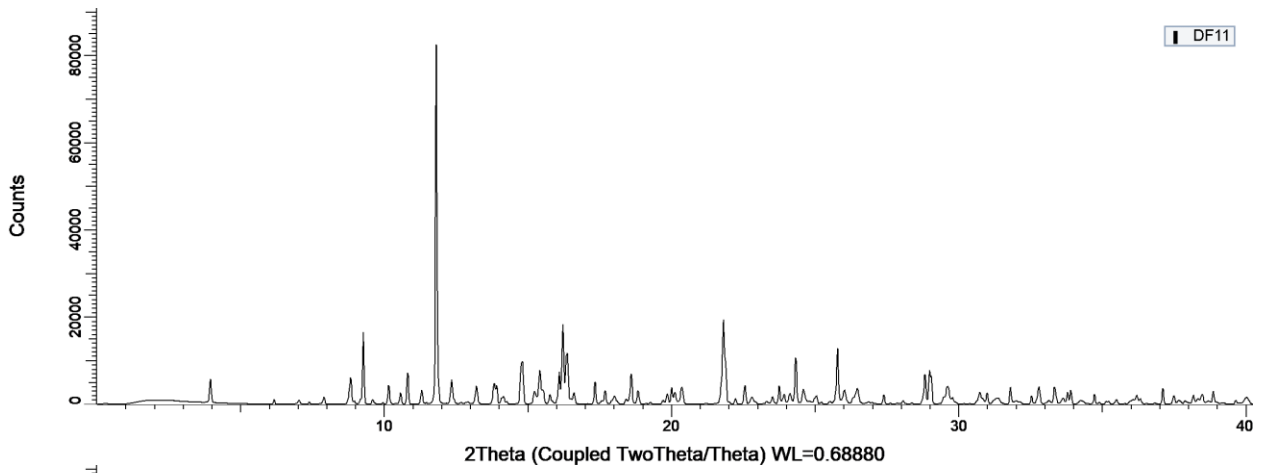
CRW2



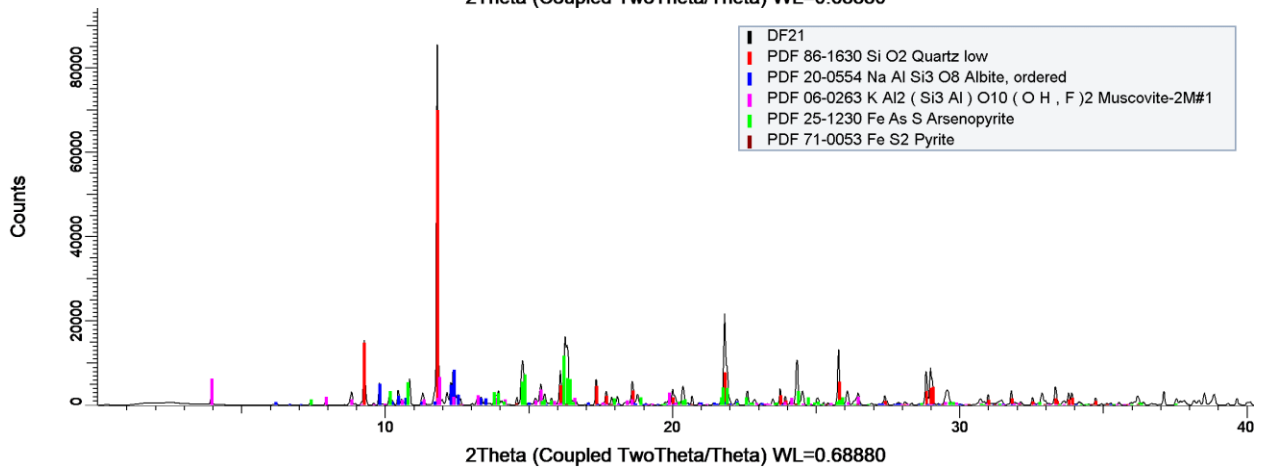
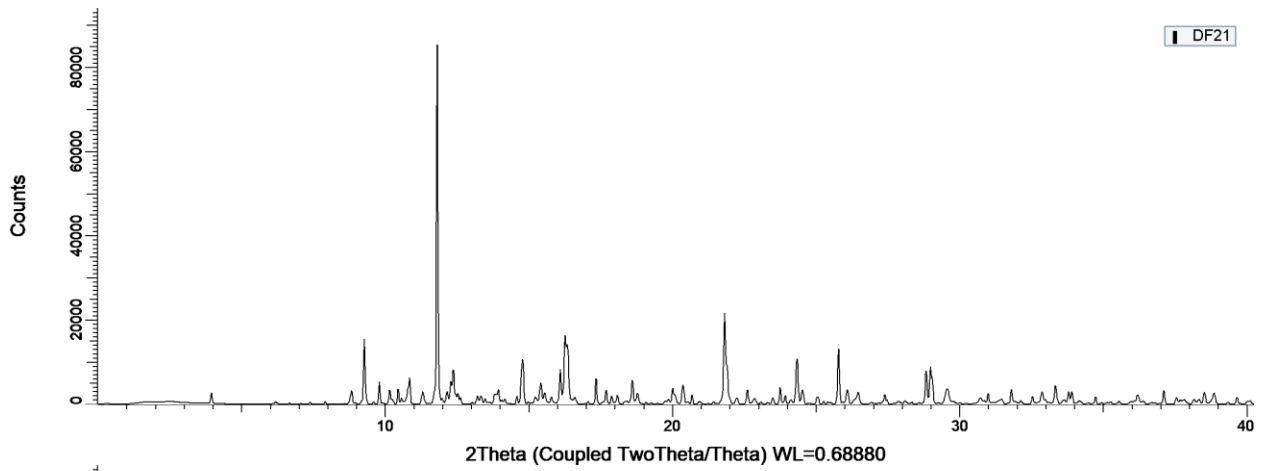
D21



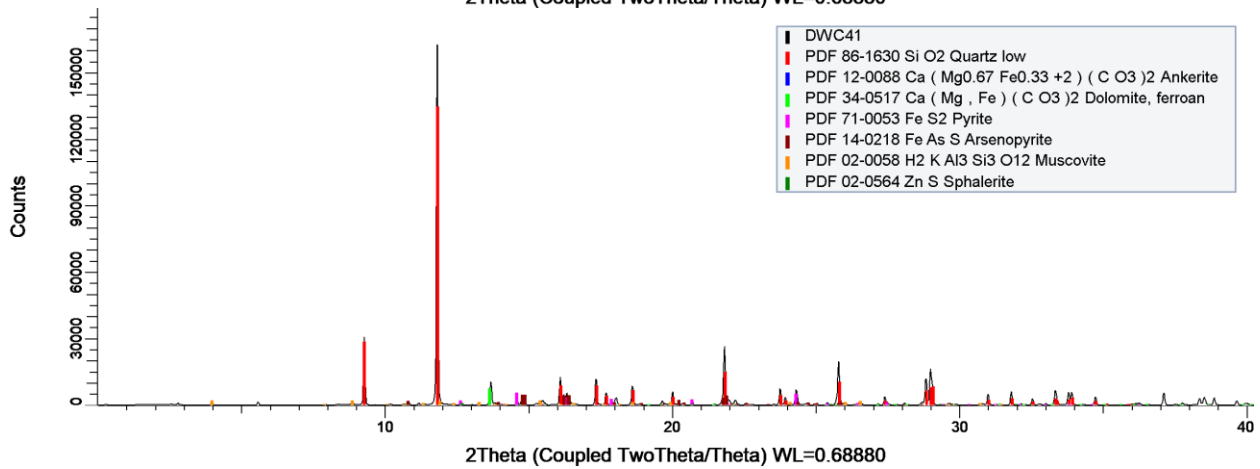
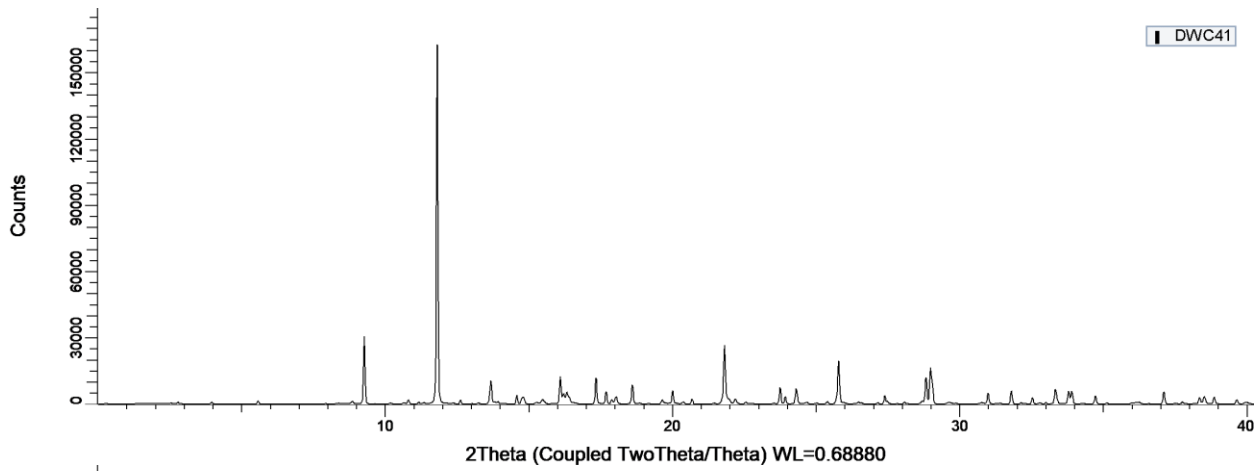
DF11



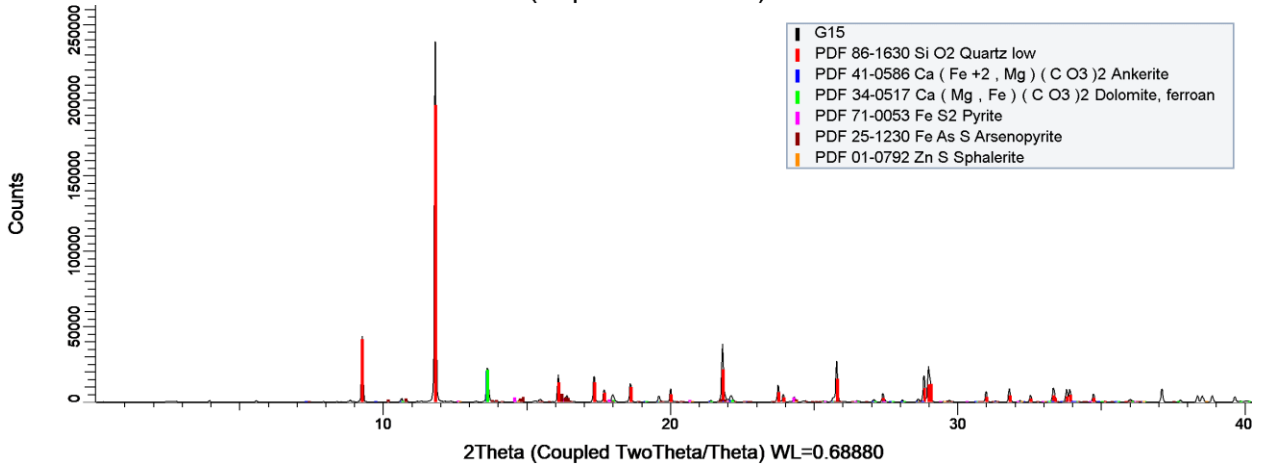
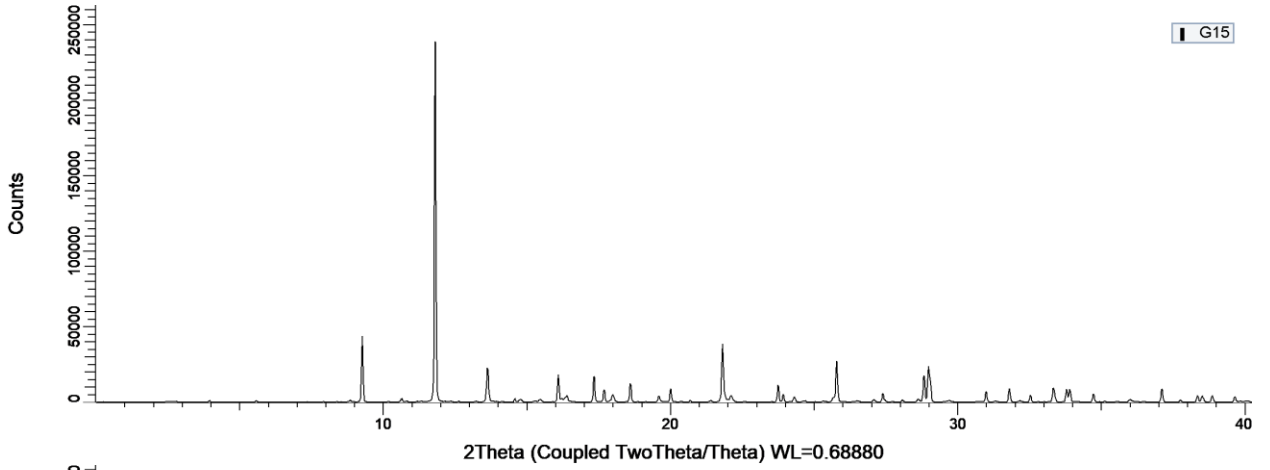
DF21



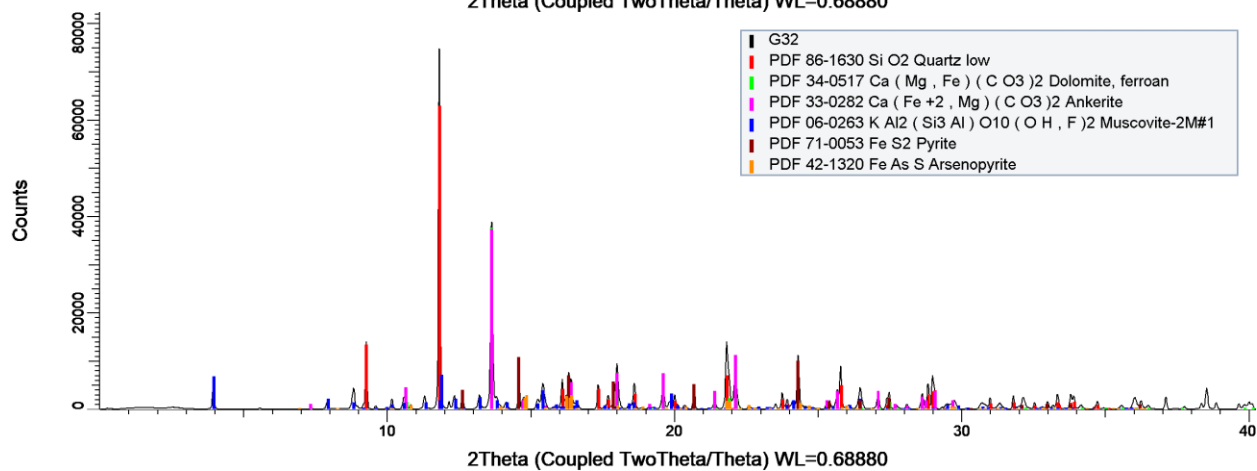
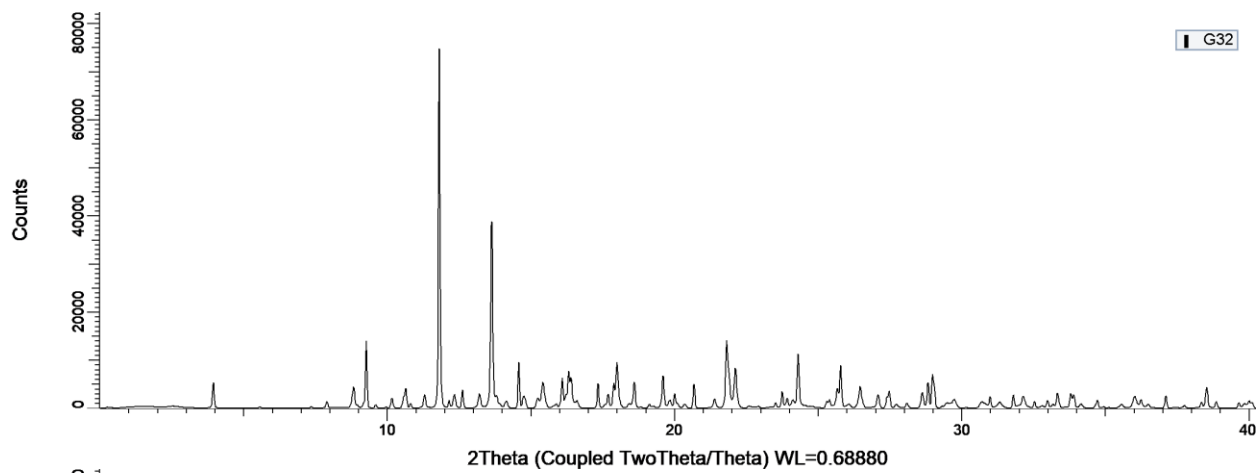
DWC41



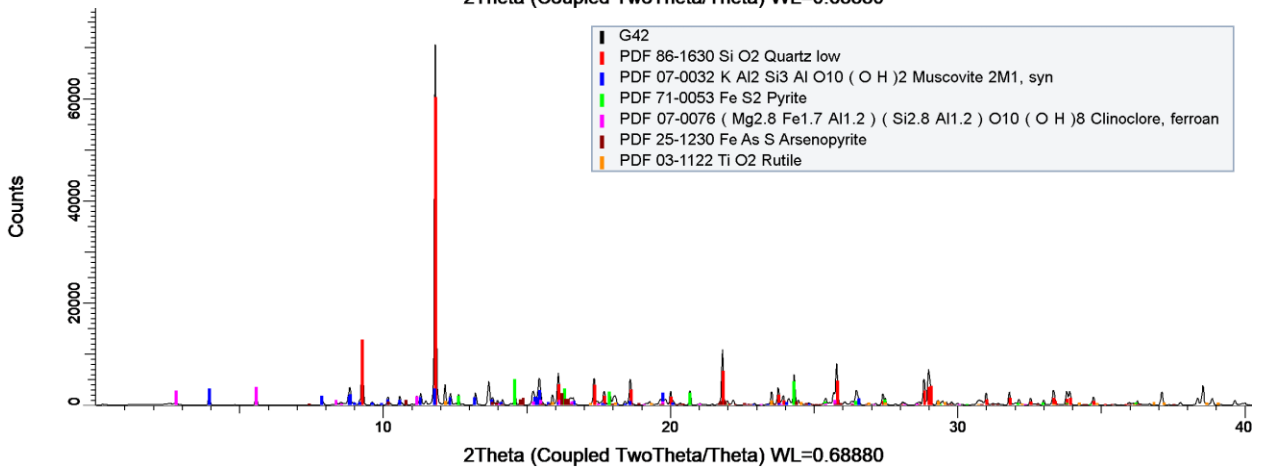
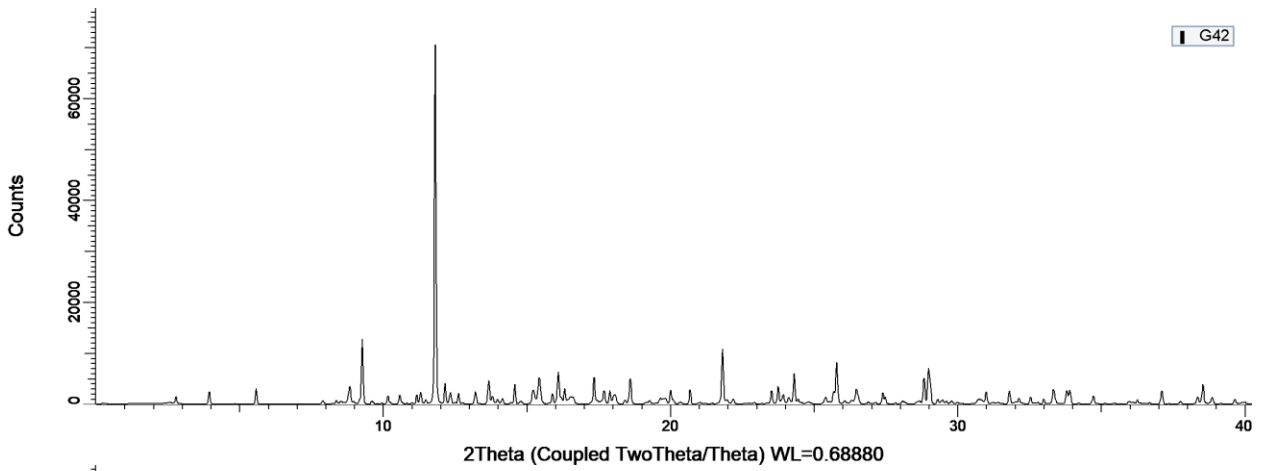
G15



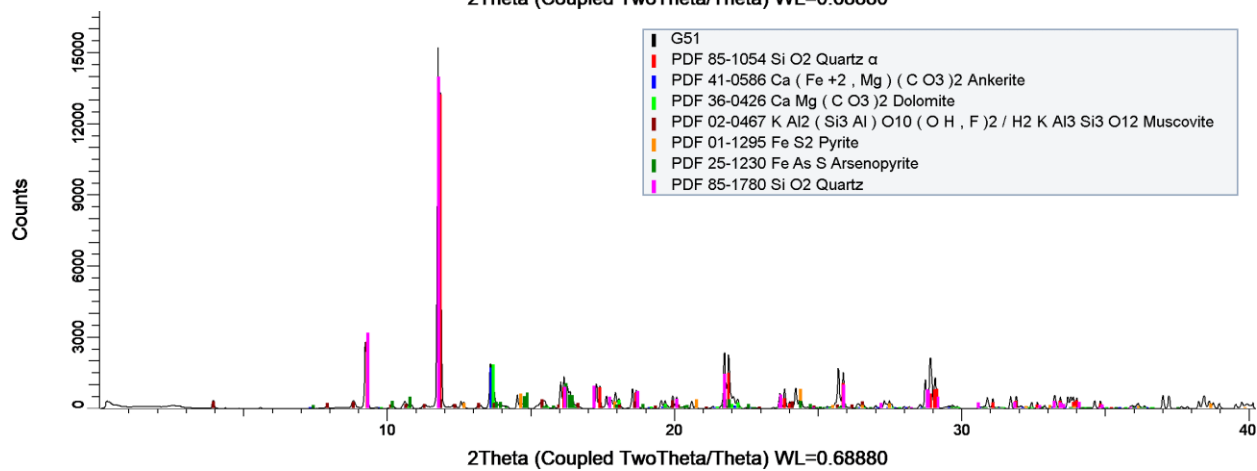
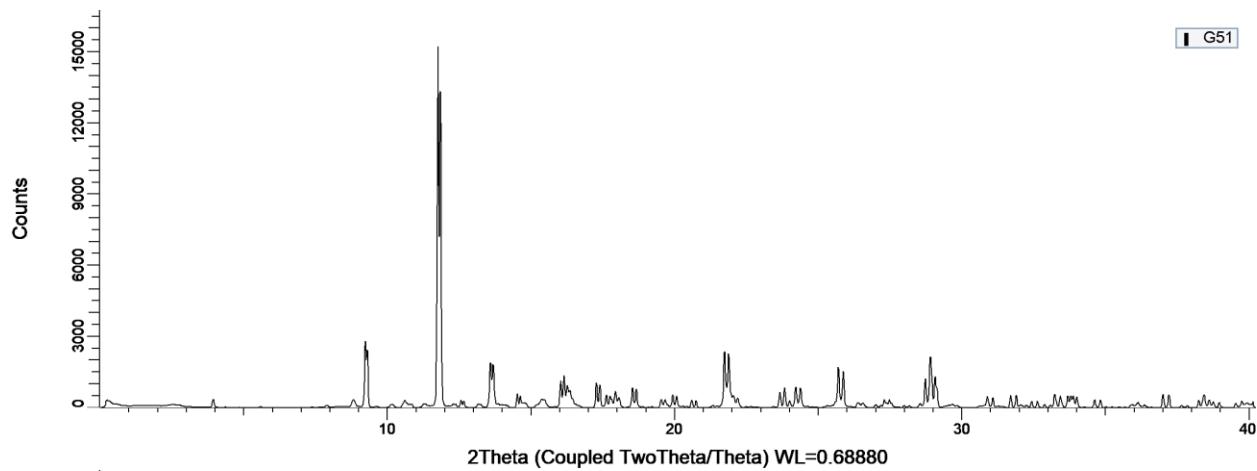
G32



G42

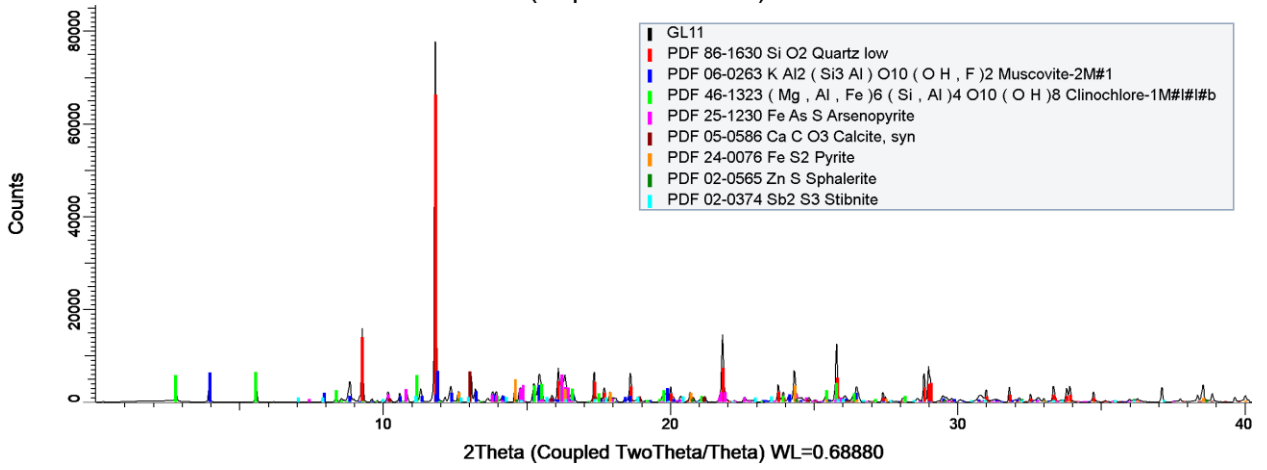
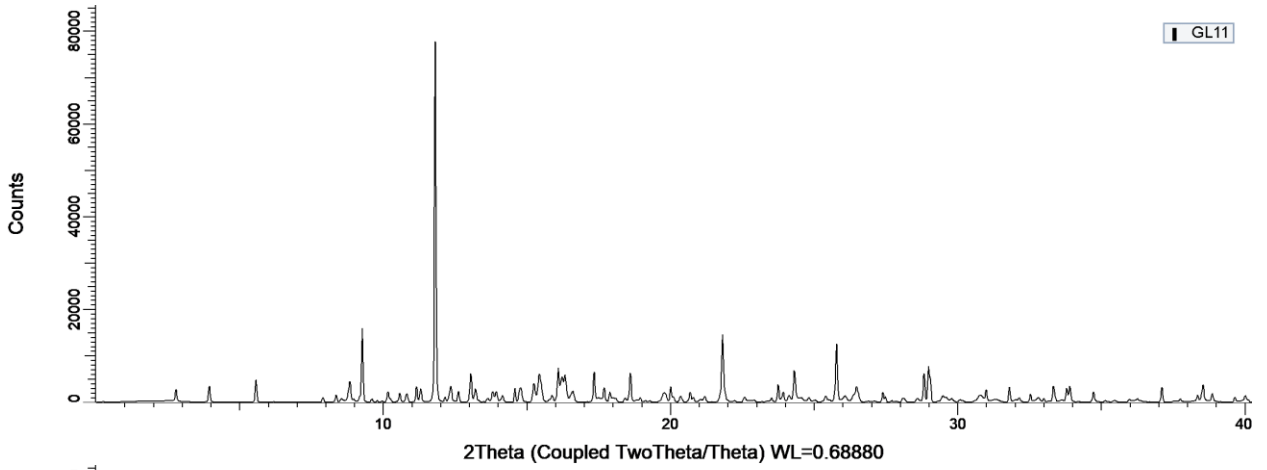


G51

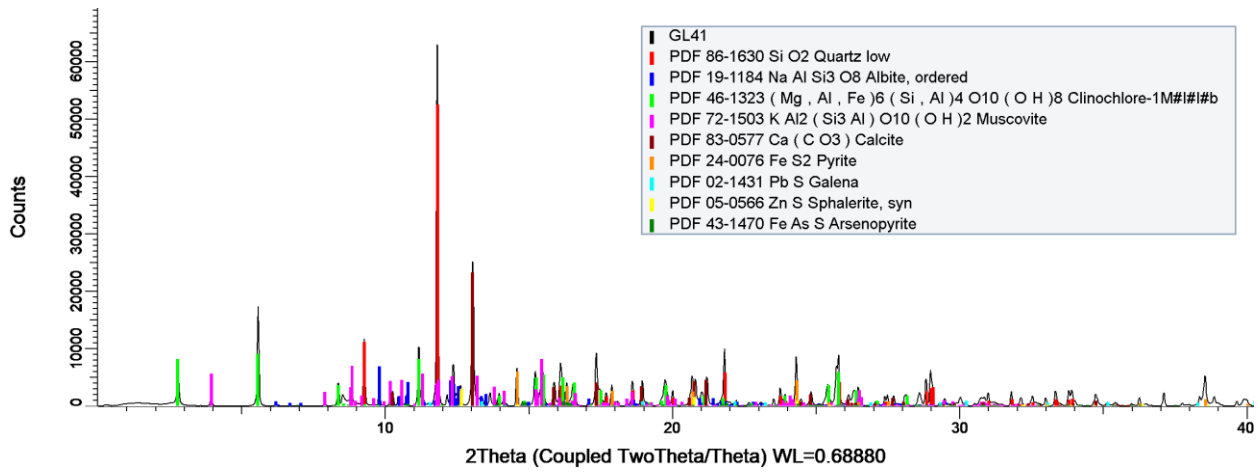
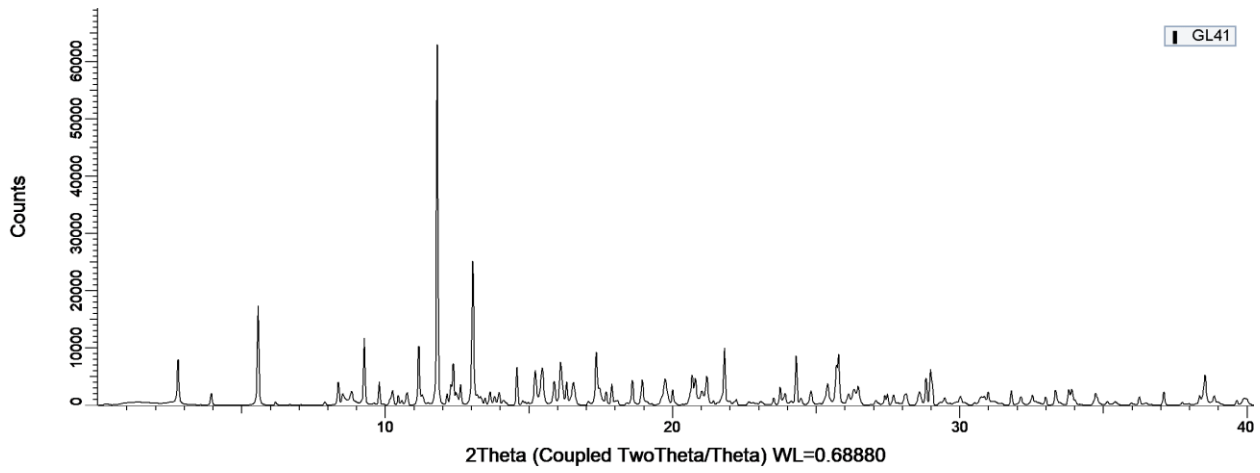


Note – remove 2nd qz

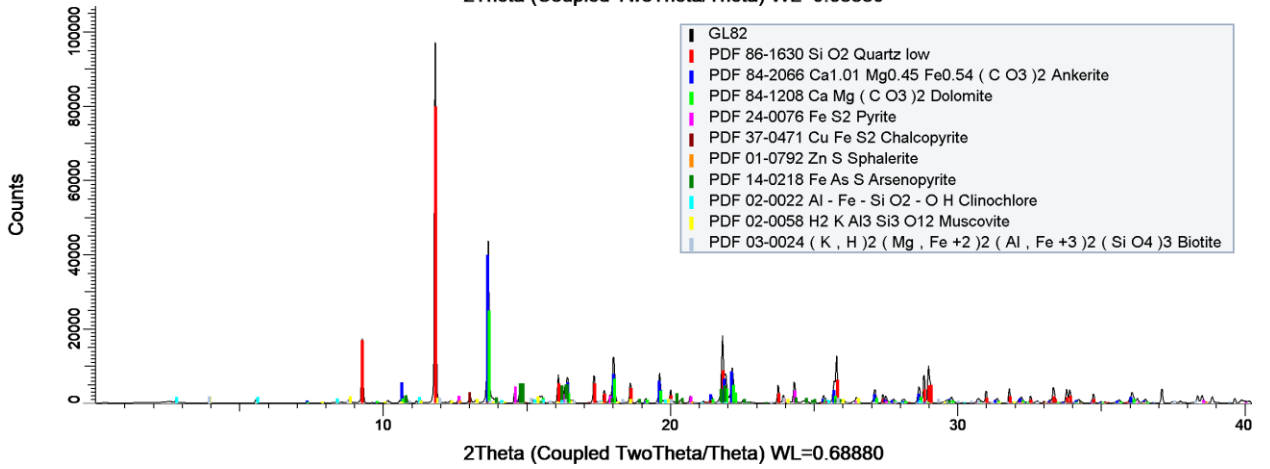
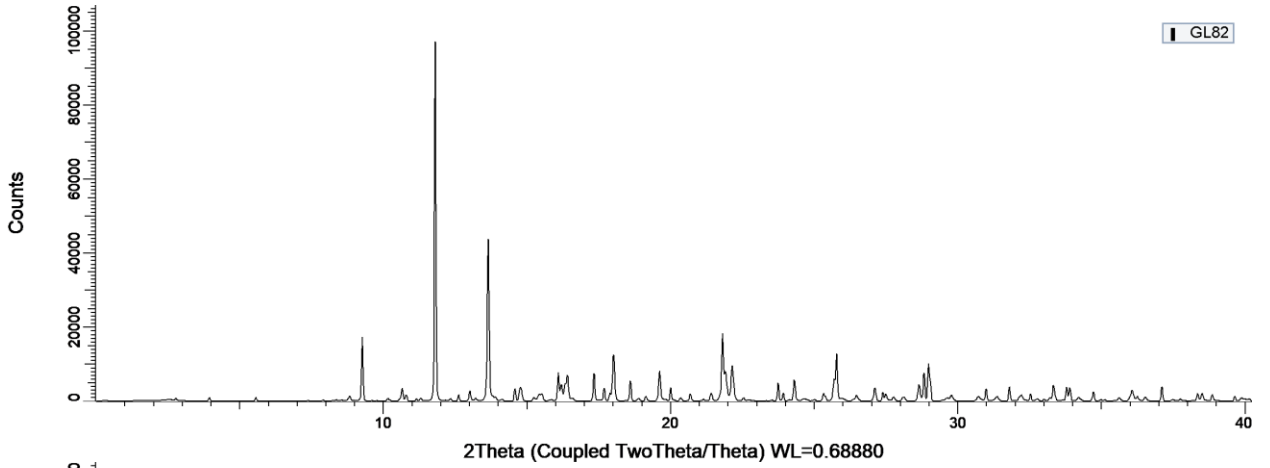
GL11



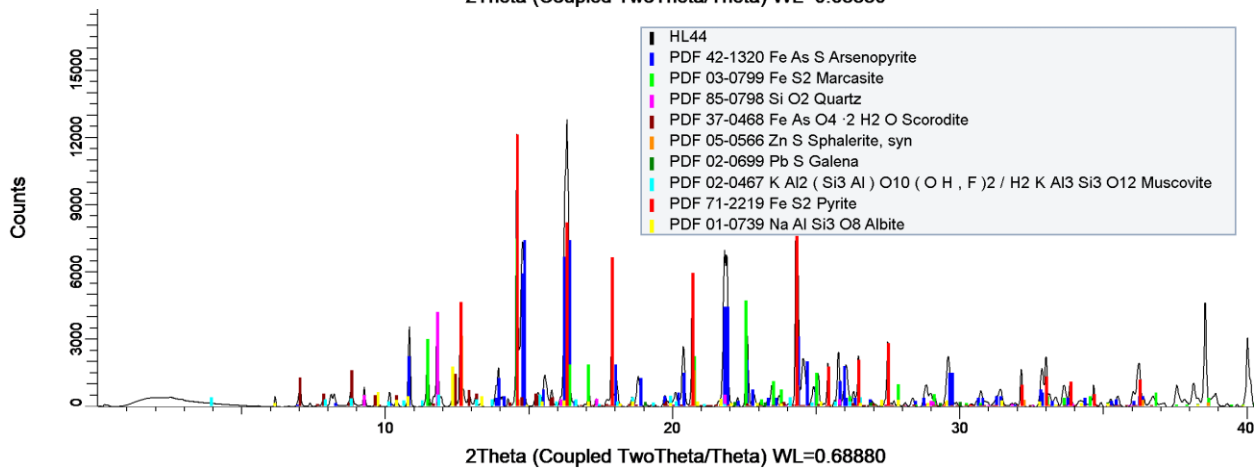
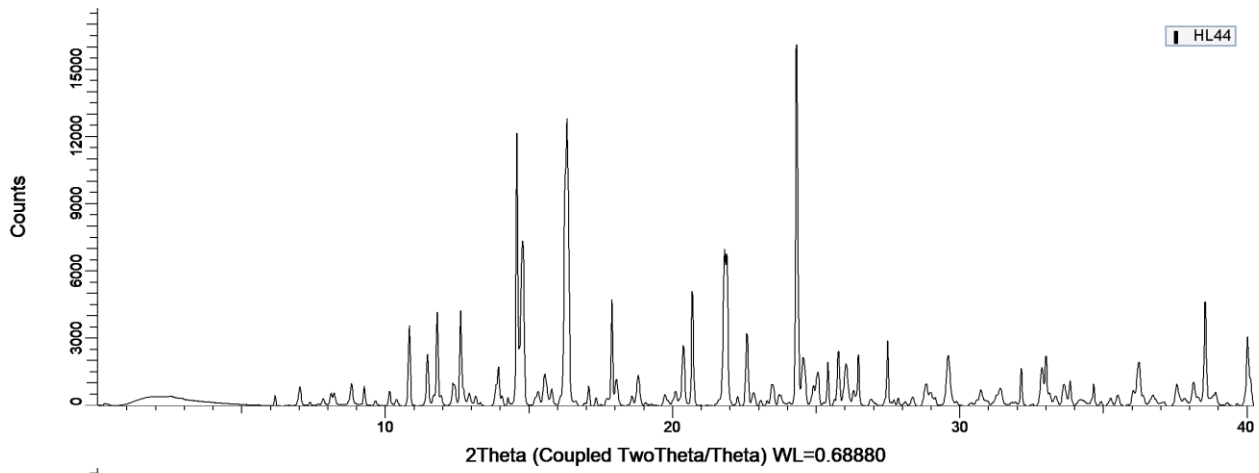
GL41



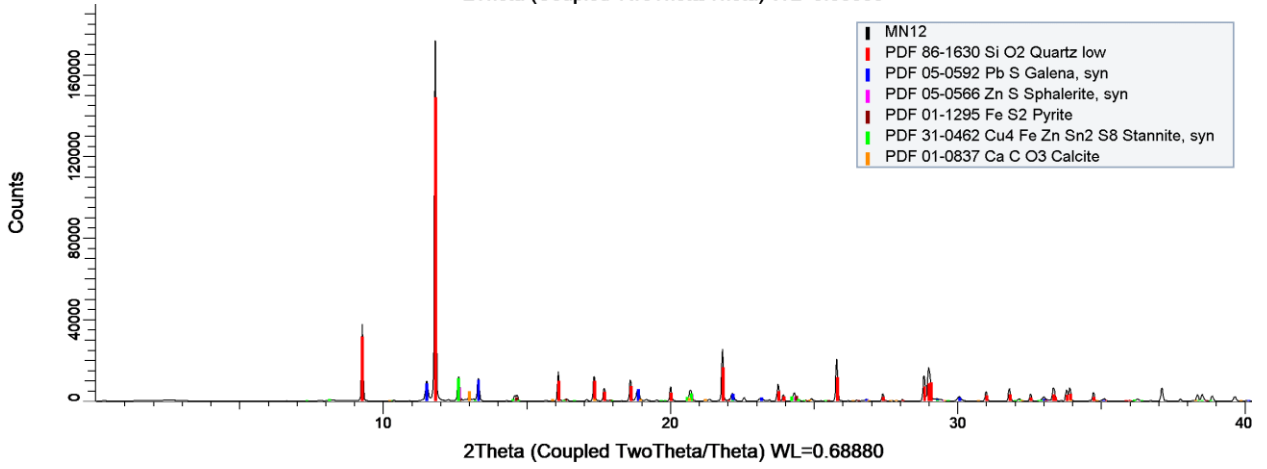
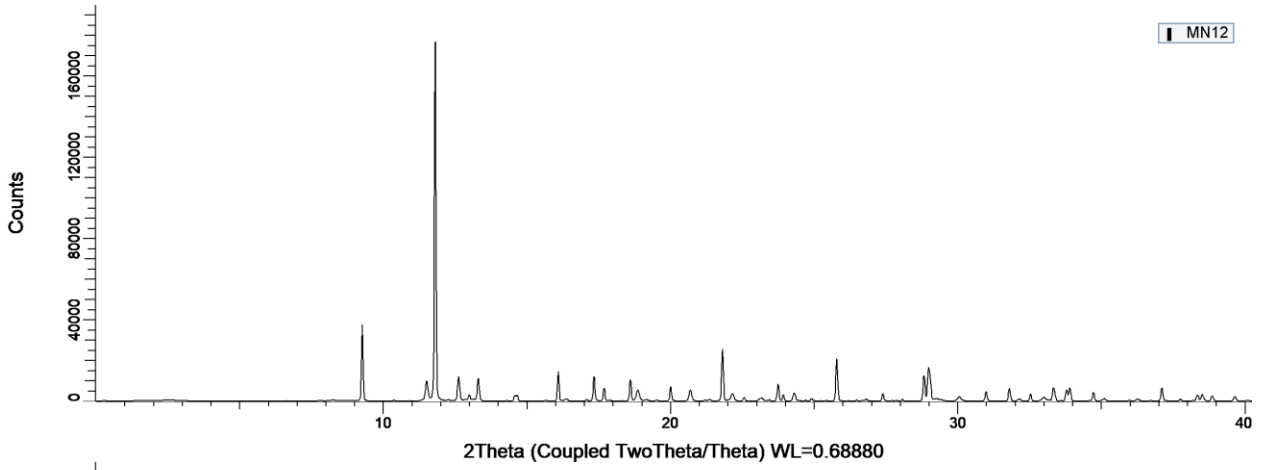
GL82



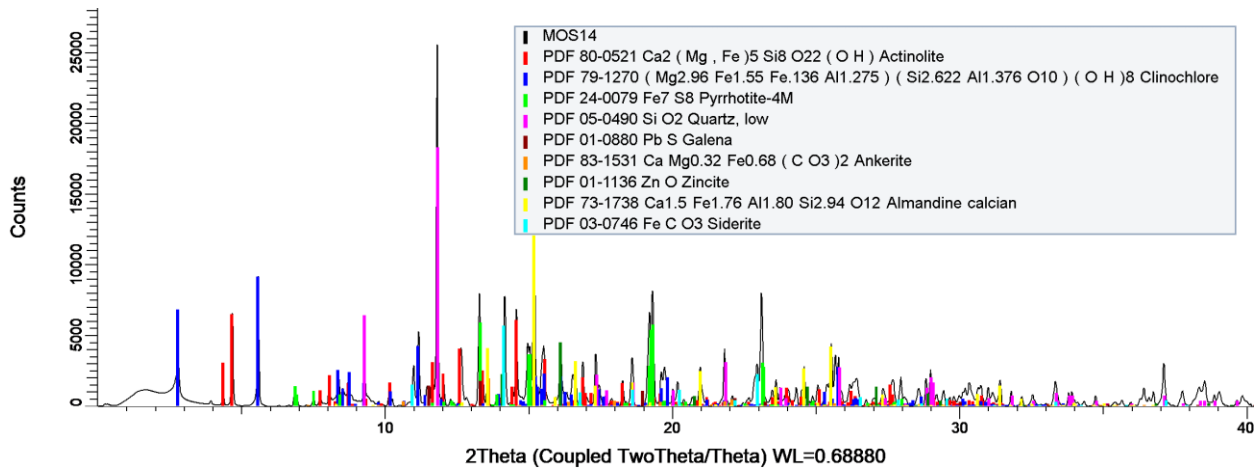
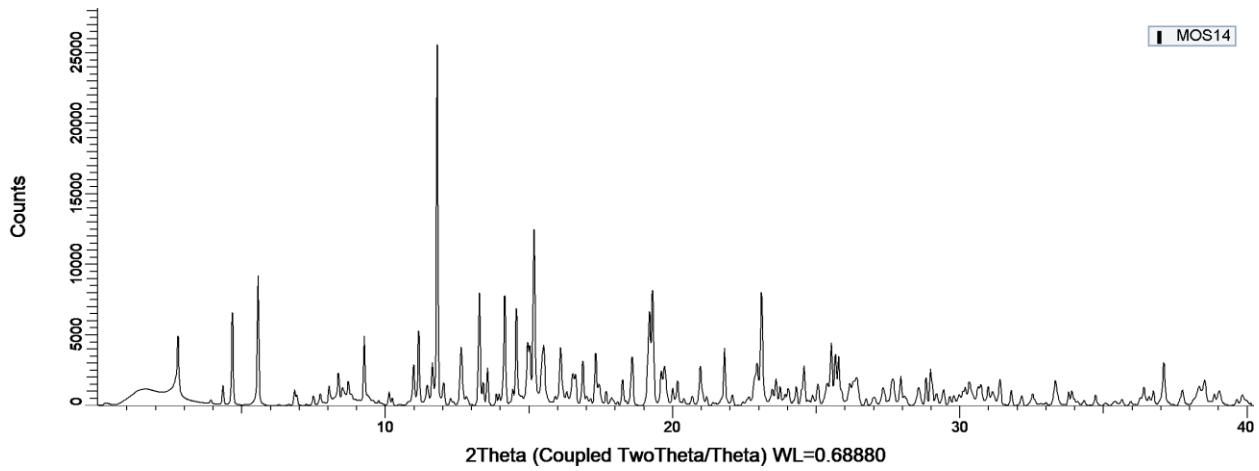
HL44



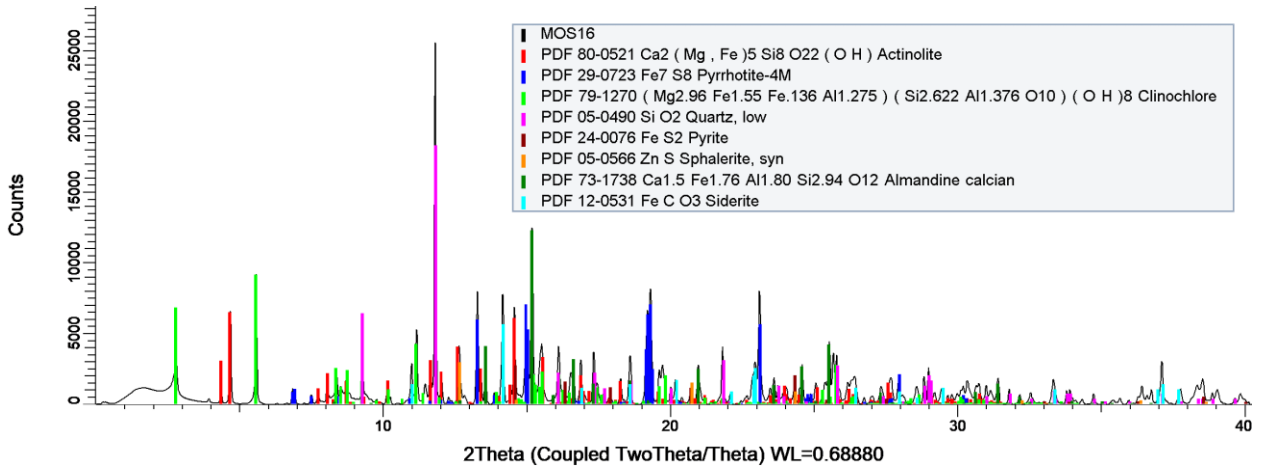
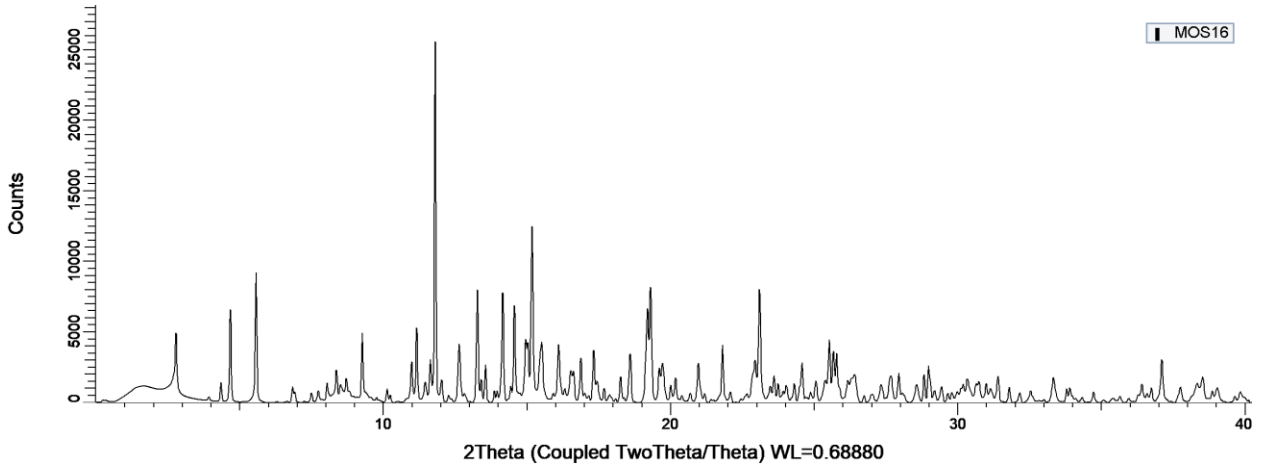
MN12



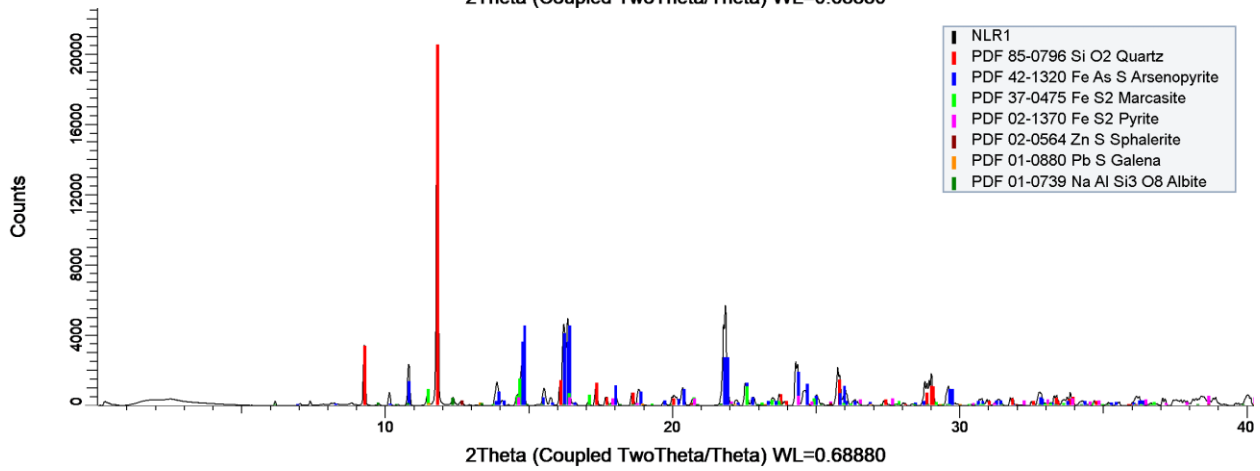
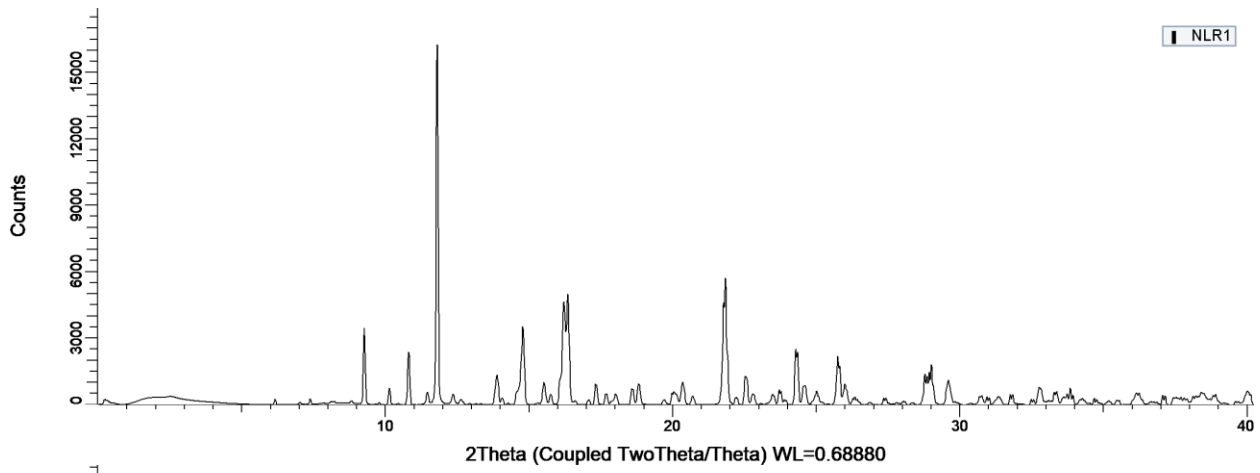
MOS14



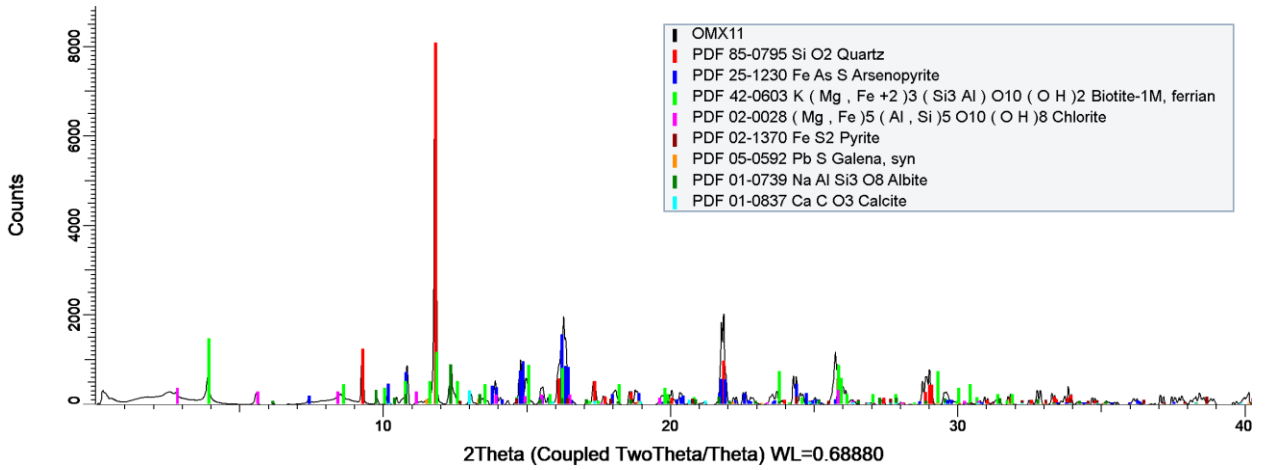
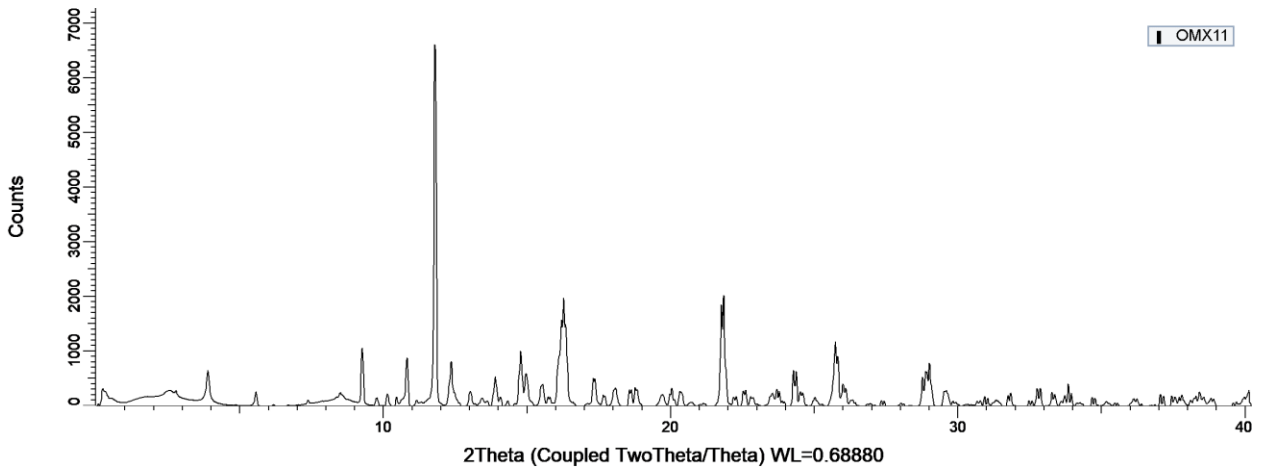
MOS16



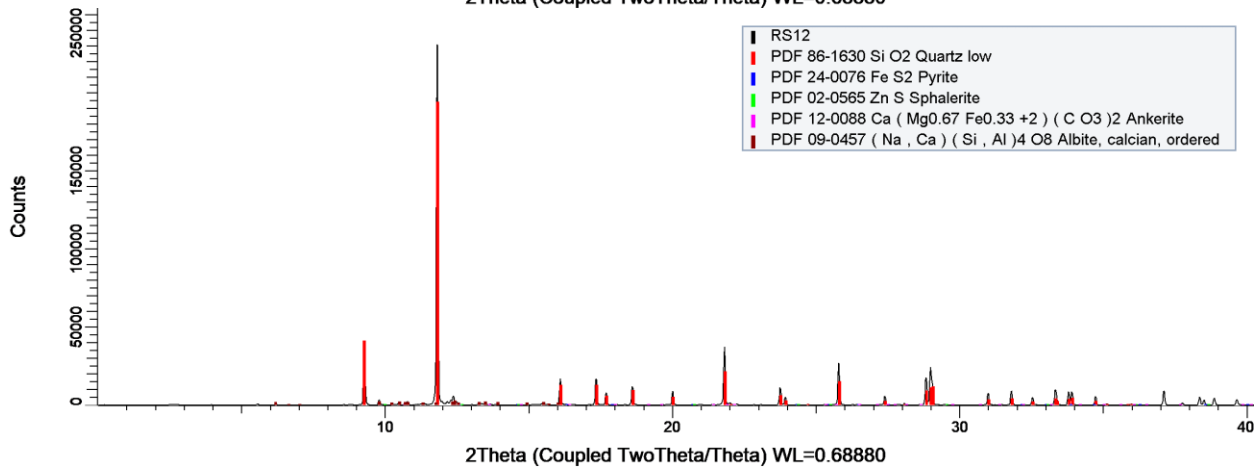
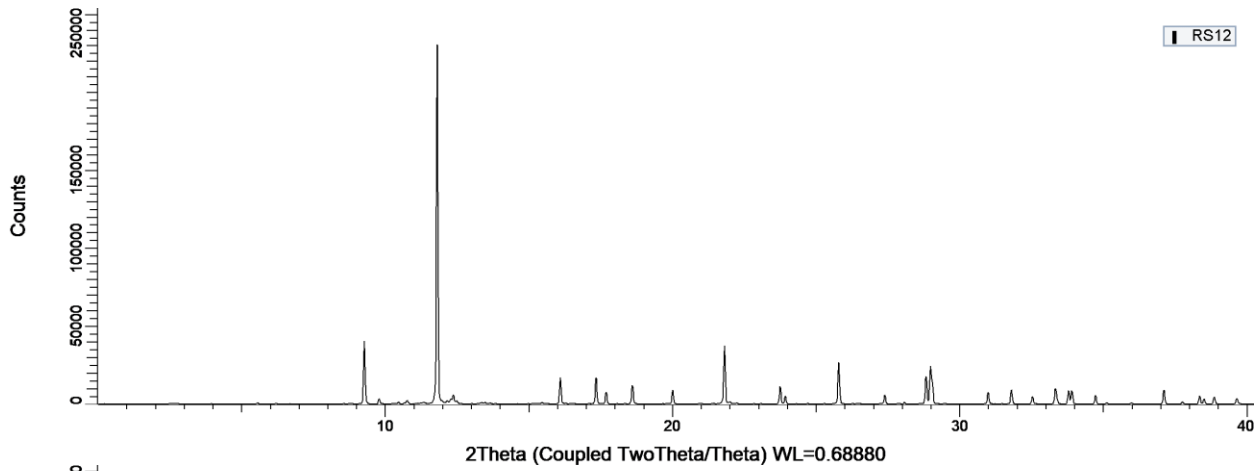
NLR1



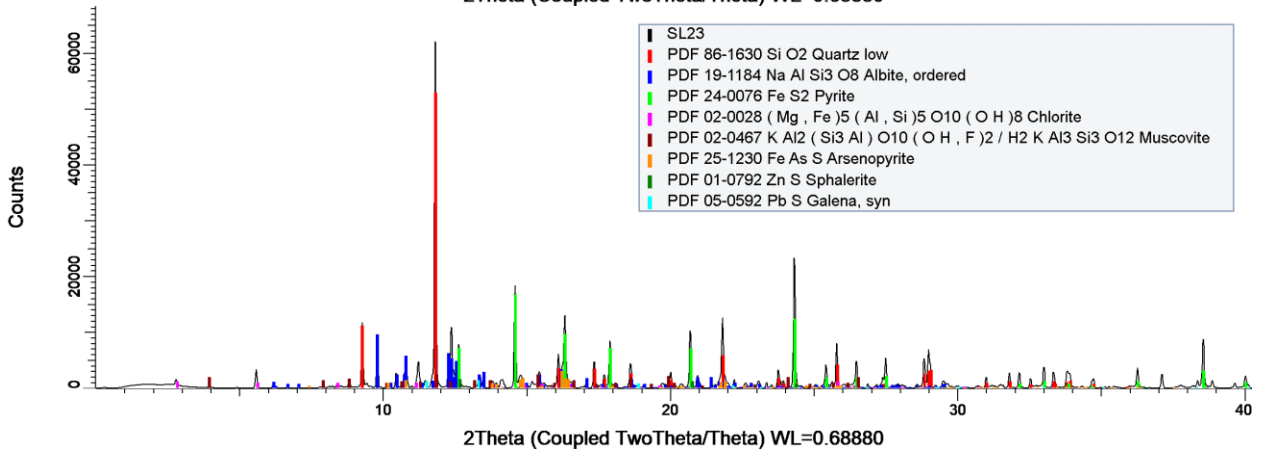
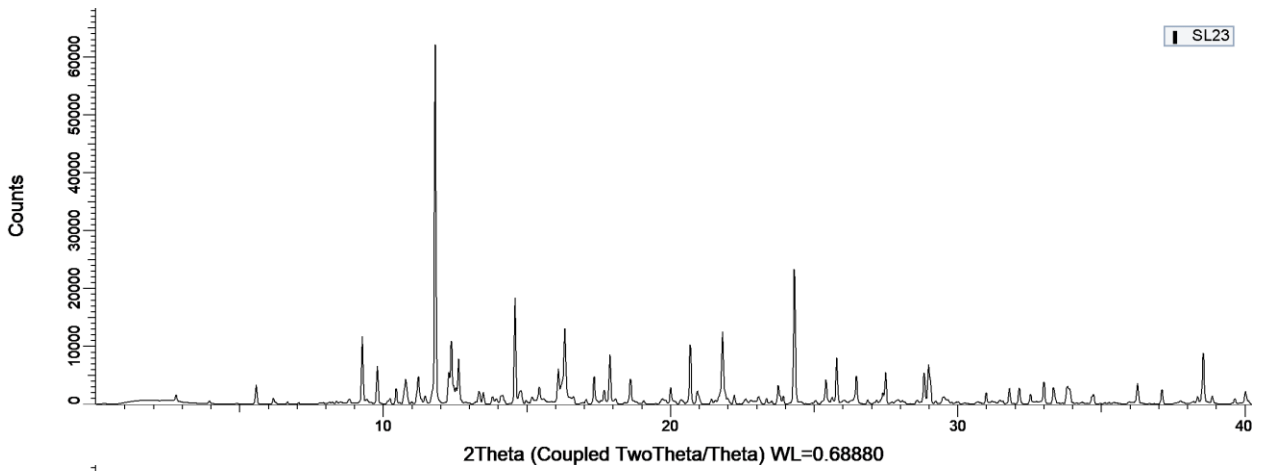
OMX11



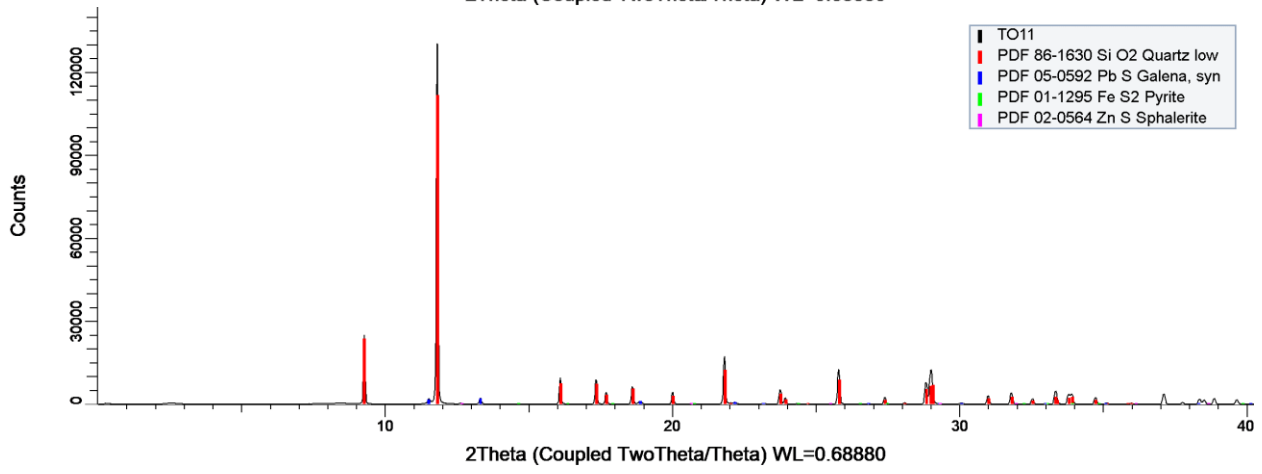
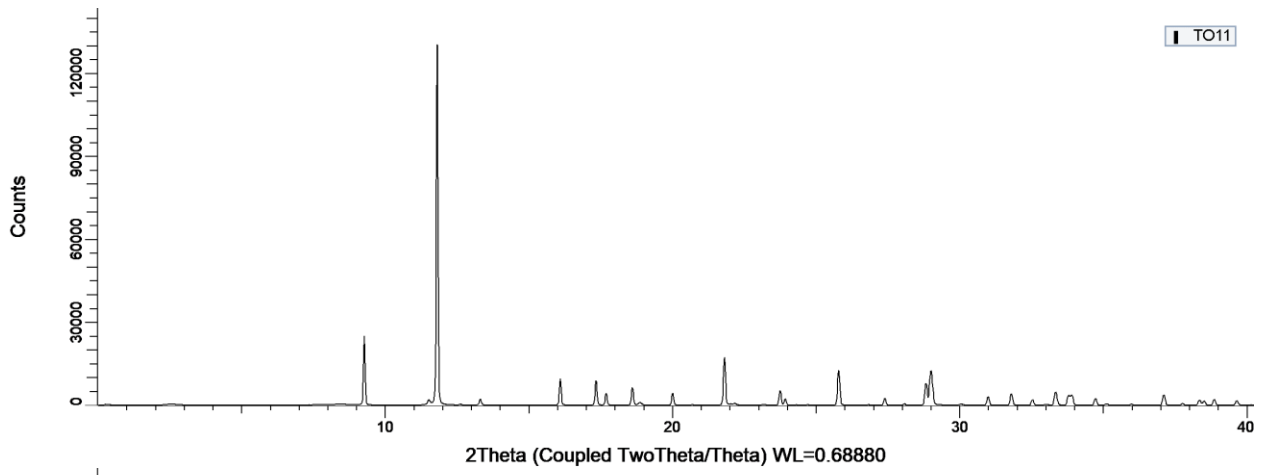
RS12



SL23

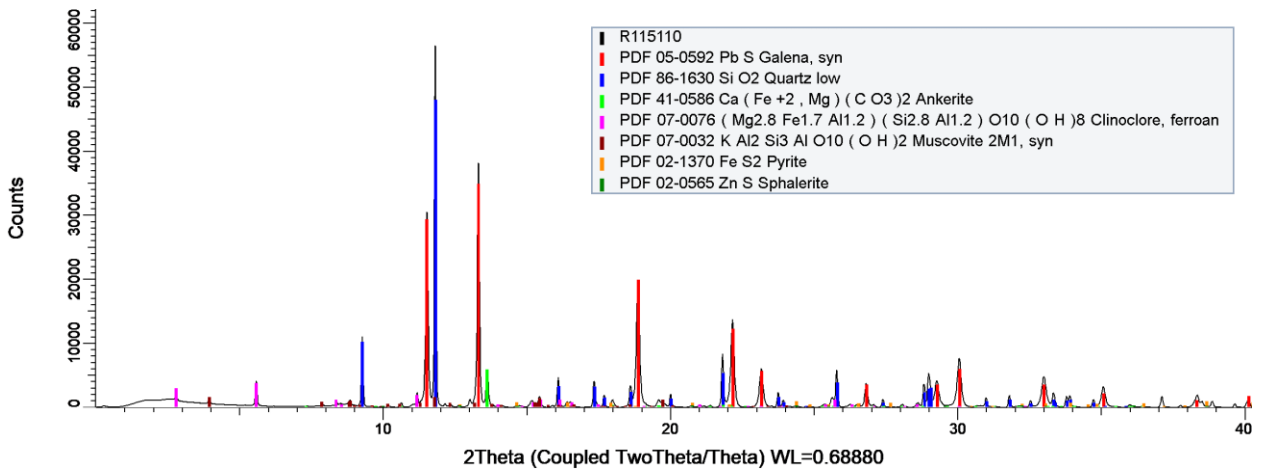
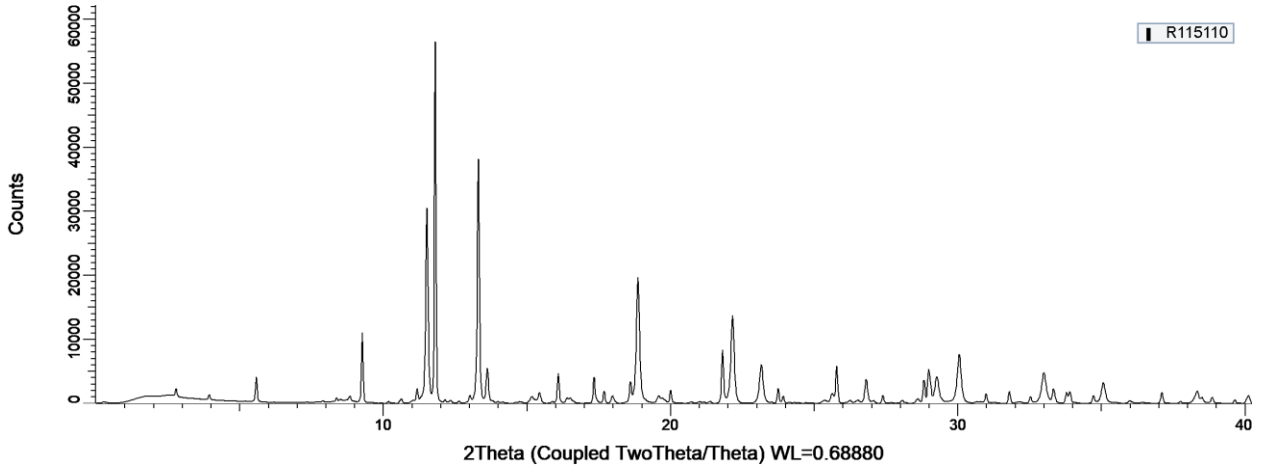


TO11

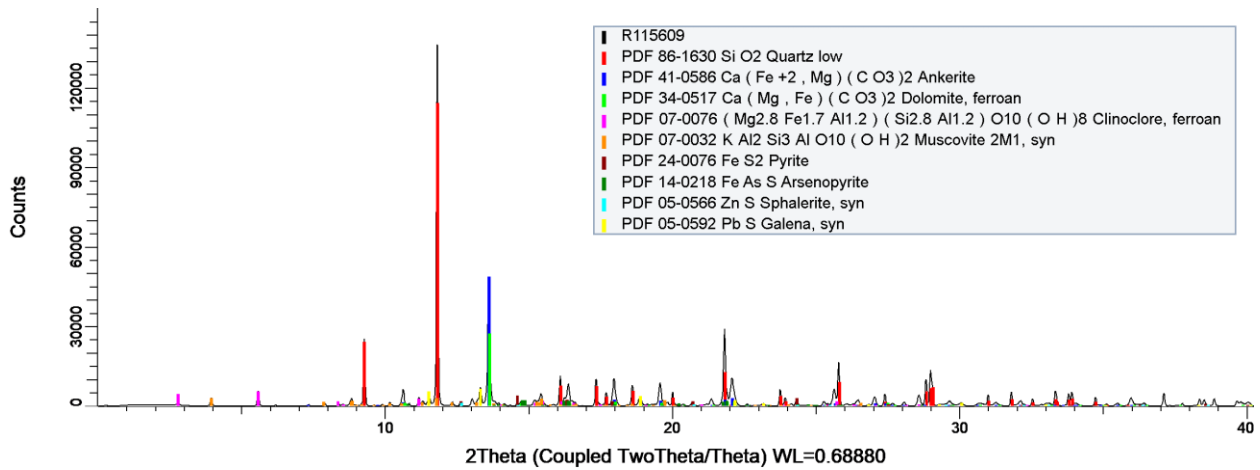
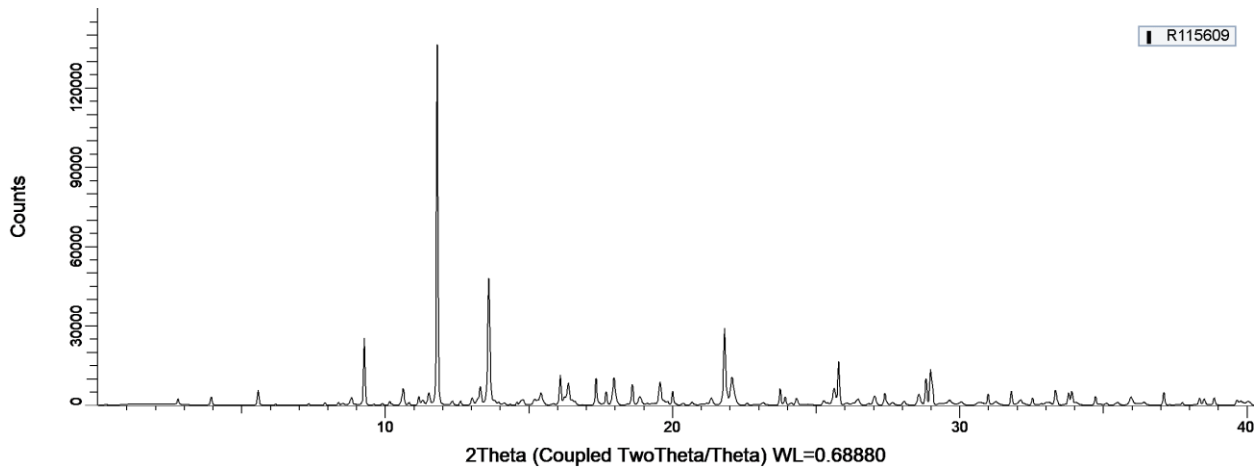


TerraX

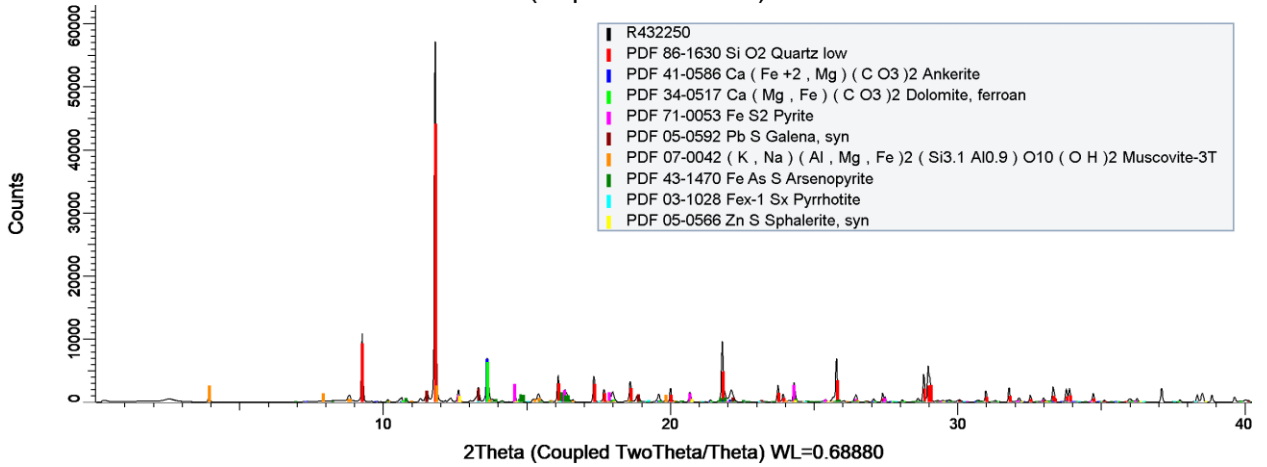
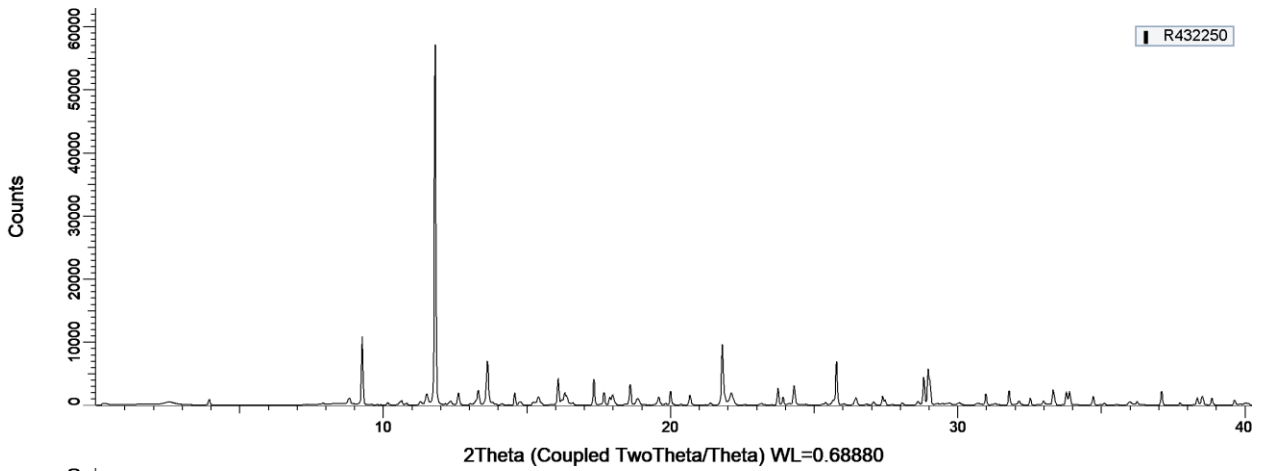
R115110



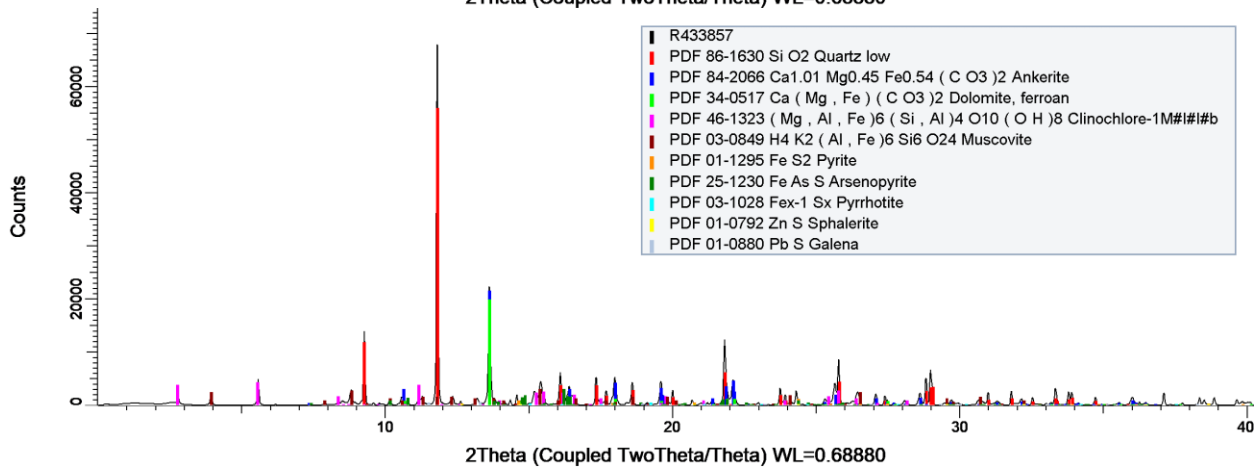
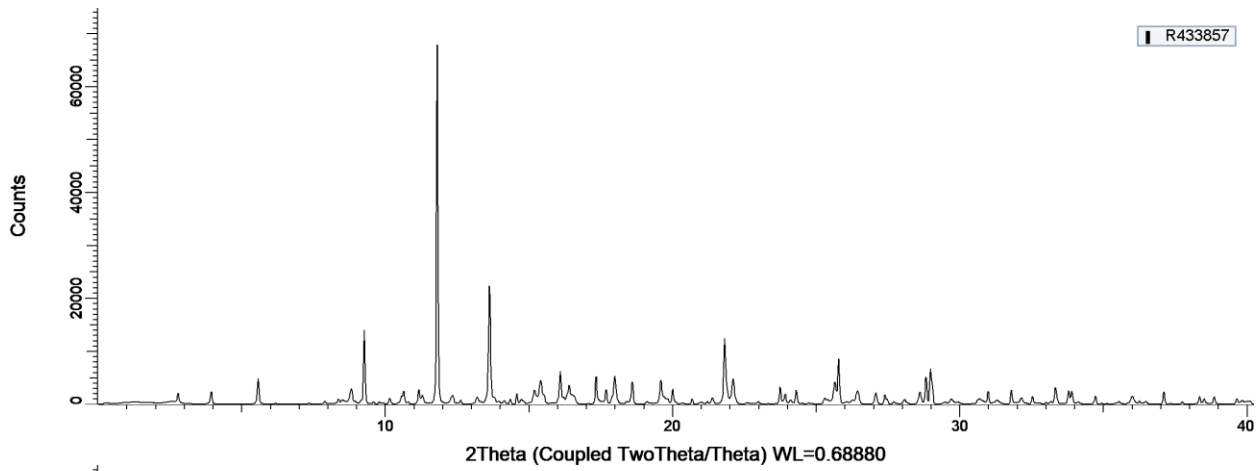
R115609



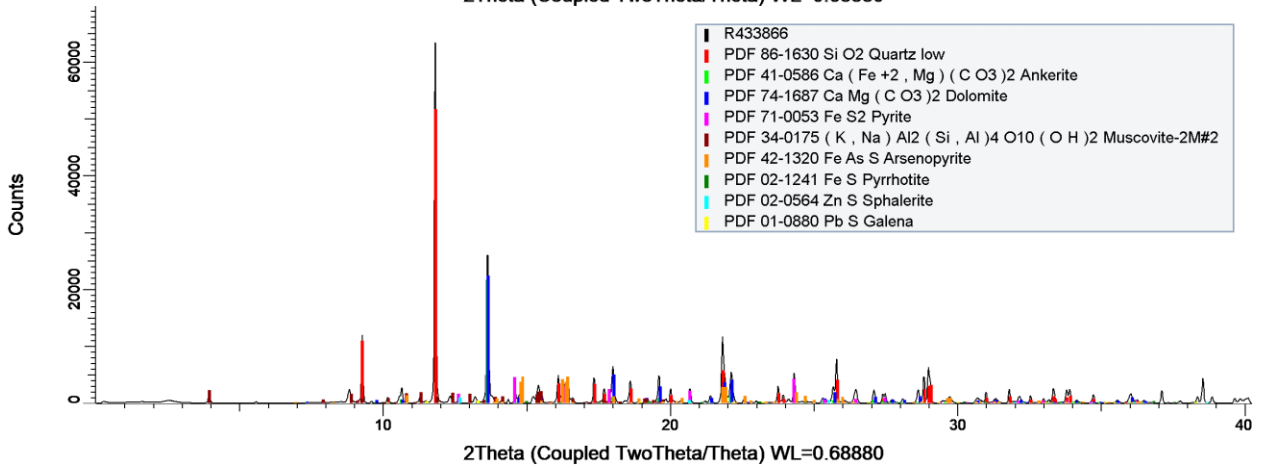
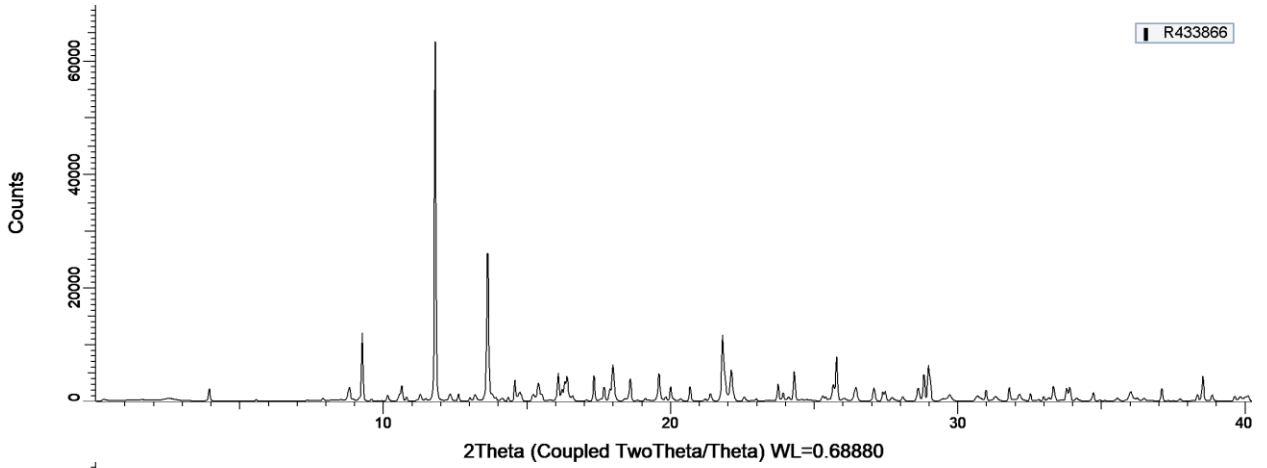
R432250



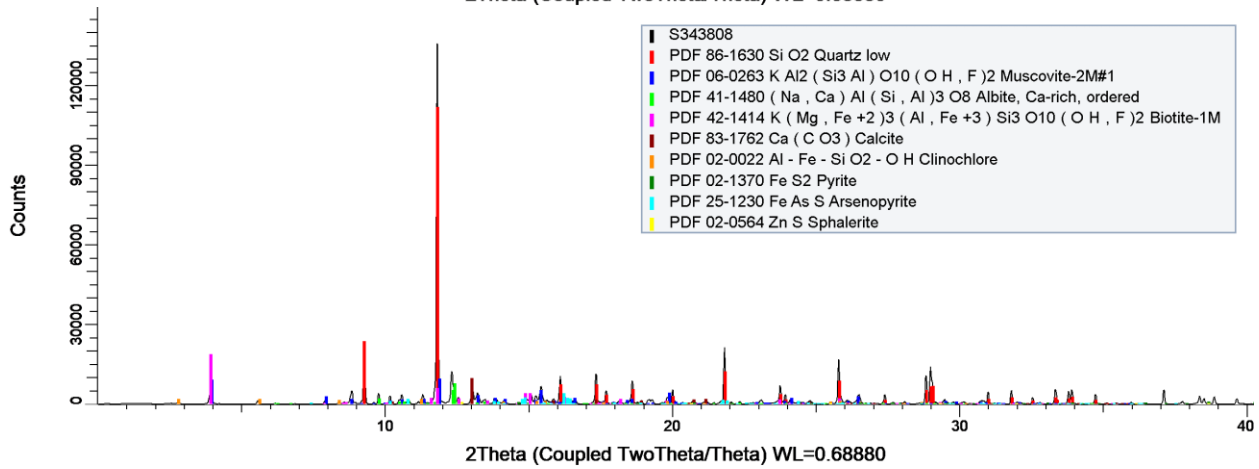
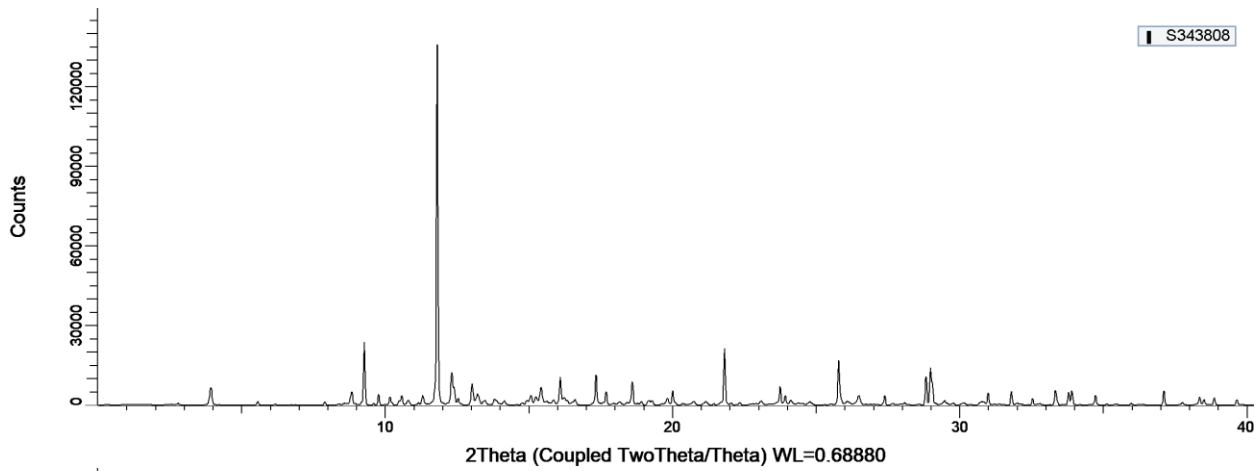
R433857



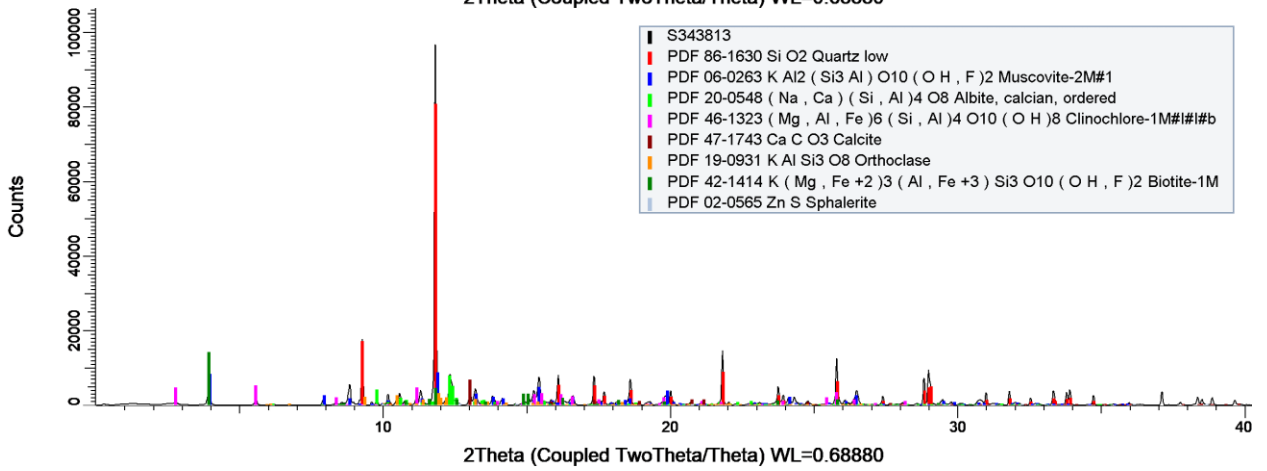
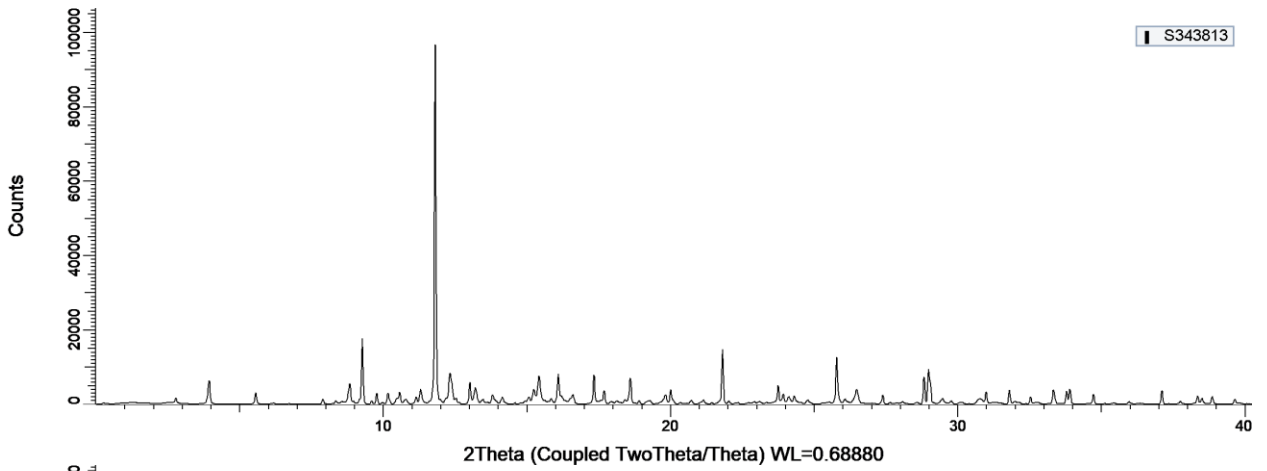
R433866

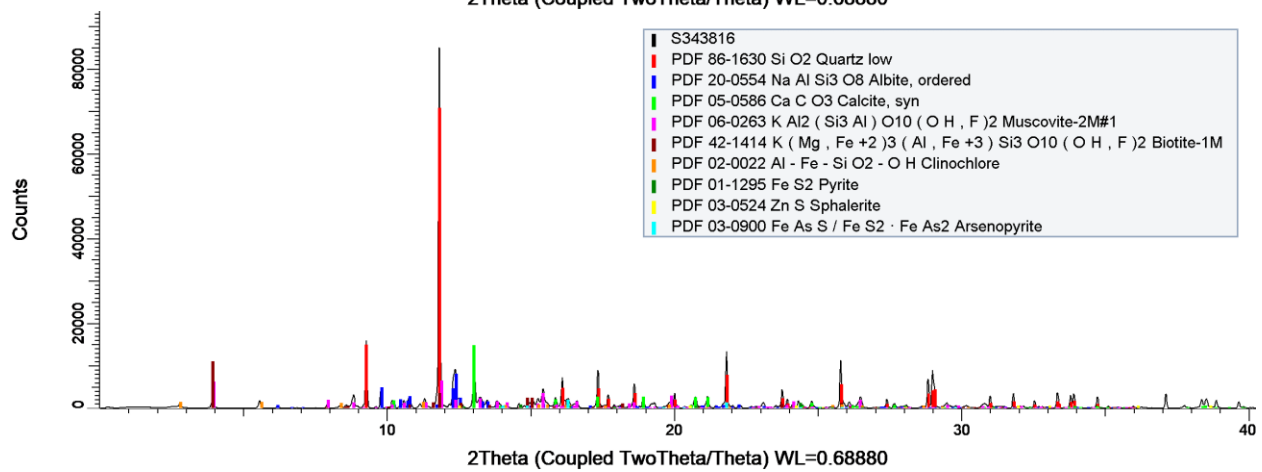
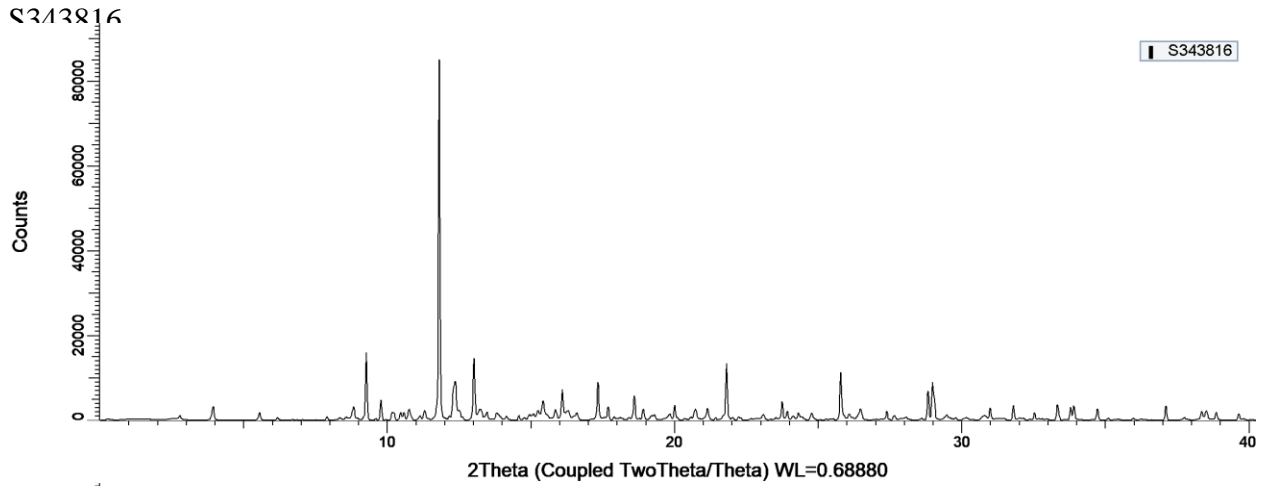


S343808

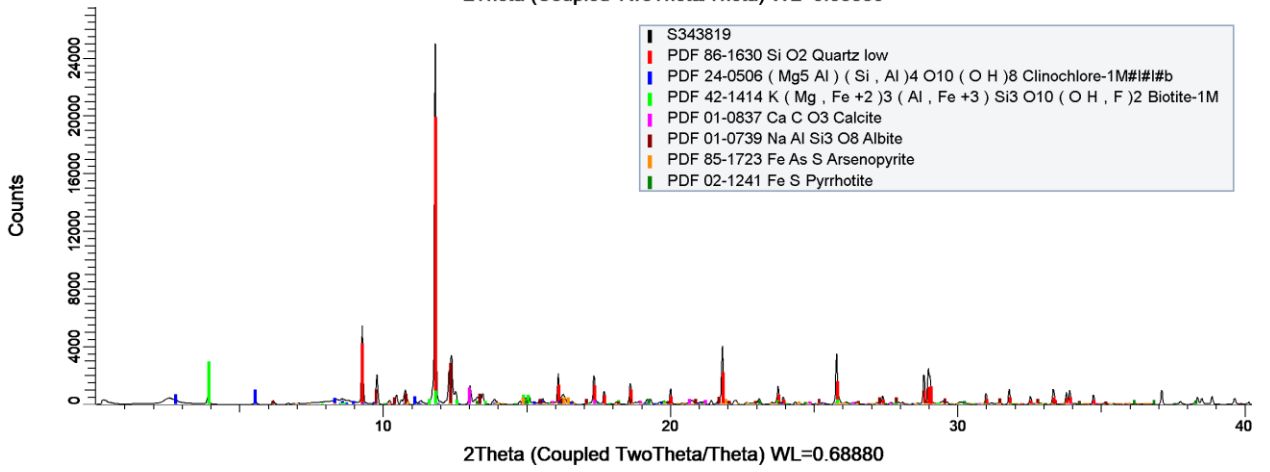
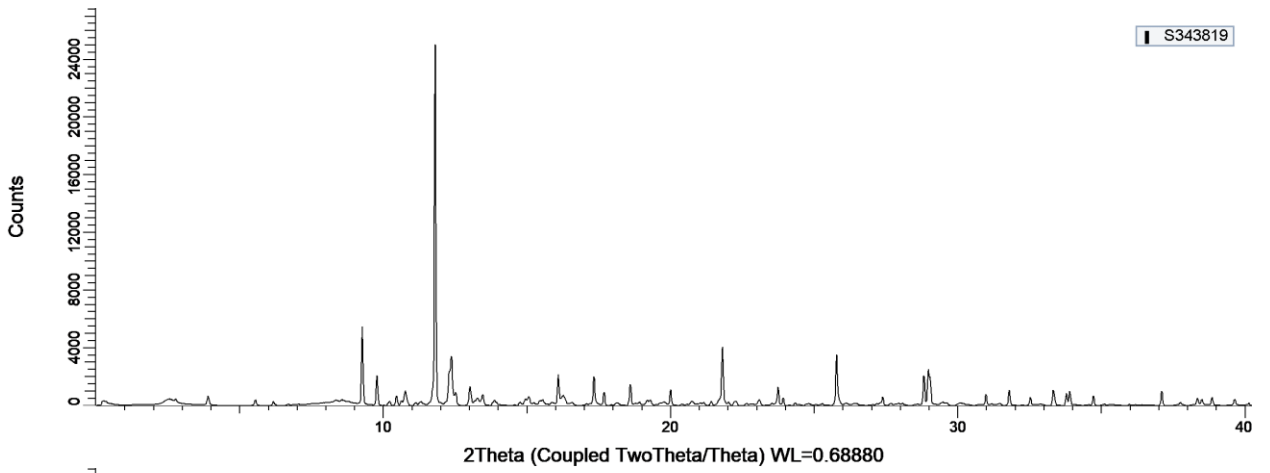


S343813

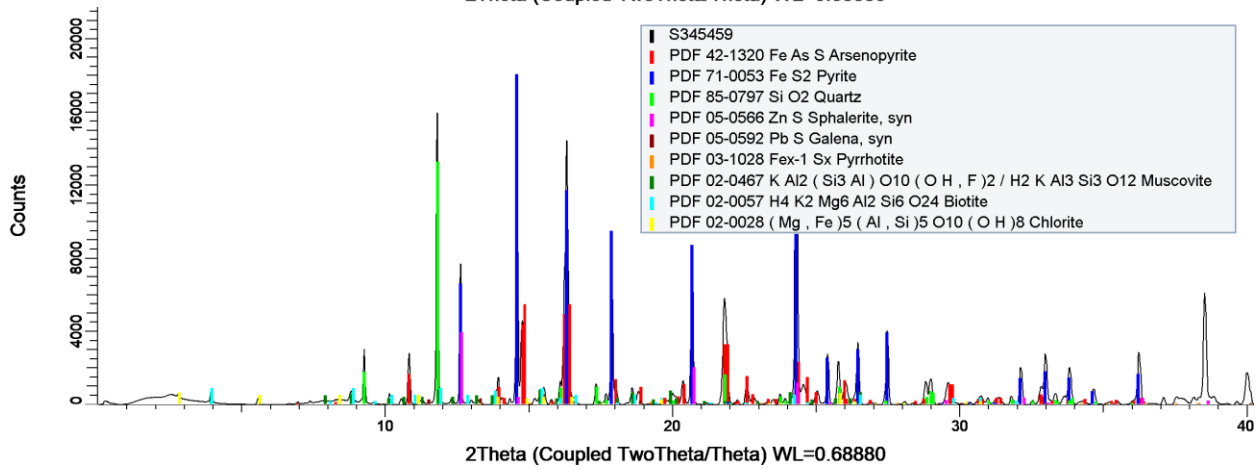
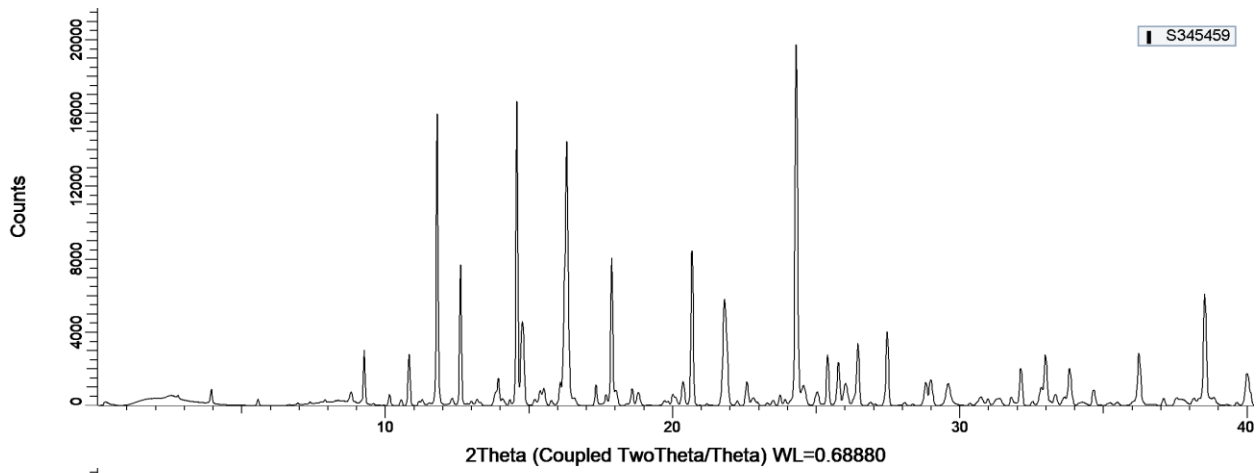




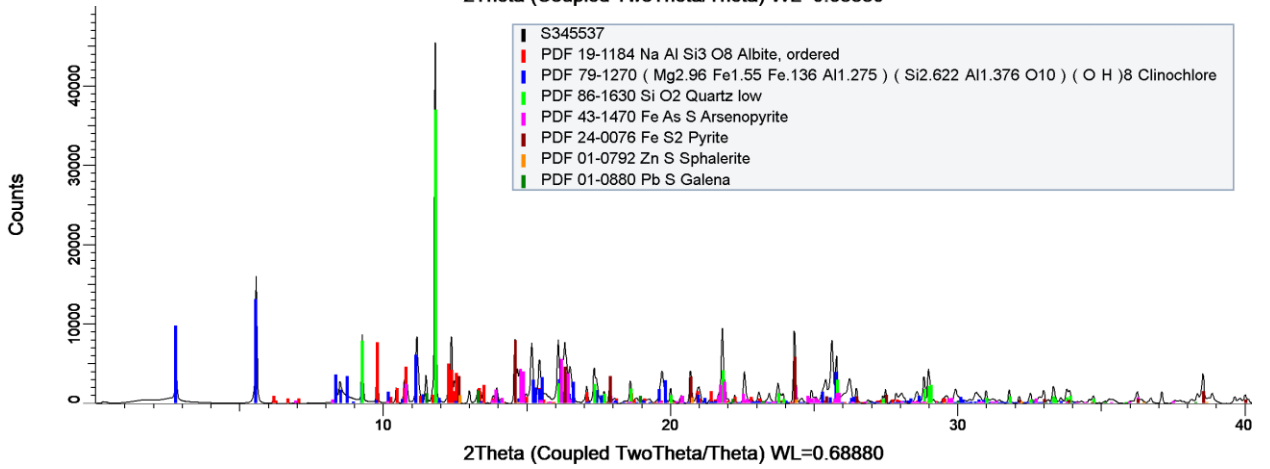
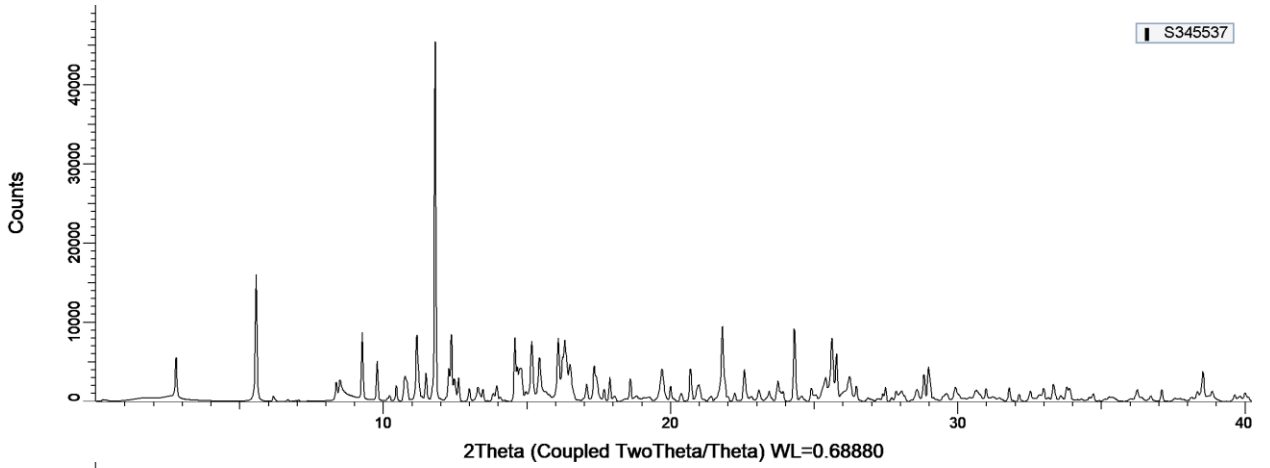
S343819



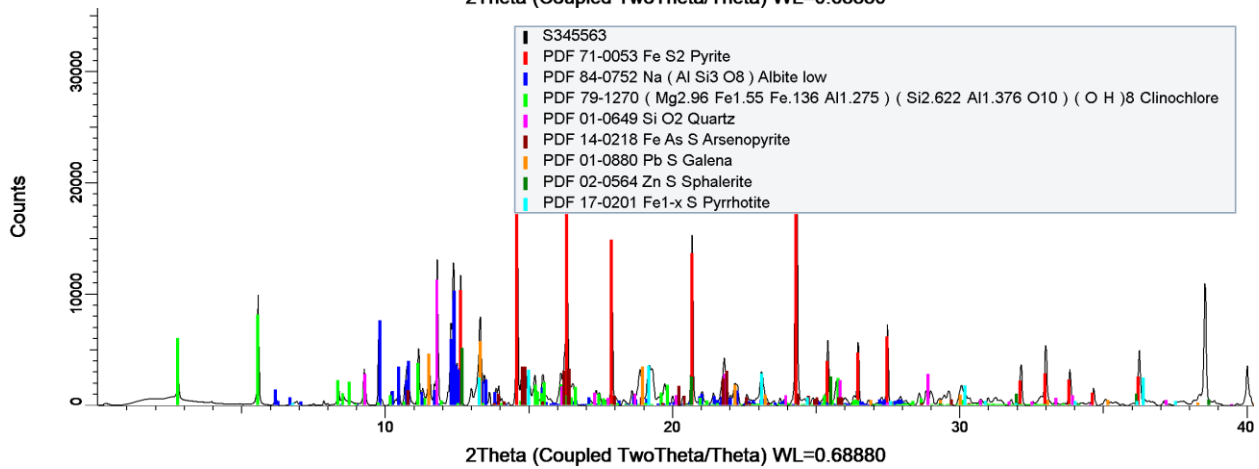
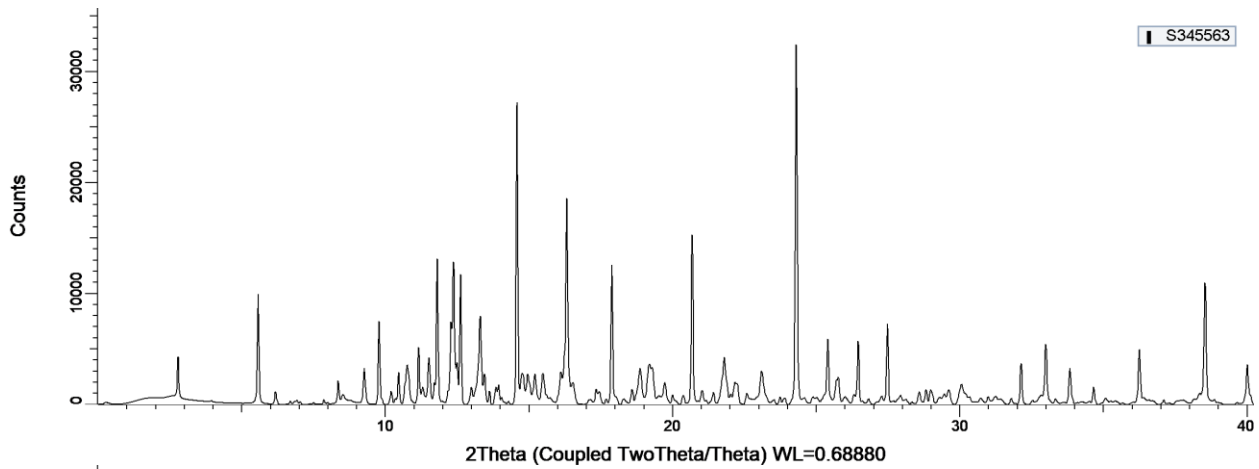
S345459



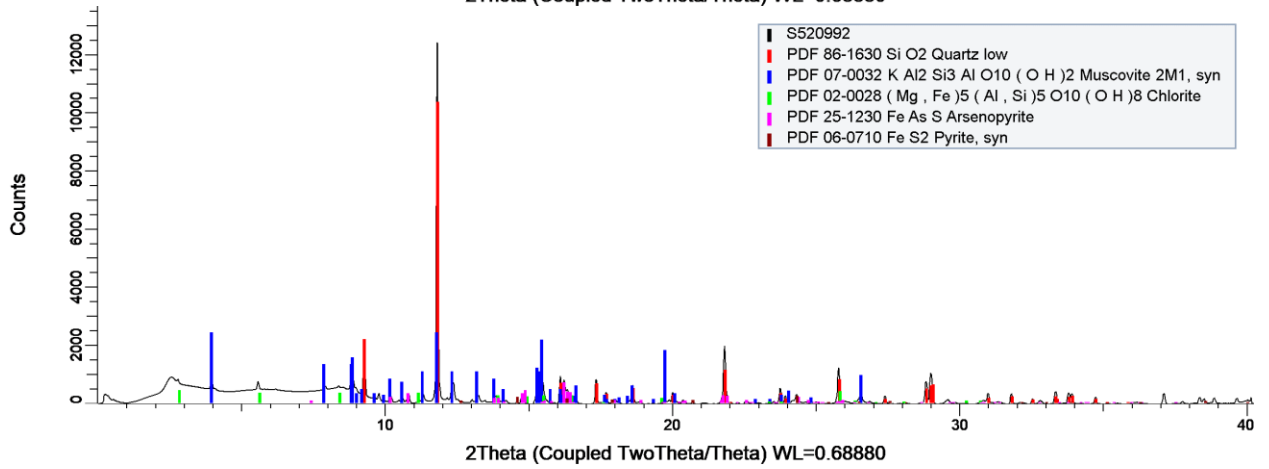
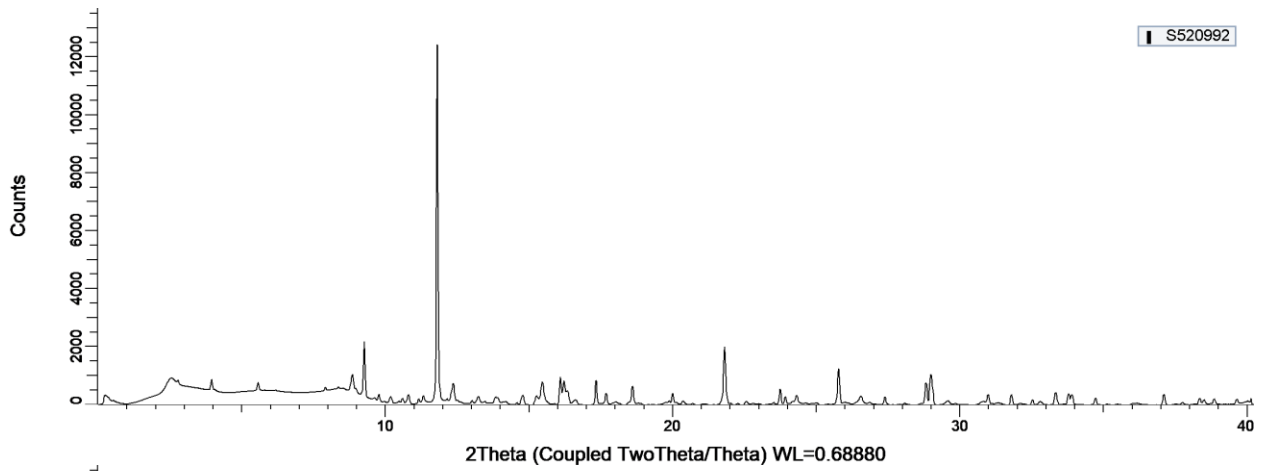
S345537



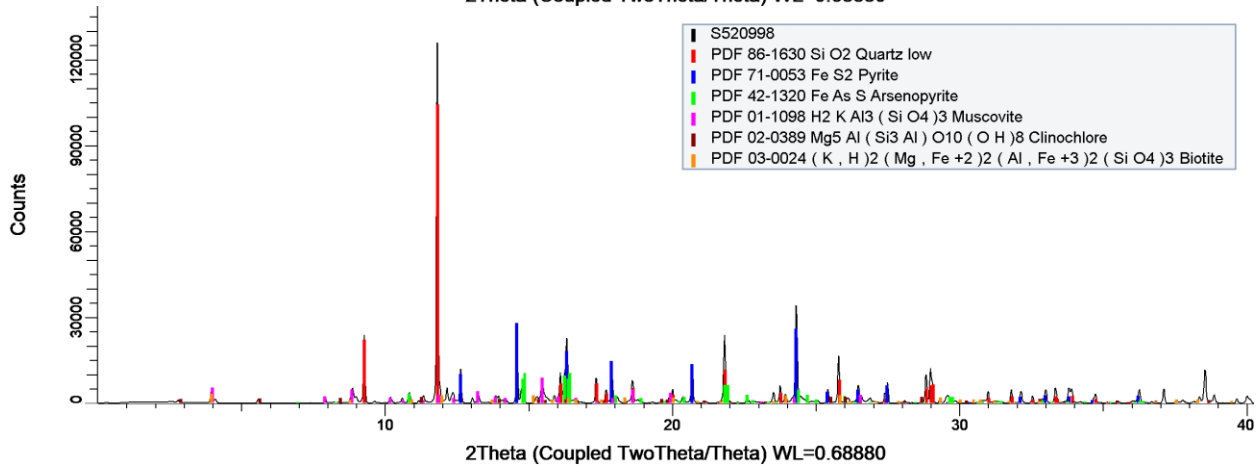
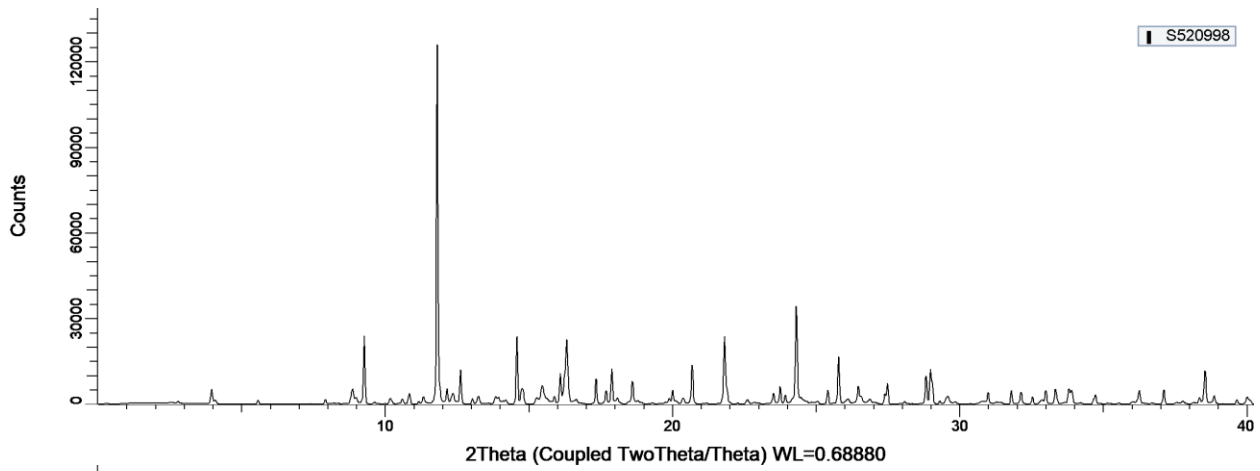
S345563



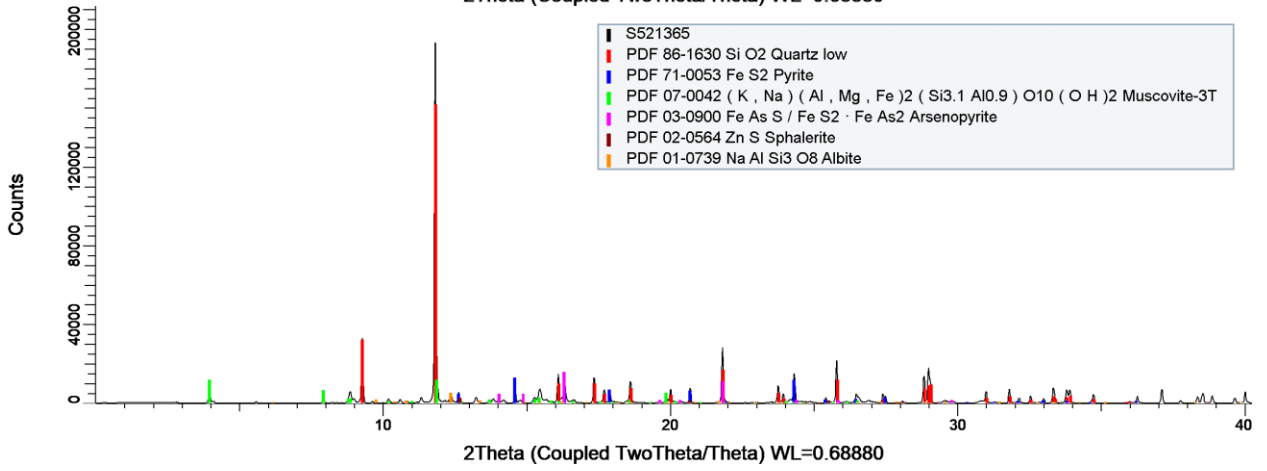
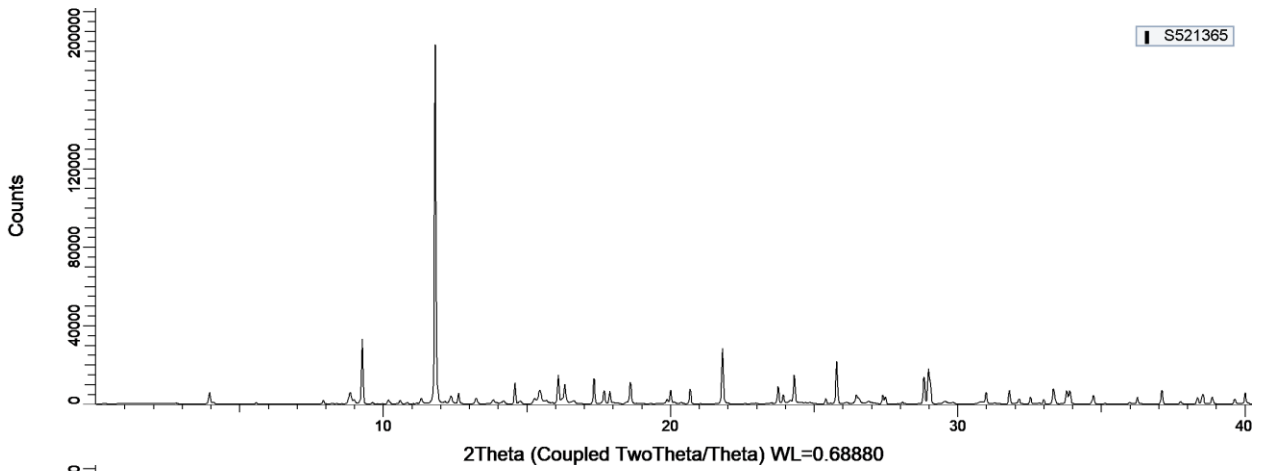
S520992



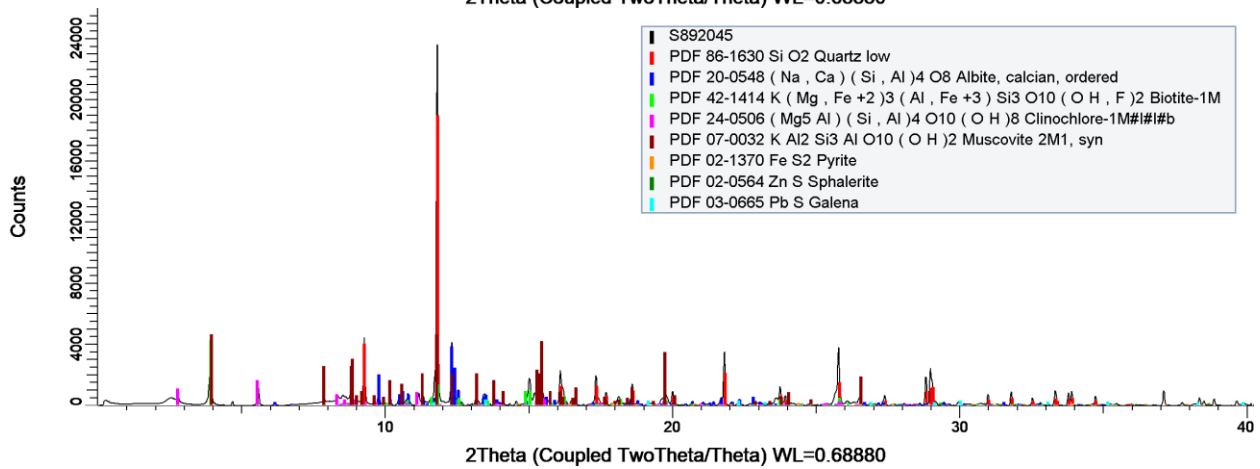
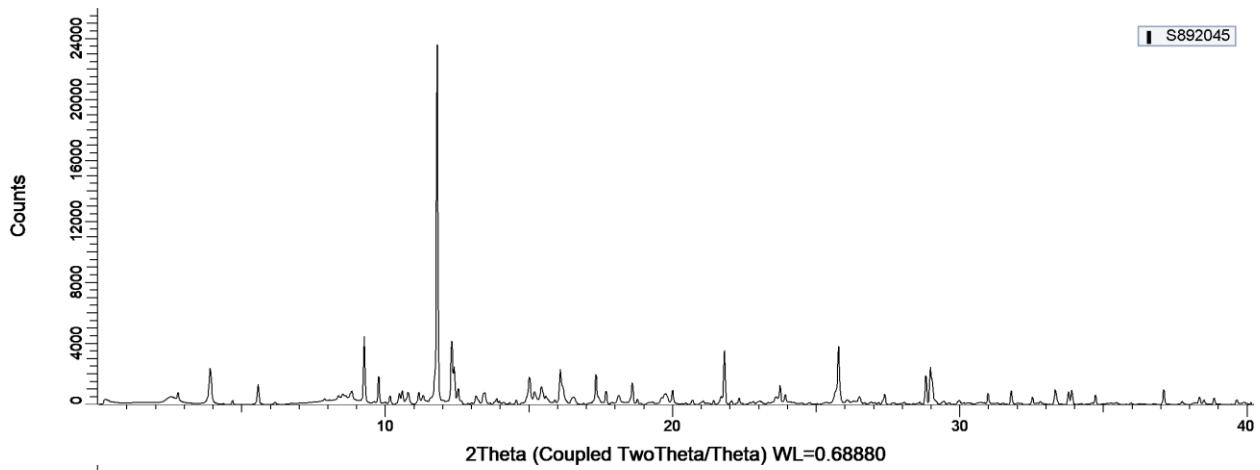
S520998

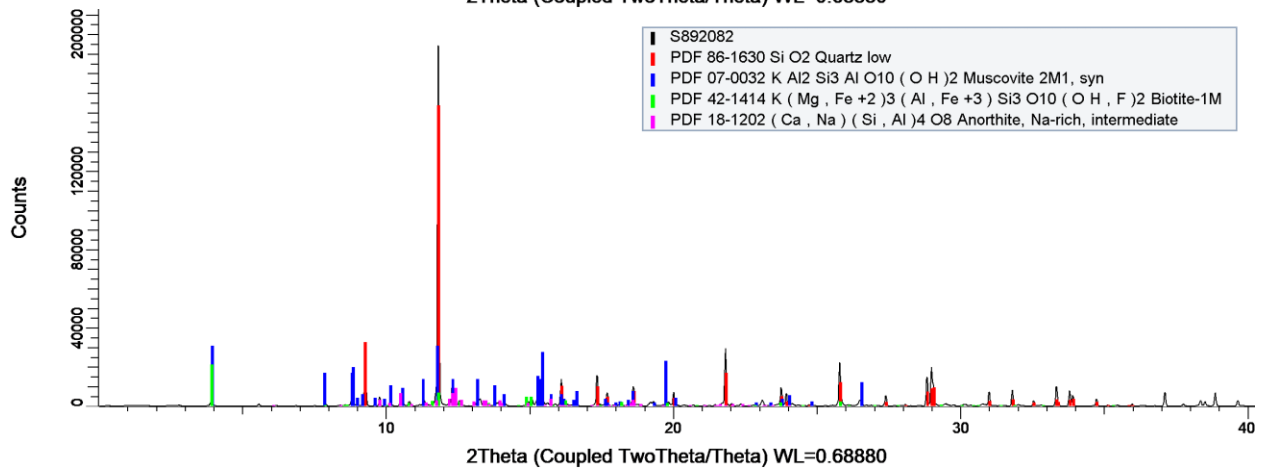
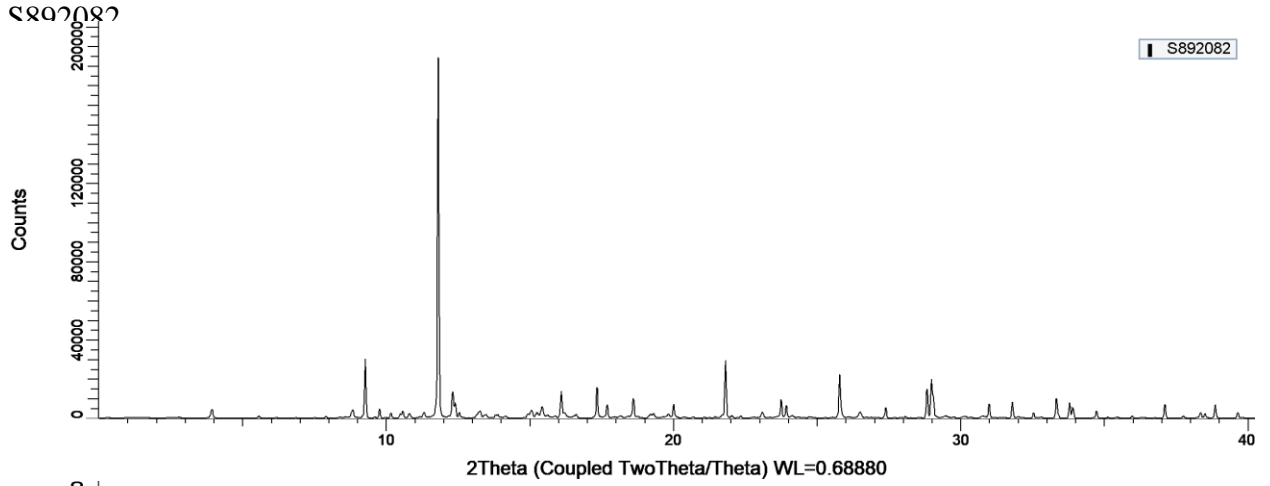


S521365

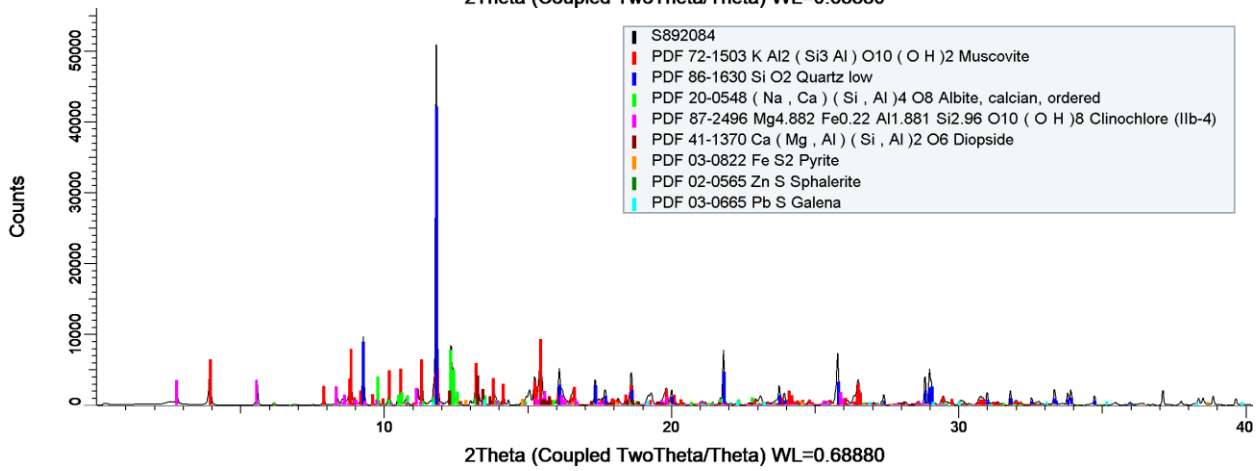
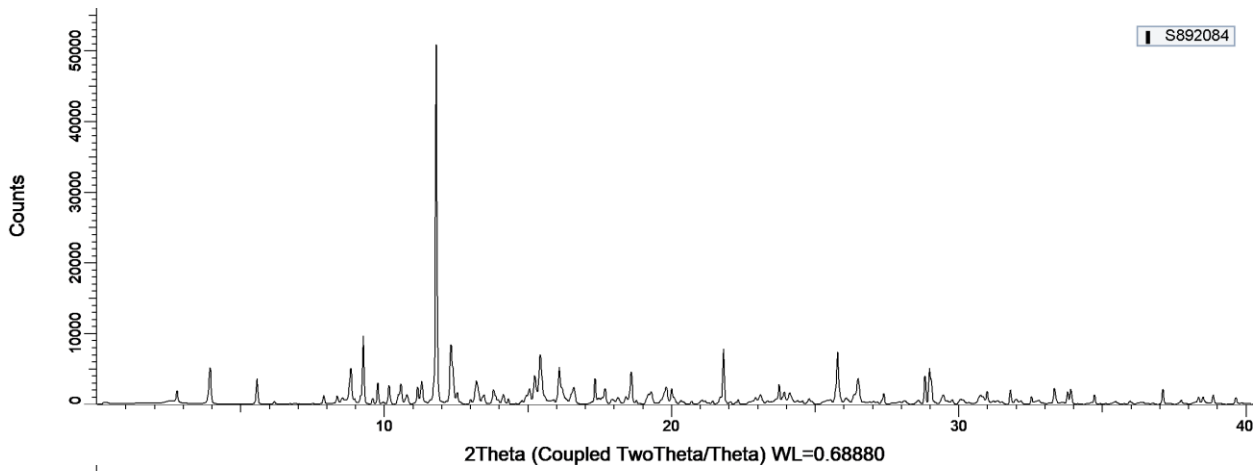


S892045

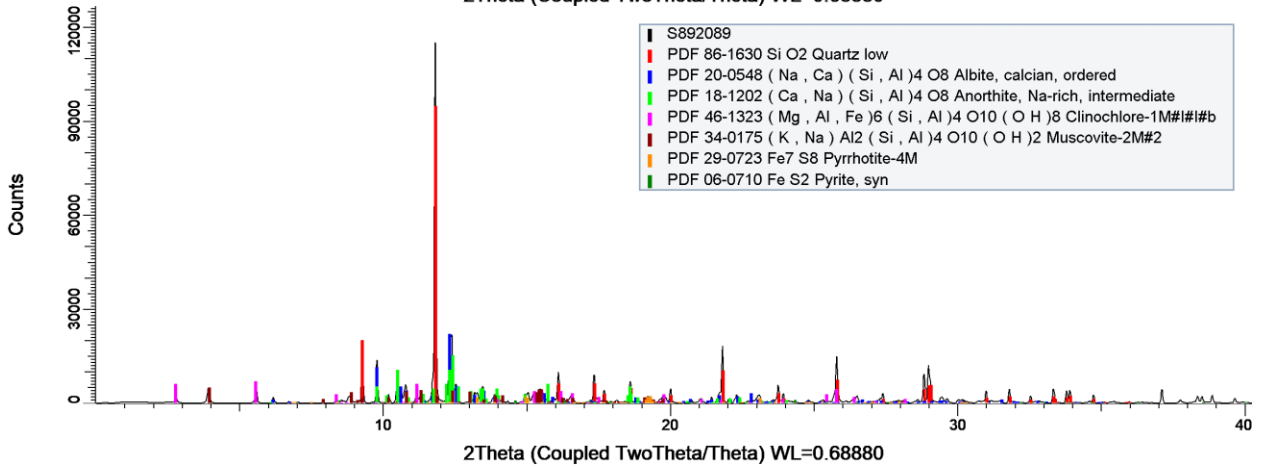
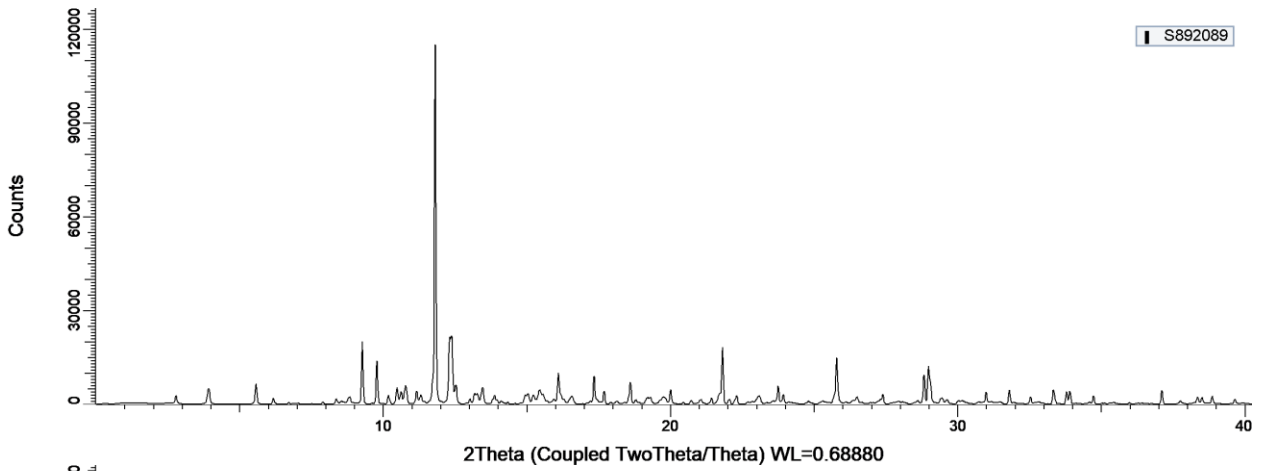




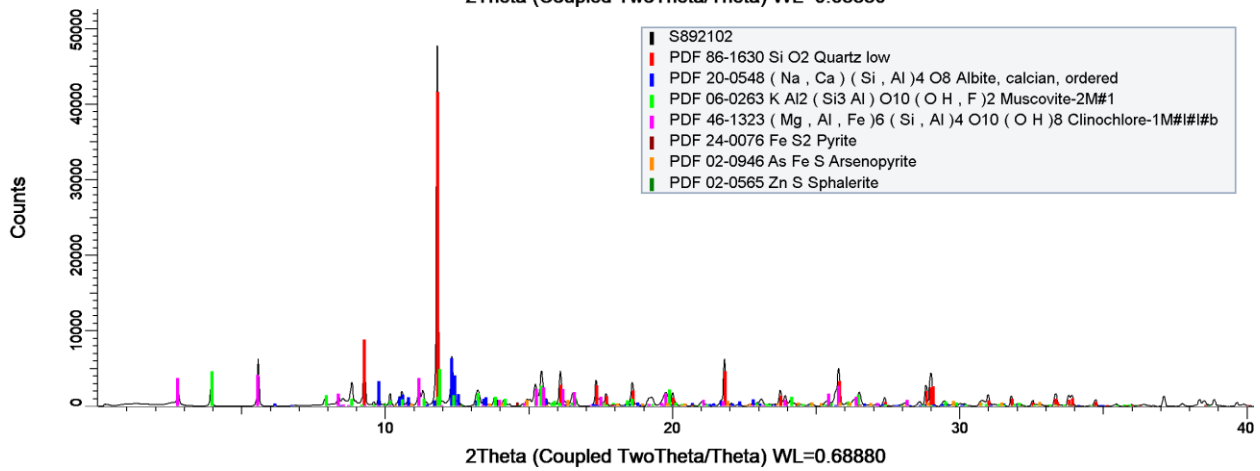
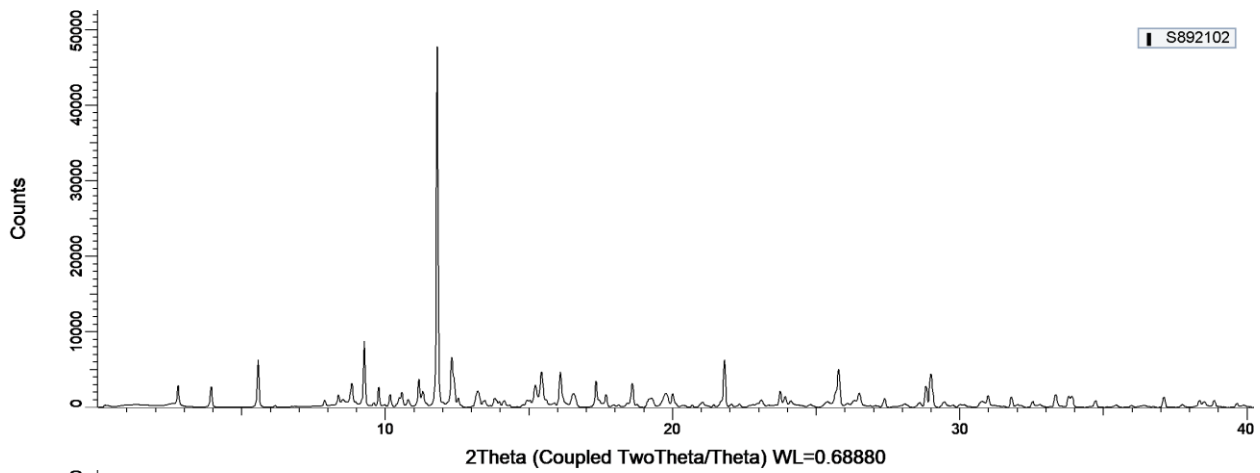
S892084



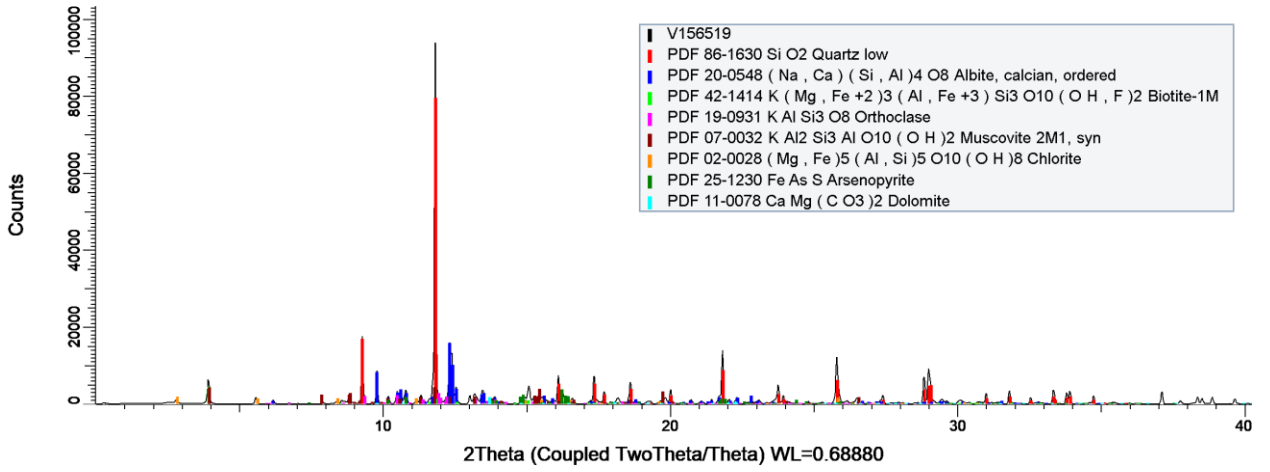
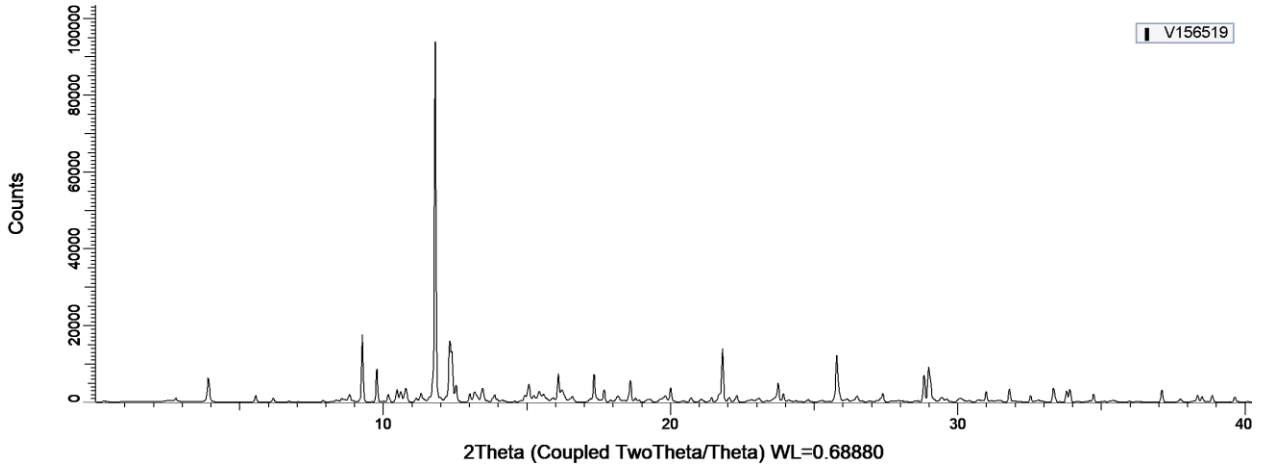
S892089



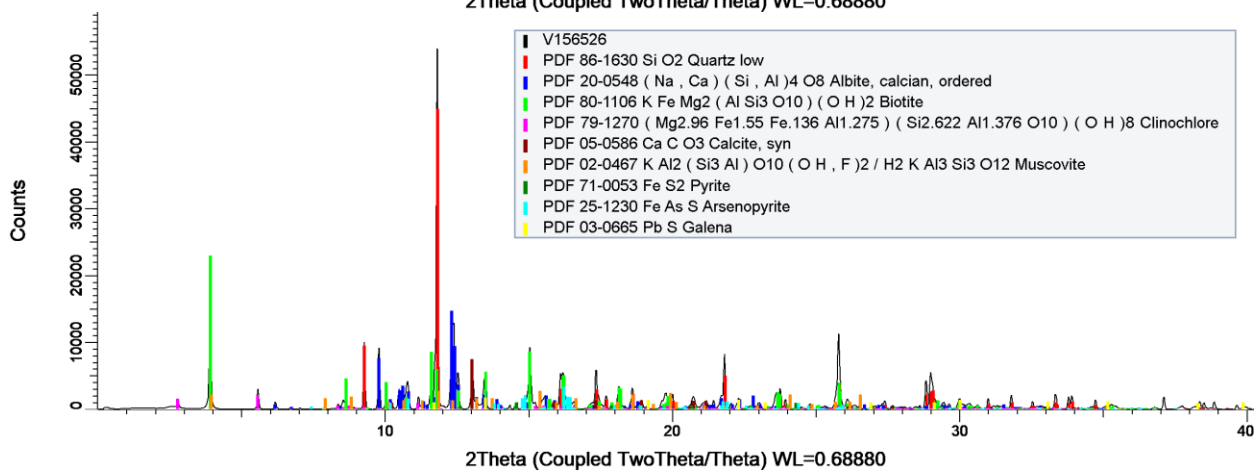
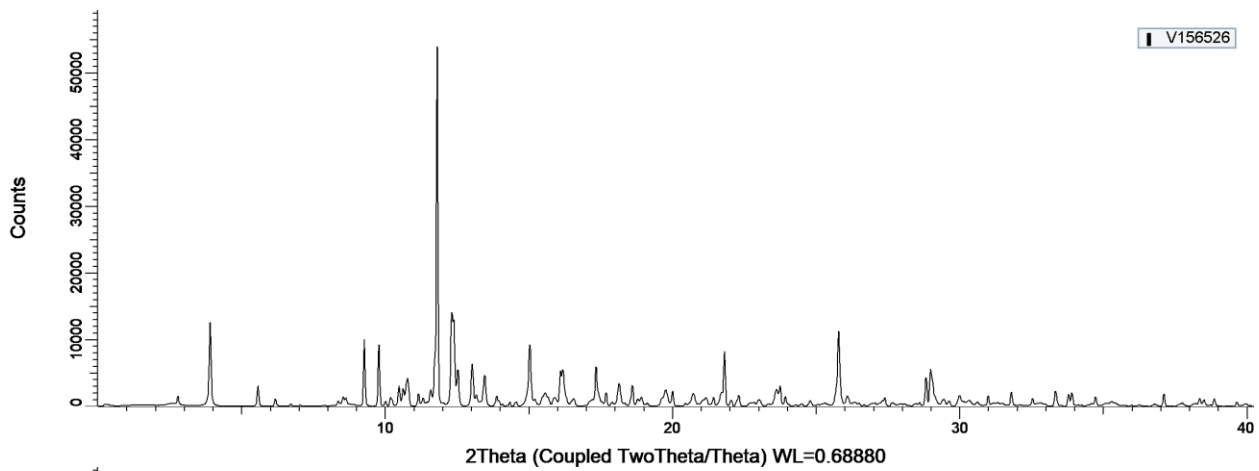
S892102



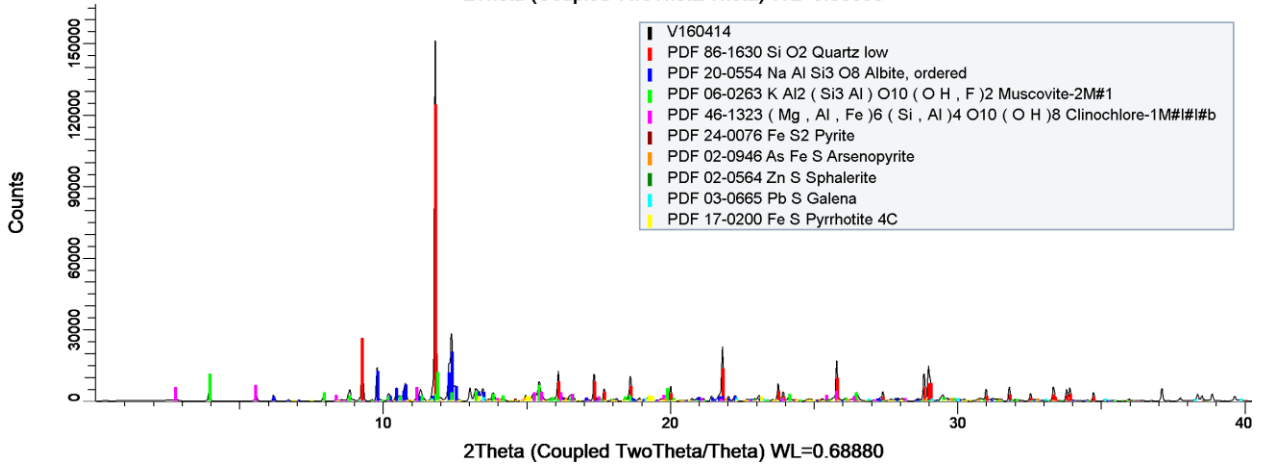
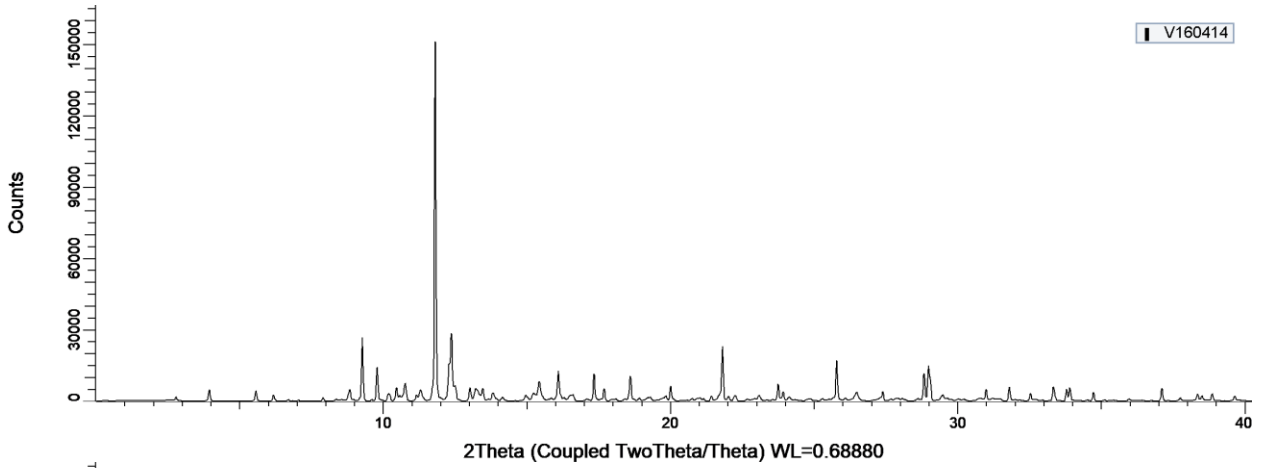
V156519



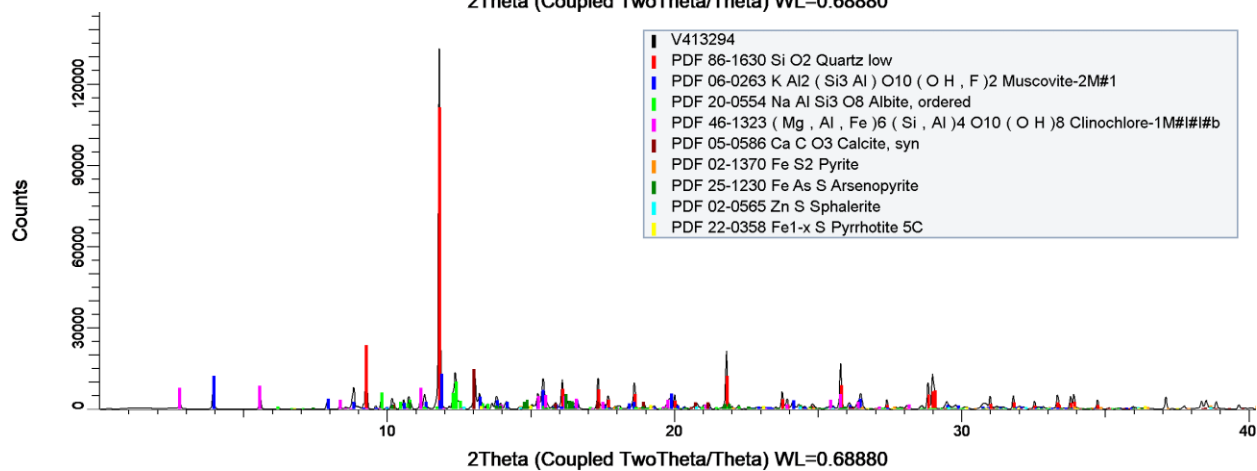
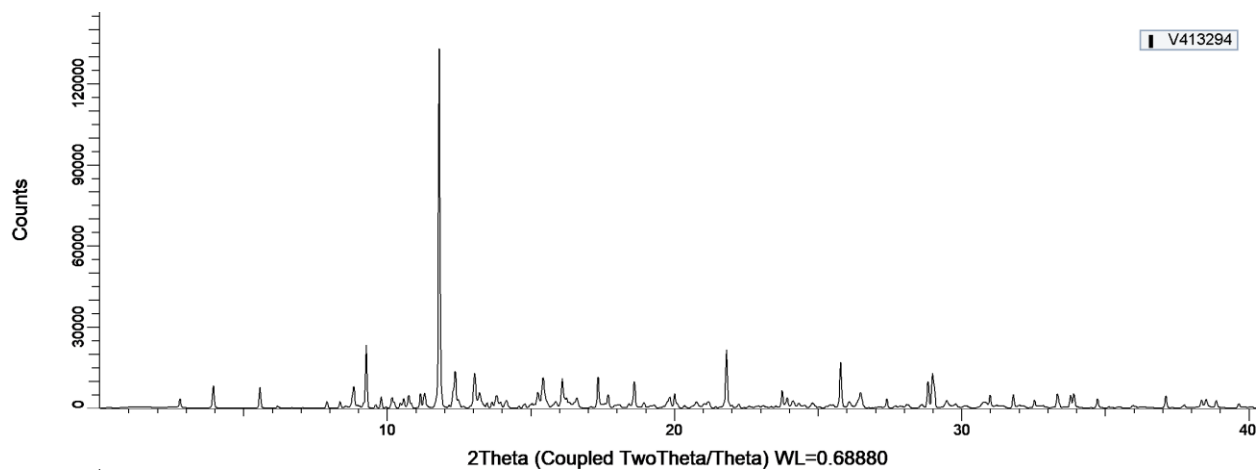
V156526



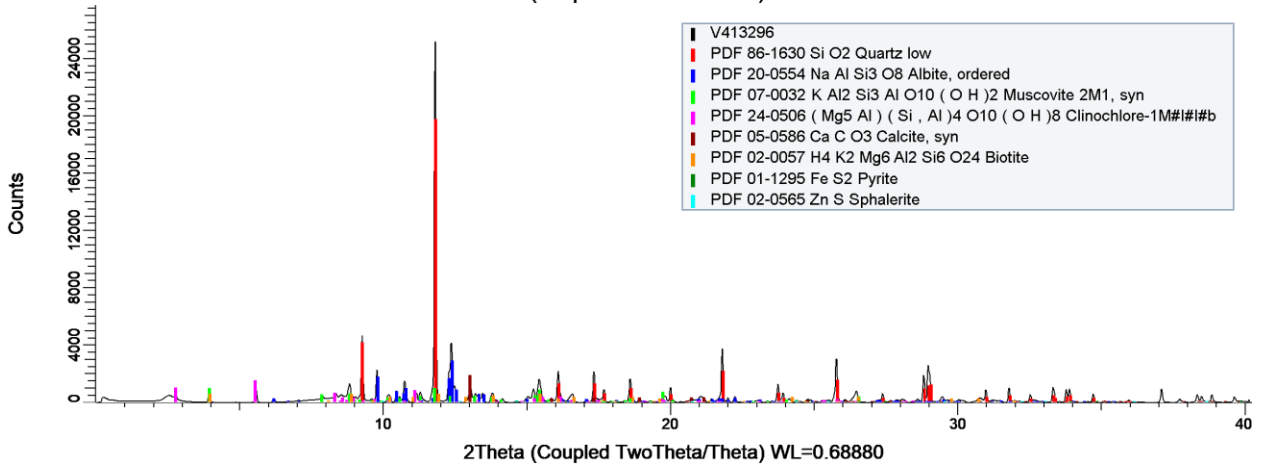
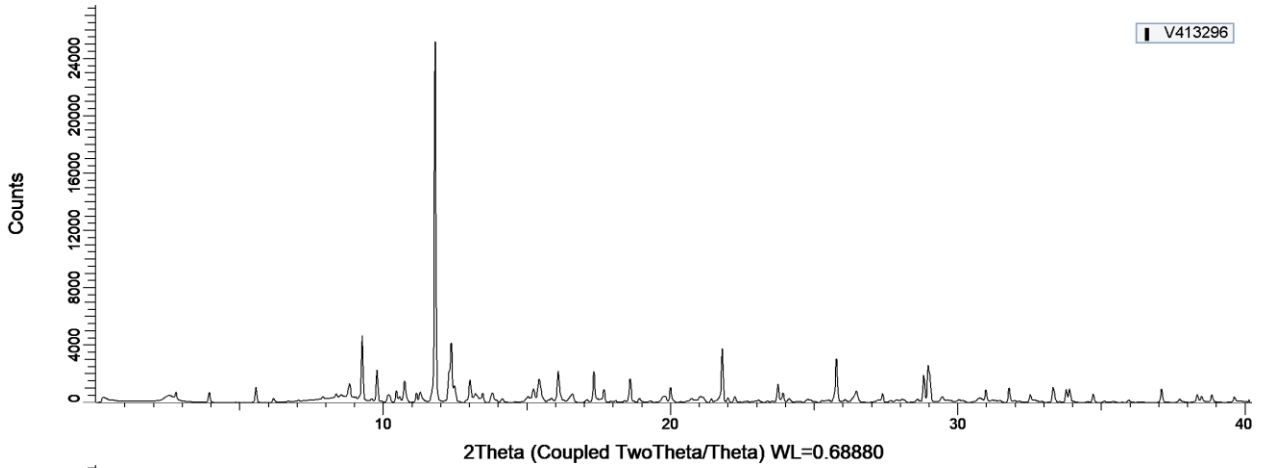
V160414



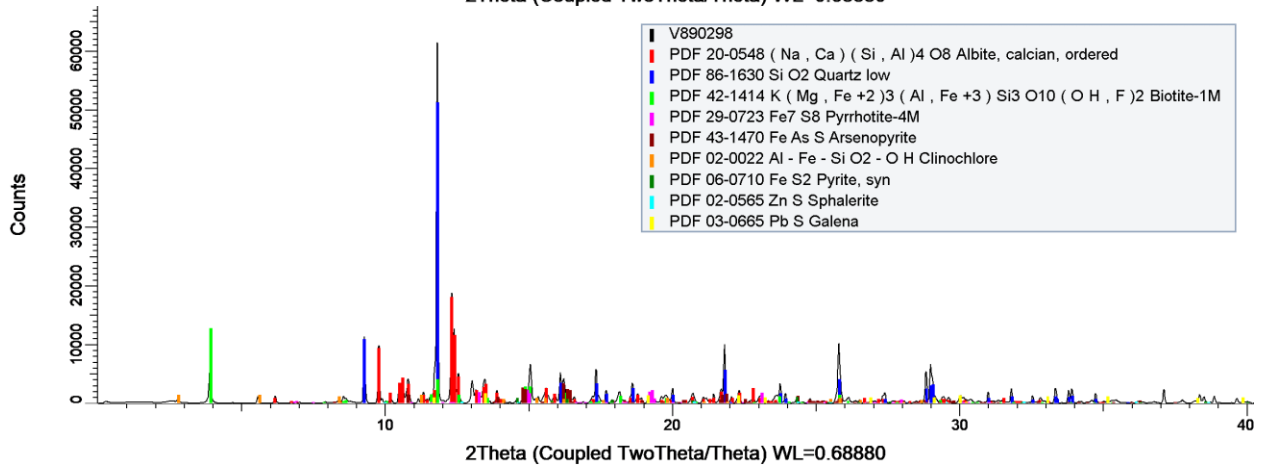
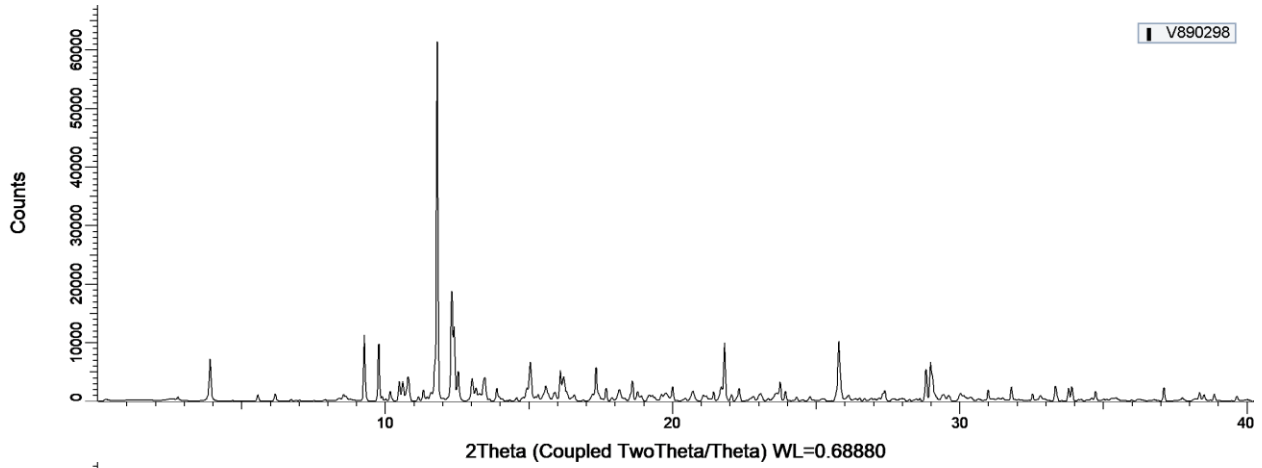
V413294



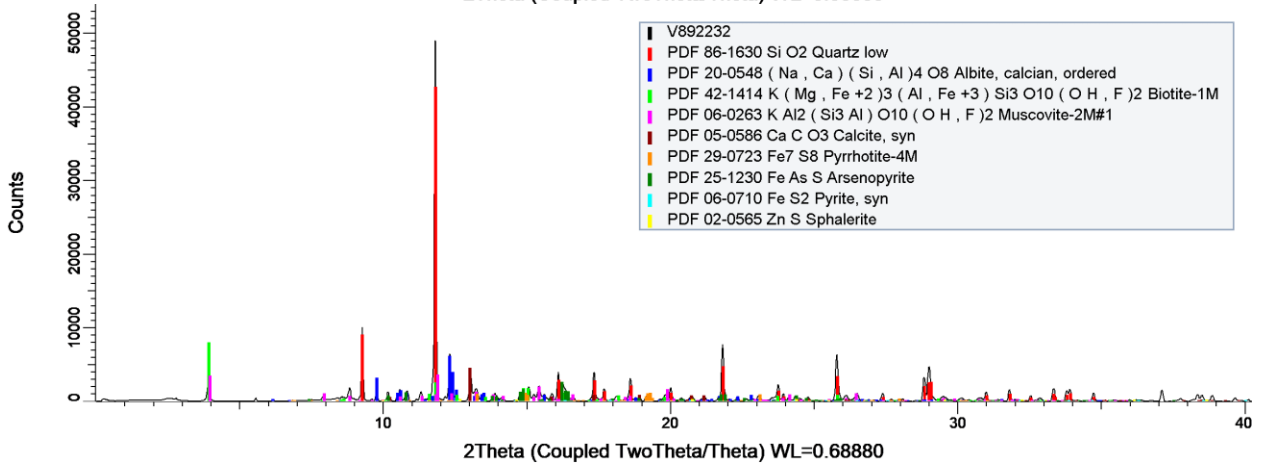
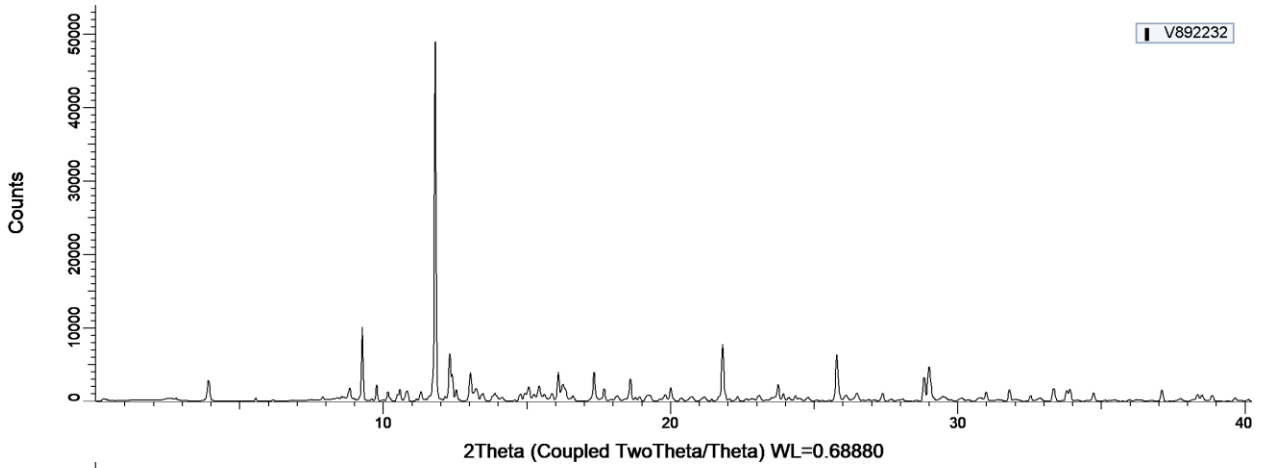
V413296



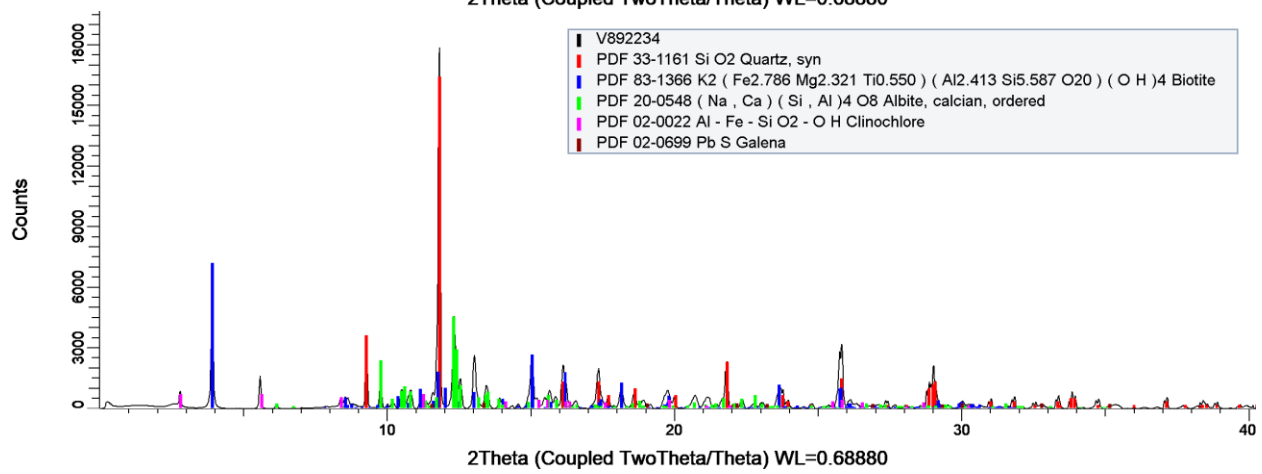
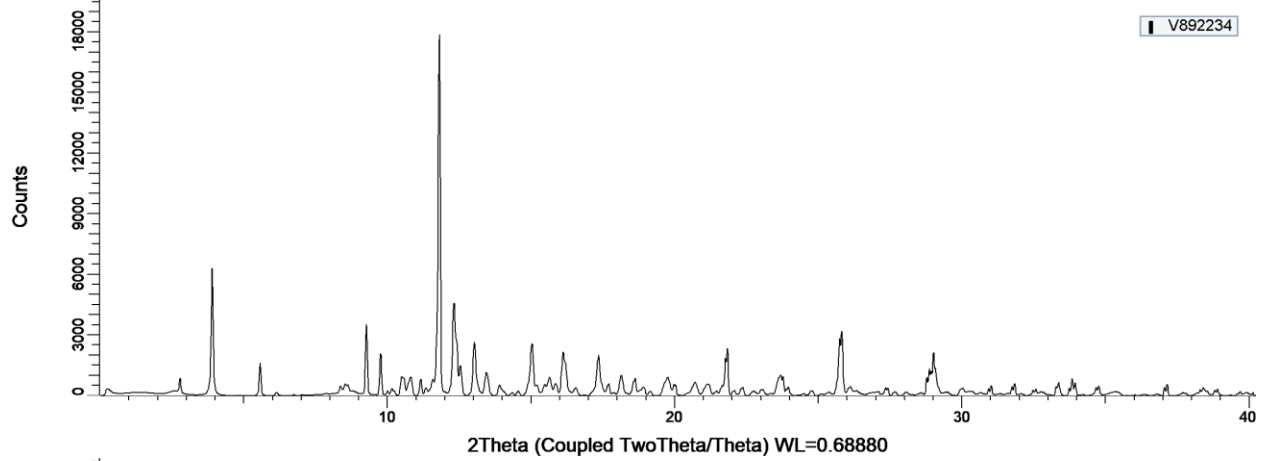
V890298



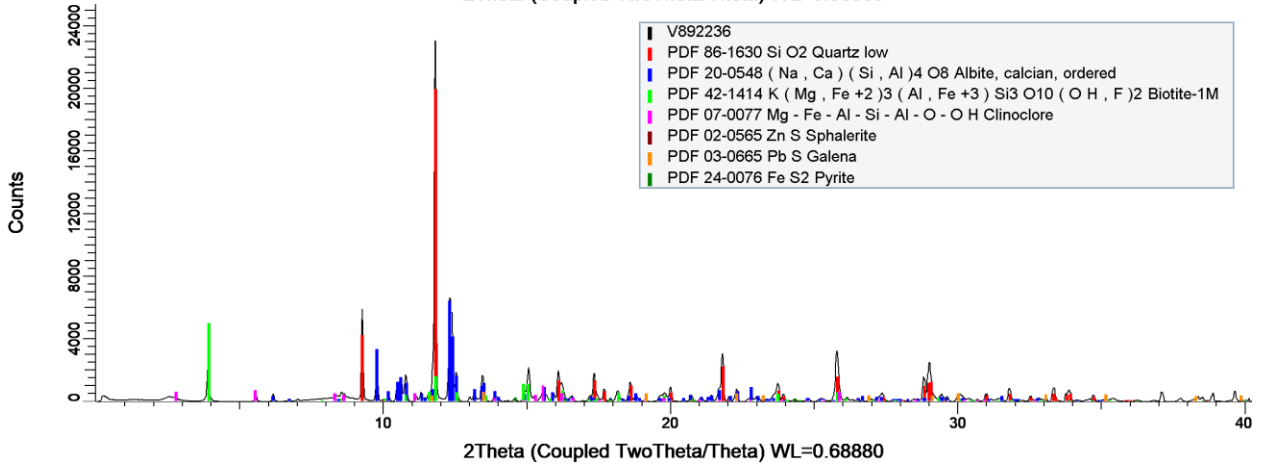
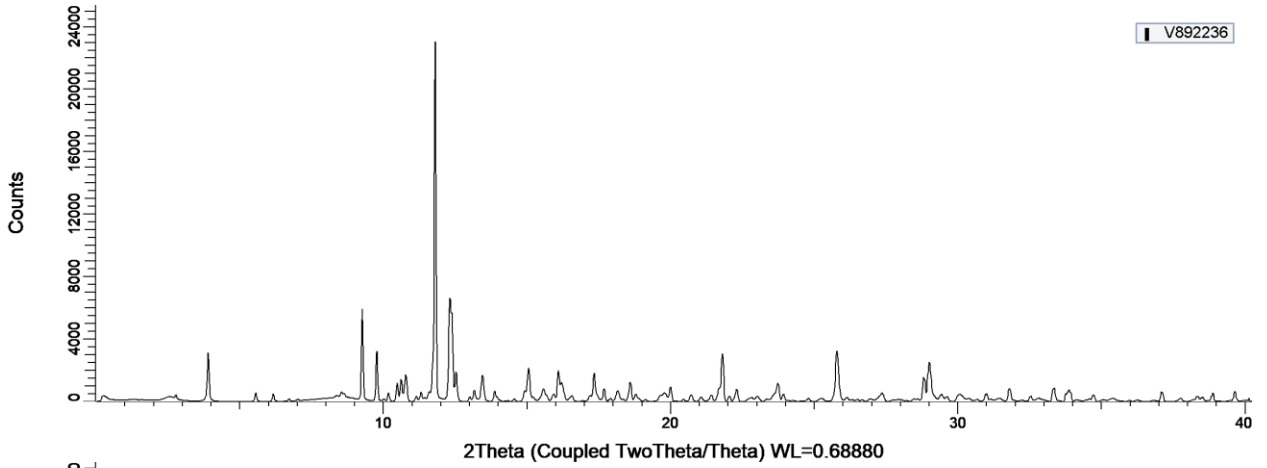
V892232



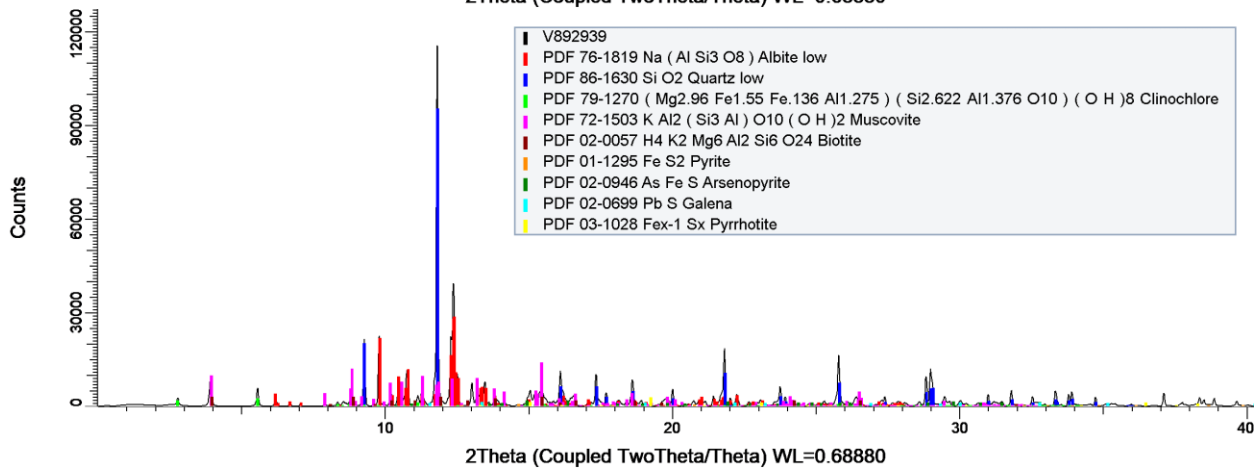
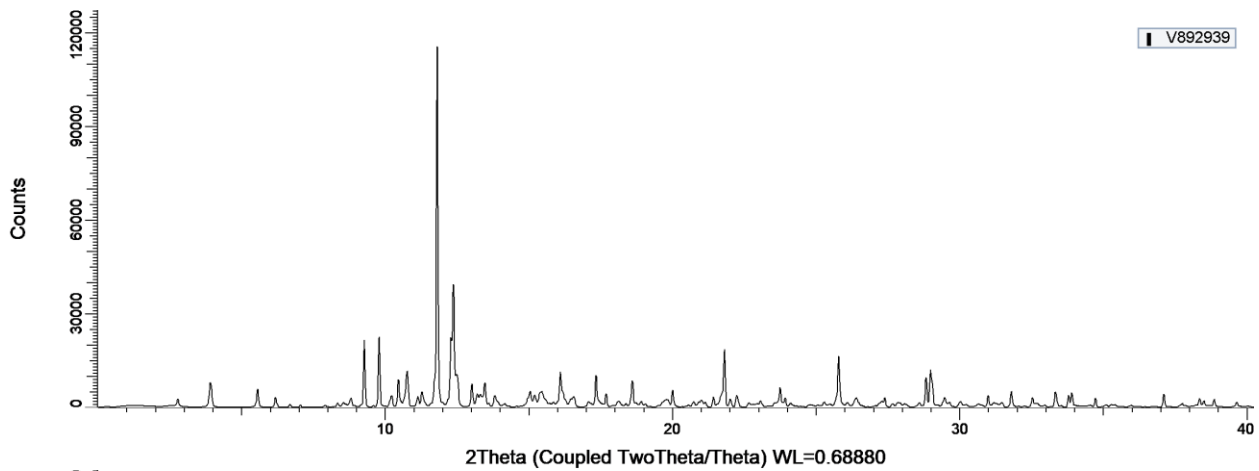
V892234



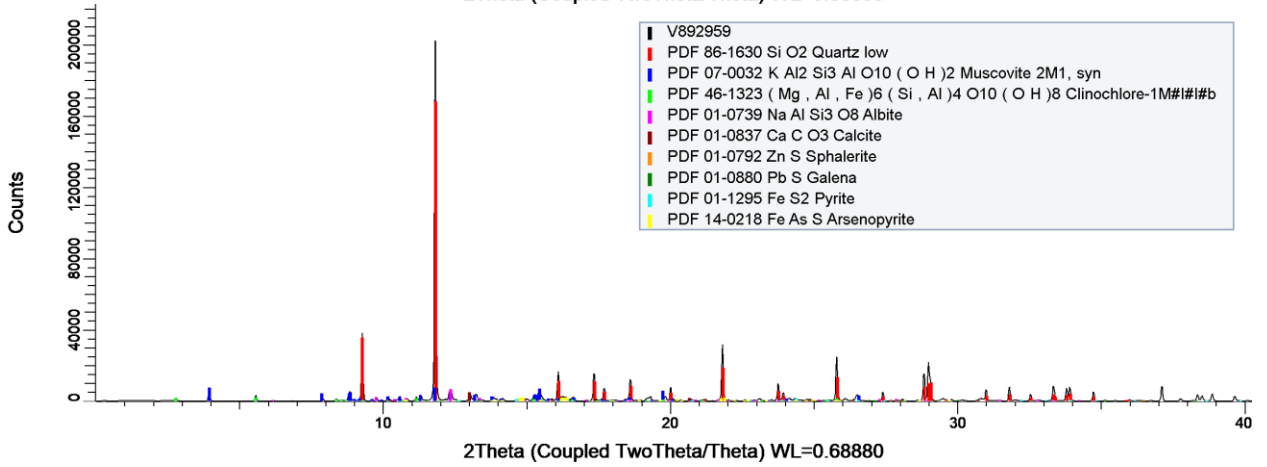
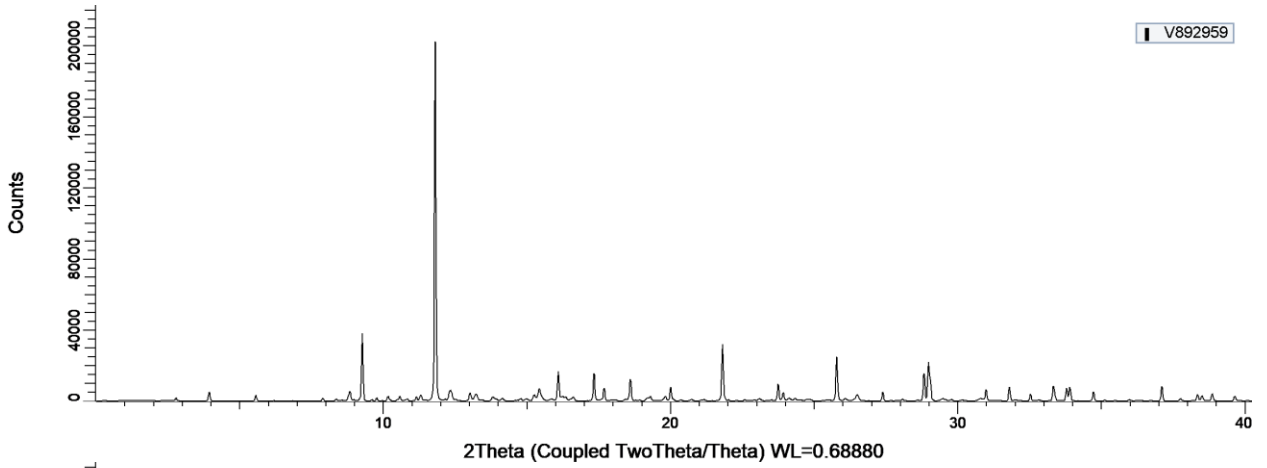
V892236



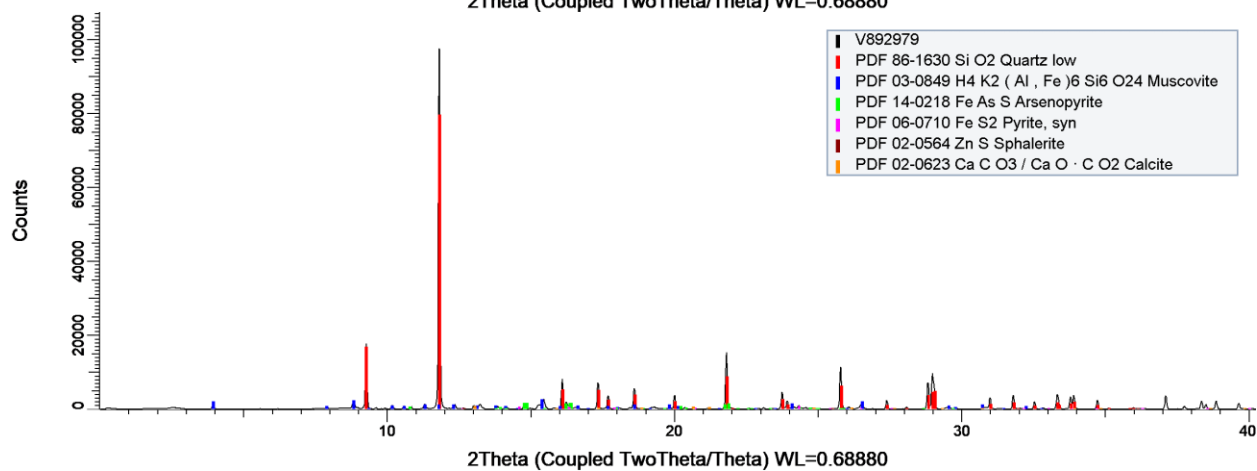
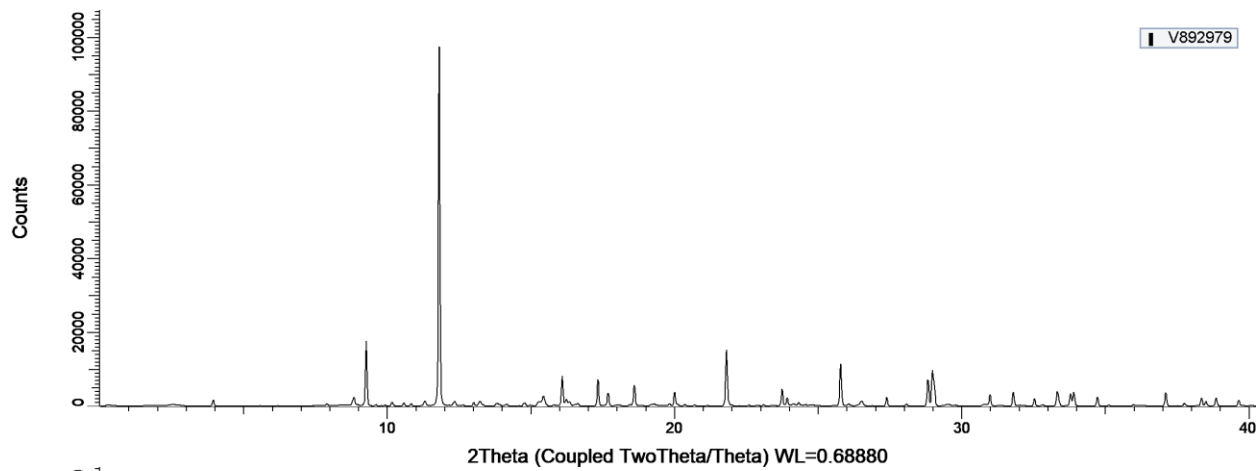
V892939



V892959

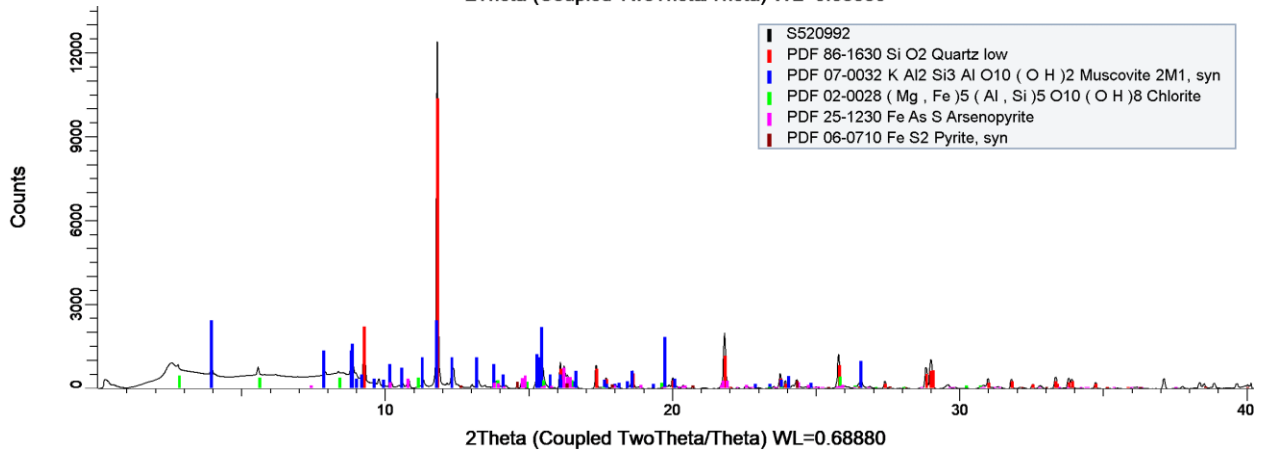
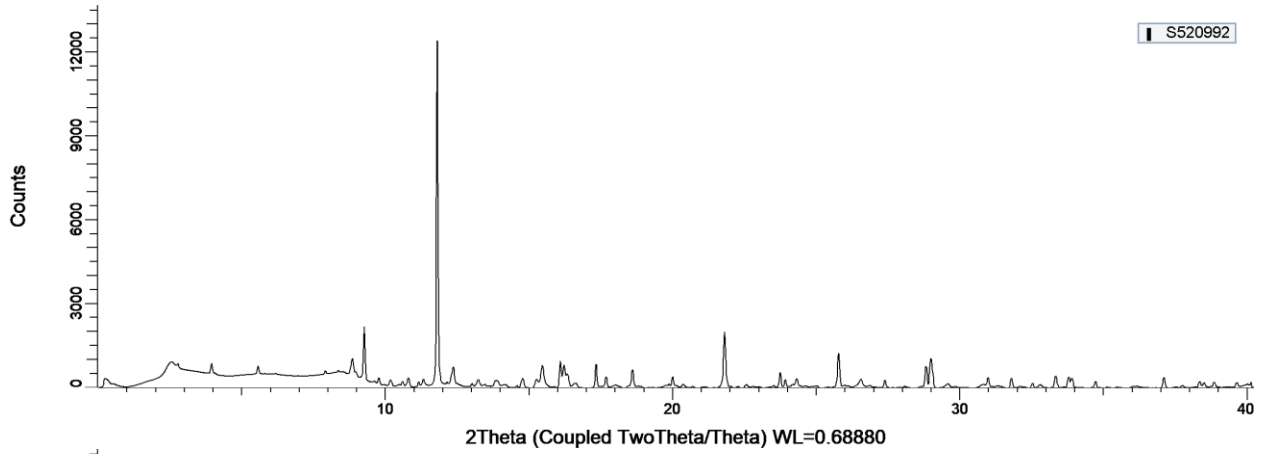


V892979

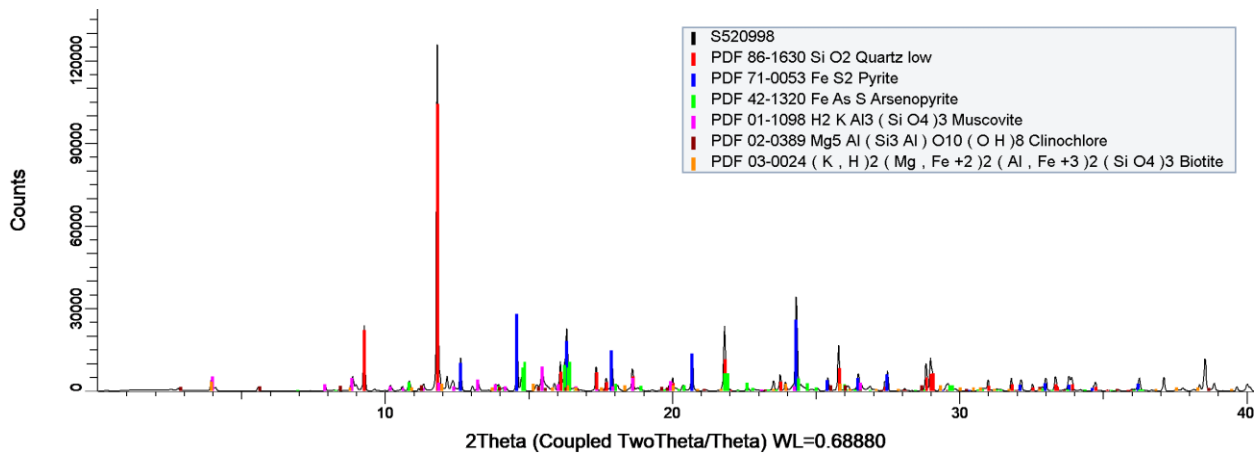
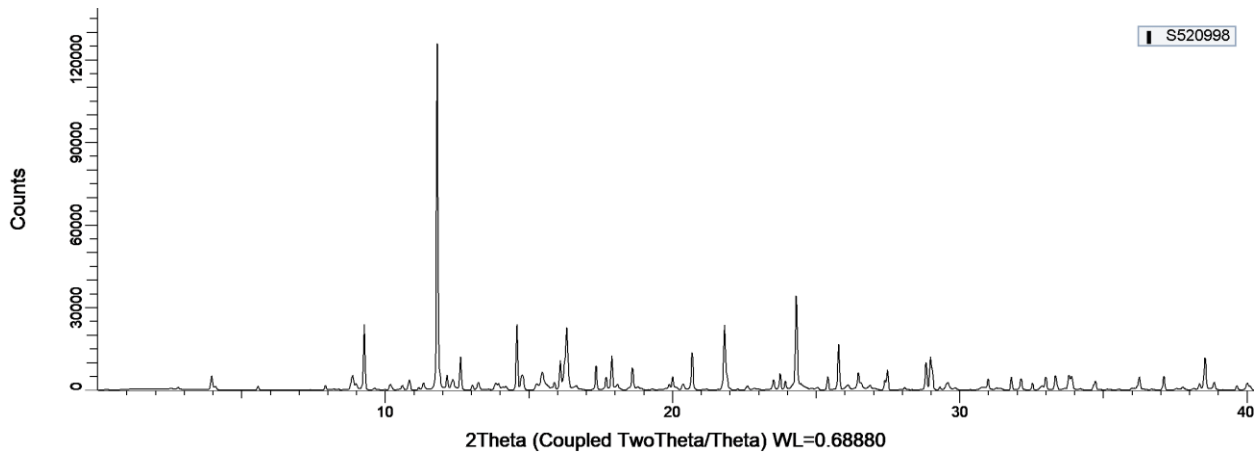


Hébert-Brent

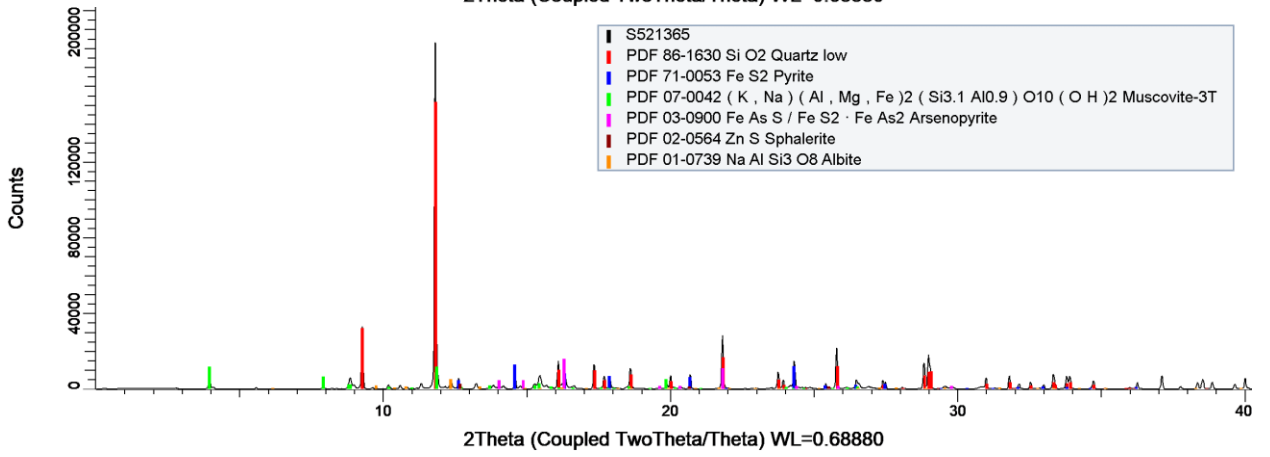
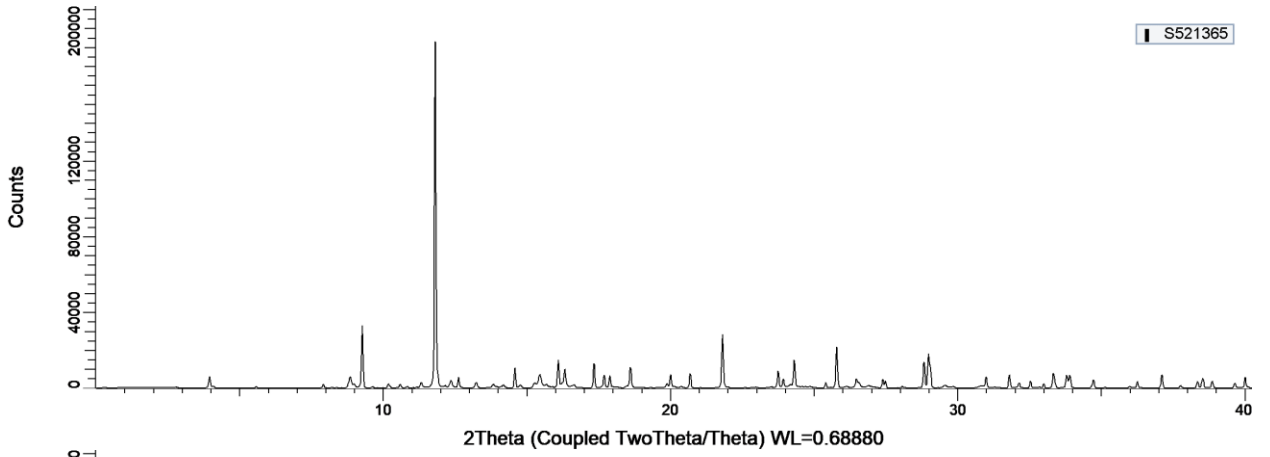
S520992



S520998



S521365



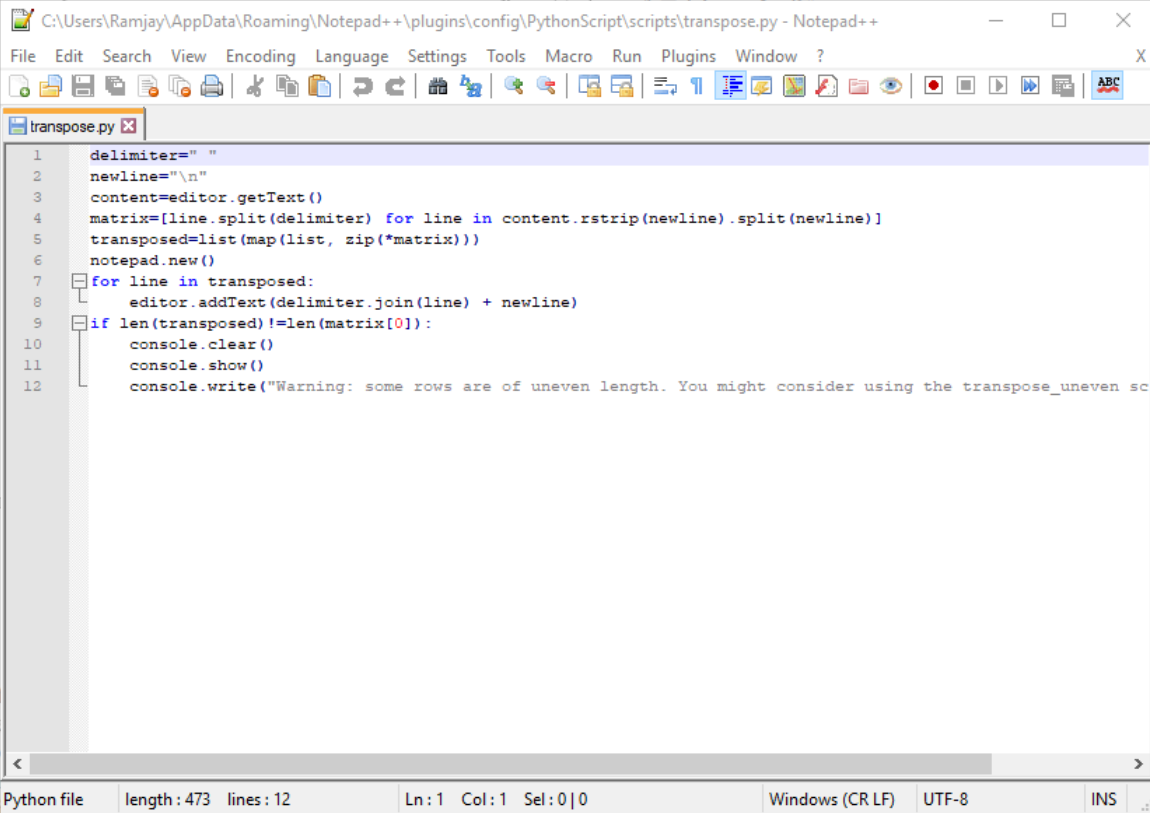
Appendix E: PyMCA Tutorial

1.1. PyMCA and steps on use

There have been numerous software packages utilized in interpreting 2-dimensional X-ray Fluorescence maps produced via synchrotron radiation. Solé et al (2007) developed the PyMCA program in the European Synchrotron Research Facility, Grenoble, France. The paper reveals the ease of use of the free program based on suitability for processing large data sets and ability to perform X-ray imaging, especially for data analysed at relatively low energies. In this work, PyMCA was mainly utilized to analyse 2-dimensional *in-situ* X-ray fluorescence maps of core samples from the Yellowknife City Gold Project. Several stack maps of elements present in the samples were produced based on the interpretations on the average fluorescence spectra for each 2-dimensional map. Information from the general 2-dimensional maps were utilized to designate spots for finer X-ray fluorescence mapping, and eventual X-ray Absorption Near Edge Structure (XANES) analyses to discern structural versus nano-gold inside sulphides, and As speciation for environmental remediation purposes.

PyMCA is a relatively straightforward program to use in analyzing 2-D X-ray Fluorescence maps from any synchrotron. It can open .edf, .mca, .hdf5, and other file types of interest. In this study, data from both the IDEAS and VESPERS beamlines at the Canadian Light Source are primarily as .txt files. The 2-dimensional files (labeled as <name>_KETEK.txt in from IDEAS, and <name_FourElementVortex.txt) are first transposed in Microsoft Excel or any third-party text processing program, such as Notepad++), and then converted to .dat. Data from both beamlines are saved as rows, and PyMCA reads data saved as columns. Alternatively, files can be saved as columns at the VESPERS beamline, eliminating this process with data collected from VESPERS.

Files can then be converted to .edf, which is a file format utilized mostly by clinical neurophysiologists for data exchange irrelevant of acquisition methods. PyMCA has an internal program which converts .mca or .dat to .edf, which simplifies analysis of data produced in ASCII (.txt or .dat) format. Individual files are to be converted, and a separate folder bearing the sample name should be created to store the .edf files, since the conversion will produce a multitude of files corresponding to each pixel of the map.



```

1 delimiter=" "
2 newline="\n"
3 content=editor.getText()
4 matrix=[line.split(delimiter) for line in content.rstrip(newline).split(newline)]
5 transposed=list(map(list, zip(*matrix)))
6 notepad.new()
7 for line in transposed:
8     editor.addText(delimiter.join(line) + newline)
9 if len(transposed)!=len(matrix[0]):
10     console.clear()
11     console.show()
12     console.write("Warning: some rows are of uneven length. You might consider using the transpose_uneven sc

```

Python file length: 473 lines: 12 Ln: 1 Col: 1 Sel: 0|0 Windows (CR LF) UTF-8 INS

Figure 1. Script utilized in Notepad++ to transpose 2-D XRF Files from both the IDEAS and VESPERS beamlines at the Canadian Light Source.

After conversion of all files have been performed, the map can then be viewed in the ROI Imaging Tool sub-program of PyMCA. Only a single .edf file needs to be selected, since PyMCA recognizes all related .edf files with the same header (i.e. <name>_00001.edf selected will also select all similarly named files). The program will then ask the user of the number of rows and columns for the maps. Note that the map dimensions should always be noted since the program will require it for display. After loading the appropriate map dimensions, a 2-dimensional XRF map GUI will pop up for data manipulation. Calibration of the fluorescence spectrum is essential for the selection of regions of interest for the maps, as well as for quantitative analyses that the user might perform. Before any calibration, the spectrum should be viewed in logarithmic y-axis scale, such that smaller peaks will be more visible. The Toggle Logarithmic Y Axis beside the Autoscale X axis button (encircled red in Fig. 4) will allow the user to view the spectrum in logarithmic scale for the y-axis. For calibration, prior knowledge of

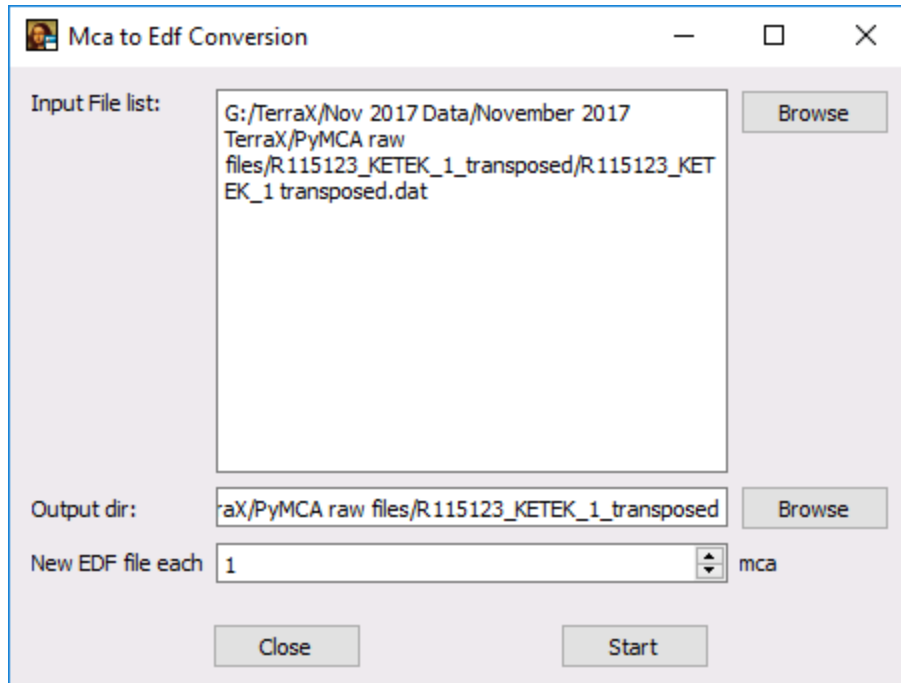


Figure 2. Conversion of .dat (or .mca) files to .edf for PyMCA.

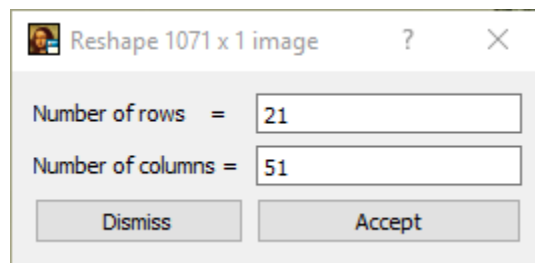


Figure 3. The dialog box in the ROI imaging tool where the program will ask for map dimensions. Note that the number of rows and columns should not be reversed. A simple trick to know the number of rows and columns is to just input the number of one section (i.e. no. of rows for no. of vertical lines, no. of columns for no. of vertical lines. The reason why the roles are reversed is due to the earlier transposing.

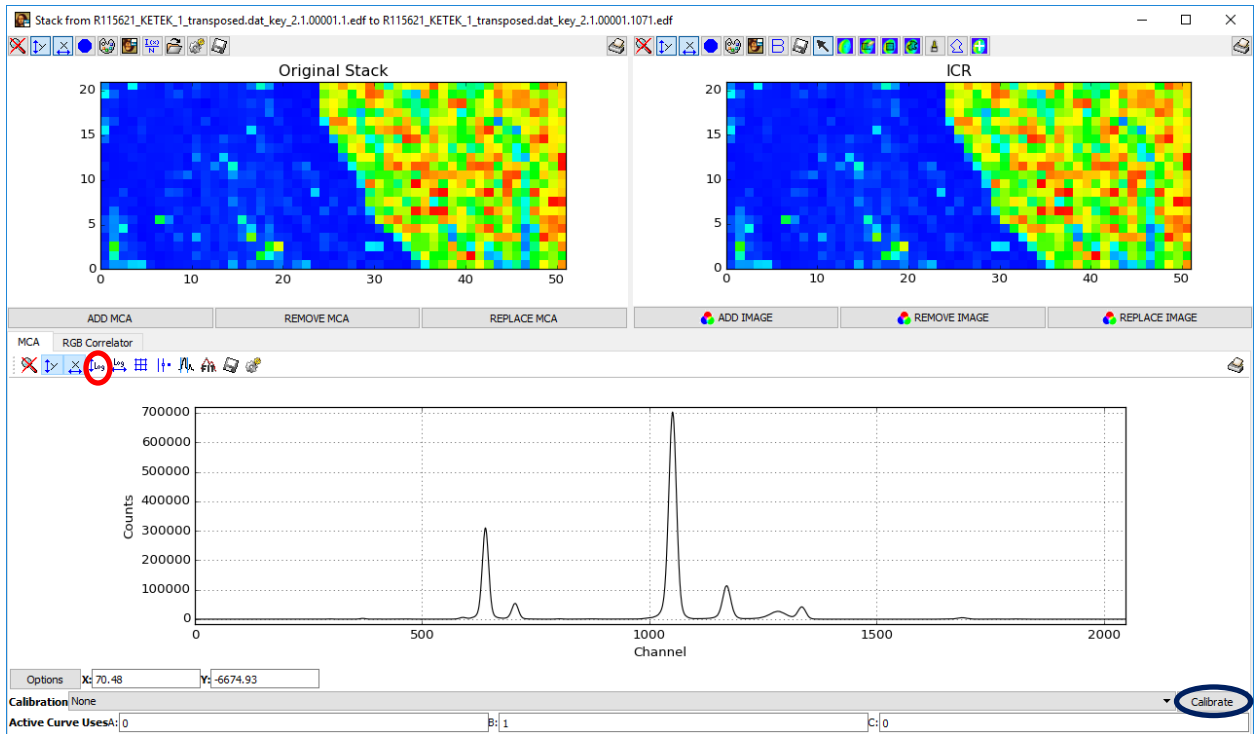


Figure 4. Interface of the ROI Imaging Tool. Note that the data has not been calibrated to the corresponding energy of the beamline yet.

the peak position of the element(s) showing the highest counts (which are Fe and As for the samples in this study) are to be collected. Upon clicking the Calibrate button (encircled blue in Fig. 4) and selecting Edit, the user will be brought to a dialog box which will allow manual selection of the most prominent peaks in the sample. Usually, one designated peak is sufficient to calibrate the spectrum. Upon clicking OK and selecting the calibration done in the Calibration drop-down list box, the spectrum will be calibrated, and the x-axis will be transformed to Energy, from the previous Channel units. The calibration can then be saved to be used as the calibrant for other data analysed with the same parameters in the same beamline, available by clicking the Calibrate button and clicking Save.

For further analysis of the elements present in the sample, the Fit function (encircled in Fig. 7) will be used to perform techniques such as background stripping, element (peak) finder, among others. The Advanced Fit tool will allow the user to define individual peaks that will correspond to the element emitting a specific energy, as well as removing background radiation for more precise semi-quantitative calculation of element abundances in the sample. Upon entering the Configure dialog box, the user will be allowed to tinker with the parameters of the analysis. In general, background stripping is set at 5000 iterations, energy at whatever the energy was set during analysis (13150, 13700, 13840, and 13400 eV for the December 2016, January 2017, June 2017, and November 2017 beamtimes, respectively), attenuators as air, and incoming and outgoing beam angles at both 45 degrees. Manual peak selection will be according to the emission lines of each element present in the sample. If there is confusion in the identity of the element in a particular

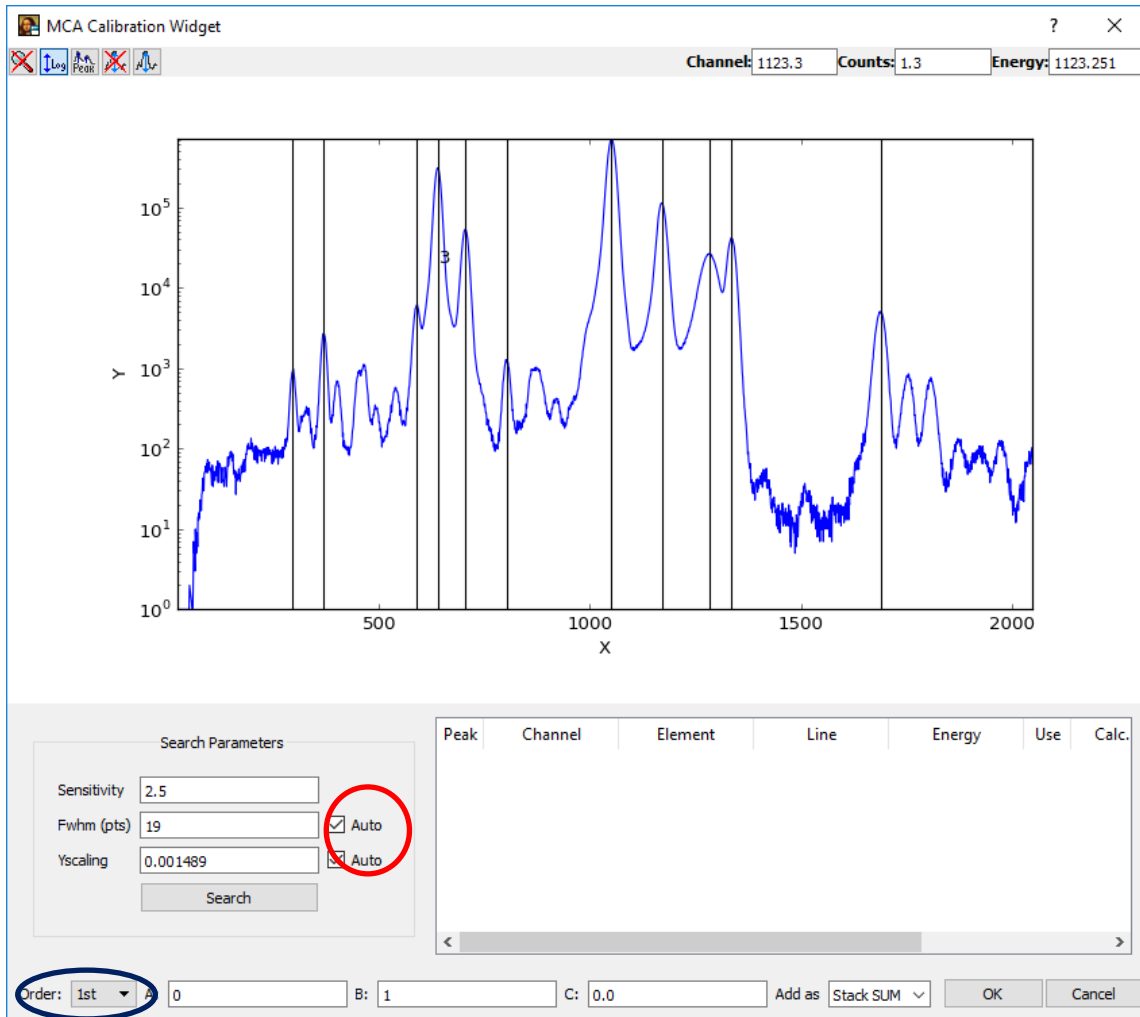


Figure 5. MCA Calibration widget dialog box. Note that the two check boxes named "Auto" (encircled red) and the Order drop-down box (encircled blue) are ticked and designated as 1st, respectively.

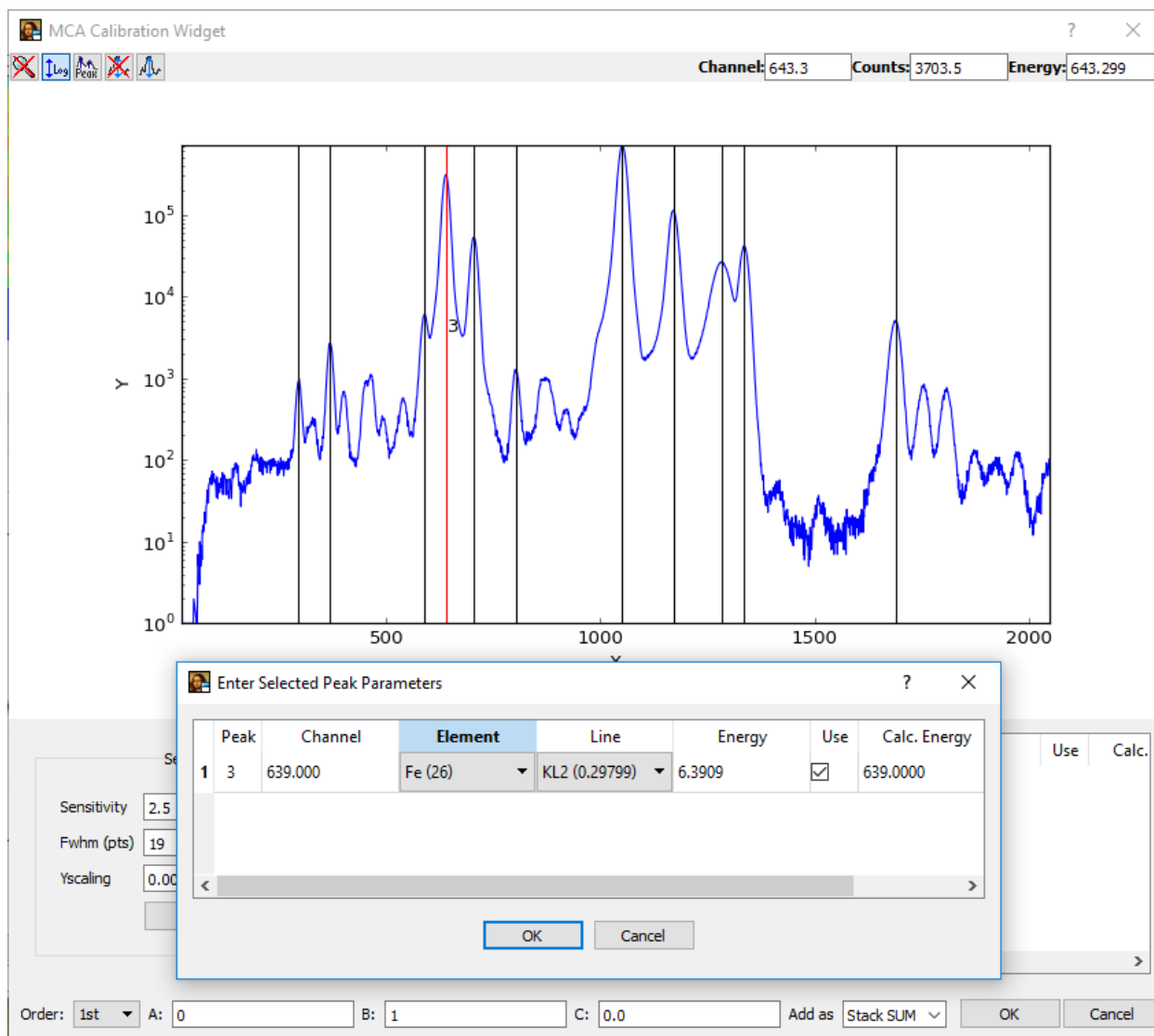


Figure 6. The selected emission line (red line) is known to correspond to the KL2 line of Fe. The user should have an idea on what element and its corresponding emission line is visible in the spectrum.

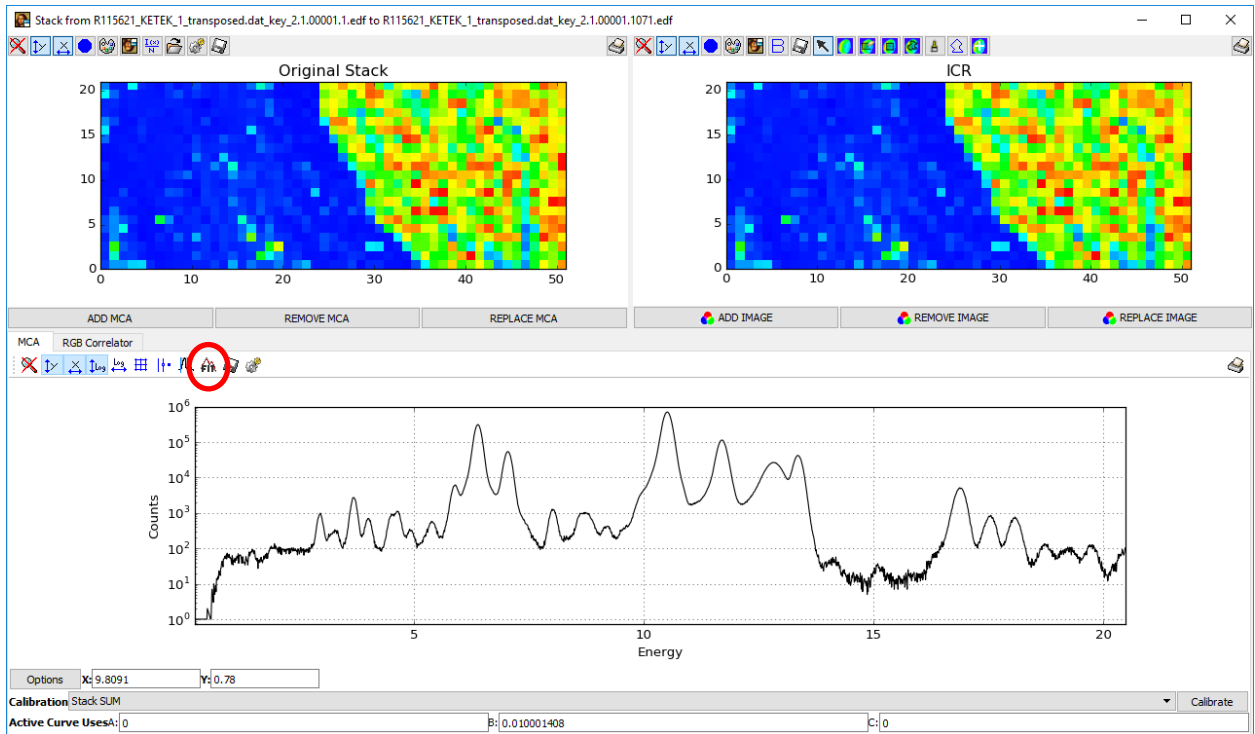


Figure 7. Calibrated spectrum in the logarithmic scale for the y-axis. The Advanced Fit button is encircled, which leads to advanced techniques such as semi-quantitative calculations and background stripping.

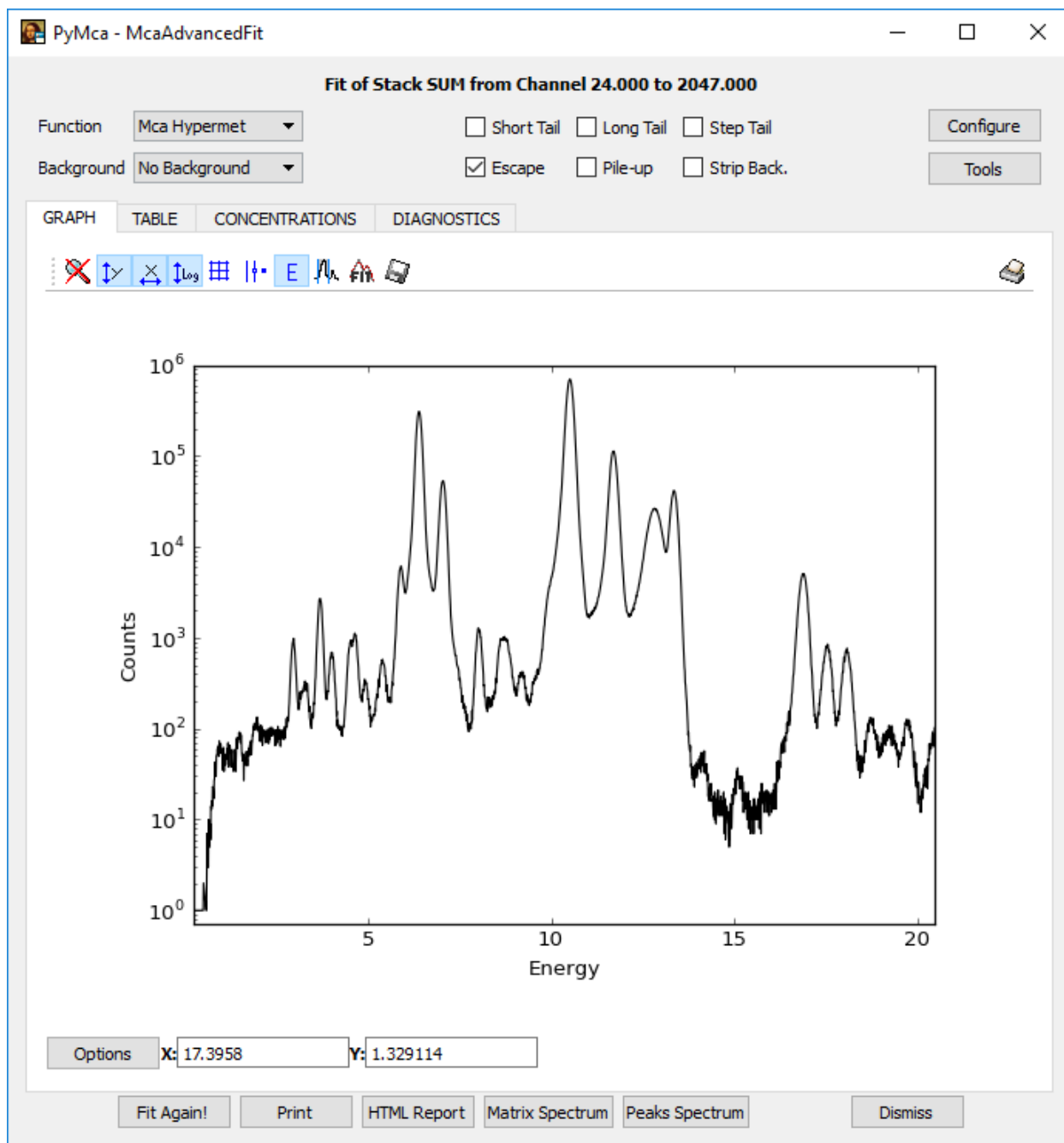


Figure 8. The Advanced Fit dialog box. This allows the configuration of specific parameters of the experiment for identification of emission lines for each element in the sample, as well as matrix corrections and background stripping.

PyMca - MCA Fit Parameters

FIT DETECTOR BEAM PEAKS PEAK SHAPE ATTENUATORS MATRIX CONCENTRATIONS XRFMC

Fit Function: Mca Hypermet

Continuum type: NO Continuum

Polynomial order: 1

Non-analytical (or estimation) background algorithm: Strip **SETUP**

SNIP Background Width: 30

Strip Background Width: 1

Strip Background Iterations: 5000

Strip Background Smoothing Width (Savitsky-Golay): 1

Strip Background use Anchors 0 0 0

Statistical weighting of data: Poisson (1/Y)

Number of fit iterations: 10

Minimum χ^2 difference (%): 0.001

Perform a fit using the selected strategy

Perform a Linear Fit Fixing non-linear Parameters to Initial Values

Limit fitting region to : *First channel* : 58 *Last channel* : 2047

Include:

Stripping Escape peaks Pile-up peaks Scattering peaks

Short tail Long tail Step tail

Load From Fit Load Save Cancel OK

Figure 9. Strip background iterations set at 5000, and stripping is included in background subtraction. Escape peaks are ticked by default, which eliminates the presence of escape peaks in the semi-quantitative analysis.

PyMca - MCA Fit Parameters

FIT DETECTOR BEAM PEAKS PEAK SHAPE ATTENUATORS MATRIX CONCENTRATIONS XRFMC

Open X-Ray Tube Setup Load Table Save Table

Use	Energy	Weight	Use	Energy	Weight	Use	Energy	Weight
<input checked="" type="checkbox"/> Energy 0	13400.000000	1.000000	<input type="checkbox"/> Energy 20		0.000000	<input type="checkbox"/> Energy 40		0.00
<input type="checkbox"/> Energy 1		0.000000	<input type="checkbox"/> Energy 21		0.000000	<input type="checkbox"/> Energy 41		0.00
<input type="checkbox"/> Energy 2		0.000000	<input type="checkbox"/> Energy 22		0.000000	<input type="checkbox"/> Energy 42		0.00
<input type="checkbox"/> Energy 3		0.000000	<input type="checkbox"/> Energy 23		0.000000	<input type="checkbox"/> Energy 43		0.00
<input type="checkbox"/> Energy 4		0.000000	<input type="checkbox"/> Energy 24		0.000000	<input type="checkbox"/> Energy 44		0.00
<input type="checkbox"/> Energy 5		0.000000	<input type="checkbox"/> Energy 25		0.000000	<input type="checkbox"/> Energy 45		0.00
<input type="checkbox"/> Energy 6		0.000000	<input type="checkbox"/> Energy 26		0.000000	<input type="checkbox"/> Energy 46		0.00
<input type="checkbox"/> Energy 7		0.000000	<input type="checkbox"/> Energy 27		0.000000	<input type="checkbox"/> Energy 47		0.00
<input type="checkbox"/> Energy 8		0.000000	<input type="checkbox"/> Energy 28		0.000000	<input type="checkbox"/> Energy 48		0.00
<input type="checkbox"/> Energy 9		0.000000	<input type="checkbox"/> Energy 29		0.000000	<input type="checkbox"/> Energy 49		0.00
<input type="checkbox"/> Energy 10		0.000000	<input type="checkbox"/> Energy 30		0.000000	<input type="checkbox"/> Energy 50		0.00
<input type="checkbox"/> Energy 11		0.000000	<input type="checkbox"/> Energy 31		0.000000	<input type="checkbox"/> Energy 51		0.00
<input type="checkbox"/> Energy 12		0.000000	<input type="checkbox"/> Energy 32		0.000000	<input type="checkbox"/> Energy 52		0.00
<input type="checkbox"/> Energy 13		0.000000	<input type="checkbox"/> Energy 33		0.000000	<input type="checkbox"/> Energy 53		0.00
<input type="checkbox"/> Energy 14		0.000000	<input type="checkbox"/> Energy 34		0.000000	<input type="checkbox"/> Energy 54		0.00
<input type="checkbox"/> Energy 15		0.000000	<input type="checkbox"/> Energy 35		0.000000	<input type="checkbox"/> Energy 55		0.00
<input type="checkbox"/> Energy 16		0.000000	<input type="checkbox"/> Energy 36		0.000000	<input type="checkbox"/> Energy 56		0.00
<input type="checkbox"/> Energy 17		0.000000	<input type="checkbox"/> Energy 37		0.000000	<input type="checkbox"/> Energy 57		0.00
<input type="checkbox"/> Energy 18		0.000000	<input type="checkbox"/> Energy 38		0.000000	<input type="checkbox"/> Energy 58		0.00
<input type="checkbox"/> Energy 19		0.000000	<input type="checkbox"/> Energy 39		0.000000	<input type="checkbox"/> Energy 59		0.00

Load From Fit Load Save Cancel OK

Figure 10. Beam energy is set in the Beam tab. This may vary for each experiment, so the user needs to write the energy level for each experiment. In the project, the energy levels were set at 13150, 13700, 13840, and 13400 eV for the December 2016, January 2017, June 2017, and November 2017 beamtimes, respectively.

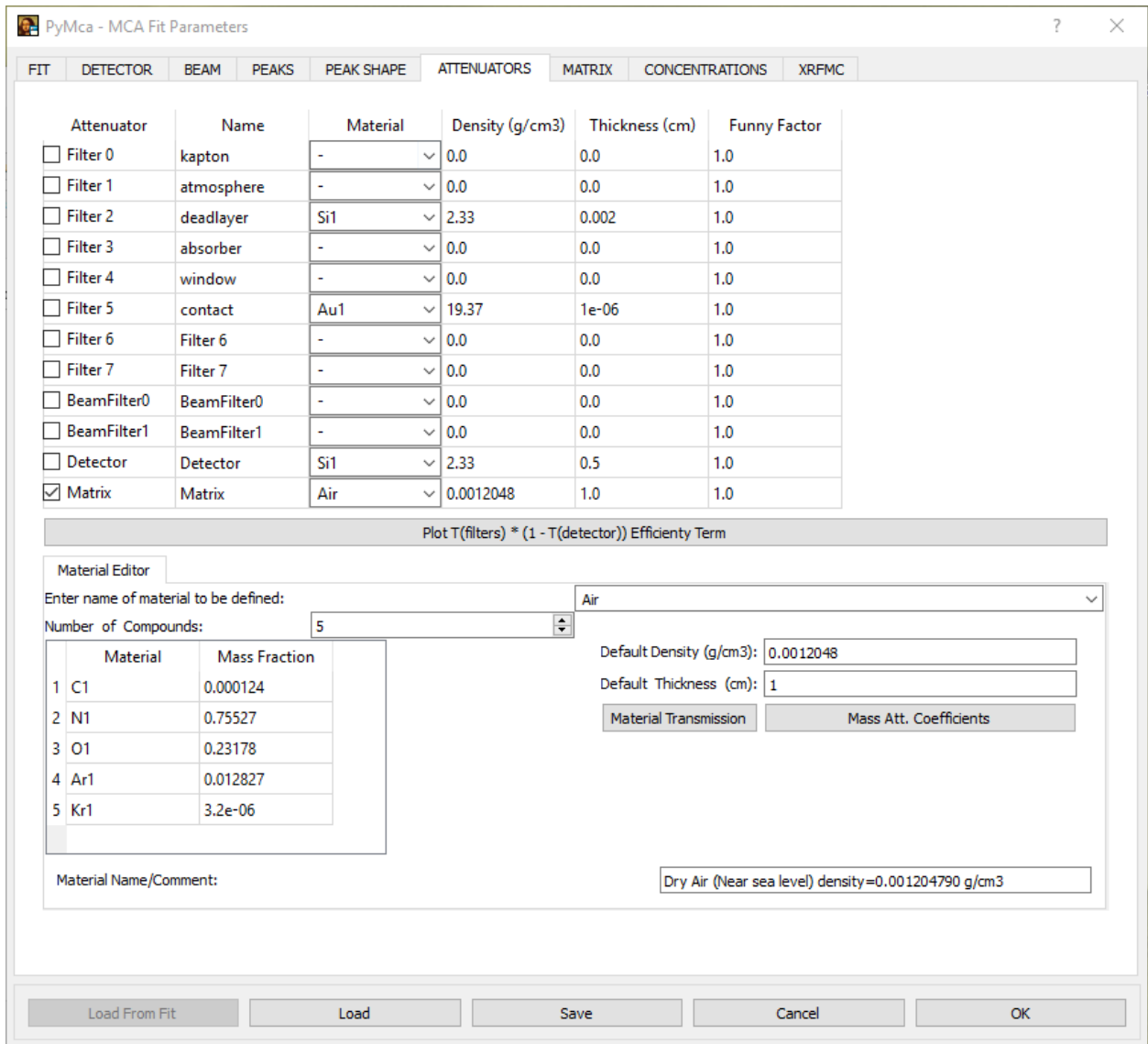


Figure 11. Attenuators tab, which allows the user to select any possible attenuators in the analyses. In the experiment, the only attenuator assumed was air in the matrix.

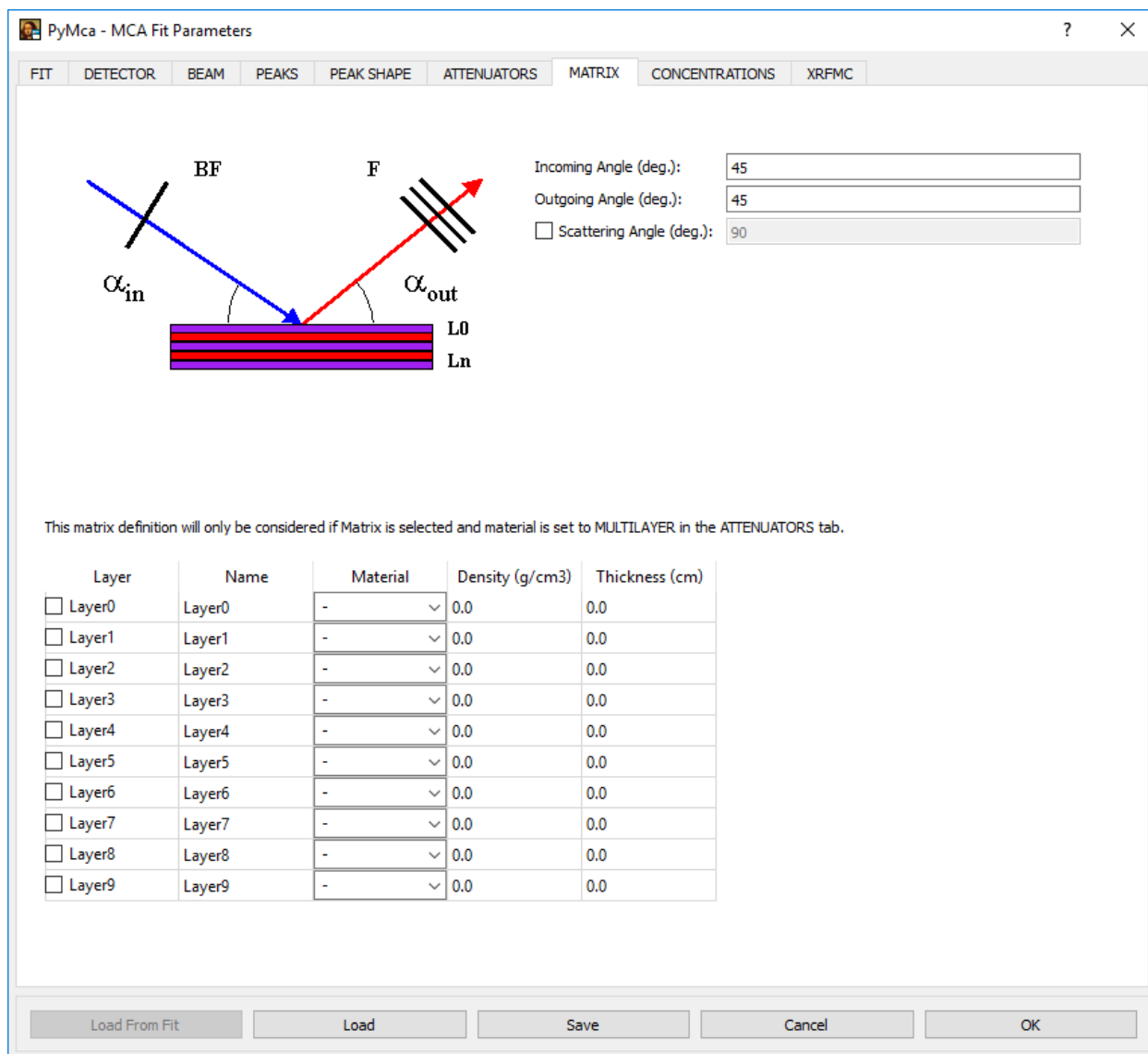


Figure 12. In the matrix tab, the incoming and outgoing angles of the beam are both set at 45 degrees, reflecting the setup of the analyses.

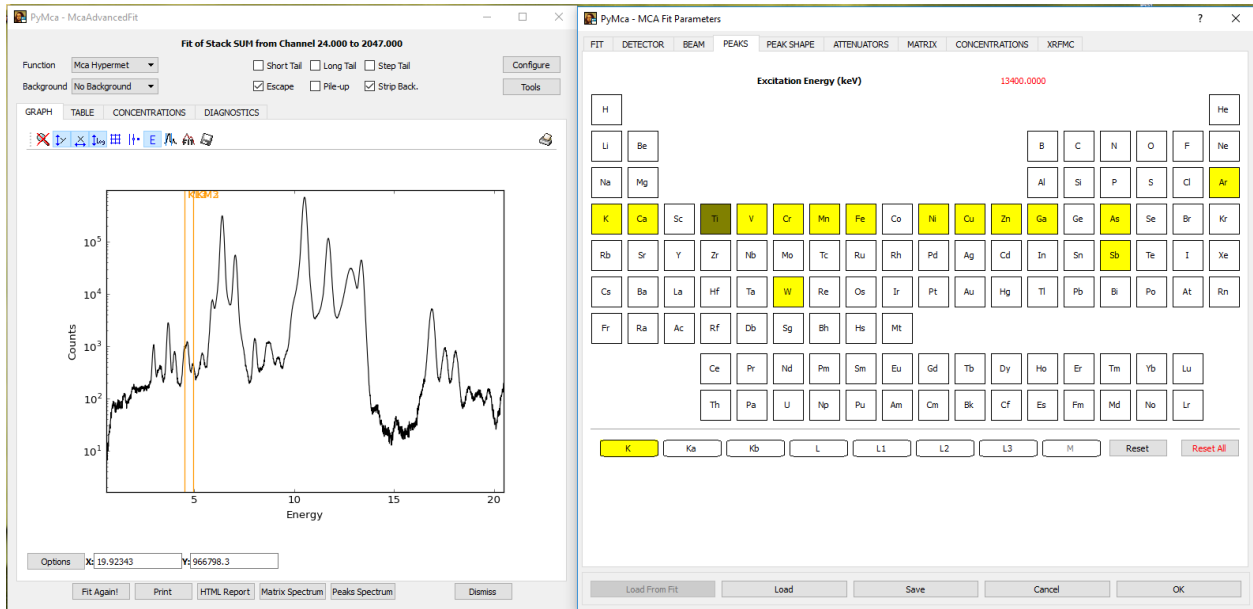


Figure 13. Peak selection tab, where the user can manually match elements and their corresponding emission lines. In this example. Ti K lines are being matched in the spectrum.

energy, the user can simply click on the position in the Advance Fit dialog box (the Fit Parameters window should be closed), and decision on what element is present is credited to the user, as seen in Fig. 14. After all peaks are identified, fitting of the elements in the spectrum will be performed. All peaks are to be identified to achieve the best fit, but there are cases that some peaks will be left unidentified. This could be attributed to noise, or the presence of pile-up peaks due to loss of some photons during dead time (Harris and Selinger, 1979). PyMCA currently has no ability to discern pile-up peaks of certain elements that may interfere with fitting. Pile-up peaks are usually ignored in this project, since they are not observable in the program, and are beyond the scope of this study. Enabling the peaks spectrum in the Advanced Fit window will allow the viewing of individual elements selected previously in the Peaks tab in the Fit Parameters window. The spectrum is usually saved as a .png image, and the user is entitled to alter the colours and line styles of each element identified (Fig. 15). The settings in the Fit Parameters window can also be saved to allow the user to utilize the same parameters on samples run with the same settings.

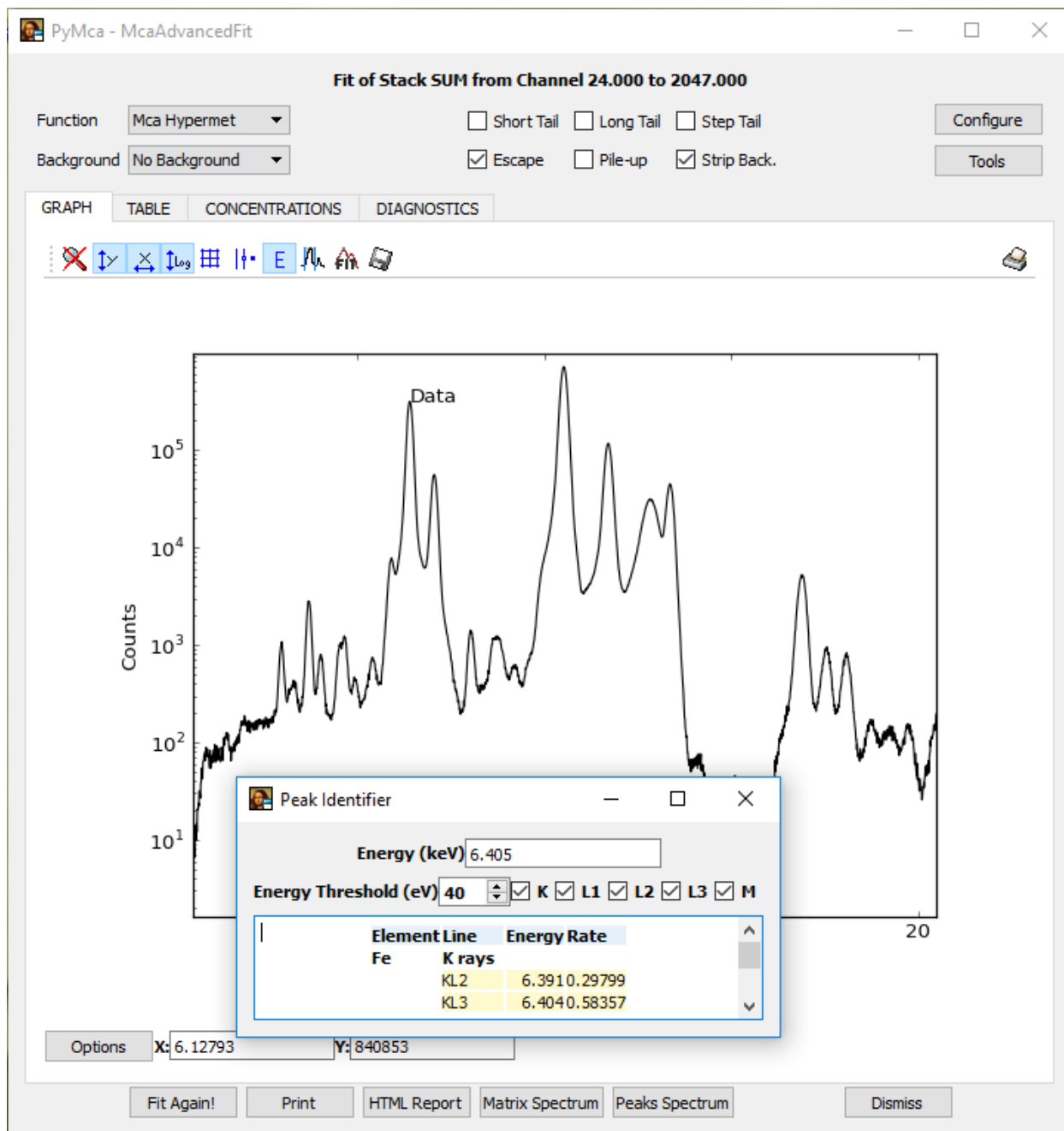


Figure 14. In cases where the peak cannot be identified, the user can simply click on the peak in the Advanced Fit window, and the Peak Identifier box will pop up, showing a list of possible elements. In this example, the selected peak (marked as Data in the example, is identified by the program as Fe.

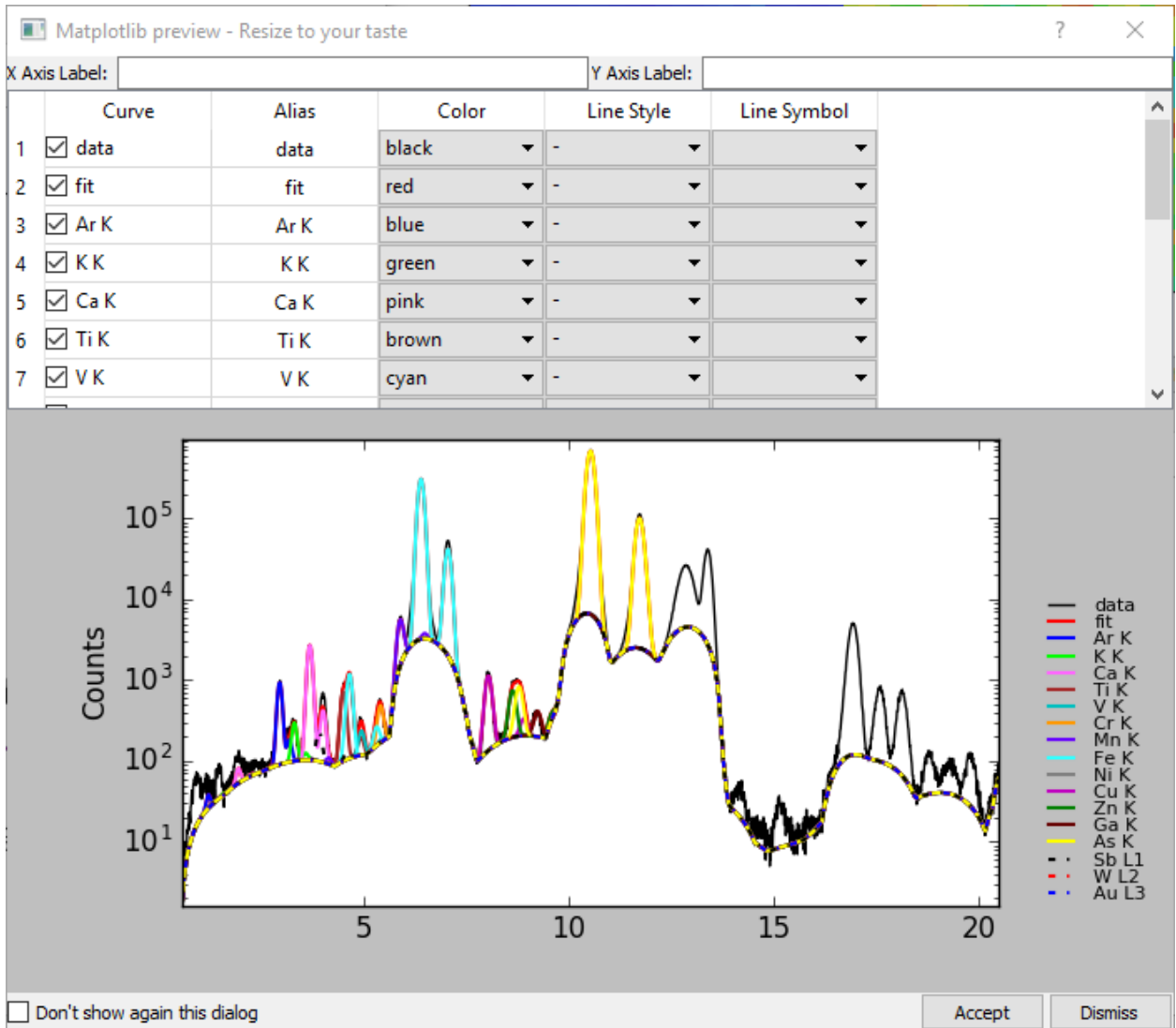


Figure 15. A snippet of the spectrum with each element showing a certain colour and line style, which can be readily edited.

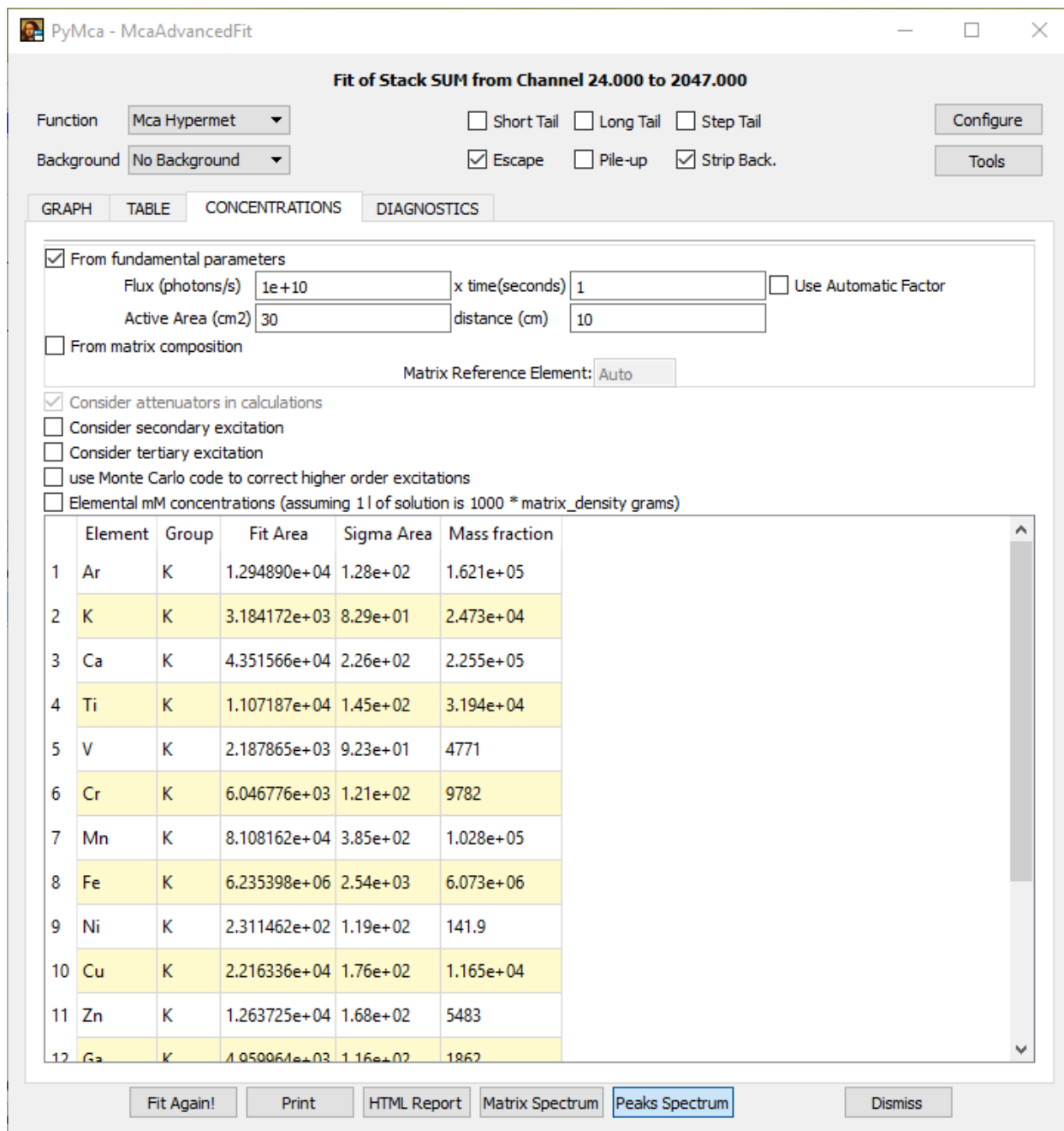


Figure 16. Concentrations tab, where absolute abundances are shown. Results here are beyond the scope of this study, since all possible attenuators were not recorded.

Absolute concentrations of each element in the analysis is viewable in the Concentrations tab in the Advanced Fit window, but corrections for this are beyond the scope of this study.

Upon returning to the first window, the user can visualize the fit of all the elements in the spectrum. Regions of Interest (ROIs) are to be made to create maps of each element in the spectrum. The ROI widget (encircled in Fig.17) is the tool for creating ROIs, and the user will be adding as many ROIs as there are elements identified. The MCA spectrum saved in the Advanced Fit window will be handy in the creation of ROIs corresponding to each element. ROI ranges are set at around 0.3 to 0.5 KeV for consistency and accurate representation of the relative abundance of each element in their corresponding 2-dimensional maps. Further tests revealed that increasing or decreasing the ROI ranges are not so crucial in the creation of maps, but some pixels will be displaying lower or higher counts for some spots. The effects of these are beyond the scope of this study, and the ranges are maintained at 0.3 to 0.5 KeV for simplicity. ROIs can also be saved to allow the user to use the same ROIs for a multitude of samples. Once the ROIs have been set, maps of each element are to be saved using the Matplotlib tool in the interface (as seen in Fig. 18). Stack maps are saved with the default parameters in the Matplotlib window for consistency. Alternatively, the user is free to set parameters to add labels, scale bars, and other settings. Note that the stack maps produced are not interpolated, providing the best representation of each pixel in the sample. Interpolating the pixels will simply alter the image to gradients, which eliminates the relationship of each pixel with each other. Saved stack maps can then be used in interpretation of element relationships.

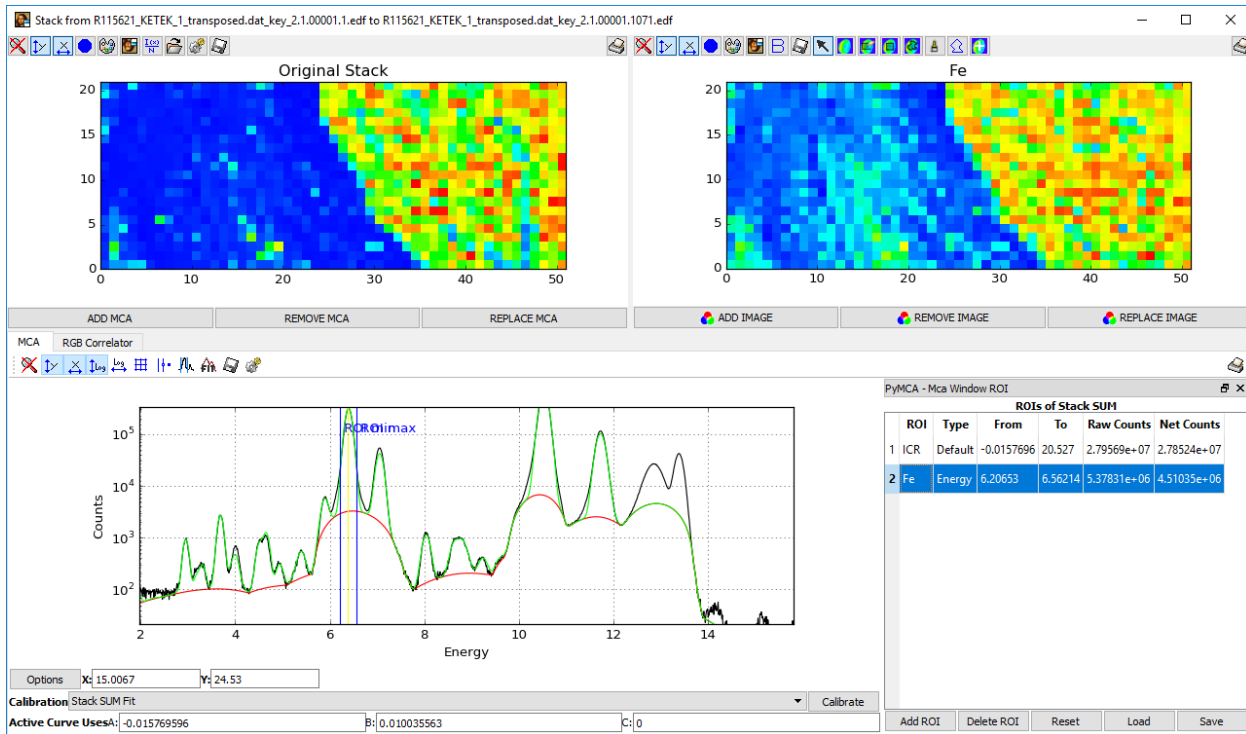


Figure 17. The ROI widget enabled with a region of interest for Fe shown. The yellow line should be very close to the peak of the element of concern, and the minimum and maximum ROIs should be at a range of 0.3 to 0.5 KeV.

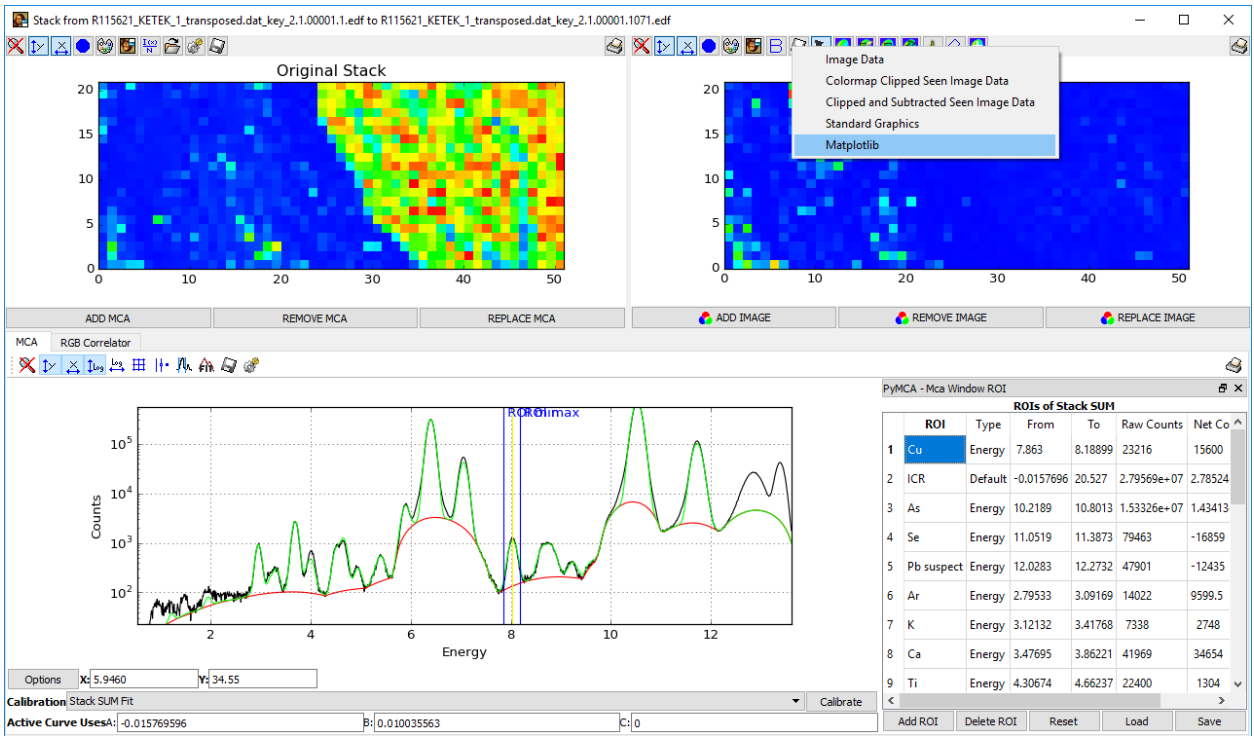


Figure 18. Selecting the Matplotlib function will allow the user to save each stack map with parameters of choice.

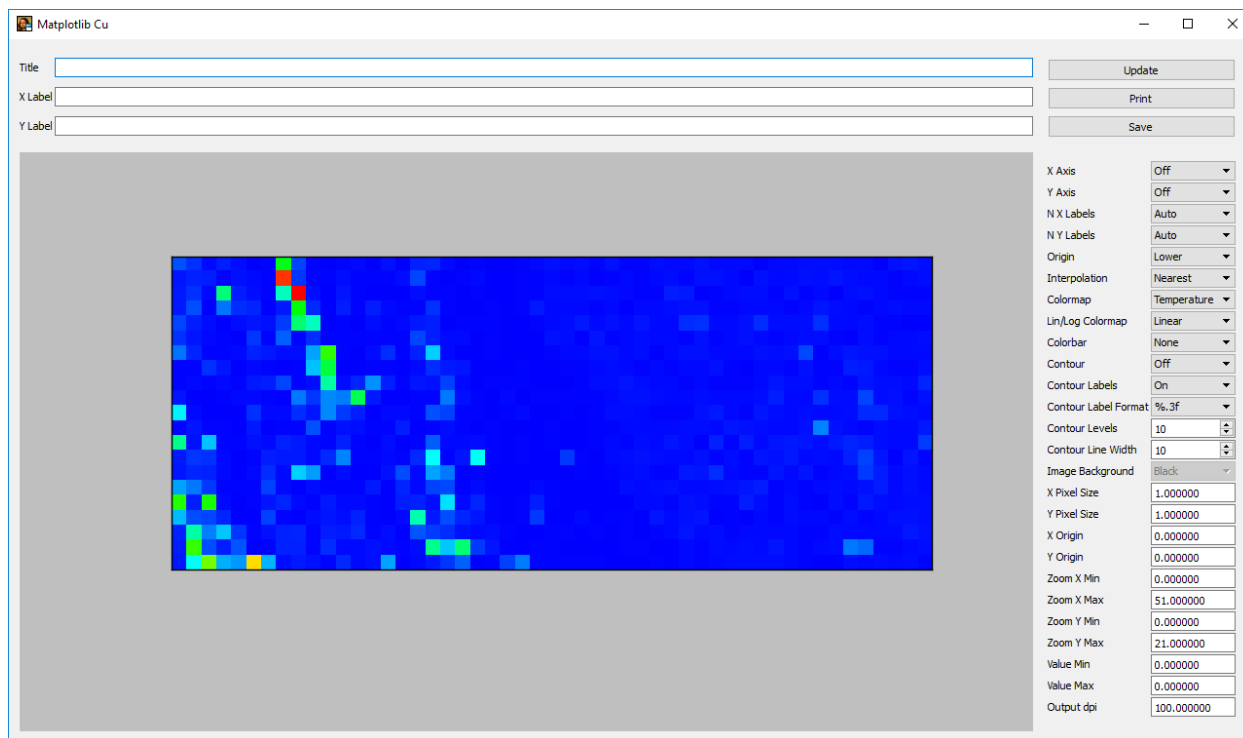


Figure 19. The Matplotlib window allows the user to personalize the stack maps. All stack maps are just saved with the default parameters.

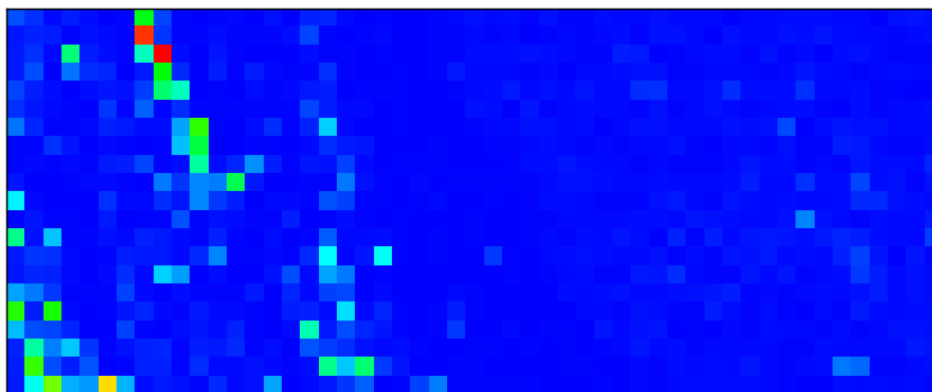


Figure 20. Sample stack map of Cu saved using the Matplotlib tool. The map can then be used in interpretation of relationships between elements,

PyMCA versus Peakaboo

Peakaboo, a software developed by Sherry et al (undated) as part of the Science Studio package for remote collection and management of data from synchrotron beamlines. The program was primarily created to interpret X-ray fluorescence data collected from the VESPERS beamline at the Canadian Light Source (McIntyre et al, 2010), but is also suited in interpreting data from other beamlines capable of producing 2-dimensional maps, such as the IDEAS beamline at the Canadian Light Source. The program was utilized to investigate for Au hotspots present in the samples analysed during the first three runs (December 2016, January 2017, and June 2017).

Upon the comparison of the Au maps interpreted via PyMCA, the author compared the maps produced with Peakaboo to the maps made via PyMCA, and some differences were pointed out. PyMCA interprets data from the bottom left to the top right, unlike Peakaboo which forces the origin at the top right. This may present problems in interpreting and comparing maps from other softwares, i.e. Peakaboo maps with PyMCA results. Unlike PyMCA, which allows the user to select a region of interest based on the preferred emission line, Peakaboo fits spectrum according to all lines of the element present. A good example of this is shown in Figure 21, where some peaks present in PyMCA are not visible in Peakaboo. More intense spots were found using PyMCA (Figure 21, right), which may be due to the difference in spectrum fitting of Peakaboo. Nevertheless, the observed spots were still analysed for Au. Thorough study of the difference between the methodology of Peakaboo in identifying spots is beyond the scope of this study.

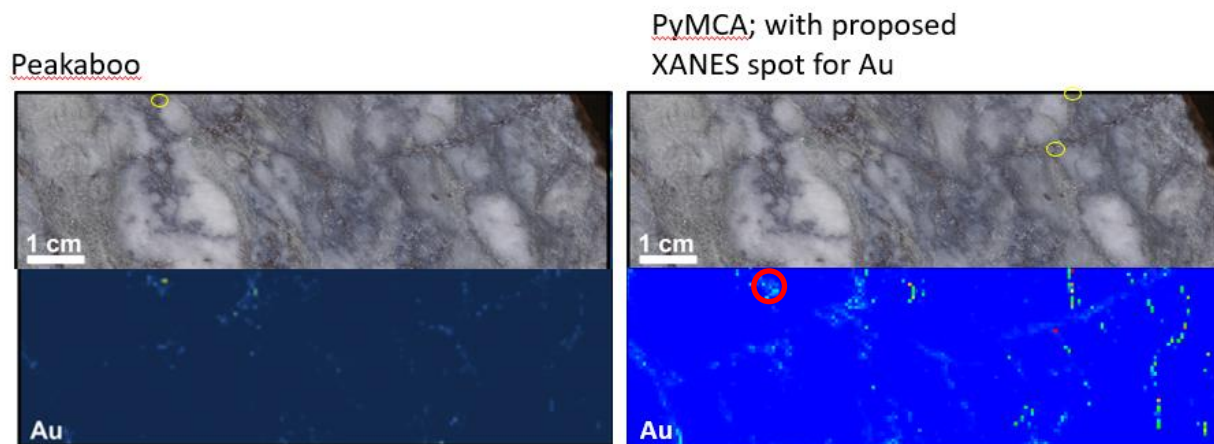
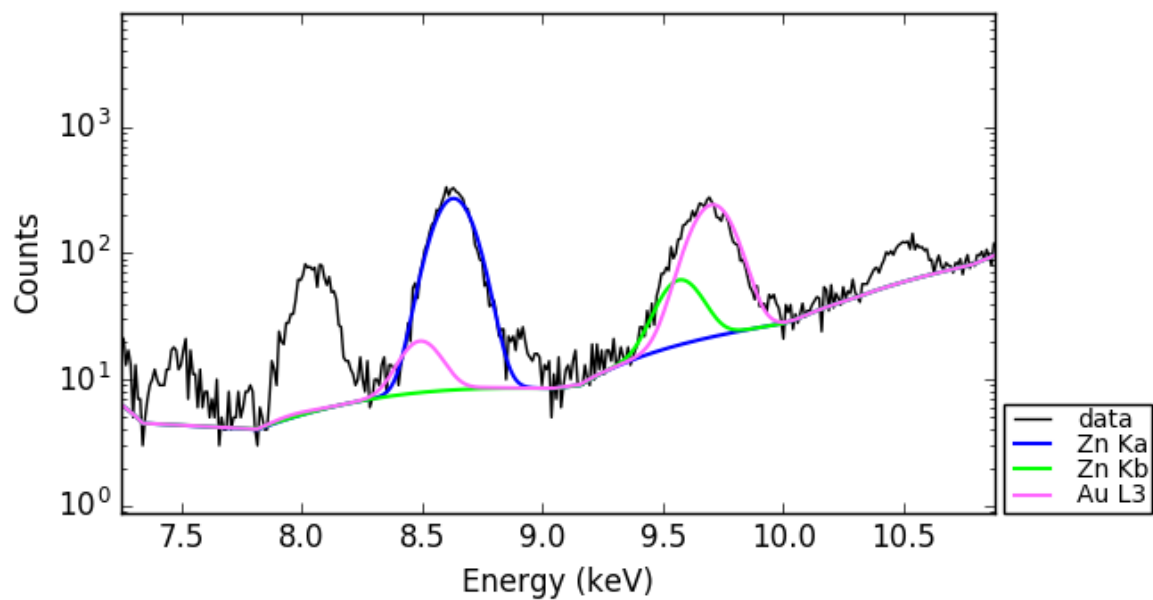
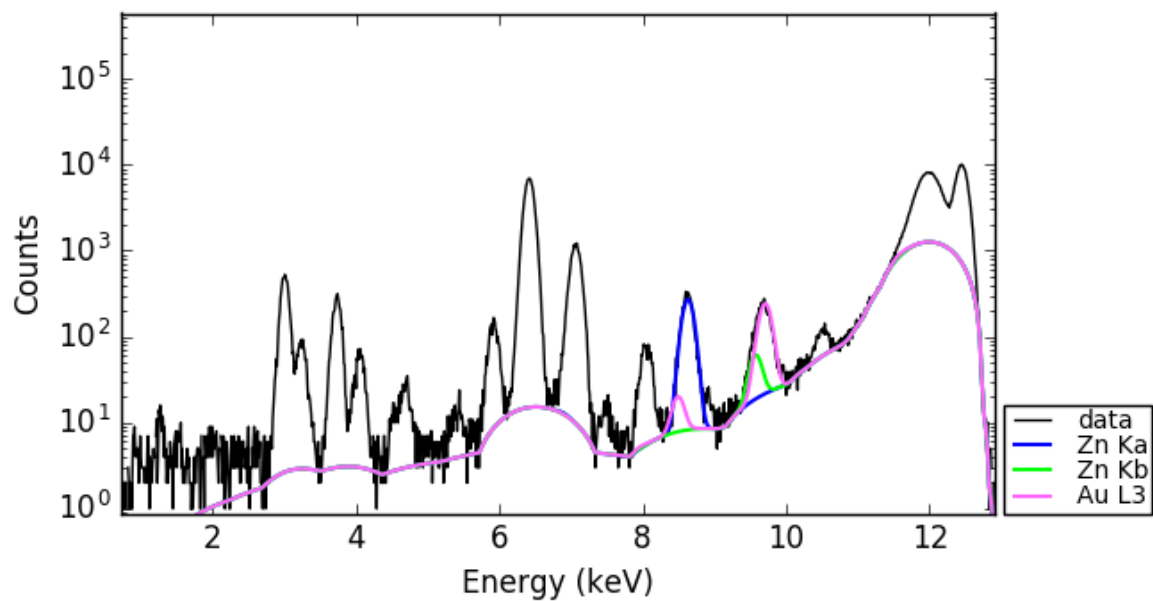


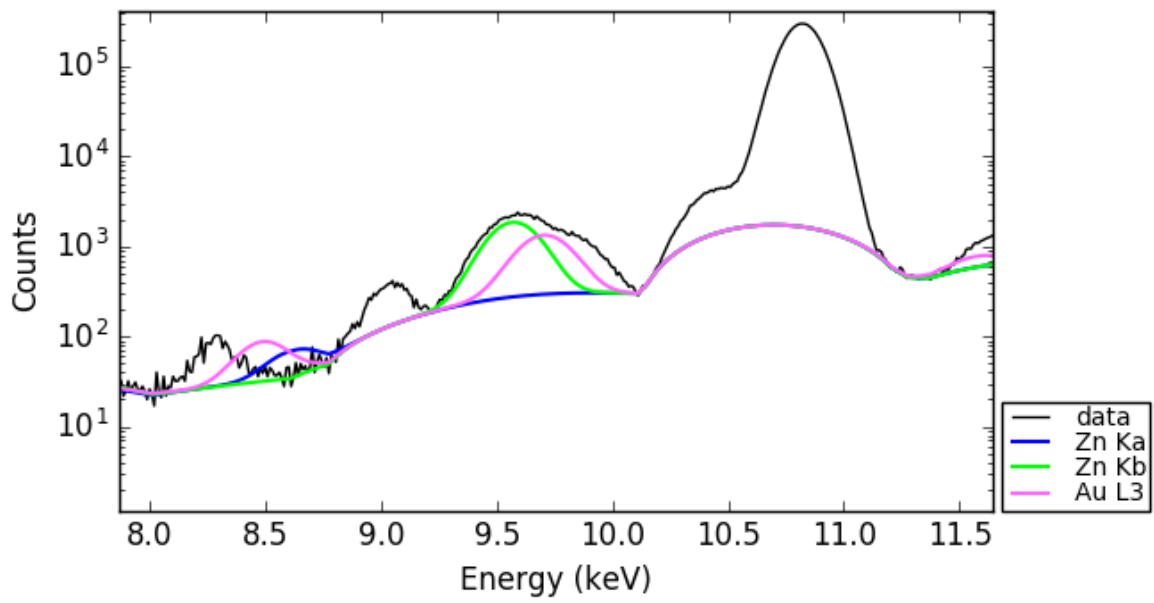
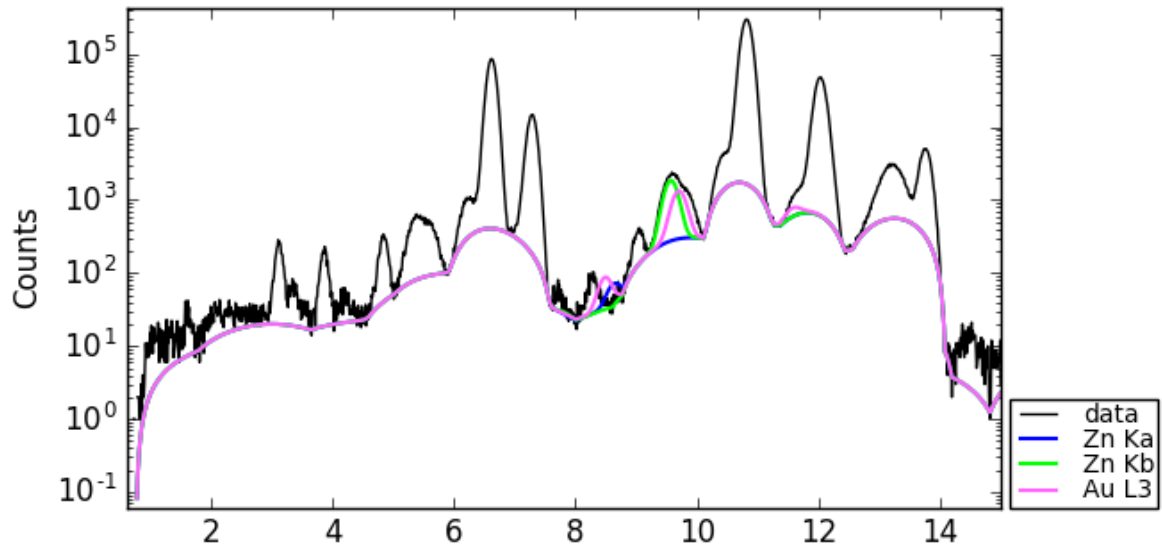
Figure 21. Peakaboo (left) versus PyMCA (right) hotspots for Au. Note that the hot pixel from Peakaboo is still present (encircled red), but spots encircled yellow in the right shows pixels not found in Peakaboo.

Appendix F: MCA spectra of samples analysed for Au XANES

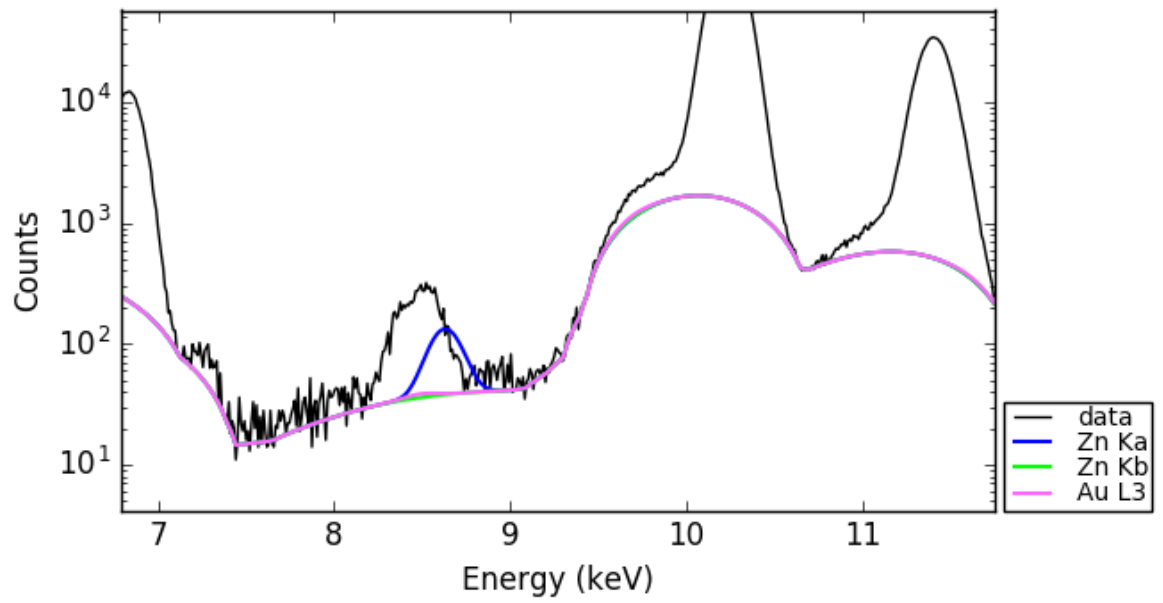
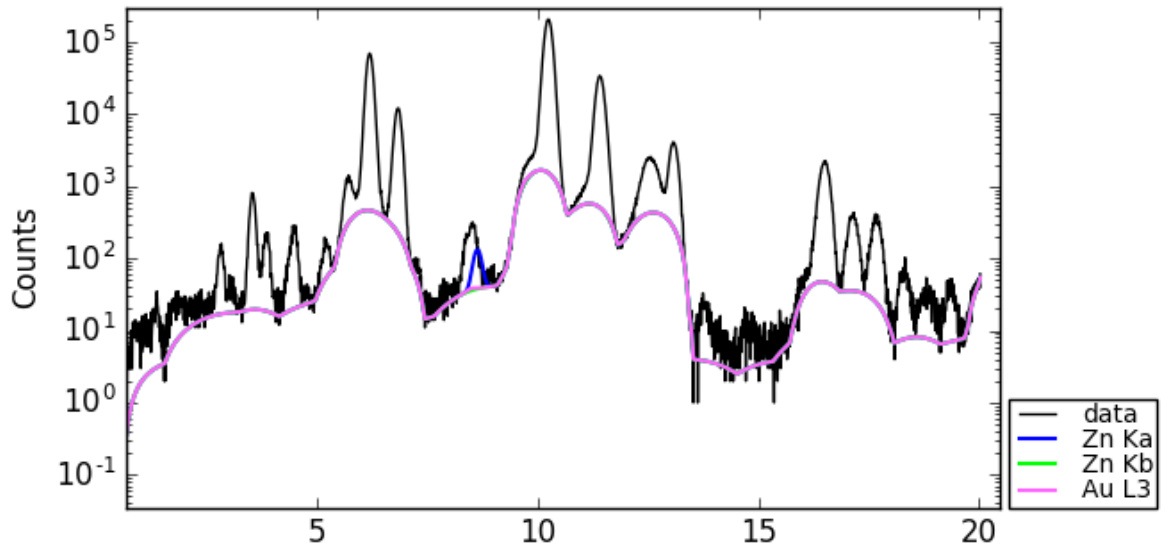
C611



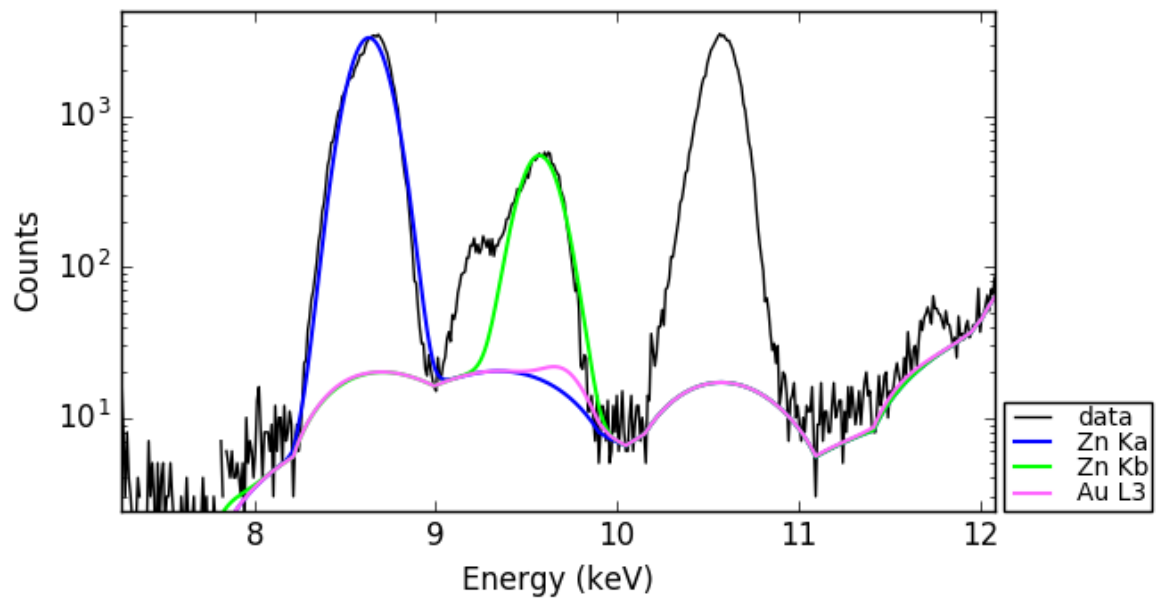
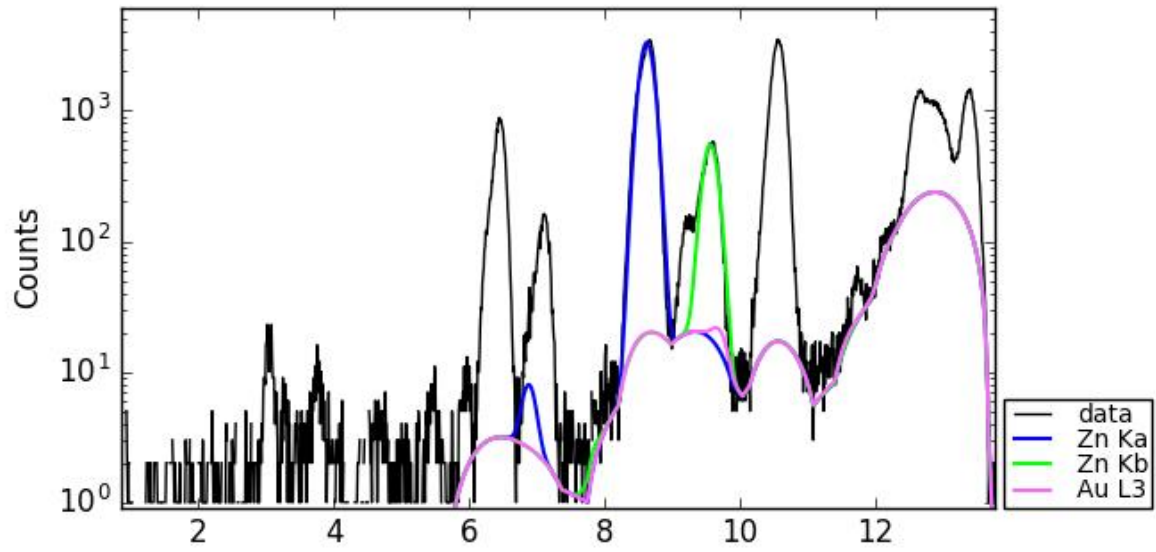
R115604



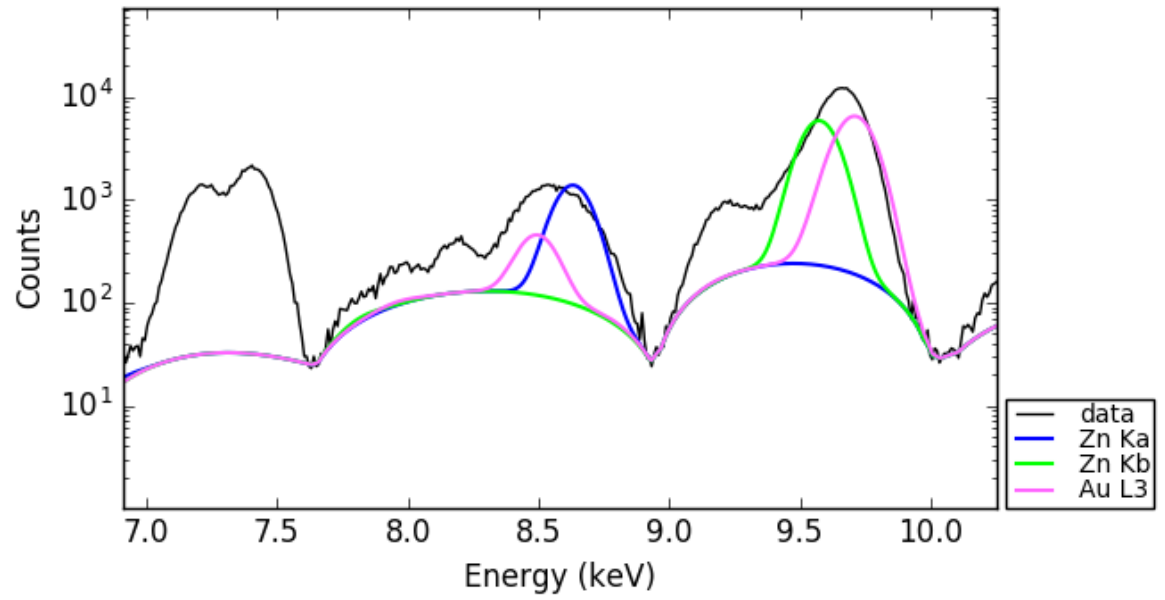
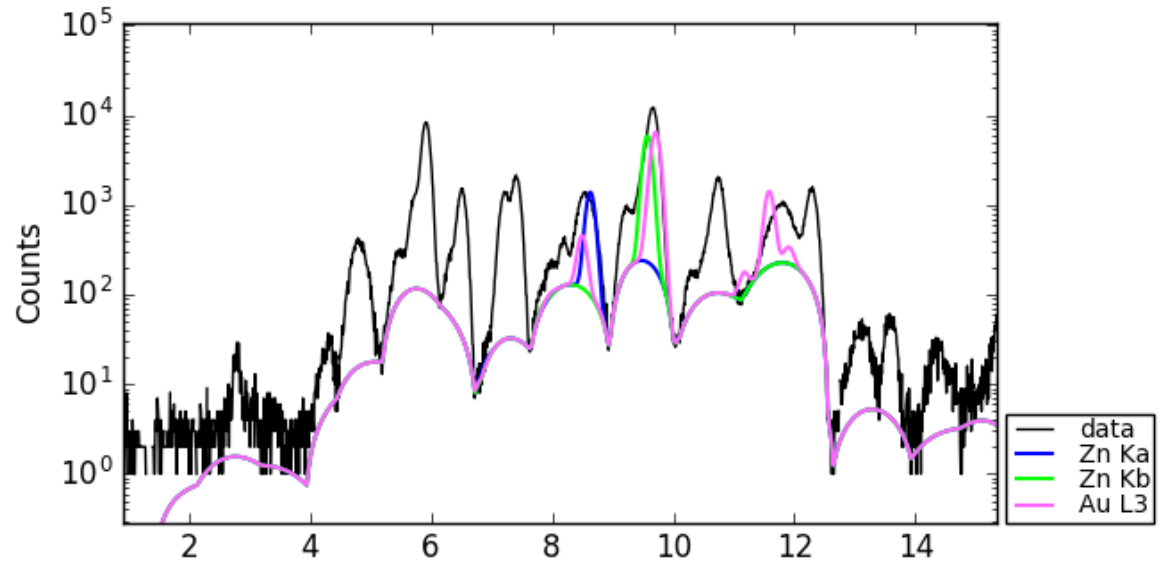
R115622



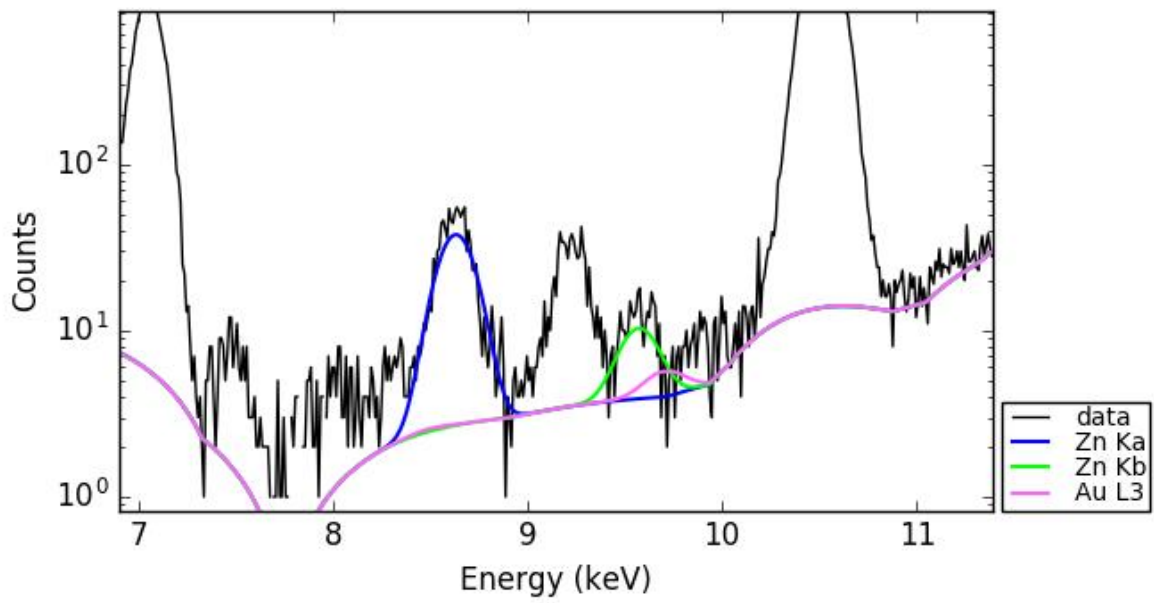
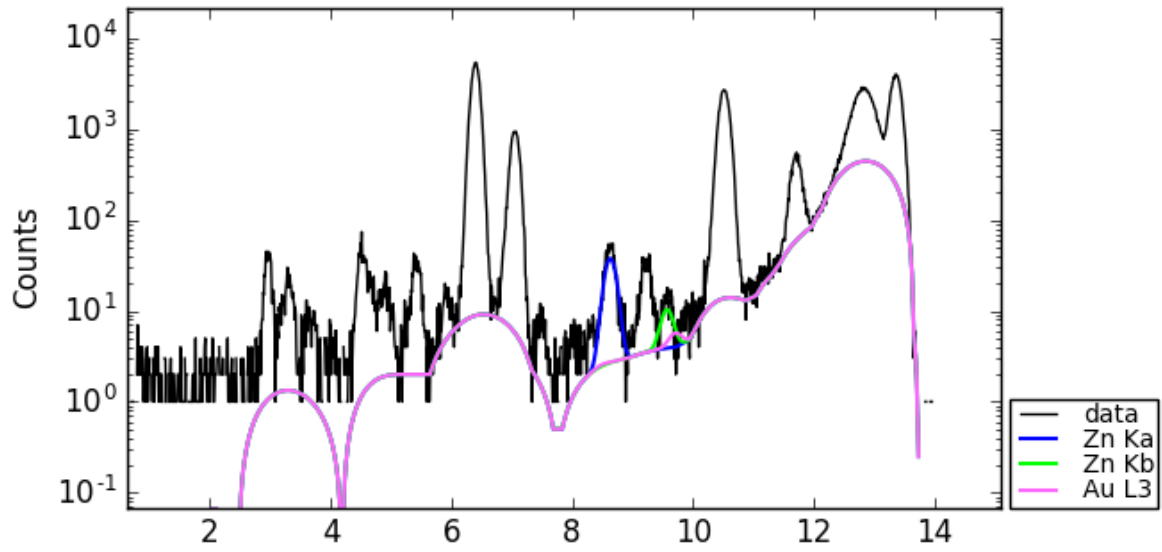
R432250



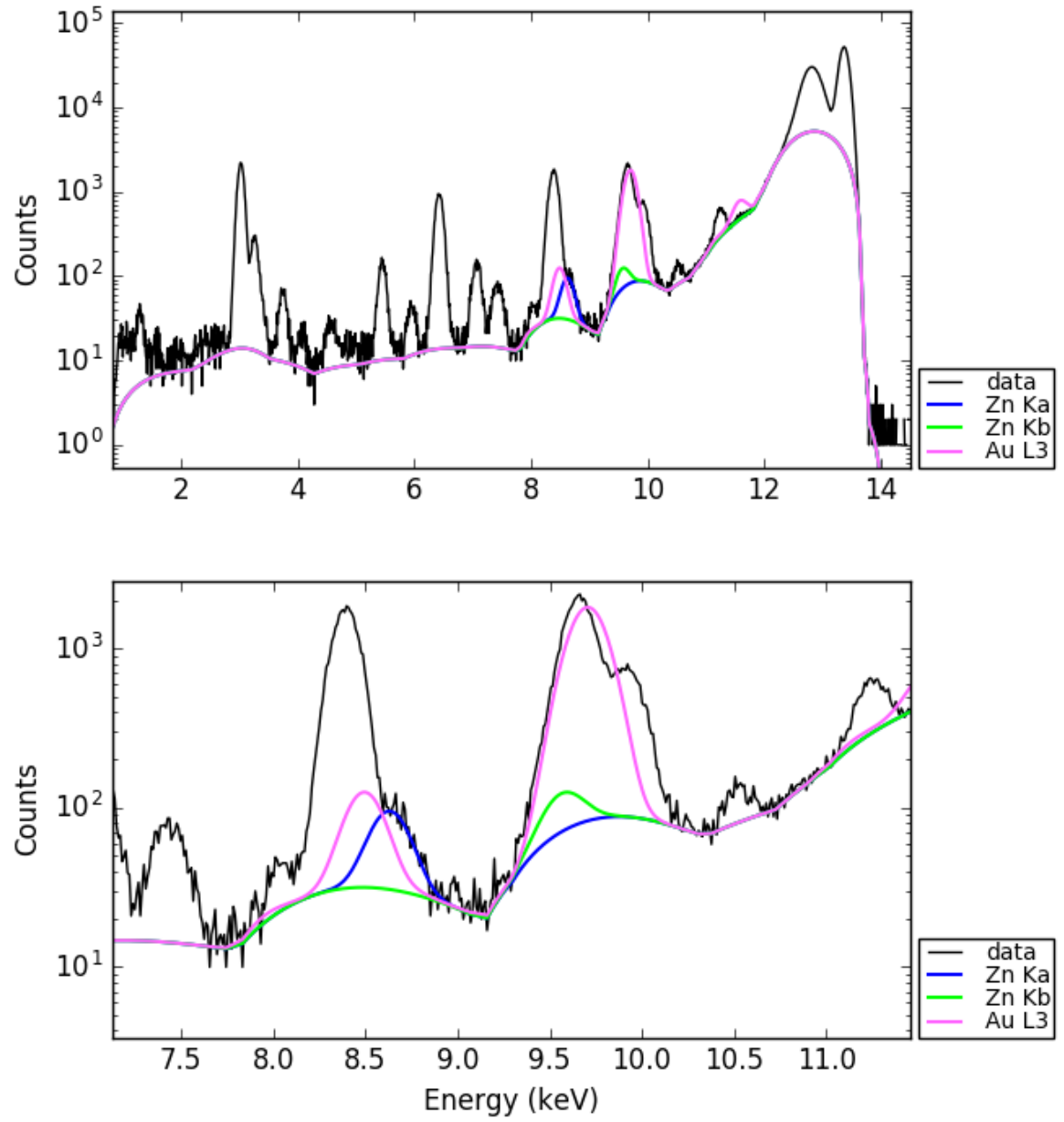
S345537



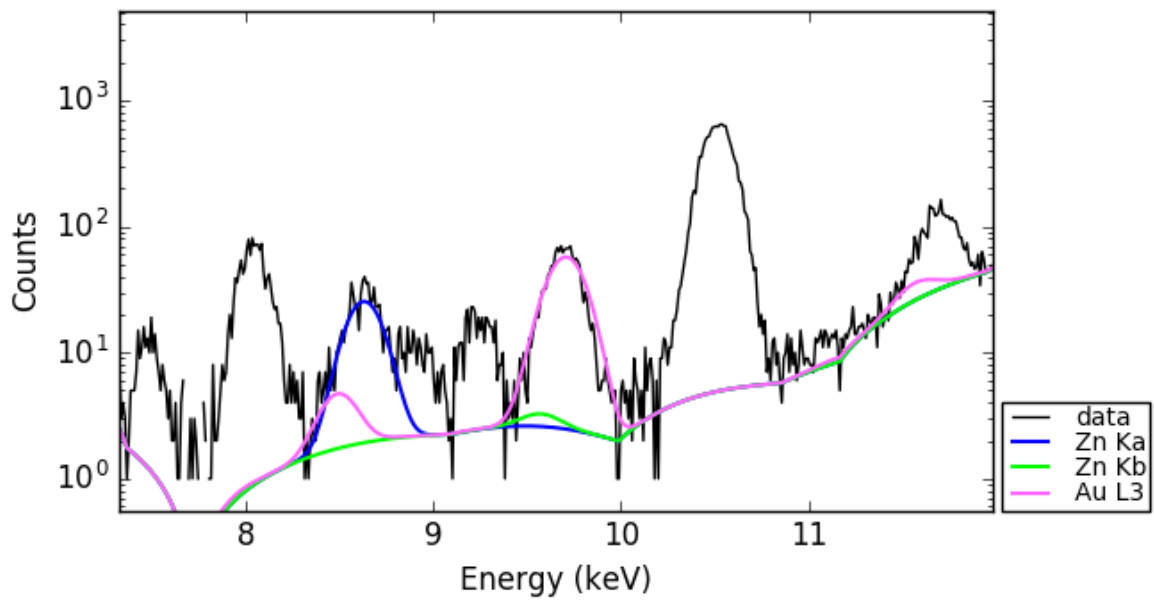
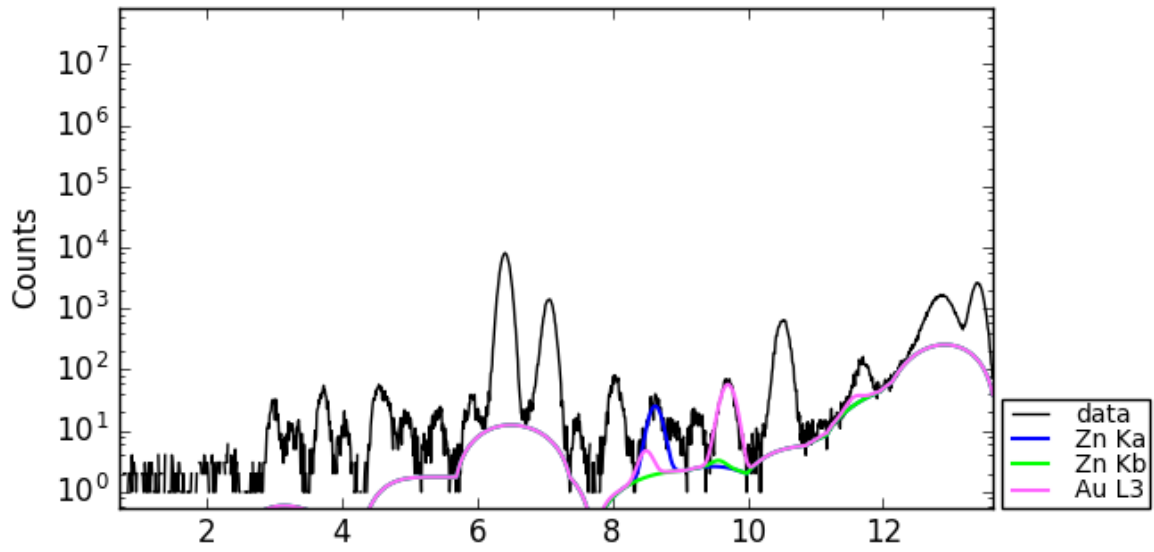
S521365



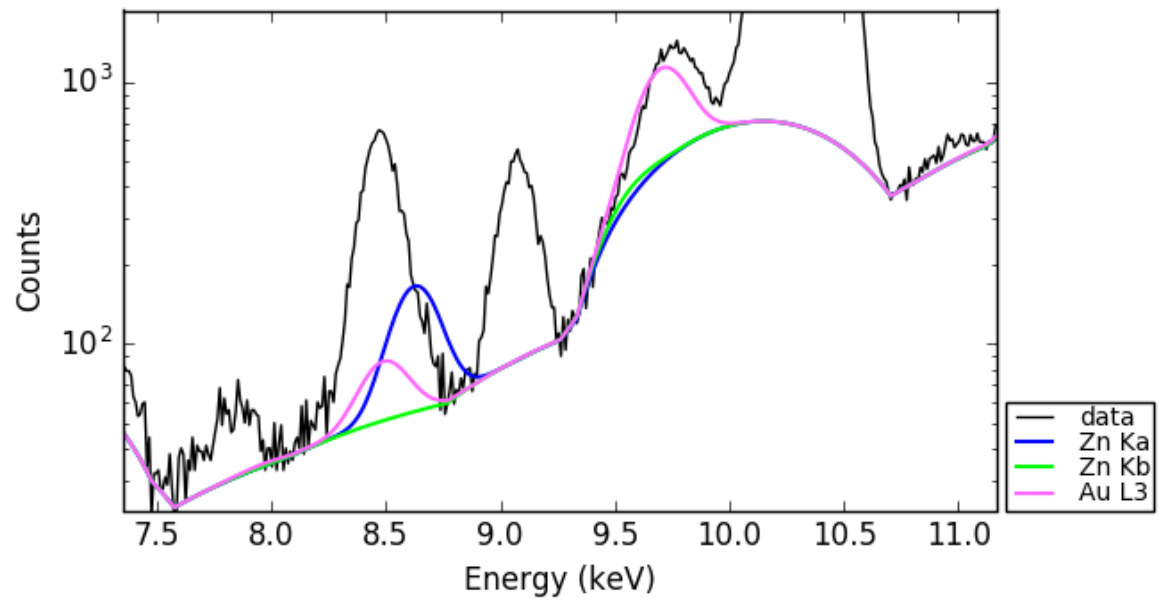
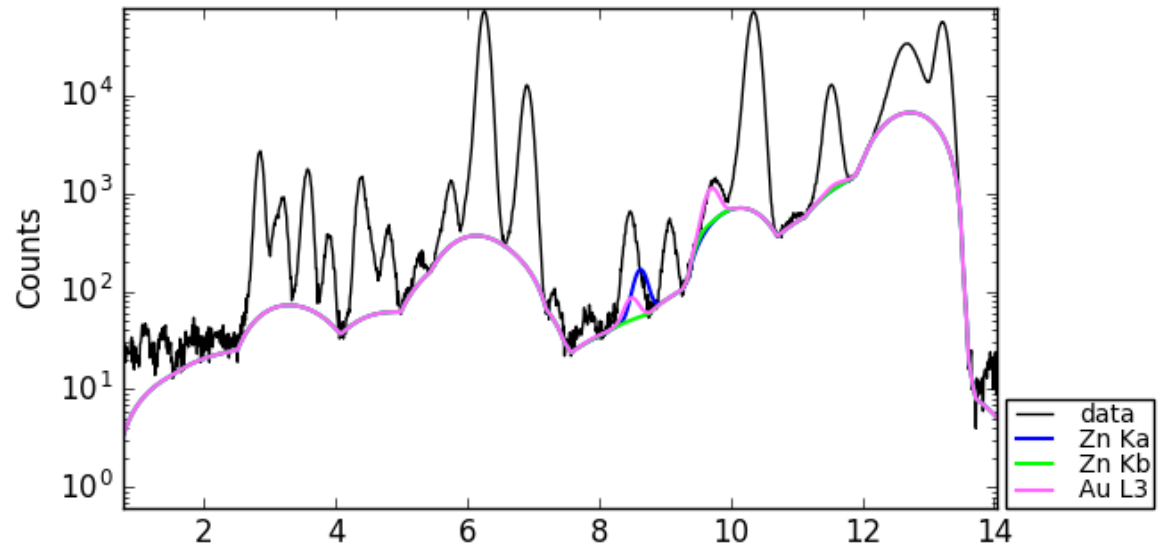
S892082



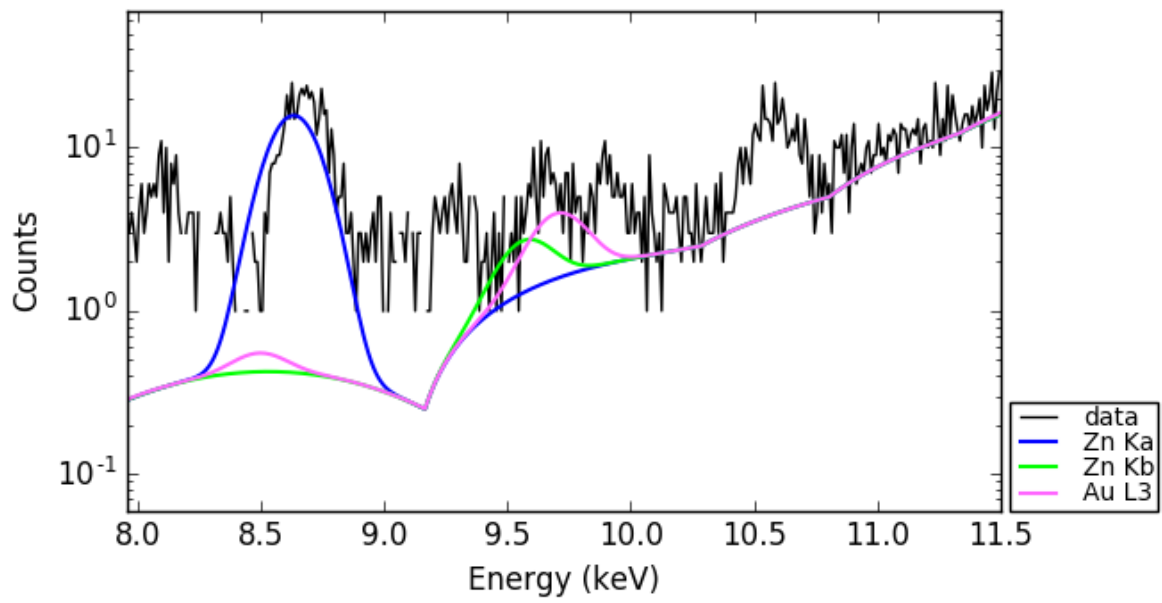
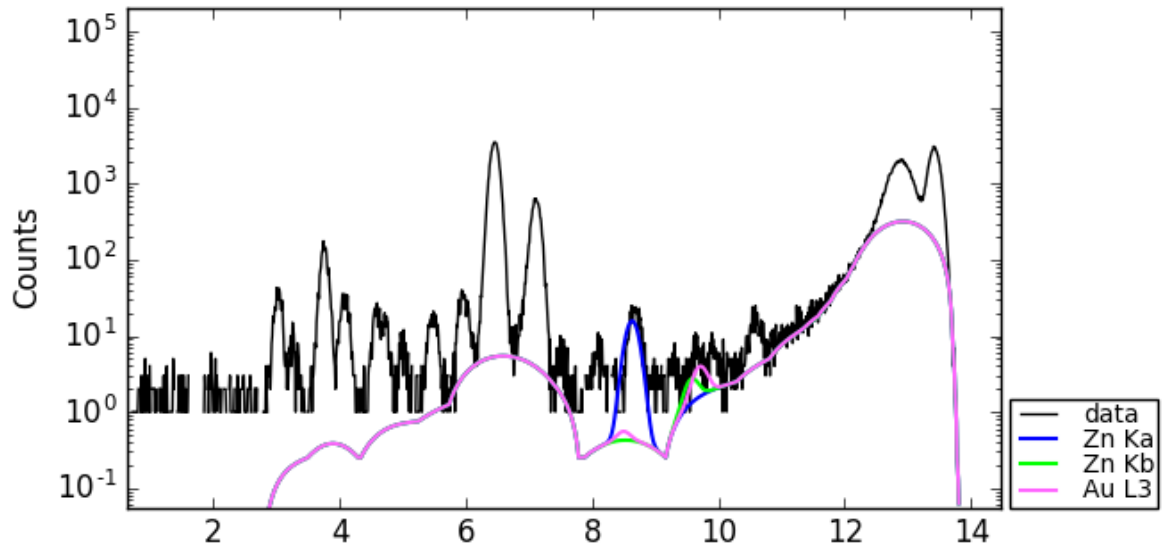
S892089



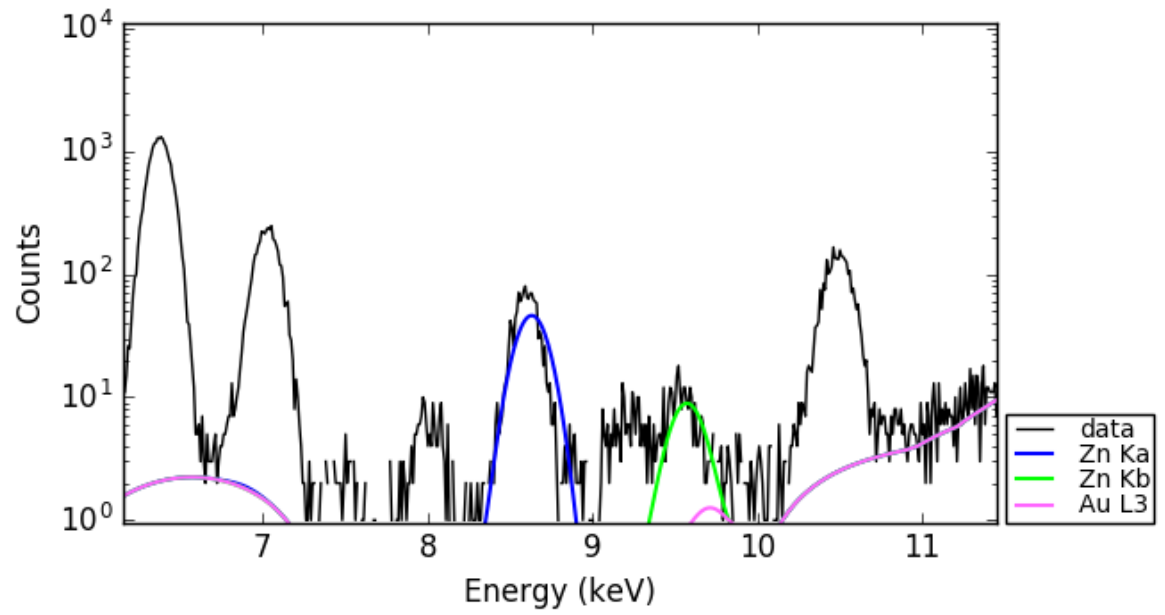
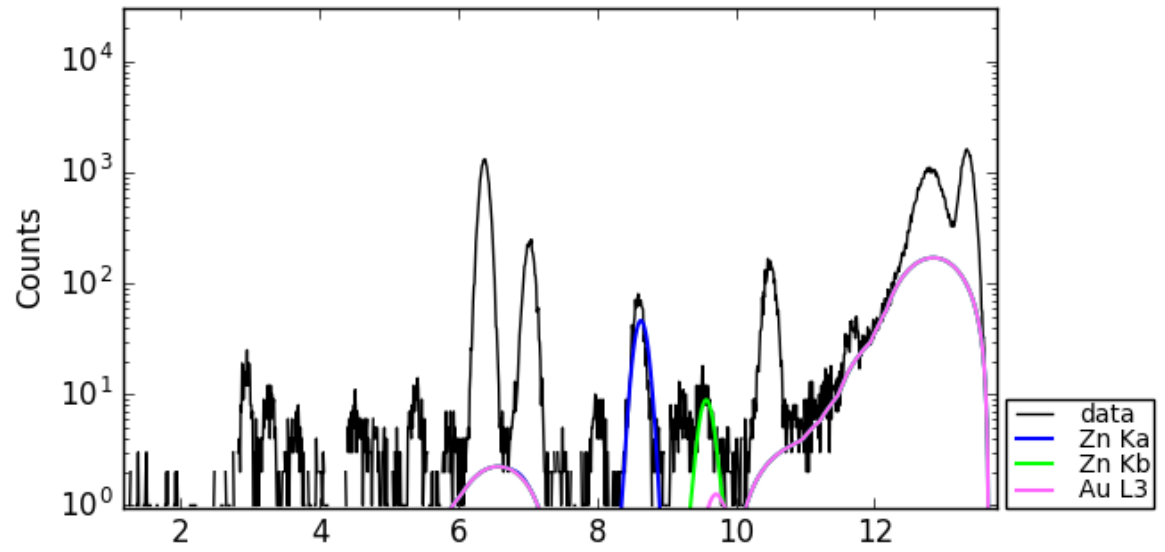
V156522



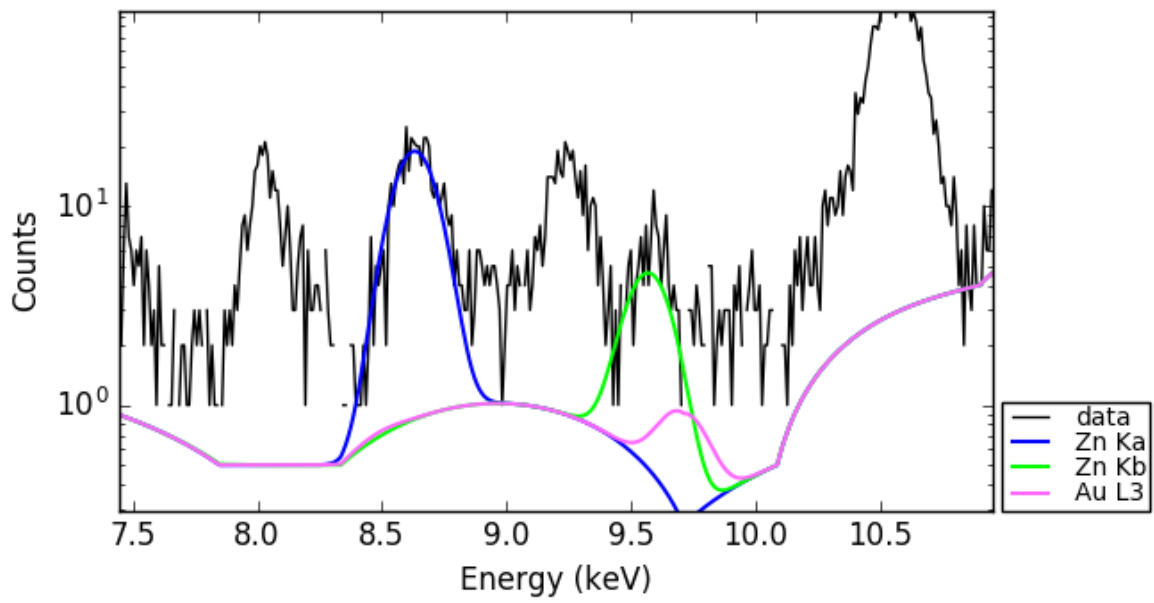
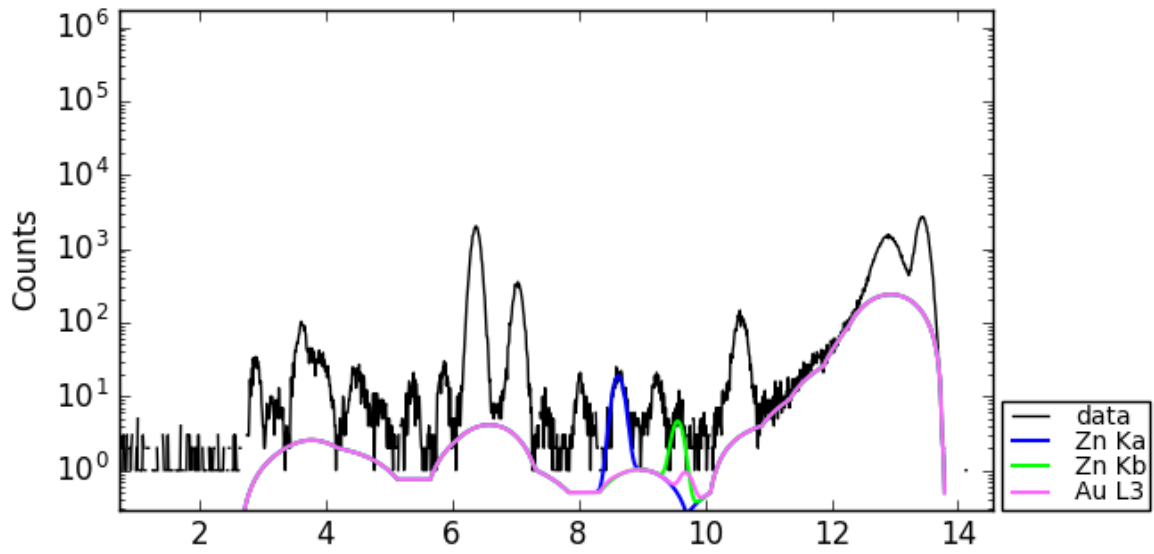
V156527



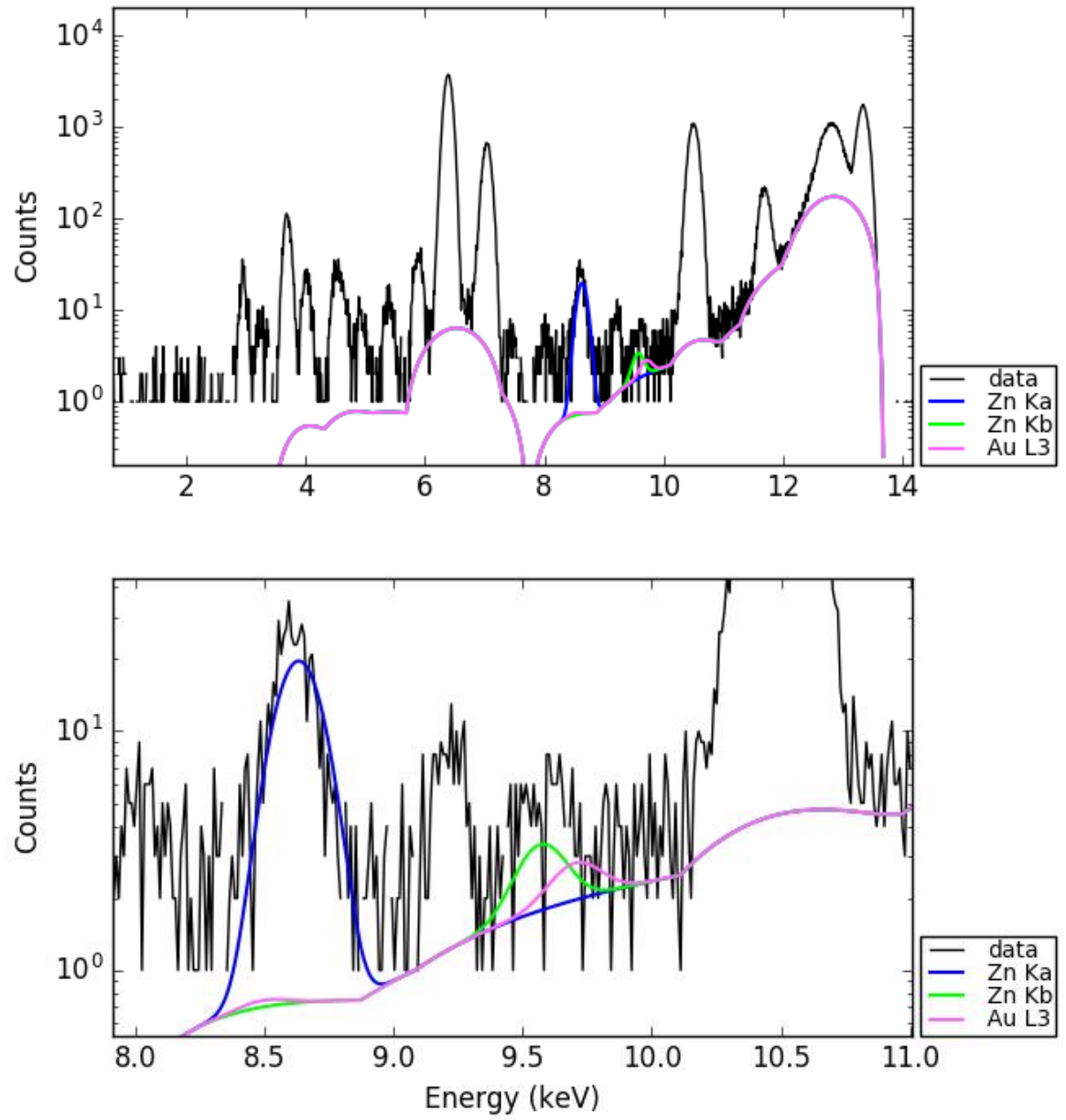
V160414



V413296



V738327



Appendix G: Other peak types to consider in identifying elements via X-ray fluorescence, and how to prevent detector oversaturation

Aside from emission (fluorescence) lines, there are other peaks to consider during data analysis, which may present some issues when identifying element peaks, also called spectral artifacts, with some examples in Figure X.

Rayleigh Scattering – elastic scattering of electrons, no energy loss

Compton Scattering – inelastic scattering of electrons, with energy loss

Summation/sum/pile-up peaks – peaks produced due to two photons from the same or different reaching the detector at the same time, producing peaks with energies equal to the sum of the energies of the photons

Escape peaks – produced due to the release of characteristic radiation of the detectors upon being hit by photons from the sample, reducing the measured energy by a certain value depending on the detector type. This is common in Ar, Si, and Ge detectors (1.7 keV for a Si detector).

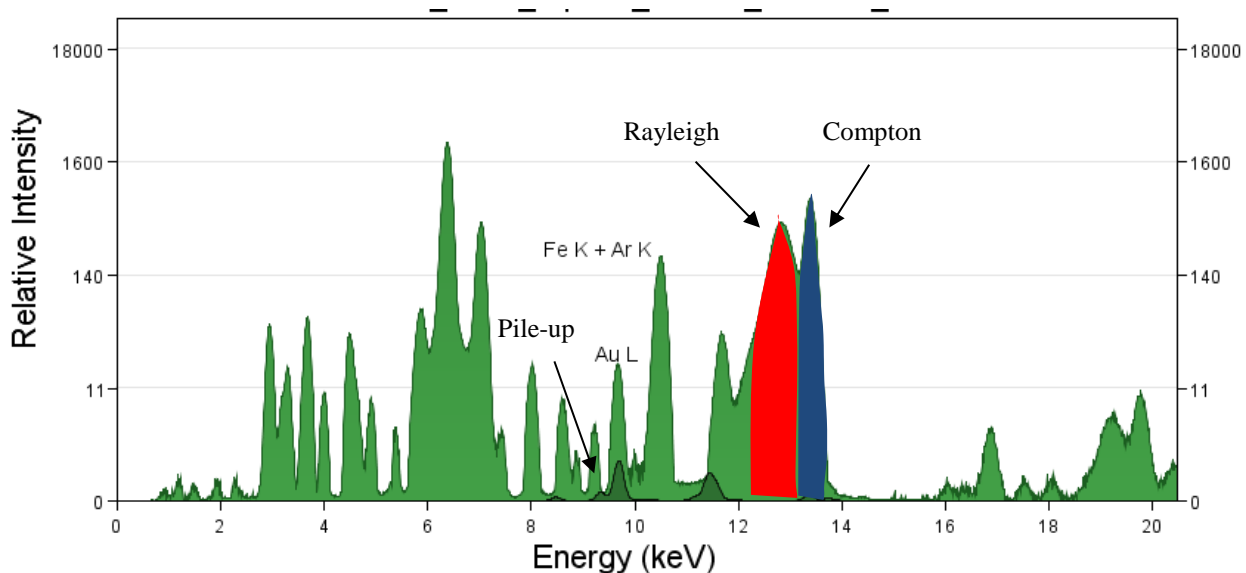


Figure X. Sample of Fe K + Ar K pile up peak close to Au L. The red peak shows a result of Rayleigh (elastic) scattering, while the blue peak shows Compton (inelastic) scattering.

What can we do if we have too much signal coming from the sample?

There will be cases where too much signal reaches the detector, resulting in high dead time percentages (>35%), which don't provide precise measurements. The following steps can be done to prevent oversaturation:

- Use filters between the sample and the beam to improve the signal-to-noise ratio
- Use a Faraday cage to cover the detector, usually a light-element metal (e.g., aluminum foil), especially in very bright beamlines
- Position the detector farther away

Note that the data collected will exhibit lower counts, but background radiation will be greatly reduced.

References:

Brouwer, Peter. "Theory of XRF: Getting acquainted with the principles." The Netherlands, PANalytical BV, 2003. Print.

Microscopy Australia. "EDS Spectral Artifacts." Microscopy Australia, 2014. Web.
<https://myscope.training/legacy/analysis/eds/spectralartefacts/>.

Curriculum Vitae

- Name:** Ramjay Jude L. Botor
- Post-secondary Education and Degrees:** University of the Philippines
Quezon City, Philippines
2011-2015 B.Sc.
- The University of Western Ontario
London, Ontario, Canada
2017-2019 M.Sc.
- Honours and Awards:** BS Geology *cum laude* graduate
2015
- Related Work Experience**
- Teaching Assistant
The University of Western Ontario
2017-2018
- Research Associate
Geoscience Foundation, Inc.
University of the Philippines
2015-2017
- Publications:**
- N.R. Banerjee, L.L. Van Loon, **R.J. Botor**, T.J. Flynn (2018). Automated Geochemical and Mineralogical Synchrotron Characterization of Bulk Geological Materials: An Innovation for the Minerals Industry. *Microscopy and Microanalysis* 24 (S2): 518-519. Print.
- R.J. Botor**, H.E. Cavallin, T.J. Flynn, L.L. Van Loon, N.R. Banerjee (2018). Understanding Gold Mineralization at the Yellowknife City Gold Project, Northwest Territories, using Synchrotron X-Ray Spectroscopy. PDAC-SEG Student Minerals Colloquium, Toronto. Poster.
- K.L. Rozon, **R.J. Botor**, C. Venier, J. Casali, L. L. Van Loon, N.R. Banerjee (2018). Geochemical Analysis of Low-Sulphidation Deposits on the La Victoria Property in the Ancash Department of the Republic of Peru. PDAC-SEG Student Minerals Colloquium, Toronto. Poster.
- H.E. Cavallin, T.J. Flynn, **R.J. Botor**, A.J. Sexton, L.L. Van Loon, N.R. Banerjee (2018) New Insights into Gold Mineralization at the Yellowknife City Gold Project using Synchrotron X-ray Spectroscopy AME Round-up Conference, Vancouver. Poster.

R. L. Flemming, J. D. Newman, **R.J. Botor**, F. Cao, C. M. Caudill, M. R. Galarneau, J. Geiger, V. L. Houde, L. E. Jenkins, Z. Li , J. M. Maris, M. Metcalf, G. D. Tolometti, A. Rupert, M. A. McCraig, G. R. Osinski (2018) Preliminary investigation of shocked carbonates from the Haughton impact structure, Devon Island, NU using X-ray diffraction and Rietveld refinement. Lunar and Planetary Science Conference, 49, Abs. #3000. Poster.

C.A. Arcilla, N. Aguda, R.J. Antonio, **R.J. Botor**, A.G. Estur (2016). Black Sand Mineral Characterization Final Report. DOST-PCIEERD. Print.